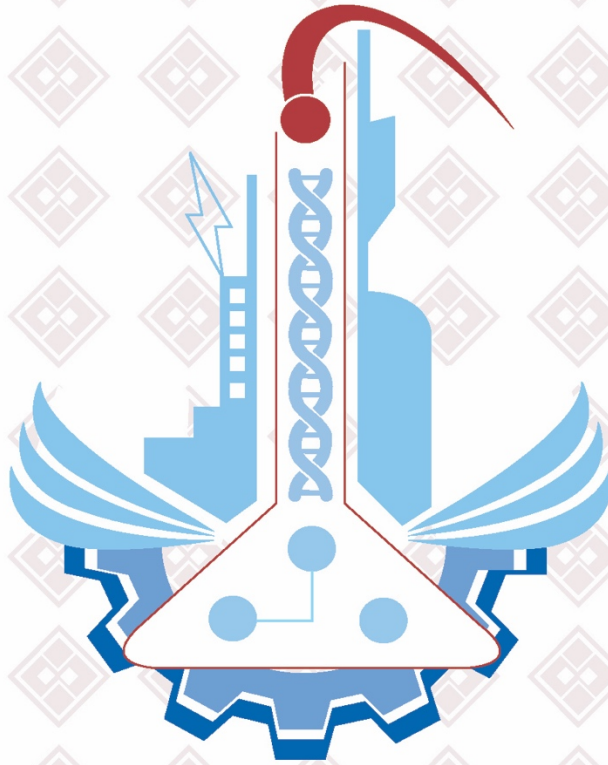


PRINTED ISSN: 1308-9080 / OLINE ISSN: 1308-9099

Volume: 19 / Number: 1 / Year: 2024

TURKISH JOURNAL OF SCIENCE & TECHNOLOGY



TURKISH JOURNAL OF SCIENCE AND TECHNOLOGY (TJST)

Year: 2024 Vol: 19 Number: 1

Address:

Fırat Universitesi
Fen Bilimleri Enstitüsü
23119, Elazig - TURKEY

Tel: 0 424 212 27 07
Fax: 0 424 236 99 55
e-mail: fenbilim@firat.edu.tr

New ISSN

Online: 1308-9099
Printed: 1308-9080

Old ISSN

Online: 1306 – 8555
Printed: 1306 – 8547

Refereed journal. Published twice a year

<https://dergipark.org.tr/tr/pub/tjst>

TURKISH JOURNAL OF SCIENCE & TECHNOLOGY (TJST)
Published by Firat University

Owner

Prof. Dr. Fahrettin GÖKTAŞ
Rector of Firat University

Editor in Chief

Assoc. Prof. Dr. Ferhat UÇAR
Firat University, Faculty of Technology
Department of Software Engineering

Responsible Director

Prof. Dr. Burhan ERGEN
Firat University, Faculty of Engineering
Department of Computer Engineering

Editor

Assoc. Prof. Dr. Nida KATI
Firat University, Faculty of Technology
Department of Metallurgical and Materials Engineering

ADVISORY BOARD

Eyüp BAĞCI

Firat University, Department of Biology,
Elazig-Turkey

Eres SOYLEMEZ

Middle East Technical University,
Department of Engineering Science,
Ankara-Turkey

Coskun BAYRAK

UALR Donaghey Collage of Eng. and
Information Tech. Dept. of Computer
Science, Little Rock, AR, USA

Hikmet GECKIL

Inonu University, Department of Biology,
Malatya-Turkey

Metin CALTA

Firat University, Fisheries Faculty,
Elazig-Turkey

Ertan GOKALP

Karadeniz Technical University,
Department of Geodesy and
Photogrametry Engineering, Trabzon-
Turkey

Abdulkadir ŞENGÜR

Firat University, Department of
Electronics and Computer Education,
Elazig-Turkey

Hasan EFEOĞLU

Ataturk University, Department of
Electrical-Electronics Engineering,
Erzurum-Turkey

Yanhui GUO

St. Thomas University, School of Science
and Technology, Miami, FL, USA

İbrahim TURKMEN

Balikesir University, Department of
Geology Engineering, Balikesir-Turkey

Deniz UNER

Middle East Technical University,
Department of Chemical Engineering,
Ankara-Turkey

M.Polat SAKA

Bahreyn University, Department of Civil
Engineering, Bahrain

Siqing XIA

Tongji Univ, State Key Lab Pollut Control
& Resource Reuse, Coll Environm Sci &
Engn, Shanghai 200092, R China

Zihni DEMIRBAG

Karadeniz Technical University,
Department of Biology, Trabzon-Turkey

Hanifi GULDEMİR

Firat University, Department of Electronics
and Computer Education, Elazig-Turkey

Nilgun GULEC

Middle East Technical University,
Department of Geology Engineering,
Ankara-Turkey

Erdogan GUNEL

West Virginia University, Department of
Statistics, Morgontown, USA

Sedigheh GHOFrani

Islamic Azad University, Electrical
Engineering Department, Tehran South
Branch, Iran

Wang XIBAO

Tianjin University, The School of
Materials Science and Engineering, China

Brain WOERNER

West Virginia University, Department of
Computer Sciences & Electrical
Engineering, Morgontown, WV, USA

A. Kadri CETIN

Firat University, Department of Biology,
Elazig-Turkey

Yusuf Kağan KADIOĞLU

Ankara University, Department of Geology
Engineering, Ankara-Turkey

Sezgin BAKIRDERE

Yıldız Technical University, Department of
Chemistry, Ankara-Turkey.

Tuncay OREN

Ottawa Univ, Fac Eng, Inform Technol.
McLeod Inst Sim.t Sci, Ottawa, ON K1N
6N5 Canada

Halil ONDER

Middle East Technical University,
Department of Civil Engineering, Ankara-
Turkey

Nazmi POLAT

Ondokuz Mayıs University, Department of
Biology, Samsun-Turkey

Mustafa DORUCU

Firat University, Fisheries Faculty,
Elazig-Turkey

Binod Chandra TRIPATHY

Mathematical Sciences Division, Institute
of Advanced Study Science and Tech.
Paschim Boragaon; Guwahati, India

Eoin CASEY

University College Dublin, Chemical and
Bioprocess Engineering, Dublin, Ireland

Farid EI-TANTAWY

Suez Canal University, Faculty of
Science, Department of Physics, Ismailia,
Egypt

Saleem HASHMI

International College of Technology,
Dublin, Ireland

Sakir ERDOĞDU

Karadeniz Technical University,
Department of Civil Engineering, Trabzon-
Turkey

Serdar SALMAN

Marmara University, Metallurgical and
Materials Engineering, İstanbul-Turkey

Firat University Turkish Journal of Science & Technology (TJST)
19-1, 2024

CONTENTS / İÇİNDEKİLER

- 1. Prediction of Air Pollution with Machine Learning Algorithms**
Hava Kirliliğinin Makine Öğrenme Algoritmaları ile Tahmin Edilmesi
Kahraman OĞUZ, Muhammet Ali PEKİN 1-12
- 2. Investigation of Antioxidant, Antimicrobial and Cytotoxic Activity of *Cydonia oblonga* Leaf on Breast Cancer (MCF-7) and Liver Cancer (HepG2) Cell Lines**
Cydonia oblonga Yaprağının Meme Kanseri (MCF-7) ve Karaciğer Kanseri (HepG2) Hücre Hatları Üzerindeki Antioksidan, Antimikrobiyal ve Sitotoksik Aktivitesinin Araştırılması
Lütfiye KADIOĞLU DALKILIÇ 13-23
- 3. DigiHuman: A Conversational Digital Human with Facial Expressions**
DigiHuman: Yüz İfadeleri ile Konuşan Dijital Bir İnsan
Kasım ÖZACAR, Munya ALKHALIFA 25-37
- 4. Ambarzumyan Theorem for Conformable Type Sturm-Liouville Problem on Time Scales**
Zaman Skalasında Uyumlu Tip Sturm-Liouville Problemi için Ambarzumyan Teoremi
Ayşe Çiğdem YAR, Tuba GÜLŞEN, Emrah YILMAZ 39-44
- 5. Determination of the Optimum Test Conditions for Measurement of Glucose Level in Liquids**
Sıvılarda Glikoz Seviyesinin Ölçülmesi İçin Optimum Test Koşullarının Belirlenmesi
Ömer Faruk GÖKTAŞ, İlyas ÇANKAYA, Esra ŞENGÜN ERMEYDAN 45-53
- 6. Automated Tuberculosis Classification with Chest X-Rays Using Deep Neural Networks -Case Study: Nigerian Public Health**
Derin Sinir Ağlarını Kullanan Göğüs Röntgenleri ile Otomatik Tüberküloz Sınıflandırması Örnek Çalışma: Nijerya Halk Sağlığı
Muhammad Zaharaddeen Abubakar, Mustafa Kaya, Mustafa Eris, Muhammad Mansur Abubakar, Serkan Karakuş, Khalid Jibril Sani 55-64
- 7. Gd Effect on Micro-Crystal Structure and Thermomagnetic Behavior of NiMnSn Magnetic Shape Memory Alloy**
NiMnSn Manyetik Şekil Hatırlamalı Alaşımının Mikro Kristal Yapısı ve Termomanyetik Davranışı Üzerindeki Gd Etkisi
Ecem ÖZEN ÖNER, Mediha KÖK 65-72
- 8. Investigation of Radon, Total Electron Content and Linear and Nonlinear Variations of Meteorological Variables Due to Earthquakes: ARIMA and Monte Carlo Modelling**
Radon, Toplam Elektron İçeriği ve Meteorolojik Değişkenlerin Depremlere Bağlı Doğrusal ve Doğrusal Olmayan Değişimlerinin İncelenmesi: ARIMA ve Monte Carlo Modellemesi
Marjan Mohammed GHAFAR, Hemn Salh, Fatih Külahcı 73-86
- 9. Increasing Strength of Clay Soils with the Use of Basalt Fiber: An Experimental Study**
Bazalt Fiber Kullanımı ile Killi Zeminlerin Dayanımının Artırılması: Deneysel Bir Çalışma
Yasemin ASLAN TOPÇUOĞLU, Zülfü GÜROCAK 87-96

10. Investigation of Charging Technologies for Electric Vehicles <i>Elektrikli Araçlar İçin Şarj Teknolojilerinin İncelenmesi</i> M. Sefa. ÇETİN, Muhsin Tunay GENÇOĞLU, Arkadiusz DOBRZYCKI	97-106
11. An Application of Robust Principal Component Analysis Methods for Anomaly Detection <i>Dayanıklı Temel Bileşenler Analizi ile Anomali Tespiti Üzerine Bir Uygulama</i> Kübra BAĞCI GENEL, Halit Eray ÇELİK	107-112
12. Expanded Perlite Mineral As a Natural Additive Used In Polylactide-Based Biodegradable Composites <i>Polilaktid Esaslı Biyobozunur Kompozitlerde Doğal Bir Katkı Maddesi Olarak Genişletilmiş Perlit Mineralinin Kullanımı</i> Erkan AKSOY, Süha TİRKEŞ, Ümit TAYFUN, Seha TİRKEŞ	113-122
13. Effect of Sulphurization Process on Vitamin, Phytosterol and Fatty Acid Levels of Some Apricot Cultivars Grown in Türkiye <i>Kükürtleme İşleminin Türkiye'de Yetiştirilen Bazı Kayısı Çeşitlerinin Vitamin, Fitosterol ve Yağ Asidi Düzeyleri Üzerine Etkisi</i> Fethi KAMIŞLI, Nazlı Gülüm MUTLU	123-132
14. Weighted Visibility Graph Based WiFi Indoor Positioning Method Using Heuristic Optimization <i>Sezgisel Optimizasyon Kullanan Ağırlıklı Görünürlük Grafi Tabanlı Kapalı Alan WiFi Konumlandırma Yöntemi</i> Turan Göktuğ ALTUNDOĞAN, Mehmet KARAKÖSE	133-145
15. Classification of the Cardiac Arrhythmia Using Combined Feature Selection Algorithms <i>Öznitelik Seçim Algoritmalarının Kombinasyonu ile Kardiyak Aritminin Sınıflandırılması</i> Murat TUNÇ, Gülnur Begüm CANGÖZ	147-159
16. Migration of a Vehicle Tracking System Running on Relational Database to Big Data Environment <i>İlişkisel Veri Tabanında Çalışan Araç Takip Sisteminin Büyük Veri Ortamına Taşınması</i> Ferhat KOÇER, Selim BAYRAKLI	161-168
17. Digital Pathology Image Reconstruction with Alternating Direction Method of Multipliers using Wavelet, Contourlet and Shearlet Transforms <i>Dalgacık, Contourlet ve Shearlet Dönüşümleri Kullanılarak Çarpanların Alternatif Yöntemi ile Dijital Patoloji Görüntüsü Geriçatılması</i> Esra ŞENGÜN ERMEYDAN, İlyas ÇANKAYA	169-178
18. Drought assessment of Yeşilirmak Basin Using Long-term Data <i>Yeşilirmak Havzası'nın uzun vadeli veriler kullanılarak kuraklığının değerlendirilmesi</i> Veysi KARTAL	179-192
19. Improved Spatial Modulation with Mapping Diversity <i>Eşleme Çeşitlemesi ile İyileştirilmiş Uzaysal Modülasyon</i> Mümtaz YILMAZ	193-202
20. Molecular Dynamics Simulation of Bauschinger Effect in Cu Nanowire with Different Crystallographic Orientation <i>Farklı Kristalografik Yönelime Sahip Cu Nano Telindeki Bauschinger Etkisinin Moleküler Dinamik Benzetimi</i> Sefa KAZANÇ, Canan AKSU CANBAY	203-211

21. Evaluation of SNP in the CDH8 and CDH10 Genes Associated with Autism Using In-Silico Tools <i>In-Silico Araçlar Kullanılarak Otizmle İlişkili CDH8 ve CDH10 Genlerindeki SNP'lerin Değerlendirilmesi</i> Azadeh REZAEIRAD, Ömer Faruk KARASAKAL, Tuğba KAMAN, Mesut KARAHAN	213-222
22. Use of 3D-CAPSNET and RNN models for 4D fMRI-based Alzheimer's Disease Pre-detection <i>4B fMRI Tabanlı Alzheimer Hastalığının Ön Tespiti için 3B-CAPSNET ve RNN Modellerinin Kullanılması</i> Ali İSMAİL, Gonca Gökçe MENEKŞE DALVEREN	223-235
23. Effect of Ferro-Alloys on the Properties of High Entropy Alloy with FeCoNiMnMoV Composition Produced by Arc-Melting Method <i>Ark-Ergitme Yöntemi ile Üretilen FeCoNiMnMoV Bileşimine Sahip Yüksek Entropili Alaşımın Özelliklerine Ferro-Alaşımın Etkisi</i> Seval Hale GÜLER	237-247
24. Physicochemical Effects of PEG Content in Alginate-based Double Network Hydrogels as Hybrid Scaffolds <i>Hibrit İskeleler Olarak Aljinat Bazlı Çift Ağ Hidrojellerindeki PEG İçeriğinin Fizikokimyasal Etkileri</i> Ozgul Gok	249-256
25. Performance Comparison of Standard Polysomnographic Parameters Used in the Diagnosis of Sleep Apnea <i>Uyku Apnesinin Teşhisinde Kullanılan Standart Polisomnografik Parametrelerin Performans Karşılaştırılması</i> Seda Arslan TUNCER, Yakup ÇİÇEK, Taner TUNCER	257-263
26. Realization of Fuzzy-PI Controller-Based Path Planning of Differential Drive Mobile Robot <i>Diferansiyel Sürüşlü Mobil Robotun Bulanık PI Denetleyici Tabanlı Yol Planlamasının Gerçekleştirilmesi</i> Ahmet TOP, Muammer GÖKBULUT	265-277
27. Comparative Analysis of Wavelet Families in Image Compression, Featuring the Proposed New Wavelet <i>Görüntü Sıkıştırma Dalgacık Ailelerinin Karşılaştırmalı Analizi ve Yeni bir Dalgacık Ailesi Önerisi</i> İbrahim ÖZ	279-294
28. Detailed Analysis of Li-ion Batteries for Use in Unmanned Aerial Vehicles <i>Li-iyon Bataryaların İnsansız Hava Araçlarında Kullanımı için Detaylı Analizi</i> Merve Nur KAYA, Zehra URAL BAYRAK	295-304

Prediction of Air Pollution with Machine Learning Algorithms

Kahraman OĞUZ^{1*}, Muhammet Ali PEKİN²

¹ Turkish State Meteorological Service, 9th Directorate of Meteorology, Ankara

² Turkish State Meteorological Service, 12th Directorate of Meteorology, Erzurum

*¹ koguz@mgm.gov.tr, ² maekin@mgm.gov.tr

(Geliş/Received: 26/12/2022;

Kabul/Accepted: 1/10/2023)

Abstract: Air pollution has become an important problem due to its threats. Air pollutants are in complex interaction with atmosphere and environment. For this reason, it is important to study air pollution issues. In recent years, studies on prediction of air pollutants with machine learning methods have gained momentum. In this study, some air pollutants are predicted with various machine learning algorithms considering meteorological factors. In machine learning phase, a separate study is conducted with various machine learning algorithms (multilayer perceptron neural network, stochastic gradient descent, ridge regression, cross decomposition) considering temperature, relative humidity, wind, pressure and air pollutant measurements of previous hour. Consistencies of these algorithms in estimating pollutant concentrations are compared. Various statistical metrics are used to analyze the consistencies. As a result, the coefficient of determination of all algorithms are found above 0.67, considering the test section. It is found that the coefficient of determination of the multilayer perceptron neural network algorithm provides better results than other algorithms.

Key words: Air pollution, machine learning, neural network, modeling, Çanakkale city.

Hava Kirliliğinin Makine Öğrenme Algoritmaları ile Tahmin Edilmesi

Öz: Hava kirliliği, canlı sağlığına yönelik tehditleri sebebiyle önemli bir problem haline gelmiştir. Hava kirliliği atmosfer ve çevre ile karmaşık ilişki içerisinde. Bu nedenle hava kirliliği ile alakalı konuların çalışılması önemlidir. Son yıllarda hava kirliticilerinin makine öğrenmesi yöntemleriyle tahmin edilmesine yönelik çalışmalar hız kazanmıştır. Bu çalışmada, meteorolojik faktörler göz önüne alınarak çeşitli makine öğrenme algoritmaları ile bazı hava kirliticilerinin tahmini yapılmıştır. Makine öğrenmesi aşamasında, bir önceki saatin sıcaklık, bağıl nem, rüzgar, basınç ve hava kirlitici ölçümleri dikkate alınarak çeşitli makine öğrenmesi algoritmaları (çok katmanlı algılayıcı sinir ağı, stokastik gradyan inişi, sırt regresyonu, çapraz ayırıştırma) ile ayrı ayrı çalışma yapılmıştır. Bu algoritmaların kirlitici konsantrasyonlarını tahmin etmedeki tutarlılıkları karşılaştırılmıştır. Tutarlılıkları analiz etmek için çeşitli istatistiksel metrikler kullanılmıştır. Sonuç olarak, test bölümü dikkate alındığında tüm algoritmaların belirleme katsayısı 0.67'nin üzerinde bulunmuştur. Çok katmanlı algılayıcı sinir ağı algoritmasının belirleme katsayısının diğer algoritmalara göre daha iyi sonuçlar verdiği tespit edilmiştir.

Anahtar kelimeler: Hava kirliliği, makine öğrenmesi, sinir ağı, modelleme, Çanakkale ili.

1. Introduction

Air pollution has significant impact on public health and environment. Population, urbanization, industrial growth, energy consumption and usage of transportation vehicles have increased significantly in the last decade worldwide. This has resulted in rised emissions of air pollutants including greenhouse gases, ambient temperature and other atmospheric variables [1]. The main factors affecting air pollutant concentration are emission sources and meteorological factors. The existence of a significant relationship between meteorological factors and air pollutant concentration has been addressed by many studies [2-4]. Transportation, chemistry and deposition of particulate matter (PM) are mainly controlled by meteorological factors. Meteorological factors not only affect each other, but also form a closely linked system with PM. The effects of meteorological conditions on PM concentration are quite complex [5]. There are various methods for estimating PM concentration. Machine learning method is one of the most frequently used prediction methods in recent years.

Machine learning is a rapidly developing field that enables computers to learn based on data. Data can come from a variety of sources, including physical experiments, computer models, or a combination of both. Machine learning method has had successful applications in many areas [6]. Over the last three decades, it has also been increasingly applied in the field of air quality prediction due to the development of statistical models based on machine learning techniques and its ability to explore, analyze and make predictions on multiple and complex datasets. The main purpose of a machine learning algorithm is to provide a model that captures the general properties and interactions of the dataset (learned) to obtain information from data and make predictions [7-8].

* Corresponding author: koguz@mgm.gov.tr. ORCID Number of authors: ¹ 0000-0001-5305-6145, ² 0000-0002-6807-890X

There are various studies on the analysis of air pollution with machine learning methods. These studies are aimed at estimating air pollution in various regions with several machine learning algorithms and examining their consistency. Several studies about prediction of air pollution with machine learning algorithms are compared in Table 1. [9] studied PM2.5 prediction with several machine learning algorithms including linear regression, random forecast and ridge regression. [10] studied prediction of air quality index with several machine learning algorithms like k-Nearest Neighbor (KNN), Gaussian Naive Bayes, support vector regression (SVM). [11] studied prediction of PM10, CO, SO2, O2 and O3 with random forest, multiple linear regression algorithms. [12] studied PM10 prediction with artificial neural network. [13] studied PM2.5 prediction with several machine learning algorithms like long short-term memory (LSTM), gradient boosting model (GRU), convolutional neural network (CNN).

Table 1. Some studies in the literature.

Pollutant	Proposed Method	Reference
SO2, PM10	Random Forest, Decision Tree	[14]
SO2, NO2, O3, CO, PM10	Random Forest	[15]
PM10, PM2.5	Support Vector Regression, Autoregressive Integrated Moving Average, Long Short-Term Memory	[16]
PM2.5	Gradient Boosting Model	[17]
PM10, PM2.5	Linear Regression, Random Forest Regressor, Gradient Boosting Regressor, K Neighbors Regressor, MLP Regressor, and Decision Tree Regressor CART	[18]
AQI	Adaptive Boosting, Artificial Neural Network, Random Forest, Stacking Ensemble, and Support Vector Machine	[19]
PM2.5	LSTM, Bi-LSTM, GRU, Bi-GRU, CNN, and a hybrid CNN-LSTM	[13]
PM10	Artificial Neural Network	[12]
PM10, CO, SO2, O2, O3	Random Forest, Multiple Linear Regression	[11]
AQI	KNN, Gaussian Naive Bayes, SVM, RF, and XGBoost	[10]
PM2.5	Linear Regression, Random Forest, KNN, Ridge and Lasso, XGBoost, and AdaBoost	[9]

In this study, we performed modeling with various machine learning algorithms (multilayer perceptron neural network, stochastic gradient descent, ridge regression, cross decomposition) by considering temperature, relative humidity, wind, pressure and air pollutant measurements of the previous hour to predict pollutant concentrations. As a result, consistencies of pollutant concentrations of PM10, SO2, NO2, NOX and O3 were compared.

2. Material and Method

2.1. Study area and data

In this study, hourly meteorological data of temperature, relative humidity, wind and pressure parameters were obtained from Çanakkale Central Meteorology Station of Turkish State Meteorological Service (latitude: 40.1410, longitude: 26.3993). PM10, SO2, NO2, NOX and O3 pollutant data were obtained from Çanakkale Central air quality station (latitude: 40.1366, longitude: 26.4055) affiliated to Ministry of Environment, Urbanization and Climate Change. Locations of the stations are shown in Figure 1. The data covers the period from 1 January 2019 to 31 December 2021. While applying the machine learning method, 80% of the data set was randomly selected as training data and 20% was used as test data.

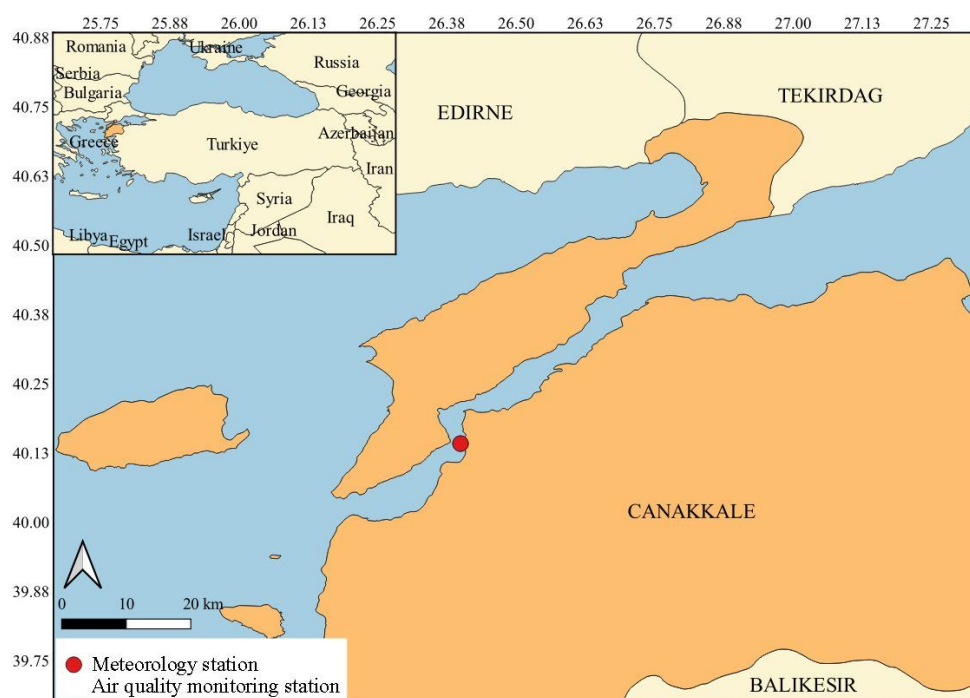


Figure 1. Locations of the meteorological and air quality.

Table 2 shows statistical information about meteorological parameters and air pollutants. PM10 average is $43.59 \mu\text{g}/\text{m}^3$, minimum and maximum values are $2.0 \mu\text{g}/\text{m}^3$ and $1003.0 \mu\text{g}/\text{m}^3$, respectively. SO₂ average is $9.58 \mu\text{g}/\text{m}^3$, minimum and maximum values are $0 \mu\text{g}/\text{m}^3$ and $183.23 \mu\text{g}/\text{m}^3$, respectively. NO₂ average is $20.62 \mu\text{g}/\text{m}^3$, minimum and maximum values are $0.26 \mu\text{g}/\text{m}^3$ and $145.86 \mu\text{g}/\text{m}^3$, respectively. NO_x average is $40.02 \mu\text{g}/\text{m}^3$, minimum and maximum values are $1.53 \mu\text{g}/\text{m}^3$ and $392.95 \mu\text{g}/\text{m}^3$, respectively. The O₃ average is $56.0 \mu\text{g}/\text{m}^3$, minimum and maximum values are $1.05 \mu\text{g}/\text{m}^3$ and $205.40 \mu\text{g}/\text{m}^3$, respectively.

Descriptive statistics of meteorological and air pollutant parameters are presented in Table 3. It was observed that the highest correlation coefficient ($r=-0.35$) of NO₂ is with wind. It was observed that the highest correlation coefficient ($r=0.558$) of O₃ is with temperature. This is followed by relative humidity with the value of $r=-0.5$. There is a weak negative relationship between NO₂ and wind. There is a moderate positive relationship between O₃ and temperature while moderate negative relationship between O₃ and relative humidity. It is clear that the relationship between other air pollutants and meteorological parameters is very weak.

Table 2. Descriptive statistics of meteorological and air pollutant parameters.

	T	RH	W	PS	PM10	SO ₂	NO ₂	NO _x	O ₃
Valid	26145	25815	26117	25979	25254	24714	24712	24521	25514
Missing	157	487	185	323	1048	1588	1590	1781	788
Mean	17.40	66.96	3.35	1014.75	43.59	9.58	20.62	40.02	56.00
Std. Dev.	7.94	16.40	2.24	6.31	35.40	9.99	14.57	28.68	26.07
Skew.	0.05	-0.34	1.41	0.29	16.09	4.35	1.73	2.54	0.22
Range	43.70	84.00	18.30	48.90	1001.00	183.23	145.60	391.42	204.35
Min.	-4.20	16.00	0.00	992.20	2.00	0.00	0.26	1.53	1.05
Max.	39.50	100.00	18.30	1041.10	1003.00	183.23	145.86	392.95	205.40

T: Temperature (°C), RH: Relative humidity (%), W: Wind (m s⁻¹), PS: Pressure (hpa).

Table 3. Correlations of the parameters used in the study.

Variable		T	RH	W	PS	PM10	SO2	NO2	NOX	O3
T	Pearson's r	—								
	p-value	—								
RH	Pearson's r	-0.6	—							
	p-value	< .001	—							
W	Pearson's r	0.048	-0.14	—						
	p-value	< .001	< .001	—						
PS	Pearson's r	-0.45	0.074	-0.12	—					
	p-value	< .001	< .001	< .001	—					
PM10	Pearson's r	0.116	-0.06	0.012	-0.06	—				
	p-value	< .001	< .001	0.063	< .001	—				
SO2	Pearson's r	-0.02	-0.05	-0.14	0.028	0.064	—			
	p-value	0.001	< .001	< .001	< .001	< .001	—			
NO2	Pearson's r	-0.13	0.171	-0.35	0.053	0.12	0.31	—		
	p-value	< .001	< .001	< .001	< .001	< .001	< .001	—		
NOX	Pearson's r	-0.14	0.16	-0.24	0.049	0.074	0.28	0.849	—	
	p-value	< .001	< .001	< .001	< .001	< .001	< .001	< .001	—	
O3	Pearson's r	0.558	-0.5	0.23	-0.3	-0.02	-0.09	-0.45	-0.47	—
	p-value	< .001	< .001	< .001	< .001	0.002	< .001	< .001	< .001	—

2.2. Multilayer Perceptron Neural Network (MLPNN)

Artificial neural network is a data processing method that mimics the neural structure of the human brain. It establishes relationships between inputs and outputs. It has parallel data processing architecture like the human nervous system [20]. Artificial neural network is one of the most used machine learning algorithms.

MLPNN is a type of feed forward artificial neural network, which uses Boolean function. MLPNN includes layers of nodes, which allow unidirectional forward connections of inputs and outputs. MLPNN consist of 3 layers including input layer, output layer and a hidden layer (between input and output layers). Data are transferred from input layer to output layer [21]. A schematic diagram of multilayer perceptron neural network presented in Figure 2.

The main aim of MLPNN is to predict future trends in a dataset given current and previous conditions. Function logic is related to modeling the connections between variables. The objective of MLPNN application is to find unknown function f with input vectors in X and output vectors in Y :

$$Y = f(X) \tag{1}$$

where $X = [n \times k]$, $Y = [n \times j]$, n is number of training patterns, k the number of input nodes/variables and j the number of output nodes/variables. The training data is represented with the matrices of X and Y . The f function is defined with regulable network weights. During training the function f is optimised, such that the network output for the input vectors in X is as close as possible to the target values in Y [22].

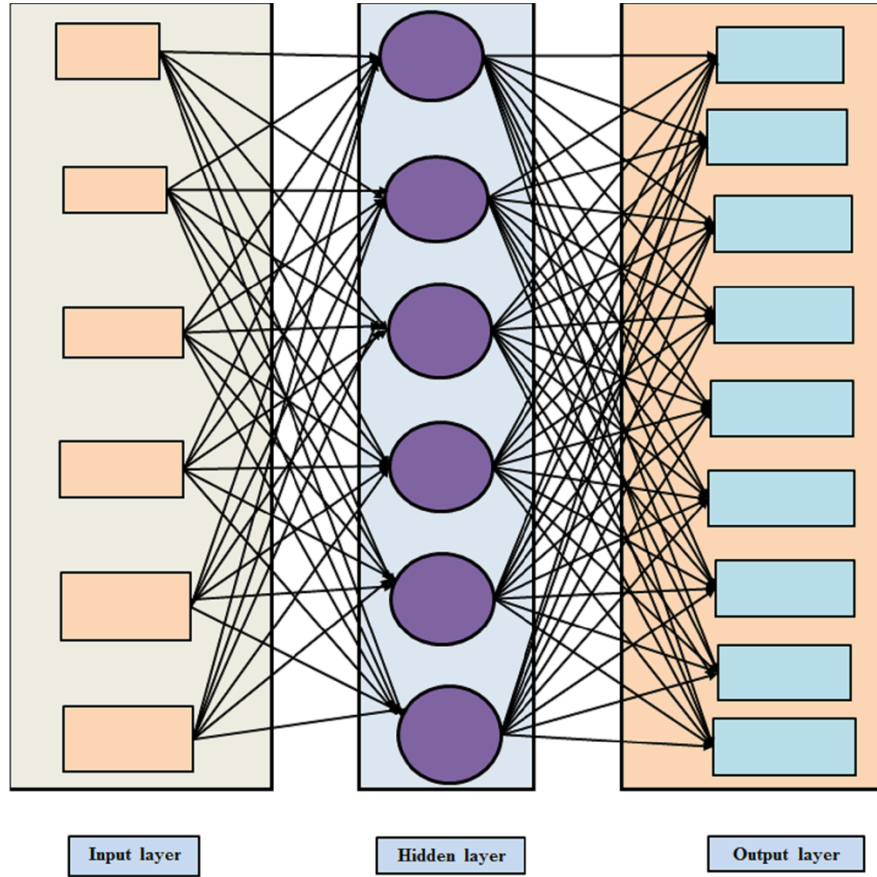


Figure 2. A schematic diagram of multilayer perceptron neural network [21].

2.3. Stochastic Gradient Descent (SGD)

SGD is another most used algorithms in machine learning. SGD is a type of optimization combining classical gradient descent with random subsampling within the target functional [23]. SGD shows good performance in convex and non-convex optimization. SGD minimizes a loss function selected through a linear function. The algorithm approximates a true gradient, considering one sample at a time, and simultaneously updates the model according to the gradient of the loss function [24].

SGD is calculated as below:

$$\theta = \theta - \alpha \nabla_{\theta} J(\theta; x^{(i)}, y^{(i)}) \quad (2)$$

where $x^{(i)}$ is training example, $y^{(i)}$ is label, θ is vector parameters of $J(\theta)$, α is learning rate [25-26].

2.4. Ridge Regression (RR)

RR is an algorithm to analyze multivariate regression data and it is the biased estimation methods. The aim is to find the factors that minimize the error sum of squares by implementing a penalty to these factors. It is durable to over-fitting and it tenders an answer to multidimensionality.

RR is calculated as below:

$$\beta^* = (X^{(T)}X + kI)^{-1} X^{(T)}Y \quad (3)$$

where β^* = (p-1)x1 dimensional vector of ridge regression coefficients, I = (p-1)x(p-1) dimensional unit matrix and k constant value, which is almost $0 \leq k \leq 1$. [27].

2.5. Cross Decomposition (CD)

CD algorithms are useful for finding relations between two matrices (datasets). Examples of cross decomposition are partial least squares regression and canonical correlation analysis. Main aim of the algorithms are to determine multidimensional aspect in the X space that clarifies the maximum multidimensional variance aspect in the Y space. The mathematical model of cross decomposition is below [28-29]:

Assuming the separations of X and Y are done in a way that maximizes the covariance between T and U:

$$X = TPT + E \quad (4)$$

$$Y = UQT + F \quad (5)$$

where, X is nxm matrix of predictors, Y is nxp matrix of responses, T nx1 projections of X, U is nx1 projections of Y, P is mx1 orthogonal loading matrix, Q is px1 orthogonal loading matrix, E is error term and F is error term.

2.6. Data Preprocessing

Data preprocessing is one of the most crucial part for machine learning. It is a data mining technique which converts raw data into a more intelligible, advantageous and fertile format. The main task for a model to be precise in estimations is that the algorithm should be able to smoothly commentate the data's features [30-31].

The data set used in the study is not complete. In time series estimates, it is required that the data set to be completed. Therefore, it is important to complete the missing data. However, this study is not a time series estimation study. Therefore, it is a convenient method to remove rows with missing columns. In our study, we removed the rows with missing columns from the data set and did not use them in the train/test stages.

In the study, the input data are scaled between 0-1. In this way, it was ensured that the different digits of the parameters were on the same scale. This ensures that the parameters have the same effect when calculating the output variable (PM10, NO2, etc.).

In this study, we used max-min normalization methodology. The max-min normalization is calculated as below:

$$x_{scaled} = \frac{x - x_{min}}{x_{max} - x_{min}} \quad (6)$$

2.7. Evaluation metrics

The R-Squared (Coefficient of determination), RMSE (Root Mean Square Error) and MAE (Mean absolute error) metrics are mainly used to evaluate model prediction performance in regression analysis. R-squared shows the coefficient of how well the values fit compared to the real values. Root Mean Square Error is very common and the standard deviation of the residuals (prediction errors). MAE shows the variation between the real and predicted values extracted by averaged the absolute difference over the data set [32].

The matrices are calculated as below:

$$r^2 = \frac{n(\sum xy) - (\sum x)(\sum y)}{\sqrt{(n\sum x^2 - (\sum x)^2)(n\sum y^2 - (\sum y)^2)}} \quad (7)$$

$$RMSE = \sqrt{\frac{1}{n} \sum (y - x)^2} \quad (8)$$

$$MAE = \frac{1}{n} \sum |y - x| \quad (9)$$

where, y is donated predicted, x is observed and n is number of samle.

3. Results and Discussions

The performance results of machine learning models are presented in Table 4. It may be seen from the table that MLPNN model performed better than others. MLPNN model estimated O3 parameter best with the scores of r=0.887, RMSE=8.81 and MAE=5.81. MLPNN then successfully estimated SO2 (r=0.783), PM10 (r=0.752),

NOX ($r=0.716$) and NO₂ (0.694), respectively. The results are close to each other when train and test scores are evaluated together.

Table 3. Performance results of machine learning models.

Parameter	Model	r ²		RMSE		MAE	
		Train	Test	Train	Test	Train	Test
NO ₂	SGD	0.697	0.691	8.05	7.99	5.2	5.22
	RR	0.697	0.692	8.04	7.99	5.17	5.19
	MLPNN	0.701	0.694	7.99	7.95	5.03	5.06
	CD	0.697	0.691	8.04	7.99	5.16	5.19
NOX	SGD	0.674	0.711	16.54	14.99	9.44	8.86
	RR	0.675	0.711	16.53	14.96	9.39	8.82
	MLPNN	0.687	0.716	16.22	14.85	9.03	8.52
	CD	0.675	0.712	16.53	14.96	9.35	8.79
O ₃	SGD	0.881	0.880	9.01	9.06	5.88	5.96
	RR	0.881	0.880	9.01	9.05	5.86	5.94
	MLPNN	0.886	0.887	8.82	8.81	5.73	5.81
	CD	0.881	0.880	9.01	9.06	5.86	5.94
PM ₁₀	SGD	0.707	0.748	18.72	16.87	6.99	6.74
	RR	0.713	0.752	18.54	16.74	6.83	6.56
	MLPNN	0.714	0.752	18.51	16.76	6.69	6.38
	CD	0.714	0.752	18.5	16.76	6.73	6.45
SO ₂	SGD	0.746	0.779	5.13	4.63	2.53	2.47
	RR	0.747	0.780	5.11	4.62	2.49	2.43
	MLPNN	0.751	0.783	5.07	4.59	2.45	2.4
	CD	0.748	0.780	5.11	4.63	2.46	2.41

Scatter plots of air pollutants according to the models are shown in Figure 3. In the scatterplots, blue graphs on the left show train results and red graphs on the right show test results. The results are mostly clustered around the regression line. The scatter plot of O₃ variable shows a more successful result than others. Variables of O₃, NOX and NO₂ are more harmonious with regression line. It is seen that PM₁₀ and SO₂ variables give the least successful results than others. It is also seen that especially large values of these two parameters deviate considerably from the regression line.

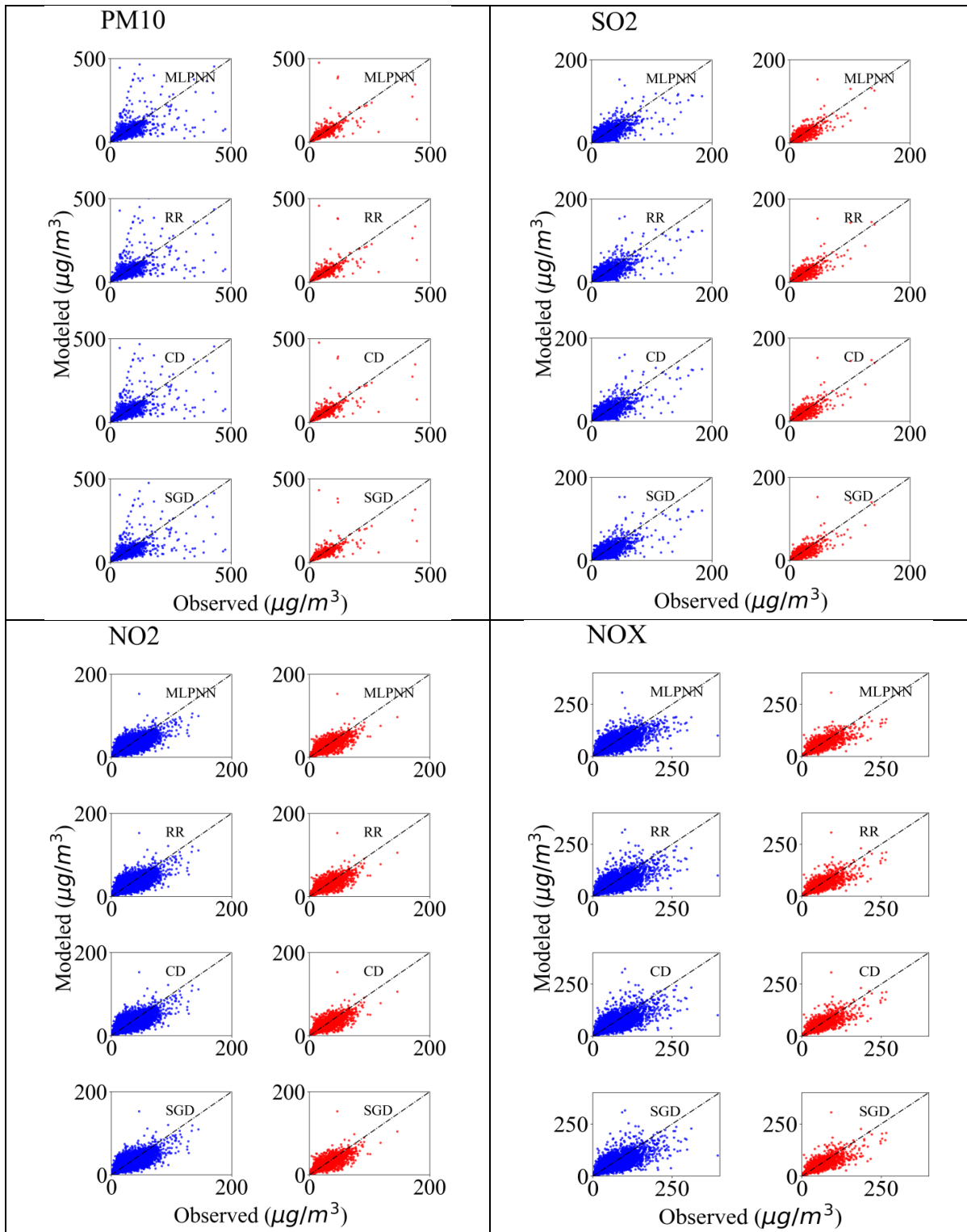


Figure 3. Scatter plots of some air pollutants according to the models.

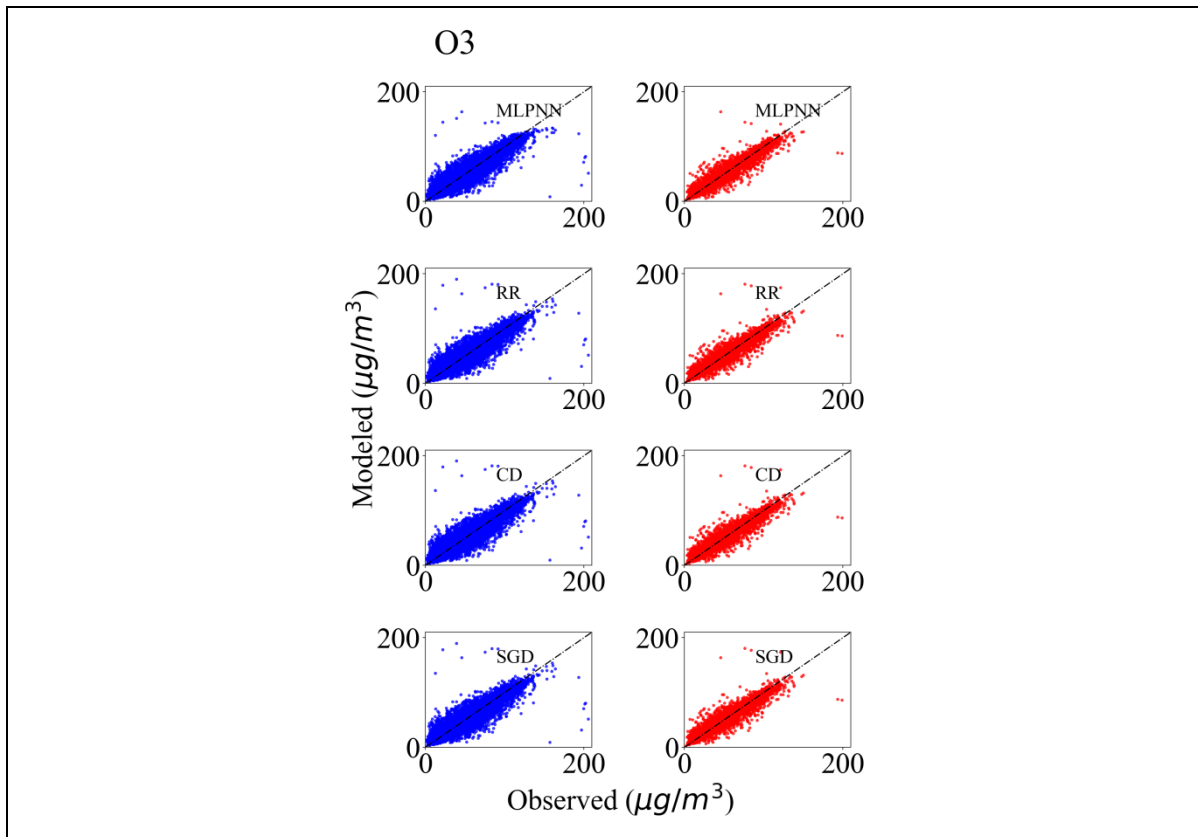


Figure 3 (cont.). Scatter plots of some air pollutants according to the models.

Error histogram graphics of the test section are shown in Figure 4. Histogram plots show the frequency distribution of the datasets. The clustering of data around zero in the error histogram indicates that the model is successful. According to the graphs, it is seen that the error amounts of O3, NOX and NO2 variables are clustered closest to 0 and its surroundings. It is also seen that PM10 and SO2 parameters are clustered a little further away from 0 compared to other parameters.

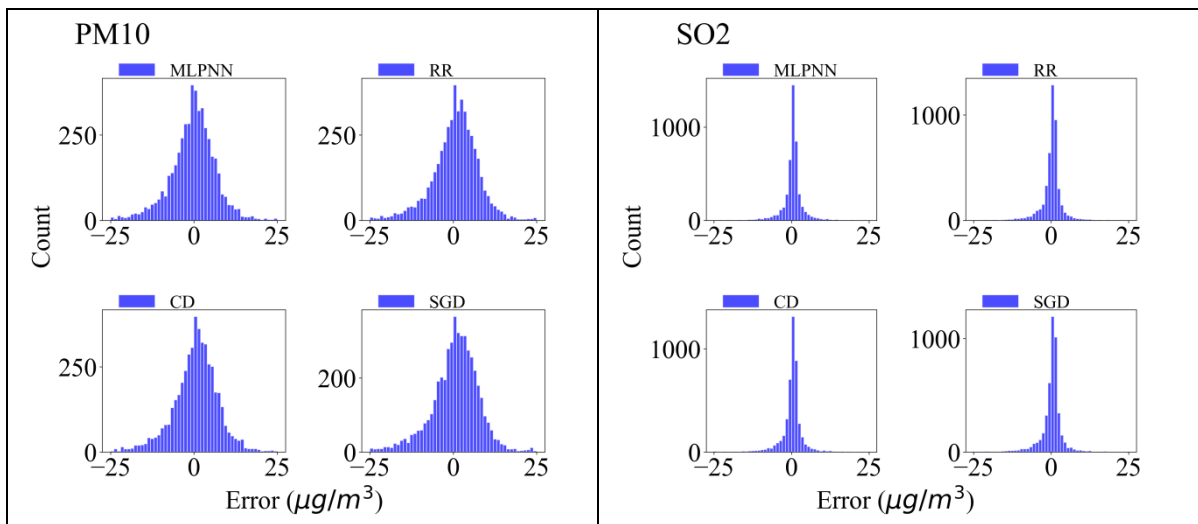


Figure 4. Error histograms of the test sections of the machine learning models.

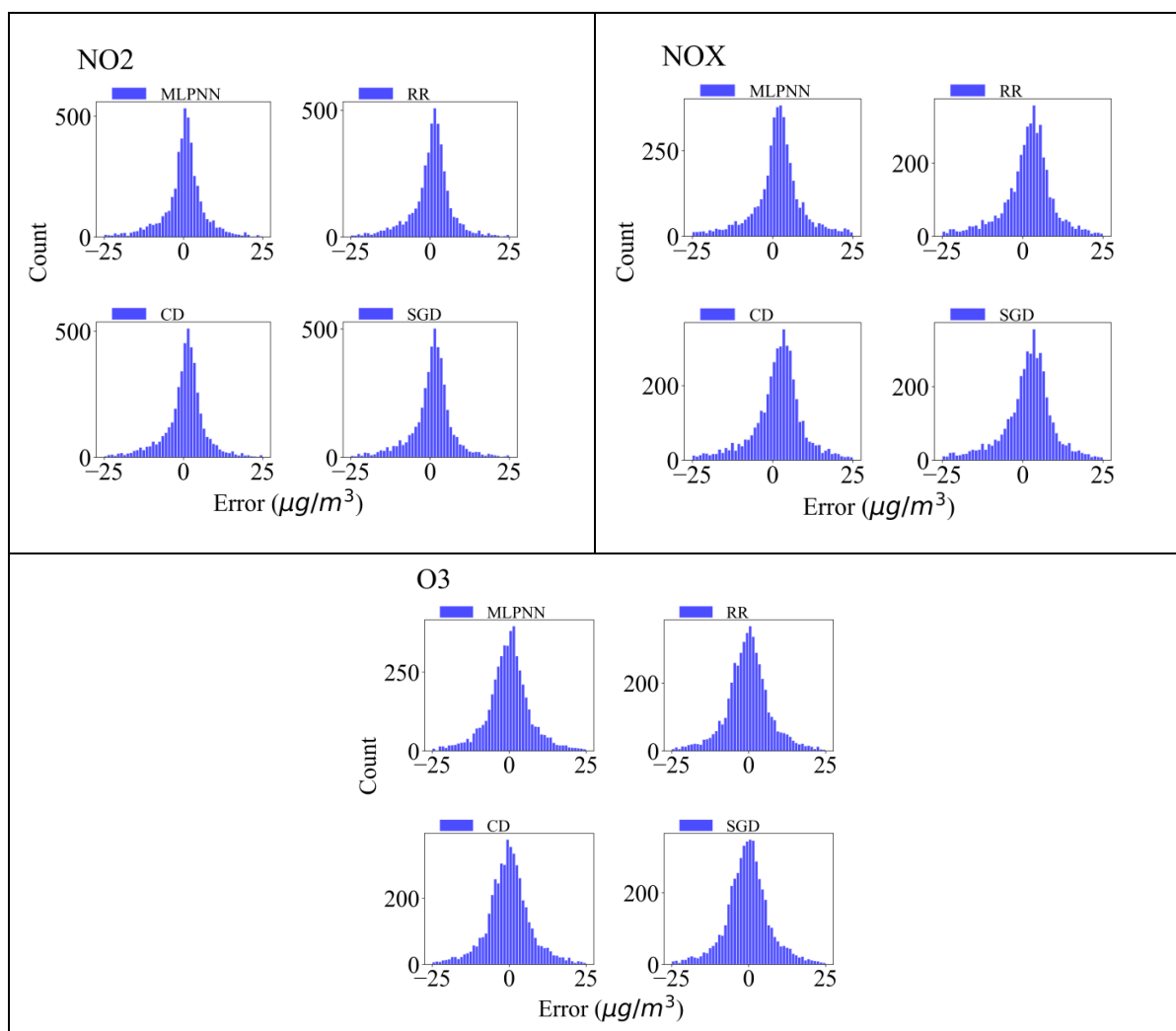


Figure 4 (cont.). Error histograms of the test sections of the machine learning models.

4. Conclusions

Air pollution is one of the most important environmental problems. Uncontrolled industrialization causes dramatic levels of air pollution and trigger environmental problems all over the world. Machine learning, which has been successfully applied in many fields nowadays, should be studied in the field of air pollution more. In this study, we performed modeling with various machine learning algorithms (multilayer perceptron neural network, stochastic gradient descent, ridge regression, cross decomposition) by considering temperature, relative humidity, wind, pressure and air pollutant measurements of the previous hour to estimate PM₁₀, SO₂, NO₂, NO_x pollutant concentrations.

According to the findings, MLPNN model is more successful than other methods for both train and test phases. Many machine learning studies stated the success of MLPNN method. Our study also confirms its success. MLPNN method is a nonlinear method and this structure gives it a clear advantage compared to other methods. Besides, O₃ variable was better predicted. The correlation of O₃ variable with the input parameters (0.558 with T, -0.5 with RH, 0.23 with W, -0.3 with PS) is higher than the correlations of other variables. It has been understood that the high correlation of the estimating variable with the input parameters increases the model performance in machine learning. From this finding, it was also understood that the O₃ variable is more correlated with temperature, humidity, wind and pressure parameters than other variables (PM₁₀, SO₂, NO₂, NO_x). The error amounts of the methods are spread homogeneously over 0 and its surroundings in most of the variables. This finding indicates that the learning process shows efficient results and the models are not biased.

Only meteorological variables and the air quality variable of the previous hour were used as input parameters in this study. Anthropogenic pollutants have also a huge impact on air quality. More successful results can be obtained if anthropogenic pollutant sources are used as input parameters. However, all the models used in this study have yielded successful results. We especially recommend the MLPNN method to be used in air quality modeling studies due to its successful performance and fast predictions. In addition, we recommend that the input variables to be used while creating the model should be selected from the parameters that show high correlation with the output variable.

Acknowledgment

The authors would like to thank Turkish State Meteorological Service and Ministry of Environment, Urbanization and Climate Change to provide data used in this study.

References

- [1] Abed Al Ahad M, Sullivan F, Demšar U, Melhem M, Kulu H. The effect of air-pollution and weather exposure on mortality and hospital admission and implications for further research: A systematic scoping review. *PloS one* 2020; 15(10): e0241415.
- [2] Hrdlickova Z, Michalek J, Kolar M, Vesely M. Identification of factors affecting air pollution by dust aerosol PM10 in Brno City, Czech Republic. *Atmos Environ* 2008; 42(37): 8661–8673.
- [3] Ei-Sharkawy MF, Zaki GR. Effect of meteorological factors on the daily average levels of particulate matter in the Eastern Province of Saudi Arabia: a cross-sectional study. *J Sci Technol* 2015; 5(1): 18–29.
- [4] Oğuz, K. Nevşehir İlinde Hava Kalitesinin ve Meteorolojik Faktörlerin Hava Kirliliği Üzerine Etkilerinin İncelenmesi. *Doğal Afetler ve Çevre Dergisi* 2020; 6(2): 391-404.
- [5] Qin YG, Yi C, Dong GL, Min JZ. Investigating the influence of meteorological factors on particulate matters: A case study based on path analysis. *Energy & Environment* 2019; 31(3): 1-13.
- [6] Panda N, Osthus D, Srinivasan G, O'Malley D, Chau V, Oyen D, Godinez H. Mesoscale informed parameter estimation through machine learning: A case-study in fracture modeling. *Journal of Computational Physics* 2020; 420: 1-15.
- [7] Alpaydin E. *Introduction to Machine Learning*. The MIT Press: Cambridge, MA, USA, 2010.
- [8] Gagliardi RV, Andenna C. A Machine Learning Approach to Investigate the Surface Ozone Behavior. *Atmosphere* 2020; 11(11): 1173.
- [9] Kothandaraman D, Praveena N et al. Intelligent Forecasting of Air Quality and Pollution Prediction Using Machine Learning, *Adsorption Science & Technology* 2022; (5086622), 15.
- [10] Kumar K, Pande BP. Air pollution prediction with machine learning: a case study of Indian cities. *Int. J. Environ. Sci. Technol.* 2022; 1-16.
- [11] Ünalı S, Yalçın N. Hava Kirliliğinin Makine Öğrenmesi Tabanlı Tahmini: Başakşehir Örneği. *Mühendislik Bilimleri ve Araştırmaları Dergisi* 2022; 4(1): 35-44.
- [12] Oğuz K, Pekin MA. Makine Öğrenme Algoritmaları ile PM10 Konsantrasyon Tahmini. *Journal of Advanced Research in Natural and Applied Sciences* 2022; 8(2): 201-213.
- [13] Bekkar A, Hssina B, Douzi S, Douzi K. Air-pollution prediction in smart city, deep learning approach. *J Big Data* 2021; 8(1): 161.
- [14] Gültepe YA Comparative Assessment on Air Pollution Estimation by Machine Learning Algorithms. *European Journal of Science and Technology* 2019; (16): 8-15.
- [15] Irmak ME, Aydılek İB. Using Ensemble Regression Algorithms for Improving the Prediction Success of Air Quality Index. *Academic Platform Journal of Engineering and Science* 2019; 7(3): 507-514.
- [16] Dobrea M et al. Machine Learning algorithms for air pollutants forecasting. 2020 IEEE 26th International Symposium for Design and Technology in Electronic Packaging (SIITME) 2020; 109-113.
- [17] Lee M, Lin L, Chen CY et al. Forecasting Air Quality in Taiwan by Using Machine Learning. *Sci Rep* 10, 2020; 4153.
- [18] Doreswamy KSH, Yogesh KM, Gad I. Forecasting air pollution particulate matter (PM2.5) using machine learning regression models. *Procedia Computer Science* 2020; 171(2020): 2057-2066.
- [19] Liang YC, Maimury Y, Chen AHL, Juarez JRC. Machine learning-based prediction of air quality. *Appl. Sci.* 10, 2020; 9151.
- [20] Haykin S. *Neural Networks: A Comprehensive Foundation*. Prentice Hall: USA, 1999.
- [21] Al-Saif AM, Abdel-Sattar M, Aboukarima AM, Eshra DH. Application of a multilayer perceptron artificial neural network for identification of peach cultivars based on physical characteristics. *PeerJ* 2021; 9(e11529).
- [22] Gardner MW, Dorling SR, Artificial neural networks (the multilayer perceptron) —a review of applications in the atmospheric sciences. *Atmospheric environment* 1998; 32(14-15): 2627-2636.
- [23] Latz J. Analysis of stochastic gradient descent in continuous time. *Stat Comput.* 2021; 31(39): 1-25.
- [24] Orange Data Mining, 2022, Stochastic Gradient Descent, available at: <https://orange3.readthedocs.io/projects/orange-visual-programming/en/latest/widgets/model/stochasticgradient.html> (accessed: 1 June 2022).
- [25] UFLDL Tutorial, 2022, Optimization: Stochastic Gradient Descent, available at: <http://deeplearning.stanford.edu/tutorial/supervised/optimizationstochasticgradientdescent/> (accessed: 15 June 2022).

- [26] Ruder, 2016, An overview of gradient descent optimization algorithms, available at: [https://ruder.io/optimizing-gradient-descent/#:~:text=Stochastic%20gradient%20descent,-Stochastic%20gradient%20descent&text=%CE%B8%3D%CE%B8%E2%88%92%CE%B7%E2%8B%85%E2%88%87%CE%B8J\(%CE%B8%3B,%3B%20y%20\(%20i%20\)%20\)%20](https://ruder.io/optimizing-gradient-descent/#:~:text=Stochastic%20gradient%20descent,-Stochastic%20gradient%20descent&text=%CE%B8%3D%CE%B8%E2%88%92%CE%B7%E2%8B%85%E2%88%87%CE%B8J(%CE%B8%3B,%3B%20y%20(%20i%20)%20)%20) (accessed: 30 June 2022).
- [27] Topal M, Eyduran E, Yağanoğlu AM, Sönmez A, Keskin S. Çoklu Doğrusal Bağlantı Durumunda Ridge ve Temel Bileşenler Regresyon Analiz Yöntemlerinin Kullanımı. Atatürk Üniversitesi Ziraat Fakültesi Dergisi 2013; 41(1): 53-57.
- [28] Scikitlearn, 2022, Cross decomposition, available at: https://scikit-learn.org/stable/modules/cross_decomposition.html (accessed: 5 July 2022).
- [29] ML-science, 2022, Cross decomposition, available at: <https://www.ml-science.com/cross-decomposition> (accessed: 5 July 2022).
- [30] Singh, 2020, Understanding Data Preprocessing, available at: <https://towardsdatascience.com/data-preprocessing-e2b0bed4c7fb> (accessed: 28 July 2022).
- [31] Baheti, 2022, A Simple Guide to Data Preprocessing in Machine Learning, available at: <https://www.v7labs.com/blog/data-preprocessing-guide> (accessed: 3 August 2022).
- [32] DataTechNotes, 2019, Regression Model Accuracy (MAE, MSE, RMSE, R-squared) Check in R, available at: <https://www.datatechnotes.com/2019/02/regression-model-accuracy-mae-mse-rmse.html> (accessed: 10 August 2022).

Investigation of Antioxidant, Antimicrobial and Cytotoxic Activity of *Cydonia oblonga* Leaf on Breast Cancer (MCF-7) and Liver Cancer (HepG2) Cell Lines

Lütfiye KADIOĞLU DALKILIÇ^{1*}

¹ Firat University, Faculty of Health Sciences, Obstetrics and Gynecology Nursing, Elazığ-Türkiye

*¹ tkadioglu85@gmail.com

(Geliş/Received: 21/07/2023;

Kabul/Accepted: 10/01/2024)

Abstract: Cancer, one of the most common pathologies in the world, has been reducing the standard of living of many people for centuries and can cause death. Many medicinal plants are widely used in cancer treatment due to their ability to improve disease symptoms and low side effects. *Cydonia oblonga* (*C. oblonga*) leaf, which is among the medicinal plants and has important health properties, is a type of plant commonly known as quince leaf. Although it originates from Asia, it is cultivated in many countries today. In this study, antioxidant, antimicrobial and cytotoxic activities of *C. oblonga* leaves on MCF-7 and HepG2 cell lines were investigated. As a method, the collected *C. oblonga* leaves were extracted in methanol and hexane solvents. The extracts were tested on MCF-7 and HepG2 cell lines using MTT Assay method for cytotoxic activity, DPPH method for antioxidant activity and well agar method for antimicrobial effects of the extract on five different microorganisms. As a results, although *C. oblonga* leaf in both cell lines hexane extract exhibited stronger cytotoxic activity than methanol extract, methanol extract was found to have stronger antioxidant effect than hexane extract. The extracts applied to microorganisms showed the best zone diameter effect on *E. coli* and the lowest effect on *B. megaterium*. In addition, it was observed that *C. oblonga* leaf has stronger antimicrobial effects than anticancer and antioxidant activity.

Key words: *Cydonia oblonga*, cytotoxic activity, antioxidant activity, antimicrobial activity.

Cydonia oblonga Yaprağının Meme Kanseri (MCF-7) ve Karaciğer Kanseri (HepG2) Hücre Hatları Üzerindeki Antioksidan, Antimikrobiyal ve Sitotoksik Aktivitesinin Araştırılması

Öz: Dünyadaki en yaygın patolojilerden biri olan kanser, yüzyıllardır birçok insanın yaşam standardını düşürmekte ve ölüme neden olabilmektedir. Birçok şifalı bitki, hastalık semptomlarını iyileştirme yetenekleri ve düşük yan etkileri nedeniyle kanser tedavisinde yaygın olarak kullanılmaktadır. Şifalı bitkiler arasında yer alan ve sağlık açısından önemli özelliklere sahip olan *Cydonia oblonga* (*C. oblonga*) yaprağı, halk arasında ayva yaprağı olarak bilinen bir bitki türüdür. Asya kökenli olmasına rağmen günümüzde birçok ülkede yetiştirilmektedir. Bu çalışmada, *C. oblonga* yapraklarının MCF-7 ve HepG2 hücre hatları üzerindeki antioksidan, antimikrobiyal ve sitotoksik aktiviteleri araştırılmıştır. Yöntem olarak, toplanan *C. oblonga* yaprakları metanol ve hekzan çözücülerinde ekstrakte edilmiştir. Ekstraktlar MCF-7 ve HepG2 hücre hatları üzerinde sitotoksik aktivite için MTT Assay yöntemi, antioksidan aktivite için DPPH yöntemi ve ekstraktın beş farklı mikroorganizma üzerindeki antimikrobiyal etkileri için well agar yöntemi kullanılarak test edilmiştir. Sonuç olarak, *C. oblonga* yaprağı her iki hücre hattında da hekzan özütü metanol özütüne göre daha güçlü sitotoksik aktivite sergilemesine rağmen, metanol özütü hekzan özütüne göre daha güçlü antioksidan etkiye sahip bulunmuştur. Mikroorganizmalara uygulanan ekstraktlar en iyi zon çapı etkisini *E. coli* üzerinde, en düşük etkiyi ise *B. megaterium* üzerinde göstermiştir. Ayrıca, *C. oblonga* yaprağının antikanser ve antioksidan aktiviteden daha güçlü antimikrobiyal etkilere sahip olduğu gözlemlenmiştir.

Anahtar kelimeler: *Cydonia oblonga*, sitotoksik aktivite, antioksidan aktivite, antimikrobiyal aktivite.

1. Introduction

Cancer is one of the most alarming diseases of the 20th century and continues to spread in the 21st century due to its persistence and increasing incidence. This is a cause for concern as one in four people have a lifetime risk of cancer [1]. Human breast cancer (MCF-7) is one of the most common cancers and has become one of the most common causes of cancer death in women [2]. Human liver cancer, of which 75-90% are hepatocellular carcinomas (HepG2), it is the third leading cause of cancer-related deaths in men and the sixth leading cause in women [3]. The progression of cancer, which is so widespread and deadly, is a multi stage process in which cells

* Corresponding author: tkadioglu85@gmail.com. ORCID Number of authors: ¹ 0000-0002-6791-3811

Investigation of Antioxidant, Antimicrobial and Cytotoxic Activity of *Cydonia oblonga* Leaf on Breast Cancer (MCF-7) and Liver Cancer (HepG2) Cell Lines

must overcome various obstacles before they become fully developed tumors. Although significant advances have been made in recent years in treatments to stop cancer growth, many patients have to fight against metastasis and tumor growth due to chemoresistance with challenging radiotherapy and chemotherapy. Researchers are therefore exploring new methods to better understand the behavior of cancer cells and develop more effective treatments. Due to some serious side effects and the medical and economic problems associated with the use of synthetic drugs for cancer treatment, herbal therapies have become popular. Herbal medicines are considered a safe, non toxic and easily accessible source of compounds that can treat cancer. Plants are believed to neutralize the effects of diseases on the body because of the active compounds they contain [4]. It has been suggested that natural antioxidants reduce the toxic effects of anticancer treatment processes and that the use of nutraceuticals may improve the treatment more, with the idea that it may help patients undergoing cancer treatment in this process [5]. Accordingly, over the years, the determination of the cytotoxic properties of natural products has gained great importance [6-9]. Quince leaf, known as *C. oblonga*, is a plant belonging to the Rosaceae family and is native to the Mediterranean region and Central Asia. This plant leaf has a long history of ethnobotanical and medicinal use [10]. The leaves of the *C. oblonga* are egg shaped or broadly elliptical, dark green and toothless on the margins, but these young leaves are petiolate. It can generally be grown in all regions in the temperate zone. Known for its antidiabetic, antimicrobial, antioxidant and UV (ultraviolet)-protective abilities, the biological phytochemicals in the leaves of this plant are also known to be a promising source of natural healing [11]. *C. oblonga* leaf is a plant recognized as an active ingredient with many characteristic properties, mainly antioxidant [12]. When the leaves of the plant are consumed by boiling and straining, it is known to have calming, antipyretic, antidiarrheal and antitussive properties [13-16]. In addition to having an important place in folk medicine, it is also considered as a good and economical source of dye [17]. *C. oblonga* leaf and fruit extracts have been found to exhibit antiproliferative activities, suggesting that this plant leaf may inhibit or reduce the growth of cancer cells [18]. Plants with antimicrobial activity are used as preservatives in foods, for medical purposes, and for their effects against parasites and microorganisms [19].

In the light of this information, the main aim of this study is to extract the leaves of *C. oblonga* plant as shown in the project flow chart in Figure 1 and to show its cytotoxic activity on MCF-7, HepG2 cell lines and to investigate its antimicrobial and antioxidant effects at different concentrations and to provide the molecular mechanisms of these activities to the literature.

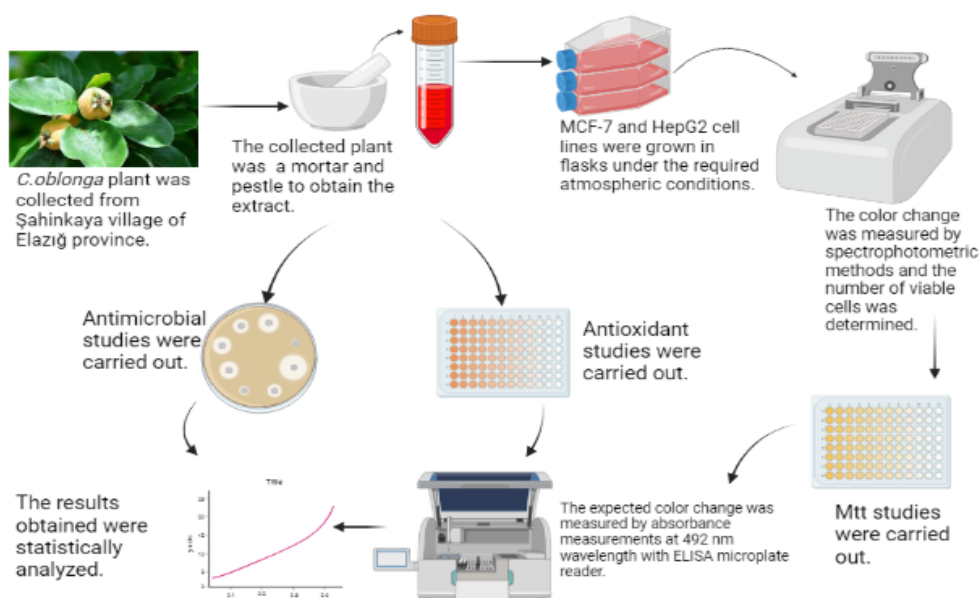


Figure 1. The overall design of the experiment showed the methods applied on *C. oblonga* leaves. Two different solvents; hexane and methanol were used to evaluate cytotoxic, antioxidant and antimicrobial activity.

2. Material and Method

2.1. Material

2.1.1. Herbal material

C. oblonga leaf was collected from Şahinkaya Village of Elazığ province in November 2022. The collected plant was kept in the laboratory of Assoc. Prof. Dr. Semih DALKILIÇ, a faculty member of the Molecular Biology and Genetics Program of the Biology Department of Firat University.

2.1.2. Microorganisms and cell lines used in the experiment

Staphylococcus aureus (*S. aureus*) ATCC 25923, *Klebsiella pneumonia* (*K. pneumonia*) ATCC 700603, *Escherichia coli* (*E. coli*) ATCC 25322, *Bacillus megaterium* (*B. megaterium*) ATCC DSM32 and *Candida albicans* (*C. albicans*) FMC17 as fungus were obtained from Fethi Sekin City Hospital central laboratory.

HepG2 and MCF-7 cancer cell lines are available in the laboratory of Assoc. Prof. Dr. Semih DALKILIÇ, one of the faculty members of the Molecular Biology and Genetics Program of the Biology Department of Firat University, and we have worked on these two cell lines.

2.2. Method

2.2.1. Extract preparation

C. oblonga leaf was pounded in a porcelain mortar and powdered. The powdered plant was weighed on a precision balance and 1 gram was taken and two separate extraction processes were carried out as 10 mL methanol and 10 mL hexane. It was incubated in a shaking oven at 37°C for 72 hours. After incubation, the extract was dried and dissolved in 10 mL Dimethyl sulfoxide (DMSO). Using Whatman No 1 filter paper, the extracts were filtered and stored at +4°C.

In order to examine the antioxidant, antimicrobial and cytotoxic activities of *C. oblonga* leaf extract, methanol, which is available in our laboratory and is a solvent frequently used in antioxidant activity studies to reveal phenolic compounds of plant extracts, and hexane, which dissolves lipophilic compounds in the plant better than many other solvents, were preferred as solvents. In addition, the fact that these two solvents have less toxicity than many other solvents is another reason why they are preferred in terms of ensuring safety in the study and working environment.

2.2.2. Cell culture

MCF-7 cells were grown in 1640 RPMI and HepG2 cells were grown in DMEM (25 mM L-Glutamine, 1% Penicillin-Streptomycin and 10% FBS (Fetal Bovine Serum)) in 75 cm² flasks at 37°C under 5% CO₂ atmosphere conditions [20]

2.2.3. MTT assay

The MTT (3-(4,5-dimethylthiazol-2-yl)-2,5-diphenyltetrazolium bromide) Assay is a technique employed to evaluate the viability, proliferation, and cytotoxicity of cells. The MTT method states that MTT is a tetrazolium salt that can pass through the cell membrane, based on its reduction by active mitochondria in living cells by taking electrons inside the cell and converting them into water-insoluble purple formazan crystals [21]. The formazan crystals were then dissolved in appropriate solvents and the color change was measured spectrophotometrically to determine the number of viable cells. Cells grown in 75 cm² flasks were washed with 5 mL of sterile Phosphate buffered saline (PBS) solution by removing the medium in the flask after 90% confluency. 1 mL of trypsin EDTA (Trypsin Ethylenediaminetetraacetic acid) was added to 75 cm² flasks and incubated at 37°C in an oven containing 5% CO₂ for 2 minutes. After the cells were detached from the surface, 5 mL of RPMI was added to inactivate trypsin EDTA. Cells removed from the flask were centrifuged at 2000 RPM (Revolutions per Minute) for 5 minutes and the supernatant was removed. The cell pellet was removed by thawing with 1000 µL RPMI and cell counting was performed using a Countess II automatic cell counter. After calculations were made, cell dilution was prepared using RPMI and 5×10³ cells were seeded in 96-well plates with 100 µL RPMI per well. In the first row, only medium was used as blank, 2.5 µg/mL Doxorubicin was used as positive control and only medium was used as negative control. Then, they were incubated in an oven at 37°C with 5% CO₂ for 24 hours. After the

Investigation of Antioxidant, Antimicrobial and Cytotoxic Activity of *Cydonia oblonga* Leaf on Breast Cancer (MCF-7) and Liver Cancer (HepG2) Cell Lines

incubation was completed, the medium in the wells was removed and 4 different concentrations of methanol and hexane extracts of *C. oblonga* leaf prepared in RPMI (100 µg/mL, 200 µg/mL, 400 µg/mL and 800 µg/mL) were added to the cells in 6 replicates. Then the cells were incubated in an oven containing 5% CO₂ at 37°C for 72 hours. At the end of the incubation period, 10 µl of MTT solution (5 mg/mL) was added to the wells containing the cells and incubated for 4 hours at 37°C in the dark containing 5% CO₂. After incubation, the medium was removed and formazan crystals were dissolved in 100 µl DMSO. The expected color change was then determined by measuring absorbance at 492 nm wavelength using an ELISA (Enzyme Linked ImmunoSorbent Assay) microplate reader [22].

2.2.4. Determination of antioxidant activity by 2,2-Diphenyl-1-Picrylhydrazyl (DPPH) Radical Scavenging Capacity

It is a method developed to assess antioxidant activity using DPPH (2,2-diphenyl-1-picrylhydrazyl) and is used to measure the free radical scavenging capacity of antioxidants against the test. It is widely used in many herbal studies and is a fast and easy method [23]. In addition, the chemicals and spectrophotometric measuring devices required for DPPH method are available in our laboratory and have been preferred in this method antioxidant tests. Antioxidant activity of *C. oblonga* leaf extracts in methanol and hexane at different concentrations was determined by DPPH radical scavenging capacity method. A lyophilized drug solution was prepared at a concentration of 5 mg/mL using methanol and hexane. The prepared solution was diluted three times and DPPH calibration curve was obtained. At the end of the specified time, absorbances were measured at 492 nm wavelength in spectrophotometer and % inhibition values were calculated. The results were calculated according to Equation 1 [24]:

$$\text{Antioxidant activity} = \frac{\text{ControlABS} - \text{SampleABS}}{\text{ControlABS}} \times 100$$

Equation 1. Formulation used in antioxidant activity calculation

2.2.5. Antimicrobial activity

Well agar method was used for antibacterial activity and *S. aureus*, *K. pneumoniae*, *E. coli*, *B. megaterium* and *C. albicans* microorganisms were used [25]. Bacteria were grown in Nutrient Broth (Biolife Lot: HE2602) and Müller-Hinton Agar (Merck Lot: VM779137) and fungi in Malt Extract Broth (Difco) before the experimental study. In order to test the antimicrobial effects of *C. oblonga* leaf extracts diluted at 25, 50, 75 and 100 mg/mL on bacterial strains, each bacterium was inoculated into Nutrient Broth with the help of a bacterial extract. The Mc Farland setting was adjusted to a turbidity of 0.5, thus achieving a dilution of 1:10 to 107 CFU/mL. 25 mL of Müller-Hinton Agar was added to the petri dishes. Petri dishes were allowed to solidify at room temperature for 10-20 minutes. On the solidified Müller-Hinton Agar, 100 µL of bacteria were inoculated evenly and then wells of the required diameter were made in Müller-Hinton Agar with the help of an agar borer (cork-borer). Compounds prepared from four different concentrations were added to 100 µL in each well and petri dishes were incubated at 37°C for 24 hours after inoculation. Clindamycin 2 mcg (Bioanalyse Lot: 171127A) was used as a positive control and DMSO as a negative control. Inhibition zones were measured with the help of a ruler [26].

2.2.6. Statistical analysis

All results were performed with SPSS 22 for Windows and one-way ANOVA was used and p < 0.05 was considered significant.

3. Results

3.1. Cytotoxic activity

As a result of the experiments, it was observed that the best result was obtained at a concentration of 250 µg/mL of *C. oblonga* leaf hexane extract used on HepG2 cancer cells, followed by the second-best result of 125 µg/mL concentration of the same extract. It was noticed that methanol 1000, 500 and 250 µg/mL concentrations did not show toxicity against cancer cells and in addition, as seen in Figure 2, methanol extract had less toxicity on cancer cells than hexane extract. Furthermore, as shown in Figure 3, 500 µg/mL concentration of *C. oblonga* leaf hexane extract had the best effect on MCF-7 cancer line, while methanol extract had any effect on MCF-7 cell line at all concentrations.

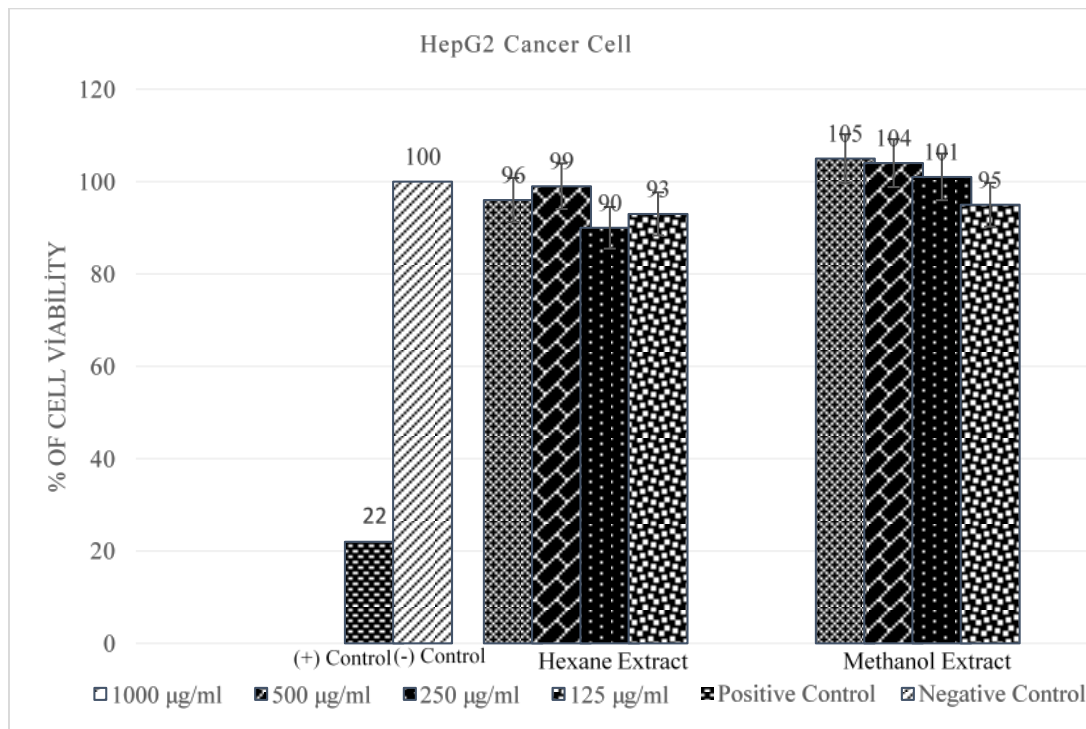


Figure 2. Cytotoxic activity of hexane and methanol extracts of *C. oblonga* leaf on HepG2 cancer cell lines. *Positive control: Doxorubicin 2.5 µg/mL, Negative control: untreated cells.

Investigation of Antioxidant, Antimicrobial and Cytotoxic Activity of *Cydonia oblonga* Leaf on Breast Cancer (MCF-7) and Liver Cancer (HepG2) Cell Lines

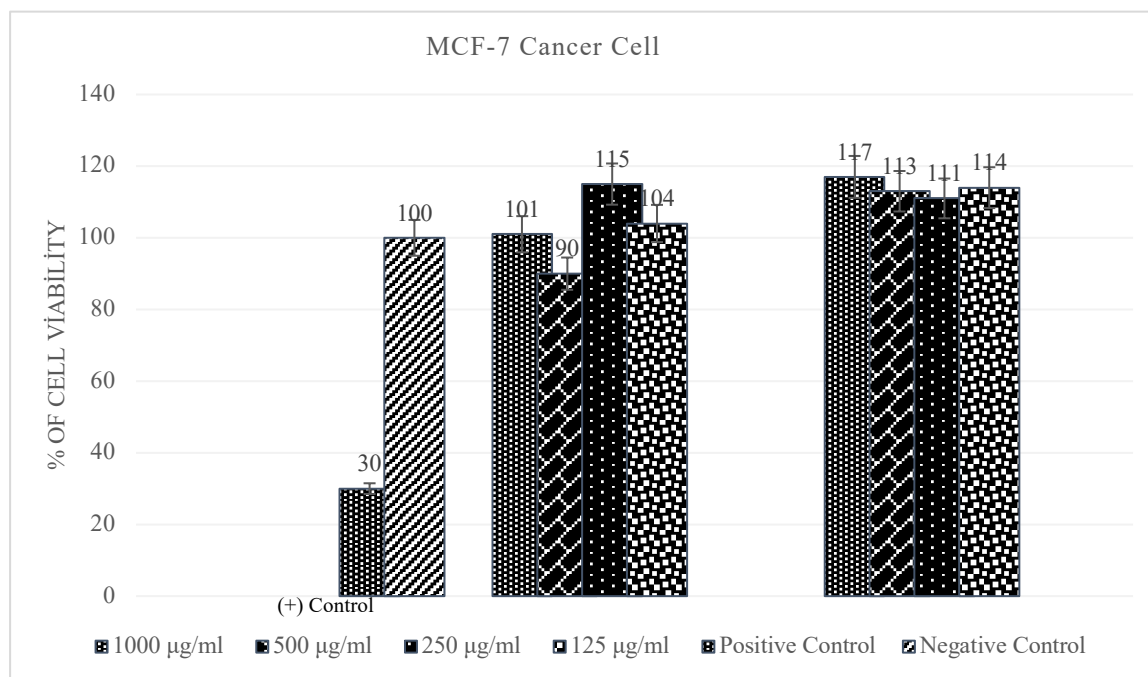


Figure 3. Cytotoxic activity of hexane and methanol extracts of *C. oblonga* leaf on MCF-7 cancer cell lines.
*Positive control: Doxorubicin 2.5 µg/mL, Negative control: untreated cells.

Cytotoxic activity results of *C. oblonga* leaf extracts were obtained by calculating the maximum inhibitory concentration (IC₅₀) value for four different concentrations (1000, 500, 250, 125 µg/mL). IC₅₀ values were calculated for both cell lines and two extracts and the results are presented in Table 1. These results differ depending on the cell line and extract type used.

Table 1. The IC₅₀ value of cytotoxic activity on cells.

MCF-7 Cell Line		
Agent	<i>C. oblonga</i> leaf hexane extract	<i>C. oblonga</i> leaf methanol extract
IC ₅₀	353.305 µg/mL	781.56 µg/mL
HepG2 Cell Line		
Agent	<i>C. oblonga</i> leaf hexane extract	<i>C. oblonga</i> leaf methanol extract
IC ₅₀	354.2317 µg/mL	139.3403 µg/mL

3.2. Antioxidant activity

Antioxidant activities of plant extracts were evaluated by DPPH method. DPPH radical inhibition percentage of *C. oblonga* leaf methanol and hexane extracts at 1000 mg/mL concentration was calculated. The results are shown in Table 2. According to the results, *C. oblonga* leaf methanol extract had 7% radical scavenging capacity and exhibited better antioxidant activity than hexane extract at a concentration of 1000 mg/mL. However, it was determined that the 1000 mg/mL concentration of *C. oblonga* leaf hexane extract did not have any scavenging capacity.

Table 2. Antioxidant activity of *C. oblonga* leaf methanol and hexane extract.

	Methanol	Hexane
Positive Control	1	1
1000 µg/ml	7	-64
Negative Control	0	0

*Positive control: 100 µL ascorbic acid and 100 µL DPPH, negative control: 200 µL DPPH.

3.3. Antimicrobial activity

The antimicrobial activity of methanol and hexane extracts of *C. oblonga* leaf plant was tested on five different microorganisms including *E. coli*, *B. megaterium*, *S. aureus*, *K. pneumoniae*, *C. albicans*. In terms of antimicrobial activity, the results were compared with the standard antibiotic clindamycin. Considering these results, as seen in Table 3 and Figure 4, 50, 75 and 100 mg/mL concentrations of the hexane extract of the plant showed the highest value with an inhibition zone of 17 mm on *E. coli*, while 25 mg/mL concentration showed the lowest zone diameter effect. The best zone diameter of the extract on *S. aureus* with 16 mm was determined at a concentration of 100 mg/mL and zone diameters of 15 mm at a concentration of 75 mg/mL, 14 mm at a concentration of 50 mg/ml and 13 mm at the lowest concentration of 25 mg/mL were measured respectively. While 25 mg/mL and 50 mg/mL concentrations of the extract showed no any effect on *B. megaterium*, the 100 mg/mL concentration showed the best inhibition zone with 14 mm effect, and the 75 mg/mL concentration showed the lowest inhibition zone with 12 mm. The concentration of 100 mg/mL with 13 mm showed the best effect on *K. pneumoniae* bacteria, while the concentration of 75 mg/mL with 11 mm showed the lowest zone diameter effect. In addition, it was noticed that 25 and 50 mg/mL concentrations showed the same effect against the bacterium with 12 mm. Concentrations of 100 and 75 mg/mL were found to have the best effect on *C. albicans* with inhibition zone diameters equal to 16 mm. The lowest zone diameter of 13 mm was measured at a concentration of 25 mg/mL, followed by a concentration of 50 mg/mL with a zone diameter of 14 mm. In general, as shown in Table 3, the hexane extract showed the best antibacterial effect on *E. coli* and the lowest effect on *B. megaterium*. Looking at the methanol extract, the best inhibition zone diameter of 15 mm in *E. coli* was observed at concentrations of 75 and 25 mg/mL. Following this, the lowest zone diameter of 14 mm was measured in both 50 and 100 mg/mL concentrations. The 50 and 75 mg/mL concentrations showed the best effect against *S. aureus* with 13 mm, while the 25 mg/mL concentration showed the lowest effect with 10 mm. Following this, inhibition zone diameter of 11 mm was measured at 100 mg/mL concentration. The methanol extract, which showed the lowest effect on *B. megaterium* with 9 mm at 25 mg/mL concentration, had no effect on the bacteria at 75 mg/mL concentration, while it showed the highest effect at 50 and 100 mg/mL concentrations with 12 mm. The highest zone diameter of 11 mm is observed at concentrations of 50 and 100 mg/mL against *K. pneumoniae* bacteria. These values were followed by 25 and 75 mg/mL concentrations of 9 mm and 10 mm, respectively. At 100 mg/mL concentration, *C. albicans* showed the best zone diameter of 15 mm, at 50 and 75 mg/mL concentrations it showed the second best effect with 14 mm, but at 25 mg/mL concentration it showed the lowest effect with 12 mm. Based on these results, as shown in Table 3 and Figure 4, *C. oblonga* leaf methanol extract showed the best antibacterial effect on *E. coli* and the lowest effect on *B. megaterium*.

The standard deviations of *C. oblonga* leaves among microorganisms were calculated and as a result, *E. coli* followed by *K. pneumoniae* showed the most significant value in both extracts, while *B. megaterium* showed less significant results compared to other bacteria. Looking at the standard deviations between concentrations, it was determined that the methanol extract gave the most significant result at 50 mg/mL, followed by the hexane extract at 100 mg/mL. At 50 mg/mL, the hexane extract gave less significant results than the other results, followed by the same extract at 25 mg/mL.

Investigation of Antioxidant, Antimicrobial and Cytotoxic Activity of *Cydonia oblonga* Leaf on Breast Cancer (MCF-7) and Liver Cancer (HepG2) Cell Lines

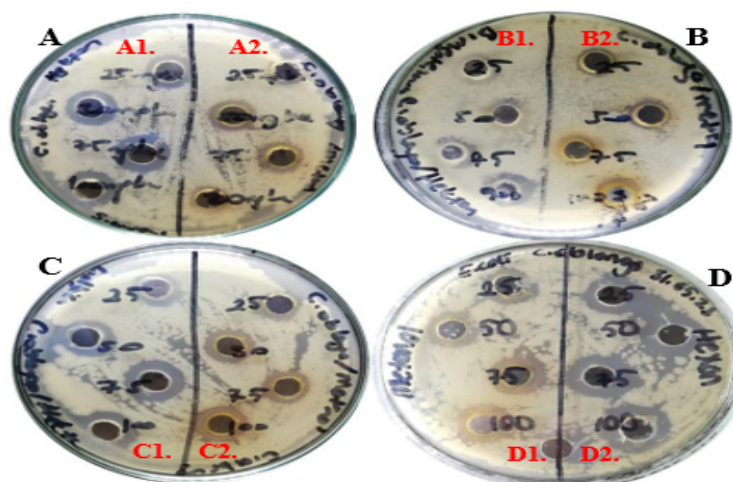


Figure 4. Zones of inhibition seen in petri dishes.

- *A: Antimicrobial effect of *C. oblonga* leaf on *S. aureus* A1: Hexane extract A2: Methanol extract
- *B: Antimicrobial effect of *C. oblonga* leaf on *B. megaterium*; B1: Hexane extract B2: Methanol extract
- *C: Antimicrobial effect of *C. oblonga* leaf on *C. albicans*; C1: Hexane extract C2: Methanol extract
- *D: Antimicrobial effect of *C. oblonga* leaf on *E. coli*; D1: Methanol extract D2: Hexane extract

Table 3. Antibacterial effect of *C. oblonga* leaf extract (zone diameters mm)

Microorganism	Concentrations (mg/mL) and zone diameters (mm)								Positive Control (Clindamycin)
	Hexane				Methanol				
	25 mg/mL	50 mg/mL	75 mg/mL	100 mg/mL	25 mg/mL	50 mg/mL	75 mg/mL	100 mg/mL	
<i>E. coli</i>	16 ± 0.7	17 ± 0.2	17 ± 0.2	17 ± 0.2	15 ± 0.5	14 ± 0.5	15 ± 0.5	14 ± 0.5	24 ± 1.6
<i>S. aureus</i>	13 ± 1.5	14 ± 0.5	15 ± 0.5	16 ± 1.5	10 ± 1.7	13 ± 1.2	13 ± 1.2	11 ± 0.7	23 ± 0.6
<i>B. megaterium</i>	*	*	12 ± 1	14 ± 1	9 ± 2	12 ± 1	12 ± 1	12 ± 1	23 ± 0.6
<i>K. pneumoniae</i>	12 ± 0	12 ± 0	11 ± 1	13 ± 1	9 ± 1.2	11 ± 0.7	10 ± 0.2	11 ± 0.7	22 ± 0.4
<i>C. albicans</i>	13 ± 1.7	14 ± 0.7	16 ± 1.2	16 ± 1.2	12 ± 1.7	14 ± 0.2	14 ± 0.2	15 ± 1.2	20 ± 2.4

* It did not show any antibacterial activity.

4. Discussion

C. oblonga leaf, commonly known as quince, is a good, low budget, easily accessible and health-promoting plant with antioxidant properties [12], [27], [28]. In the studies, it was determined that *C. oblonga*, which was found to have higher phenolic compound content and stronger antioxidant capacity compared to other plants used in the studies, could be valuable in nutraceuticals as an antioxidant source and would reveal new possible applications of the plant [29]. DPPH test, ABTS (2,2-azinobis(3-ethylbenzothiazollin-6-sulfonic acid) and ferric acid reducing antioxidant assays showed that *C. oblonga* had the highest antioxidant potential [30]. When the leaves of the plant and *Camellia sinensis* (*C. sinensis*) known as green tea, were compared, DPPH method was applied with methanolic extracts and as a result, EC₅₀ values were determined as 21.6 µg/mL and 12.7 µg/mL and it was statistically revealed that *C. sinensis* had a higher capacity (p<0.005). However, considering the high phenolic content of *C. oblonga* leaves compared to peel, seed or pulp, the EC₅₀ values of 600, 1700 and 2000 µg/mL for the peel were determined that the leaf would have a higher antioxidant effect (EC₅₀ 21.6 µg/mL) [31]. Quince fruit, compared to apple, is characterized by the presence of compounds such as 4-caffeoyl shikimic acid,

4-caffeoyl quinic acid, quercetin-3,7-diglucoside, kaempferol-3-O-rhamnoside and kaempferol-7-O-glucoside, while it lacks dihydrochalcone compounds. However, quince peel has the highest phenolic content, while the most abundant compound in quince pulp is 3-O-caffeoylquinic acid [29]. *C. oblonga* Mill. leaves were examined for their antioxidant activity along with their in vivo antidiabetic activity and the highest ABTS radical scavenging effect, reducing power and total antioxidant activity were observed in *C. oblonga* [32]. Parts of the plant were evaluated in three different ways: fresh frozen, oven dried and sun dried. According to the observations, fresh frozen fruit gave results close to normal nutritional values, but the oven dried plant retained antioxidant activity better than sun dried and frozen plants [33]. Methanolic extracts were prepared from various parts of *C. oblonga* plant and the bark was found to have the best antioxidant capacity [34]. *C. oblonga* leaf extract showed concentration dependent growth inhibitory activity against human colon cancer cells and no any effect against renal adenocarcinoma cells. However, seed extracts of the plant had no any effect on cell growth in colon cancer, but effective antiproliferative activity detected in kidney cancer cells [18]. When two different extracts of *C. oblonga* were extracted as lipophilic wax extract and aqueous fermented extract and their cytotoxic effects on human HepG2, A549 (human non-small cell lung cancer cell line) and HeLa cell lines were evaluated, it was determined that the aqueous fermented extract played a more effective role than lipophilic extracts, but this would vary depending on the exposure time [35]. In colorectal cancer, polyphenol-rich extracts of *C. oblonga* bark inhibited colon adenocarcinoma LS174 cells in a quantity dependent manner [36]. MTS (5-(3-carboxymethoxyphenyl)-2-(4,5-dimethyl-thiazole)-3-(4-sulfophenyl) tetrazolium, inner salt assay) testing of *C. oblonga* petals, leaves and fruit pellet on BT-20 (human breast cancer cell line), HepG2 and Caco-2 (human colorectal cancer cell line) human cancer lines showed that these three *C. oblonga* extracts strongly reduced cell growth and had low toxicity on HepG2 and Caco-2 cell lines [37]. When RD (Rabdomiyosarkom) and L2OB cancer cells were exposed to the methanol extract of *C. oblonga* seed, it was reported that it had a cytotoxic effect at the first 1000 and 500 µg/mL, but this cytotoxic activity changed depending on the concentration in the following time [38]. The antimicrobial effect of ethanol, acetone and water extracts of *C. oblonga* plant seeds on *K. pneumonia*, *E. coli*, *E. aerogenes* (*Enterobacter aerogenes*) bacteria were examined and it was determined that the seed had the most effective antimicrobial effect in the ethanolic extract and *E. coli* showed the highest sensitivity, while the aqueous extract was only effective on *E. aerogenes* bacteria [39]. With the application of *C. oblonga* seed extract to different bacterial strains, quince seed extract was found to have antimicrobial effect against gram positive *S. aureus* and gram negative *E. coli* and *P. aeruginosa* (*Pseudomonas aeruginosa*) bacteria and the MIC (Minimal inhibitory concentration) value against these bacteria was 500 µg/mL [40]. Regarding the antimicrobial effect of the plant, gram negative bacteria were more sensitive to the extracts, while the extracts obtained from *C. oblonga* flour showed growth inhibitory effect on *Aspergillus niger* (*A. niger*) [41]. To promote the full reuse of this plant, biologically active extracts and fiber concentrates of the plant were extracted and found to exhibit in vitro antioxidant activity as well as antimicrobial activity against food borne fungi and bacteria, suggesting that various extracts of the plant could be pioneers in the use of natural preservatives in foods [42]. Dye was obtained from the extract of *C. oblonga* plant in order to work on recovery to nature and dyeing process was carried out with various chemicals as a coloring agent on wool. When the properties of the extract used as a dye were tested, it has been shown to have strong antimicrobial activity on gram positive and gram negative bacteria [43]. In the study conducted with silver nanoparticles from *C. oblonga* leaves, the antimicrobial activity of these nanoparticles was examined and tested on gram negative *E. coli*, gram positive *S. aureus* and *C. albicans* and MIC values were determined as 0.0552, 0.1535 and 0.0383 mg L⁻¹ [44].

The analyzed studies showed that the leaves and various parts of *C. oblonga* showed high antioxidant activity compared to some other plants. It was observed that different solvents from the solvents used in cytotoxic activity studies may show good activity, the same solvents such as methanol used in our study showed similar effects, followed by antimicrobial activity studies also showed similar effects especially on *E. coli*, supporting the results of our study.

5. Conclusions

While hexane extract of *C. oblonga* showed better anticancer effect than methanol extract, when antioxidant activity was considered, methanol extract showed better antioxidant activity than hexane. In terms of antimicrobial activity, the best zone diameter was observed in *E. coli* bacteria and the lowest zone diameter was observed in *B. megaterium* at both concentrations. As a result, it is concluded that *C. oblonga* leaf exhibits significant anticancer, antimicrobial and antioxidant activities in an in vitro model and therefore, it may be one of the important therapeutic herbal agents.

References

- [1] Roy PS and Saikia BJ, "Cancer and Cure: A Critical Analysis," *Indian J. Cancer*, 2016; 53(3): 441.
- [2] Khan MI, et. al., "Anticancer Properties of Medicinal Plants and Their Bioactive Compounds against Breast Cancer: A Review on Recent Investigations," *Environ. Sci. Pollut. Res. Int.*, 2022; 29(17): 24411-24444.
- [3] London WT and Mcglynn KA, "Liver Cancer," in *Cancer Epidemiology and Prevention*, D. Schottenfeld and J. F. Fraumeni, Eds., Oxford University Press., 2006; 763–786.
- [4] Khan T, et. al., "Anticancer Plants: A Review of the Active Phytochemicals, Applications in Animal Models, and Regulatory Aspects," *Biomolecules*, 2019; 10(1): 47.
- [5] Maiuolo J, et al., "Nutraceuticals and Cancer: Potential for Natural Polyphenols," *Nutrients*, 2021; 13(11): 3834.
- [6] Chemoprevention of Prostate Cancer through Dietary Agents: Progress and Promise," *Cancer Epidemiology, Biomarkers & Prevention*, American Association for Cancer Research, 2023; 16(11): 2193.
- [7] Johnson JJ, Bailey HH, and Mukhtar H, "Green tea polyphenols for prostate cancer chemoprevention: A translational perspective," *Phytomedicine*, 2010; 17(1): 3-13.
- [8] Johnson JJ, Bailey HH, and Mukhtar H, "*Curcumin* for chemoprevention of colon cancer," *Cancer Lett.*, 2007; 255(2): 170–181.
- [9] Saleem M, "Lupeol, a novel anti-inflammatory and anti-cancer dietary triterpene," *Cancer Lett.*, 2009; 285(2): 109-115.
- [10] Devkota HP, Dirar AI, Hassan M, and Logesh R, "Chapter 10 - *Cydonia oblonga* Mill," in *Himalayan Fruits and Berries*, T. Belwal, I. Bhatt, and H. Devkota, Eds., Academic Press, 2023; 91–99.
- [11] Sabir S, et. al., "Pharmacognostic and clinical aspects of *Cydonia oblonga*: A review," *Asian Pac. J. Trop. Dis.*, 2015; 5(11): 850-855.
- [12] García-Alonso M, Pascual-Teresa S, Santos-Buelga C, and J. C. Rivas-Gonzalo, "Evaluation of the antioxidant properties of fruits," *Food Chem.*, 2004; 84(1): 13-18.
- [13] Oliveira AP, Pereira JA, Andrade PB, Valentão P, Seabra RM, and Silva BM, "Phenolic Profile of *Cydonia oblonga* Miller Leaves," *J. Agric. Food Chem.*, 2007; 55(19): 7926-7930.
- [14] Gründemann C, Papagiannopoulos M, Lamy E, Mersch-Sundermann V, and Huber R, "Immunomodulatory properties of a lemon-quince preparation (Gencydo®) as an indicator of anti-allergic potency," *Phytomedicine*, 2011; 18(8-9): 760-768.
- [15] Essafi-Benkhadir K, Refai A, Riahi I, Fattouch S, Karoui H, and Essafi M, "Quince (*Cydonia oblonga* Miller) peel polyphenols modulate LPS-induced inflammation in human THP-1-derived macrophages through NF- κ B, p38MAPK and Akt inhibition," *Biochem. Biophys. Res. Commun.*, 2012; 418(1): 180–185.
- [16] Abliz A et al., "Effect of *Cydonia oblonga* Mill. leaf extract on serum lipids and liver function in a rat model of hyperlipidaemia," *J. Ethnopharmacol.*, 2014; 151(2): 970-974.
- [17] Cerempei A, Mureşan EI, Cimpoeşu N, Carp-Cărare C, and Rimbu C, "Dyeing and antibacterial properties of aqueous extracts from quince (*Cydonia oblonga*) leaves," *Ind. Crops Prod.*, 2016; 94: 216-225.
- [18] Carvalho M, Silva BM, Silva R, Valentão P, Andrade PB, and Bastos ML, "First Report on *Cydonia oblonga* Miller Anticancer Potential: Differential Antiproliferative Effect against Human Kidney and Colon Cancer Cells," *J. Agric. Food Chem.*, 2010; 58(6): 3366–3370.
- [19] Faydaoğlu E and Sürücüoğlu M, "Tıbbi ve Aromatik Bitkilerin Antimikrobiyal, Antioksidan Aktiviteleri ve Kullanım Olanakları," *Erzincan Univ. J. Sci. Tech.*, 2014; 6(2): 233 - 265.
- [20] Dalkılıç LK, Dalkılıç S, and Uygur L, "Investigation of apoptotic, cytotoxic, and antioxidant effects of *Juglans regia* against MDA-MB-231 and A549 cell lines," *Int. J. Plant Based. Med.*, 2023; 3(1): 62–67.
- [21] Dalkilic S, Dalkilic LK, İnci S, Korkmaz İ, and Kirbag S, "Investigation of Cytotoxic Effect of *Black Mulberry* (*Morus nigra* L.) Fruit," *Indian J. Tradit. Knowl. (IJTK)*, 2021; 20(1): 54-58.
- [22] Dalkılıç S, Korkmaz İ, Dalkılıç LK, Akay G, and Fidan S, "In vitro cytotoxic effects of *Smilax aspera* L. roots on cancer cell lines," *Food Biosci.*, 2022; 46: 101501.
- [23] Kedare SB and Singh RP, "Genesis and development of DPPH method of antioxidant assay," *J. Food Sci. Technol.*, 2011; 48(4): 412-422.
- [24] Abed SN et al., "Phytochemical Composition, Antibacterial, Antioxidant and Antidiabetic Potentials of *Cydonia oblonga* Bark," *Molecules*, 2022; 27(19): 6360.
- [25] Duraipandiyar V, Ayyanar M, and Ignacimuthu S, "Antimicrobial activity of some ethnomedicinal plants used by Paliyar tribe from Tamil Nadu, India," *BMC Complement. Altern. Med.*, 2006; 6(35): 1-7.
- [26] Pekdemir S, Özen Öner E, Pekdemir ME, Dalkılıç S, and Kadioğlu Dalkılıç L, "*C. moschata* Leaves Extract on Physicochemical and Biological Properties of Biodegradable PCL/PLA Blend Film," *J. Polym. Environ.*, 2022; 30(9): 3645-3655.

- [27] Fattouch S et al., "Antimicrobial Activity of Tunisian Quince (*Cydonia oblonga* Miller) Pulp and Peel Polyphenolic Extracts," J. Agric. Food Chem., 2007; 55(3): 963–969.
- [28] Hamazu Y, Yasui H, Inno T, Kume C, and Omanyuda M, "Phenolic Profile, Antioxidant Property, and Anti-influenza Viral Activity of Chinese Quince (*Pseudocydonia sinensis* Schneid.), Quince (*Cydonia oblonga* Mill.), and Apple (*Malus domestica* Mill.) Fruits," J. Agric. Food Chem., 2005; 53(4): 928–934.
- [29] Sut S, Dall'Acqua S, Poloniato G, Maggi G, and Malagoli M, "Preliminary evaluation of quince (*Cydonia oblonga* Mill.) fruit as extraction source of antioxidant phytoconstituents for nutraceutical and functional food applications," J. Sci. Food Agric., 2019; 99(3): 1046–1054.
- [30] Zhang L et al., "The UHPLC-QTOF-MS Phenolic Profiling and Activity of *Cydonia oblonga* Mill. Reveals a Promising Nutraceutical Potential," Foods, 2021; 10(6): 1230.
- [31] Khoubnasabjafari M and Jouyban A, "A review of phytochemistry and bioactivity of quince (*Cydonia oblonga* Mill.)," Academic Journals, 2010; 5(16): 3577-3594.
- [32] Orhan DD and Orhan N, "Assessment Of In-Vitro Antidiabetic - Antioxidant Effects Of *Helianthus Tuberosus*, *Cydonia oblonga* And *Allium Porrum*," Turk. J. Pharm. Sci., 2016; 13(2): 60–67.
- [33] Gheisari HR and Abhari KH, "Drying method effects on the antioxidant activity of quince (*Cydonia oblonga* Miller) tea," Acta. Sci. Pol. Technol. Aliment., 2014; 13(2): 129–134.
- [34] Silva BM, Andrade PB, Valentão P, Ferreres F, Seabra RM, and Ferreira MA, "Quince (*Cydonia oblonga* Miller) Fruit (Pulp, Peel, and Seed) and Jam: Antioxidant Activity," J. Agric. Food Chem., 2004; 52(1): 4705–4712.
- [35] Al-Snafi A, "Anticancer effects of Arabian medicinal plants (part 1) - A review," IOSR J. Pharm., 2017; 7(4): 63–102.
- [36] Benarba B and Pandiella A, "Colorectal cancer and medicinal plants: Principle findings from recent studies," Biomed. Pharmacother., 2018; 107: 408–423.
- [37] Pirvu L, Stefanu A, Neagu G, Albu B, and Pintilie L, "In Vitro Cytotoxic and Antiproliferative Activity of *Cydonia oblonga* flower petals, leaf and fruit pellet ethanolic extracts. Docking simulation of the active flavonoids on anti-apoptotic protein Bcl-2," Open Chem., 2018; 16(1): 591–604.
- [38] Al-Khazraji S, "In - Vitro Study of Cytotoxic Effect of *Cydonia Oblonga* Seeds Extract on Some Cancer Cell Lines," Int. J. Sci. Technol., 2013; 8(4): 74–79.
- [39] Alizadeh H, Rahnema M, Semnani SN, and Hajizadeh N, "Detection of Compounds and Antibacterial Effect of Quince (*Cydonia oblonga* Miller) Extracts in vitro and in vivo," J. Biol. Act. Prod. Nat., 2013; 3(5-6): 303–309.
- [40] Shaida B, Singh NB, and Singh K, "In-Vitro Evaluation of Anti-Inflammatory and Anti-Microbial Properties of Ethanolic Extract of *Cydonia Oblonga* Seeds," J. Sci. Ind. Res., 2020; 79(1): 49-51.
- [41] Islam F, et al., "Chemical and biological properties of *Cydonia oblonga* L. flour: a concurrent review," Int. J. Food Prop., 2023; 26(1): 1167–1176.
- [42] Pereira A, et al., "Upcycling Quince Peel into Bioactive Ingredients and Fiber Concentrates through Multicomponent Extraction Processes," Antioxidants (Basel), 2023; 12(2): 260.
- [43] Cerempei A, Mureşan EI, Cimpoeşu N, Carp-Cărare C, and Rimbu C, "Dyeing and antibacterial properties of aqueous extracts from quince (*Cydonia oblonga*) leaves," Ind. Crops Prod., 2016; 94: 216–225.
- [44] Baran M, "Synthesis, characterization and investigation of antimicrobial activity of silver nanoparticles from *Cydonia oblonga* leaf," Appl. Ecol. Environ. Res., 2019; 17(2): 2583–2592.

DigiHuman: A Conversational Digital Human with Facial Expressions

Kasım ÖZACAR^{1*}, Munya ALKHALIFA²

^{1,2} Computer Engineering Department, Engineering Faculty, Karabuk University, Karabuk, Türkiye

^{*1} kasimozacar@karabuk.edu.tr, ² munia.khalifa@gmail.com

(Geliş/Received: 24/05/2023;

Kabul/Accepted: 06/09/2023)

Abstract: Recently, Artificial Intelligence (AI)-powered chatbots and virtual humans have assumed significant roles in various domains due to their ability to interact with users and perform tasks based on their intended purpose. Virtual humans have received considerable attention in various industries due to their lifelike human appearance, behaviour, and ability to convey emotions, especially in virtual reality contexts. Conversely, chatbots are finding use in a wide range of applications and represent a promising feature of human-computer interaction due to their efficient communication with humans. Therefore, this study aims to develop a real-time chatbot that can effectively convey emotions through facial expressions, thereby promoting realistic communication. To achieve this, several advanced AI models were employed to address different aspects, including speech recognition, emotion synthesis, and response generation. The methodology, models used, components, and results are explained in detail, and the results of the user study are also presented.

Keywords: human-computer interaction, artificial intelligence, virtual human, chatbot, conversational agent.

DigiHuman: Yüz İfadeleri ile Konuşan Dijital Bir İnsan

Öz: Yapay zeka destekli sohbet robotları ve sanal insanlar, oluşturulma amaçlarına bağlı olarak farklı görevleri yerine getirmek için kullanıcılarla aralarında iletişim kurma yetenekleri nedeniyle son zamanlarda birçok uygulamada önemli rol üstlenmişlerdir. Sanal insanlar, gerçekçi insan formları, davranışları ve özellikle sanal gerçeklik ortamında deneyimlendiklerinde duygusal geri bildirim iletme yetenekleri nedeniyle farklı sektörlerde büyük ilgi görmektedir. Diğer taraftan, sohbet robotları insanlarla iletişim kurmadaki yüksek verimlilikleri nedeniyle insan bilgisayar etkileşimi için en umut verici örneklerden biri olarak çeşitli uygulamalarda kullanılmaktadır. Bu nedenle, bu çalışmada başarılı bir iletişim ve gerçekçi davranış sergilemesi için yüz ifadeleri aracılığıyla duyguları iletme yeteneğine sahip bir gerçek zamanlı sohbet robotu oluşturması amaçlanmıştır. Bunun için sırasıyla; konuşma tanıma, duygu sentezi, yanıt üretme gibi çeşitli özellikler için çoklu geliştirilmiş yapay zeka modelleri uygulanmıştır. Çalışma kapsamında yaklaşım, kullanılan tüm modeller, bileşenler ve sonuçları kapsamlı bir şekilde açıklanmış ve kullanıcı testleri sonuçları da açıklanmıştır.

Anahtar kelimeler: insan-bilgisayar etkileşimi, yapay zeka, sanal insan, chatbot, konuşma ajanı.

1. Introduction

Metaverse technology is expected to contribute to and shape numerous substantial areas of our lives, including social media, commerce, education, and entertainment, and consequently, Metaverse requires intelligent conversational agents capable of delivering human-like responses to serve users in this evolving digital landscape. Furthermore, these agents are expected to imitate human behaviour within conversations, enabling them to comprehend human language, engage in responses within the appropriate context, and even grasp his/her feelings. Although numerous conversational agents or chatbots designed for conversation are available, they typically revolve around text or speech interactions and often lack certain human-like qualities. For instance, these bots lack a physical embodiment, leading to the absence of bodily gestures. Additionally, they may lack distinct personalities and fail to engage with individuals on an emotional level.

When considering an effective exchange between two people, persuasion and emotion come to mind. Persuasion is achieved primarily in face-to-face communications because the conversation mainly affects facial gestures and expressions, besides other body gestures like head nodding and hand gestures. Accordingly, an intelligent agent should be able to provide relevant information and respond to user questions and comments. It should conduct communication through persuasive responses with appropriate facial expressions and gestures. Emotions and facial expressions lead us to a hot topic: Human-Computer Interaction (HCI) introduced: virtual humans or digital humans. Virtual humans or embodied agents enhance HCI by taking advantage of pre-existing social skills, such as body language, and making interactions seem more natural. Therefore, the objective of developing a more human-centered and engaging speech-based face-to-face interactive system will lead to the term Embodied Conversational Agent (ECA). ECA will be represented by a character looking like a human, talking, understanding, expressing emotions, and responding to you. The more realistic an embodied agent is, the

* Corresponding author: kasimozacar@karabuk.edu.tr. ORCID Number of authors: ¹ 0000-0001-7637-0620, ² 0000-0003-0364-201X

more influential communication and face-to-face communication leave a very good impression on people and will serve the industry better.

Building such a high-fidelity agent requires employing both HCI and AI solutions. Realistic natural interaction and emotional intelligence are essential [1]. Consequently, we need to implement multiple improved models for various features such as speech recognition [2], emotion synthesis [3], response generating [4], and facial animation as they are very needed [5]. Despite creating or employing Convolutional Neural Network (CNN) and Natural Language Processing (NLP) models, in this paper, we concentrate on the problem of building human-agent real-time interaction with the ability to convey emotions through facial expressions to establish successful communication and realistic behaviour. The paper's contributions are structured as follows:

- Introduction of conversational digital human with facial emotions.
- A literature review and discussion of prior research in the field.
- A comprehensive explanation of our approach encompasses all the constituent models, components, and achieved outcomes.
- Conducting a user study to evaluate the system's overall performance.

2. Literature Review

At present, technologies and daily life applications are moving towards the digital trend. Embodied Conversational agents are considered a worldwide example that has been around for a very long time for digitalizing human behaviour and interactions. Conversational activities among people involve complex behaviour expressed through speech and gestures, which include facial expressions, hand gestures, head movement and eye gaze. This led to the idea of modelling the human body as well as making it intelligent by combining two systems together: AI and HCI, for many different purposes in different applications and businesses.

An ECA acts as an intelligent entity through conversations by understanding humans and responding back to them using text or voice, both of which are the most commonly widespread techniques. We can find ECAs becoming quite popular through wide industry applications, for example, education, health, business, information retrieval and e-commerce [6]. The main part of an ECA is the chatbot, which is a machine model that processes and simulates the flow of human conversation either in close-domain or open-domain. Chatbots are not necessarily but mostly integrated into interfaces to facilitate user-computer interaction either through text, speech, or both.

Throughout history, chatbots have greatly improved since the date that first enlightened the world with the idea of chatbot, which was in 1950 when Alan Turing suggested the Turing Test, stating the well-known question, "Can machines think?" since then, researchers have begun to compete in introducing different chatbots (Turing, 1950). Chatbots started as text chatbots and are still being used in many industries. Then, speech chatbots were introduced and worked mostly as virtual assistants. To choose the right bot for the industry, many features should be considered, including the domain, the way of processing input and producing output, and its goal [7].

Eliza was the first chatbot developed in 1966, and it aimed to be a psychotherapist. Early Conversational agents such as Eliza depended on predefined simple pattern matching [8]. In 1972, PARRY was introduced to the world and was considered an improvement over ELIZA [9]. After that, in 1995, ALICE, or the Artificial ELinguistic Internet Computer Entity, was developed and was considered to be the most human computer. ALICE introduced AIML, which stands for Artificial Intelligence Markup Language, which is a markup language for manual-defined conversations. Another text-based chatbot is SmarterChild [10], which was developed in 2001 to be used in messenger applications.

Chatterbot software, such as Cleverbot, has been introduced commercially. It uses approaches such as rule-based response generation but is enhanced with techniques for learning new responses. After that came the next step of chatbot creation, which was virtual personal assistants. They became quite well-known and used in daily life tasks by people as they interact with them using voice. The most known examples of virtual assistants are Apple Siri, Amazon Alexa, Microsoft Cortana, IBM Watson, and Google Assistant.

Creating virtual characters necessitates the use of a variety of research skills. Different skills are needed to combine multiple modules within one agent. What plays the most essential role in communication and conversation is the face, which transmits verbal and nonverbal knowledge. Pre-research has introduced new tools like Xface [11], which is an open-source project and a tool to build Embodied Conversational Agents (ECAs) [12].

Text-based and vocal Conversational agents have gained fair popularity in virtual assistant applications. However, various studies, projects, and workgroups have shown that to enhance the reality of interactions with Information and Communications Technology (ICT) systems, it is better to employ embodied interactions. Previous research and projects were done employing a virtual human-like MiraculousLife [13] and CaMeLi [14], which led to the result that the avatar should express more with its facial expressions and give more appropriate reactions. Even though [9] developed successful avatars for virtual social worlds, they lack facial expressions, making the agent seem dull and emotionless.

Due to the rapidly increasing interest in chatbots, particularly post-2016, researchers are striving to develop chatbots that closely emulate human conversational behaviour, resulting in a more human-like interaction. This led to the concept of integrating chatbots into virtual humans. This integration aims to improve human-machine interaction through conversation domains and behaviours, including expressions, acting, and animations. However, sometimes, they are not considered entirely intelligent even though they have bodies and talking heads [15].

Prior studies have not successfully met the essential criteria for enabling a human-like, face-to-face conversation within an intelligent Human-Computer Interaction (HCI) system interface. This goal necessitates establishing the external interface level functions combined with the internal logical level that controls how the system will operate in a behavioural way. In other words, we should take into consideration that a system must give most of the rights that a conversation would consist of between two people, including speech domain, verbal and non-verbal speech acquisition through voice and gestures, and the ability to interrupt while talking and convey emotions.

Although digital humans have been adapted for the entertainment industry, including movies and video games, they are now becoming more prevalent and involved in our daily lives. However, the field still suffers from problems in giving the avatar the concept of a lifelike human. As a result, the field of digital human research continues to improve its realism and overcome its current limitations. Therefore, this research pursues several areas that utilize novel state-of-the-art techniques related to the socialization of digital humans.

The first step towards achieving a real human is its appearance, which falls in the field of computer graphics, and this requires the use of comprehensive deep techniques for remaking a human as a digital one. The choice of tools and techniques is not direct. By following [16], we can understand the difference between the high-quality, expensive approach and the less one in the remaking stage, thus leading to knowing how to relate perception to quality. Despite the focus on external appearance, other research, like [17], focuses on the anatomical side that includes features like skin, muscles, and bones.

Another fact to add is the focus on the balance between the body and the model itself. Alvarado et al [18] did this by proposing a rendering technique to model the deformation of the ground as a result of movement. Nonetheless, a lifelike digital human does not occur through the physical features only but through socialism as well. [18] addressed the aspect of real communication by engaging AI deep learning methods.

With this challenging compilation, it is evident that HCI has advanced so much in recent years and improved in many digital human-related applications and aspects such as lip-syncing and gestures. This inspired us to make use of such novel techniques and try to present a new ECA that will focus on multiple conversational behaviours through verbal speech to non-verbal speech. Our primary objective is to provide a wide speech domain chatbot that will cover a variety of possible topics along with emotion-conveying ability. Our system is considered a combination of skills and novel techniques that are presented by former research, all integrated as one system model manifested as a virtual human in the most straightforward possible way.

3. A Conversational Digital Human with Facial Expressions

Our approach is an embodied conversational agent that can understand and convey emotions, interact with users, and use facial expressions. This requires deploying multiple neural network models. We show our system structure and workflow in Figures 1 and 2, which consist of two parts. In Figure 1, we have three models combined that work simultaneously. These models are speech recognition, response generation, and emotion recognition. We get two inputs when a user talks to the avatar: the utterance that the user said and the face of the user in the video frames while saying that utterance. After that, we convert the input speech to text using the speech recognition model for the avatar to understand what the user says and replies. Then, the resulting text will be fed to the response generator to be analyzed, and a proper reply will be generated as the first output.

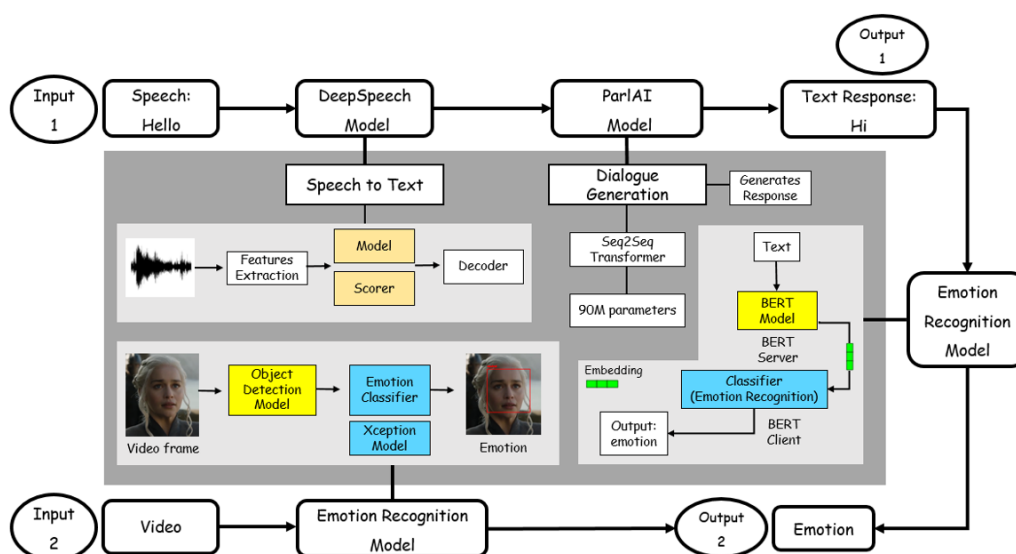


Figure 1. Our system’s workflow between the models and with their architectures.

At the same time, our efforts are directed at establishing suitable emotions for the avatar's presentation. Thus, the system will process two inputs: images and text. There will be two emotion outputs, each extracted from different models: the CNN model and the NLP model. CNN will output the first emotion by taking video frames as input, and then the second emotion will be extracted from the response text by the NLP model. Having two similar emotions will be fine; however, we pick the one with a more significant probability if they differ.

In the second part of the system, we work on the Unity Game Engine's side. The two outputs from the previous part are sent to Unity as inputs. As shown in Figure 2, the system synthesizes the text that generates the speech for the response; it also takes the emotion to map the appropriate facial expression through blendshapes and runs the lip-syncing feature in the project. As a result, the avatar speaks back to the user while showing emotion on its face.

3.1. Emotion recognition

Recognizing human emotion is a key component in the study of human-computer interfaces (HCIs) to empathize with people [12,19-20]. Conveying emotion has a crucial contribution to effective human-computer interaction [21].

As the agent should act realistically, we aim to get the accurate emotion to map the appropriate facial expression over the agent's face while conversing with the user. For this purpose, we followed two techniques to combine their results. During the prediction, we compare the probability of predictions done by each predictor to obtain the more accurate one.

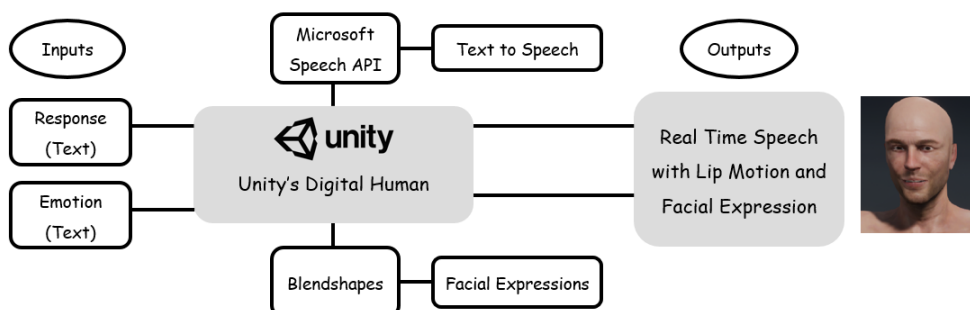


Figure 2. The architecture shows the Unity Game Engine part when combined with result of the deep learning model.

Table 1. Evaluation metrics for text-based emotion recognition model.

F1-Score	0.93
Precision	0.87
Recall	0.83
Accuracy	0.84

3.1.1. Text-based emotion recognition

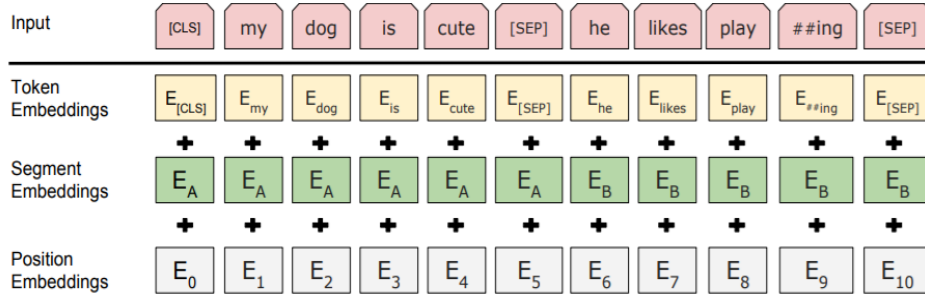


Figure 3. Input representation in BERT includes the sum of embeddings of tokens, segmentation embeddings, and position embeddings, denoted as (E) [20].

When talking about analyzing text, then Sentiment Analysis comes to mind, which is a method that uses Natural Language Processing (NLP) to extract beliefs, thoughts, views, and emotions from the text but associates three categories, like "positive" or "negative" or "neutral," for classifying the views regarding a text [22]. Following the same scheme, we get the idea of emotion recognition, which involves analyzing the text and recognizing what type of emotion it implies.

Our agent will respond to the user with a sentence, and to accomplish this, we employ an NLP model that analyzes the response. This analysis aims to detect any hidden emotion within the text, ultimately leading to the generation of an appropriate facial expression corresponding to that emotion.

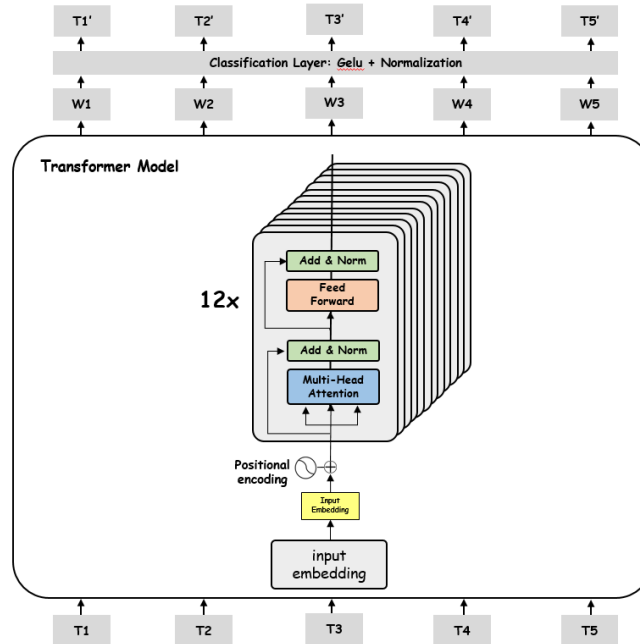


Figure 4. The Transformer (T) based BERT base architecture with twelve encoder blocks.

For this purpose, we fine-tuned Google's BERT pre-trained model that Google AI language researchers recently introduced as a Machine Learning technique built upon state-of-art techniques for NLP tasks [23]. ktrain framework [24] was used as a wrapper for the model to facilitate and accelerate the BERT training process.

The reason for choosing BERT is because it is pre-trained on a massive data corpus, giving it a large knowledge repository and substantial contribution to the NLP community. BERT can be downloaded and fine-tuned on any dataset for NLP tasks. The deep bidirectionality of BERT allows it to learn information from both sides, right and left, as displayed in Figure 3, of the context within the training step, which utilizes adapting it to achieve NLP tasks [25].

BERT architecture is illustrated in Figure 3, which simplifies how the input is processed. In addition, it is essential to mention that BERT has two architectures, BASE and LARGE, that differ in the count of heads in attention modules in encoders, parameters, layers, and units in hidden layers. Our work uses the BERTBASE, which consists of the following values: *parameters=110M, encoders=12, hidden layers units=768, heads in attention modules=12*. In accordance with GLUE benchmarks, BERT performed better than its predecessors. Although BERTLARGE improved BERTBASE's performance, we used the basic one because the dataset is not extremely large, so it does not require a vast network model such as the large BERT version.

BERT is widely used on the basic NLP tasks of classifying a piece of text, which suits our aim in this part of the work as we aim to categorize sentences into emotions classes. In Figure 4, we summarize the architecture of BERTBASE model that we deployed.

We used the following for training the model:

- Ktrain wrapper for Keras,
- Dataset combines three main datasets: daily dialogue, emotion-stimulus, and isear, which includes 7934 inputs for training and 3393 inputs for validation,
- learning rate = 2×10^{-5} , which follows the 1-cycle learning rate policy [26],
- 20 epochs,
- activation function = GeLU.

The resulting output will be one of seven emotions: happy, sad, angry, scared, neutral, surprised, and disgusted. The model achieved 83% accuracy, and the evaluation metrics for the text-based emotion recognition model are shown in Table 1; the evaluation metrics for the real-time video-based emotion recognition model are shown in Table 2, respectively.

3.1.2 Video-based emotion recognition

Another approach is to make the agent draw an expression similar to the user's expression by understanding how the user feels. For an appropriate reaction toward a human, the agent will detect the emotion through the expression revealed on the human's face because it is asserted that video-based facial expression is the most informative method for the machine's perception of emotions [27].

This part of the work requires using two models: one for detecting the human's face and the other for detecting the emotion extracted from the human's facial expression. We use the Cascade Classifier for face detection, a machine-learning model for image object detection. For detecting emotions, we operate on a CNN model to learn features and classify emotions.

For this purpose, we fine-tuned one of ImageNet's pre-trained models [28], the Xception model [29], which is pre-trained on the ImageNet database. ImageNet is an image recognition project aiming to classify an image into up to 1000 categories. ImageNet's Xception model consists of 29 layers and is extended from the Inception model architecture but uses depthwise separable convolutions instead of the standard Inception modules; therefore, it scored higher accuracy than other models such as VGG16, VGG19, ResNet50, and Inception V3.

We illustrate the workflow of the Xception architecture in Figure 5. For fine-tuning the model, we used the following:

- fer2013 dataset = 35.9k images. 80% is for training, and 20% is for validation.
- Keras library
- 100 training epochs
- Adam optimizer, learning rate = 0.001 and is reduced when validation loss is not improving
- ReLU and Softmax activation functions

It is worth mentioning that we generated real-time data augmentations for the images using Keras's built-in class ImageDataGenerator. The output will fall into one of these emotion categories: "anger," "disgust," "fear," "joy," "sadness," "surprise" and "neutral." Evaluation methods have been applied again to this model; the resulting accuracy is 76%, and other measures are displayed in Table 2.

Table 2. Evaluation metrics for real-time video-based emotion recognition model.

F1-Score	0.75
Precision	0.83
Recall	0.68
Accuracy	0.76

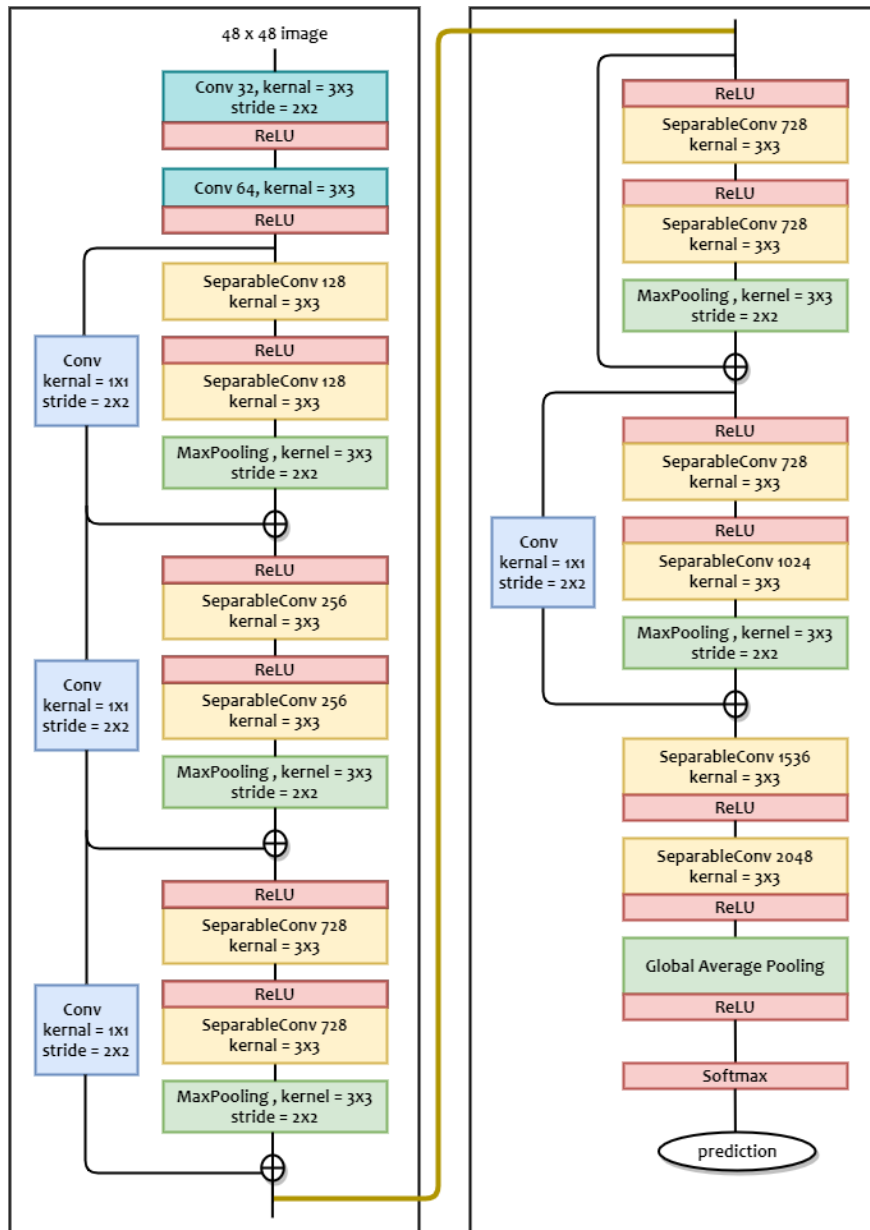


Figure 5. Architecture of Xception network model used for emotion detection from video.

3.2. Dialogue generation

Building an open-domain chatbot is considered a challenge in the ML field, requiring extensive research and a long time. Therefore, we avoid going through the process of building one, and instead, we use the model proposed by [30], which is shared by the ParlAI framework [31]. In this paper, we focus on the Transformer, which allows us to build different chatbots and then fine-tune them. We chose the Generator model, which in its architecture is almost equivalent to the standard seq2seq model introduced by [32], but huger provided three sizes (90M, 2.7B, 9.4B). Rather than retrieving the replicates from a fixed dataset, the generator generates the replicates. We use the 90M model for our project.

The animation of the digital human face involves mapping emotion-relevant facial expressions and applying lip movements to synchronize them with speech when the agent speaks.

3.3. Facial animation

3.3.1. Emotional facial expression

A human's perception, intent, and verbal and nonverbal expressions are expressed effectively through emotional facial expressions; thus, this part of the work is a key major for completing the project. Multiple techniques have been introduced to generate animations, like blendshapes [33-34], bone positions, or a facial action coding system (FACS) [35].

Blendshapes are a well-known technique within digital productions. We can define a blendshape as a geometry deformation for creating looks for the mesh, which means it is originally a group of deformed versions of the mesh blended with the neutral or the regular version of the mesh. Besides being practical for representing various appearances for models, such a technique is also very effective and common in animations and facial expressions.

A blendshape is a linear union of facial targets to create expressive facial expressions and muscle actions [36]. In the virtual human project, we can configure 6 facial expressions for the fundamental emotions according to [37] basic emotions: joy, sadness, anger, fear, surprise, and disgust. We access these emotions through coding to apply proper facial expressions during conversations between the user and the virtual human.

3.3.2. Lip syncing

Lip synchronization means matching lip movement with the speech sound. Lip syncing consists of combining three main stages: facial muscle movements, phonemes, and visemes. We will briefly explain each of them: The phoneme is the smallest unit in a language, like the m sound in Mother and th in thread, whereas visemes are the visual representations of phonemes and are used for approximating visual similarities between phonemes. Therefore, the hierarchy of facial muscle movements, phonemes, and visemes generates the following workflow: facial muscle movements create the phonemes, and phonemes turn into visemes.

Though the virtual human project provides lip synchronization to be generated both in real-time and from a pre-recorded audio clip, we aim for real-time lip animation, which means synchronizing sound live from a microphone input with accurate lip movement to accomplish a virtual computer-generated human, which accordingly is done through blendshapes again.

3.4. Speech-to-text

Baidu's DeepSpeech [38] is a deep learning neural network model architecture that manipulates the process of Automatic Speech Recognition and gets an implementation by Mozilla [39], which uses Tensorflow for more straightforward implementation and will be deployed for our system to understand and convert the user's speech to text. The input of the model is the spectrogram, and the output will be a sequence of character probabilities. The architecture includes 3 non-recurrent layers, one bidirectional recurrent layer, and one non-recurrent layer.

Achieving speech-to-text conversion requires the conversion of speech from sound waves to electrical waves. Then, once an analog-to-digital converter converts it to digital data, models can start working on audio to convert it into text.

The hidden Markov Model (HMM) is a widely accepted approach to handling tasks related to speech recognition. Fortunately, there are Python APIs that provide speech recognition services. Through Python, we can get speech recognition packages such as PocketSphinx, Google Cloud Speech, Watson Developer Cloud, and SpeechRecognition.

From the previously mentioned packages, we pick SpeechRecognition, which is a library that comprises multiple APIs for speech-related tasks, for instance, the Google speech API. This API supports the default API

key integrated within the library. To choose the Google web speech API, we set the `recognize_google()` method for the Recognizer class.

3.5. Text-to-speech

To achieve the agent response to humans, we need to synthesize the speech, producing audible output. We preferred using Unity's plugin to synthesize the speech from within Unity instead of deploying a model like Wavenet [40]. To achieve this objective, we utilized the "Microsoft Windows Text-to-Speech API" plugin. This plugin involves creating a wrapper around the Microsoft Speech API in Unity. The underlying technology relies on Windows COM capabilities, introduced with Windows Vista. When the virtual human application in Unity starts running, this wrapper launches the text-to-speech engine, resulting in speech by reading the generated text through the provided function.

3.6. Integrating into unity

Starting with the Unity part, some models need to work in parallel, meaning that running them together at once is required. For instance, when the user is talking, we already know that the user's speech will be converted into text immediately once the user starts finishing a sentence. Also, while the user is talking, we know that emotions appear on that person's face, which means that real-time video capturing has started detecting the emotion from the face. Thus, while the user's speech is being converted with the speech recognition model, the video-based emotion recognition model will also work to extract facial expressions for emotion. To make two processes run together, we used threading in Python. Threads improve performance through parallelism, so we use them to run models together to get outputs simultaneously.

After obtaining the outputs, we utilize communication protocols in networking to send these outputs data with Python-Unity socket communication. Data will be sent to a port through sockets in Python, and then we use the UDP client in Unity to read this data from a socket. We have emotion and response as text data to be sent from Python to C# in Unity. Thus, the C# client will send a connection request to the Python server, and when accepted, the server creates a thread for the client that runs in the background to listen for the requests. For each server client, a socket will be responsible for sending and receiving the data between them. The rest of the output process will be held within Unity C# scripts. All models were combined in one Python virtual environment using Anaconda's command prompt and were called from one Python script, respectively. Using this method, models will keep running and give results in real-time interaction with the agent.

4. User Study

In our study, participants interact with the agent for 10-15 minutes. We first specify tasks and assign each participant a task to carry on the conversation with the agent. Participants wore a Meta Quest 2 Virtual Reality device with a wired connection to start a conversation with the embodied agent. After the conversation, we let the participants give their feedback by filling out a survey consisting of 10 questions or themes that concentrate on several sides of the system to evaluate the overall performance from the users' point of view. Participants followed the Likert scales for filling out the survey, composed of the following scales: strongly disagree, disagree, neutral, agree, and strongly agree, by spending approximately five minutes to finish, concluding the study in twenty minutes total time. The statements and the tasks are shown in Table 3.

We recruited 6 participants (4 females) with an average age of 24 to 30 (Mean:25.1). During the study, they were seated singly in a room while running the system on a PC opposite them. Headphones with microphones were given to the users to talk with the agent. Each user was given a task to talk about with the agent after introducing each. As summarized in Table 3, the first user gets to talk about the first task, which is personal hobbies and interests. Then, the second user talks about movies and video games. The third user talks about holidays and travelling. The fourth user talks about personal issues and problems. The fifth user generally talks about people and what he hates and loves, and finally, the last user asks the agent personal questions and answers in the case being asked.

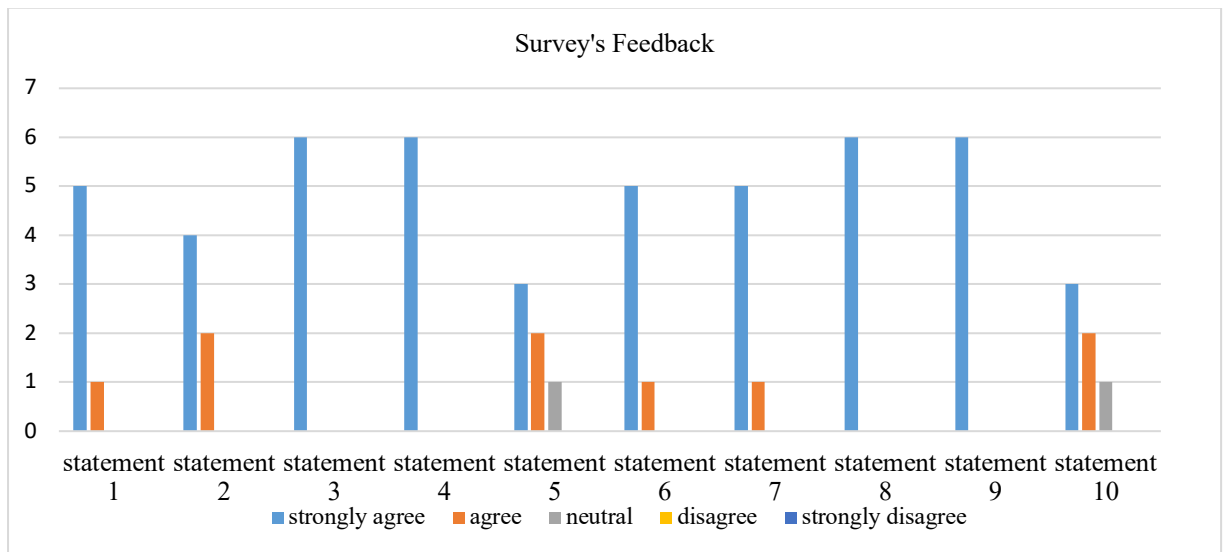


Figure 6. The results of the survey are shown as a graph. For the 1st statement, 5 users strongly disagree, while only one agrees. For the 2nd statement, 4 users strongly disagree, but 2 agree. For both the 3rd and 4th statements, all participants strongly agreed. In the 5th statement, 3 strongly disagreed, 2 agree, and 1 gave a neutral response. For the 6th and 7th statements, 5 strongly agree, and 1 agrees. All participants strongly agreed on the 8th and 9th statements. For the 10th statement, 3 strongly agrees, 2 agree, and 1 is neutral. In all statements, none of the users gave negative feedback by disagreeing or strongly disagreeing.

Table 3. The list of themes or statements asked in the survey (top). The list of tasks given to users to talk about with the agent (bottom).

Statement 1	The agent has human-like interaction.
Statement 2	The agent was persuasive in interaction.
Statement 3	The agent was entertaining and not dull.
Statement 4	The conversation was not boring.
Statement 5	The agent provided quick responses
Statement 6	The agent replied with responses related to the task
Statement 7	The agent provided accurate answers responses.
Statement 8	The agent was expressive in emotions.
Statement 9	The agent reacted to the context with proper emotions.
Statement 10	The overall system, including emotions, conversation, and interaction was realistic.

Task 1	Personal hobbies and interests
Task 2	Movies and video games
Task 3	Holidays and travelling
Task 4	Personal issues and problems
Task 5	People, things to hate and love
Task 6	Personal questions.

5. Results and Discussion

Applying expressive and emotional interaction is the key insight of our work to generate a realistic Conversational agent. To do this, we conducted a user study by arranging conversations between the avatar and multiple users to determine how convincing our model was. As a result, many of the users were satisfied as most of the participants gave positive feedback, proving that our multi-modal avatar can be successful but requires more improvement; we believe that it will make it deployable in many industries for particular goals. Results are summarized in Figure 6, which illustrates the participant's feedback on every theme.

Going through these ratings and starting with the first statement, which refers to how much the digital agent was able to deliver a real interaction, five of the users were fully satisfied with the human-like behaviour by strongly agreeing on it, and more precisely, it was approved in terms of the lip-syncing ability. On the other hand, one person rated the agent with a normal agreement, elaborating that the agent should act differently from one user to another.

Regarding the second statement, which discusses how persuasive the agent was, we received positive feedback from all subjects, but only two of them saw a lack in the persuasion part. These two users commented on the lack of body language during the conversation. Their expectations included hand gestures and head movements to indicate agreement or disagreement when the avatar responded to a question. Despite this, the agent was still approved in the name of entertainment, with all users strongly agreeing. Without a doubt, the key to a successful end-to-end conversation is to have interesting topics, a variety of ideas to talk about, and non-ending responses that prove the agent is not acting boring or dull.

For the fifth statement, we asked the subjects for their opinion on the speed of the agent's responses. One user found it slow during some answers, to which he pointed out that a human's reaction is naturally fast whenever he or she is asked. We also noticed that another user had chosen the "agree" feedback for this, for which he emphasized that there were some moments when he felt that the agent was lagging in the answer as if it didn't understand the question correctly or it took a few seconds to find a correct answer. He also justified this by saying that this is still something that can happen with people because sometimes it takes a moment to think about what to say. For the next ratings, we took the accuracy of the conversation into account and asked our subjects to give their feedback.

Regarding statements 6 and 7, one user gave a less agreeable opinion on both points because she found that one of the answers was not what she expected for her question. This might have happened because the question had a metaphor, and the agent was not able to process the metaphor. However, we believe that this is normal in our case, as the bot is trained on normal everyday conversation data, not deep literature data, and the dataset itself can improve this.

In our study, our focus was emotions. Thus, we proposed two questions on whether the agent was expressive about his feelings and if he was successful in conveying them properly according to the context. All users gave strongly agreed positive feedback. In the final stage of the test, we asked for the final opinion of each participant about the system, including all aspects and whether it was considered too real for them. Though the overall ratings were acceptable as we did not receive any negative feedback, the "agree" and "neuter" votes were still because the system was slow in some reactions and overall lacked gestures.

With this, we conclude our discussion, considering the previous results and realizing that our proposed system will need improvement in terms of movement, whether head or hand gestures. In addition, it should have a whole body to give it more advantages, and it should create its personality like any other natural person has a personality.

5. Conclusion

As machines have become a part of our lives, serving us in every industry, machines need to communicate with humans and enhance their social capabilities. To achieve realistic natural communication and effects on users, the machine or the bot should mimic natural human behaviour and hold humane aspects such as human voice, chatting, emotions, gestures, and expressions. Therefore, this study has demonstrated the potential of combining various advanced AI models to create open-domain conversational chatbots that not only communicate efficiently with users but also provide a friendly virtual avatar and establish realistic interaction with users by conveying emotions through facial expressions. To achieve this, we combined a virtual human with multiple models, each responsible for a task, including speech understanding, speech generation, emotion understanding, emotion generation, and chatting. Although the preliminary study's findings suggest that users generally found their interactions with open-domain conversational virtual avatars to be acceptable, it is evident that additional enhancements are necessary to make these interactions even more lifelike and realistic.

We plan to improve the interaction of the avatar in our future work by providing more realistic interactions with a whole body with more gestures.

References

- [1] Robert PH, König A, Amieva H, Andrieu S, Bremond F, Bullock R, Ceccaldi M, Dubois B, Gauthier S, Konigsberg pa, nave s. recommendations for the use of serious games in people with Alzheimer’s disease, related disorders and frailty. *Frontiers in Aging Neuroscience*. 2014; 6:54.
- [2] Xiong W, Wu L, Allea F, Droppo J, Huang X and Stolcke A. The Microsoft 2017 conversational speech recognition system. In: 2018 IEEE International Conference on Acoustics, Speech and Signal Processing (ICASSP); 15-20 April 2018; Calgary, AB, Canada. pp. 5934-5938.
- [3] Skerry-Ryan RJ, Battenberg E, Xiao Y, Wang Y, Stanton D, Shor J, Weiss R, Clark R, Saurous RA. Towards end-to-end prosody transfer for expressive speech synthesis with tacotron. In: International Conference on Machine Learning; 10-15 Jul 2018; Stockholm, Sweden. pp. 4693-4702.
- [4] Zhang WE, Sheng QZ, Alhazmi A, Li C. Adversarial attacks on deep-learning models in natural language processing: A survey. *ACM Transactions on Intelligent Systems and Technology (TIST)*. 2020 Apr 1;11(3):1-41.
- [5] Hyneman W, Itokazu H, Williams L, Zhao X. Human face project. In: *ACM Siggraph 2005 Courses*; 31 Jul 2005; Los Angeles, CA, USA: pp. 5-es.
- [6] Shawar BA, Atwell E. Chatbots: Are they Really Useful? *Journal for Language Technology and Computational Linguistics* 2007; 22(1):29-49.
- [7] Adamopoulou E, Moussiades L. An overview of chatbot technology. In: *IFIP international conference on artificial intelligence applications and innovations*; 5–7 June 2020; Neos Marmaras, Greece: pp. 373-383.
- [8] Griol D, Sanchis A, Molina JM, Callejas Z. Developing enhanced conversational agents for social virtual worlds. *Neurocomputing*. 2019;354: 27-40.
- [9] Weizenbaum, J. ELIZA—a Computer Program for the Study of Natural Language Communication between Man and Machine. *Commun.* 1966, 9(1), 36–45.
- [10] Molnár G, Szücs Z. The role of chatbots in formal education. In: *IEEE 16th International Symposium on Intelligent Systems and Informatics*; 13-15 Sep 2018; Subotica, Serbia. pp. 197-202.
- [11] Balci K, Not E, Zancanaro M, Pianesi F. Xface open-source project and smil-agent scripting language for creating and animating embodied conversational agents. In: *the 15th ACM international conference on multimedia*; 25-29 Sep 2007; Augsburg, Germany. pp. 1013-1016.
- [12] Aneja D, McDuff D, Shah S. A high-fidelity open embodied avatar with lip syncing and expression capabilities. In: *2019 International Conference on Multimodal Interaction*; 14-18 Oct 2019; Suzhou, China. pp. 69-73.
- [13] Stainer-Hochgatterer A, Wings-Kölgen C, Cereghetti D, Hanke S, Sandner E. Miraculous-life: An avatar-based virtual support partner to assist daily living. In: *ISG 2016 World Conference of Gerontechnology*; 28-30 Sept 2016; Nice, France. pp. 95-96.
- [14] Nijdam NA, Konstantas D. The CaMeLi framework—a multimodal virtual companion for older adults. In: *Intelligent Systems and Applications (IntelliSys 2016)*: 21–22 September 2016; London, UK. pp. 196-217.
- [15] Don A, Brennan S, Laurel B, Shneiderman B. Anthropomorphism: from ELIZA to Terminator 2. In: *the SIGCHI conference on Human Factors in Computing Systems*; 1 Jun 1992; San Francisco, CA, USA. pp. 67-70.
- [16] Bartl A, Wenninger S, Wolf E, Botsch M, Latoschik ME. Affordable but not cheap: A case study of the effects of two 3D-reconstruction methods of virtual humans. *Front. Virtual Real.* 2021;2: 694617.
- [17] Komaritzan M, Wenninger S and Botsch M. Inside humans: creating a simple layered anatomical model from human surface scans. *Front. Virtual Real.* 2021; 2:694244.
- [18] Regateiro J, Volino M and Hilton A. Deep4D: a compact generative representation for volumetric video. *Front. Virtual Real.* 2021; 2:739010.
- [19] Liu Z, Shan Y, Zhang Z. Expressive expression mapping with ratio images. In: *the 28th annual conference on Computer graphics and interactive techniques*; 1 Aug 2001; Los Angeles, CA, USA. pp. 271-276.
- [20] Queiroz RB, Cohen M, Musse SR. An extensible framework for interactive facial animation with facial expressions, lip synchronization and eye behavior. *Computers in Entertainment (CIE)*. 2010;7(4):1-20.
- [21] Lee M, Lee YK, Lim MT, Kang TK. Emotion recognition using convolutional neural network with selected statistical photoplethysmogram features. *Applied Sciences*. 2020;10(10):3501.
- [22] Kharde V, Sonawane P. Sentiment analysis of twitter data: a survey of techniques. *International Journal of Computer Applications*. 2016, 139(11):5-15.
- [23] Kenton JD, Toutanova LK. Bert: Pre-training of deep bidirectional transformers for language understanding. In: *Proceedings of naacL-HLT*; Jun 2-7 2019; Minneapolis, MN, USA: pp. 4171-4186.
- [24] Maiya AS. ktrain: A low-code library for augmented machine learning. *The Journal of Machine Learning Research*. 2022;23(1):7070-5.
- [25] Alammam J. The Illustrated Transformer. <https://jalammar.github.io/illustrated-transformer>. Accessed 20 April 2021.
- [26] Smith LN. A disciplined approach to neural network hyper-parameters: Part 1--learning rate, batch size, momentum, and weight decay. *arXiv preprint arXiv:1803.09820*. 2018.
- [27] Sun Y, Sebe N, Lew MS, Gevers T. Authentic emotion detection in real-time video. In: *Computer Vision in Human-Computer Interaction: ECCV 2004 Workshop on HCI*; 16 May 2004; Prague, Czech Republic. pp. 94-104.
- [28] Deng J, Dong W, Socher R, Li LJ, Li K, Fei-Fei L. Imagenet: A large-scale hierarchical image database. In: *IEEE conference on computer vision and pattern recognition*; 20-25 Jun 2009; Miami, FL, USA. pp. 248-255.
- [29] Chollet F. Xception: Deep learning with depthwise separable convolutions. In: *the IEEE conference on computer vision and pattern recognition*; 21-26 Jul 2017; Honolulu, HI, USA. pp. 1251-1258.

- [30] Roller S, Dinan E, Goyal N, Ju D, Williamson M, Liu Y, Xu J, Ott M, Shuster K, Smith EM, Boureau YL. Recipes for building an open-domain chatbot. arXiv preprint arXiv:2004.13637. 2020.
- [31] Miller AH, Feng W, Fisch A, Lu J, Batra D, Bordes A, Parikh D, Weston J. Parlai: A dialog research software platform. In: the 2017 Conference on Empirical Methods in Natural Language Processing: System Demonstrations; 9-11 September 2017; Copenhagen, Denmark. pp. 79-84.
- [32] Vaswani A, Shazeer N, Parmar N, Uszkoreit J, Jones L, Gomez AN, Kaiser Ł, Polosukhin I. Attention is all you need. *Advances in neural information processing systems*. 2017;30.
- [33] Smith AP. Muscle-based facial animation using blendshapes in superposition. Doctoral dissertation, Texas A&M University, 2007.
- [34] Li T, Bolkart T, Black MJ, Li H, Romero J. Learning a model of facial shape and expression from 4D scans. *ACM Trans. Graph.* 2017;36(6):194-1.
- [35] Prince EB, Martin KB, Messinger DS, Allen M. Facial action coding system. 2015.
- [36] Anjyo K. Blendshape Facial Animation, *Handbook of Human Motion*. Bertram Müller. Switzerland: Springer Cham, 2018; pp. 2145–2155.
- [37] Ekman P. An argument for basic emotions. *Cognition & Emotion*. 1992;6(3-4):169-200.
- [38] Hannun A, Case C, Casper J, Catanzaro B, Diamos G, Elsen E, Prenger R, Sathesh S, Sengupta S, Coates A, Ng AY. Deep speech: Scaling up end-to-end speech recognition. arXiv preprint arXiv:1412.5567. 2014.
- [39] Mozilla DeepSpeech, <https://github.com/mozilla/DeepSpeech>. Accessed 1 May 2021.
- [40] Oord AV, Dieleman S, Zen H, Simonyan K, Vinyals O, Graves A, Kalchbrenner N, Senior A, Kavukcuoglu K. Wavenet: A generative model for raw audio. arXiv preprint arXiv:1609.03499. 2016.

Ambarzumyan Theorem for Conformable Type Sturm-Liouville Problem on Time Scales

Ayşe Çiğdem YAR¹, Tuba GÜLŞEN², Emrah YILMAZ^{3*}

¹ Department of Mathematics, Institute of Science, Firat University, Elazığ, Türkiye.

^{2,3} Department of Mathematics, Faculty of Science, Firat University, Elazığ, Türkiye.

¹ ayseyar23@gmail.com, ² tubagulsen87@hotmail.com, ^{3*} emrah231983@gmail.com

(Geliş/Received: 13/08/2023;

Kabul/Accepted: 09/11/2023)

Abstract: In this study, we give an Ambarzumyan type theorem for a Sturm-Liouville dynamic equation which includes conformable type derivative on time scales with conformable Robin boundary conditions. Under certain conditions, we prove that potential function can be determined by using only first eigenvalue.

Key words: Ambarzumyan Theorem, Conformable Derivative, Sturm-Liouville Equation, Time Scale.

Zaman Skalasında Uyumlu Tip Sturm-Liouville Problemi için Ambarzumyan Teoremi

Öz: Bu çalışmada, uygun Robin sınır koşullarına sahip zaman skalasında uyumlu türev içeren bir Sturm-Liouville dinamik denklemi için Ambarzumyan tipi bir teorem veriyoruz. Belirli koşullar altında potansiyel fonksiyonun yalnızca birinci özdeğer kullanılarak belirlenebileceğini kanıtıyoruz.

Anahtar kelimeler: Ambarzumyan Teoremi, Uyumlu Türev, Sturm-Liouville Denklemi, Zaman Skalası.

1. Introduction

A time scale \mathbb{T} is a non-empty, arbitrary, closed subset of \mathbb{R} . Time scale theory was introduced by Hilger to combine continuous and discrete analysis [1]. This theory allows generalization of existing concepts and better interpretation of physical phenomena. Especially after 2000s, this way of thinking has received a lot of attention and has applied quickly to numerous areas in mathematics. Similarly, the reflections of this idea in spectral theory began to be seen in a short time. Sturm-Liouville theory on \mathbb{T} was firstly studied by Erbe and Hilger in 1993 [2]. In this context, the properties of the eigenvalues and eigenfunctions of the Sturm-Liouville problem were discussed in many studies on \mathbb{T} for different type derivatives (see [3]-[12]). As in classical spectral theory, it is very valuable to obtain results about inverse problems in this theory. Therefore, it is aimed to provide an important literature contribution to the studies on inverse problems for Conformable Sturm-Liouville equation on \mathbb{T} in our study.

The inverse spectral problem is the problem of obtaining the coefficient functions of an operator using various data. One of these data is the set of eigenvalues obtained under the given conditions of the problem. Although there are many studies on inverse problems for different operators in classical case, there isn't much study related to inverse spectral problems on \mathbb{T} with conformable derivative. Before expressing our results for inverse problems involving conformable derivatives on \mathbb{T} , it would be useful to briefly mention the first study done on this subject for classical case.

Ambarzumyan's theorem is the first known work in the literature for the steady state Sturm-Liouville problem by Ambarzumyan, who has made very important studies in mathematical physics [13]. He considered following problem of critical importance in mathematical physics and proved that if q is continuous on $(0,1)$ and eigenvalues of the problem,

$$\begin{cases} -y''(t) + q(t)y(t) = \lambda y(t), t \in (0,1) \\ y'(0) = y'(1) = 0, \end{cases}$$

are given as $\lambda_n = n^2\pi^2$, $n \geq 0$, then $q \equiv 0$. In fact, the result obtained here is an exceptional case [13]. In general, a single spectrum is not sufficient to obtain the potential function. Notwithstanding, this study opens an important path for mathematicians studying on spectral theory.

* Corresponding author: emrah231983@gmail.com. ORCID Number of authors: ¹ 0000-0002-2310-4692, ² 0000-0002-2288-8050, ³ 0000-0002-7822-9193.

After this study, Ambarzumian type theorems have been generalized in various ways for different equations and problems. Although this theorem was an exceptional case, it gave an idea to the mathematicians working on this subject at that time that the operator could be determined using spectral data. Based on this idea, two spectra, a spectrum, a normative constant set, and finally a nodal point set were used. Freiling and Yurko have recently interpreted Ambarzumyan's theorem in a different way [14]. They proved that it is sufficient to determine q by only the first eigenvalue instead of whole spectrum and formulated Ambarzumyan's theorem as below:

- $q \equiv \lambda_0$ provided that $\lambda_0 = \int_0^1 q(t)dt$.

Later, Yurko generalized this different approach to a large class of self-adjoint differential operators with arbitrary self-adjoint boundary conditions [15]. This special type of Ambarzumyan theorem was proved by Özkan in 2018 for the Sturm-Liouville dynamical equation on \mathbb{T} (see [16]).

In this study, we discussed and proved the theorem discussed by Özkan from a different aspect using conformable derivative on \mathbb{T} . Thus, we have determined how the conformable derivative, which is one of the most useful and functional versions of the fractional derivative, works in the Ambarzumyan theorem.

2. Preliminaries

Before expressing the main results, it needs to be reminded some basic notions on \mathbb{T} [17-19]. Let $a = \inf \mathbb{T}$ and $b = \sup \mathbb{T}$. Forward and backward jump operators $\sigma, \rho : \mathbb{T} \rightarrow \mathbb{T}$ are defined by

$$\sigma(t) = \inf\{s \in \mathbb{T} : s > t\}, \rho(t) = \sup\{s \in \mathbb{T} : s < t\}$$

respectively, for $t \in \mathbb{T}$ where $a < t < b, t < \sup \mathbb{T}, \inf \emptyset = \sup \mathbb{T}, \sup \emptyset = \inf \mathbb{T}$ and \emptyset indicates empty set. If \mathbb{T} is bounded, one can write $\sigma(b) = b$ and $\rho(a) = a$. The related forward-step function is defined by [18,19]

$$\mu: \mathbb{T}^\kappa \rightarrow \mathbb{R}^+, \mu(t) = \sigma(t) - t.$$

Here, $\mathbb{T}^\kappa = \mathbb{T} \setminus \{b\}$ is bounded above and b is left-scattered; otherwise $\mathbb{T}^\kappa = \mathbb{T}$. This is often used when trading with a first-order delta derivative. Similarly, the n -dimensional version of this set can be defined. $f: \mathbb{T} \rightarrow \mathbb{R}$ is right side continuous at $t \in \mathbb{T}$ if there is some $\delta > 0$ such that $|f(t) - f(s)| < \varepsilon$ for all $s \in [t, t + \delta)$ and $\varepsilon > 0$. The set of all these functions on \mathbb{T} is denoted by $C_{rd}(\mathbb{T})$. One can define $f^\Delta(t)$ to be the value for $t \in \mathbb{T}^\kappa$, if one exists, there is a neighborhood U of t such that for all $s \in U$ and $\varepsilon > 0$

$$|[f^\sigma(t) - f(s)] - f^\Delta(t)(\sigma(t) - s)| < \varepsilon|\sigma(t) - s|.$$

f is Δ -differentiable on \mathbb{T}^κ if $f^\Delta(t)$ exists for all $t \in \mathbb{T}^\kappa$. Let $f \in C_{rd}(\mathbb{T})$. Then, there exists a function F such that $F^\Delta(t) = f(t)$, and Δ integral is constructed by

$$\int_a^b f(t)\Delta t = F(b) - F(a).$$

Now, let's examine the problem on which we have built this study and expressed by Özkan on \mathbb{T} [16].

Let \mathbb{T} be bounded, $a = \inf \mathbb{T}$ and $b = \sup \mathbb{T}$. Ozkan considered $\ell = \ell(q, h_a, h_b)$ generated by below Sturm–Liouville dynamic equation

$$\ell y = -y^{\Delta\Delta}(t) + q(t)y^\sigma(t) = \lambda y^\sigma(t), t \in \mathbb{T}^{\kappa^2}, \tag{2.1}$$

subject to boundary conditions

$$y^\Delta(a) - h_a y(a) = 0, \tag{2.2}$$

$$y^\Delta(\rho(a)) - h_b y(\rho(a)) = 0, \tag{2.3}$$

where $q(t)$ is real-valued, continuous on $\mathbb{T}, h_a, h_b \in \mathbb{T}, a \neq \rho(b), 1 + h_a \mu(a) \neq 0, 1 + h_b \mu(\rho(b)) \neq 0$ and λ is a spectral parameter [16]. The following theorem is the Freiling-Yurko version of the Ambarzumyan theorem on the time scale.

Theorem 2.1. [16] Let λ_1 be the first eigenvalue of (2.1) – (2.3). If

$$\lambda_1 = \frac{1}{\rho(b)-a} \left\{ h_a - h_b + \int_a^{\rho(b)} q(t) \Delta t \right\},$$

then $q(t) \equiv \lambda_1$ on \mathbb{T}^{κ^2} and $h_a = h_b = 0$.

The proof of this theorem was made by Özkan using the basic properties of the time scale and the dynamic equation structure. In the next section, properties of conformable derivative and integral will be expressed and Theorem 2.1 will be generalized to conformable derivative on \mathbb{T} .

3. Main Results

Different versions of the fractional derivative have been described and generalized over the years. The most common fractional derivatives are Riemann-Liouville, Caputo, Grünwald-Letnikov, Wely, Riesz. For more information about the characteristics of these fractional concepts, we refer to [20].

For these fractional derivative types, different ideas have been put forward over time due to the difficulties in the applications and the difficulties experienced. Recently, Khalil et al. give a new fractional derivative "conformable" [21]. Unlike other types, this new version satisfies properties "derivative of product and quotient of two functions". Apart from this, the chain rule, which has an important place in applications, has taken a simpler form in this derivative.

Definition 3.1. [21,22] Conformable fractional derivative of $f: [0, \infty) \rightarrow \mathbb{R}$ with order α , is defined by

$$(T_\alpha f)(t) = \lim_{\varepsilon \rightarrow 0} \frac{f(t+\varepsilon t^{1-\alpha}) - f(t)}{\varepsilon}, \quad (3.1)$$

for all $t > 0$ and $0 < \alpha \leq 1$. If f is α -differentiable on some $(0, \alpha)$, then $\lim_{t \rightarrow 0^+} (T_\alpha f)(t)$ exists and

$$(T_\alpha f)(0) = \lim_{t \rightarrow 0^+} (T_\alpha f)(t). \quad (3.2)$$

In the next theorem, we will recall the necessary and important properties of conformable derivative.

Theorem 3.2. [21] Let f, g be α -conformable differentiable at $t > 0$ and $0 < \alpha \leq 1$. Then

- i. $T_\alpha(af + bg) = a(T_\alpha f) + b(T_\alpha g), \forall a, b \in \mathbb{R}$.
- ii. $T_\alpha(t^p) = pt^{p-\alpha}, \forall p \in \mathbb{R}$.
- iii. $T_\alpha(\lambda) = 0$, for $f(t) = \lambda, \lambda \in \mathbb{R}$.
- iv. $T_\alpha(fg) = f(T_\alpha g) + g(T_\alpha f)$.
- v. $T_\alpha\left(\frac{f}{g}\right) = \frac{g(T_\alpha f) - f(T_\alpha g)}{g^2}$.
- vi. $(T_\alpha f)(t) = t^{1-\alpha} \frac{df}{dt}(t)$ when f is α -conformable differentiable.

Definition 3.3. α -conformable integral of regulated function $h: \mathbb{T} \rightarrow \mathbb{R}$ is defined by [23]

$$\int h(t) \Delta^\alpha t = \int h(t) t^{\alpha-1} \Delta t. \quad (3.3)$$

α -Conformable fractional integral of h reduces to classical Conformable fractional integral for $\mathbb{T} = \mathbb{R}$ and $\alpha = 1$ [21]. And, it reduces to indefinite integral on \mathbb{T} for $\alpha = 1$ [21]. If indefinite α -Conformable fractional integral of h order α is

$$H_\alpha(t) = \int h(t) \Delta^\alpha t,$$

then, Cauchy α -Conformable fractional integral of h is [24]

$$\int_a^b h(t)\Delta^\alpha t = H_\alpha(b) - H_\alpha(a),$$

for all $a, b \in \mathbb{T}$.

Now it is time to define our conformable problem and prove Ambarzumyan theorem on \mathbb{T} . Consider conformable Sturm-Liouville boundary value problem by

$$Ly = -T_\alpha(T_\alpha y(t)) + q(t)y^\sigma(t) = \lambda y^\sigma(t), \quad t \in [a, \rho(b)] \quad (3.4)$$

$$T_\alpha(y(a)) - h_a y(a) = 0, \quad (3.5)$$

$$T_\alpha(y(\rho(b))) - h_b y(\rho(b)) = 0, \quad (3.6)$$

where $a \neq \rho(b)$, $1 + h_a \mu(a) a^{\alpha-1} \neq 0$, $1 + h_b \mu(\rho(b)) (\rho(b))^{\alpha-1} \neq 0$, λ is spectral parameter and $L = L(q, h_a, h_b)$.

Definition 3.4. [16] The values of λ when equation (3.4) has non-zero solutions satisfying (3.5) and (3.6) are eigenvalues and corresponding non-trivial solutions are eigenfunctions. Additionally, the set of all eigenvalues for (3.4) – (3.6) is real and below bounded [18].

Definition 3.5. [16] A solution y of (3.4) has a zero at $t \in \mathbb{T}$ if $y(t) = 0$, and it has a node between t and $\sigma(t)$ if $y(t)y(\sigma(t)) < 0$.

Lemma 3.6. [3] Eigenvalues of (3.4) – (3.6) can be arranged as $-\infty < \lambda_1 < \lambda_2 < \lambda_3 < \dots$, and an eigenfunction corresponding to λ_{k+1} has exactly k generalized zeros on (a, b) .

Proof. Assume that x and y are solutions to the equations $ly + \lambda y^\sigma = 0$ and $lx + \rho_v x^\sigma = 0$, respectively where $\rho_v \in \mathbb{R}$, $1 \leq v \leq k$, and also $\tilde{x} = x + \tilde{x}_1$, $S = \frac{\tilde{x}}{y}(xT_\alpha y - yT_\alpha x)$. If $\lambda_{k+1} < \infty$, $y = y(\cdot, \lambda)$, let's assume $x = 0$, $x_v = x_v$, $1 \leq v \leq k$, $k \in \mathbb{N}_0$, $p_v = \lambda_v$, $\lambda = \lambda_{k+1}$. In this situation, $S_\alpha(a) = S_\alpha(\rho(b)) = 0$, and the rest of the proof is the similar in [3].

Lemma 3.7. $y^\sigma(a) \neq 0$ and $y^\sigma(\rho(b)) \neq 0$ provided that $y(t)$ is eigenfunction of (3.4) – (3.6).

Proof. We get

$$y^\sigma(a) = y(a) + \mu(a)a^{1-\alpha}T_\alpha(y(a)) = y(a)[1 + h_a \mu(a)a^{\alpha-1}],$$

and

$$y^\sigma(\rho(b)) = y(\rho(b))[1 + h_b \mu(\rho(b))(\rho(b))^{\alpha-1}].$$

Here by the properties of time scale calculus, we allege that $y^\sigma(a) \neq 0$ and $y^\sigma(\rho(b)) \neq 0$. Otherwise, either $T_\alpha(y(a)) = 0$ or $T_\alpha(\rho(b)) = 0$ holds by (3.4) ve (3.5). It implies that $y(t) = 0$ which contradicts to be an eigenfunction. Hence, the assumptions $1 + h_a \mu(a)a^{\alpha-1} \neq 0$, $1 + h_b \mu(\rho(b))(\rho(b))^{\alpha-1} \neq 0$ completes the proof. Now, together with the following theorem, the Freiling-Yurko version of the Ambarzumyan theorem will be expressed in a time scale including conformable derivative.

Theorem 3.8. Let λ_1 be the first eigenvalue of the problem (3.4) – (3.6).

$$\lambda_1 = \frac{\alpha}{(\rho(b))^{\alpha-\alpha}} \left\{ h_a - h_b + \int_a^{\rho(b)} q(t)\Delta^\alpha t \right\},$$

Implies that $q(t) = \lambda_1$.

Proof. By (3.4), we obtain

$$\begin{aligned} \frac{T_\alpha(T_\alpha y_1(t))}{y_1^\sigma(t)} &= q(t) - \lambda_1, \\ T_\alpha \left(\frac{T_\alpha(y_1)}{y_1} \right) &= \frac{T_\alpha(T_\alpha y_1) y_1 - T_\alpha y_1 T_\alpha y_1}{y_1^\sigma y_1} \\ &= \frac{T_\alpha(T_\alpha y_1)}{y_1^\sigma} - \frac{(T_\alpha y_1)^2}{y_1^\sigma y_1}. \end{aligned}$$

Since $\frac{T_\alpha(T_\alpha y_1)}{y_1^\sigma} = q(t) - \lambda_1$, it yields

$$\frac{(T_\alpha y_1)^2}{y_1^\sigma y_1} = -T_\alpha \left(\frac{T_\alpha y_1}{y_1} \right) + q(t) - \lambda_1.$$

If we apply conformable integration to both sides of above equality from a to $\rho(b)$, we get

$$\int_a^{\rho(b)} \frac{(T_\alpha y_1)^2}{y_1^\sigma y_1} \Delta^\alpha t = \frac{T_\alpha(y_1(a))}{y_1(a)} - \frac{T_\alpha(y_1(\rho(b)))}{y_1(\rho(b))} + \int_a^{\rho(b)} [q(t) - \lambda_1] \Delta^\alpha t.$$

On the other hand, since $\frac{(T_\alpha y_1)^2}{y_1^\sigma y_1} > 0$ and $\Delta^\alpha t = t^{\alpha-1} \Delta t$, the result of the above expression is obtained as follows

$$\int_a^{\rho(b)} \frac{(T_\alpha y_1)^2}{y_1^\sigma y_1} \Delta^\alpha t = h_a - h_b + \int_a^{\rho(b)} q(t) \Delta^\alpha t - \frac{\lambda_1}{\alpha} [(\rho(b))^\alpha - a^\alpha] = 0.$$

Considering the conditions of the problem, we get

$$T_\alpha y_1(t) \equiv 0 \Rightarrow y_1(t) = c \Rightarrow q(t) = \lambda_1.$$

This completes the proof.

Example 3.9.

Let us consider below conformable Sturm-Liouville problem

$$-T_{0.5}(T_{0.5} y(t)) + q(t) y^\sigma(t) = \lambda y^\sigma(t), \quad t \in [1, \rho(3)]$$

$$T_{0.5}(y(1)) - y(1) = 0, \quad (h_a = 1)$$

$$T_{0.5}(y(\rho(3))) - y(\rho(3)) = 0, \quad (h_b = 1).$$

Using Theorem 3.7 and properties of delta conformable derivative, we get

$$\begin{aligned} \lambda_1 &= \frac{0.5}{(\rho(3))^{0.5} - 1^{0.5}} \left\{ 1 - 1 + \int_1^{\rho(3)} q(t) \Delta^{0.5} t \right\} \\ &= \frac{1}{2(\sqrt{\rho(3)} - 1)} \int_1^{\rho(3)} q(t) t^{-0.5} \Delta t \\ &= \frac{1}{2(\sqrt{\rho(3)} - 1)} \int_1^{\rho(3)} \frac{q(t)}{\sqrt{t}} \Delta t \end{aligned}$$

Then, it implies

$$q(t) = \lambda_1.$$

Here, the order of conformable derivative and the time scale studied can be chosen arbitrarily.

4. Conclusions

In this study, a Freiling-Yurko type Ambarzumyan theorem, which has been proved on the time scale before, is considered and proven to include a conformable derivative on the time scale. The results obtained are very important in terms of the application of the fractional derivative to inverse spectral theory on the time scale. The theorem proved is made more concrete with an example for some special cases. This study can be done for other kinds of fractional derivative and inverse problems other than Ambarzumyan theorem can be proved.

References

- [1] Hilger S. Analysis on measure chains– a unified approach to continuous and discrete calculus. *Results Math* 1990; 18(1-2): 18–56.
- [2] Erbe L, Hilger S. Sturmian theory on measure chains. *Differ Equ Dyn Syst* 1993; 1(3): 223–244.
- [3] Agarwal RP, Bohner M, Wong PJY. Sturm-Liouville eigenvalue problems on time scales. *Appl Math Comput* 1999; 99(1-2): 153–166.
- [4] Amster P, De Nápoli P, Pinasco JP. Eigenvalue distribution of second-order dynamic equations on time scales considered as fractals. *J Math Anal Appl* 2008; 343(1): 573–584.
- [5] Amster P, De Nápoli P, Pinasco JP. Detailed asymptotic of eigenvalues on time scales. *J Differ Equ Appl* 2009; 15(3): 225–231.
- [6] Guseinov GSh. Eigenfunction expansions for a Sturm-Liouville problem on time scales. *Int J Differ Equ* 2007; 2(1): 93–104.
- [7] Guseinov GSh. An expansion theorem for a Sturm-Liouville operator on semi-unbounded time scales. *Adv Dyn Syst Appl* 2008; 3(1): 147-160.
- [8] Davidson FA, Rynne BP. Eigenfunction expansions in L^2 spaces for boundary value problems on time-scales. *J Math Anal Appl* 2007; 335(2): 1038–1051.
- [9] Davidson FA, Rynne BP. Self-adjoint boundary value problems on time scales. *Electron J Differ Equ* 2007; 175(2): 1–10.
- [10] Huseynov A, Bairamov E. On expansions in eigenfunctions for second order dynamic equations on time scales. *Nonlinear Dyn Syst Theory* 2009; 9(1): 77–88.
- [11] Kong Q. Sturm-Liouville problems on time scales with separated boundary conditions. *Results Math* 2008; 52(1-2): 111-121.
- [12] Rynne BP. L^2 spaces and boundary value problems on time scales. *J Math Anal Appl* 2007; 328(2): 1217–1236.
- [13] Ambarzumyan VA. Über eine Frage der Eigenwerttheorie. *Z Physik* 1929; 53: 690-695.
- [14] Freiling G, Yurko VA. *Inverse Sturm–Liouville Problems and Their Applications*, Nova Science: Hauppauge, 2001.
- [15] Yurko VA. On Ambarzumyan-type theorems. *Appl Math Lett* 2013; 26(4): 506-509.
- [16] Ozkan AS. Ambarzumyan-type theorems on a time scale. *J Inverse Ill-posed Probl* 2018; 26(5): 633-637.
- [17] Atkinson FV. *Discrete and Continuous Boundary Problems*. New York: Academic Press, 1964.
- [18] Bohner M, Peterson A. *Dynamic Equations on Time Scales. An Introduction with Applications*. Boston: Birkhäuser, 2001.
- [19] Bohner M, Peterson A. *Advances in Dynamic Equations on Time Scales*. Boston: Birkhäuser, 2003.
- [20] Kilbas A, Srivastasa H, Trujillo J. *Theory and Applications of Fractional Differential Equations*. Math Studies, New York: North-Holland, 2006.
- [21] Khalil R, Al Horani M, Yousef, A, Sababheh M. A new definition of fractional derivative. *J Comput Appl Math* 2014; 264: 65-70.
- [22] Martinez F, Martinez I, Kaabar MKA, Ortiz-Munuera R, Paredes S. Note on the Conformable Fractional Derivatives and Integrals of Complex-valued Functions of a Real Variable. *Int J Appl Math* 2020; 50(3): 609-615.
- [23] Benkhetrou N, Hassani S, Torres DFM. A conformable fractional calculus on arbitrary time scales. *J King Saud Univ Sci* 2016; 28(1): 93-98.
- [24] Gulsen T, Yilmaz E, Goktas S. Conformable fractional Dirac system on time scales. *J Inequal Appl* 2017; 161(2017): 1-10.

Determination of the Optimum Test Conditions for Measurement of Glucose Level in Liquids

Ömer Faruk GÖKTAŞ^{1*}, İlyas ÇANKAYA², Esra ŞENGÜN ERMEYDAN³

^{1,2,3}Department of Electrical and Electronics Engineering, Faculty of Engineering and Natural Sciences, Ankara Yıldırım Beyazıt University, Ankara, Türkiye

¹ofgoktas@aybu.edu.tr, ²ilyas.cankaya@aybu.edu.tr, ³esrasengunermeydan@aybu.edu.tr

(Geliş/Received: 29/09/2023;

Kabul/Accepted: 30/10/2023)

Abstract: Diabetes is a disease that affects more than 400 million people worldwide and currently lacks a cure. Monitoring blood sugar levels is crucial in minimizing the effects of this disease and protecting against its complications. Invasive and minimally invasive methods are commonly used traditional approaches for detecting and monitoring blood sugar levels. However, these methods bring along psychological and infectious risks. Currently, efforts are being made to develop a non-invasive method for determining blood sugar levels. Microwaves offer the possibility of non-invasive glucose measurement as they do not cause any harmful effects on human tissue. Furthermore, the complex permeability of blood is sensitive to glucose concentration in the microwave band. In literature, most of the studies are done with vector network analyzers (VNA) to detect blood sugar level noninvasively. In this study, an expensive and bulky VNA is replaced by an affordable microwave source and RMS power detector. The influence of the type and diameter of the test tube material used for non-invasive determination of sugar levels is examined with this setup. Additionally, the effect of the distance between the Vivaldi antennas used during measurements and the test tube is investigated. The results indicate that measurements performed using plastic test tubes yield better results compared to glass test tubes. Moreover, reducing the diameter of the test tube leads to improved outcomes. It has been observed that accurate results cannot be obtained if the antennas and the test tube are too close (<0.5 cm) or too far (>4.5cm) from each other.

Key words: Microwaves, Non-invasive glucose detection, Glucose detection, Diabetes, Vivaldi antenna

Sıvılarda Glikoz Seviyesinin Ölçülmesi İçin Optimum Test Koşullarının Belirlenmesi

Öz: Diyabet, dünya çapında 400 milyondan fazla insanı etkileyen ve şu anda tedavisi bulunmayan bir hastalıktır. Kan şekerinin takibi bu hastalığın etkilerini en aza indirmek ve komplikasyonlarından korunmak açısından çok önemlidir. İnvaziv ve minimal invaziv yöntemler, kan şekeri seviyelerinin tespiti ve izlenmesinde yaygın olarak kullanılan geleneksel yaklaşımlardır. Ancak bu yöntemler psikolojik ve bulaşıcı riskleri de beraberinde getirmektedir. Şu anda kan şekeri seviyelerini invazif olmayan bir yöntem geliştirerek belirlemek için çaba sarf edilmektedir. Mikrodalgalar insan dokusu üzerinde herhangi bir zararlı etkiye neden olmadığından, invaziv olmayan glikoz ölçümü olanağı sunmaktadır. Ayrıca kanın kompleks geçirgenliği mikrodalga bandındaki glikoz konsantrasyonuna duyarlıdır. Literatürde kan şekeri düzeyinin invazif olmayan bir şekilde tespit edilmesine yönelik çalışmaların çoğu vektör ağ analizörleri (VNA) ile yapılmaktadır. Bu çalışmada pahalı ve hantal bir VNA'nın yerini uygun fiyatlı bir mikrodalga kaynağı ve RMS güç dedektörü almıştır. Bu kurulumla şeker seviyelerinin invaziv olmayan tespiti için kullanılan test tüpü malzemesinin türü ve çapının etkisi incelenir. Ayrıca ölçümler sırasında kullanılan Vivaldi antenleri ile test tüpü arasındaki mesafenin etkisi araştırılmıştır. Sonuçlar, plastik test tüpleri kullanılarak yapılan ölçümlerin cam test tüplerine göre daha iyi sonuçlar verdiğini göstermektedir. Ayrıca test tüpünün çapının azaltılması daha iyi sonuçlara yol açar. Antenlerin ve test tüpünün birbirine çok yakın (<0,5 cm) veya çok uzak (>4,5 cm) olması durumunda doğru sonuçların alınamayacağı görülmüştür.

Anahtar kelimeler: Mikrodalga, İnvazif olmayan glikoz tespiti, Glikoz tespiti, Diyabet, Vivaldi anten

1. Introduction

Diabetes is one of the important chronic diseases characterized by very high sugar levels in the blood [1]. Diabetes occurs when the body cannot produce enough insulin or cannot use insulin effectively. Two hours after eating, the human blood glucose level should ideally remain below 140 mg/dl. Higher levels can, over time, result in significant harm to the heart, blood vessels, eyes, kidneys, and nerves. The incidence of diabetes in the last century is directly related to poor lifestyles such as low physical activity and poor diet. The World Health Organization (WHO) reports that roughly 422 million individuals globally suffer from diabetes in 2023, with most residing in low to middle-income nations. Each year, diabetes is the direct cause of 1.5 million deaths[1]. Given that diabetes can lead to severe damage to vital organs, potentially resulting in life-threatening complications, there must be a continuous and reliable process for monitoring blood sugar levels. Many of the devices in use today require a blood sample and are invasive methods that are often

* Corresponding author: ofgoktas@aybu.edu.tr. ORCID Number of authors: ¹ 10000-0002-2021-4052, ² 20000-0002-6072-3097, ³ 30000-0002-5953-4301.

painful for patients [2]. In addition, some commercial devices used today offer some solutions for continuous monitoring of blood sugar, but these devices are expensive and short-lived [3]. Machine learning methods are widely used in different fields of medicine, and they can also be used to determine the level of glucose in the blood [4]–[6]. Therefore, cost-effective and non-invasive technology is required for safe and continuous monitoring of blood glucose.

In order to monitor the glucose level in the blood, various researchers propose variety of methods spanning different frequency ranges. Non-invasive methods can be divided into electromagnetic-based and electrochemical-based methods. Many studies have been carried out using electrochemical-based methods [7]–[10]. These studies showed a subtle and delayed relationship between blood glucose levels and measured values. However, it is premature to evaluate the feasibility of these studies. Because the studies are still in their nascent stage [11]. In methods based on electromagnetism, a range of wavelengths within the electromagnetic spectrum are employed. After interaction with the human body, the relationship between the size, phase and frequency of the measured signal and the glucose level in the blood is investigated [2], [12]–[14]. In the last decade, interest in detecting blood glucose levels using microwaves has increased [15]–[19]. The behavior of electromagnetic waves in a material depends on the dielectric properties of the material. These features form the basis of the primary design of the microwave frame [20], [21]. Evaluation of the dielectric properties of blood is of great importance for successful microwave diagnosis and treatment. In recent years, researchers have turned to studying blood glucose dielectric properties to pave the way for non-invasive and microwave band blood glucose monitoring systems. The relationship between microwave absorption and glucose concentration in human blood samples via the complex refractive index has been demonstrated in previous studies [22]–[24]. In recent times, artificial intelligence methods have gained popularity for assessing glucose concentrations in blood samples [25]–[27].

The present work seeks to pave the way for monitoring blood glucose levels using the vivaldi antenna at 5.5 GHz as a microwave sensor. In this study, an expensive and bulky VNA was replaced with an affordable microwave source and RMS power detector. The effect of the type and diameter of the test tube material used for the non-invasive determination of sugar levels is examined with this setup. In addition, the effect of the distance between the Vivaldi antennas used during the measurements and the test tube was examined. The primary advancement offered by the study presented here is the elimination of the need for costly equipment like a VNA to serve as a signal generator within the proposed experimental framework. Additionally, this research lays the groundwork by establishing the most favorable test conditions, setting a benchmark for similar studies in the literature.

2. Material and Methods

2.1. S-Parameters

Two-port S parameters are established by considering the propagation of waves along transmission lines with actual characteristic impedance Z_0 connected to each of the network's ports, as illustrated in Figure 1 [28].



Figure 1. Illustration of a two-port circuit

$$V_1^- = S_{11}V_1^+ + S_{12}V_2^+, \quad V_2^- = S_{21}V_1^+ + S_{22}V_2^+ \quad (1)$$

where S_{ij} are the individual S parameters. The equations mentioned above are represented in matrix form as follows,

$$\begin{bmatrix} V_1^- \\ V_2^- \end{bmatrix} = \begin{bmatrix} S_{11} & S_{12} \\ S_{21} & S_{22} \end{bmatrix} \begin{bmatrix} V_1^+ \\ V_2^+ \end{bmatrix} \quad (2)$$

Individual S parameters are derived by measuring the incident and reflected waves with loads $Z_L = Z_0$ at the network's ports. In the case of the output line, where the load doesn't dissipate power, $V_2^+ = 0$, thus [18],

$$S_{11} = \frac{V_1^-}{V_1^+} \Big|_{V_2^+=0} \quad (3)$$

and the transmission parameter is [18]

$$S_{21} = \frac{V_2^-}{V_1^+} \Big|_{V_2^+ = 0} \quad (4)$$

2.2. Cole – Cole and Debye Models

The dielectric constant values of different tissues are determined through the application of various models, such as the Debye model or the Cole–Cole model. In accordance with the Cole–Cole model, the estimation of dielectric constants can be achieved using equation 5

$$\hat{\epsilon}(w) = \epsilon_c'(\omega) - j\epsilon_c''(\omega) = \epsilon_\infty + \sum_n \frac{\Delta\epsilon_n}{1+(j\omega\tau_n)^{1-\alpha_n}} + \frac{\sigma_i}{j\omega\epsilon_0} \quad (5)$$

where, ϵ_∞ is the high frequency permittivity, $\Delta\epsilon_n$ is the magnitude of the dispersion, ω is the angular frequency, $\epsilon_c'(\omega)$ is the frequency dependent dielectric constant, $\epsilon_c''(\omega)$ is the frequency dependent dielectric loss, σ_i is the static ionic conductivity, n is the order of the Cole–Cole model, α_n is the parameter that allows for the broadening of the dispersion, and τ_n is the relaxation time constant [29]. In case of $\alpha_n = 0$ the equation reduces to Debye model and the term with the static conductance can be omitted for materials with low conductivity. Solutions of glucose/water can also be modelled with this model.

2.3. Vivaldi Antenna

Two vivaldi antennas were used for the study. Developed by Gibson in 1979, the Vivaldi antenna is used with very wide bandwidth characteristics and directional radiation patterns [30]. Vivaldi antenna offers advantages such as wide bandwidth, high directivity and bandwidth can be changed by changing some antenna parameters (shape, length, dielectric constant and dielectric thickness etc.). However, they are expensive due to the difficulties in the manufacturing phase. The structure of a vivaldi antenna is given in Figure 2 .

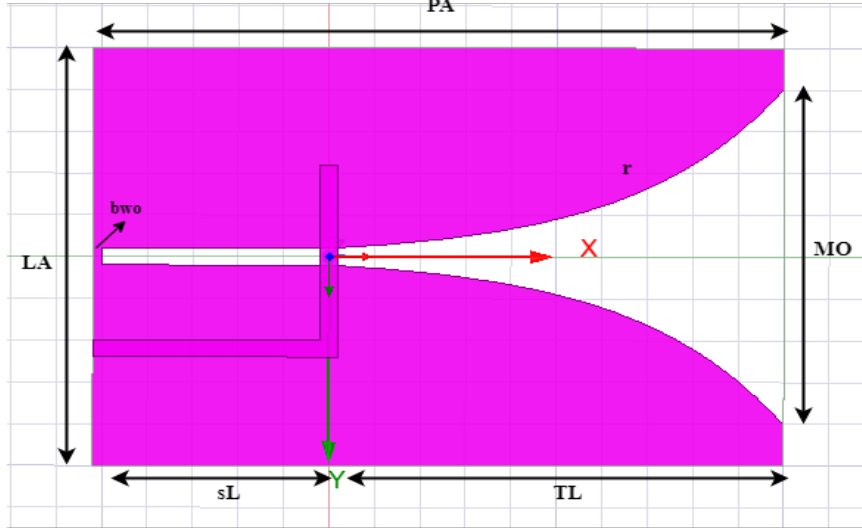


Figure 2. Vivaldi antenna

Dimension parameters of Vivaldi Antenna are antenna opening mouth (MO), slot-line length (sL), tapered length (TL), tapered rate (r), antenna width (LA), back-wall offset (bwo) and length (PA). The process of antenna design starts with establishing the fundamental antenna parameters on paper, laying the foundation for the upcoming steps. Once these parameters are determined, the next phase involves creating a virtual model of the antenna. This modeling is facilitated by an antenna simulation software, where the design is tested and analyzed based on the predetermined parameters. It's worth noting that the dimensions and size attributes of the antenna play a crucial role in determining its bandwidth and overall performance. Adjustments in these parameters can have a significant impact on how effectively the antenna operates within its intended frequency range [31].

The width (LA) and length (PA) of the antenna is determined by equation (6,7)

$$PA \approx \frac{c}{f\sqrt{\epsilon_r}} \quad (6)$$

$$LA \approx \frac{1}{2} \times \frac{c}{f\sqrt{\epsilon_r}} \quad (7)$$

where LA is an antenna width, PA is a length, f is frequency, c is a speed of light and ϵ_r is a relative permittivity. In the design of Vivaldi antenna, the dimensions of tapered rate determine and tapered length calculation using equation (8). The slope level of the taper slot of Vivaldi antenna greatly affects the beam width, bandwidth and gain. In addition, the mouth opening value can be found using equation (9) [31].

$$u = \pm s \times \exp(r \times t) \quad (8)$$

$$\pm \frac{MO}{2} = \pm \frac{s}{2} \times \exp(r \times TL) \quad (9)$$

2.4. Experimental Setup and Measurements

The schematic diagram of experimental setup for monitoring the blood glucose level is shown in Figure 3. In the proposed system, the 5.5 GHz signal produced by the microwave wideband synthesizer is transmitted to the transmitting antenna via a coaxial cable. Here, electromagnetic waves interacting with the sample are collected in the receiving antenna and come to the power detector via the coaxial cable.

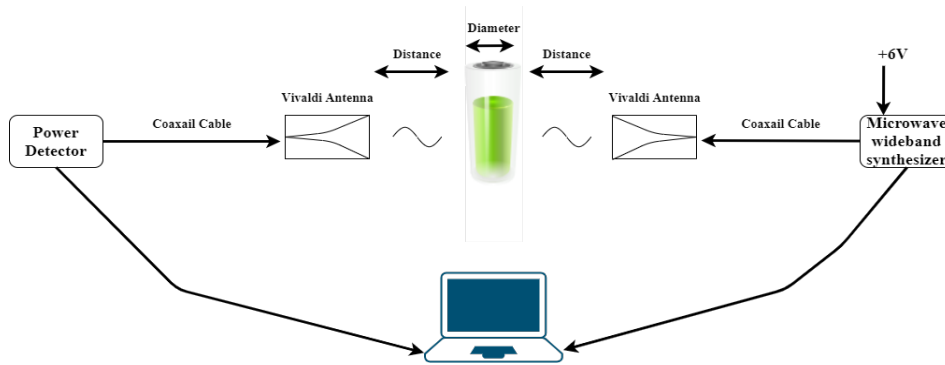


Figure 3. Schematic diagram of experimental setup

The primary benefit of the system we've implemented is its ability to bypass the vector network analyzer, a component frequently referenced in prior studies. This omission presents a significant cost-saving advantage. Furthermore, given the VNA's substantial size, it becomes impractical for long-term integration into commercial devices intended for everyday human use. Thus, by eliminating the VNA, our system paves the way for more streamlined and user-friendly applications. In the study, the effect of the sample cup material (glass, plastic, etc.) on the measurement results was also investigated. The results of the measurements made using glass and plastic containers are presented in Table 1.

Table 1. Comparison of plastic and glass material

	Air	Plastic	Glass	Distilled Water	
				Plastic	Glass
-4 dBm	-25.6	-24.5	-28.8	-33.3	-33
-1 dBm	-19.8	-18.8	-22.3	-29.9	-31.2
+2 dBm	-16.5	-15.6	-18.9	-27	-28.9
+5 dBm	-14.1	-13.4	-17.6	-25.1	-27

When the measurement results made with air, empty plastic, empty glass, and plastic and glass tubes filled with pure water were examined, it was seen that the measurements made with plastic gave better results when compared to glass ones. In addition, the measurement results obtained for 50mg/dl, 125mg/dl, 250mg/dl, 500mg/dl and 1000mg/dl

glucose solutions are given in Table 2. When these results were examined, it was seen that the measurement results made with the plastic cup gave better results than the glass.

Table 2. Measurements made in solutions of various glucose concentrations using a plastic cup

	50 mg/dL		125 mg/dL		250 mg/dL		500 mg/dL		1000 mg/dL	
	Plastic	Glass	Plastic	Glass	Plastic	Glass	Plastic	Glass	Plastic	Glass
-4 dBm	-33.5	-34.9	-33.7	-34.5	-33.8	-33	-33.9	-32.5	-33.9	-34
-1 dBm	-29.9	-31.1	-29.7	-31.3	-29.1	-31.2	-29.4	-31.7	-29.8	-31.5
+2 dBm	-26.8	-28.6	-26.5	-29	-25.6	-28.5	-25.9	-29.5	-26.8	-29
+5 dBm	-24.2	-27	-24.1	-27.6	-24.3	-27.1	-24.5	-27	-24.8	-27.1

With the plastic material giving better results than glass, the effects of the diameters of the plastic sample cups on the measurement results were investigated. Sample cups with diameters of 20.5 mm and 22.8 mm were used and these cups are shown in Figure 4.

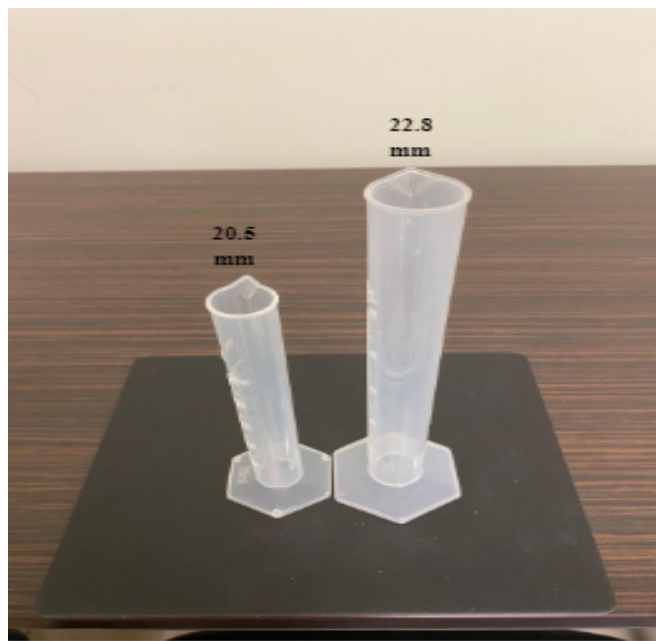


Figure 4. Plastic sample cups of 20.5 mm and 22.8 mm

The measurement results with 20.5 mm and 22.8 mm plastic cups are given in Table 3. When Table 3 is examined, it is seen that there is an improvement in the data obtained from the power detector with the reduction of the measuring cup diameter.

Table 3. Effect of measuring cups with diameters of 20.5 mm and 22.8 mm on measurement results

	50 mg/dL		125 mg/dL		250 mg/dL		500 mg/dL		1000 mg/dL	
	22.8 mm	20.5 mm	22.8 mm	20.5 mm	22.8 mm	20.5 mm	22.8 mm	20.5 mm	22.8 mm	20.5 mm
-4 dBm	-33.5	-33.4	-33.7	-33.2	-33.8	-33.1	-33.9	-33.4	-33.9	-33.7
-1 dBm	-29.9	-29.1	-29.7	-28.5	-29.1	-28.7	-29.4	-28.5	-29.8	-29.1
+2 dBm	-26.8	-25.2	-26.5	-25.9	-25.6	-25.1	-25.9	-25.7	-26.8	-26.2
+5 dBm	-24.2	-23.7	-24.1	-23.8	-24.3	-23.7	-24.5	-23.6	-24.8	-23.9

In the research thus far, the impact of both the measuring cup's material (plastic versus glass) and its diameter (20.5 mm and 22.8 mm) on the results is explored. From our observations, plastic cups outperform their glass counterparts, and cups with a smaller diameter yield better outcomes. In the next part of the research, the effect of the distance of the receiving and transmitting antennas to the measuring cup on the measurement result is examined.

The objective of antenna simulation is to evaluate and determine whether the designed antenna model aligns with the predefined specifications. In the context of this research, the antennas in consideration are commercial products sourced from China. Unfortunately, these products lack detailed datasheets and a Gerber file. To overcome this limitation and gain insights into the approximate characteristics of the antenna, a modeling process is proposed. We employed the

ANSYS-HFSS software, a leading tool in the electromagnetic simulation domain, to recreate and analyze the antenna's behavior and performance. The size parameters of the modeled antenna and the design of the antenna are presented in Figure 5.

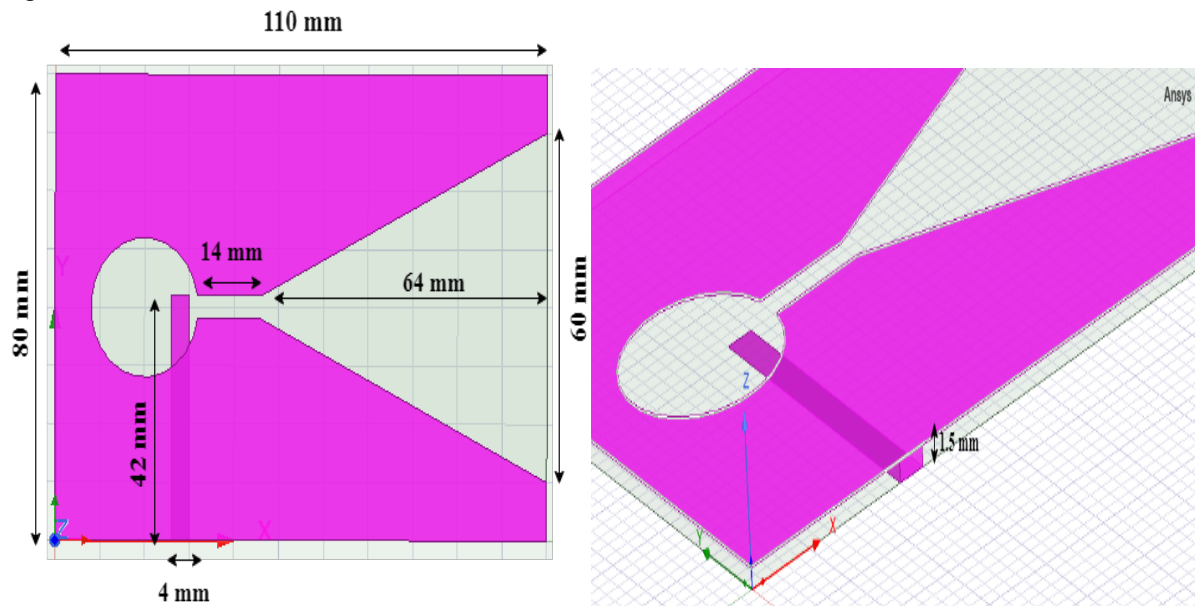


Figure 5. Vivaldi antenna view from the upper z-axis and vivaldi antenna thickness

In order to examine the distance of the antennas to the measuring cup, the setup in Figure 6 was set up. Measurements were taken as 0.5 cm, 1.5 cm, 2.5 cm, 3.5 cm and 4.5 cm distances from the antennas to the measuring cup.

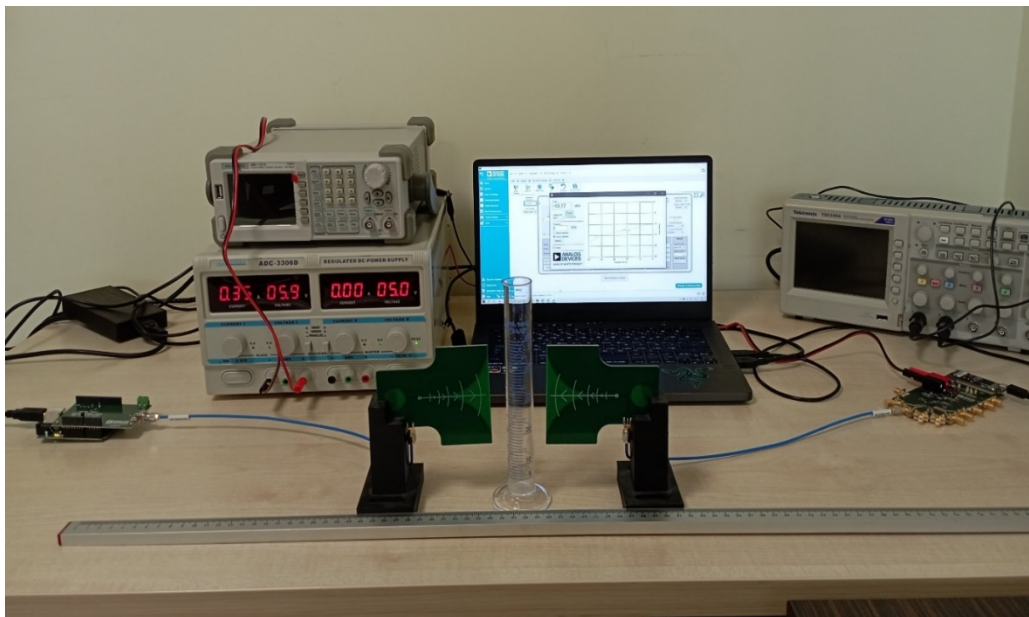


Figure 6. Experimental setup

With the installation in Figure 5, both the distance of the antennas to the test tube and the effect of the diameters were examined together. Plastic test tubes with diameters of 22.8 mm and 20.5 mm were used for the measurements. The glucose solution concentrations used during the experiment are 50 mg/dL, 125 mg/dL, 250 mg/dL, 500 mg/dL and 1000 mg/dL.

Table 4. Effect of the distance between the antennas and the test tube on the measurement results.

Distance between sample and antenna: 0.5 cm										
	50 mg/dL		125 mg/dL		250 mg/dL		500 mg/dL		1000 mg/dL	
	22.8 mm	20.5 mm	22.8 mm	20.5 mm	22.8 mm	20.5 mm	22.8 mm	20.5 mm	22.8 mm	20.5 mm
-4 dBm	-34	-32.5	-34.1	-33.2	-34.3	-33.5	-34.5	-34	-35	-32
-1 dBm	-32.5	-28.8	-33	-27.8	-32.9	-30.5	-33.5	-30.8	-33	-30.9
+2 dBm	-31.6	-26.3	-31.5	-25.9	-31.4	-27.1	-31.4	-26.8	-31.3	-28.1
+5 dBm	-30.2	-24.1	-29.5	-23.4	-30.1	-25.2	-27.9	-25.6	-30.1	-25.8
Distance between sample and antenna: 1.5 cm										
	50 mg/dL		125 mg/dL		250 mg/dL		500 mg/dL		1000 mg/dL	
	22.8 mm	20.5 mm	22.8 mm	20.5 mm	22.8 mm	20.5 mm	22.8 mm	20.5 mm	22.8 mm	20.5 mm
-4 dBm	-33.6	-32.7	-33.4	-32.5	-34.1	-33.2	-33.1	-32.8	-32.5	-32.4
-1 dBm	-28.7	-28.4	-29.8	-27.7	-30.5	-28.1	-28.4	-28.2	-27.8	-27.4
+2 dBm	-25.6	-25.1	-27.7	-24.6	-28.2	-24.3	-27.7	-24.7	-25.4	-25.1
+5 dBm	-24.1	-24.1	-25.2	-22.8	-25.7	-22.3	-24	-22.3	-23.3	-22.2
Distance between sample and antenna: 2.5 cm										
	50 mg/dL		125 mg/dL		250 mg/dL		500 mg/dL		1000 mg/dL	
	22.8 mm	20.5 mm	22.8 mm	20.5 mm	22.8 mm	20.5 mm	22.8 mm	20.5 mm	22.8 mm	20.5 mm
-4 dBm	-33.5	-33.4	-33.7	-33.2	-33.8	-33.1	-33.9	-33.4	-33.9	-33.7
-1 dBm	-29.9	-29.1	-29.7	-28.5	-29.1	-28.7	-29.4	-28.5	-29.8	-29.1
+2 dBm	-26.8	-25.2	-26.5	-25.9	-25.6	-25.1	-25.9	-25.7	-26.8	-26.2
+5 dBm	-24.2	-23.7	-24.1	-23.8	-24.3	-23.7	-24.5	-23.6	-24.8	-23.9
Distance between sample and antenna: 3.5 cm										
	50 mg/dL		125 mg/dL		250 mg/dL		500 mg/dL		1000 mg/dL	
	22.8 mm	20.5 mm	22.8 mm	20.5 mm	22.8 mm	20.5 mm	22.8 mm	20.5 mm	22.8 mm	20.5 mm
-4 dBm	-36.6	-35.1	-36.4	-34.8	-37	-34.2	-35.3	-34.1	-34.8	-33.9
-1 dBm	-32.7	-30.1	-33.1	-29.8	-32.8	-29.4	-32.6	-28.9	-31.6	-29.5
+2 dBm	-29.3	-26.5	-30.1	-26.8	-30.5	-26.5	-30.3	-26.2	-30.7	-25.6
+5 dBm	-28.8	-24.9	-28.1	-23.8	-27.8	-24.7	-27.6	-24	-28.8	-23.9
Distance between sample and antenna: 4.5 cm										
	50 mg/dL		125 mg/dL		250 mg/dL		500 mg/dL		1000 mg/dL	
	22.8 mm	20.5 mm	22.8 mm	20.5 mm	22.8 mm	20.5 mm	22.8 mm	20.5 mm	22.8 mm	20.5 mm
-4 dBm	-35.1	-33.1	-35.7	-32.9	-36.2	-32.5	-36.8	-32.8	-36.4	-32.1
-1 dBm	-32.3	-28.6	-31.5	-28.2	-32.3	-28.4	-32.9	-28.1	-32.7	-28.4
+2 dBm	-30.1	-25.6	-30.4	-25.4	-29.1	-24.8	-30	-24.7	-29.8	-25
+5 dBm	-29.2	-23.5	-28.5	-23	-28.5	-23	-28.8	-23.1	-28.6	-22.6

The 5.5 GHz signal generated by the microwave wideband synthesizer is directed to the sample by the transmitting antenna. Signals passing through the sample are collected by the receiving antenna on the opposite side and sent to the power detector. When the data obtained from the power detector in Table 4 are examined, signal distortions occurred when the antennas and the sample were too close ($< 1.5\text{ cm}$) or too far ($> 4.5\text{ cm}$) away. In addition, the data obtained at 1.5 cm, 2.5 cm and 3.5 cm were found to be consistent within themselves. As it is consistent with the Table 3, 20.5 mm results are superior to 22.8 mm ones.

3. Conclusion

As a result, in this study, it is aimed to determine the optimum test conditions for glucose level determination with a non-invasive method at 5.5 GHz. In this context, firstly, the test tube material was examined and it was seen that better results were obtained in plastic material than in glass material. The reason for this is that the signals coming to the glass material are more scattered than the plastic material. Then, the effects of the diameters of the plastic test tubes on the measurement results were examined. By reducing the diameter of the measuring cup, better data were obtained in the power detector. In the last study, the effect of the distance of the antennas from the sample cup on the measurement results was investigated. When these results were examined, it was observed that the signal was scattered when the antennas were adjacent to the sample cup and the distance increased. As a future work, it is aimed to obtain healthier and more reliable data by taking signals as continuous data and applying signal processing algorithms. In addition, antenna structures will be compared by taking measurements at different frequencies with various antenna types.

4. Acknowledgements

This work has been supported by Ankara Yıldırım Beyazıt University Scientific Research Projects Coordination Unit under grant number #2423.

References

- [1] International Diabetes Federation, "IDF Diabetes Atlas 2021 _ IDF Diabetes Atlas," IDF official website. 2021.
- [2] Gonzales WV, Mobashsher AT, and Abbosh A, "The progress of glucose monitoring—A review of invasive to minimally and non-invasive techniques, devices and sensors," *Sensors (Switzerland)*, vol. 19, no. 4. 2019, doi: 10.3390/s19040800.
- [3] Mahnashi Y, Qureshi KK, Al-Shehri A, and Attia H, "Microwave-Based Technique for Measuring Glucose Levels in Aqueous Solutions," in *2023 International Microwave and Antenna Symposium, IMAS 2023*, 2023, pp. 1–4, doi: 10.1109/IMAS55807.2023.10066913.
- [4] Ermeydan EŞ, Değirmenci A, Çankaya İ, and Erdoğan F, "Patolojik Görüntülerin Sıkıştırılmış Algılamasında Ölçüm Matrisi ve Geri Çatma Algoritmalarının Etkileri," *Düzce Üniversitesi Bilim ve Teknol. Derg.*, vol. 8, no. 1, 2020, doi: 10.29130/dubited.626880.
- [5] Degirmenci A, "Performance Comparison of kNN, Random Forest and SVM in the Prediction of Cervical Cancer from Behavioral Risk," *Int. J. Innov. Sci. Res. Technol.*, vol. 7, no. 10, 2022.
- [6] Değirmenci A, Çankaya İ, Gümüşkaya Öcal B, and Karal Ö, "TCGA Verilerinden H&E ile Boyanmış Örneklerden Mesane Kanseri Derecelendirmesi," *Gazi Üniversitesi Fen Bilim. Derg. Part C Tasarım ve Teknol.*, vol. 11, no. 2, 2023, doi: 10.29109/gujsc.1232028.
- [7] Zhang J, Hodge W, Hutnick C, and Wang X, "Noninvasive diagnostic devices for diabetes through measuring tear glucose," *Journal of Diabetes Science and Technology*, vol. 5, no. 1. 2011, doi: 10.1177/193229681100500123.
- [8] Malik S, Gupta S, Khadgawat R, and Anand S, "A novel non-invasive blood glucose monitoring approach using saliva," 2015, doi: 10.1109/SPICES.2015.7091562.
- [9] Guo D, Zhang D, Zhang L, and Lu G, "Non-invasive blood glucose monitoring for diabetics by means of breath signal analysis," *Sensors Actuators, B Chem.*, vol. 173, 2012, doi: 10.1016/j.snb.2012.06.025.
- [10] Gao W, et al., "Fully integrated wearable sensor arrays for multiplexed in situ perspiration analysis," *Nature*, vol. 529, no. 7587, 2016, doi: 10.1038/nature16521.
- [11] Shaker G, Chen R, Milligan B, and Qu T, "Ambient electromagnetic energy harvesting system for on-body sensors," *Electron. Lett.*, vol. 52, no. 22, 2016, doi: 10.1049/el.2016.3123.
- [12] Xue Y, Thalmayer AS, Zeising S, Fischer G, and Lübke M, *Commercial and Scientific Solutions for Blood Glucose Monitoring—A Review*, vol. 22, no. 2. 2022.
- [13] Kang JW, et al., "Direct observation of glucose fingerprint using in vivo Raman spectroscopy," *Sci. Adv.*, vol. 6, no. 4, 2020, doi: 10.1126/sciadv.aay5206.
- [14] Ebrahimi A, Scott J, and Ghorbani K, "Microwave reflective biosensor for glucose level detection in aqueous solutions," *Sensors Actuators, A Phys.*, vol. 301, p. 111662, 2020, doi: 10.1016/j.sna.2019.111662.
- [15] Govind G and Akhtar MJ, "Metamaterial-inspired microwave microfluidic sensor for glucose monitoring in aqueous solutions," *IEEE Sens. J.*, vol. 19, no. 24, 2019, doi: 10.1109/JSEN.2019.2938853.
- [16] Saleh G, Ateeq IS, and Al-Naib I, "Glucose level sensing using single asymmetric split ring resonator," *Sensors*, vol. 21, no. 9, 2021, doi: 10.3390/s21092945.
- [17] Omer AE, Gigoyan S, Shaker G, and Safavi-Naeini S, "WGM-Based Sensing of Characterized Glucose- Aqueous Solutions at mm-Waves," *IEEE Access*, vol. 8, 2020, doi: 10.1109/ACCESS.2020.2975805.
- [18] Gökaş ÖF, Çankaya İ, and Ermeydan EŞ, "Milimetre dalga bandında invazif olmayan bir yöntem ile sivilarda glikoz seviyesinin belirlenmesi," pp. 1235–1248, 2022, doi: 10.17482/uumfd.1125289.
- [19] Zhang R, et al., "Noninvasive Electromagnetic Wave Sensing of Glucose," doi: 10.3390/s19051151.
- [20] Smulders PFM, Buysse MG, and Huang MD, "Dielectric properties of glucose solutions in the 0.5-67 GHz range," *Microw. Opt. Technol. Lett.*, vol. 55, no. 8, 2013, doi: 10.1002/mop.27672.
- [21] Lazebnik M, et al., "A large-scale study of the ultrawideband microwave dielectric properties of normal, benign and malignant breast tissues obtained from cancer surgeries," *Phys. Med. Biol.*, vol. 52, no. 20, 2007, doi: 10.1088/0031-9155/52/20/002.
- [22] Alison JM and Sheppard RJ, "Dielectric properties of human blood at microwave frequencies," *Phys. Med. Biol.*, vol. 38, no. 7, 1993, doi: 10.1088/0031-9155/38/7/007.
- [23] Gennarelli G, Romeo S, Scarfi MR, and Soldovieri F, "A microwave resonant sensor for concentration measurements of liquid solutions," *IEEE Sens. J.*, vol. 13, no. 5, pp. 1857–1864, 2013, doi: 10.1109/JSEN.2013.2244035.
- [24] Topsakal E, Karacolak T, and Moreland EC, "Glucose-dependent dielectric properties of blood plasma," 2011 30th URSI Gen. Assem. Sci. Symp. URSIGASS 2011, pp. 1–4, 2011, doi: 10.1109/URSIGASS.2011.6051324.
- [25] Agrawal H, Jain P, and Joshi AM, "Machine learning models for non-invasive glucose measurement: towards diabetes management in smart healthcare," *Health Technol. (Berl.)*, vol. 12, no. 5, 2022, doi: 10.1007/s12553-022-00690-7.
- [26] Kumar A, et al., "High-sensitivity, quantified, linear and mediator-free resonator-based microwave biosensor for glucose detection," *Sensors (Switzerland)*, vol. 20, no. 14, 2020, doi: 10.3390/s20144024.
- [27] Yilmaz T, Foster R, and Hao Y, "Towards accurate dielectric property retrieval of biological tissues for blood glucose monitoring," *IEEE Trans. Microw. Theory Tech.*, vol. 62, no. 12, 2014, doi: 10.1109/TMTT.2014.2365019.

- [28] Pozar DM, David M - Microwave engineering-Wiley (2012), vol. 4. 2011.
- [29] Nella A, Aldhaferi RW, Kamili JB, and Sobahi NM, "A non - invasive method of glucose monitoring using FR4 material based microwave antenna sensor," 2023.
- [30] Gibson PJ, "VIVALDI AERIAL.," 1979, doi: 10.1109/euma.1979.332681.
- [31] Maruddani B, Sandi E, and Fadhil Naufal Salam M, "Design and Implementation of Low-cost Wideband Vivaldi Antenna for Ground Penetrating Radar," KnE Soc. Sci., vol. 3, no. 12, 2019, doi: 10.18502/kss.v3i12.4118.

Automated Tuberculosis Classification with Chest X-Rays Using Deep Neural Networks -Case Study: Nigerian Public Health

Muhammad Zaharaddeen Abubakar¹, Mustafa Kaya^{2*}, Mustafa Eris³, Muhammad Mansur Abubakar⁴, Serkan Karakuş⁵, Khalid Jibril Sani⁶

^{1,2,3,6} Digital Forensic Engineering, Faculty of Technology, Firat University, Elazığ, Türkiye

⁴ Computer Engineering, Faculty of Engineering, Firat University, Elazığ, Türkiye

⁵ Software Engineering, Faculty of Engineering, Firat University, Elazığ, Türkiye

* mkaya@firat.edu.tr

(Geliş/Received: 26/12/2022;

Kabul/Accepted: 13/02/2024)

Abstract: Tuberculosis, a contagious lung ailment, stands as a prominent global mortality factor. Its significant impact on public health in Nigeria necessitates comprehensive intervention strategies. Detecting, preventing, and treating this disease remains imperative. Chest X-ray (CXR) images hold a pivotal role among diagnostic tools. Recent strides in deep learning have notably improved medical image analysis. In this research, we harnessed publicly available and proprietary CXR image datasets to construct robust models. Leveraging pre-trained deep neural networks, we aimed to enhance tuberculosis detection. Impressively, our experimentation yielded remarkable outcomes. Notably, f1-scores of 98% and 86% were attained on the respective public and private datasets. These results underscore the potency of deep neural networks in effectively identifying tuberculosis from CXR images. The study emphasizes the promise of this technology in combating the disease's spread and impact.

Key words: Deep learning, Tuberculosis (TB), ResNet, MobileNet, Data augmentation.

Derin Sinir Ağlarını Kullanan Göğüs Röntgenleri ile Otomatik Tüberküloz Sınıflandırması Örnek Çalışma: Nijerya Halk Sağlığı

Öz: Bulaşıcı bir akciğer rahatsızlığı olan tüberküloz, önde gelen küresel ölüm faktörü olarak karşımıza çıkıyor. Nijerya'da halk sağlığı üzerindeki önemli etkisi, kapsamlı müdahale stratejilerini gerektirmektedir. Bu hastalığın tespit edilmesi, önlenmesi ve tedavi edilmesi hâlâ zorunludur. Tanı araçları arasında göğüs röntgeni (CXR) görüntüleri çok önemli bir role sahiptir. Derin öğrenmedeki son gelişmeler, tıbbi görüntü analizini önemli ölçüde iyileştirdi. Bu çalışmada, sağlam modeller oluşturmak için kamuya açık ve tescilli CXR görüntü veri kümelerinden yararlandık. Önceden eğitilmiş derin sinir ağlarından yararlanarak tüberküloz tespitini geliştirmeyi hedefledik. Etkileyici bir şekilde, deneylerimiz dikkate değer sonuçlar verdi. Özellikle, ilgili açık ve özel veri setlerinde %98 ve %86'lık f1 puanlarına ulaşıldı. Bu sonuçlar, CXR görüntülerinden tüberkülozun etkili bir şekilde tanımlanmasında derin sinir ağlarının gücünün altını çiziyor. Çalışma, bu teknolojinin hastalığın yaygın etkisiyle mücadelede umut vaat ettiğini belirliyor.

Anahtar kelimeler: Derin öğrenme, Tüberküloz, ResNet, MobileNet, Veri artırma.

1. Introduction

Tuberculosis (TB) is a contagious bacterial infection that usually attacks the lungs, which is known as Mycobacterium Tuberculosis. Morbidity and mortality of the disease can be reduced if it's been detected at its early stage. TB is a curable disease that is mostly cured using the global recommended strategy for TB control, known as DOTS (Directly Observed Treatment, Short Course), a strategy that Nigeria and other largely affected countries follow. The DOTS strategy is for patients on medication to have support from individuals to observe them while being on medication [1].

TB was declared a global public health emergency issue in 1993 after being initially neglected, and the DOTS strategy was launched as part of indicators in Millennium Development Goals; of the Stop TB Strategy [2] and [3]. TB is one of the top 10 leading causes of death globally, the first leading cause of a single infectious disease, and the leading killer of HIV-positive people. In 2016, 10.4 million people approximately fell ill with TB and over 25% of those people are from Africa [4 – 7].

TB is one of the major public health problems in Nigeria, a country of 169 million inhabitants, with the country currently ranking among the top 10, out of 22 high TB burdened countries of the world and fourth highest

* Corresponding author: mkaya@firat.edu.tr. ¹ 0000-0002-0240-6827, ²0000-0002-0160-4469, ³0000-0002-1757-8496, ⁴0000-0001-8410-0057, ⁵0000-0001-5639-1408, ⁶0000-0003-2593-243X

in Africa (after South Africa, Ethiopia, and DR Congo) [8, 9]. Due to the rate of the disease in the region, TB is considered a national emergency problem in Nigeria.

In a study conducted in 2020, B. Odume et al. investigated the impact of the COVID-19 epidemic on the findings of tuberculosis cases in Nigeria. It was emphasized that after the global epidemic, the TB program urgently needs to adapt to the new normal and strengthen the patient-centered approach to TB care, adopt digital health technology, increase awareness, and increase community-based active TB case finding [10].

However, Various approaches to automated detection have been attempted in the last decade, and in recent years, Machine learning (ML) is not a strange term for the general public, ML-based techniques with deep learning (DL) are attracting lots of attention in big data analysis. DL algorithms have become a popular choice for solving biomedical diagnostic problems [11, 12], whereby data is filtered through a cascade of multiple layers using chest X-ray (CXR) images. The most recommended method of TB diagnosis is by using the computer-aided diagnosis (CAD) framework, which plays a significant role in the mass screening of TB by classifying the CXR images, helping expert radiologists to read the images which is a time-consuming task that leads to fatigue-based diagnosis, error-prone, and lack of availability of diagnostic expertise.

DL techniques, such as convolutional neural networks (CNNs) have demonstrated great promise and performance in image classification and are now widely adopted by the research communities [13]. These models have been applied in different fields of medicine such as; brain tumor [14], breast cancer [15], COVID-19 [16], Heart failure [17], Diabetes detection [18], and detection of thoracic pathologies [19].

However, several studies have used custom CNN models in their research to classify TB positive and negative from CXR images. F. Pasa et al [20] built a custom deep-learning CNN model with five (5) convolutional blocks, similar to AlexNet [21]. In their study, they scored an Accuracy of 86.2% and an AUC of 88.4% on the Maryland (MC), and Shenzhen (SZ) datasets combined. They believe their model is competitive even if comparison with other techniques is difficult, hence argued that saliency maps and gradient-weighted class activation mapping (Grad-CAMs) are useful tools for an in-depth visual explanation of TB, which they believe will provide an approximate visual diagnosis and might in-turn be a useful additional tool for clinicians.

Y. Xiong [22] also designed a custom CNN model called (TB-AI) which was originally trained on the Google CIFAR-10 dataset. The custom model was trained using 201 samples which were collected as test and used to examine Tb-AI. Meanwhile, further pre-processing techniques were carried out to have enough data to curb the problem of training a few datasets which might result in type one error and type two error even though they claim to have a human pathologist on the ground to analyze inconsistencies between their model and human. TB-AI scored 97.94% sensitivity score and a specificity of 83.65% score.

1.1. Related works

E. J. Hwang et al [23] developed a custom DCNN-based automatic detection (DLAD) model made up of 27 layers with 12 residual connections, trained via a semi-supervised localization approach and only a portion of the training data was annotated. The last layer of the model was made up of Image classification and lesion localization (segmentation of the lung), using 60,768 CXRs images collected from Seoul National University Hospital (SNUH), to classify TB, and further performance of their model was tested on 6 independent datasets to confirm the generalization performance. Certified radiologists labeled and annotated the CXR images and the performance of the model was further observed by other physicians and high cutoffs were set for Sensitivities and specificities, and scored 98% through in-house validation. Which demonstrated excellent performance in TB detection, outperforming physicians and other several studies such as P. Rajpurkar et al [24].

Meanwhile, some other studies used pre-trained CNNs with the concept TL to binary classify TB into positive and negative. T. Rahman et al [25] were able to detect TB and score state-of-the-art performance ahead of other studies reviewed, using some image preprocessing techniques, data augmentation, and image segmentation using two different U-Net models, with the help of three available public datasets (NLM, Belarus, and RSNA). They used 9 pre-trained DL CNN techniques, with the help of TL, from their pre-trained initial weights, they trained, validated, and hence tested to obtain binary classification of TB from the combined datasets, where the result yielded the best results compared to other studies under review.

S. Hwang et al [26] also believe DCNN for TB screening is a promising DL method for various visualization tasks since it enables end-to-end training from feature extraction to classification as agreed with other various studies, without the need for manual feature extraction. Hence, they developed a custom DCNN for automatic TB screening on AlexNet, and further used TL to binary detect TB infections on the three available public datasets, and scored the performance of 96%, 93%, and 88% in terms of AUC for three real field datasets. The study also shows that TL of pre-trained networks resolves the difficulties in handling high-resolution medical images and training huge parameters with a limited number of CXR images, and also states that transferring low-level filters from a pre-trained model based on large-scale images is very effective for training.

R. Hooda [27] presented an ensemble of three standard architectures used for binary image classification with AlexNet, GoogLeNet, and ResNet. where the architectures were all trained from scratch. The dataset is the combination of four public datasets which consist of 1.133 images that were pre-processed using augmentation to increase the number of images as in [25] and other similar studies. Their ensemble model achieves an accuracy of 88% and an AUC of 93%. They believe in a DL-based CAD system, segmenting lung region is not mandatory as opposed to [24].

M. H. A. Hijazi et al [28] also used the two publicly available datasets MC and SZ, in which they first pre-processed the CXRs images to retain only the Region of Interest (ROI). And also used two different pre-trained architectures; VGG 16 and InceptionV3, and further developed a custom CNN architecture with 15 layers to detect TB from the preprocessed CXR images, where the process took less time to complete training. And further performed an ensemble of the architectures, where it scored the best accuracy of 91.0%, sensitivity of 89.6%, and specificity of 90.7% than the individual architecture.

S. K. T. Hwa, M. H. A. Hijazi et al [29] also used the publicly available datasets MC and SZ similar to other literature, in which they first pre-processed the CXRs images to obtain edge feature using Canny Edge detector, which they believe CXR images with more unusual edges could increase the detection rate. They perform an ensemble of two pre-trained CNN architectures as in [25] and [28]. They believe sensitivity is considered more in medical image analysis; hence their work was to get a high sensitivity score.

Furthermore, some studies used private datasets, such as; P. Lakhani and B. Sundaram [30] that used four de-identified HIPAA-compliant datasets exempt from review by the institutional review board (which is believed to be one of the problems of medical datasets), They employed two different DCNNs which were AlexNet and GoogLeNet to binary classify the TB CXR images by training from scratch and by using pre-trained networks on ImageNet (where the pre-trained network performed better), and further perform augmentation with multiple preprocessing techniques which further increased accuracy. Ensembles were further performed on the best-performing algorithms using AlexNet and GoogLeNet architecture with an AUC score of 99%. For cases where the classifiers had type one error, an independent board-certified cardiothoracic radiologist interpreted the result without seeing the model result. Their study also shows that even with CAD systems there is a need for cardiothoracic radiologist experts to further give verdict on the result.

1.2. Innovations and contributions

Most of the studies in the literature used different techniques for binary classification of CXR images using different public and private datasets and different techniques ranging from custom DCNNs to binary classifying of TB.

In our study, we present the use of several pre-trained DCNN architectures to make binary classifications on our private dataset from the western Africa region, Nigeria in particular as most of the studies in the literature are from Europe and Asia, and we further compare our result using the same models on public available dataset from Europe and Asia. Hence, we achieved an accuracy of 94% for both VGG16 and mobile Net version one (MobileNetV1) as the best performing models, with precision, recall, f1-score, specificity, and sensitivity at 94% respectively for the latter and 94% precision, 94% recall, 94% f1-score, 96% specificity, and 92% sensitivity for the former. Whereas for our public dataset, we achieved 99% accuracy, sensitivity, specificity, precision, recall, and f1-score respectively with VGG16 and VGG19, and 99% sensitivity, with 100% accuracy, specificity, precision, recall, and f1-score with MobileNetV1, as our best performing DCNN models while using the public dataset.

The proposed approach is presented in Section 2. The discussion and results are described in Section 3. The conclusion and future work are presented in Section 4.

2. Materials

This study involves two separate datasets; (I) a processed public dataset that includes NLM (National Library of Medicine USA), Belarus, and RSNA (Radiological Society of North America) from T. Rahman et al Kaggle repository, and (II) A private identified dataset in compliance with the Health Insurance and Accountability Act from Nigeria (West Africa). TB case images of the Nigerian people in private datasets consist of images obtained with different imaging devices and are generally of low resolution and quality. On the other hand, the images obtained from the public data set have higher resolution and can be used directly. Positive and negative image counts in public and private datasets are shown in Table 1. From Table 1. the public dataset consists of a total of 7000 CXR images with 3500 as negative and 3500 as positive. Meanwhile, our private dataset consists of a total of 4415 unprocessed CXR images with different pixel values with 3073 as negative and 1342 as positive as shown in Table 2. The two separate datasets were divided into three sets; (I) used for training, (II) validation, and (III)

testing of the architectures. The images were divided randomly in the ratios 80:10:10, with 80% in the training set as it requires more images for training. Thus, the training set for the public data contains 5600 images out of 7000 images, and validation and testing contain 700 each. Whereas, on the private data and 3530 training images out of 4415 images, validation and testing contain 441 each. Hence data augmentation was performed on the positive data of the private dataset only to balance the dataset CXR images. The validation set was used for selecting the proper values of hyper-parameters while training and the testing set was only used for model evaluation to calculate the performance of the architecture.

Table 1. Class-wise image counts in the public and private datasets

Dataset	Positive Data	Negative Data	Total
Public Dataset	3500	3500	7000
Private Dataset	1342	3073	4415

For our private data collection; (I) A mobile X-ray unit was used, provided by the US government, nomenclature X-ray portable apparatus (NSN 6525-01-523-1989), (II) A fixed stationed X-ray unit Philip model of 150kv capacity, (III) A Kodak digital image processing unit (CR140) were used.

Meanwhile a computer with an Intel core i7-3632QM CPU @2.20GHz processor and 16GB RAM, alongside privately obtained GPUs from Google Colab pro+ were used for data preprocessing via TensorFlow (Keras) framework library and Python programming language for the classification of TB in our study.

3. Method

The methodology of this study was carried out in three different stages as listed below and shown schematically in Figure 1.

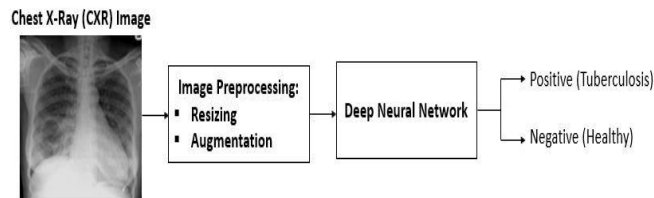


Figure 1. Schematic flow of the study

- I. The public dataset was used for the binary classification of TB positive and negative cases using several trained DCNN models as shown in Table 4,
- II. The private dataset was also used for the binary classification of TB positive and negative cases using the same pre-trained models from the first method as shown in Table 3. respectively.
- III. The pre-trained model's configuration was tweaked to form a custom model by training some layers and leaving out some layers, or by adding/reducing dense layers to classify the TB positive and negative cases on our two separated datasets.

3.1. Preprocessing

The sizes of the private dataset CXR images varied with no actual standard, hence the datasets were preprocessed to resize the CXR images 224*224 to obtain a standard for the dataset, whereas most of the DCCNs models accept 224*224 except for NasNet which accept only 331*331 as input shape, hence we also converted the images from grayscale to Blue, Green, Red (BGR) to obtain three channels since pre-trained models accept only 3 channels, and further store it into a NumPy array, which we further normalized it to fit into the different DCNNs models used. Whereas the public dataset has standards the same preprocessing techniques carried out on

the private dataset as stated above were carried out to obtain a similar dimension of images and to carry out the same comparison.

3.2. Preprocessing

Table 2. Class-wise image counts in the augmented dataset

Dataset	Total	Positive Data	Negative Data	Train	Test	Valid
Public	7000	3500	3500	5600	700	700
Private	6000	3000	3000	4800	600	600

From Table 2. To improve our classification performance knowing DL requires a huge amount of data and the amount of dataset available in our study is limited and not balanced, we used different data augmentation techniques to increase the number of our positive data to 3000 and gave away some negative images, rather than collecting new data which proved to be a problem, and the augmentation technique will help to avoid overfitting. This technique in turn expands the diversity of data available for training models and helps us have balanced data for both positive and negative classification. The built-in Keras framework for data augmentation was used. However, in this study, different image augmentation techniques (re-scaling, zoom, and fill mode) were utilized to generate more images, as shown in Figure 2. In this work, the original image zoom range was set to 20% max, with fill mode set to reflect for convenience.

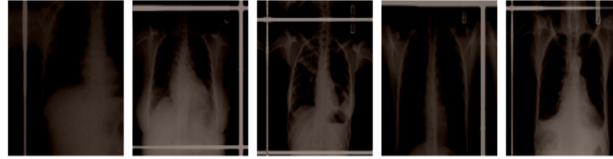


Figure 2. Sample images from the augmented dataset

3.3. Performance evaluation

Many different methods were used in the literature for the performance evaluation of the DCNN models. In our study, the performances of the classification methods were evaluated with sensitivity, specificity, precision, and F1 scores given in Equations 1-5 respectively. The binary classification of the negative and positive class of our models was hence schematically presented with the help of a confusion matrix to showcase the indicators; True Positive, (TP), True Negative (TN), False Positive (FP), and False Negative (FN) as result where the model correctly predicts the positive, negative class, and incorrectly predicts the positive, negative class, respectively.

$$\text{Accuracy} = (\text{TP}+\text{TN})/(\text{TP}+\text{FN}) + (\text{FP}+\text{TN}) \quad (1)$$

$$\text{Sensitivity} = (\text{TP})/(\text{TP}+\text{FN}) \quad (2)$$

$$\text{Specificity} = (\text{TN})/(\text{FP}+\text{TN}) \quad (3)$$

$$\text{Precision} = (\text{TP})/(\text{TP}+\text{FP}) \quad (4)$$

$$\text{F1 Score} = (2\text{TP})/(2\text{TP}+\text{FN}+\text{FP}) \quad (5)$$

The F1 score is a critical evaluation metric commonly used in medical image classification tasks and other binary classification scenarios. It strikes a balance between precision (the ratio of true positive predictions to the total predicted positives) and recall (the ratio of true positive predictions to the total actual positives).

In medical image classification, such as detecting diseases like tuberculosis from chest X-rays, both precision and recall are of utmost importance. A high precision ensures that the positive predictions made by the model are highly reliable, reducing false positives. This is crucial in medical settings to avoid unnecessary follow-up tests or

treatments. On the other hand, a high recall indicates that the model is adept at identifying the actual instances of the disease, reducing false negatives, and ensuring that no cases are overlooked.

The F1 score combines precision and recall into a single metric, providing a comprehensive measure of a model's performance. It is particularly useful when the class distribution is imbalanced, which is often the case in medical scenarios where diseases might be rare. A high F1 score implies a model that strikes a strong balance between accurate positive predictions and comprehensive disease detection.

In medical image classification, a high F1-score signifies that the model is both accurate in identifying the disease and comprehensive in capturing most cases, instilling confidence in its clinical applicability and potential to aid medical professionals in accurate diagnosis.

4. Results and discussions

Table 3. Performance of different models for the classification of TB with private data

Models	Acc.	Weighted Average				
		Sen.	Spe.	Pre.	Recall	F1 Score
VGG 16	94	94	94	94	94	94
VGG 19	92	92	92	92	92	92
ResNet152	84	86	82	85	84	84
RestNet50V2	92	94	89	84	84	92
ResNet152V2	92	92	91	92	92	92
ResNet101V2	92	90	94	92	92	92
MobileNetV1	94	92	96	94	94	94
MobileNetV2	90	88	91	90	90	90
InceptionV3	90	89	91	90	90	90
InceptionRNetV2	90	89	90	89	89	89

The motivation behind this study is to use a private data set from a highly affected region and to compare it with a more prepared public dataset from a different region, hence examining both regions' datasets by using different pre-trained and custom DCCN algorithms to assist physicians in the diagnosis of TB in affected populations. In our Study, the CXR images were binary classified (+ve and -ve). For each DCNN model used, the learning rate was set to 0.0001 and the epoch set to 150 respectively. The activation function was set to Softmax and categorical cross-entropy was employed to train the model. Table 3 shows the results obtained from the training while using public data (the weighted average of the training result was considered for all the models in the method). Whereas Table 4 shows the result obtained from the training while using our private dataset (the weighted average of the training result from the classification table was considered for all the models in the method).

Table 4. Performance of different models for the classification of TB with public data

Models	Acc.	Weighted Average				
		Sen.	Spe.	Pre.	Recall	F1 Score
VGG 16	99	99	99	99	99	99
VGG 19	99	99	99	99	99	99
ResNet152	82	78	87	82	82	82
RestNet50V2	97	99	95	97	97	97
ResNet152V2	98	98	97	98	98	98
ResNet101V2	99	97	100	99	99	99
MobileNetV1	100	99	100	100	100	100
MobileNetV2	99	100	97	99	99	99
InceptionV3	97	99	95	97	97	97
InceptionResNet	98	97	99	98	98	98

This study has several limitations such as; Some CXR-images of our private data are skewed and have no standard due to the machines being used in collecting and storing the images and without having a radiologist or expert to look at the data after preprocessing, some of the images pose a large scale of the black area which we cropped some part of that because which we believe it can be a problem. Nonetheless, we believe that our results could establish a foundation for future prospective research for the detection of TB. Furthermore, regarding the data used for testing, validation, and training, due to human error and the fact that all images were obtained from one center, ignite the possibility that some patients' CXR images found in the test set might also be found in the training set even after a very careful scrutinizing of the data. Additional images were also excluded due to size or standard set while preprocessing the data.

In our first method using pre-trained models to train our public data, we obtained a state-of-the-art performance as in T. Rahman et al [25], and a good result while using the second method for the binary classification.

A general comparison with other studies can be achieved while using our private data as it has shown great promise, and is competitive, which implies that our study performs well. Figure 3. using the confusion matrix systematically explains the performance of our models on our datasets in detecting TB, Figure 3. in our binary classification shows that our model wrongly classified eleven (11) patients to be TB-negative when they were TB-positive patients, and predicted twenty-five (25) patients to be TB positive while they were negative with a sensitivity and specificity of 92%, and 96% respectively meanwhile all other predictions were correct. In Figure 3. a) Binary classification, which happened to be our best-performing model while using our public dataset it wrongly predicted one (1) patient to be TB negative when they were TB positive patients and also predicted two (2) patients to be TB positive when they were actually TB negative. Then, respectively, in Figure 3. b) the public data set, which was trained with the VGG16 model, and in c) and d), the private data set was used with the VGG16 and MobileNet models, and confusion matrices were given.

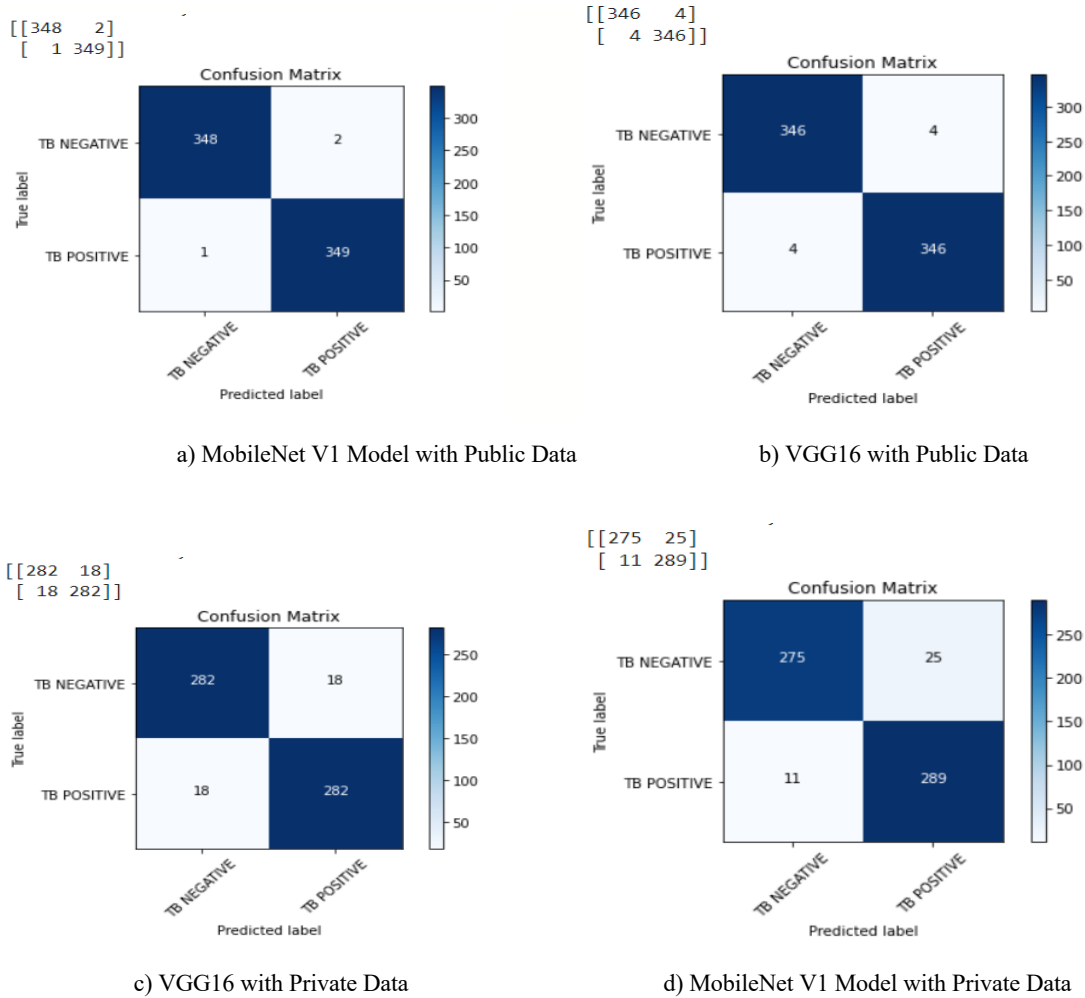


Figure 3. Confusion Matrix of Optimal Models on Public and Private Datasets

5. Conclusion

In conclusion, a pre-trained deep convolutional neural network has been proposed to effectively detect tuberculosis from CXR images. Several pre-trained deep convolutional neural networks were applied to the public and private CXR images. These pre-trained models used in our experiment includes: VGG16, VGG19, ResNet152, ResNet50V2, ResNet101V2, ResNet152, MobileNetV1, MobileNetV2, InceptionV3, and InceptionResNet. The result of this experiment shows that MobileNetV1 achieved the best performance when applied to the public dataset. And for our private dataset, VGG16 and MobileNetV1 achieved the best performance. The performance of the deep learning model applied on the private dataset was observed to be less than that of the public dataset due to different factors, such as; demography of data collection, number of data obtained from the different regions, type of machines used, personal, and many more. However, the results in this proposed study demonstrate the effectiveness of DCCNs in predicting tuberculosis disease from CXR images.

In conclusion, this study demonstrated the effectiveness of deep neural networks (DNN) in tuberculosis detection from chest X-ray images. Our best model achieved impressive f1-scores of 98% and 86% on public and private datasets, respectively.

This underscores the robustness of DNNs in accurately identifying tuberculosis cases, showcasing their potential as a valuable tool for enhancing disease detection efforts. These findings carry significant implications for tuberculosis detection in Nigeria, a country where the disease is a substantial public health concern. The utilization of advanced image analysis techniques, as evidenced by our study, could significantly aid healthcare professionals in swiftly and accurately identifying tuberculosis cases. This could potentially lead to earlier interventions, reduced transmission rates, and improved patient outcomes.

From a forward-looking perspective, future research in this area could explore the integration of multi-modal data, such as combining X-ray images with clinical data or other diagnostic modalities. Furthermore, investigating the generalizability of the deep learning models across different populations and settings would enhance the applicability of these technologies on a broader scale. Additionally, efforts could be directed toward creating user-friendly tools for real-time decision support in clinical practice, further enhancing the impact of tuberculosis detection initiatives in resource-constrained environments.

References

- [1] Desmon S. "Taking a Deep Dive into Why Nigeria's TB Rates are So High," 2018. <https://ccp.jhu.edu/2018/10/22/nigeria-tb-rates-high-tuberculosis/> (Last accessed Aug. 29, 2023).
- [2] WHO. "The End TB Strategy Global strategy and targets for tuberculosis prevention, care and control after 2015," 2015, <https://apps.who.int/iris/rest/bitstreams/1271371/retrieve>. (Last accessed Aug. 29, 2023).
- [3] Alcantra MF, Liu C, Liu B, Brunette M, Zhang N, Sun T, Zhang P, Chen Q, Li Y, Albarracin CM, Peinado J, Garavito ES, Garcia LL, Curioso WH. "Improving tuberculosis diagnostics using deep learning and mobile health technologies among resource-poor communities in Perú," *Smart Heal.*, vol. 1–2, no. March, pp. 66–76, 2017, doi: 10.1016/j.smhl.2017.04.003.
- [4] WHO. Global Tuberculosis report 2016, <https://apps.who.int/iris/bitstream/handle/10665/250441/9789241565394-eng.pdf?sequence=1> (Last accessed Aug. 29, 2023)
- [5] Harries AD *et al.*. "Deaths from tuberculosis in sub-Saharan African countries with a high prevalence of HIV-1," *Lancet Infect. Dis.*, vol. 357, no. 9267, pp. 1519–1523, 2001, doi: 10.1016/S0140-6736(00)04639-0.
- [6] CDC A. "Tuberculosis," Tuberculosis in Africa. <https://africacdc.org/disease/tuberculosis/#:~:text=TB,Africa CDC>, (Last accessed Aug. 29, 2023).
- [7] WHO. "World Tuberculosis Day," 2018. <https://www.afro.who.int/health-topics/tuberculosis-tb>. (Last accessed Aug. 29, 2023).
- [8] Vassall A and Gidado M. "Post-2015 Development Agenda: Nigeria Perspectives: Tuberculosis," pp. 1–40, 2015.
- [9] Chukwu O and Okoeguale B. "FIRST National TB Prevalence Survey 2012, Nigeria," Nigeria, 2012. [Online]. Available: https://www.who.int/tb/publications/NigeriaReport_WEB_NEW.pdf. (Last accessed Aug. 29, 2023).
- [10] Odume B, Falkun V, Chukwuogo O, Ogbudebe C, Useni S, Nwokoye N, Aniwada E, Olusola Faleye B, Okekearu I, Nongo D, Odusote T, and Lawanson A. Impact of COVID-19 on TB active case finding in Nigeria, *Public Health Action*. 2020 Dec 21; 10(4): 157–162. doi: 10.5588/pha.20.0037
- [11] WHO. "Chest Radiography in Tuberculosis," WHO Libr. Cat. Data, p. 44, 2016, [Online]. Available: http://www.who.int/about/licensing/copyright_form%0Ahttp://www.who.int/about/licensing/copyright_form. (Last accessed Aug. 29, 2023).
- [12] Wang S and Summers RM. "Machine learning and radiology," *Med. Image Anal.*, vol. 16, no. 5, pp. 933–951, 2012, doi: 10.1016/j.media.2012.02.005.
- [13] Lopes UK and Valiati JF. "Pre-trained convolutional neural networks as feature extractors for tuberculosis detection," *Comput. Biol. Med.*, vol. 89, pp. 135–143, 2017, doi: 10.1016/j.compbimed.2017.08.001.
- [14] Chen B, Zhang L, Chen H, Liang K, and Chen X. "A novel extended Kalman filter with support vector machine based method for the automatic diagnosis and segmentation of brain tumors", *Comput. Methods Programs Biomed.* 2021 Mar;200:105797. doi: 10.1016/j.cmpb.2020.105797. PMID: 3331787
- [15] Houssein EH, Emam MM, Ali AA, and Suganthan PN. "Deep and machine learning techniques for medical imaging-based breast cancer: A comprehensive review," *Expert Syst. Appl.*, no. April, p. 114161, 2020, doi: 10.1016/j.eswa.2020.114161.
- [16] Ozturk T, Talo M, Yildirim EA, Baloglu UB, Yildirim O, and Rajendra Acharya U. "Automated detection of COVID-19 cases using deep neural networks with X-ray images," *Comput. Biol. Med.*, vol. 121, no. April, p. 103792, 2020, doi: 10.1016/j.compbimed.2020.103792.
- [17] Olsen CR, Mentz RJ, Anstrom KJ, Page D, and Patel PA. "Clinical applications of machine learning in the diagnosis, classification, and prediction of heart failure: Machine learning in heart failure," *Am. Heart J.*, vol. 229, pp. 1–17, 2020, doi: 10.1016/j.ahj.2020.07.009.
- [18] Chaki J, Thillai Ganesh S, Cidham SK, and Ananda Theertan S. "Machine learning and artificial intelligence based Diabetes Mellitus detection and self-management: A systematic review," *J. King Saud Univ. - Comput. Inf. Sci.*, no. xxxx, 2020, doi: 10.1016/j.jksuci.2020.06.013.
- [19] Rajpurkar P *et al.*. "Deep learning for chest radiograph diagnosis: A retrospective comparison of the CheXNeXt algorithm to practicing radiologists," *PLoS Med.*, vol. 15, no. 11, pp. 1–17, 2018, doi: 10.1371/journal.pmed.1002686.
- [20] Pasa F, Golkov V, Pfeiffer F, Cremers D, and Pfeiffer D. "Efficient Deep Network Architectures for Fast Chest X-Ray Tuberculosis Screening and Visualization," *Sci. Rep.*, vol. 9, no. 1, pp. 2–10, 2019, doi: 10.1038/s41598-019-42557-4.
- [21] Krizhevsky A, Sutskever I, and Hinton GE. "ImageNet Classification with Deep Convolutional Neural Networks,"

- Commun. ACM, vol. 60, no. 6, pp. 84–90, June 2017. doi = 10.1145/3065386
- [22] Xiong Y, Ba X, Hou A, Zhang K, Chen L, and Li T. “Automatic detection of mycobacterium tuberculosis using artificial intelligence,” *J. Thorac. Dis.*, vol. 10, no. 3, pp. 1936–1940, 2018, doi: 10.21037/jtd.2018.01.91.
- [23] Hwang EJ *et al.*. “Development and Validation of a Deep Learning-based Automatic Detection Algorithm for Active Pulmonary Tuberculosis on Chest Radiographs,” *Clin. Infect. Dis.*, vol. 69, no. 5, pp. 739–747, 2019, doi: 10.1093/cid/ciy967.
- [24] Rajpurkar P *et al.*. “CheXaid: deep learning assistance for physician diagnosis of tuberculosis using chest x-rays in patients with HIV,” *npj Digital Med.*, vol. 3, no. 1, pp. 1–8, 2020, doi: 10.1038/s41746-020-00322-2.
- [25] Rahman T *et al.*. “Reliable tuberculosis detection using chest x-ray with deep learning, segmentation, and visualization,” *IEEE Access.*, August, 2020, doi: 10.1109/access.2020.3031384.
- [26] Hwang S, Kim HE, Jeong J, and Kim HJ. “A novel approach for tuberculosis screening based on deep convolutional neural networks,” *Med. Imaging 2016 Comput. Diagnosis*, vol. 9785, p. 97852W, 2016, doi: 10.1117/12.2216198.
- [27] Hooda R, Mittal A, and Sofat S. “Automated TB classification using an ensemble of deep architectures,” *Multimed. Tools Appl.*, vol. 78, no. 22, pp. 31515–31532, 2019, doi: 10.1007/s11042-019-07984-5.
- [28] Hijazi MHA, Yang LQ, Alfred R, Mahdin H, and Yaakob R. “Ensemble deep learning for tuberculosis detection,” *Indones. J. Electr. Eng. Comput. Sci.*, vol. 17, no. 2, pp. 1014–1020, 2019, doi: 10.11591/ijeecs.v17.i2.pp1014-1020.
- [29] Hwa SKT, Hijazi MHA, Bade A, Yaakob R, and Jeffree MS. “Ensemble deep learning for tuberculosis detection using chest X-ray and canny edge detected images,” *Int. J. Artif. Intell.*, vol. 8, no. 4, pp. 429–435, 2019, doi: 10.11591/ijai.v8.i4.pp429-435.
- [30] Lakhani P and Sundaram B. “Deep Learning at Chest Radiography: Automated Classification of Pulmonary Tuberculosis by Using Convolutional Neural Networks.” *Radiology*, vol. 284, no. 2, pp. 574–582, Aug., 2017. doi: 10.1148/radiol.2017162326. Epub 2017 Apr 24. PMID: 28436741.

Gd Effect on Micro-Crystal Structure and Thermomagnetic Behavior of NiMnSn Magnetic Shape Memory Alloy

Ecem ÖZEN ÖNER^{1*}, Mediha KÖK²

^{1,2} Department of Physics, Faculty of Science, Fırat University, Elazığ, Turkey
^{*1} e.ozenoner@firat.edu.tr, ² msoglu@firat.edu.tr

(Geliş/Received: 13/07/2023;

Kabul/Accepted: 09/10/2023)

Abstract: In this study, the rare earth Gadolinium (Gd) element was added to the NiMnSn alloy, which is an alternative to the NiMnGa alloy group, with the increasing popularity of magnetic shape memory alloys. Since rare earth elements have strategic importance for our country in recent years, Gd element has been preferred in this study. X-rays and SEM-EDX analysis were performed to determine the morphological properties of the crystal structure and microstructure of the alloys. Magnetic measurements of the alloys were made with the physical property measuring device and it was determined that the magnetization values decreased with the addition of Gd.

Key words: Magnetic shape memory alloy, Smart materials, Rare earth element, Gadolinium

NiMnSn Manyetik Şekil Hatırlamalı Alaşımının Mikro Kristal Yapısı ve Termomanyetik Davranışı Üzerindeki Gd Etkisi

Öz: Bu çalışmada, manyetik şekil hatırlamalı alaşımlarının artan popüleritesi ile NiMnGa alaşım grubuna bir alternatif olan NiMnSn alaşımına nadir toprak gadolinyum (Gd) elemanı ilave edildi. Son yıllarda nadir toprak unsurları ülkemiz için stratejik bir öneme sahip olduğundan, bu çalışmada Gd element tercih edilmiştir. Kristal yapının morfolojik özelliklerini ve alaşımların mikro yapısını belirlemek için X-ışınları ve SEM-EDX analizi yapıldı. Alaşımların manyetik ölçümleri fiziksel özellik ölçüm cihazı ile yapılmıştır ve mıknatıslanma değerlerinin Gd ilavesiyle azaldığı belirlenmiştir.

Anahtar kelimeler: Manyetik şekil hatırlamalı alaşım, Akıllı malzemeler, Nadir toprak elementleri, Gadolinyum

1. Introduction

Smart materials; Materials whose structure can change significantly with external factors such as pressure, humidity, electric or magnetic field, light, temperature, acidity of the environment (pH) or chemical components are called materials [1-4]. Today, smart materials are classified into many subheadings. To give an example of smart materials; piezoelectric, thermoelectric etc., chromic materials (thermochromic, photochromic etc.), rheological materials (magneto-rheological, electro-rheological etc.) alloys can be given [3,5]. Magnetic shape memory alloys (MSMA) are smart materials that exhibit a magnetic field induced strain (MFIS). Compared to thermally activated shape memory alloys such as NiTi, MSHA's response is much faster (less than a millisecond compared to a few seconds), making them a good candidate material for use in actuator applications [6-10].

In this study, Gadolinium (Gd), which is one of the strategically important rare earth elements, was added to reduce the transformation temperature of the NiMnSn magnetic shape memory alloy. At temperatures above 20 °C, Gd is paramagnetic. Gadolinium was identified by Jean de Marignac in 1880 by spectroscopy of the mineral gadolinite, and he named this element Gadolinium after the mineral gadolinite [6,11,12]. This mineral is named after the Swedish/Finnish chemist Johan Gadolin, who discovered and characterized it in the 18th century. Gadolinium has been the benchmark magnetocaloric material for room temperature magnetic cooling since Brown's pioneering work in 1976. Gadolinium is readily available and has a relatively high magnetocaloric effect and a Curie temperature around room temperature [13-15]. The aim of this study, in order to see the effect of Gd element on NiMnSn magnetic shape memory alloy, various characterization analyzes were performed by preparing different ratios. X-ray (XRD) diffraction method analysis was performed to have information about the atomic arrangement of the material. SEM-EDX analysis was performed in order to see the changes in the surface of the alloys made by changing the amounts of the elements. Since it is a magnetic alloy, magnetization measurements were made.

* Corresponding author: e.ozenoner@firat.edu.tr. ORCID Number of authors: ¹ 0000-0001-8784-8044, ² 0000-0001-7404-4311

2. Experimental

In this study, high purity powdered (99.9%) Ni, Mn, Sn and Gd elements were used. For alloy production, each alloy is designed to be 10 g. Alloys codes; Ni₅₀Mn₃₈Sn₁₂ (Gd0), Ni₅₀Mn₃₄Sn₁₂Gd₄ (Gd4), Ni₅₀Mn₃₂Sn₁₂Gd₆ (Gd6), Ni₄₆Mn₃₈Sn₁₂Gd₄ (Gd44), Ni₄₄Mn₃₈Sn₁₂Gd₆ (Gd66). The production of pelletized NiMnSn-Gd magnetic shape memory alloys was made by arc melting method. The melting process was carried out several times while the samples were in the system, thus homogenizing the alloys in the system. Post-production alloys have become bulk. In bulk alloys, a second homogenization process was carried out by keeping the alloys in an ash furnace at 900 °C for 24 hours. In this study, the crystal structures of the produced NiMnSn-Gd alloys were determined at room temperature using a Bruker D8 X-ray diffractometer at room temperature. For this study, the samples were mechanically polished and chemically etched in 20 ml of HCl + 5 g FeC₃-H₂O + 96 mL methanol solution, then the microstructures and chemical compositions of all alloys were determined using a Hitachi brand scanning electron microscope. Magnetic measurement is important to analyze the properties of magnetic shape memory alloys rather than traditional shape memory alloys. Transitions and changes between phases in the structure of the sample can be thoroughly analyzed and evaluated. The magnetization measurements of the Gd0, Gd4, Gd44, Gd6, Gd66 alloy samples were precisely measured with the Quantum Design PPMS 7 (Physical Properties Measurement System) device at room temperature between -6 Tesla and 6 Tesla.

3. Result and Discussion

Figure 1 shows the results obtained from the x-ray diffractogram of Gd undoped and doped NiMnSn alloy at room temperature. The results obtained are supported by the literature [16-18]. In the Gd0 alloy, precipitate phases were also observed together with peaks belonging to the martensite phase. Here, the martensite phase exhibits the characteristic 10 M modified orthorhombic martensite crystal structure [16]. The precipitate phases are thought to be due to insufficient homogenization during the production of the alloy. In the x-ray diffractograms of Gd4 and Gd44 alloys, the number and intensity of peaks belonging to martensite phases increased unlike the main alloy. This may be due to the contribution of Gd element to NiMnSn alloy. Along with the martensite phase, precipitate phases were also observed. In the x-ray diffractograms of Gd6 and Gd66 alloys, unlike other alloys, peaks belonging to the austenite (A) L21 phase were observed. In Gd66 alloy, unlike Gd6 alloy, there are also peaks belonging to the martensite phase with low intensity. The other result extracted from the XRD curve is the crystal size (D) of the alloys obtained using (1), Scherrer's equation, which depends on some parameters including width at half maximum (FWHM), Bragg angle (θ), wavelength [19]:

$$D = K \lambda / (B \cos \theta) \quad (1)$$

where, B indicates the Full width at half maximum FWHM of the sharpest x-ray curve, K is the shape factor (K = 0.9) and the wavelength of the beam $\lambda K\alpha(\text{Cu})$ applied in the measurement was taken as 1.5406 Å. Figure 2 shows the average crystal size comparison of Gd doped NiMnSn alloy. It was observed that the crystal size of Gd-doped NiMnSn alloys increased compared to the Gd0 main sample.

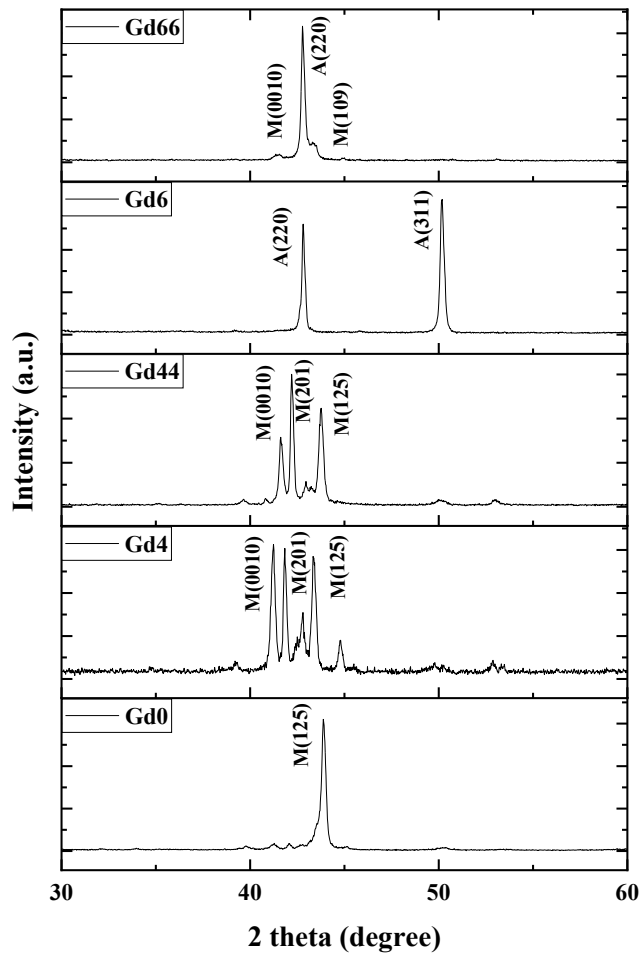


Figure 1. XRD results of Gd0, Gd4, Gd44, Gd6 and Gd66 samples

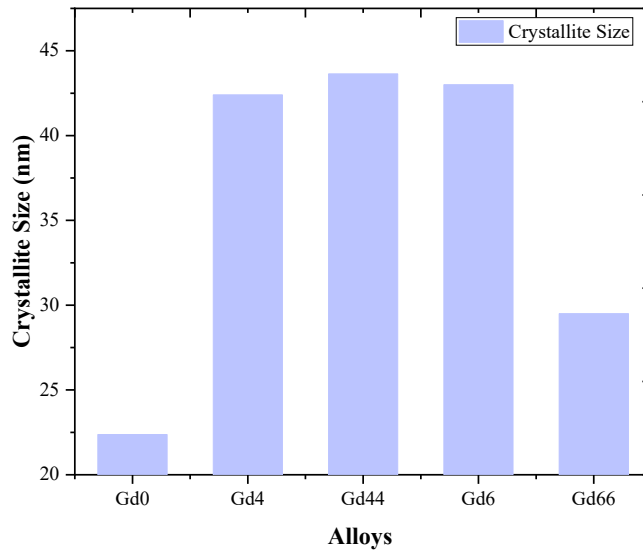


Figure 2. Comparison of crystal size of NiMnSn-Gd alloy

Scanning Electron Microscopy (SEM) technique was used to analyse the effect on the microstructure of NiMnSn-Gd shape-memory alloy and measurements were made at room temperature. The results are shown in Figures 3-4. Figure 3 shows the SEM image of the Gd0 master sample. According to the SEM image, needle type and parallel martensite plates are seen in the main NiMnSn alloy [20]. In addition, bump-shaped precipitate phases were occasionally observed. The reason for the formation of precipitate phases is that the full martensite phase (M) could not be obtained during and after the heat treatment during and after production. In addition, the regions marked in yellow show the voids formed. The reason for these voids may be the air bubbles formed during the melting of the alloying elements melted during production. Figure 4. a-b shows the SEM images of gadolinium doped Gd4 and Gd44 alloys taken at room temperature. In Gd4 alloy, nickel element ratio is higher, manganese element ratio is lower and Gd ratio is equal compared to Gd44 alloy. Considering these results, if we compare the images of the two alloys, the precipitate phase is observed in high density in Gd4 alloy, while the precipitate phase is very rare in Gd44 alloy and the size of the precipitate phases is enlarged. According to these results, the increase in nickel content increased the precipitate phases. Apart from precipitate phases, martensite plates and voids were observed in both alloys. Since the transformation temperatures of these alloys are almost close to room temperature, it is natural to see martensite plates. Figure 5. a-b shows the SEM images of two types of NiMnSnGd alloys doped with 6% Gd. In the alloys given with the codes Gd6 and Gd66, while the Gd ratio is constant at 6%, the nickel ratio is higher and the manganese ratio is lower in Gd6 alloy compared to Gd66 alloy. Similar to Gd4 and Gd44 alloys, the amount of precipitate phase increased depending on the nickel content. With the effect of Gd element, the flatness of the precipitate phases increased. It was also observed that the volume and number of voids increased. Another important result is the reduction of martensite plates. Since the austenite→ martensite transformation temperature of these alloys is below room temperature, it is normal that the appearance of martensite plates decreases. SEM analysis shows images of both martensite and austenite phases (A) of the alloys. In addition, the austenite phase contains more Mn compared to the martensite phase (M). Saini et al. [21] obtained similar results for a Ni₄₆Cu₄Mn₄₅Sn₅ shape memory alloy and found that the SEM image is a mixture of martensite and austenite phases. They also stated that the needle-like component in the images represents the martensite phase, which is characteristic of martensitic transformation.

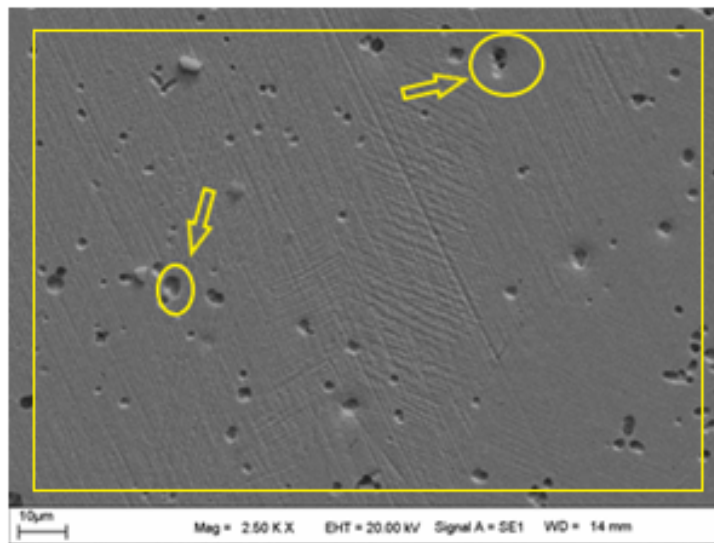


Figure 3. SEM image of Gd0 alloy

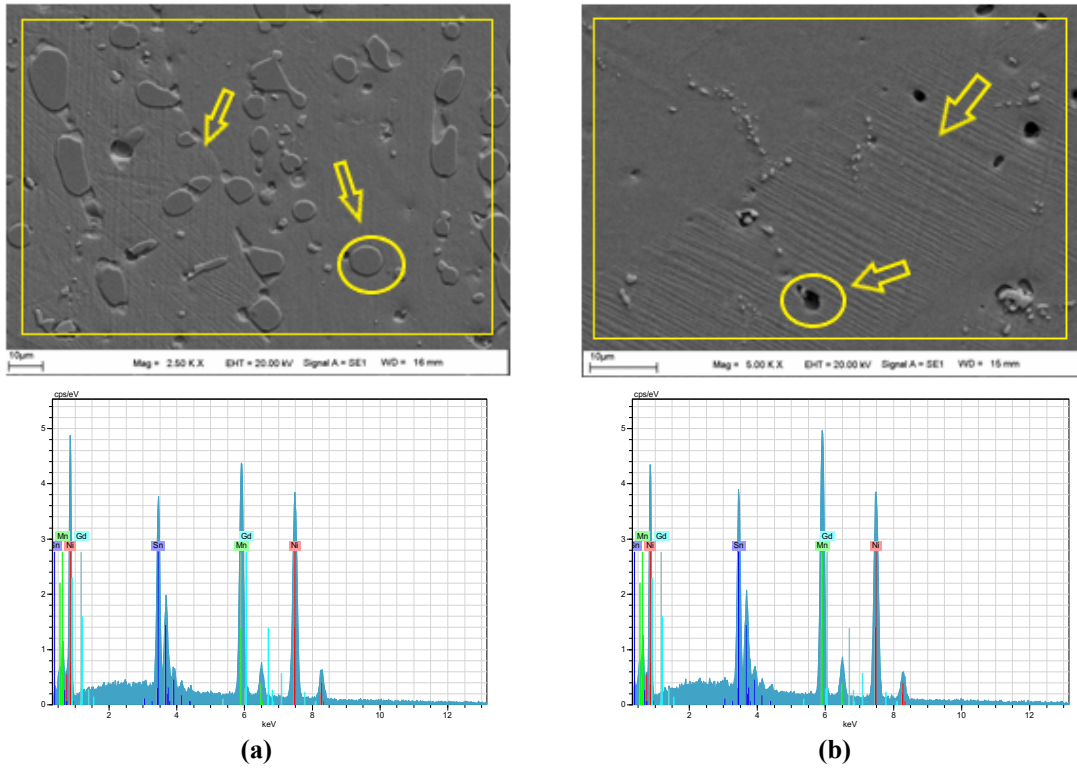


Figure 4. a) SEM image of Gd4 alloy b) SEM image of Gd44 alloy

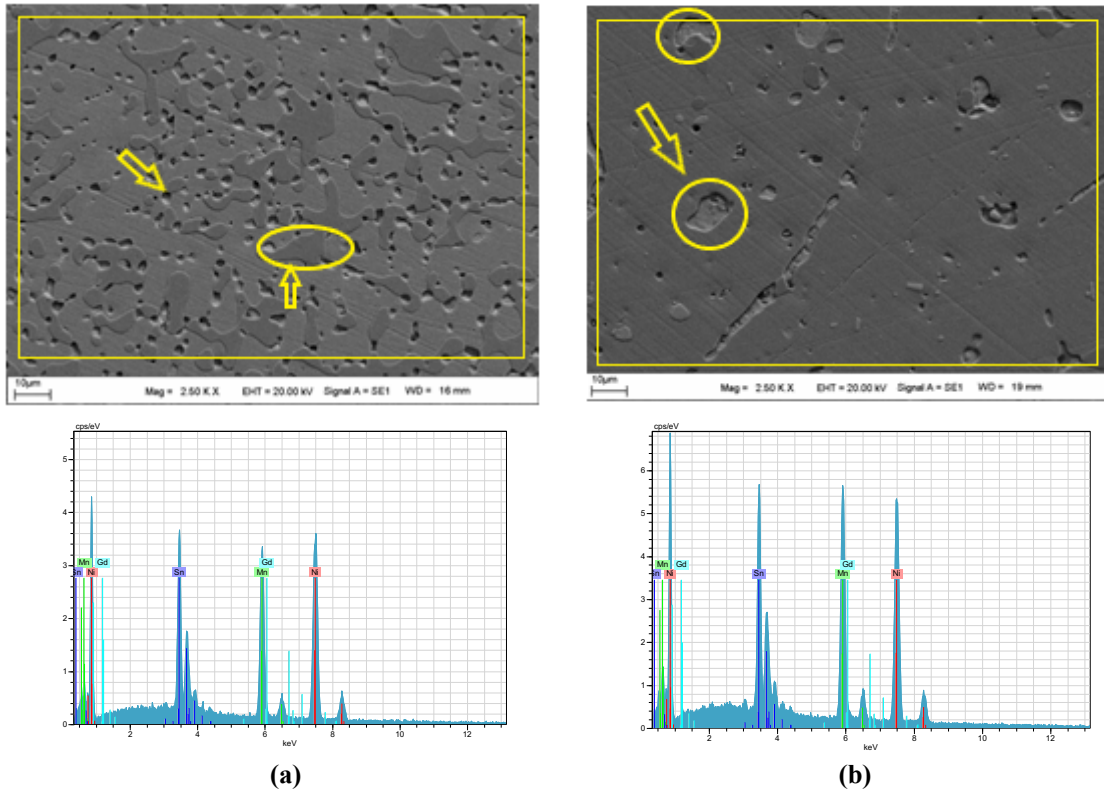


Figure 5. a) SEM image of Gd6 alloy b) SEM image of Gd66 alloy

Figure 6 shows the magnetization values of NiMnSn-Gd alloys at room temperature in 6T external magnetic field. According to these results, in general, there is a decrease in magnetization value with Gd doping for 6 Tesla external magnetic field. If Gd4, Gd44, G6 and Gd66 alloys prepared by changing the ratio of nickel and manganese are compared among themselves, it is concluded that decreasing the nickel ratio is more effective than manganese in decreasing the magnetization value for all of them.

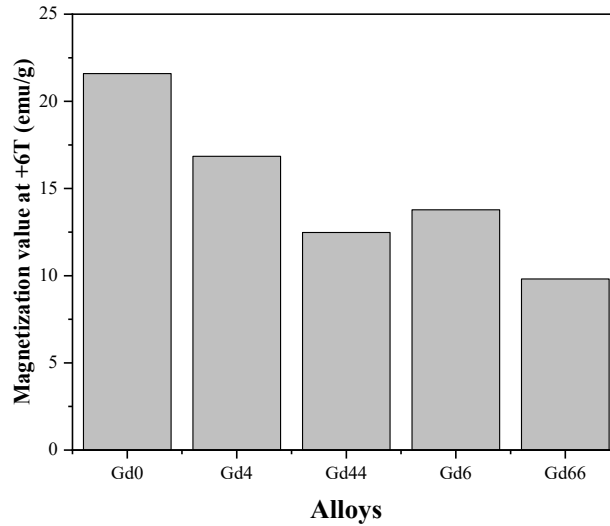


Figure 6. Comparison of saturation values of NiMnSGd alloys

Figure 7 a-e shows the magnetization measurements of the base NiMnSn alloy and Gd doped NiMnSn alloys in the temperature range of -120 °C to 100 °C under 1 Tesla magnetic field. These measurements were performed at a heating-cooling rate of 1 °C/min. The measurements made using the PPMS device could not be measured for higher temperatures, since the maximum temperature that the device can reach is 100 °C. It is known from previous study[14] that the transformation temperature of Gd0 alloy is between 84 and 120 °C. The thermomagnetic hysteresis formation in Figure 7.a. could not be completed because the system did not reach 120 °C, but the beginning of the hysteresis is seen. In Gd4, Gd44 and Gd66 alloys, hysteresis was found to occur at the points where austenite→martensite, martensite→austenite transformation occurred. In Gd6 alloy, as seen in our previous study[14], no transformation hysteresis is observed in the magnetization hysteresis since a low energy transformation occurs.

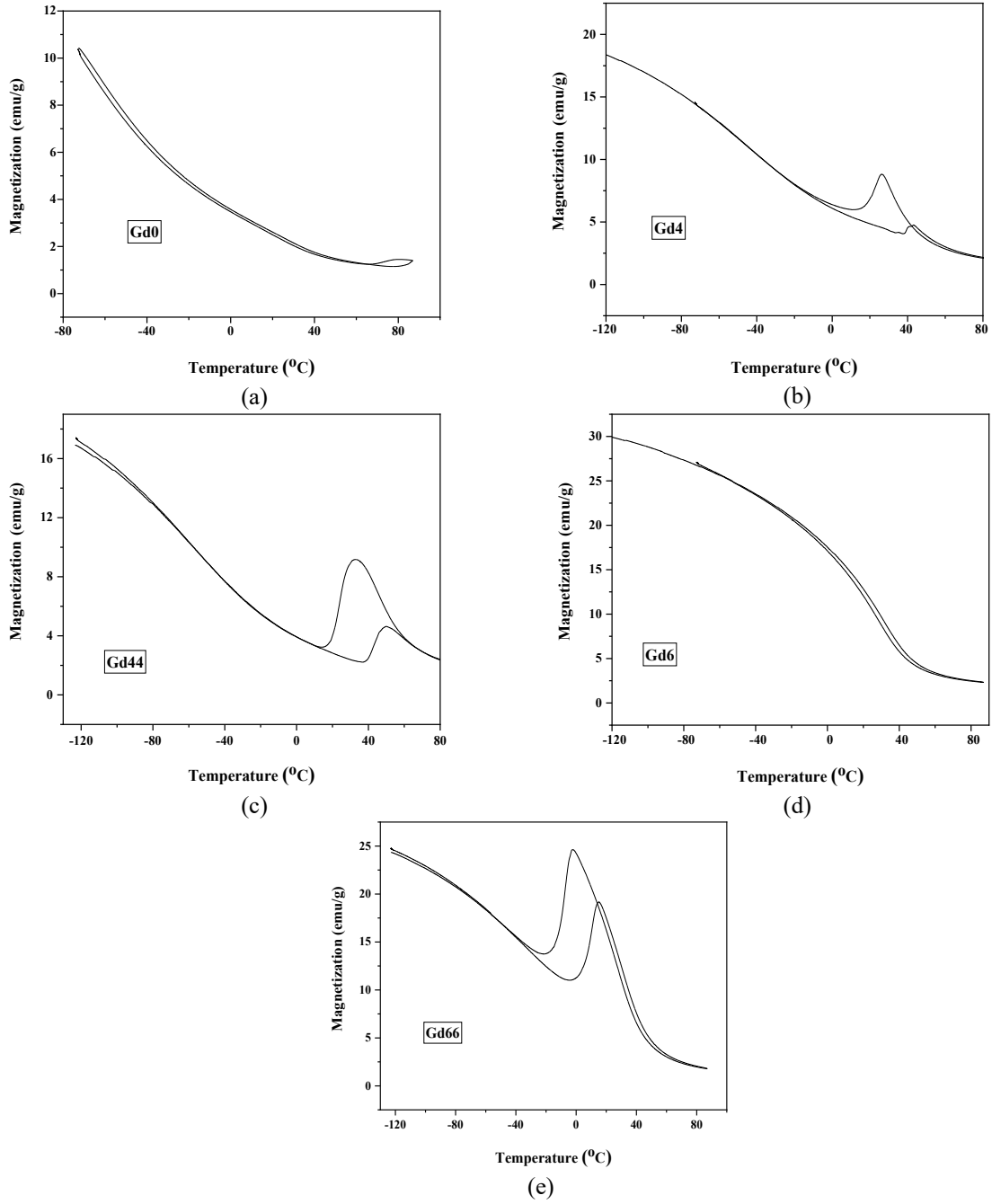


Figure 7. Variation of magnetization with temperature of alloys a) Gd0, b) Gd4, c) Gd44, d) Gd6, e) Gd66

Conclusions

In this study, the effect of Gd doping of NiMnSn magnetic shape-memory alloy on the microcrystalline structure and thermomagnetic hysteresis of the alloy was investigated. As a result of microstructure and crystal structure investigations, peaks belonging to the martensite phase of the NiMnSn alloy without Gd were found, while peaks belonging to the precipitate phases and austenite phase were found with Gd doping. Needle-type martensite plates and V-type martensite plates were observed in SEM images. After thermomagnetic measurements, a wide magnetic hysteresis was found in Gd4, Gd44 and Gd6 alloys. The starting and ending points of this hysteresis were found to coincide with austenite and martensite phase temperatures.

Acknowledgements

The authors would like to thank the financial support provided by the Research Universities Support Program of Firat University (ADEP) (Project Number: ADEP.23.02). Also, this article is a part of the Ph.D. thesis of Ecem Özen Öner.

References

- [1] Otsuka K and Wayman CM. Shape memory materials. Cambridge university press; 1999.
- [2] Castillo-Villa PO, Mañosa L, Planes A, Soto-Parra DE, Sánchez-Llamazares JL, Flores-Zúñiga H and Frontera C. Elastocaloric and magnetocaloric effects in Ni-Mn-Sn (Cu) shape-memory alloy. *Journal of Applied Physics* 113 (2013); 053506.
- [3] Wayman C. Some applications of shape-memory alloys. *Jom* 32 (1980); 129.
- [4] Lagoudas DC. Shape memory alloys: modeling and engineering applications. Springer 2008.
- [5] Addington M and Schodek D. Smart materials and technologies. *Archit. Urbanism* 5 (2005); 8.
- [6] Milleret A. 4D printing of Ni–Mn–Ga magnetic shape memory alloys: a review. *Materials Science and Technology* 38 (2022); 593.
- [7] Qader İN, Mediha K, Dağdelen F and Aydogdu Y. A review of smart materials: researches and applications. *El-Cezeri* 6 (2019); 755.
- [8] Cai W, Meng X and Zhao L. Recent development of TiNi-based shape memory alloys. *Current Opinion in Solid State and Materials Science* 9 (2005); 296.
- [9] Dhaka R, D’Souza S, Maniraj M, Chakrabarti A, Schlagel D, Lograsso T and Barman S. Photoemission study of the (1 0 0) surface of Ni₂MnGa and Mn₂NiGa ferromagnetic shape memory alloys. *Surface Science* 603 (2009); 1999.
- [10] Murakami Y, Shindo D, Oikawa K, Kainuma R and Ishida K. Magnetic domain structures in Co–Ni–Al shape memory alloys studied by Lorentz microscopy and electron holography. *Acta materialia* 50 (2002); 2173.
- [11] Blomqvist L, Nordberg GF, Nurchi VM and Aaseth JO. Gadolinium in Medical Imaging—Usefulness, Toxic Reactions and Possible Countermeasures—A Review. *Biomolecules* 12 (2022); 742.
- [12] Tian X, Shi D, Zhang K, Li H, Zhou L, Ma T, Wang C, Wen Q and Tan C. Machine-learning model for prediction of martensitic transformation temperature in NiMnSn-based ferromagnetic shape memory alloys. *Computational Materials Science* 215 (2022); 111811.
- [13] Bahl CRH and Nielsen KK. The effect of demagnetization on the magnetocaloric properties of gadolinium. *Journal of Applied Physics* 105 (2009); 013916.
- [14] Öner E and Kök M. Evaluation of thermal, electrical and magnetic properties of NiMnSnGd shape memory alloys by changing Gd amount for keeping the tin ratio constant. *The European Physical Journal Plus* 136 (2021); 463.
- [15] Deniz CZ and Kök M. Investigation of the thermal and microstructural changes of CuAlNiNb quaternary shape memory alloys by different niobium amount. *The European Physical Journal Plus* 133 (2018); 288.
- [16] Xing C, Zhang H, Long K, Xiao Y, Zhang H, Qiu Z, He D, Liu X, Zhang Y and Long Y. The effect of different atomic substitution at Mn site on magnetocaloric effect in Ni₅₀Mn₃₅Co₂Sn₁₃ alloy. *Crystals* 8 (2018); 329.
- [17] Pathak AK, Dubenko I, Stadler S and Ali N. The effect of partial substitution of In by Si on the phase transitions and respective magnetic entropy changes of Ni₅₀Mn₃₅In₁₅ Heusler alloy. *Journal of Physics D: Applied Physics* 41 (2008); 202004.
- [18] Sun H, Jing C, Zeng H, Su Y, Yang S, Zhang Y, Bachagha T, Zhou T, Hou L and Ren W. Martensitic Transformation, Magnetic and Mechanical Characteristics in Unidirectional Ni–Mn–Sn Heusler Alloy. *Magnetochemistry* 8 (2022); 136.
- [19] Kök M, Qader İN, Mohammed SS, Öner E, Dağdelen F and Aydogdu Y. Thermal stability and some thermodynamics analysis of heat treated quaternary CuAlNiTa shape memory alloy. *Mater Res Express* 7 (2019); 015702.
- [20] Qader İN, Kök M and Dağdelen F. Effect of heat treatment on thermodynamics parameters, crystal and microstructure of (Cu-Al-Ni-Hf) shape memory alloy. *Physica B: Condensed Matter* 553 (2019); 1.
- [21] Saini D, Singh S, Banerjee M and Sachdev K. Structural Transformation and Hysteresis Behaviour of Ni₄₆Cu₄Mn₄₅Sn₅ Alloy Synthesized by Ball Milling Method. *Macromolecular Symposia* 2017; 1700015.

Investigation of Radon, Total Electron Content and Linear and Nonlinear Variations of Meteorological Variables Due to Earthquakes: ARIMA and Monte Carlo Modelling

Marjan Mohammed GHAFAR¹, Hemn Salh^{2*}, Fatih Külahcı³

¹ Department of Physics, College of Science, University of Halabja, Halabja, Iraq

² Department of Physics, Faculty of Science and Health, Koya University, Koya KOY45, Iraq

³ Firat University, Science Faculty, Physics Department, Nuclear Physics Division, TR-23119, Elazığ, Harput, Turkey

¹ Marjan.ghafar@uoh.edu.iq, ² hemn.salh@koyauniversity.org, ³ fatihkulahci@firat.edu.tr

(Geliş/Received: 18/01/2023;

Kabul/Accepted: 04/05/2023)

Abstract: An Integrated Autoregressive Moving Average (ARIMA) - Monte Carlo Simulation (MCS) is proposed to analyze and model the anomalies of atmospheric and ground gases by an earthquake along the North Anatolian Fault Zone (Türkiye). Earthquakes, Soil radon gas and Total Electron Content (TEC) showed simultaneous anomalies. There are positive relationships between these three parameters. Also, positive relations between Rn, meteorology, and atmosphere are detected. The proposed ARIMA model and MCS for the Rn-TEC-Earthquake relationships of the measured data gave statistically significant results. This model and simulation showed statistically significant changes in the effects of microearthquakes, which are more difficult to detect than large earthquakes, especially on the ionospheric TEC.

Key words: Total Electron Content, Earthquake precursors, ARIMA, Monte Carlo Simulation

Radon, Toplam Elektron İçeriği ve Meteorolojik Değişkenlerin Depremlere Bağlı Doğrusal ve Doğrusal Olmayan Değişimlerinin İncelenmesi: ARIMA ve Monte Carlo Modellemesi

Öz: Kuzey Anadolu Fay Zonu (Türkiye) boyunca meydana gelen bir depremin atmosferik ve yer gazlarındaki anormallikleri analiz etmek ve modellemek için Entegre Otoregresif Hareketli Ortalama (ARIMA) - Monte Carlo Simülasyonu (MCS) önerilmiştir. Depremler, Toprak radon gazı ve Toplam Elektron İçeriği (TEC) eşzamanlı anormallikler gösterdi. Bu üç parametre arasında pozitif ilişkiler vardır. Ayrıca Rn, meteoroloji ve atmosfer arasında da pozitif ilişkiler tespit edilmiştir. Ölçülen verilerin Rn-TEC-Deprem ilişkileri için önerilen ARIMA modeli ve MCS istatistiksel olarak anlamlı sonuçlar vermiştir. Bu model ve simülasyon, tespit edilmesi büyük depremlere göre daha zor olan mikrodepremlerin, özellikle iyonosferik TEC üzerindeki etkilerinde istatistiksel olarak anlamlı değişiklikler olduğunu gösterdi.

Anahtar kelimeler: Toplam Elektron İçeriği, Deprem öncüleri, ARIMA, Monte Carlo simülasyonu

1. Introduction

Earthquake formations are among the most difficult geological phenomena occurrences that exist on the Earth's surface as a consequence of various parameter influences. Soil radon gas (²²²Rn) alone is insufficient because of the Earth's structure, air pressure, environmental warming, temperature, and interior, among other influences [1–4]. An earthquake is a sudden movement induced by fissures in the Earth's crust [5] and is the result of a large amount of energy moving for heat energy, seismic wave energy, and plastic deformation energy, and then only a seismic wave is considered for the earthquake. The idea of magnitude has been included to make estimating earthquake energy clear [6]. The changes in the composite materials' physical, chemical, and other characteristics that result from the accumulation of stress in the crust are known as the precursors of an earthquake.

Seismologists may detect these actions and use them as a basis for earthquake forecasts [6–9]. While an uncolored gas, radon has a half-life of approximately four days. The most stable isotope of radium that exists is ²²²Rn, the heaviest noble gas. Radium is the primary source of radon in the Earth's crust, Therefore, the amount of radium is mostly equal to the amount of uranium since around 80% of the Rn that is released into the atmosphere is detected in the top few meters of the earth, in rocks and soil. Depending on the type of rock and mineral, different amounts of uranium and radium can be discovered in soil. On average, ²³⁸U is present in 24 Bq/kg of soil worldwide [10]. The study of Rn release rates from the Earth's crust has implications in several fields of earth and atmospheric sciences for quantifying activities ranging from monitoring atmospheric sources to transportation. Radon gas and its offspring can be used. All of this research needs a thorough knowledge of the processes that regulate the amounts of Rn emanation from rocks, minerals, and soil [11]. Rn atoms cannot leave a solid grain due

* Corresponding author: hemn.salh@koyauniversity.org. ORCID Number of authors: ¹ 0000-0002-1343-5594, ² 0000-0002-2367-2980, ³ 0000-0001-6566-4308

to the low solid diffusion coefficients (1×10^{-25} - 1×10^{-27} m²/s) present. It is commonly assumed that parent Ra undergoes radioactive decay and that Rn escapes from the mineral grain as a result of the recoil. Ra decay produces Rn atoms, which frequently escape grains due to recoil and internal space in grains. The molecular diffusion coefficients of air and water can be transmitted by diffusion via processes of Rn removal from the subsurface and subsequent transportation to the atmosphere [12, 13].

For forecasting earthquakes, ²²²Rn has been utilized [14–16], and ²²²Rn has been used for seismic activity monitoring since the Tashkent (M 5.2) earthquake. Six years before the Tashkent earthquake, the study area was considered [17]. As a result, the data also reveals the radon growth rates previous to the earthquake. In many parts of the world, the movement of the Earth's crust has led to new techniques for earthquake prediction [18–20][21–23]. These predicting areas include a variety of strategies with significant effects. These methods include magnetic area, compression, decline, seismic velocity wave, shell resistance, slide down, gravitational effects, and radon measurements, and the data indicate that earthquakes could cause radon levels to increase. There was a significant variance in soil radon gas before the earthquake in Chamoli, India, in 1999 [24, 25], Radon gas was recorded abnormally after the North Indian earthquake of 1997 (M 5.4) due to the observation of an underground water source. Compared to typical soils, radon gas levels are greater [26]. Although the earth's crust typically emits very little radon into the atmosphere, Before the production of volcanic activity and seismic occurrences, fault lines in geothermal in uranium and radon irregularities are seen [27].

Ions and free electrons in the ionosphere, an area of the atmosphere at altitudes between 60 and 1100 km, reflect a small number of electromagnetic waves [28]. The number of free electrons along 1m² of the beam path is represented by atmospheric TEC [29]. The TECU unit, which is used to quantify TEC and is equal to 10¹⁶ electrons.m⁻², is used to directly investigate the ionosphere's composition [30]. The recipient's zenith and Slant Total Electron Content are used to determine the recipient's free electron content in the slant line between the receiver and the satellite. Using Vertical TEC, TEC is measured (STEC) [31]. The ionosphere can be affected by geomagnetic forces, diurnal and seasonal influences, solar interference, and earthquakes, which result in irregularities in the ionosphere [32]. Because that can account for ionosphere changes caused by this activity, the TEC is an essential study factor for the relation between pre-earthquake and seismic activities. This is because the Earth's crust has experienced seismic and pre-earthquake events that stress rocks. Stresses cause the positive electrical charge of stones inside the crust of the earth. When positive charges develop, they generate a potential difference on the outer surfaces of the stones, which generates a charge transfer that may travel quickly and thus be away from its source position. Charges flow upward due to the operation of the electric field lines between the Earth's crust and the ionosphere's bottom. It reached the ionosphere's bottom due to a change in the ionosphere's electron equilibrium [33]. If TEC disruptions might be used to direct earthquake monitoring, such a disturbance in total electron content also may signal significant seismic prediction, where these disruptions might be used in an earthquake predicting system to improve earthquake alert systems, thus saving hundreds of lives [34]. Ionosphere abnormalities are caused by earthquakes, solar interference, seasonal and diurnal impacts, and geomagnetic influences, among other factors [35, 36]. Ionospheric changes have been detected as earthquake precursors in more than 20 nations [37, 38].

This research aims to estimate the formation of radon gas in soil which is closely related to seismic events, as well as variations in ionospheric TEC while accounting for earthquakes, and to correlate together utilizing Monte Carlo Simulation. Some meteorological factors are also taken into account while analyzing this relation. The results revealed significant conclusions about the TEC-Rn-Earthquake triad co-change.

2. Analysis of data and the Study Area

One of the countries with the most seismic activity is Türkiye, It is seismically affected by The North Anatolian Activity Zone (NAFZ), which affects the region's north while causing a 1,600 km-long surface rupture for dextral strike-slip movement, The place is located on the North Anatolian Fault's eastern side and serves as a research location, and this is an important region in terms of development and future expansion due to earthquake disasters in 1942 and 1943, with magnitudes of 7.6 and 7.2, respectively [32, 39, 40]. Türkiye's Tokat Province's research district is known as Yolkonak. This region is located near the NAFZ, one of Türkiye's major fault zones. The Tokat Region and the middle Black Sea are where the NAFZ is situated. It covers the area between north latitude and (longitude 36o.89443, latitude 40o.53932). The topographic maps are illustrated in Figure 1.

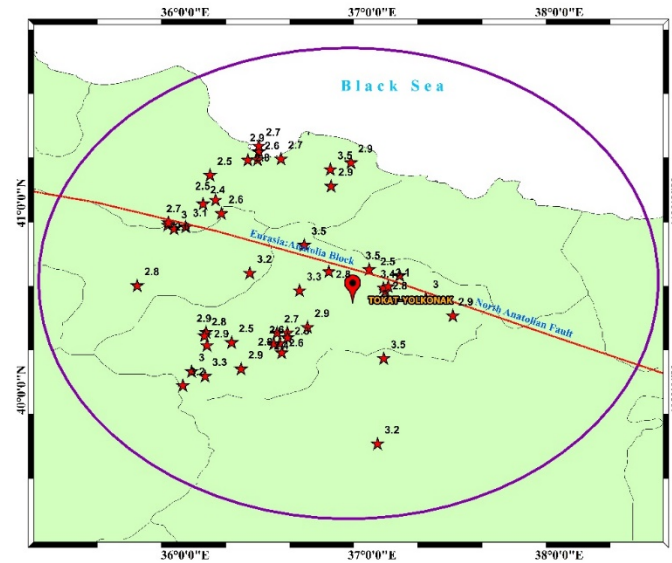


Figure 1. The exact location of the radon monitoring station and studied earthquakes along the North Anatolian Fault zones in T rkiye.

The data for the ^{222}Rn time series was provided by the Government of T rkiye Ministry of Interior's Emergency and Disaster Management Agency (AFAD) [41]. From 4 March 2007 to 10 February 2010, soil radon was monitored using an alpha particle detector at approximately one meter deep in the soil at 15-minute intervals. Alpha Nuclear Corporation, Canada, created the detecting, version 611-Alpha Meter Assume a 400 mm² stainless steel silicon diffusing cross-detector container with an aluminium Mylar covering [42]. The sensing surface of the detector is 450 mm². Because this detection works much better in a dark, dry environment, it is enclosed beneath a thin opaque film or membrane. Since the film is 0.25 mm thick and made of aluminized Mylar, it has a sufficiently low density to allow for the efficient transit of alpha particles in addition to water vapour and light. The TR Meteorology General Directorate offers daily mean steam pressure (hPa), dry bulb temperature, wet bulb temperatures, and soil temperature at deeper distances of 10, 20, and 50 cm to examine the influence of meteorological parameters on the ^{222}Rn during the observation period [43]. The seismic data were collected by Bogazici University, Kandilli Center, and the Earthquake Research Institute [44]. Furthermore, the regularized estimate procedure for GPS data was used in this study to generate three mid-latitude stations' VTEC values, Istanbul, (41.06N, 29.01E), Ankara, (39.53N, 32.45E), and Gebze (40.47N, 29.27E), via Laboratory for Ionosphere Research (IONOLAB)[45] [46–52].

3. Result and Discussion

3.1 Monte Carlo Modeling and the Autoregressive Integrated Moving Average Method

The (ARIMA) Autoregressive Integrated Moving Average prediction test is utilized for predicting. Several times preceding terms should be taken into account and expressed as a series of different models depending on the time series model. A MATLAB application is utilized to evaluate whether seismic activity in the study region could be the cause of any radon data anomalies. It provides a workstation for developing the ideal ARIMA model through Monte Carlo simulations to predict future radon time series. To select the best ARIMA model, 80 percent of the total Rn data is imported and used as the train data set. The remaining 20 percent is then used to evaluate the Monte-Carlo simulation data prediction. The ARIMA model can be used only with stationary data (45,46]. Because the Rn train data set's t-static is higher than the crucial value and is thus deviated by one degree. The partial autocorrelation function (PACF) and autocorrelation functions (ACF) indicate that the data are stationary. The moving average q orders and autoregressive p orders may also be found using the ACF and PACF plots. As shown in Figure 2. Initially, train data is used to apply ARIMA (p, d, q). The chosen time series model is thus ARIMA (4,1,13), which has the formula given in (1):

$$(1 - \phi_1 L - \dots - \phi_4 L^4)(1 - L)y_t = C + (1 + \theta_1 L - \dots - \theta_{13} L^{13})\varepsilon_t, \quad (1)$$

In this equation, ϕ and θ and are the model's input parameters, ε_t represents the error at time t and C is a constant amount.

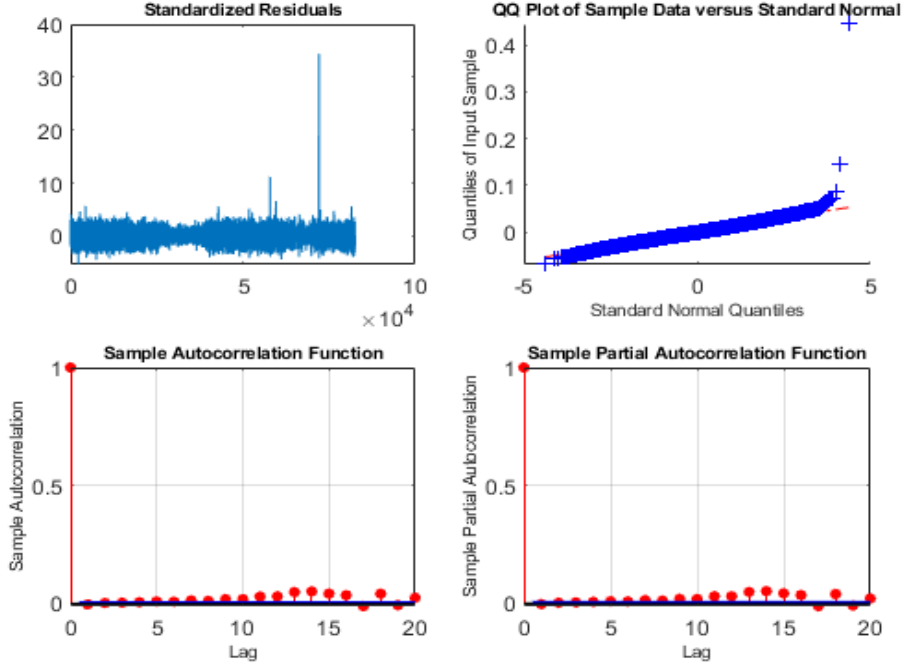


Figure 2. Partial autocorrelation function and autocorrelation function plots (lower part); the standardized residuals and the quantile-quantile of the ARIMA model residuals (upper part).

Figure 2 shows the histogram of the model's residuals, which shows that they follow the standard distribution, and the accuracy of the fitted model's residues is examined. Figure 2 shows the q-q plot of the model's residuals. It can be seen that there appear to be irregularities despite a few minor tail variances. The normal distribution's value and both residues' values combined, indicate that ARIMA (4,1,13) is an appropriate model.

MCS is a mathematical approach to decision-making and statistical analysis. It is useful in many fields, including nuclear energy, engineering, high-energy physics and atomic, research and development, the environment, and transportation [56–59]. It identifies the best with worst situations in all possible outcomes and displays all possible outcomes with each option, typically using probabilities (PDF) [60] as well as how to apply these inputs to the distribution MCS performs multiple analyses and, A PDF indicates that this helps in providing a range of potential outcomes based on the number of uncertainties as well as the range of input values associated with such uncertainties. The usage of PDFs, which can take several forms like Gaussian, lognormal, or uniform, is the most sensible and trustworthy method for defining uncertainties in a risk modelling job. Randomly calculated probability distribution functions (PDFs) are used to sample data during MCS. Each sample set's iteration is specified, and the data is provided as displayed in this data sample. The MCS technique displays not just potential outcomes but also information on the PDFs that these outcomes produce [61, 62]. The Monte-Carlo simulation tries four distinct pathways and forecasts 20% of data time steps based on the ARIMA model. It appears suitable, as demonstrated in Figure 3, which also shows the Monte-Carlo forecast probability boundaries. The red lines represent lower and higher limits, the green lines represent radon, and the black line indicates the Monte Carlo average.

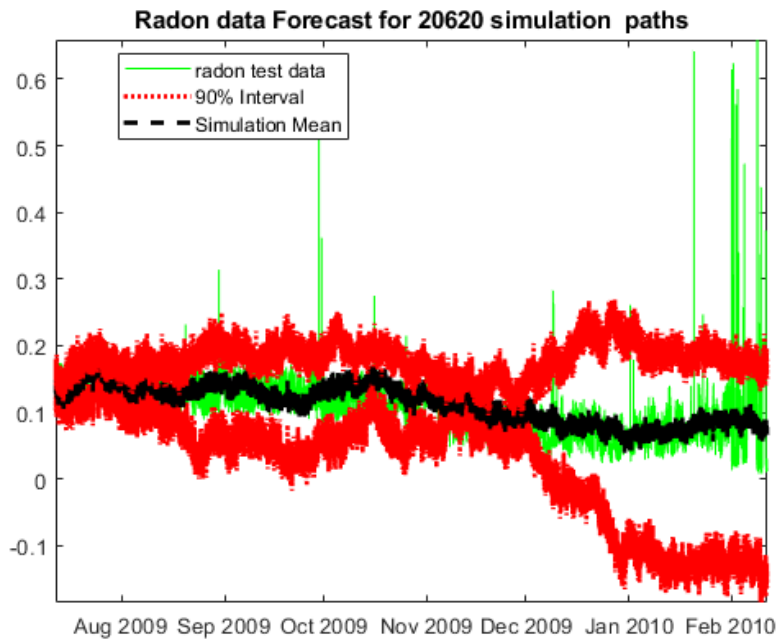


Figure 3. The mean of Monte Carlo Simulation Rn forecasts with lower and upper bounds.

3.2 Non-Seismic Related Variations in Radon Gas Concentration in Soil and Air

Figure 4 shows the radon time series analyzed between March 2007 and February 2010. It has been shown that the Rn concentration varies over time. There is no notable variation in the radon level from the beginning of March to the end of November 2007; therefore, its concentration varies around this standard ($150 \text{ Bq} \cdot \frac{1}{\text{m}^3}$). As a result, the Rn level began to fall progressively beginning in mid-October.

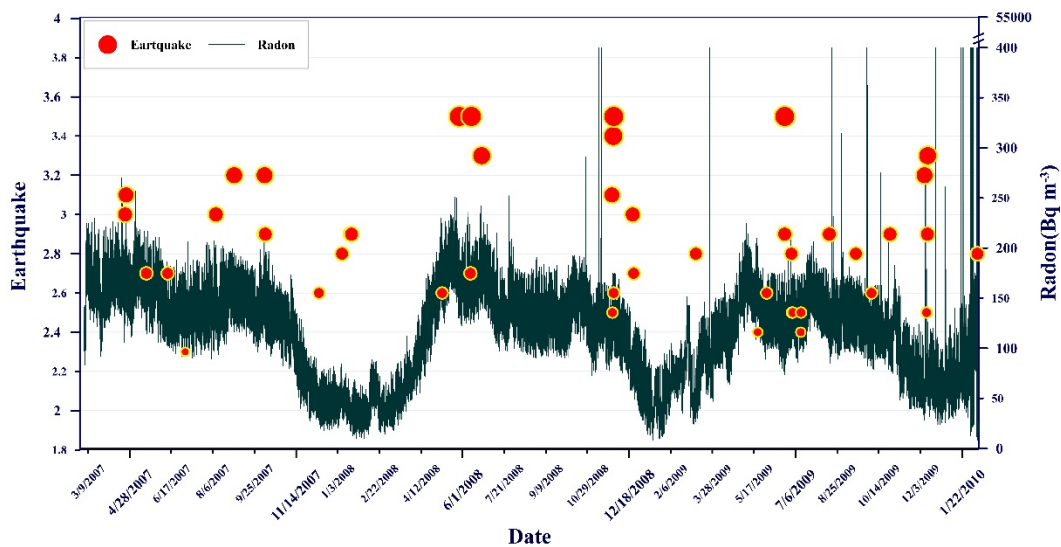


Figure 4. The studied Rn time series data.

In comparison to the end of 2007, when the Rn content reached its lowest concentration of around ($150 \text{ Bq} \cdot \frac{1}{\text{m}^3}$), the Rn concentration fluctuations in December 2007, January, and February 2008 are insignificant.

The Rn level progressively rose to start in March 2008, with spring being the time of year with the maximum Rn concentration. Until the end of the summer, there was a high concentration of Rn, which progressively lowered until the 2009 winter. The seasonal cycle of soil air Rn concentrations may continue until 2010. This variation in Rn concentration is seasonal. Vertical fissures in the clay open up throughout the summer due to increased permeability and Rn concentrations [63]. Earthquake stress in the earth's crust has a considerable influence on Rn emission. Rn gas flow has also been observed to be influenced by temperature variations between soil and air. At temperatures below $-10\text{ }^{\circ}\text{C}$, Rn may be extracted from an air stream for activated charcoal, cooling to liquid N_2 on glass wool at $-196\text{ }^{\circ}\text{C}$, and soil CO_2 at $-78.5\text{ }^{\circ}\text{C}$. Rn condenses on the surface at around $-150\text{ }^{\circ}\text{C}$ even though the partial pressure of soil ^{222}Rn is quite low in environmental conditions [64]. Due to the inverse relationship between temperature and relative humidity in the air, the rising surface soil moisture content is connected to higher air and soil temperatures. In comparison to lower temperatures, higher Rn emanation levels are expected [65].

Variations in air pressure are a result of flux from the Earth's atmosphere on the ground [64]. Frontal system routes are associated with 1%-2% pressure fluctuations, which are thought to have resulted in 20–60% variances in ^{222}Rn flux on the earth's surface [66]. High indoor Rn levels are generally attributed to a pressure difference between the basement and the rest of the residence. Most buildings have high levels of indoor radon, which is caused by the living area/basement pressure differential. The lower basement pressure creates a suction effect. Since the air pressure at the surface is greater than the air pressure at the ground level, Rn gas must be released into the atmosphere [65].

3.3 Possible Seismic Activity Associated Variations in Soil-Air Radon Gas Concentration

During the years 2007-2010, earthquake activity in the research region of Tokat province was documented by Bogazici University, Kandili Observatory, and the Research Center for Seismic. It has been discovered that there are around 45 earthquakes with magnitudes ranging from 2.3 ML and 3.5 ML. As shown in Figure 5, The earthquakes are related to the time-series data in which the radon data are collected, and the seismic data are related to the Rn concentration.

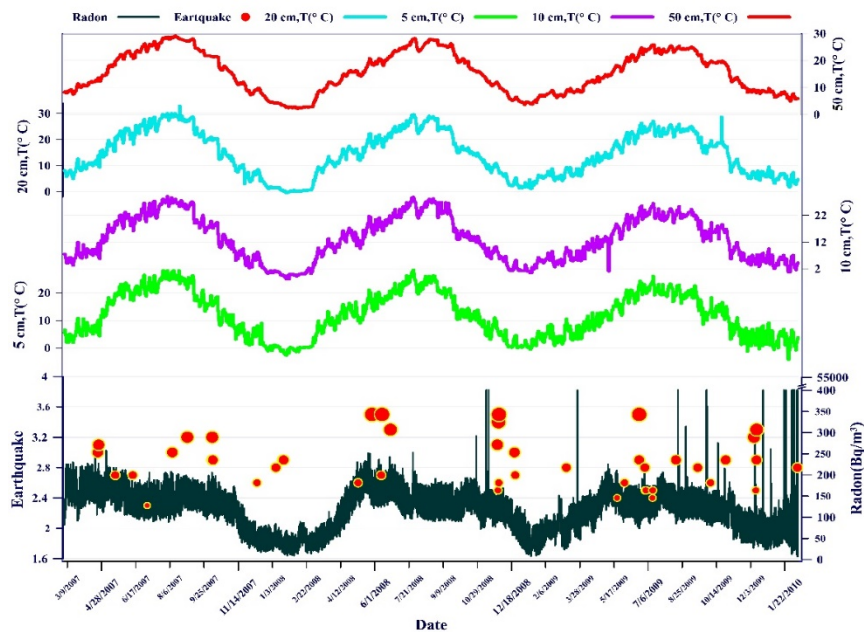


Figure 5. The variations of the radon concentration with soil temperature at (5, 10, 20, and 50 cm) depths.

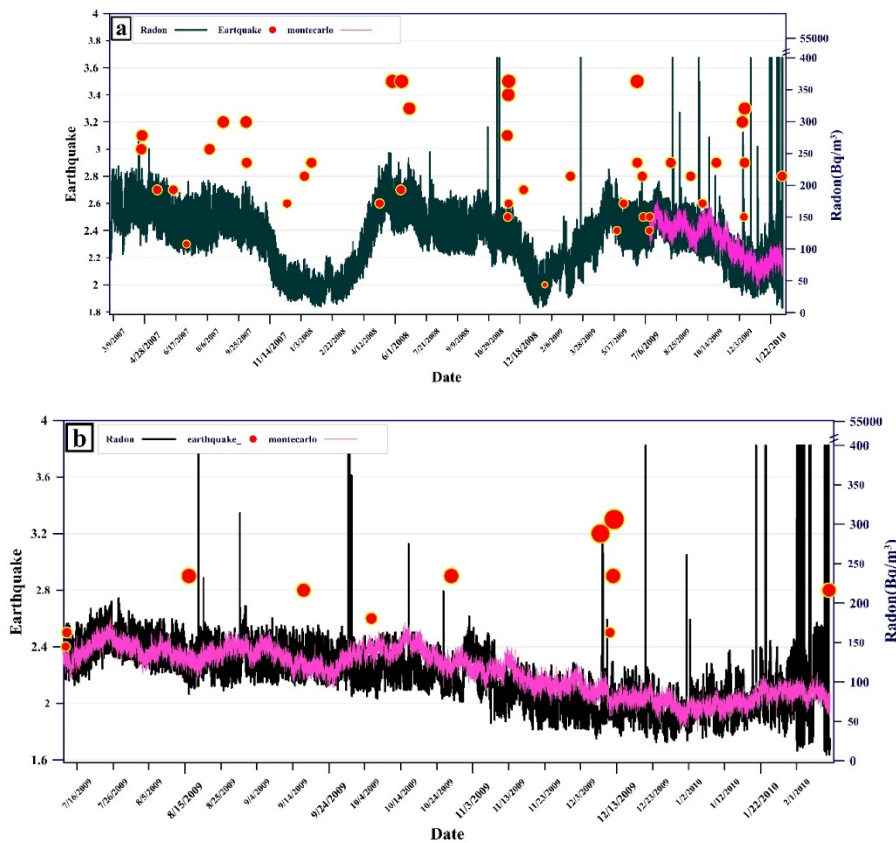


Figure 6. (a) The training and evaluation parts of the radon data with all earthquakes in the study area, (b) The MCS forecasted radon data.

Seven of these occurred in 2007, with the largest having a magnitude of 3.2 ML. There is some variance in radon concentration. As a result, the previously indicated seasonal variance occurred. In 2008, there were about 14 earthquakes, three of which had magnitudes of ML=3.4, and 3.5, 3.5 in July and May, respectively, in Sehitler-(Tokat) [South East 0.9 km], Mescitkoy-Almus (Tokat) [South 5.0 km], and in Gokal-Erbaa (Tokat) [South West 4.5 km], Rn levels reached their peak a month following these earthquakes. All of these factors influence Rn release from the earth's surface [67]. The largest number of Rn disturbances and eighteen earthquakes were recorded in 2009. When compared to other locations, the seismic distance was then closer. In the studied region in 2010, there were just two earthquakes recorded. Figure 5 shows the relation between Rn and soil temperature. Subsurface drilling, gas releases, tensions, earthquakes, and volcanic eruptions, all of these factors influence Rn release from the earth's surface, among other geochemical and geophysical factors. The link between Rn fluctuations and atmospheric and weather changes is shown reasonably in Figure 5.

3.4 Radon anomaly detection using Monte Carlo Simulation

Figure 6(a) shows how the radon data is split into a "train" set of 80 percent for use in determining the best ARIMA model and a "test" set of 20 percent for use in measuring the accuracy of the MCS data prediction. Figure 6 (a) begins with two 2.4 and 2.5 micro-earthquakes. Due to the minor earthquakes, radon didn't change significantly. Later, on August 15, 2009, as a result of these earthquakes, there were two Rn irregularities, parallel to Rn is the Monte Carlo line. The fourth seismic event, measuring 2.9 magnitudes, occurred on September 16, 2009. The Rn concentration didn't increase immediately after the earthquake, but it did grow over time. Following the occurrence of these earthquakes' Rn anomalies, four earthquakes occurred in December 2009. Soil permeability shows that seismic fault lines, geothermal sources, uranium resources, and other potential energy sources are all present in the Anatolian Fault Zone, where the research was conducted and volcanic zones are theoretically specified, the Rn concentration increases. Rock, soil, mineral, and uranium mine tailings all naturally emit radon

^{222}Rn into the surrounding environment. Higher levels of Rn emission occur at warmer air and soil temperatures than at cooler ones, resulting in a positive Rn anomaly when the exposed moisture content temperature rises. Significant factors include the magnitude of the earthquake and the distance from the epicentre. The magnitude of the earthquake and its distance from the monitoring station have a significant impact on the peak intensity and width of the Rn anomaly.

3.5 Variations in the ionospheric Total Electron Content (TEC)

TEC is an essential study measure because it may explain ionosphere changes caused by pre-earthquake and seismic events. For three locations in the research region, Figure 7 shows the temporal radon with total electron. Figure 7 shows the findings of a triple examination of earthquake-TEC and Rn Anomalies. As an example, one may study this figure from the perspectives of numerous basic components. On the other hand, the number of these parts can be increased (similar to the variations during 2007 and 2008), Earthquake-Rn-TEC causes abnormalities very instantly, according to analysis. In the red column, the Rn gas concentration in the soil is seen to have been released as a consequence of several earthquakes. The blue and yellow columns illustrate this, similar fill-discharge trends are seen. For all three TEC stations, these abnormalities usually show consistent behaviour.

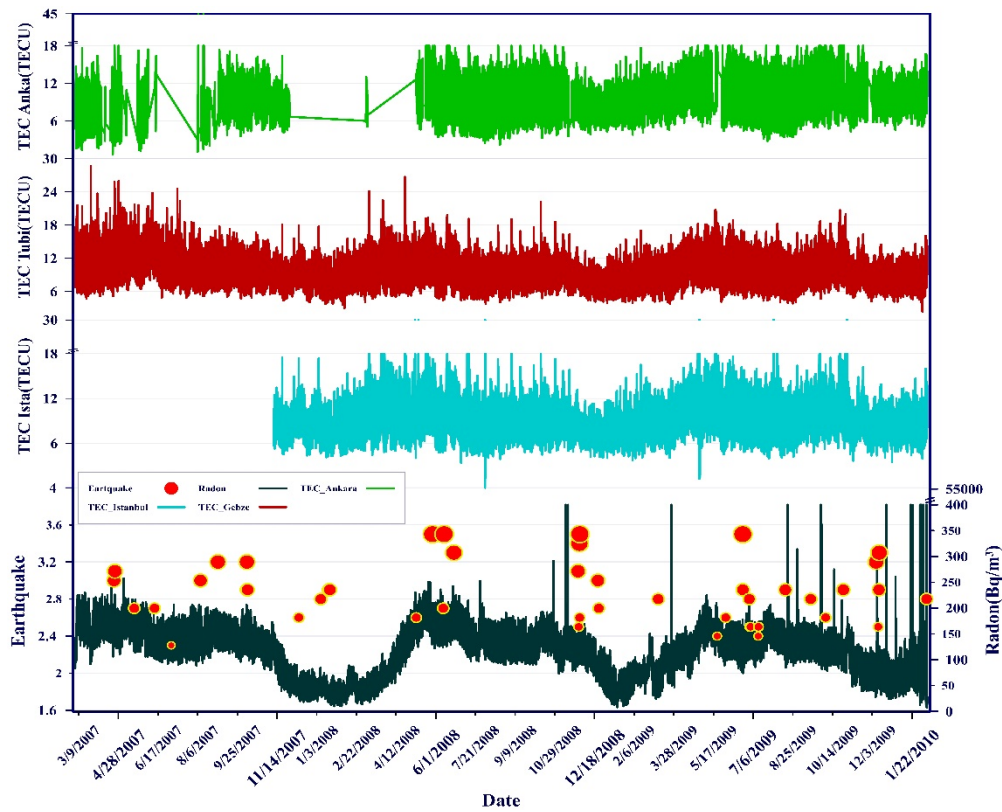


Figure 7. Radon time series, earthquake magnitude, and total electron content for three stations Tubi (Gebze), Ista (Istanbul), Anka (Ankara).

The graph did not begin at the origin since there is missing data from November 2007 until the start of the green line, which represents the TEC in the Ista station in Istanbul. the Tubi (Gebze) station's total electron content during the previous study period is represented by the purple line. The total content is shown as a brown line. In Anka (Ankara) station, the electron data was interrupted in 2007 and resumed in 2008. The limits by the standard deviation of the equation given, applied 10 days before and 5 days after the observation day, are used to determine whether the daily TEC result is within confident intervals of average and standard deviation, see the equations (2) and (3) as follows:

$$\text{Upper Bound} = \text{mean} + 2 \text{ stdev}, \quad (2)$$

$$\text{Lower Bound} = \text{mean} - 2 \text{ stdev}, \quad (3)$$

Figure 8(a) demonstrates that the anomaly at the three stations is comparable. Due to three days of TEC abnormalities at the Ista-station before and after the earthquake variation, shows a TEC anomaly that was discovered five days before the earthquake measuring 2.8 on the Richter scale on September 16, 2009. Predictions made using both Rn concentration and MCS tend to be accurate. Figure 8(b) shows the M_L 3.2 earthquake that occurred on December 7, 2009, on the Richter scale. Three days before the earthquake and immediately following it, TEC anomalies were seen with decreasing TEC values. While the daily fluctuations in Rn concentration before the earthquake were greater than the fluctuations seen afterwards, some Rn anomalies persisted. Although the Monte Carlo line and radon are nearly parallel, so often, it is not reasonable. As shown in Figure 8(b), on December 11, 2009, a most latest earthquake was 3.0 on the Richter scale. Nevertheless, forty-eight hours later, the quantity of TEC increased for three days, seemingly unrelated to the seismic. The intense seismic activity may have caused the abnormally large number of electrons to indicate a GPS signal that can be received at a greater distance from the epicenter. The TEC irregularity shows that there may be background noise blocking GPS signals in the high atmosphere under the influence of the generating force from the region surrounding the epicenter [68]. This might be caused by magnetic storms and solar, and plasma level concentration indicates that significant ionosphere irregularities are often associated with plasma upward drift near seismogenic locations [69].

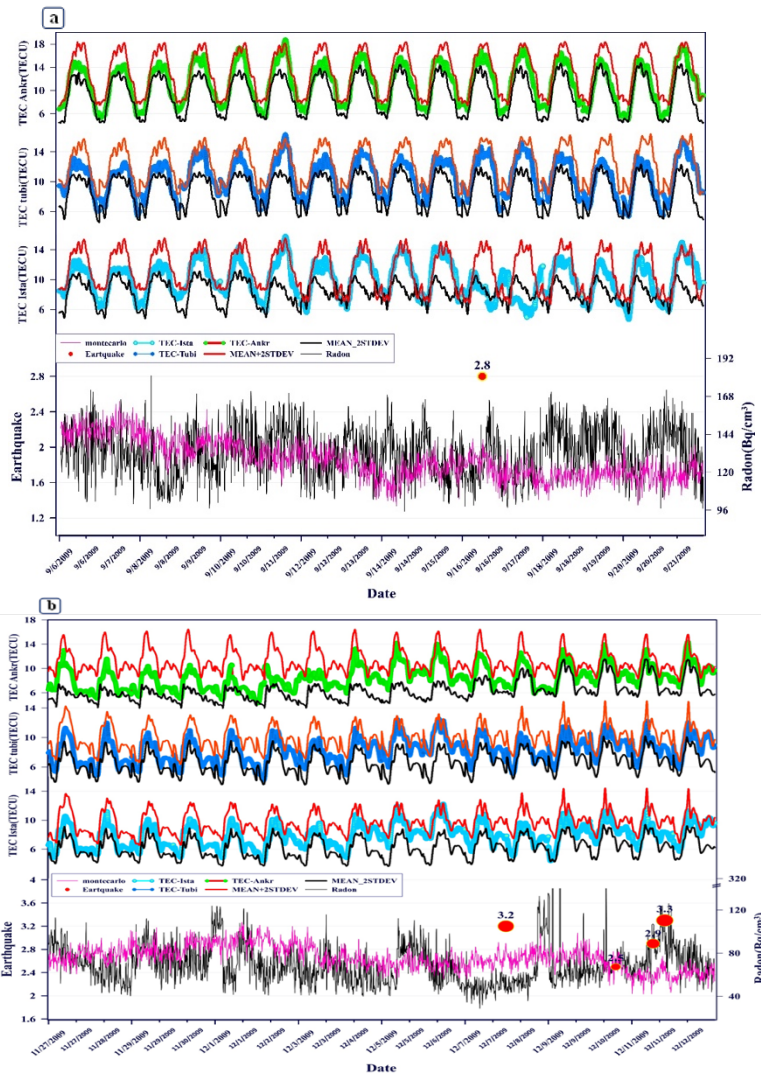


Figure 8 (a) TEC and radon variation before and after an earthquake M_L 2.9 on September 16, 2009, (b) TEC and radon variation before and after an earthquake M_L 3.2 on December 7, 2009.

4. Conclusions

In Yolkonak/Tokat, Türkiye, the study examined changes in Rn content in soil gas over around four years. At a depth of 1 m, fluctuations in the radon concentration have been seen that are both seasonal and non-seasonal. Regarding seasonal fluctuations, wintertime appears to have the lowest Rn concentration, It is increased in the summer because of the effects of metrological factors on radon transport typical processes such as diffusion. Before the August and December 2009 microearthquakes, Monte Carlo simulations with growing radon levels revealed non-seasonal variations (anomalies). The North Anatolian Fault Zone (NAFZ) earthquake may be anticipated by these anomalies. In these situations, variations in the total amount of electrons in the ionospheric atmosphere seem to be linked to radon anomalies. For instance, Rn levels increased and total electron concentration exceeded upper boundaries before the earthquake on December 12, 2009. However, the MCS method generates the PDF by calculating using all available data, unlike interpreting a single variable, resulting in optimal simulation optimization. When MCS is applied in combination using the Model (ARIMA), statistical outputs with high reliability are created with high reliability. Using the ARIMA-MCS approach in data interpretation is useful for this study. We advocate for the application of various artificial intelligence approaches in various investigations. Similar to the investigation of soil Rn gas time series, warmer seasons are characterized by much greater positive rises in Rn anomalies than cold ones. These rises are caused by a decrease in moisture during hotter seasons, the rise in temperature causes soil pores to expand and the spaces between soil particles to grow, the Moon's gravitational movements have a positive influence on soil, a decrease in rainfall, and the resulting dryness. These seasonal fluctuations are useful for measuring earthquake-Rn change. Rn surface changes are directly influenced by variations in air pressure. Rn is positively correlated with both meteorological changes and atmospheric changes. Rn-TEC and Earthquakes have a positive correlation.

Acknowledgments

We would like to thank Boğaziçi Kandilli Observatory (<http://www.koeri.boun.edu.tr/scripts/lasteq.asp>) for earthquake data, AFAD (Ministry of Interior Disaster and Emergency Management Presidency, <https://en.afad.gov.tr/>) for Rn data, IONOLAB (<http://www.ionolab.org/index.php?page=index&language=en>) for TEC data, TR Meteorology General Directorate (<https://www.mgm.gov.tr/eng/forecast-cities.aspx>) for meteorology data.

References

- [1] Külahci F, Inceöz M, Doğru M, Aksoy E, Baykara O. Artificial neural network model for earthquake prediction with radon monitoring. *Applied Radiation and Isotopes*. 67, 212-219 (2009). <https://doi.org/10.1016/J.APRADISO.2008.08.003>
- [2] Anisimov SV, Dmitriev EM, Aphinogenov KV, Guriev AV, Kozmina AS. Variability of radon distribution in the atmospheric surface layer over the land of middle latitudes. *IOP Conf Ser Earth Environ Sci*. 231, (2019). <https://doi.org/10.1088/1755-1315/231/1/012006>
- [3] Kulali F, Akkurt I, Özgür N. The effect of meteorological parameters on radon concentration in soil gas. *Acta Phys Pol A*. 132, 999-1001 (2017). <https://doi.org/10.12693/APhysPolA.132.999>
- [4] Fuente M, Rábago D, Goggins J, Fuente I, Sainz C, Foley M. Radon mitigation by soil depressurisation case study: Radon concentration and pressure field extension monitoring in a pilot house in Spain. *Science of the Total Environment*. 695, (2019). <https://doi.org/10.1016/j.scitotenv.2019.133746>
- [5] MILNE J. The California Earthquake of April 18, 1906. *Nature* 1910 84:2128. 84, 165-166 (1910). <https://doi.org/10.1038/084165a0>
- [6] Pulinet S. *The Possibility of Earthquake Forecasting: Learning from nature*. IOP Publishing Ltd 2018 (2018)
- [7] Mahmood I, M.F. Shahzad MI, Qaiser S. Investigation of atmospheric anomalies associated with Kashmir and Awaran Earthquakes. *J Atmos Sol Terr Phys*. 154, 75-85 (2017). <https://doi.org/10.1016/j.jastp.2016.12.018>

- [8] Huang F, Li M, Ma Y, Han Y, Tian L, Yan W, Li X. Studies on earthquake precursors in China: A review for recent 50 years, (2017)
- [9] Akyol AA, Arikan O, Arikan F. A Machine Learning-Based Detection of Earthquake Precursors Using Ionospheric Data. *Radio Sci.* 55, (2020). <https://doi.org/10.1029/2019RS006931>
- [10] Nazaroff WW. Radon transport from soil to air. *Reviews of Geophysics.* 30, 137-160 (1992). <https://doi.org/10.1029/92RG00055>
- [11] Hosoda M, Tokonami S, Suzuki T, Janik M. Machine learning as a tool for analysing the impact of environmental parameters on the radon exhalation rate from soil. *Radiat Meas.* 138, (2020). <https://doi.org/10.1016/J.RADMEAS.2020.106402>
- [12] Ye Q, Singh RP, He A, Ji S, Liu C. Characteristic behavior of water radon associated with Wenchuan and Lushan earthquakes along Longmenshan fault. *Radiat Meas.* 76, 44-53 (2015). <https://doi.org/10.1016/j.radmeas.2015.04.001>
- [13] Rikitake T. Predictions and precursors of major earthquakes: the science of macro-scopic anomalous phenomena. Terra Scientific Publishing Company (2001)
- [14] Rikitake T. Earthquake prediction. *Earth Sci Rev.* 4, 245-282 (1968). [https://doi.org/https://doi.org/10.1016/0012-8252\(68\)90154-2](https://doi.org/https://doi.org/10.1016/0012-8252(68)90154-2)
- [15] Birchard GF, Libby W.F.: Soil radon concentration changes preceding and following four magnitude 4.2–4.7 earthquakes on the San Jacinto Fault in southern California. *J Geophys Res Solid Earth.* 85, 3100-3106 (1980)
- [16] King CY. Radon emanation on San Andreas Fault. *Nature* 1978 271:5645. 271, 516-519 (1978). <https://doi.org/10.1038/271516a0>
- [17] Ulomov VI, Zakharova A.I., Nauk N.V.U.-D.A., undefined 1967. The Tashkent earthquake of April 26, 1966, and its repeated shocks. mathnet.ru.
- [18] Kūlahcı F, Zeki Ş. On the Correction of Spatial and Statistical Uncertainties in Systematic Measurements of ²²²Rn for Earthquake Prediction. *Geophysics* . 35, 449-478 (2014). <https://doi.org/10.1007/s10712-013-9273-8>
- [19] Tse ST, Rice JR. Crustal earthquake instability in relation to the depth variation of frictional slip properties. *J Geophys Res.* 91, 9452 (1986). <https://doi.org/10.1029/jb091ib09p09452>
- [20] Muhammad A, Kūlahcı F, Salh H, Hama RA. Long Short Term Memory networks (LSTM)-Monte-Carlo simulation of near surface ionization using radon. *J Atmos Sol Terr Phys.* (2021). <https://doi.org/10.1016/j.jastp.2021.105688>
- [21] Wattanakorn, K, Wiboolsake S. Soil gas radon as an earthquake precursor: Some considerations on data improvement. *Radiat Meas.* 29, 593-598 (1998). [https://doi.org/10.1016/S1350-4487\(98\)00079-1](https://doi.org/10.1016/S1350-4487(98)00079-1)
- [22] Ghosh D, Deb A, Sengupta R, Patra KK, Bera S. Pronounced soil-radon anomaly-Precursor of recent earthquakes in India. *Radiat Meas.* 42, 466-471 (2007). <https://doi.org/10.1016/j.radmeas.2006.12.008>
- [23] Kuo T, Su C, Chang C, Lin C, Cheng W, Liang H, Lewis C, Chiang C. Application of recurrent radon precursors for forecasting large earthquake near Antung, Taiwan. *Radiat Meas.* 45, 1049-1054 (2010). <https://doi.org/10.1016/j.radmeas.2010.08.009>
- [24] Singh M, Kumar M, Jain R, Chatrath R. Radon in ground water related to seismic events. (2019)
- [25] Virk, Walia HS. Helium/radon precursory signals of Chamoli Earthquake, India. *Radiat Meas.* 34, 379-384 (2001). [https://doi.org/https://doi.org/10.1016/S1350-4487\(01\)00190-1](https://doi.org/https://doi.org/10.1016/S1350-4487(01)00190-1)

- [26] Viñas R, Darwich A, Soler V, Martín-Luis MC, Quesada ML, de la Nuez J. Processing of radon time series in underground environments: Implications for volcanic surveillance in the island of Tenerife, Canary Islands, Spain. *Radiat Meas.* 42, 101-115 (2007). <https://doi.org/10.1016/j.radmeas.2006.07.002>
- [27] Kūlahci F, Inceöz M, Dođru M, Aksoy E, Baykara O. Artificial neural network model for earthquake prediction with radon monitoring. *Applied Radiation and Isotopes.* 67, 212-219 (2009). <https://doi.org/10.1016/J.APRADISO.2008.08.003>
- [28] Inyurt S, Peker S, Mekik C. Monitoring potential ionospheric changes caused by the Van earthquake (<i>M</i>=7.2). *Ann Geophys.* 37, 143-151 (2019). <https://doi.org/10.5194/angeo-37-143-2019>
- [29] Arikan F, Arikan O, Erol CB. Regularized estimation of TEC from GPS data for certain midlatitude stations and comparison with the IRI model. *Advances in Space Research.* 39, 867-874 (2007). <https://doi.org/10.1016/j.asr.2007.01.082>
- [30] Géodésique, des sciences naturelles. C. Mapping and predicting the Earth's ionosphere using the Global Positioning System. (1999)
- [31] Langley, RB. Monitoring the Ionosphere and Neutral Atmosphere with GPS.
- [32] Inyurt S, Peker S, Mekik C. Monitoring potential ionospheric changes caused by the Van earthquake . *Ann Geophys.* 37, 143-151 (2019). <https://doi.org/10.5194/angeo-37-143-2019>
- [33] Viti M, Mantovani E, Cenni N, Vannucchi A. Interaction of seismic sources in the Apennine belt. *Physics and Chemistry of the Earth, Parts A/B/C.* 63, 25-35 (2013). <https://doi.org/10.1016/j.pce.2013.03.005>
- [34] Hammerstrom JA, Cornely PR. Total Electron Content (TEC) Variations and Correlation with Seismic Activity over Japan. (2016). <https://doi.org/10.22186/JYI.31.4.13-16>
- [35] Namgaladze AA, Zolotov OV, Karpov MI, Romanovskaya YV. Manifestations of the earthquake preparations in the ionosphere total electron content variations. *Nat Sci (Irvine).* 4, 848-855 (2012). <https://doi.org/10.4236/NS.2012.411113>
- [36] Li M, Parrot M. Statistical analysis of the ionospheric ion density recorded by DEMETER in the epicenter areas of earthquakes as well as in their magnetically conjugate point areas. *Advances in Space Research.* 61, 974-984 (2018). <https://doi.org/10.1016/j.asr.2017.10.047>
- [37] Liu J.Y., Chen C.H., Chen Y.I., Yang W.H., Oyama K.I., Kuo K.W. A statistical study of ionospheric earthquake precursors monitored by using equatorial ionization anomaly of GPS TEC in Taiwan during 2001-2007. *J Asian Earth Sci.* 39, 76-80 (2010). <https://doi.org/10.1016/j.jseaes.2010.02.012>
- [38] Li M, Parrot M. Statistical analysis of the ionospheric ion density recorded by DEMETER in the epicenter areas of earthquakes as well as in their magnetically conjugate point areas. *Advances in Space Research.* 61, 974-984 (2018). <https://doi.org/10.1016/j.asr.2017.10.047>
- [39] Şengör AMC, Zabcı C. The North Anatolian Fault and the North Anatolian Shear Zone. *World Geomorphological Landscapes.* 481-494 (2019). https://doi.org/10.1007/978-3-030-03515-0_27
- [40] Allen CR. Active Faulting in Northern Turkey. (1969)
- [41] Ministry of interior DAEMP. Disaster And Emergency Coordination Board, <https://en.afad.gov.tr/disaster-and-emergency-coordination-board>
- [42] Thomas D.M., Cotter J.M., Holford D. Experimental design for soil gas radon monitoring. *Journal of Radioanalytical and Nuclear Chemistry Articles.* 161, 313-323 (1992). <https://doi.org/10.1007/BF02040478>

- [43] Turkish State Meteorological Service Official Web Sites, <https://www.mgm.gov.tr/eng/forecast-cities.aspx>
- [44] Boğaziçi University. Earthquake Catalog - BOUN KOERI Regional Earthquake-Tsunami Monitoring Center, <http://www.koeri.boun.edu.tr/sismo/2/earthquake-catalog/>
- [45] Sezen U, Arikan F, Arikan O, Ugurlu O, Sadeghimorad A. Online, automatic, near-real time estimation of GPS-TEC: IONOLAB-TEC. *Space Weather*. 11, 297-305 (2013)
- [46] Arikan F, Deviren MN, Lenk O, Sezen U, Arikan O. Observed Ionospheric Effects of 23 October 2011 Van, Turkey Earthquake. *Geomatics, Natural Hazards and Risk*. 3, (2012). <https://doi.org/10.1080/19475705.2011.638027>
- [47] Tuna H, Arikan O, Arikan F. Model based Computerized Ionospheric Tomography in space and time. *Advances in Space Research*. 61, (2018). <https://doi.org/10.1016/j.asr.2018.01.031>
- [48] Arikan F, Sezen U, Toker C, Artuner H. Improved IONOLAB-TEC Space Weather Service GIM-TEC. (2015)
- [49] Gulyaeva TL, Arikan F, Stanislawska I. Earthquake aftereffects in the Equatorial Ionization Anomaly region under geomagnetic quiet and storm conditions. *Advances in Space Research*. 60, 406-418 (2017). <https://doi.org/10.1016/j.asr.2017.03.039>
- [50] Deviren MN, Arikan F. IONOLAB-MAP. An automatic spatial interpolation algorithm for total electron content. *Turkish Journal of Electrical Engineering and Computer Sciences*. 26, 1933-1945 (2018). <https://doi.org/10.3906/elk-1611-231>
- [51] Karatay S, Arikan F, Arikan O. Investigation of total electron content variability due to seismic and geomagnetic disturbances in the ionosphere. *Radio Sci*. 45, (2010). <https://doi.org/10.1029/2009RS004313>
- [52] Arikan F, Shukurov S, Tuna H, Arikan O, Gulyaeva TL. Performance of GPS slant total electron content and IRI-Plas-STECh for days with ionospheric disturbance. *Geod Geodyn*. 7, 1-10 (2016). <https://doi.org/10.1016/j.geog.2015.12.009>
- [53] Salh H, Kūlahcı F, Aközcan S. A mobile simulation and ARIMA modeling for prediction of air radiation dose rates. *Journal of Radioanalytical and Nuclear Chemistry* 2021 328:3. 328, 889-901 (2021). <https://doi.org/10.1007/S10967-021-07726-8>
- [54] Rycroft MJ, Nicoll KA, Aplin KL, Harrison RG. Recent advances in global electric circuit coupling between the space environment and the troposphere. *J Atmos Sol Terr Phys*. 90-91, 198-211 (2012). <https://doi.org/10.1016/j.jastp.2012.03.015>
- [55] Jeřkovský M, Javorník A, Breier R, Slučiak J, Povinec PP. Experimental and Monte Carlo determination of HPGe detector efficiency. *J Radioanal Nucl Chem*. 322, 1863-1869 (2019). <https://doi.org/10.1007/s10967-019-06856-4>
- [56] Abdolhamidzadeh B, Abbasi T, Rashtchian D, Abbasi SA. A new method for assessing domino effect in chemical process industry. *J Hazard Mater*. 182, 416-426 (2010). <https://doi.org/10.1016/j.jhazmat.2010.06.049>
- [57] Zhao Y, Nielsen CP, Lei Y, McElroy MB, Hao J. Quantifying the uncertainties of a bottom-up emission inventory of anthropogenic atmospheric pollutants in China. *Atmos Chem Phys*. 11, 2295-2308 (2011). <https://doi.org/10.5194/acp-11-2295-2011>
- [58] Aalizadeh R, Nika MC, Thomaidis NS. Development and application of retention time prediction models in the suspect and non-target screening of emerging contaminants. *J Hazard Mater*. 363, 277-285 (2019)

- [59] K lahc  F. Environmental Distribution and Modelling of Radioactive Lead (210). A Monte Carlo Simulation Application. 15-32 (2020). https://doi.org/10.1007/978-3-030-21638-2_2
- [60] Muhammad A, K lahc  F, Salh H, Hama Rashid PA. Long Short Term Memory networks (LSTM)-Monte-Carlo simulation of soil ionization using radon. *J Atmos Sol Terr Phys.* 221 105688 (2021). <https://doi.org/10.1016/j.jastp.2021.105688>
- [61] K lahc  F, Ak zcan S, G nay O. Monte Carlo simulations and forecasting of Radium-226, Thorium-232, and Potassium-40 radioactivity concentrations. *J Radioanal Nucl Chem.* 324, 55-70 (2020). <https://doi.org/10.1007/s10967-020-07059-y>
- [62] Lindmark A, Rosen B. Radon in soil gas Exhalation tests and in situ measurements. *Science of The Total Environment.* 45, 397-404 (1985). [https://doi.org/https://doi.org/10.1016/0048-9697\(85\)90243-8](https://doi.org/https://doi.org/10.1016/0048-9697(85)90243-8)
- [63] Schery SD, Gaeddert DH. Measurements of the effect of cyclic atmospheric pressure variation on the flux of 222Rn from the soil. *Geophys Res Lett.* 9, 835-838 (1982). <https://doi.org/10.1029/GL009I008P00835>
- [64] Baskaran M. Physical, Chemical and Nuclear Properties of Radon: An Introduction. *Radon: A Tracer for Geological Geophysical and Geochemical Studies.* 1-14 (2016). https://doi.org/10.1007/978-3-319-21329-3_1
- [65] Clements WE, Wilkening MH. Atmospheric pressure effects on 222Rn transport across the Earth-air interface. *Journal of Geophysical Research* (1896-1977). 79, 5025-5029 (1974). <https://doi.org/https://doi.org/10.1029/JC079i033p05025>
- [66] Nazaroff W, Nero A. Radon and its decay products in indoor air. (1988)
- [67] Tariq MA, Shah M, Hern andez-Pajares M, Iqbal T. Pre-earthquake ionospheric anomalies before three major earthquakes by GPS-TEC and GIM-TEC data during 2015–2017. *Advances in Space Research.* 63, 2088-2099 (2019). <https://doi.org/https://doi.org/10.1016/j.asr.2018.12.028>
- [68] Shah MT, Ahmad MA, Naqvi J, Jin S. Seismo ionospheric anomalies before the 2007 M7.7 Chile earthquake from GPS TEC and DEMETER. *J Geodyn.* 127, 42-51 (2019). <https://doi.org/https://doi.org/10.1016/j.jog.2019.05.004>

Increasing Strength of Clay Soils with the Use of Basalt Fiber: An Experimental Study

Yasemin ASLAN TOPÇUOĞLU^{1*}, Zülfü GÜROCAK²

^{1,2} Department of Geological Engineering, Faculty of Engineering, Fırat University, Elazığ, Türkiye

*¹ yaslan@firat.edu.tr, ² zgurocak@firat.edu.tr

(Geliş/Received: 01/12/2023;

Kabul/Accepted: 14/01/2024)

Abstract: Due to the increase in population, the demand for buildings increases. The engineering properties of the soils on which these structures will be built may not always meet the desired conditions. In such cases, soil improvement methods are used. One of these methods is additive used stabilization, in which additives such as lime, fly ash, volcanic ash and tuff, silica fume, and blast furnace slag are used. This method has been used successfully for years. However, in recent years, interest in the use of different types of fibers has increased. Some of these fibers are glass, basalt, polypropylene, and carbon. Basalt fibers have begun to attract attention in soil reinforcement applications due to the properties of their raw material, basalt rock, which is widely distributed in nature, natural, and has high strength. In this study, the effect of basalt fiber reinforcement on the unconfined compressive strength of high plasticity bentonite clay was revealed. For this purpose, 12 mm long basalt fiber in different proportions (1%, 2%, 3%, 4%, and 5%) was used as reinforcement in bentonite clay, and the optimum fiber ratio that provided the maximum increase in strength was determined. According to the results of the study, when 12 mm long basalt fiber was used as reinforcement in bentonite clay, the maximum strength value was obtained at a 4% basalt fiber ratio. However, the strength value decreased in the sample where 5% BF was used. It has been determined that basalt fiber reinforcement improves the strength properties of bentonite clay.

Key words: Basalt fiber, bentonite clay, reinforcement, unconfined compressive strength.

Bazalt Fiber Kullanımı ile Killi Zeminlerin Dayanımının Artırılması: Deneysel Bir Çalışma

Öz: Nüfusun artışına bağlı olarak yapılara olan talepte artmaktadır. Bu yapıların inşa edileceği zeminlerinde mühendislik özellikleri her zaman istenilen şartları sağlamayabilir. Böyle durumlarda zeminlerin iyileştirilmesi yöntemlerine başvurulmaktadır. Bu yöntemlerden biri de kireç, uçucu kül, volkanik kül ve tuf, silis dumanı, yüksek fırın cürufu gibi katkıların kullanıldığı katkılı stabilizasyondur. Bu yöntem yıllardır başarılı bir şekilde uygulanmaktadır. Fakat son yıllarda farklı türde fiberlerin kullanımına olan ilgi artmıştır. Bu fiberlerden bazıları cam, bazalt, polipropilen ve karbonur. Özellikle bazalt fiberler, hammaddesi olan bazalt kayacının doğada geniş yayılım göstermesi, doğal olması ve dayanımın yüksek olması gibi özelliklerinden dolayı zemin güçlendirme uygulamalarında oldukça dikkat çekici olmaya başlamıştır. Bu çalışmada yüksek plastisiteli bentonit kilinin serbest basınç dayanımında bazalt fiber takviyesinin etkisi ortaya konmuştur. Bu amaçla 12 mm uzunluğunda ve farklı oranlarda (%1, %2, %3, %4 ve %5) bazalt fiber, bentonit kilinde takviye olarak kullanılmış ve dayanımda maksimum artışı sağlayan optimum fiber oranı belirlenmiştir. Çalışmanın sonuçlarına göre, 12 mm uzunluğundaki bazalt fiber bentonit kilinde takviye olarak kullanıldığında maksimum dayanım değeri %4 bazalt fiber oranında elde edilmiştir. Ancak %5 BF kullanılan örnekte dayanım değeri azalmıştır. Bazalt fiber takviyesinin bentonite kilinin dayanım özelliklerini iyileştirdiği belirlenmiştir.

Anahtar kelimeler: Bazalt fiber, bentonit kili, güçlendirme, serbest basınç dayanımı.

1. Introduction

The use of fiber (glass, polypropylene, basalt, etc.) as an alternative to traditional methods in soil improvement has shown remarkable development in recent years. Ekinçioğlu [1] defines fibers as materials that can be found naturally or produced by humans, one dimension of which is much larger than the other dimension, and has a higher strength and elasticity modulus than the larger shape of the same material. Of the two types of fibers, natural and artificial, the artificial one is used more. Artificial fibers are preferred because they have high strength, are light, flexible and highly resistant to environmental effects [2]. Glass fiber [3-8], polypropylene fiber [8-12] and carbon fiber [13] are used as reinforcement in several studies and studies using these fibers as reinforcement stated that improvements in soil properties occurred.

One of these fiber is basalt fibers (BF), which has attracted attention in recent years and is produced from basalt rock. The raw material of BF is basalt rock, which is a volcanic rock that is widely distributed in nature and easy to access. BFs have superior properties such as high chemical resistance and resistance to temperature and microorganism effects. The fact that no additives are used during production is also an advantage for BFs. When

* Corresponding author: yaslan@firat.edu.tr. ORCID Number of authors: ¹ 0000-0002-3135-5926, ² 0000-0002-1049-8346

soil reinforcement studies with BF reinforcement are examined, it is seen that BF length and rate are important for successful reinforcement.

As a matter of fact, Gao et al. [14] used BF reinforcement in clayey soil and stated that the fiber ratio in which the maximum strength was determined was 0.25% and the fiber length was 12 mm. Gisymol & Ramya [15] found that the maximum increase in the strength of the organic soil with 10 mm length and 0.05% BF reinforcement occurred after 28 days of curing, while Kenan & Özocak [16] found that the optimum fiber ratio was 1.5% in their study on a silty soil. Pandit et al. [17] showed that according to the results of experimental studies using BF reinforcement in the soil, the maximum dry unit weight value of the soil increased and the optimum water content value decreased with the 4% ratio of BF. Moreover, Ocakbaşı [18] reported that the maximum strength value in the soil was increased by 2% BF and she stated that the fiber length was determined as 24 mm. Sungur et al. [19], determined that the shear strength increases up to a fiber length of 15 mm in BF reinforced clay soil, and the shear strength values decrease at a fiber length greater than that. Terzi [20] added 6 mm, 12 mm and 24 mm long BF to high plasticity clay at the rate of 0, 1.0, 1.5, 2.0 and 2.5% by weight. As a result of experimental studies, the maximum cohesion value was determined in the 12 mm long 1.5% BF reinforced sample, and the maximum internal friction angle was determined in the 24 mm long 2% BF reinforced sample. Zhao et al. [21] examined the reinforcing effect of BF and polypropylene fiber on low plasticity clay in their study. In the study, it was suggested that the effect on strength could be maximized when the fiber length was 10 - 13 mm and the additive ratio was 0.2%. Also, Jia et al. [22] determined that the shear strength and cohesion of silty clay increased with basalt fiber reinforcement. It has been noted that the shear strength of reinforced silty clay is maximum when the fiber content is approximately 0.2%. The researchers stated that a single fiber is tightly surrounded by the surrounding clay particles, which creates a gripping effect that can increase soil strength. It has been stated that the fibers in certain areas are interwoven to form a fiber network, and the binding effect of this fiber network can effectively restrain the surrounding soil particles and increase the strength of the soil. It has been stated that the gripping effect and the binding effect are the main mechanisms of fiber reinforcement. Gürocak and Aslan Topçuoğlu [23] conducted experimental studies on the samples prepared by using 20, 25, 30 and 35% water content in kaolin clay by using BF (0, 1, 2, 3%). According to the test results, they stated that the maximum strength value was obtained with 1% BF reinforcement and 25% water content. Aslan Topçuoğlu and Gürocak [24] carried out experimental studies using 6 mm long BF reinforcement in different proportions in bentonite clay. According to the results obtained from the study, the optimum fiber ratio that provides the maximum improvement in unconfined compressive strength was determined to be 4%. Song et al. [25] stated that the use of basalt fiber in low plasticity clay soil increased the shear and compressive strength of the soil and that the fiber ratio that provided the maximum increase in strength was 0.3%.

When fiber is added to the soil, the mechanism between the fiber and the soil is explained as follows; When the appropriate amount of fiber is added to the soil, the fiber binds to the soil particles and forms a fiber - soil column. When exposed to external forces, discrete soil-fiber columns interact with each other to form an approximately three-dimensional fiber - soil network and serve to limit the displacement and deformation of soil particles. Thus, the mechanical properties of the soil improve [25]. When the fiber ratio in the soil is very low, the fiber spacing is wide and the intersection between fiber - soil columns is difficult, so an effective fiber - soil network does not form. When the soil is exposed to external force, the stress is mainly transferred and carried by the scattered fiber - soil columns and the forces between the soil particles themselves. Gradually, as the fiber ratio increases, the fiber spacing decreases, which enables adjacent fiber to soil columns to easily intersect to form an effective fiber to soil network. Thus, when the soil is subjected to external force, the force is mainly carried by the forces between the fiber - soil network and the soil particles. When the fiber ratio is high, it becomes difficult to distribute the fibers properly due to the accumulation of many fiber filaments in clusters on the soil due to electrostatic interaction [14].

In the studies briefly summarized above, fiber reinforcement of different lengths and rates was used in different soil types. In these studies, it is clear that the effect of fiber reinforcement depends on the type of soil, fiber ratio and length. Unlike the soil type chosen in the studies, bentonite clay (B) was preferred in this study because it has higher plasticity. It has been tried to reveal the importance of basalt fiber reinforcement, especially in the unconfined compressive strength of clay soils with high plasticity. The fiber ratio was kept within a wide range (1%, 2%, 3%, 4%, 5%), thus aiming to reveal more clearly the effect of the fiber ratio on unconfined compressive strength. For this purpose, different amounts of BF with a length of 12 mm were used as reinforcement in bentonite and the changes in the strength values were determined. The fiber ratio that gives maximum strength on the soil was determined and the effectiveness of fibers used less or more than this ratio was evaluated separately. The results obtained from the study will contribute to future studies on the use of BF in soil reinforcement.

2. Materials and Methods

In this study, bentonite was used as the clayey soil, and BF, whose use has increased in recent years and whose database still needs to be strengthened with new studies, was used as the reinforcement material.

2.1. Bentonite clay and basalt fiber

Bentonite clay, which is a clay mineral that belongs to the montmorillonite family and is formed as a result of the chemical decomposition or degradation of volcanic ash, lava and tuff rich in aluminum and magnesium content Önem [26], Akbulut [27], consists of chemically hydrated aluminum and magnesium silicates. In the experimental studies, pure bentonite clay produced in the Tokat - Reşadiye (Turkey) clay quarry was used (Figure 1), and according to the results of the XRF analysis performed on the clay, it was determined to be Na - Bentonite type clay [28].

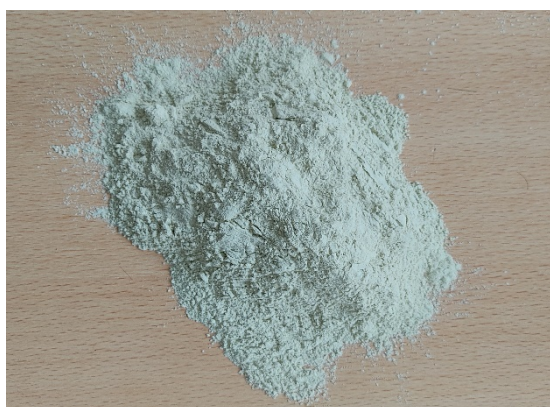


Figure 1. Bentonite clay used in the study.

BF produced from basalt, which is a hard, fine - grained, dark - colored volcanic rock widely found in the world, is used for reinforcement soils due to its economical, natural, and high strength properties. Basalt has the property of melting when heated, like thermos - plastic materials [29]. BF with a length of 12 mm was used in the study (Figure 2) and was purchased from a fiber selling company. The physical and mechanical properties of BF are given in Table 1.



Figure 2. Unseparated (a) and separated (b) basalt fiber used in the study.

Table 1. Mechanical and physical properties of BF were used in the study.

Feature	Value
Length fiber (mm)	12
Diameter of monofilament (μm)	15 \pm 1,5
Humidity, Max (%)	2
Modulus of elasticity (GPa)	90
Tensile strength (MPa)	3000
Thermal conductivity (W/mK)	0.031- 0.038
Elongation at break (%)	3.5
Density (g/cm^3)	2.63

2.2. Laboratory studies

Firstly, liquid limit (LL), plastic limit (PL), and standard proctor tests were carried out on bentonite in the laboratory studies. In the second stage, unconfined compressive strength tests were carried out after the mixtures in which different amounts of BF were used as reinforcement in B were compressed at optimum water content. Laboratory studies were carried out at Firat University, Department of Geological Engineering, Rock - Soil Mechanics Laboratory.

2.2.1. Liquid and plastic limit tests

At this stage of laboratory studies, the LL and PL values of unreinforced B were determined according to the ASTM D4318 - 17e1 [30] standard. For this purpose, a total of 15 tests were carried out. According to the test results, the average LL and PL values of unreinforced B were found to be 507% and 41%, and the plasticity index (PI) value was calculated to be 466%. It was determined that the clay used in this study was the high plasticity (CH) clay according to the Unified Soil Classification System (USCS) (Table 2).

Table 2. Results of consistency limits

Feature	Value
LL (%)	507
PL (%)	41
PI (%)	466
Soil class (USCS)	CH

2.2.2. Sample preparation and standard proctor experiments

Firstly, BF separated by compressor was added to the clay, which was dried in an oven at 105°C for 24 hours and mixed with the help of a mixer (Figure 3). B samples reinforced with BF were mixed again with a mixer by spraying distilled water at optimum water content, and a separate manual mixing process was applied in order to ensure homogeneous distribution of the fibers in B and to prevent fiber aggregation/agglomeration. In this study, the mixing time was determined to be 10 minutes and five separate mixtures were prepared. BF ratios used in the mixtures are shown in Table 3. The optimum water content (w_{opt}) value and maximum dry density (γ_{dmax}) value of B were determined by standard proctor tests performed in accordance with the ASTM D698 - 12e2 [31] standard. The test was carried out by letting a 2.5 kg load fall freely from a height of 30.5 cm on the soil and compressing the soil in three layers in the formwork (Figure 4). According to the proctor test results, w_{opt} value was determined as 38.50% and γ_{dmax} value was determined as 12.36 kN/m^3 (Figure 5).



Figure 3. Preparation of B and BF mixtures.



Figure 4. Proctor test and taking cylindrical samples.

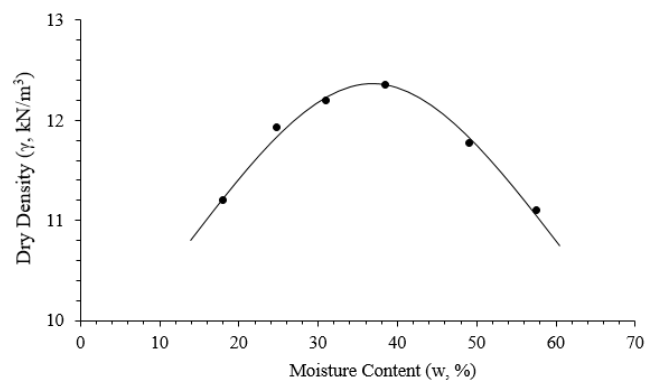


Figure 5. w - γ graph of the clay used in the study.

Table 3. BF rates used in experimental studies.

BF Length (mm)	BF Rate (%)	Sample Name
	0	B
	1	B + 1% BF
12	2	B + 2% BF
	3	B + 3% BF
	4	B + 4% BF
	5	B + 5% BF

2.2.3. Unconfined compressive tests

According to the ASTM D2166M - 16 [32] standard, unconfined compressive tests were carried out on cylindrical soil samples whose length is twice the diameter length to determine the compressive strength (q_u) of the soil. Experiments were carried out on 35 cylindrical specimens compressed to optimum water content and reinforced with 12 mm long BF (Figure 6).

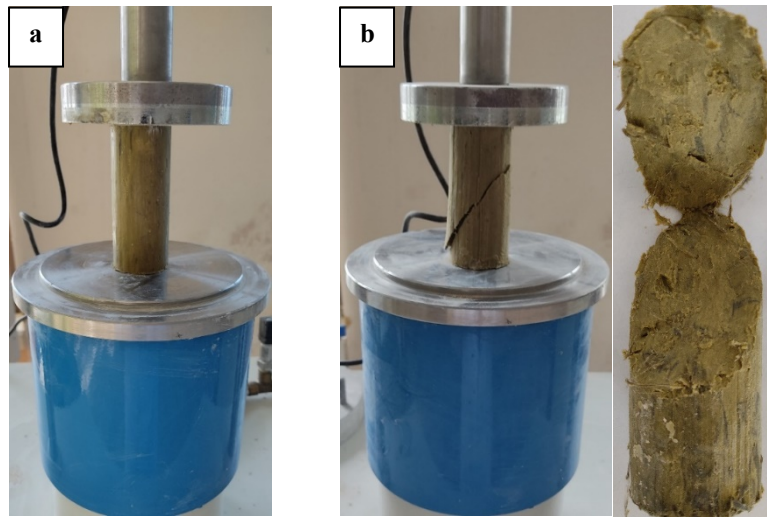


Figure 6. Unconfined compressive strength (a) before sample and (b) after sample.

According to the results of the unconfined compressive tests, the average q_u value of the unreinforced B was determined as 206.93 kPa. The average q_u values of the BF reinforced samples were found to be in the range of 202.74 - 267.66 kPa (Table 4). The failures that occurred in the samples after the unconfined compressive tests are given in Figure 7.



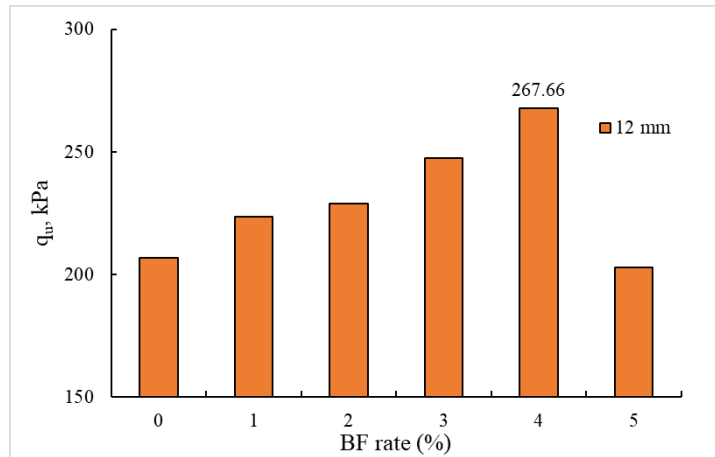
Figure 7. Samples after unconfined compressive test.

Table 4. q_u values of unreinforced and BF reinforced samples.

BF Length (mm)	Sample Name	Average q_u (kPa)	Standard Deviation (SD)
12	B	206.93	6.27
	B + 1% BF	223.64	7.06
	B + 2% BF	229.00	5.13
	B + 3% BF	247.42	8.10
	B + 4% BF	267.66	5.69
	B + 5% BF	202.74	4.82

3. Results and Discussion

With the experimental studies, it was tried to determine the changes in the unconfined compressive strength values of the unreinforced and BF reinforced B samples. In addition, the optimum fiber ratio, which provides the best improvement in strength, was determined. The average q_u value of unreinforced B is 206.93 kPa. The sample in which the maximum strength was determined with BF reinforcement is B + 4% BF, and its q_u value is 267.66 kPa. The lowest q_u value was determined as 202.74 kPa in the B + 5% BF sample (Table 4, Figure 8). This BF ratio was determined as 4%.

**Figure 8.** Relationship between q_u - BF ratio in unreinforced and BF reinforced clay samples.

The increases in the q_u values of the reinforced samples with 1, 2, 3, and 4% BF compared to unreinforced B were found as 8.08, 10.67, 19.57, and 29.35%, respectively. However, there is a decrease of 2.02% in the 5% BF reinforced sample (Table 5, Figure 9).

Table 5. Percentage changes in q_u values of unreinforced and reinforced clay samples.

BF Length (mm)	Sample Name	q_u (% Change)
12	B	-
	B + 1% BF	8.08
	B + 2% BF	10.67
	B + 3% BF	19.57
	B + 4% BF	29.35
	B + 5% BF	-2.02

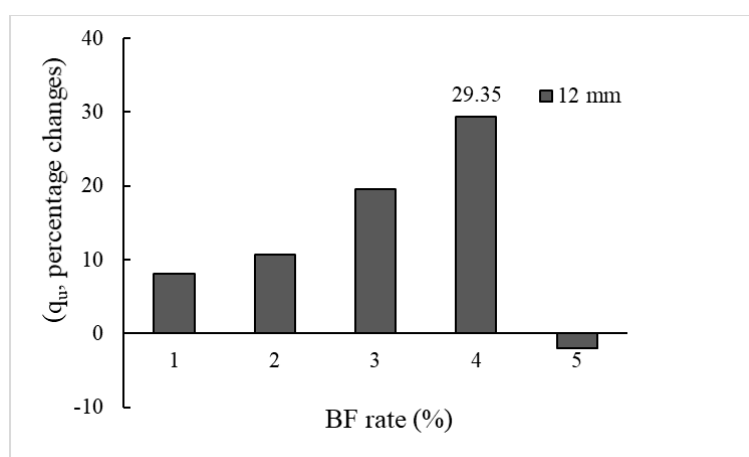


Figure 9. The relationship between percentage changes of q_u - BF ratio of unreinforced and reinforced clay samples.

The q_u value of clay increased up to 4% BF reinforcement but decreased with 5% BF reinforcement. The reason for this is the difficulty in aggregating and dispersing the fibers in the soil as the fiber ratio increases. When the fiber ratio is high in the soil, electrostatic interaction occurs between the fibers. For this reason, the fibers that are not homogeneously dispersed in the soil are collected in clusters, and thus the strength decreases [14, 25].

In addition, the fibers clustered in increasing fiber ratios do not have direct contact with the soil particles; thus, the grip effect between the fibers and the soil weakens. Excessive fiber concentration tends to create a weak structural surface in the soil, resulting in a decrease in soil strength [13]. In this study, q_u values increase up to 4% BF, and at 5% BF addition, the strength decreases as the grip effect between the fiber and the soil decreases due to fiber agglomerations. When the literature is examined, if the soil type is clay, the optimum BF ratio changes due to the type of reinforced clay.

When BF reinforcement is used in a low plasticity clay soil, the optimum BF ratio that provides maximum improvement in soil properties varies between 0.2 and 1.5% [14, 19, 21, 23, 25]. In high plasticity clays, the optimum BF ratio varies between 1.5 and 4% [18, 20, 24]. These studies showed that not only the BF ratio but also the type of reinforced soil and fiber length are important in soil reinforcement. The bentonite clay used in this study has much higher plasticity than the clays used in the literature. Therefore, the optimum BF ratio of 4% can be recommended for maximum strength in this bentonite clay with such high plasticity. In the study conducted by Aslan Topçuoğlu and Gürocak [24] using BF reinforcement in bentonite clay, 6 mm long BF was used. The optimum BF ratio that provides maximum strength with BF reinforcement was found to be 4%. The maximum strength value is 237.48 kPa. In this study, BF with a length of 12 mm was used and the optimum BF ratio was determined as 4%. However, the maximum q_u value corresponding to the optimum BF ratio is 267.66 kPa. The maximum q_u value determined by using a 12 mm long BF is 12.71% higher than the maximum q_u value determined by using a 6 mm long BF. In other words, using the same ratio but different lengths of BF resulted in obtaining different q_u values. In this study, increasing the BF length has a significant effect on obtaining higher q_u values. Accordingly, the plasticity of the clay, the fiber ratio and length affect the unconfined compressive strength.

4. Conclusions

In this study, using BF as reinforcement, the effect of BF ratio on the strength properties of high plasticity clay soil was determined. In unconfined compressive tests, the average strength value of unreinforced B was determined as 206.93 kPa. The average q_u values of BF reinforced mixtures vary between 202.74 - 267.66 kPa. In BF reinforced samples, q_u values increased up to 4% BF addition. By using 4% BF, the q_u value increased by 29.35% compared to unreinforced clay. However, with 5% BF reinforcement, there was a decrease of 2.02% compared to the q_u value of unreinforced clay. As the increasing fiber ratio caused fiber aggregation, the strength values decreased. Since the clustered fibers do not have direct contact with the soil particles, the grip effect between the fibers and the soil is weakened and excessive fiber concentration reduces the strength of the soil [13]. This study also revealed that q_u values increase with increasing BF length. In this study using 12 mm BF on the same type of soil and in another study using 6 mm BF [24], different strength values were determined and higher strength values were obtained in samples using 12 mm BF. Additionally, based on the findings of this study, one can assert that the optimum fiber ratio rises with an increase in the soil's plasticity. In studies where BF reinforcement was used,

it is clear that the soil type, fiber ratio and length have an effect on the strength of the soil. In addition, mixing soil and BF homogeneously during the preparation of samples for experimental studies is very important in obtaining healthier and more reliable results. This experimental research on the reinforcement of high plasticity bentonite clay with basalt fiber is important in terms of providing a theoretical basis for engineering applications. The data obtained from this study will contribute to the studies and literature on the use of BF, which is abundant and naturally found in nature, has high strength and is environmentally friendly, in soil reinforcement and road base improvement in engineering.

Acknowledgement

There is no conflict of interest with any person/institution in the prepared article. YAT and ZG prepared the study concept and design, performed the experiments, and analysed and interpreted the data.

References

- [1] Ekincioglu Ö. Mechanical behavior of cement based composites reinforced with hybrid fibres-an optimum design. Master's thesis, Istanbul Technical University, Istanbul, Türkiye, 2003.
- [2] Aral M. Mechanical behavior of cement based composites with hybrid fibres-an optimum design, Master Thesis, İstanbul Technical University, Istanbul, Türkiye, 2006.
- [3] Maher MH, Ho YC. Mechanical properties of kaolinite/fiber soil composite. *J. Geotech. Eng.* 1994; 120(8): 1381-1393.
- [4] Fındıkçı B. Bentonit kilinin cam fiber ile iyileştirilmesi 2020, Master Thesis, Kocaeli University.
- [5] Naidu GG, Ramakrishna R, Babu GE. Strengthening of soil by adding lime and glass fiber as stabilizing materials for the construction of high rise buildings. *IOP Conf. Series: Materials Science and Engineering* 2021; 1126 (2021): 1-8.
- [6] Kekeç E, Sert S, Arslan E, Bol E, Özocak A. Experimental investigation on the variation in shear strength of clayey soil reinforced with randomly distributed alkali-resistant glass fiber. *Sakarya University Journal of Science* 2022; 26(3): 438-447.
- [7] Sharo AA, Alawneh AS, Al zghool HN, Rabab'ah SR. Effect of alkali-resistant glass fibers and cement on the geotechnical properties of highly expansive soil. *Journal of Materials in Civil Engineering* 2022; 34(2).
- [8] Rajabi AM, Ghorashi SMS, Yeganeh MM. The effect of polypropylene and glass fibers on strength and failure behavior of clayey sand soil. *Arabian Journal of Geosciences* 2023; 16(6).
- [9] Puppala AJ, Musenda C. Effects of fiber reinforcement on strength and volume change in expansive soils. *Transportation Research Record* 2000; 1736: 134-140.
- [10] Iasbik I, De Lima DC, Carvalho CAB, Silva CHC, Minette E, Barbosa PSA. Geotechnical characterization of a clayey soil stabilized with polypropylene fiber using unconfined compression and resilient modulus testing data, in *Resilient Modulus Testing for Pavement Components*. ASTM Special Technical Publication (STP 1437) 2002; 114-125, West Conshohocken, PA, USA.
- [11] Al-Kareem KWA, Fattah MY, Hameedi MK. Compressibility and strength development of soft soil by polypropylene fiber. *International Journal of GEOMATE* 2022; 22(93): 91-97.
- [12] Uday RA, Kiran D, Arun Kumar GS, Prakash KG, Maddodi BS. Effect of polypropylene macro fiber on geotechnical characteristics of black cotton soil: an experimental investigation and correlation analysis. *Eng. Sci.* 2023; 21, 775: 1-10.
- [13] Bao X, Huang Y, Jin Z, Xiao X, Tang W, Cui H, Chen X. Experimental investigation on mechanical properties of clay soil reinforced with carbon fiber. *Construction and Building Materials* 2021; 280: 1-9.
- [14] Gao L, Hu G, Xu, N, Fu J, Xiang C, Yang C. Experimental study on unconfined compressive strength of basalt fiber reinforced clay soil. *Advances in Materials Science and Engineering* 2015; 1-8.
- [15] Gisymol PG, Ramya K. A study on the effect of basalt fiber in organic soil. *IOSR Journal of Mechanical and Civil Engineering (IOSR-JMCE)* 2017; 14(4):13-17.
- [16] Kenan A, Özocak A. Effect of basalt fiber addition on shear strength of silty soils. *International Symposium on Natural Hazards and Disaster Management* 2018: 918-924.
- [17] Pandit VM, Rohit C, Tushar K, Ayushi C, Bhushan G, Deepali C. Study of basalt fiber on compaction characteristics of black cotton soil. *6th International Conference on Recent Trends in Engineering & Technology (ICRTET)* 2018: 850-853.
- [18] Ocakbaşı P. The effect of basalt fiber addition on undrained shear strength of clayey soils. Master's Thesis, Sakarya University, Sakarya, Türkiye, 2019.
- [19] Sungur A, Yazıcı MF, Keskin SN. Experimental research on the engineering properties of basalt fiber reinforced clayey soil. *European Journal of Science and Technology Special Issue* 2021; 28: 895-899.
- [20] Terzi S. Contribution of basalt fiber to shear strength of clayey soils. Yüksek Lisans Tezi, Master's Thesis, Sakarya University, Sakarya, Türkiye, 2021.
- [21] Zhao N, Wu H, Huang Z. Strength behavior of red clay reinforced by basalt chopped fiber, *Arabian Journal of Geosciences* 2021: 1-9.
- [22] Jia Y, Zhang J, Wang X, Ding Y, Chen X, Liu T. Experimental study on mechanical properties of basalt fiber-reinforced silty clay. *Cent. South Univ.* 2022; 29: 1945-1956
- [23] Gürocak Z, Aslan Topçuoğlu Y. The effect of basalt fiber use on the unconfined compressive strength of low plasticity clay. *Gümüşhane University Journal of Science and Technology* 2023; 13(3): 688-701.
- [24] Aslan Topçuoğlu Y, Gürocak Z. Determination of the optimum basalt fiber ratio for maximum strength in sodium bentonite clay reinforcement. *DUJE (Dicle University Journal of Engineering)* 2023; 14(3): 479-487

- [25] Song Y, Geng Y, Dong S, Ding S, Xu K, Yan R, Liu F. Study on mechanical properties and microstructure of basalt fiber-modified red clay. *Sustainability* 2023; 15: 4411.
- [26] Önem Y. *Sanayi Madenleri*. Kozan Ofset, Ankara, 2000.
- [27] Akbulut A. *Bentonit*. MTA Eğitim Serisi-32, Ankara, 1996.
- [28] Aslan Topçuoğlu Y. The effect of different additive materials on the engineering properties of soils. PhD Thesis, Fırat University, Elazığ, Türkiye, 2020.
- [29] Jamshaid H, Mishra R. A green material from rock: basalt fiber-a review. *The Journal of the Textile Institute* 2015; 107(7): 923-937.
- [30] Standard Test Methods for Liquid Limit, Plastic Limit and Plasticity Index of Soils. American Society for Testing and Materials, ASTM D4318-17e1, 2017.
- [31] Standard Test Methods for Laboratory Compaction Characteristics of Soil Using Standard Effort, American Society for Testing and Materials ASTM D698- 12e2, 2012.
- [32] Standard Test Method for Unconfined Compressive Strength of Cohesive Soil, American Society for Testing and Materials ASTM D2166M-16, 2016.

Investigation of Charging Technologies for Electric Vehicles

Muhammed Sefa ÇETİN^{1*}, Muhsin Tunay GENÇOĞLU², Arkadiusz DOBRZYCKI³

^{1,2} Department of Electrical and Electronics Engineering, Faculty of Engineering, Firat University, Elazığ, Türkiye.

³ Institute of Electrical Engineering and Electronics, Faculty of Control, Robotics and Electrical Engineering, Poznan University of Technology, Poznan, Poland.

*¹ mscetin@firat.edu.tr, ² mtgencoglu@firat.edu.tr, ³ arkadiusz.dobrzycki@put.poznan.pl

(Geliş/Received: 01/12/2023;

Kabul/Accepted: 14/01/2024)

Abstract: In today's world, internal combustion engine vehicles are widely used. These vehicles cause harmful emissions as they use fossil fuels for engine propulsion and vehicle movement. To address this issue, electric vehicles have been considered as a solution. In electric vehicles, electric motors are used instead of traditional internal combustion engines and the necessary electrical energy is supplied from battery packs. In this way, electric vehicles do not cause harmful emissions to the environment. If the energy required for electric vehicle charging stations is obtained from renewable energy systems, electric vehicles will be zero-emission vehicles. Battery packs, that provide energy for electric vehicles, typically consist of rechargeable Lithium-ion battery groups and they can be charged using fast charging technology. In this study, the future of transportation, electric vehicles and the standards and technologies used in electric vehicle charging stations have been examined. Additionally, an electric vehicle system has been designed using MATLAB/SimScope.

Key words: Electric vehicles, charging stations, charging technologies.

Elektrikli Araçlar İçin Şarj Teknolojilerinin İncelenmesi

Öz: Günümüzde, içten yanmalı motorlu araçlar yaygın olarak kullanılmaktadır. Bu araçlar, motor tahriki ve araç hareketi için fosil yakıt kullandıkları için zararlı emisyonlara sebep olurlar. Elektrikli araçlar bu soruna bir çözüm olarak düşünülmüştür. Elektrikli araçlarda, geleneksel içten yanmalı motorlar yerine elektrikli motorlar kullanılır. Elektrikli motorların çalışması için gerekli olan enerji ise batarya paketlerinden sağlanmaktadır. Bu sayede, elektrikli araçlar zararlı emisyonlara sebep olmazlar. Elektrikli araç şarj istasyonları için gerekli enerji yenilenebilir enerji sistemlerinden sağlanırsa, elektrikli araçlar sıfır emisyonla sahip araçlar olacaktır. Elektrikli araçlara enerji sağlayan batarya paketleri, yenilenebilir Lithium-ion batarya gruplarından oluşmaktadır. Bu bataryalar hızlı şarj teknolojisi kullanılarak şarj edilebilirler. Bu çalışmada; geleceğin ulaşım tercihi olan elektrikli araçlar, şarj istasyonlarında kullanılan standartlar ve teknolojiler incelenmiştir. Ayrıca, MATLAB/SimScope yardımıyla bir elektrikli araç sistemi tasarlanmıştır.

Anahtar kelimeler: Elektrikli araçlar, şarj istasyonları, şarj teknolojileri.

1. Introduction

With the increase in the population, the use of vehicles is also on the rise. The use of internal combustion engines contributes to CO₂ emissions. The significant share of the transportation sector in CO₂ emissions is a crucial issue that needs attention [1]. A common idea around the world as a solution to this issue has developed in the form of electric vehicles (EVs). EVs provides quieter, greener and more economical transportation by using electrical energy as fuel. It is obvious that electric cars will have a significant impact on the automotive industry in the future. It is thought that EVs will not only save fuel but also reduce environmental pollution and carbon emissions [2].

At the outset, the limited proliferation of EVs was attributed to elevated production costs. Nevertheless, the resurgence of interest in EVs can be attributed to advancements in battery technology and charging infrastructure. However, persistent challenges impede the ubiquitous adoption of EVs and their full displacement of conventional internal combustion vehicles. The progress of this technology is hindered by factors such as battery costs, full charge range, charging time, the unavailability of the existing grid infrastructure and both the environmental and economic impacts of EVs. Consequently, the majority of studies related to EVs focus on battery packs and charging technologies.

Through studies focused on charging technologies, the charging management systems of EVs are continually advancing. Novel charging management systems offer innovative solutions in areas such as grid integration, smart charging, energy storage, and user experience. These systems can be categorized as Smart Grid Integration, Vehicle-to-Grid (V2G), Adaptive Charging Algorithms, Energy Storage Integration, Advanced Remote

* Corresponding author: mscetin@firat.edu.tr. ORCID Number of authors: ¹ 0000-0001-5587-0001, ² 0000-0002-1774-1986, ³ 0000-0001-5640-685X

Management, Payment Integration, and Pricing. These developments aim to provide electric vehicle owners with a more flexible, efficient, and user-friendly charging experience [3,4].

The charging technologies of EVs are continually evolving. Presently, various charging technologies such as Home Charging, Public Alternating Current (AC) Charging Stations, Fast Direct Current (DC) Charging Stations, Inductive and Capacitive Wireless Charging Technologies, and High-Power Density and Lightweight Charging Cables are available. This study examines the existing charging technologies [5].

This study investigates the operational principles, impacts and charging technologies of EVs. Furthermore, the adequacy of the existing charging station infrastructure in the countries and the adverse effects of EVs on the distribution grid are discussed. Standards for EV charging stations and information regarding vehicle charging technologies are provided. A sample EV is designed and relevant parameters are calculated. The EV is modeled using reference project in the MATLAB/Simscape environment.

2. Electric Vehicles

EV is a type of vehicle in which the traditional internal combustion engine and electric motor are not used together, but only the electric motor is used. Vehicle movement is provided only by the electric motor. An EV system consists of an electric motor, high-capacity battery, power electronics and charger. Vehicle movement is provided by electrical energy taken from high-capacity batteries.

EV battery packs consist of Lithium-ion batteries. With today's technology, the battery type with the highest cell voltage per unit cell and the highest energy density per unit mass is Lithium-ion batteries. These batteries; It is more preferred than other battery types due to its lack of memory effect, very low self-discharge and high cycle life [6]. Due to these advantages, Lithium-ion batteries are also widely used in EVs [7]. In Figure 1, an electric vehicle system is presented.

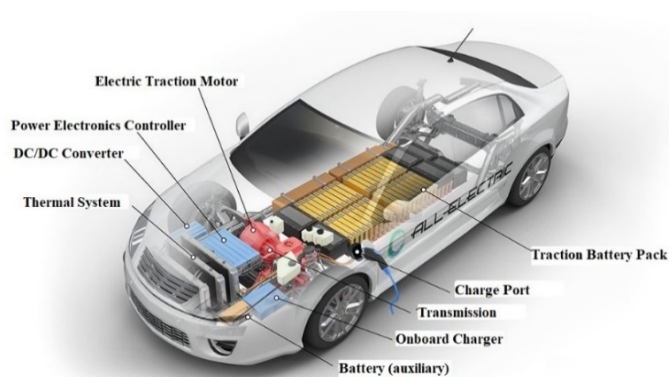


Figure 1. Electric vehicle system [8].

The advantages of EVs can be enumerated; encompassing a reduced frequency of breakdowns and maintenance requirements due to a lower number of mechanical components, quiet operation, the electric motor being comparatively more economical and having a simpler structure in contrast to traditional internal combustion engines. Furthermore, EVs can be powered by renewable energy sources and they possess the capability for hybrid operation.

In addition to these advantages, there are also some disadvantages of EVs that hinder the widespread adoption of these vehicles. Furthermore, similar to internal combustion engine vehicles, the proliferation of EVs is accompanied by various effects. These effects can be considered under three main categories: economic, environmental and grid-related impacts.

Undoubtedly, one of the most significant impacts of EVs will be on the grid. One of the major challenges preventing the widespread adoption of EVs is perhaps the unpreparedness of grid infrastructure for the extensive use of EVs. As the demand for EVs increases, the need for charging stations will also grow. With the increase in demand, the charging of EV will have a negative impact on the grid [9].

This situation can give rise to issues such as sudden and localized loading, grid harmonics, phase imbalances, overloading of equipment, voltage drops and so on. Additionally, the non-compliance of existing regulations with new developments will pose a problem [10]. The control of new-generation loads like EVs can be achieved using smart grid management algorithms. In this way, the charging load of the EV can be managed intelligently and negative effects can be reduced [11].

The selection of areas for the installation of EV charging stations is crucial in terms of distribution grid reliability and energy efficiency [12]. In addition, the balance of the electrical distribution network is also very important and all components must work together. An integrated grid system should be used to balance the load from EV charging stations [13]. Charging stations integrated into the grid system must be designed appropriately for grid reliability and balance [14]. Smart grid systems, grid management software and energy storage systems should be utilized to enhance grid stability and reliability [15]. At this point, all these solutions are of critical importance for the spread of EVs.

3. Electric Vehicle Charging Standards

In this section, charging station standards for EVs for only wired charging technologies are mentioned. Charging stations provide the infrastructure necessary for EVs to charge their batteries from external sources [16]. The charging process is carried out through charging equipment or charging stations. Factors such as the way batteries are charged, charging speed and charging frequency affect the reliability, durability and performance of the battery. There are two charging technologies in terms of charging speed: AC and DC charging. Therefore, the selection of the correct charging device and charging method is crucial for the accurate charging of batteries [1].

The increasing using of EVs leads to a growing demand for charging among EV owners. Consequently, the installation of more charging stations becomes necessary. The installation of charging stations and the use of EVs are interdependent systems. Therefore, countries and companies need to invest in the charging infrastructure required for the expanded use of EVs [16].

Since the voltage and frequency values of the electrical networks of different regions are different, the structures of the charging stations will also be different. Accordingly, leading countries in EVs technology have established EVs charging standards.

These standards include:

- SAE (Society of Automotive Engineers) Standards
- IEC (International Electromechanical Commission) Standards
- CHAdeMO Standards

In Europe, charging stations adhere to IEC standards. In addition, some companies include CHAdeMO standard sockets in their charging stations. However, different countries have charging stations adhering to various standards, including SAE, IEC and CHAdeMO.

3.1. SAE standards

Although established in the United States, it operates globally in the automotive sector. Numerous standards have been developed by the SAE. However, the SAE J1772 standard stands out for EVs [17]. According to this standard, charging speed is expressed in specific levels. Each level has a specified charging speed limit and vehicle charging ports are designed in accordance with this standard [16]. Table 1 shows the electrical parameters of the SAE J1772 standard.

Table 1. Electrical parameters of the SAE J1772 standard [18].

Source	Level	Voltage (V)	Max. Current (A)	Max. Power (kW)
AC	Level 1	120	12	1,44
		120	16	1,92
	Level 2	208-240	>20 ≤80	19,2
DC	Level 1	200-500	80	40
	Level 2	200-500	200	100

3.2. IEC standards

IEC is an organization that develops standards in the field of electric, electronic and related technologies [13]. For EVs, the IEC 61851 standard stands out. This standard, which is used in Europe and China, has similar requirements to the J1772 standard. Instead of the term “levels” used in the SAE standard, “modes” are used in the IEC standard. [16]. Table 2 shows the electrical parameters of the IEC 61851 standard.

Table 2. Electrical parameters of the IEC 61851 standard [18].

Source	Mode	Phase	Max. Voltage (V)	Max. Current (A)
AC	Mode 1	1	≤ 250	≤ 16
		3	≤ 480	
	Mode 2	1	≤ 250	≤ 32
		3	≤ 480	
	Mode 3	1	≤ 250	≤ 32
		3	≤ 480	
DC	Mode 4	-	≤ 1000	≤ 400

3.3. CHAdeMO standards

CHAdeMO is a fast-charging standard developed by Japanese automotive companies and is primarily used in Japan [19]. The CHAdeMO standard is used for DC fast charging and many fast-charging stations worldwide support this standard [16]. Table 3 shows the electrical parameters of the CHAdeMO standard.

Table 3. Electrical parameters of the CHAdeMO standard [18].

Standard	Voltage (V)	Max. Current (A)	Max. Power (kW)
CHAdeMO	500	125	62,5

4. Charging Technologies for Electric Vehicles

In this section, the charging technologies of EVs, both wired and wireless, have been examined.

4.1. Wired charging technologies

AC charging charges the battery more slowly. On the other hand, DC charging can charge at higher power and is generally used on highways and in areas with heavy traffic. DC charging is faster than AC charging and can charge 80% of the battery in about 30-45 minutes. However, DC charging stations cost more than AC charging stations [20].

The DC charging method is carried out using an off-board charger and this method enables the power received from the AC network to be directly converted to DC. In this way, AC power is converted to DC power without using any extra equipment. However, since DC charging stations have high voltage and current values, their investment costs are higher [1].

Different charging technologies are employed at each station depending on the structure of the charging station. EV manufacturers need to adapt their vehicles to different countries and markets. Therefore, there are charging station standards. The purpose of establishing these standards is to prevent potential damage to batteries during charging and enable manufacturers to make their vehicles suitable for use in different countries.

There are three types of EVs charging station structures used worldwide. The structure of the station, where an EV will be charged, determines the type of connector to be used. When the structure of the charging station changes, the equipment used also changes. The essential equipment used during EV charging includes the plug, connector (on the cable from the source to the vehicle), inlet (on the vehicle) and socket [21]. In Figure 2, charging cable connector types used in EVs are presented [22].

Type-1: It is an AC charging connection point designed according to the SAE J1772 standard, commonly used in the United States and Japan. These connectors typically support 120 V and 240 V AC charging levels. Type 1 connectors are used for AC Level 1 charging and are designed for slow charging processes [16].

Type-2: These types of charging cable connectors are also known as Mennekes connectors and are widely used in AC charging stations in Europe. This charging port is designed in accordance with the IEC standard and is commonly used by most AC Level 2 charging devices. Unlike the Type 1 socket, this connector features control and safety pins that enable communication between the EV and the charging device [16].

GB/T: It is the connector type defined by GB/T 20234 standards created in China and used only in China. The GB connector type is similar to the Type 2 connector mentioned in the IEC standard. It supports single-phase charging with 16/32 A current and 250 V output voltage. It is similar to Type 2 connectors in appearance and structure. However, these two connectors do not overlap functionally [16].

Combo Connector: The first DC fast charging standard is the CHAdeMO standard introduced by Japan. However, eight major automotive manufacturers (Audi, BMW, Chrysler, Daimler, Ford, General Motors, Porsche and Volkswagen) have decided to support the combo socket, which combines AC and DC charging defined in IEC and SAE standards in a single connector/input duo. CHAdeMO standard sockets only support DC charging. For this reason, vehicles using the CHAdeMO standard will always need two connector input pairs, separate for AC and DC charging. This is a negative situation that increases the production cost of the vehicle. CHAdeMO standard connectors will be replaced by combo connectors in countries other than Japan in the future, as they are not combo compatible [16]. The combo connector is an improved version of the type 2 connector with a fast-charging attachment. It also supports AC and DC charging up to 170 kW [23].

Tesla Supercharger: This technology is exclusively used in Tesla EVs. Thanks to this technology, the vehicle can be charged up to 80% within 30 minutes [24].

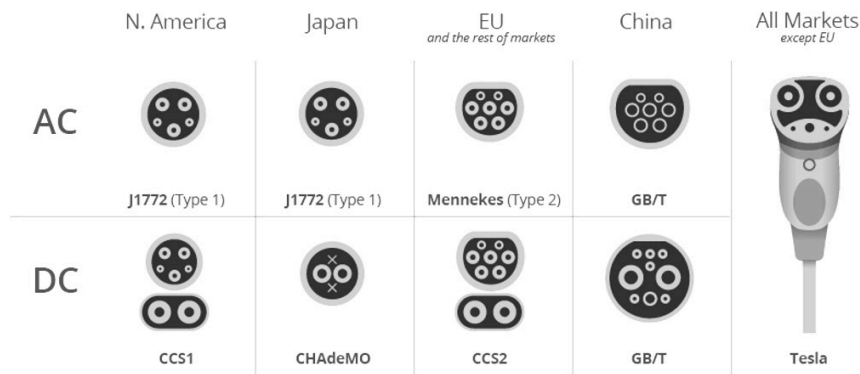


Figure 2. Connector types [22].

The large differences in the standards of charging stations and the types of sockets used reduce the accessibility of EV charging stations. Therefore, in parallel with the development of EV technology, the number of current socket types should be reduced to a single connector type [16].

4.2. Wireless charging technologies

Wireless charging includes a set of technologies used to charge electrical devices or vehicles without using a cable. Wireless charging technologies are supported by many electrical device and automobile manufacturers. These technologies provide the user with the advantage of getting rid of cable clutter and providing a more convenient charging experience. Capacitive Power Transfer (CPT) and Inductive Power Transfer (IPT) technologies are widely used. There are also Mixed Wireless Power Transfer (MWPT) and Magnetic Gear Wireless Power Transfer (MGWPT) technologies [25]. But CPT and IPT are detailed in this study.

CPT: Capacitive wireless charging is a technology that transfers energy using electrostatic capacity instead of electromagnetic induction. A capacitive coupling is created between the device and the capacitors on the charging plate. This system is a wireless charging method that transmits energy using the change of electric field between two capacitor plates. CPT transfers energy using the change of electrostatic capacitance. Energy transfer is achieved through capacitance changes between the capacitors in the charging tray and the capacitors in the vehicle. In this process, the electric field shows low loss. That's why they are suitable for charging EVs [26].

IPT: Inductive wireless charging is based on the principle of magnetic induction. A magnetic field is created between the device and the coils on the charging plate. Energy transfer occurs through the magnetic field. Thanks to the IPT magnetic induction principle, a magnetic connection is established between the coils on the charging

tray and the coils in the vehicle to ensure energy transfer between magnetic fields. Inductive charging generally allows for high energy transfer rates because it transfers energy through magnetic fields. This provides faster charging times. That's why they are suitable for charging EVs [27].

Both technologies (CPT and IPT) enable wireless charging of EVs, but the preferred technology may vary depending on the situation in which it will be used and user needs. For example, CPT can be used in situations with low power needs or over shorter distances, while IPT may generally be the more common choice due to its advantages such as wide availability and high energy transfer rates [28].

Wireless charging technologies allow users to charge their EVs in a more comfortable and convenient way. However, energy transfer efficiency and speed can often be lower than wired charging systems. Therefore, it is currently used mostly in home and office environments and is still considered an area under development.

5. Method

In this article, a modeling study has been conducted in order to examine the charging mechanism and performance parameters of EV. The parameters of EV were calculated and found to be used in modeling. In order to apply these calculated values to the EV, an exemplary project runnable in the MATLAB/Simscape environment was utilized. This reference model encompasses the motor, generator, battery, drive system, transmission and other transmission components, providing a comprehensive representation of an EV [29]. In Figure 3, MATLAB/Simscape model is presented.

The performance parameters of an electric vehicle can be classified as Range, Charging Speed, Acceleration and Top Speed, Battery Capacity, Energy Efficiency, Suspension and Handling. In this study, Acceleration and Maximum Speed parameters will be initially examined. Subsequently, Range, Charging Speed, and Battery Capacity parameters will be scrutinized. The performance parameters will be analyzed by comparing them with the average data of an electric vehicle.

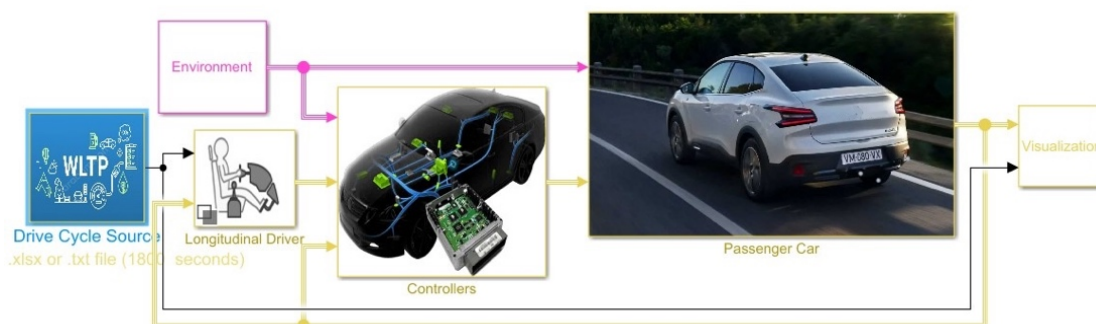


Figure 3. MATLAB/Simscape model.

Firstly, to examine the acceleration parameter, the time for the vehicle to reach a speed of 100 km/h will be considered. An average electric vehicle is expected to reach this speed in approximately 10 seconds. To achieve this speed within this time frame, the motor power should be 100 kW, and the torque should be 265 Nm. In the design process, an Internal Permanent-Magnet Synchronous Motor (IPMSM) with these values was selected. This chosen motor provides its maximum torque in the range of 0-3600 RPM. It can deliver its maximum power (100 kW) up to 10,000 RPM. Utilizing these characteristics, the maximum speed was found to be approximately 149 km/h from Equation 1 [30]. The power requirement at this speed is approximately 42 kW. With these motor values, the gradeability of the vehicle is a maximum of 37.6%, decreasing to 8.1% at the maximum speed. The power and torque of the electric motor are crucial for achieving the desired acceleration and gradeability of the vehicle. The motor power was calculated using Equation 2, and Equation 3 was used to analyze the acceleration parameter [30]. The parameters used in these calculations and the results are provided in Table 5.

According to these values, when creating the MATLAB/Simscape model, the energy consumption was found to be approximately 160 Wh/km in the WLTP (Worldwide Harmonized Light Vehicles Test Procedure) Class 3 cycle. To achieve an approximate range of 300 km, the battery capacity needs to be 50 kWh. For the design of a battery pack with these specifications, a total of 4,428 batteries were used, configured as 108 series and 41 parallel, as specified in Table 6. Additionally, the modeling was done with reference to CCS (Combined Charging System)

technology because a vehicle with fast charging capabilities, capable of charging in approximately 30 minutes, is desired. The designed vehicle achieved a fast-charging power of approximately 100 kW. CCS is an appropriate standard for many EVs to utilize fast charging infrastructure. It is widely used in both Europe and North America, providing fast charging capabilities at various power levels.

While modeling the battery pack, the Lithium-ion NCA type battery coded NCR18650BD, which is currently on the market, was used as a reference. This battery, which finds its place in many application areas today, is widely preferred especially in EVs and power units [31]. Modeling has been carried out, taking into account the features of EVs that are commonly used and accessible across the world [32]. Table 5 and Table 6 shows the calculated values for the designed EV. The following equations (1) to (10) were used to obtain these values.

$$V_{max} = \frac{n_{max} \cdot \pi \cdot r}{30 \cdot i} \times \frac{1km}{1000m} \times \frac{3600s}{1h} \quad (1)$$

$$P_{mot} = \left[\left(\frac{1}{2} \rho A_f C_d v^2 + mg f_r \cos \alpha + mg \sin \alpha \right) \times v / \eta_{drv} \right] \quad (2)$$

$$t = \int \frac{m \cdot 1,03}{T_m \frac{i}{\eta_{drv}} - \left(mg f_r + \frac{1}{2} g C_d A_f v^2 \right)} dV \quad (3)$$

The block uses these equations (4-10) to determine the combined voltage of the battery network [29]. Table 4 shows the variables that used in equations 4-10.

$$V_T = E_m - I_{batt} R_o - \sum_1^n V_n \quad (4)$$

$$V_n = \int_0^t \left[\frac{I_{batt}}{C_n} - \frac{V_n}{R_n C_n} \right] dt \quad (5)$$

$$SOC = \frac{-1}{C_{batt}} \int_0^t I_{batt} dt \quad (6)$$

$$I_{batt} = \frac{I_{in}}{N_p} \quad (7)$$

$$V_{out} = N_s V_T \quad (8)$$

$$P_{BattLoss} = I_{batt}^2 R_o + \sum_1^n \frac{V_n^2}{R_n} \quad (9)$$

$$Ld_{Ah} = \int_0^t I_{batt} dt \quad (10)$$

Table 4. Variables used in equations 4-10 [29].

Variables	
SOC	State of Charge
E_m	Battery Open-Circuit Voltage
I_{batt}	Per Module Battery Current
I_{in}	Combined Current Flowing From the Battery Network
R_o	Series Resistance
N_p	Number Parallel Branches
N_s	Number of RC Pairs in Series
V_{out}, V_T	Combined Voltage of the Battery Network
V_n	Voltage for n -th RC Pair
R_n	Resistance for n -th RC Pair
C_n	Capacitance for n -th RC Pair
C_{batt}	Battery Capacity
$P_{BattLoss}$	Battery Network Power Loss

Table 5. Calculated values for the general parameters of designed EV.

Parameters	Values
Motor Power (P_{mot})	100 kW
Max. Torque (3600 RPM) (T_m)	265 Nm
Max. Power RPM (n_{max})	10000 RPM
Reduction Gear Ratio (i)	8
Max. Speed (V_{max})	~149 km/h
Mass (m)	1750 kg
Drag Coefficient (C_d)	0,27
Frontal Area (A_f)	2,464 m ²
Driveline Efficiency (η_{drv})	0,88
Tire Radius (r)	0,316 m
Rolling Friction (f_r)	0,01

Table 6. Calculated values for the battery packs of designed EV.

Parameters	Values
Per Module Battery Voltage	3,73 V
Per Module Battery Capacity	3037,3 mAh
Number of Cells in Series and Parallel (108 series x 41 parallel)	4428
Battery Voltage (25 °C, %60 SOC)	402,84 V
Battery Capacity (25 °C)	124,53 Ah
Battery Energy	~50 kWh
Continuous Discharge Current	125 A
Max. Discharge Current (5C - 10 sec)	625 A
Charge Current (Nominal 1C - Max. 2C)	125 A – 250 A

The individually calculated parameters for the designed vehicle were entered as data into the Workspaces in MATLAB/Simscape blocks. Both the accuracy of these calculated values was tested and the use of applications

in the MATLAB/Simscape environment served as a reference for subsequent studies. Comments regarding the design are presented in the conclusion section.

6. Conclusion

EVs are considered the future choice of transportation due to their advantages over internal combustion engine vehicles. However, unresolved issues have prevented EVs from fully replacing traditional vehicles. In order for the existing distribution network to handle the EV charging load, it needs to be prepared using smart grid systems. Increasing the number of stations with fast-charging technologies is essential for both short and long-distance journeys to be easily achievable. Thus, the charging duration problem can be resolved. The abundance of diverse charging technologies diminishes the accessibility of charging stations. Therefore, charging technologies should be reduced to a single type. Additionally, it is crucial for EV charging stations to be powered exclusively by renewable energy sources to ensure the zero-emission nature of EVs. Significant investment costs are required to address these challenges.

When examining the studies related to EVs, it is observed that emphasis is placed on battery and charging technologies. This is because the most significant obstacles to the widespread adoption of EVs are associated with these parameters. Particularly, the unpreparedness of grid infrastructure for the charging load introduced by EVs makes this issue a crucial matter to address. If these problems, which are briefly mentioned in this study, are resolved, the obstacles to EV replacing traditional vehicles will be eliminated.

In this study, the values of the vehicles taken as reference were tried to be reached while designing an EV. These reference vehicles are readily accessible in the world and represent EV of average level. A vehicle with an average range of 300 kilometers and the ability to be charged in approximately 30 minutes using fast-charging technology has been designed. The Simscape model used incorporates the WLTP Class 3 driving cycle, where the kilometer-based consumption is approximately 160 Wh [32]. When the energy value of our vehicle's battery pack is compared to this value, it is observed that the designed vehicle has an approximate range of 300 kilometers. Additionally, considering the nominal charging current value, a fast-charging power value of approximately 100 kW is obtained. This value is suitable for fast charging and an EV with this capacity can be charged in approximately 30 minutes with the fast-charging option.

Simulation and modeling studies facilitate the design of all systems. This enables predictions to be made regarding the performance and status of EVs. Moreover, modeling studies are crucial in terms of cost and time. In this study, the parameters related to the designed vehicle and the existing projects in the MATLAB/Simscape environment can serve as references for future studies.

Acknowledgement

Muhammed Sefa ÇETİN has been supported by The Scientific and Technological Research Council of Türkiye (TÜBİTAK) under the Directorate of Science Fellowships and Grant Programmes (BİDEB) 2211-A National PhD Scholarship Program.

References

- [1] Bora Y. A review of electric vehicles. MSc, Yıldız Technical University, Istanbul, Türkiye, 2017.
- [2] Çetin MS, & Gençoğlu MT. Electric vehicles and charging technologies. Power Systems National Congress (ETUK); 01-02 November 2023; İzmir, Türkiye. (pp. 1-12).
- [3] Mohammed SAQ, Jung JW. (2021). A Comprehensive State-Of-The-Art Review Of Wired/Wireless Charging Technologies For Battery Electric Vehicles: Classification/Common Topologies/Future Research Issues. IEEE Access 2021; 9, 19572-19585.
- [4] Dost PKH, Spichartz P, Sourkounis C. Charging Behavior Of Users Utilizing Battery Electric Vehicles And Extended Range Electric Vehicles Within The Scope Of A Field Test. IEEE Transactions on Industry Applications 2018; 54(1): 580-590.
- [5] Acharige SS, Haque ME, Arif, MT, Hosseinzadeh N, Hasan KN, Oo AMT. Review Of Electric Vehicle Charging Technologies, Standards, Architectures, And Converter Configurations. IEEE Access 2023.
- [6] Turğut M. Design and implementation of battery management system for electric vehicles. MSc, Karabük University, Karabük, Türkiye, 2018.
- [7] Çetin MS, Karakaya B, Gençoğlu MT. Modelling of Lithium-Ion Batteries for Electric Vehicles. Firat University Journal of Engineering Science 2021; 33(2): 755-763. doi: 10.35234/fumbd.953296.
- [8] Çetin MS, Güler, H, Gençoğlu MT. Fuzzy logic based battery control system design for electric vehicles. Innovations in Intelligent Systems and Applications Conference (ASYU); 06-08 October 2021; Elâzığ, Türkiye. (pp. 1-4). IEEE.
- [9] Dobrzycki A, Çetin MS, Gençoğlu MT. Harmonics generated during the electric vehicle charging process. 2. International Conference on Advances and Innovations in Engineering (ICAIE); Elâzığ, Türkiye. (pp. 173-178).

- [10] Rigan M. Battery management system design of electric vehicles. MSc, Kahramanmaraş Sütçü Imam University, Kahramanmaraş, Türkiye, 2020.
- [11] Şengör İ. Optimum operation of electric vehicle parking lots considering demand side flexibility in electric distribution system. PhD, Yıldız Technical University, Istanbul, Türkiye, 2019.
- [12] Ahmad F, Iqbal A, Ashraf I, Marzband M, Khan I. Placement of electric vehicle fast charging stations using Grey Wolf Optimization in electrical distribution network. IEEE International Conference on Power Electronics, Smart Grid, and Renewable Energy (PESGRE); 02-05 January 2022; Trivandrum, India. (pp. 1-6). IEEE.
- [13] Das HS, Rahman MM, Li S, Tan CW. (2020). Electric Vehicles Standards, Charging Infrastructure, and Impact on Grid Integration: A Technological Review. Journal of Renewable and Sustainable Energy Reviews 2020; 120, 109618.
- [14] Liu Y, Li X, Liang Y, Zeng S, Li M. Assessment of impacts on integration of disorderly EV charging load to flexible distribution network. 11th International Conference on Power, Energy and Electrical Engineering (CPEEE); 26-28 February 2021; Kyoto, Japan. (pp. 139-142). IEEE.
- [15] Araújo AV, Araujo DN, Vasconcelos AS, Júnior WDAS, Rosas PAC, de Medeiros LH, Ji T. A proposal for technical and economic sizing of energy storage system and PV for EV charger stations with reduced impacts on the distribution network. The 26th International Conference and Exhibition on Electricity Distribution (CIRED); 20-23 September 2021. doi:10.1049/icp.2021.1832.
- [16] Polat Ö. Stochastic modelling of electric vehicle charging load and its impacts on low voltage distribution networks. PhD, Istanbul Technical University, Istanbul, Türkiye, 2015.
- [17] Özcan M.E. Distribution integration of electric vehicles. PhD, Marmara University, Istanbul, Türkiye, 2019.
- [18] Zoroğlu B, Yapıcı AT, Kurt ÜG. Electric vehicle status of standards and electric vehicle charging stations in Turkey. International Marmara Sciences Congress (IMASCON); 04-05 December 2020; Kocaeli, Türkiye. (pp. 299-308).
- [19] Durmuş FS, Kaymaz H. Electric Vehicle Charging Methods. Journal of Intelligent Transportation Systems and Applications (JITSA) 2020; 3(2): 123-139.
- [20] <https://zes.net/SA>
- [21] Dericioglu C, Yirik E, Unal E, Cuma MU, Onur B, Tumay M. A Review of Charging Technologies for Commercial Electric Vehicles. International Journal of Advances on Automotive and Technology 2018; 2(1): 61-70.
- [22] <https://bestchargers.eu/blog/different-types-of-ev-charging-connectors/>
- [23] https://www.mobilityhouse.com/int_en/knowledge-center/charging-cable-and-plug-types
- [24] İpek B. Electric vehicles, electric charging stations and electric vehicle quantity future forecast for Turkey. MSc, Istanbul Technical University, Istanbul, Türkiye, 2022.
- [25] Mohamed AA, Shaier AA, Metwally H, Selem SI. Wireless Charging Technologies For Electric Vehicles: Inductive, Capacitive, And Magnetic Gear. IET Power Electronics 2023; 1-27. doi: 10.1049/pel2.12624
- [26] Regensburger B, Sinha S, Kumar A, Maji S, Afridi KK. High-Performance Multi-MHz Capacitive Wireless Power Transfer System For EV Charging Utilizing Interleaved-Foil Coupled Inductors. IEEE Journal of Emerging and Selected Topics in Power Electronics 2020; 10(1): 35-51.
- [27] Amjad M, Farooq-i-Azam M, Ni Q, Dong M, Ansari EA. Wireless Charging Systems For Electric Vehicles. Renewable and Sustainable Energy Reviews 2022; 167: 112730.
- [28] Bai HK, Costinett D, Tolbert LM, Qin R, Zhu L, Liang Z, Huang Y. Charging Electric Vehicle Batteries: Wired And Wireless Power Transfer: Exploring EV Charging Technologies. IEEE Power Electronics Magazine 2022; 9(2): 14-29.
- [29] https://ch.mathworks.com/help/autoblks/ug/electric-vehicle-reference-application.html?s_tid=srchtitle_Reference%20Application_4
- [30] Ehsani M, Gao Y, Longo S, & Ebrahimi K. Modern Electric, Hybrid Electric, And Fuel Cell Vehicles. Boca Raton, Florida, USA: CRC press, 2018.
- [31] Şahin H. Development of an electric vehicle powered by a fuel cell-battery hybrid power source. PhD, Fırat University, Elazığ, Türkiye, 2022.
- [32] <https://ev-database.org/>

An Application of Robust Principal Component Analysis Methods for Anomaly Detection

Kübra BAĞCI GENEL^{1*}, Halit Eray ÇELİK^{2,3}

^{1,2} Department of Econometrics, Faculty of Economics and Administrative Sciences, Van Yüzüncü Yıl University, Van, Türkiye

³ Department of Computer Engineering, Engineering Faculty, Khoja Akhmet Yassawi International Kazakh- Turkish University, Kazakhstan

*¹ kubrabagci@yyu.edu.tr, ² ecelik@yyu.edu.tr

(Geliş/Received: 05/05/2023;

Kabul/ Accepted: 01/03/2024)

Abstract: Ensuring a secure network environment is crucial, especially with the increasing number of threats and attacks on digital systems. Implementing effective security measures, such as anomaly detection can help detect any abnormal traffic patterns. Several statistical and machine learning approaches are used to detect network anomalies including robust statistical methods. Robust methods can help identify abnormal traffic patterns and distinguish them from normal traffic accurately. In this study, a robust Principal Component Analysis (PCA) method called ROBPCA which is known for its extensive use in the literature of chemometrics and genetics is utilized for detecting network anomalies and compared with another robust PCA method called PCAGRID. The anomaly detection performances of these methods are evaluated by injecting synthetic traffic volume into a well-known traffic matrix. According to the application results, when the normal subspace is contaminated with large anomalies the ROBPCA method provides much better performance in detecting anomalies.

Key words: Anomaly detection, outlier, Principal Component Analysis, robust statistics.

Dayanıklı Temel Bileşenler Analizi ile Anomali Tespiti Üzerine Bir Uygulama

Öz: Dijital sistemlere yönelik artan sayıda tehdit ve saldırılar sebebi ile güvenli bir ağ ortamı sağlamak önemli bir problemdir. Anomali tespiti gibi yöntemlerin uygulanması, herhangi bir anomal trafik hacminin tespit edilmesine yardımcı olabilmektedir. Dayanıklı istatistiksel yöntemler de dahil olmak üzere ağ anomalilerini tespit etmek için çeşitli istatistiksel ve makine öğrenmesi yaklaşımları kullanılmaktadır. Dayanıklı yöntemler, anormal trafik modellerini belirlemeye ve bunları normal trafikten doğru bir şekilde ayırmaya yardımcı iyi bir araçtır. Bu çalışmada, ağ anomalilerini tespit etmek için kemometri ve genetik literatüründe yaygın kullanımıyla bilinen ROBPCA adlı dayanıklı bir Temel Bileşen Analizi (PCA) yöntemi kullanılmış ve PCAGRID adlı başka bir dayanıklı PCA yöntemi ile karşılaştırılmıştır. Bu yöntemlerin anomali tespit performansları, iyi bilinen bir trafik matrisine sentetik trafik hacmi enjekte edilerek değerlendirilmiştir. Uygulama sonuçlarına göre anomali tespitinde ROBPCA yöntemi daha iyi performans sağladığı görülmüştür.

Anahtar kelimeler: Anomali tespiti, aykırı değer, dayanıklı istatistik, Temel Bileşenler Analizi.

1. Introduction

Network security has become more important due to the rapid development of network technologies. Providing a stable network is a critical task considering even some basic services use network technologies. To fulfill this task, anomaly detection is one of the approaches to detecting abnormal behaviors in the traffic volume. Anomaly detection is also effective with unknown attack patterns, unlike the signature-based approaches.

Although machine learning methods are promising and generally used in detecting network anomalies, statistical approaches are also frequently utilized in related fields successfully. Robust versions of the classical statistical methods can be useful in solving many statistically related computer network issues, and their potential as a tool for detecting anomalies [1]. Principal Component Analysis (PCA) known as a classical data reduction technique has been widely used in network anomaly detection over the last 20 years. To use the dimension reduction method for detecting outliers i.e., anomalies, the PCA is regarded as a classification procedure and utilized to detect outlying and normal observations. Since outliers can seriously bias or influence estimates that may be of substantive interest [2] it is not desirable for a statistical method to be sensitive to outliers even though the objective is to detect the outliers. The outcomes caused by this sensitivity are extensively discussed in previous studies [3–5] on network anomaly detection. Consequently, these works suggested that using robust methods may be beneficial to cope with such problems as subspace contamination and sensitive false positive rates. Due to the potential costs of an incorrect classification, robust methods are considered in critical cases, such as the detection of network anomalies.

* Corresponding author: kubrabagci@yyu.edu.tr. ORCID Number of authors: ¹ 0000-0002-6679-9738, ² 0000-0001-7490-8124

In this study, two robust PCA methods called the ROBPCA [6] and PCAGRID [7] are considered. The reason for considering these methods is based on a study by [8] that compares the outlier detection performances of many robust PCA methods throughout a simulation study. According to their study, amongst the many robust PCA algorithms, the ROBPCA and PCAGRID algorithms stand out in detecting anomalies. Motivated by this, performances of the ROBPCA and PCAGRID methods for detecting network anomalies are compared through a well-known traffic matrix. In addition, PCAGRID is recognized for its ability to yield precise estimates in cases of uncontaminated datasets while also demonstrating robustness when dealing with contaminated data [8]. The PCAGRID and ROBPCA, have versatile applications across different fields. The efficiency of these methods in outlier detection is compared in the studies from various fields (see [9, 10]) including chemometrics, and time series analysis, recently. Chen et al. [9] showed that the PCAGRID method had performed better in terms of false positives over the ROBPCA algorithm for both simulated and real biological data with varying outlieriness levels and Kazemi et al. [10] pointed out the PCAGRID is computationally faster than the ROBPCA method. Although the PCAGRID method has already been used in network anomaly detection previously [1], the ROBPCA method is utilized by [11] in the field of cybersecurity for detecting outliers most recently. Consequently, these two methods continue to find applications across various fields for detecting outliers. Considering the methods have advantageous features, the studies to detect network anomalies using these methods, are quite limited. This study contributes to the literature by evaluating the performance of two established robust PCA methods, ROBPCA and PCAGRID, for the purpose of network anomaly detection. Building upon prior research that highlighted their effectiveness in various research areas, our work emphasizes their applicability to network security by comparing their recalls of varying sizes of injections.

The rest of the study is organized as follows. In section 2, related literature is reviewed. Then, the methods used in the study are briefly described and the application scheme is explained. In section 4, the anomaly detection performances of the robust PCA methods are evaluated. In section 5, the study is finalized with a discussion of the results in light of previous studies.

2. Literature

In this section, some of the studies that addressed the advantages of using robust PCA methods in anomaly detection are reviewed. Lakhina et al. [12] pioneered the use of a PCA-based approach for network anomaly detection. Subsequently, many studies have contributed to this field. After the study of Lakhine et al., [12] there have been studies [3] and [13] concerning the sensitivity of the PCA for traffic anomaly detection and stated that using robust methods may overcome this problem. In this manner, Pascoal et al. [1], proposed a new detection scheme that utilizes a robust PCA method, the PCAGRID for detecting outliers after a robust feature selection step. They showed that the robust PCA successfully detected the anomalies in different traffic conditions. Wang et al. [14] proposed the Relaxed Principal Component Pursuit method as a new decomposition model and discussed the limitations of the classical PCA when the traffic matrix is contaminated with large anomalies. Kudo et al. [15] stated that considering a robust PCA method may perform better even though their PCA-based anomaly detection scheme is able to decrease the false alarm rate. Also, they proposed a detection scheme using the daily or weekly periodicity of the traffic matrix to avoid normal subspace contamination problems. Subspace contamination problem is explained as, problems encountered such as a high false alarm rate, due to contamination of normal subspace with the presence of very large anomalies [3]. By this means, Matsuda et al. [16] utilized an existing robust PCA method for the network anomaly detection scheme in [15] which is based on the periodicity of the traffic volume. They considered the Minimum Covariance Determinant (MCD) estimator MCD to be a robust covariance estimation method also included in the ROBPCA algorithm. Also applied the mentioned scheme to the Abilene data set. Hadri et al. [17] proposed a nonlinear feature extraction method called Nonlinear Fuzzy Robust PCA for anomaly detection is effective with noisy data as well. They showed that the Nonlinear Fuzzy Robust PCA method resulted in low false positive alarms using well-known KDDcup99 and NSL-KDD data. There are several studies in network intrusion detection literature employing PCA-based methods. Fernandes et al. [5] reviewed some of these studies on network anomaly detection including a detailed discussion of PCA-based methods as well. In recent years, the PCA has continued to be used in many network anomaly detection systems mostly in combination with various other approaches. For example, Vilaca et al., [18] introduce a semi-supervised machine learning model called RPCA-MD, which utilizes robust PCA and Mahalanobis Distance to automatically identify anomalies in network traffic and detect potential attacks, offering a promising solution for enhanced network security addressing the issue of botnet attacks. Wang et al., [19] combined PCA and Single-Stage Headless Face Detector algorithms offering superior detection speed and accuracy in experiments conducted using IDS2017 and IDS2012 datasets, making it a promising solution for efficient traffic attack detection in network security. Lu [20] proposes an anomaly detection system based on PCA to enhance the security of networked medical devices,

and the evaluation using real-world data demonstrates its effectiveness in detecting malicious attacks with a high detection rate and a low false alarm rate.

3. PCA-Based Outlier Detection

In this section, the PCA-based robust ROBPCA, and PCAGRID methods are described briefly. Since the methods introduced by [6, 7] before, a brief description of the methods is only given.

As mentioned the classical PCA is a statistical method generally used for dimension reduction. It is based on transforming relatively large numbers of variables into fewer unrelated variables by finding orthogonal linear combinations of original variables with the greatest variance [1]. The PCAGRID is introduced by Croux et al. [7] as a robust PCA method that uses the projection pursuit algorithm. It is based on finding projections of the data that have maximal dispersion with the grid search algorithm. Instead of using the variance, the algorithm employs a robust scale estimator called the Median Absolute Deviation. Similarly, the ROBPCA method includes both projection pursuit and robust covariance estimation. In the robust estimation of covariance, the MCD method is employed in the algorithm. In both methods, each observation is classified using different outlying scores based on distance, as normal observations and anomalies. See also [6] for more information on the ROBPCA method. The ROBPCA and PCAGRID methods are implemented by using the functions of LIBRA, which is a library of MATLAB published by [21], and the "rrcov" package featured in the R application, respectively.

4. Data and Application

4.1. Abilene data set and synthetic outliers

The traffic matrix used in this study is based on the traffic volumes measured on the origin-destination (OD) flows in the Abilene network on 1-8 March 2004. Abilene is a backbone network that connects various US campuses consisting of 12 nodes and 30 links. The Abilene dataset is a well-known data that continues to be used in various intrusion detection studies such as, [14–16]. It is available in [22]. The topology of the Abilene network is given in Figure 1. 12 nodes (n1-n12) and 30 links (e1-e30) of the Abilene network are visualized in the network topology.

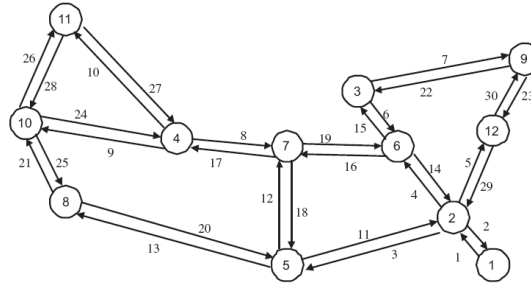


Figure 1. Abilene Network Topology [15].

For evaluating the anomaly detection performance of the PCAGRID and ROBPCA methods, synthetic anomalies are injected randomly into the Abilene traffic matrix which consists of 2016 observations and 144 variables. Anomalies are injected into traffic volumes measured in generated random places between the links e1-e7. The data is contaminated with different sizes of anomalies. As suggested in [23] the large anomalies injected as 10 times larger than the given traffic volume and small anomalies are injected as 2 times larger than the given traffic volume. Moreover, 1.2, 1.5, 8, and 12 times larger injections from background traffic volume are injected to examine both methods' recall (detection) performances in more detail.

4.2. Application scheme

The proposed application scheme is given as follows

1. Create random numbers using discrete uniform distribution ($I_{1 \times n}$) to determine where to inject n synthetic anomalies. $n=100$.

For, $i=1 \dots n$,

2. set $i=1$

3. Add synthetic traffic into the original traffic volume ($X_{2016 \times 144}$) for the corresponding element given in $I_{1 \times 1}$ and store injected data as a new data matrix (X_i).
4. Implement the ROBPCA for X_i using the “robpca” function in the LIBRA, MATLAB library.
5. Extract outlier score from $flag_{2016 \times 1}$ matrix obtained by implementing the “robpca” function. If the corresponding element of $flag$ matrix (injection) is labeled as 0, classify observation as an outlier, and if it is 1, classify it as regular observation.
6. Set $i=i+1$ and repeat 3-5 steps.

Consequently, a detection rate as given in equation 1, is obtained by considering outcomes in each loop. A similar scheme is followed for the PCAGRID method by using the PcaGrid function of the "rrcov" package featured in the R software. The ROBPCA method initializes a parameter denoted as 'alpha,' which serves as a control parameter to regulate the algorithm's sensitivity to outliers. Alpha is a continuous variable within the range of 0.5 to 1, with a default value set at 0.75. Here default value of this parameter is chosen since the injections are not more than %25 of the data (around %1). The PCAGRID is also implemented using default parameter settings as well.

$$\text{Detection rate} = \frac{\text{True positives}}{\text{False negatives} + \text{True positives}} \quad (1)$$

4.3. Application

In this section, anomaly detection performances of the ROBPCA and PCAGRID methods are compared by injecting synthetic anomalies into the Abilene dataset. The number of principal components to be used in the ROBPCA and PCAGRID algorithms is determined with the help of the scree plots. A scree plot is a practical tool used in deciding the number of PCs. The anomaly detection rate is considered a measure of detection performance.

Scree plots of eigenvalues for the ROBPCA algorithms are given in Figure 2.

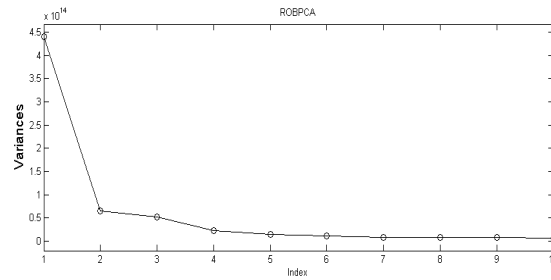


Figure 2. Scree plot for the ROBPCA method.

Scree plots of eigenvalues for the PCAGRID algorithm is given in Figure 3.

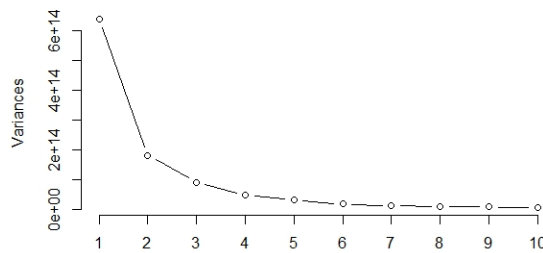


Figure 3. Scree plot for the PCAGRID method.

According to Figure 2 and Figure 3, it is decided to consider the first 4 PCs by taking into account the level-off point on the line.

Hair et al. [24] stated that the percentage of total explained variance of at least 60% is a satisfactory rate. A high variance explanation rate (86%) is reached by considering 4 PCs.

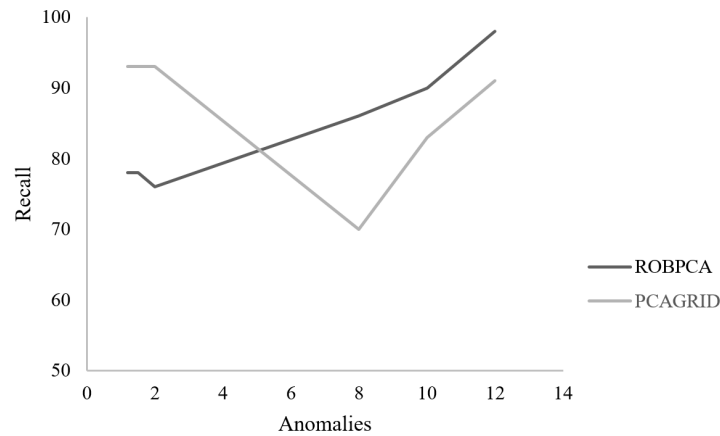


Figure 4. Detection rates for different sizes of injected anomalies.

Detection rates for various injections are given for both methods in Figure 4. With the ROBPCA algorithm, the %98, %90, %86, %76, %78, and %78 of injections are detected for 12, 10, 8, 2, 1.5 and 1.2 sized injections, respectively. With the PCAGRID algorithm, the %91, %83, %70, %94, %93, and %93 detection rates are obtained for 12, 10, 8, 2, 1.5 and 1.2 sized injections, respectively. Consequently, it can be said that the PCAGRID method is effective in detecting small anomalies better than ROBPCA. Moreover, although in larger anomalies the ROBPCA performed better, the PCAGRID reached higher detection rates overall. According to the results, it is seen that the ROBPCA provides better performance in detecting larger network anomalies and PCAGRID provides better performance in detecting smaller network anomalies. Also, anomaly detection rates are consistent with previous studies, such as [12] and [25] which reached around a % 90 detection rate. The false alarm rate is not given since it would require a data cleaning process. Also, it is seen that the ROBPCA method, which has been successfully used in chemometrics and genetics [9, 26, 27] can be adapted to network anomaly detection as well.

5. Conclusion

In this study, the anomaly detection performance of two robust PCA methods, ROBPCA and PCAGRID, across various injection scenarios are investigated. First, the background traffic volume is contaminated with synthetic anomalies by injecting them into random links of Abilene data. Then, it is examined whether these two methods can detect these outliers. Results show that the ROBPCA method performed better when the data are contaminated with large anomalies and the PCAGRID method is superior in recall of small anomalies. Consequently, the two methods that are highly popular in different fields, such as chemometrics, biology, and engineering, have been applied to network anomaly detection, providing significant performance in the subjected area, which should be investigated in more detail in future studies.

References

- [1] Pascoal C, Oliveira MR de, Valadas R, et al. Robust feature selection and robust PCA for internet traffic anomaly detection. 2012 Proceedings IEEE INFOCOM 2012[Online] 2012.
- [2] Zimmerman DW. A Note on the Influence of Outliers on Parametric and Nonparametric Tests. *J Gen Psychol* Routledge 1994; 121(4):391–401.
- [3] Ringberg H, Soule A, Rexford J, et al. Sensitivity of PCA for Traffic Anomaly Detection. *SIGMETRICS Perform. Eval. Rev. Association for Computing Machinery: New York, NY, USA* 2007; 35(1):109–20.
- [4] Brauckhoff D, Salamatian K, May M. Applying PCA for Traffic Anomaly Detection: Problems and Solutions. *IEEE INFOCOM 2009* 2009[Online] 2009.
- [5] Fernandes G, Rodrigues JJPC, Carvalho LF, et al. A comprehensive survey on network anomaly detection. *Telecommun Syst* 2019; 70(3):447–89.
- [6] Hubert M, Rousseeuw PJ, Branden K Vanden. *ROBPCA: A New Approach to Robust Principal Component Analysis*. Technometrics Taylor & Francis 2005; 47(1):64–79.
- [7] Croux C, Filzmoser P, Oliveira MR. Algorithms for Projection–Pursuit robust principal component analysis. *Chemometrics and Intelligent Laboratory Systems* 2007; 87(2):218–25.
- [8] Pascoal C. and Oliveira MR and PA and VR. Detection of Outliers Using Robust Principal Component Analysis: A Simulation Study. *Combining Soft Computing and Statistical Methods in Data Analysis 2010*[Online] Springer Berlin Heidelberg: Berlin, Heidelberg 2010.

- [9] Chen X, Zhang B, Wang T, et al. Robust principal component analysis for accurate outlier sample detection in RNA-Seq data. *BMC Bioinformatics* 2020; 21(1):269.
- [10] Kazemi M, Rodrigues PC. Robust singular spectrum analysis: comparison between classical and robust approaches for model fit and forecasting. *Comput Stat* 2023;
- [11] Burr B. Intruder Alert: Dimension Reduction and Density-Based Clustering for a Cybersecurity Application. 2021[Online] Ottawa 2021.
- [12] Lakhina A, Crovella M, Diot C. Diagnosing Network-Wide Traffic Anomalies. *Proceedings of the 2004 Conference on Applications, Technologies, Architectures, and Protocols for Computer Communications 2004*[Online] Association for Computing Machinery: New York, NY, USA 2004.
- [13] Abdelkefi A, Jiang Y, Wang W, et al. Robust Traffic Anomaly Detection with Principal Component Pursuit. *Proceedings of the ACM CoNEXT Student Workshop 2010*[Online] Association for Computing Machinery: New York, NY, USA 2010.
- [14] Wang Z, Hu K, Xu K, et al. Structural analysis of network traffic matrix via relaxed principal component pursuit. *Computer Networks* 2012; 56(7):2049–67.
- [15] Kudo T, Morita T, Matsuda T, et al. PCA-based robust anomaly detection using periodic traffic behavior. 2013 IEEE International Conference on Communications Workshops (ICC) 2013[Online] 2013.
- [16] Matsuda T, Morita T, Kudo T, et al. Traffic anomaly detection based on robust principal component analysis using periodic traffic behavior. *IEICE Transactions on Communications* The Institute of Electronics, Information and Communication Engineers 2017; 100(5):749–61.
- [17] Hadri A, Chougali K, Touahni R. A Network Intrusion Detection Based on Improved Nonlinear Fuzzy Robust PCA. 2018 IEEE 5th International Congress on Information Science and Technology (CiSt) 2018[Online] 2018.
- [18] Vilaça ESC, Vieira TPB, Sousa RT de, et al. Botnet traffic detection using RPCA and Mahalanobis Distance. 2019 Workshop on Communication Networks and Power Systems (WCNPS) 2019[Online] 2019.
- [19] Wang Z, Han D, Li M, et al. The abnormal traffic detection scheme based on PCA and SSH. *Conn Sci Taylor & Francis* 2022; 34(1):1201–20.
- [20] Lu W. Detecting Malicious Attacks Using Principal Component Analysis in Medical Cyber-Physical Systems. In: Traore I, Woungang I, Saad S, Eds. *Artificial Intelligence for Cyber-Physical Systems Hardening* Springer International Publishing: Cham 2023; pp. 203–15.
- [21] Verboven S, Hubert M. LIBRA: a MATLAB library for robust analysis. *Chemometrics and Intelligent Laboratory Systems* 2005; 75(2):127–36.
- [22] Zhang Y. Abilene Data. <https://WwwCsUtxasEdu/~yzhang/Research/AbileneTM/> [Online].
- [23] Nagaraja S, Jalaparti V, Caesar M, et al. P3CA: Private Anomaly Detection Across ISP Networks. *Privacy Enhancing Technologies 2011*[Online] Springer Berlin Heidelberg: Berlin, Heidelberg 2011.
- [24] Hair JF, Black WC, Babin BJ, et al. *Multivariate data analysis: Pearson new international edition*. Essex: Pearson Education Limited 2014; 1(2).
- [25] Rubinstein BIP, Nelson B, Huang L, et al. ANTIDOTE: Understanding and Defending against Poisoning of Anomaly Detectors. *Proceedings of the 9th ACM SIGCOMM Conference on Internet Measurement 2009*[Online] Association for Computing Machinery: New York, NY, USA 2009.
- [26] Shieh AD, Hung YS. Detecting Outlier Samples in Microarray Data 2009; 8(1).
- [27] Granzotto C, Sutherland K, Arslanoglu J, et al. Discrimination of Acacia gums by MALDI-TOF MS: applications to micro-samples from works of art. *Microchemical Journal* 2019; 144:229–41.

Expanded Perlite Mineral As a Natural Additive Used In Polylactide-Based Biodegradable Composites

Erkan AKSOY^{1*}, Süha TİRKEŞ², Ümit TAYFUN³, Seha TİRKEŞ⁴

¹ Project and Technology Office, Rectorate, Bartın University, 74100, Bartın, Türkiye

² Welding Technology and NDT Center, Middle East Technical University, Ankara, Türkiye

³ Department of Basic Sciences, Bartın University, Bartın 74110, Türkiye

⁴ Department of Chemical Engineering, Atılım University, Ankara, Türkiye

¹ eaksoy@bartin.edu.tr, ² stirkes@metu.edu.tr, ³ utayfun@bartin.edu.tr, ⁴ seha.tirkes@atilim.edu.tr

(Geliş/Received: 23/08/2023;

Kabul/Accepted: 02/03/2024)

Abstract: Polylactide (PLA) is a biodegradable polymer derived from natural resources used in various applications ranging from medical to packaging. In this study, biocomposites were developed by combining perlite mineral (PER), a natural filler material, with a biodegradable PLA matrix in incorporated contaminations of 2.5%, 5%, 10%, and 15%. The purpose of this work is to obtain composites having low production costs while retaining their main properties. Mixing force measurements, tensile, Shore hardness, impact tests, melt flow indices (MFI), and scanning electron microscopy (SEM) evaluations were carried out on composite samples to determine the processing, mechanical, melt flow, and morphological aspects of the developed composites. When the tensile test data were reviewed, minor decreases in the tensile strength and % elongation parameters were noticed with perlite loadings. The inclusion of perlite powder significantly reduced the impact strength value of PLA. Composites with high amounts of PER displayed elevated hardness values. While the MFI results were analyzed, it was deduced that the addition of PER increased the melt flow characteristics of the PLA polymer. At low PER quantities, SEM micrographs displayed that PER particles were homogeneously distributed in the PLA phase. The particle homogeneity in the composite morphology deteriorated as the PER loading ratio in the composites rose. According to the overall results, the highest performance among composites was achieved in the sample including 2.5% PER, and this sample was considered to be the most suitable option for applications regarding PLA-based biocomposite material purposes.

Keywords: Biocomposites, polylactide, perlite, polymeric composites, biodegradable polymer.

Polilaktid Esaslı Biyobozunur Kompozitlerde Doğal Bir Katkı Maddesi Olarak Genişletilmiş Perlit Mineralinin Kullanımı

Öz: Polilaktit (PLA), tıptan paketlemeye kadar çeşitli uygulamalarda kullanılan, doğal kaynaklardan elde edilen ve biyolojik olarak parçalanabilen bir polimerdir. Bu çalışmada, biyokompozitler, doğal bir dolgu malzemesi olan perlit mineralinin (PER) biyolojik olarak parçalanabilen bir PLA matrisi ile %2.5, %5, %10 ve %15'lik ekleme oranlarında harmanlanarak hazırlanmıştır. Geliştirilen kompozitlerin işleme, mekanik, erime akışı ve morfolojik özelliklerini belirlemek için kompozit numuneler üzerinde karıştırma kuvveti ölçümleri, çekme, Shore sertliği, darbe testleri, erime akış indisleri (MFI) ve taramalı elektron mikroskobu (SEM) değerlendirmeleri yapılmıştır. Çekme testi verileri incelendiğinde, perlit yüklemeleri ile çekme mukavemeti ve % uzama parametrelerinde ufak düşüşler görülmüştür. Perlit tozunun dahil edilmesi, PLA'nın darbe dayanımı değerini önemli ölçüde azaltmıştır. Yüksek miktarda PER içeren kompozitler, yüksek sertlik değerleri göstermiştir. MFI sonuçları analiz edildiğinde, PER ilavesinin PLA polimerinin erime akış özelliklerini arttırdığı bulunmuştur. Düşük PER miktarlarında, SEM mikrografları, PER partiküllerinin PLA fazında homojen bir şekilde dağıldığını ortaya çıkarmıştır. Kompozit morfolojisindeki partikül homojenliği, kompozitlerdeki PER yükleme oranı arttıkça bozulmuştur. Genel sonuçlara göre kompozitler arasında en yüksek performans %2,5 PER içeren numunede elde edilmiş ve bu numunenin PLA esaslı biyokompozit malzeme amaçlı uygulamalar için en uygun seçenek olduğu değerlendirilmiştir.

Anahtar kelimeler: Biyokompozitler, polilaktid, perlit, polimerik kompozitler, biyobozunur polimer.

1. Introduction:

Minerals are commonly employed as reinforcements for polymeric materials due to their low cost and ease of processing. Perlite is a naturally occurring mineral that is a type of amorphous volcanic silica glass with high water content. When heated, this aluminosilicate can expand 30 times its initially formed volume. Türkiye has the highest perlite deposits, accounting for over fifty percent of the world's total. The other countries with substantial perlite abundance include Japan, Greece, Hungary, Iran, USA, Italy, Mexico, and Iran. In addition to the low-cost plastic additive, coatings, flooring, insulation goods, concrete, lightweight structural components, medicines, dental substances, detergents, soapy products, and water filtering applications have all found uses for perlite

* Corresponding author: eaksoy@bartin.edu.tr, ORCID Number of authors: ¹ 0000-0002-0083-2574, ² 0000-0002-1255-4524, ³ 0000-0001-5978-5162, ⁴ 0000-0002-9131-9951.

mineral [1-9]. As a porous volcanic rock, perlite mineral donates weight-reduction in addition to a decrease in production cost as it is used as a filler material [10,11].

Perlite mineral was evaluated as reinforcing material for various polymers in experimental studies according to the literature. In these research studies, perlite inclusions yielded performance improvements for thermal conductivity characteristics in the case of heat storage behavior of poly (ethylene glycol) (PEG) [12], mechanical characteristics of polystyrene (PS) based composites [13], decline in the drug release rate of poly (methacrylic acid) (PMAA) regarding drug delivery application [14]. Additionally, the bone tissue efficiency of hydroxyapatite (HA) was investigated after the integration of perlite [15]. Melt flow properties of acrylonitrile-butadiene-styrene terpolymer (ABS) involving perlite powder were reported in which process parameters were not affected by mineral incorporation related to additive manufacturing application of ABS [16]. The thermal and mechanical performance of poly (vinyl alcohol) (PVA) composites was also optimized with the help of perlite additions [17]. Biodegradable chitosan polymer was filled with expanded perlite which produced composites that showed viscoelastic behavior [18]. Perlite-incorporated polyaniline exhibited a reduction in electrical conductivity compared to unfilled polymers [19]. The flame retardant effect of perlite was also postulated by its integration with polypropylene (PP) composites involving wood flour [20] and expandable graphite [21]. Polyethylene (PE) was compounded with perlite in several research works. In these studies, thermal stability and mechanical strength of composites were reported [22-28]. Thermal insulation behaviors of polyurethane foam (PUF) [29] and epoxy resin [30] loaded with perlite powder were also studied. PLA-based composites involving perlite were fabricated in two research affords according to the literature survey. In one of these studies, perlite addition with high loading amounts (from 20 to 50%) to PLA was evaluated by limited characterization methods including thermal and structural properties [31]. In another publication dealing with PLA/perlite composites, nanosized perlite was used with filling ratios ranging from 1 to 7% by weight. Similarly, the thermal decomposition and crystallinity of composites were reported [32].

Poly lactide (PLA) is a broadly accessible thermoplastic made from materials that are renewable and biodegradable. As a result of these features, polylactide has great potential as a substitution for petroleum-based products. However, in circumstances needing a high level of mechanical resistance, polylactide's strength in its unadulterated condition is frequently inadequate. As a result, a great deal of effort has been expended in researching solutions to this material property defect. The biomedical industry has employed PLA, a biodegradable aliphatic polyester with good qualities for many polymer applications, mostly because of its high cost, which is the result of high-priced polymerization and purifying procedures. The main application area of PLA and related composites is the packaging industry due to its biodegradable character. The use of PLA in textile, transportation, biomedical, and building sectors also exhibits an increasing trend as well as recently being applied as a filament feedstock material in the additive manufacturing process [33-36].

In this work, the PLA matrix was compounded with expanded perlite to achieve low-priced and reduced-weight biocomposites with optimized performances. The resulting composites can be employed as 3D filament material thanks to the wide use of PLA in this application area. The novelty of the study lies in the experimental evaluation of perlite inclusion on mechanical, mixing force, and melt-flow behavior of PLA composites since these properties were not reported in similar research works dealing with PLA/PER composite systems [31,32] as discussed in the literature survey. Melt-blending method was applied to develop composite samples due to its practical integration into high-level production stages in the industry. Mechanical characteristics are crucial factors for PLA as it is used as a packaging material. For this reason, mechanical strength parameters of produced composites were investigated employing tensile, hardness, and impact resistance tests. Reduction of weight for the composite material is highly required in vehicles. The inclusion of a natural mineral in bio-based PLA yields a green composite that retains biodegradable and environmentally friendly behavior. Melt flow measurements were performed since this characterization provides processing ability in the case of developing 3D printed parts via PLA-based composite filaments utilizing additive manufacturing techniques. Besides cost-reduction using low-cost perlite mineral, the force values exerted in the melt-blending process were recorded since it affects the total production cost in industrial manufacturing steps. Morphological analysis was carried out to visualize the dispersion quality of perlite particles in composite morphologies.

2. Experimental

2.1. Materials and instruments:

Expanded perlite with a bulk density of 300–1000 kg/m³ and an average particle size of 40 µm was obtained from Eti Maden, İzmir, Türkiye. The commercial name of PLA polymer was Ingeo Biopolymer which was purchased by Natureworks LLC, USA.

In this study, Xplore Instruments program was employed to quantify force values throughout the extrusion process. The screw force values in the melt were determined using the micro-compounder's rheological software as a function of mixing time. Lloyd LR 30 K universal tensile testing machine was used for tensile properties of composites in accordance with ASTM D-638 standard. Hardness analysis was carried out using an EBP Electromechanical Equipment digital shore hardness tester according to the ASTM D2240 procedure. Coesfeld impact tester was utilized to investigate the impact resistance of composite samples having dimensions of 7.6x2.0x50 mm³ by ASTM D256 standard method. MFI measurements were performed in accordance with ASTM D1238 via Coesfeld Meltfixer LT under the conditions of a 2.16 kg standard load at 190°C. The JSM-6400 Electron Microscope, a field emission scanning electron microscope, was used for observing the morphological characteristics of composite materials. A small coating of gold was applied to the surfaces of the cracked samples from the impact test to establish conductive surfaces.

2.2. Preparation of composites:

Before compounding, PLA pellets and PER powder were vacuum-dried at 80 °C for 6 hours to reduce moisture content. Co-rotating twin screw extruder (Micro-compounder, 15 ml, Xplore Instruments, Netherlands) was utilized for developing composites. In the PLA matrix, PER was compounded by loading ratios of 2.5, 5, 10, and 15 % by weight. Process temperature of 190°C, screw speed of 100 rpm, and mixing time of 5 minutes were applied during the melt-bending process. Using an injection molding equipment (Micro-injector, Daga Instruments, USA), test specimens in the shape of dog bones with dimensions of 7.6x2.0x80 mm³ were prepared. The gauge length of the injection-molded specimens was 50 mm. A barrel temperature of 195°C, a mold temperature of 50°C, and an injection pressure of 8 bar were used in the injection molding process.

3. Results and Discussions:

3.1 Tensile properties of PLA and PLA/PER composites:

The characteristic tensile stress curves versus the percentage strain of PLA and composites were visualized in Figure 1.

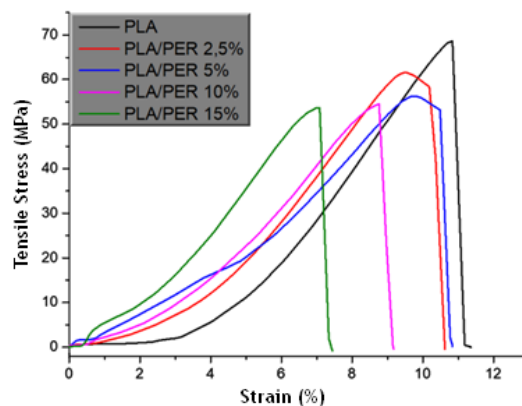


Figure 1. Stress vs. strain curves of PLA and composite samples.

PLA displayed brittle behavior according to its stress vs. strain curve since no necking property at the ultimate strength value. On the contrary, necking behavior was observed for composites filled with low amounts (2.5% and 5%) of PER as curves exhibited a small decline before the breaking point. This finding revealed that PLA/PER composites showed ductile characteristics in low concentrations of PER inclusions. Composites involving high adding amounts (10% and 15%) of PER yielded a brittle tendency similar to unfilled PLA. The necking tendency of a polymer is linked to its ductile property, in which polymer chains resist tensile deformation throughout the test. In this case, PER particles promote the ductility of brittle PLA polymer as they were incorporated with low amounts due to their homogeneous dispersion. On the contrary, weak points in polymer structure were formed for highly-filled PER particles stemming from their poor dispersion in the PLA matrix. The incorporation of PER regardless of its concentration caused the increase in the initial tensile strength of PLA.

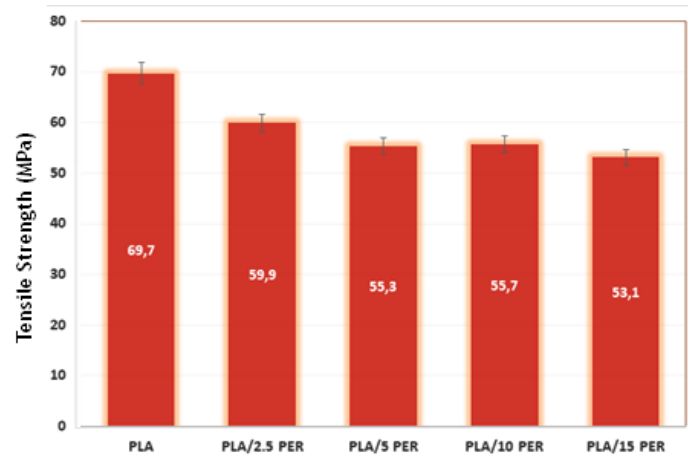


Figure 2. Tensile strength data of PLA and composite samples.

The ultimate tensile strength data of samples were demonstrated as bar graphs in Figure 2. The tensile strength of PLA was reduced by inclusions of PER according to Figure 2. PLA/2.5 PER reached maximum strength value among composites. Further additions of PER caused a slight decrease with a reduction ratio of 7.7% in the tensile strength of composites. Particulate geometry of PER particles might be responsible for this decrease as similar findings were reported in studies dealing with the mechanical performance of PER-filled polymers [13,16,28].

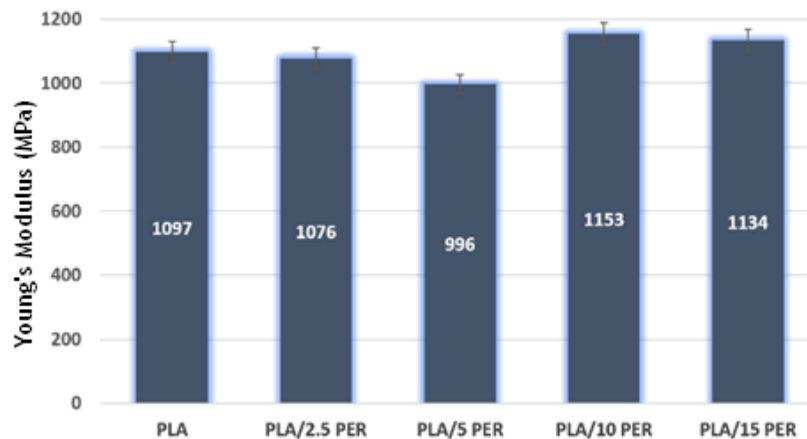


Figure 3. Young's modulus data of PLA and composite samples.

Figure 3 represents Young's modulus values of PLA and relevant composites. PLA/10 PER and PLA/15 PER samples gave higher modulus compared to unfilled PLA where nearly a 5% increase was obtained. This result implied that the addition of high amounts of PER resulted in the improvement of Young's modulus of PLA.

Young's modulus of composites involving high amounts of PER was found to be higher since compounding high amounts of PER increases the hardness and brittleness of the PLA matrix. On the other hand, a small decline was observed for composites containing low amounts of PER. As displayed with elongation data of samples in Figure 4, percent elongation and elongation at break parameters of PLA showed a decreasing trend with PER loadings. Obtaining higher elongation values in composites involving low amounts of PER relative to highly PER-filled composites might be caused by the necking tendency of PLA/2.5 PER and PLA/5 PER as stated in Figure 1.

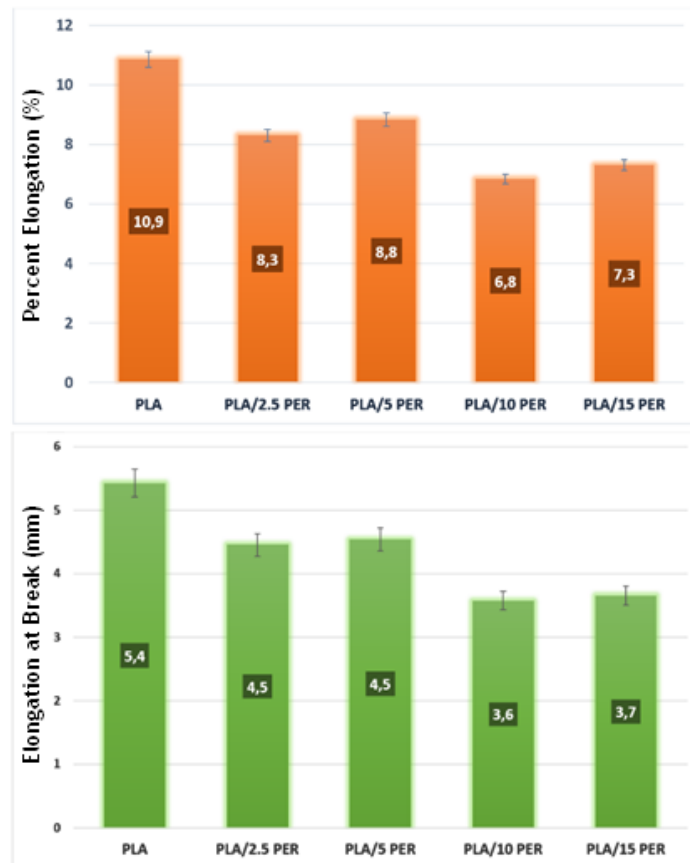


Figure 4. Elongation data of PLA and composite samples.

3.2 Impact resistance of PLA and PLA/PER composites:

The impact properties of PLA and composites are shown in Figure 5. The impact strength of unfilled PLA was reduced proportionally with the increase in the concentration of PER. Lowering in impact resistance was found to be more significant for highly-filled PLA/PER composites where a 31% reduction was calculated. Particulate geometry of PER powder resulted in the propagation of cracks exhibiting a negative effect against impact deformation of the PLA matrix due to the disorientation of load transfer with the inclusion of PER particles. Generally, plate-like additives such as graphite and mica donate impact strength thanks to the high surface area of their layers resulting in the load-bearing capacity during deformation [37-40].

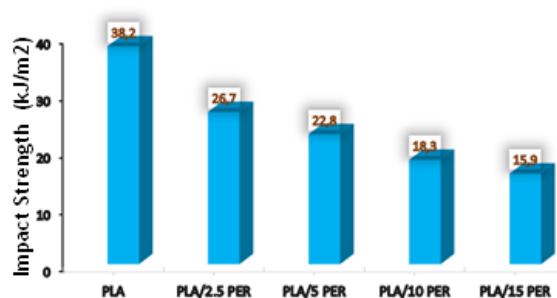


Figure 5. Impact strength data of PLA and composite samples.

3.3 Hardness performance of PLA and PLA/PER composites:

A and D type Shore hardness results of unfilled PLA and PER-involved PLA composites are postulated in Table 1.

Table 1. Shore hardness data of samples.

Sample code	Shore A	Shore D
PLA	95.0±0.1	86.0±0.1
PLA 2,5 PER	95.5±0.1	86.5±0.1
PLA 5 PER	96.0±0.1	88.0±0.1
PLA 10 PER	97.0±0.2	88.5±0.1
PLA 15 PER	97.5±0.1	89.5±0.2

As listed in Table 1, the Shore hardness of unfilled PLA was enhanced with the integration of PER into the composite structure. Hardness values of composites were found to be increased as the PER concentrations were elevated. Higher hardness values were obtained after PER inclusions thanks to the rigidity of the polymer increased with the concentration of mineral additive [34]. According to hardness findings, the correlation between Shore A and Shore D was achieved.

3.4 Force measurements of PLA and PLA/PER composites:

The exerted force values recorded during the melt-mixing process are given in Figure 5. This parameter provides experimental information before production planning related to the fabrication expenditure of resulting composite materials prior to high-scale manufacturing stages.

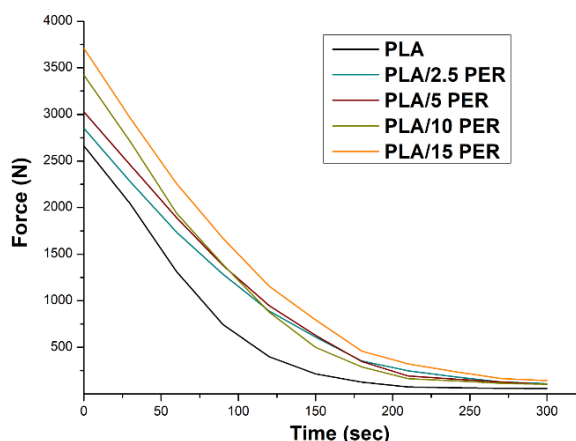


Figure 6. Force measurements of PLA and composites.

As displayed by force versus time curves in Figure 6, PER additions caused an increase in mixing force values since powder inclusions yielded improvement in shear force stemming from enhanced melt viscosity during the extrusion process. Elevated force values were obtained with an increase in the amount of PER due to the aggregation tendency of PER particles in the case of their higher concentrations [41-43].

3.5 Melt-flow behavior of PLA and PLA/PER composites:

In order to evaluate the viscosity of macromolecular melts, melt-flow index analysis is widely applied for thermoplastics. MFI parameters of PLA and relevant composites are shown in Figure 7.

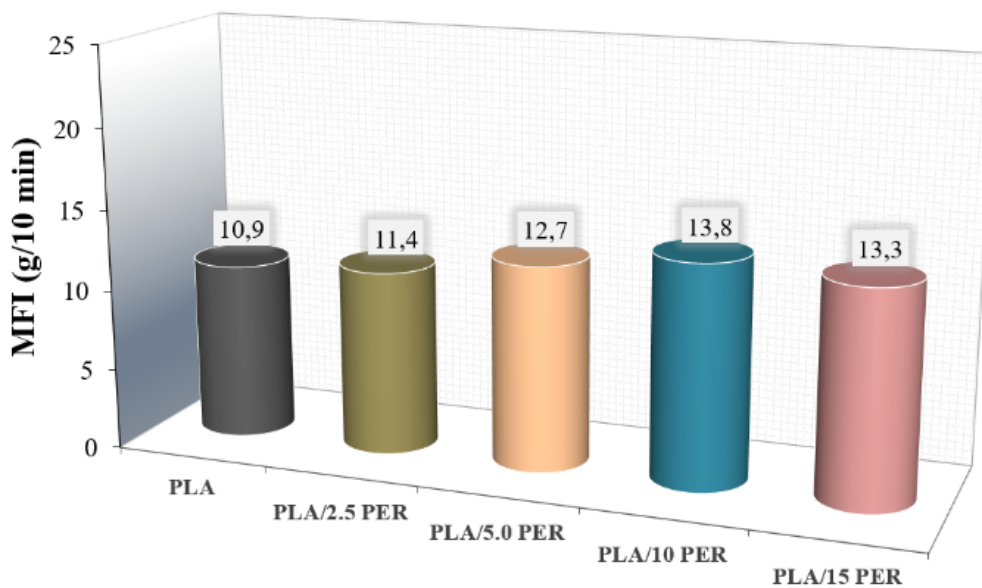


Figure 7. MFI data of PLA and composite samples.

PER-incorporated composites gave relatively higher MFI values compared to unfilled PLA. The increasing amount of MFI was found to be remarkable for composite samples containing higher amounts of PER whereas lower filling ratios of PER displayed very close MFI values to PLA. As an overall observation regarding the melt-flow behavior of PER-loaded PLA composites, MFI parameters of composites were found to be in a narrow range concerning unfilled PLA. This result indicates that PER addition caused no restriction to additive manufacturing application of PLA-based composites as the production of the 3D printing process is considered. The correlation between MFI measurements and additive manufacturing is previously stated in related research work which implied that the printability of polymer is highly affected by its melt-flow characteristics [44-48].

3.6 Morphological analysis of PLA and PLA/PER composites:

Morphological characterization of composite samples was carried out via SEM micro-images as visualized in Figure 8.

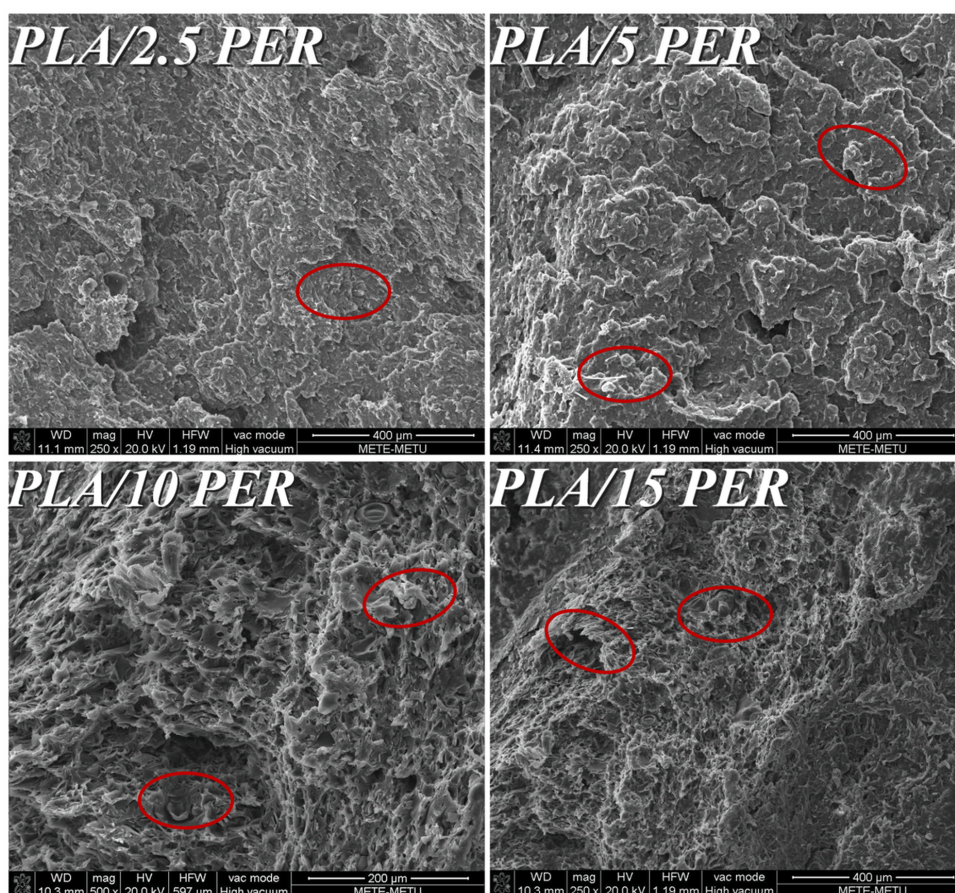


Figure 8. SEM micro-images of composites.

According to SEM micro-images of PLA/2.5 PER and PLA/5 PER samples, PER particles exhibited homogeneously dispersed morphology into the PLA matrix. Conversely, the dispersion homogeneity of PER disoriented as their added content increased due to the tendency for forming agglomeration was favored in the PER phase by particle-particle interactions despite particle-polymer interactions. This finding provided visual evidence for the reduction in related performances of composites described in earlier sections.

4. Conclusion

PLA is a thermoplastic material derived from renewable resources that is considered a green choice for petroleum-derived plastics. Perlite, on the other hand, is a naturally occurring volcanic glass mineral that is frequently used in horticulture, construction, and industrial applications due to its unique properties. While the combination of PLA and perlite offers several advantages, the specific properties and applications of the composite depend on factors such as the perlite ratio of PLA, processing methods, and the intended use of the material. Specifically, in this study, 2.5% PER-added PLA, while exhibiting the highest impact strength compared to other PER-filled PLAs, was considered to be the most suitable option. The properties of PLA and perlite composites can be adjusted by changing the composition and processing parameters. This customizability allows manufacturers to tailor the material to specific application requirements and expand its potential uses. Due to the porous nature of perlite, it can potentially decompose more efficiently than pure PLA, allowing microorganisms to access the material more easily. What's more, it can offer greater sustainability. The use of PLA reduces reliance on petroleum-based plastics and perlite is a naturally occurring resource. The low content of PER is suggested in the case of PLA-based composites since optimum results were obtained for this loading level in this study.

References

- [1] Singh M, Garg M. Perlite-based building materials-a review of current applications, *Construct. Build. Mater* 1991; 5(2): 75-81.
- [2] Aksoy Ö, Alyamaç E, Mocan M, Sütçü M, Özveren-Uçar N, Seydibeyoğlu MÖ. Characterization of perlite powders from Izmir, Türkiye region, *Physicochem. Prob. Miner. Proc* 2022; 58(6): 155277.
- [3] Burriesci N, Arcoraci C, Antonucci P, Polizzotti G. Physico-chemical characterization of perlite of various origins, *Mater. Lett* 1985; 3(3): 103-110.
- [4] Daza A, Santamaria C, Rodríguez-Navarro DN, Camacho M, Orive R, Temprano F. Perlite as a carrier for bacterial inoculants, *Soil Biol. Biochem* 2000; 32(4): 567-572.
- [5] Altuntaş E, Arıkan AK. Odun-plastik kompozit malzemelerde genişletilmiş perlit kullanımının araştırılması, *Mobilya ve Ahşap Malzeme Araştırmaları Dergisi* 2022; 5(2): 142-154
- [6] Gencil O, Bayraktar OY, Kaplan G, Arslan O, Nodehi M, Benli A. et al., Lightweight foam concrete containing expanded perlite and glass sand: Physico-mechanical, durability, and insulation properties, *Construct. Build. Mater* 2022; 320: 126187.
- [7] Öncül MK. Türkiye perlit endüstrisi, *Scientific Mining J* 1976; 15(1): 35-43
- [8] Biazar E, Keshel SH, Niazi V, Shiran NV, Saljooghi R, Jarrahi M, Arbastan AM. Morphological, cytotoxicity, and coagulation assessments of perlite as a new hemostatic biomaterial, *RSC Adv* 2023; 13(9): 6171-6180.
- [9] Turanlı L, Dernek C. The use of perlite in cement and concrete systems in the world and Turkey, *Sürdürülebilir Mühendislik Uygulamaları ve Teknolojik Gelişmeler Dergisi* 2022; 4(2): 88-97.
- [10] Çoban O, Yılmaz T. Volcanic particle materials in polymer composites: A review, *J. Mater. Sci* 2022; 57: 16989–17020.
- [11] Raji M, Nekhlaoui S, El Hassani IE, Essassi EM, Essabir H, Rodrigue D, Bouhfid R. Utilization of volcanic amorphous aluminosilicate rocks (perlite) as alternative materials in lightweight composites, *Compos. Part B Eng* 2019; 165: 47-54.
- [12] Zhang X, Wen R, Tang C, Wu B, Huang Z, Min X, Huang Y, Liu Y, Fang M, Wu X. Thermal conductivity enhancement of polyethylene glycol/expanded perlite with carbon layer for heat storage application, *Energy Build* 2016; 130: 113-121.
- [13] Oliveira AG de, Jandorno Jr JC, Rocha EB da, Sousa AM de, Silva AL da. Evaluation of expanded perlite behavior in PS/Perlite composites, *Appl. Clay Sci* 2019; 181: 105223.
- [14] Mahkam M, Vakhshouri L. Colon-specific drug delivery behavior of pH-responsive PMAA/perlite composite, *Int. J. Mol. Sci* 2010; 11(4): 1546-1556.
- [15] Koç S. Pumice and perlite co-substituted hydroxyapatite: Fabrication and characterization, *MANAS J. Eng* 2020; 8(2): 132-137.
- [16] Alghadi AM, Tirkes S, Tayfun U. Mechanical, thermo-mechanical and morphological characterization of ABS based composites loaded with perlite mineral, *Mater. Res. Express* 2019; 7(1): 015301.
- [17] Tian H, Tagaya H. Dynamic mechanical property and photochemical stability of perlite/PVA and OMMT/PVA nanocomposites, *J. Mater. Sci* 2008; 43: 766-770.
- [18] Çabuk M. Electrorheological properties of biodegradable chitosan/expanded perlite composites, *J Turkish Chem. Soc. Sect. A Chem* 2016; 3(3): 119-130.
- [19] Arsalani N, Hayatifar M. Preparation and characterization of novel conducting polyaniline–perlite composites, *Polym. Int* 2005; 54(6): 933-938.
- [20] Özdemir F. Perlit içeriğinin odun plastik kompozitlerin yanma dayanımına etkisi, *Bartın Orman Fakültesi Dergisi* 2020; 22(3): 852-860.
- [21] Mattausch H, Laske S, Hohenwarter D, Holzer C. The effect of mineral fillers on the rheological, mechanical and thermal properties of halogen-free flame-retardant polypropylene/expandable graphite compounds, *AIP Conf. Proc* 2015; 1664: 180002.
- [22] Öktem GA, Tincer T. A study on the yield stress of perlite-filled high-density polyethylenes, *J. Mater. Sci* 1993; 28: 6313-6317.
- [23] Sahraeian R, Hashemi SA, Esfandeh M, Ghasemi I. Preparation of nanocomposites based on LDPE/Perlite: mechanical and morphological studies, *Polym. Polym. Compos* 2012; 20(7): 639-646.
- [24] Atagür M, Sarıkanat M, Uysalman T, Polat O, Elbeyli İY, Seki Y, Sever K. Mechanical, thermal, and viscoelastic investigations on expanded perlite–filled high-density polyethylene composite, *J. Elastom. Plast* 2018; 50(8): 747-761.
- [25] Öktem GA, Tincer T. Preparation and characterization of perlite-filled high-density polyethylenes. I. Mechanical properties, *J. Appl. Polym. Sci* 1994; 54(8): 1103-1114.
- [26] Öktem GA, Tincer T. Preparation and characterization of perlite-filled high-density polyethylenes. II. Thermal and flow properties, *J. Appl. Polym. Sci* 1994; 54(8), 1115-1122.
- [27] Sahraeian R, Esfandeh M. Mechanical and morphological properties of LDPE/perlite nanocomposite films, *Polym. Bull* 2017; 74: 1327-1341.
- [28] Heidari BS, Davachi SM, Sahraeian R, Esfandeh M, Rashedi H, Seyfi J. Investigating thermal and surface properties of low-density polyethylene/nanoperlite nanocomposites for packaging applications, *Polym. Compos* 2019; 40(7): 2929-2237.
- [29] Ai MX, Cao LQ, Zhao XL, Xiang ZY, Guo XY. Preparation and characterization of polyurethane rigid foam/expanded perlite thermal insulation composites, *Adv. Mater. Res* 2010; 96: 141-144.

- [30] Rolon BG, Flores JB, Gutierrez VE. Design and manufacture of a fiber pyro expanded perlite/epoxy composite for thermal insulation, *Int. J. Adv. Technol* 2017; 8(03): 191.
- [31] Tian H, Tagaya H. Preparation, characterization and mechanical properties of the polylactide/perlite and the polylactide/montmorillonite composites, *J. Mater. Sci* 2007; 42: 3244–3250
- [32] Aval ST, Davachi SM, Sahraeian R, Dadmohammadi Y, Heidari BS, Seyfi J, Hejazi I, Mosleh I, Abbaspourrad A. Nanoperlite effect on thermal, rheological, surface and cellular properties of poly lactic acid/nanoperlite nanocomposites for multipurpose applications, *Polym. Test* 2020; 91: 106779.
- [33] Pang X, Zhuang X, Tang Z, Chen X. Polylactic acid (PLA): Research, development and industrialization, *Biotechnol. J* 2010; 5(11): 1125-1136.
- [34] Dike AS. Preparation and characterization of calcite loaded poly (lactic acid) composite materials, *Erzincan Univ. J. Sci. Technol* 2020; 13(1): 162-170.
- [35] Ebrahimi F, Dana HR. Poly lactic acid (PLA) polymers: From properties to biomedical applications, *Int. J. Polym. Mater. Polym. Biomater* 2022; 71(15): 1117-1130.
- [36] Sreekumar K, Bindhu B, Veluraja K. Perspectives of polylactic acid from structure to applications, *Polym. Renew. Resour* 2021; 12(1-2): 60-74.
- [37] Alhaj I, Tirkas S, Hacıoglu F, Tayfun U. Investigation of mechanical, thermal and melt flow performance of polycarbonate hybrid composites containing mica flakes and glass fiber, *Adv. Mater. Lett* 2020; 11(4): 20041501.
- [38] Mishra PK, Senthil P, Adarsh S, Anoop MS. An investigation to study the combined effect of different infill pattern and infill density on the impact strength of 3D printed polylactic acid parts, *Compos. Commun* 2021; 24: 100605.
- [39] Arslan Ç, Tayfu Ü, Dogan M. Examination of perlite-polymer interface interactions in polypropylene-based composites via several compatibilizers. *Hittite J. Sci. Eng.* 2023; 10(4), 323-329.
- [40] Leluk K, Frąckowiak S, Ludwiczak J, Rydzkowski T, Thakur VK. The impact of filler geometry on polylactic acid-based sustainable polymer composites, *Molecules* 2020; 26(1): 149.
- [41] Ahmed S, Jones FR. A review of particulate reinforcement theories for polymer composites, *J. Mater. Sci* 1990; 25: 4933-4942.
- [42] Kaplan A, Erdem A, Arslan C, Savas S, Tayfun U, Dogan M. The roles of filler amount and particle geometry on the mechanical, thermal, and tribological performance of polyamide 6 containing silicon-based nano-additives, *Silicon* 2023; 15 (7): 3165-3180.
- [43] Zare Y. Study of nanoparticles aggregation/agglomeration in polymer particulate nanocomposites by mechanical properties, *Compos. Part A Appl. Sci. Manuf* 2016; 84:158-164.
- [44] Tayfun Ü, Yılmaz VM, Arslan Ç, Eklemeli imalat yönteminde filament olarak kullanılan polimerik malzemeler, *J. Smart Systems* 2023; 2 (1), 45-67.
- [45] Tayfun Ü, Tirkeş S, Doğan M, Tirkeş S, Zahmakıran M. Comparative performance study of acidic pumice and basic pumice inclusions for acrylonitrile–butadiene–styrene-based composite filaments, *3D Print. Addit. Manuf* 2024; 11 (1), 276-286.
- [46] Wang S, Capoen L, D'hooge DR, Cardon L. Can the melt flow index be used to predict the success of fused deposition modelling of commercial poly (lactic acid) filaments into 3D printed materials?, *Plast. Rubber Compos* 2018; 47(1): 9-16.
- [47] Cisneros-López EO, Pal AK, Rodriguez AU, Wu F, Misra K, Mielewski DF, Kiziltas A, Mohanty AK. Recycled poly (lactic acid)-based 3D printed sustainable biocomposites: a comparative study with injection molding, *Mater. Today Sustain* 2020; 7: 100027.
- [48] Kumar R, Singh R, Farina I. On the 3D printing of recycled ABS, PLA and HIPS thermoplastics for structural applications, *PSU Res Rev* 2018; 2(2): 115-137.

Effect of Sulphurization Process on Vitamin, Phytosterol and Fatty Acid Levels of Some Apricot Cultivars Grown in Türkiye

Fethi KAMIŞLI^{1*}, Nazlı Gülüm MUTLU²

^{1*} Department of Chemical Engineering, Faculty of Engineering, Firat University, Turkey.

²Department of Occupational Health and Safety, Faculty of Health Sciences, Bingöl University, Turkey.

^{1*}fkamisli@firat.edu.tr, ²ngmutlu@bingol.edu.tr

(Geliş/Received: 06/09/2023;

Kabul/Accepted: 26/03/2024)

Abstract: Two kinds of fresh apricot (*Prunus armeniaca* L.) samples were sulphurized in various concentrations of sodium metabisulfite solution at different immersion times. The sulphur contents in fresh apricot samples and in the apricot samples dried in open air for a week were determined as a function of immersion time. Variations of vitamins of K1, D2, E and phytosterols were determined as a function of sulphur content of two kinds of fresh apricot samples. It was observed that amount of vitamins of K1, D2 and E decreased with increasing concentrations of sodium metabisulfite solution and prolonging immersion time. Moreover, it was observed that there was no regular relationship between sulfur content and phytosterol changes in both apricot samples. While fatty acids such as palmitic acid, myristic acid and oleic acid were determined in all apricot samples, the palmitoleic acid, stearic acid and arachidonic acid were encountered in some samples.

Key words: Apricot, sulphurization, vitamins, physterols, fatty acids.

Kükürtleme İşleminin Türkiye'de Yetiştirilen Bazı Kayısı Çeşitlerinin Vitamin, Fitosterol ve Yağ Asidi Düzeyleri Üzerine Etkisi

Öz: İki çeşit kayısı örnekleri farklı daldırma sürelerinde çeşitli Sodyum metabisülfit konsantrasyonlarında kükürtleldi. Taze ve açık havada bir hafta kurutulmuş kayısı örneklerinin kükürt içerikleri daldırma süresinin fonksiyonu olarak belirlendi. İki çeşit kayısı örneklerinin kükürt içeriğine bağlı olarak K1, D2 ve E vitaminlerinin ve fitosterollerin değişimleri saptandı. Sodyum metabisülfit konsantrasyonunun ve daldırma süresinin artmasıyla K1, D2 ve E vitaminlerinin miktarlarının azaldığı gözlemlendi. Ayrıca, her iki kayısı örneklerinde de kükürt içeriğiyle fitosterol değişimleri arasında düze'nlili bir ilişkinin olmadığı gözlemlendi. Palmitik asit, miristik asit ve oleik asit gibi yağ asitleri bütün kayısı numunelerinde saptanırken, pamitoleik asit, stearik asit ve araşidonik asit bazı kayısı örneklerinde bulunmuştur.

Anahtar kelimeler: Kayısı, Kükürtleme, vitaminler, fitosteroller, yağ asitleri.

1. Giriş

Apricot named as *Prunus armeniaca* L. which can be produced in the various parts of the World is one of the most important fruits. Apricot cultivation depends upon the soil compositions, its variety and climate conditions. The nutrition values, quality and yield of the apricot depend on processing method, variety, climate conditions and soil composition where apricot trees are cultivated. Apricot can be considered an important foodstuff on account of the nutrients and its minerals. Since the harvest period for apricots is short and the fresh apricots are quickly deteriorated, the large amount of apricot all over the world has to be consumed in fresh or be conserved with some preservation method to consume later. Therefore, some preservation methods such as drying and treatment with some chemicals are necessary to consume this fruit in different times and places from its producing time and place. It is reported that 20-25 % of the fresh apricots around the world are dried and processed products of the canned apricots, apricot jam, nectar marmalade, jelly and cream [1]. By preservation of this fruit, the economic loss of the fruit can be decreased and nutrition loss can be protected. The preservation methods will most likely protect the perishable foodstuff from spoilage and supply economic value by exporting. The drying of foodstuff with and without pretreatment prevents or retards microbial or non-microbial spoilages. The pretreated apricots with the sulphur contained substances should be dried since water dependent activities can be either prevented or retarded by drying process and Millard reactions can be either prevented or retarded by sulphurization. Moreover, the drying period of time is shortened for the pretreated apricots since shells of apricots are injured during sulphurization, allowing to remove moisture easily. The sulphurization that can be done by sulphur dioxide, bisulfites and metabisulfites is one of the most important effective methods used to prevent or retard browning reactions in the foodstuffs. Although the sulphurization prevents or retards browning reactions in the foodstuff, it should be done

*Corresponding author: fkamisli@firat.edu.tr, ORCID numbers of authors: ¹0000-0002-1769-3785, ²0000-0003-0210-5175

carefully since sulphur content in apricots is necessary to be less than 2000 ppm that is a maximum allowable value.

Enzymatic and non-enzymatic reactions can take place during drying and storage of apricots. The formation of intermediate carbonyl products owing to series reactions in foodstuff can be called as non-enzymatic browning reactions that result in undesired brownian pigments with polymerization. The formed intermediate carbonyl products and reducing sugars react directionally with sulfites during the non-enzymatic reactions to prevent melanoids of those intermediate products. Ascorbic acid called as the reducing substance in enzymatic Brownian reactions inhibits color deterioration by reducing the o-kinons to the o-phenols while the ascorbic acid cracks down. The amount of ascorbic acid should be more than enough in reaction medium since ascorbic acid is consumed out, there will be no inhibitors on browning reactions. Furthermore, the ascorbic acid is consumed out by the oxygen having important role in browning reactions that can be retarded with reduction of the oxygen in reaction medium. Glaucous and fructose having, respectively, free aldehydes and ketones are called as the reducing sugars. The nutrition value of the foodstuff can be decreased with Millard reaction reducing sugar with proteins or amino acids.

In apricot drying, the sliced, halved or whole samples of apricot are commonly exposed to either directly to sun lights or conventional hot air that can be heated by sun lights ([2], [3]). Drying process and pretreatment of apricot samples affect quality of apricot, which is subject of several researchers ([4], [5], [6]). Horoz et al. [7] used hot air and microwave together to dry apricot samples in which quality of the dried apricot samples was compared with conventional drying process and it is claimed that the quality of apricot dried in the combined drying process (hot air +microwave) is better than that of the dried in conventional method. Albanese et al. [5] used hot air and infrared together to dry apricot in which quality of dried samples was compared with the sun drying apricot and it was claimed that the quality of apricot dried in this process is better than those dried in the sun lights. The combined drying process for the sulphurized and unsulphurized apricot samples was investigated by Ozbek et al. [8] to determine difference from the conventional drying method/methods in terms of hardness, color, retention of vitamin C, antioxidant activity, total phenolic content and β -carotene of apricot samples. According to food legislation, the allowable largest sulphur content is 2000 mg/kg (ppm) in dehydrated fruits. The sulphur dioxide preserves the texture and color of apricots and thus taste characteristics by inhibiting browning reactions and microbial deteriorations, which makes the dried apricots attractive to the consumers. It was reported by Pala et al. [9] that the amount of carbon hydrates, protein, oil, moisture, cellulose, total acid and ash in apricot depend upon variety of the apricot. Belloso and Barrichero [10] stated that some kinds of apricots are more suitable for drying to give vitamins, high calorific values and mineral rich products. The contents of minerals, vitamins, appearances and calorific values affected by the preservation method namely sulphurization and drying processes determine the quality of a foodstuff. Vitamins A, E and C having antioxidant roles against oxidative damage and cofactors for many enzymes must be taken into body ([11], [12], [13]).

In the sulphurization process, the fresh apricot can be sulphurized with either water soluble sulfite salts such as $\text{Na}_2\text{S}_2\text{O}_5$ and $\text{K}_2\text{S}_2\text{O}_5$ or sulphur dioxide used to preserve their color and to exterminate microbial agents that cause spoilage. The apricot samples are dried in open-air sun drying before and after removing stones from apricot. Pizzoferrato et al. [14] reported that sulfites are converted into the harmless products such as sulfate ions by oxidizing or removing from the foodstuff by evaporating. Polyphenol oxidase activity is prevented by decreasing pH of the solution used for sulphurization of apricot lower than 4.2 [15]. On the other hand, non-enzymatic browning reactions were accelerated in alkaline solution or neutral medium [16]. It was reported that the prevention of the browning reactions of litchi pericarp can arise from inhibition of polyphenol oxidase activity and stabilization of anthocyanins. Non-enzymatic and enzymatic browning reaction in vegetables and fruits can be prevented by sulphurization process ([17], [2]). The formation of H_2SO_3 increases with increasing sulphur concentration in the treatment solution, which results in values of larger titratable acidity [18].

In none of the reviewed papers, the variations of K1, D2, E and phytosterols in two kinds of apricot samples locally known hacihaliloglu and kabaaşı with concentrations of sodium metabisulphite (SMBS) solution and immersion times and thus, sulphur contents were not investigated. Therefore, in this study, variations of K1, D2, E (α -tocopherol and σ -tocopherol) vitamins and phytosterols as a function of immersion time were examined for various concentrations of SMBS solution. Moreover, amounts of fatty acids such as the myristic acid, oleic acid, palmitic acid, stearic acid palmitoleic acid and arachidonic were tried to determine in all apricot samples sulphurized in various concentrations of SMBS solution at different immersion times.

2. Material and Method

The chemicals used in the sulphurization and titration preprocesses were 37 % HCl, $\text{Na}_2\text{S}_2\text{O}_5$, 35% H_2O_2 , NaOH, Brome phenol, Ethyl alcohol that were in analytical grade and purchased from Sigma Chemical Co. (Darmstadt, Germany).

Two different kinds of apricot samples locally known as hacihaliloglu and kabaası (*Prunus armeniaca* L.) existed in the apricot research center in Malatya, Turkey were collected in the same side of the tree with the same size, the same ripeness (pH = 4.25-4.35 for hacihaliloglu, pH = 4.30-4.50 for kabaası) and the same appearance for each kind of the apricot samples to use in the experimental study. The harvested apricots samples were put into plastic bags and transferred to the laboratory and the apricot specimens in the plastic bags were kept in refrigerator at 5 °C. pH of fresh hacihaliloglu and kabaası apricot samples was measured to be in ranges of 4.25-4.35 and 4.30-4.50, respectively. In order to measure pH values of apricot samples, the apricot samples were homogenized in the homogenizer having three fold the distilled water of the apricot weight and the mixture was filtered using Whatman No.1 filter paper. The pH values of the apricot samples were measured using Mettler Toledo Delta pH meter.

The hacihaliloglu apricot is one of the important apricot type to dry in Malatya, Turkey. This fruit has an average size (25 -35 g) in yellow color with reddish cheek and less water content, and shell of this fruit is thin and it is a luscious fruit. Kabaası apricot type has a large size (30-45 g) with oval and symmetric shape and the shell of this fruit in the yellow color is thick and it is a very luscious fruit.

All apricot samples used in the study were sulphurized with sodium metabisulfite ($\text{Na}_2\text{S}_2\text{O}_5$) that releases SO_2 when it dissolves in water. In other words, it forms sulphurous acid (H_2SO_3), bisulfite (HSO_3)⁻¹ and sulphur three oxide (SO_3)⁻² in water. Sodium metabisulfite ($\text{Na}_2\text{S}_2\text{O}_5$) solutions were prepared in various concentrations namely 5, 15 and 20 % (w/v) to sulphurize apricot samples at different immersion times.

After sulphurization with various concentrations of sodium metabisulfite (SMBS) at different immersion times namely 15, 45, 60 and 90 minutes, all apricot samples were dried in open air for a week to determine the effect of drying process on the sulphur content of the apricot samples. As it is known, the drying, one of the oldest preservation method, is used to preserve food stuffs since beginning of human's history. The water content of food decreases with drying times and thus, water-dependent microbial deterioration in the food stuff is either decreased or entirely preserved with decreasing water activity [19]. In this study, the apricot samples were taken out from immersion utensils and placed on the cloths to be dried in open air. After three days of the drying, the stones of apricot samples were taken out and the apricot samples were shaped by hands and the shaped apricot samples were left to be dried in the open air for another four days. The dried apricot samples were put into the sterilized bags and closed carefully and then placed in a deep freeze at -60 °C and kept in there until being analyzed for determining sulphur contents of apricot samples.

3. Sulphur, Vitamins and Fatty Acids Analysis

3.1.1 Determination of sulphur in the apricot samples

The 5 g apricot sample treated with the certain concentration of SMBS solutions and certain immersion times were taken into homogenizer and made it slurry with 50 ml the distilled water. This slurred apricot sample (homogenized sample) was put in a round-bottom flask and 40 ml 15 % HCl was added into it. All remains of slurred apricot sample were transferred to the round-bottom flask by washing homogenizer with 100 ml distilled water. The flow of N_2 was adjusted to be 40 bubbles per minutes in the round-bottom flask since flow rate of N_2 is the most critical factor in performing experiment. N_2 and the releasing gas consisting of SO_2 and SO_3 were taken into 10 ml of 3 % H_2O_2 solution in a trap tube connected to the outlet of a condenser. The mixture (homogenized apricot sample + distilled water + 15 % HCl) in the round-bottom flask was boiled under the condenser mounted on the top of the round-bottom flask for 60 minutes to release sulphur compounds in the sulphurized apricot samples. The homogenized apricot samples were boiled in the presence of HCl to release the sulphur compounds in the apricot samples since HCl solution damages the structure of apricots [15] and damages become more pronounced by increasing acid concentration and temperature [20].

The reaction being taken place in the trap tube containing 10 ml of 3 % H_2O_2 solution can be written as in Equation (1).



The solution in the trap tube was put into a flask and added 2-3 drops of brome phenol indicator and then exposed to titration with 0.1 M NaOH solution to determine sulphur contents of apricot samples. The following formula derived from the naturalization reaction between NaOH and H_2SO_4 was used to calculate amount of sulphur in the apricot samples since the neutralization reaction as shown in Equation (2) can take place in the titration process.



$$S(\text{ppm}) = 16000 \frac{M_{\text{NaOH}} V_{\text{NaOH}}}{W_{\text{apricot}}}$$

Here S stands for amount of sulphur in ppm, M molarity of NaOH solution, V volume of NaOH in L and W weight of apricot sample in kilograms.

3.2 Preparation of apricot samples for vitamins and oil analysis

All slurred apricot samples were centrifuged at 600 rpm for 10 minutes to obtain pellets from the apricot slurry. 2 g of pellets was taken into falcon tube and 10 ml hexane propyl alcohol with butylated hydroxytoluene (BHT) was added into the tube and homogenized in the homogenizer. After homogenization process, the samples were again centrifuged at 600 rpm for 10 minutes and supernatant being formed at the top of tubes was taken and filtered with Whatman No.1 filter paper for analysis of vitamins and oils.

3.2.1 Analysis of vitamins

5 ml methanol-potassium hydroxide was added to the supernatant and the obtained solution was kept in an oven at 85 °C for 20-30 minutes. After the tube was removed from the oven 5 ml distilled water was put into the tube, after that 10 ml hexane propyl alcohol was added and the tube was waited at the room temperature for 12 hours for a phase separation. The supernatant (upper phase) being formed at the top of tube was taken and placed in the oven at 37 °C to evaporate. After evaporation takes place, 1 ml acetonitrile/methanol was added into the tubes with remains of the samples and vortexed and then the samples were taken into 1 ml vials. Analyses were performed by HPCL (Shimadzu, Kyota, Japan) in which acetonitrile/methanol (60 % v +40 % v) was used as a mobile phase at rate of 1 ml/s. The UV detector was used to determine amount of a vitamin. Supelcosil LC18 (14x46 cm, 5 µm, sigma, USA) was used as column. Amounts of vitamin E, D and K were determined with the HPCL according to the method described in the papers by Catignani [21] and Miller, Lorr & Yang [22]. Detection wave length for vitamin E was chosen to be 296 nm and for vitamin D2 and K1 were chosen to be 265 nm.

3.2.2 Analyses of fatty acids

5 ml of 2 % methanolic H₂SO₄ was added into the supernatant obtained from homogenization process and resulting solution was vortexed and incubated at 55 °C for 12 hours. 5 ml of 5 % NaCl was added into the solution after cooling down at the end of the incubation [23]. 5 ml n-hexane was added to methyl ester of fatty acid formed in reaction medium. The levels of all specimens in tubes were made to be equal and they were closed and were made upside-down. After having been waited at room temperature for 5 hours, the supernatant was taken and 5 ml of 2 % KHCO₃ solution was added and the sample tubes were closed and made them upside-down and were waited for 3 hours. After this period of time, the supernatant was taken into small tubes exposed in the oven at 37 °C to evaporate. After the evaporation process was completed, the tubes with remains were filled 1 ml n-hexane to solve those remains and then samples were put into vials in which samples were analyzed with Shimadzu GC17. 25 m long, 0.25 µm inner radius, 25 µm film thickness of capillary column (Machery-Nagel, Germany) was used to analyze the sample. During fatty acids analyses, the injection temperature was kept constant at 240 °C and detector temperature at 280 °C and the program for column temperature was adjusted from 120 °C to 220 °C. An increase in the temperature was adjusted to be 5 °C/min. up to 200 °C and after this point, the increase in the temperature was adjusted to be 4 °C/min. up to 220 °C. Nitrogen was used as a carrying gas.

During analysis, methyl ester of standard fatty acid was injected into the GC to determine the time for each fatty acid of a sample analyzed. After performing this operation, the amount of fatty acids was calculated with unit of mg/kg using class GC10 program.

3.2.2.1 Analyses of phytosterol

The determination of phytosterol in oils was carried out according to the method described in ISO 12228-1:2014. In this method, ethanolic potassium hydroxide solution is used to saponify oil by boiling under reflux. The sterols have to be separated from fatty acid anions and the unsaponified mater isolated by solid-phase extraction an

aluminum oxide column (Merck, Darmstadt, Germany). Also the thin-layer chromatography (Merck, Darmstadt, Germany) was used to separate sterols from other unsaponified matters. The separated sterols were determined by GC using betulin as internal standard. 25 m long, 0.25 μm inner radius, 25 μm film thickness of capillary column (Machery-Nagel, Germany) was used to analyze the sample. The conditions applied for temperature here were the same as in fatty acids analysis.

4. Results and Discussion

As mentioned previously, two kinds of fresh apricot samples locally know hacihaliloglu and kabaası were sulphurized in various concentrations of SMBS solution at different immersion times. The Sulphur contents of apricot samples as a function of immersion time for various concentrations of SMBS solution were determined for both kinds of fresh and dried apricot sample. Variations in vitamins and phytosterols of two kinds of fresh apricot samples as a function of immersion time for various concentrations of SMBS solution were also determined.

For each run, the values given in either graphics or tables for the sulphur content, vitamins K1, D2, E and phytosterol and fatty acids were the average value of three apricot specimens that were treated at the same time.

4.1 Variation of sulphur with immersion time

In order to determine the effect of immersion time and concentration of SMBS solution on the sulphur content in apricot samples, two kinds of apricot samples locally known as hacihaliloglu and kabaası at the same size, the same ripeness, and the same appearance were collected from the same tree for each kind of apricot sample. While some of the samples were put into the sterilized bags and put in refrigerator to use later, some of them were immediately immersed into the SMBS solutions at 5 %, 15 % and 20 % (w/v) for 15, 45, 60 and 90 minutes of immersion times.

The sulfur contents of fresh hacihaliloglu apricot samples immersed into various concentrations of SMBS solutions as a function of immersion times. It was observed that the sulphur contents of apricot sample increase with increasing immersion time at each concentration of the SMBS solution. The sulphur contents of apricot samples also increase with increasing the concentrations of the SMBS solution. The maximum sulphur content of the apricot samples was obtained at the maximum concentration and the maximum immersion time namely 20 % of the SMBS solution and 90 minutes of immersion time, respectively.

The sulphur content of the fresh kabaası apricot samples immersed into 5 %, 15 % and 20 % of SMBS solution as a function of immersion time. As in hacihaliloglu apricot samples, the sulphur contents of kabaası apricot samples increase with increasing immersion times and the concentration of the SMBS solution. While minimum sulphur content of apricot specimens was obtained at the shortest immersion time and the lowest concentration of the SMBS solution, the maximum sulphur content of apricot samples was obtained at the longest immersion time and largest concentration of the SMBS solution. While the sulphur content of hacihaliloglu apricot samples increase with immersion time, those of kabaası apricot samples become almost constant after the immersion time of 45 minutes at high concentrations namely 15 % and 20 % of the SMBS solution.

When the sulphur contents of the fresh hacihaliloglu and kabaası apricot samples immersed into 5 % of the SMBS solution are compared, it will be seen that the sulphur content of both kinds of apricot samples are close to one another. However, the sulphur contents of the fresh hacihaliloglu and kabaası apricot samples are different from one another at the high concentration namely 15 % and 20 % SMBS solution for all immersion times. Although the amount of sulphur absorbed by both kinds of apricot specimens increase with increasing immersion times, the sulphur contents of kabaası apricot samples were found to be higher than those of hacihaliloglu for all immersion times at high concentrations namely 15 % and 20 % SMBS solutions. While sulphur content of hacihaliloglu apricot samples increase linearly with immersion time at all concentrations of the SMBS solution, those of kabaası apricot samples became almost constant after the immersion time of 45 minutes at high concentration namely 15 % and 20% of the SMBS solutions.

4.2 Effect of drying on sulphur content of apricot samples

Two kinds of apricot samples locally known as hacihaliloglu and kabaası sulphurized in the 5, 15 and 20 % SMBS solutions for the immersion times of 15, 45, 60 and 90 minutes were dried in open air for seven days. The variation of sulphur content in the dried apricot samples as a function of immersion times and the concentrations of the SMBS solution were also determined for hacihaliloglu and kabaası apricot samples. As expected, the trend for sulphur content obtained during sulphurization was observed to be maintained after drying process. In other words, the apricot samples with the highest or the lowest sulphur content in the sulphurization had the highest or the

lowest sulphur content after drying, respectively. While the sulphur contents of the fresh hacihaliloglu and kabaası apricot samples sulphurized in 5 % of SMBS solution were close to one another for all immersion times, the sulphur contents of the dried hacihaliloglu and kabaası apricot samples were found to be different from one another for all immersion times. Before drying, the sulphur contents of hacihaliloglu apricot samples were less than those of kabaası apricot samples for concentrations higher than 5 % SMBS solution. After drying, the trend for sulphur content of apricot samples was maintained. The existed difference between the sulphur contents of the hacihaliloglu apricot samples and that of the kabaası apricot samples increased with drying. This can be attributed to the structure of kabaası apricot samples allows water to evaporate more than that of hacihaliloglu. The levels of moisture, carbohydrate, cellulose, nutrient, mineral contents, calorific values, vitamins depend on variety of apricot. Therefore, the apricot variety is an important parameter and some kinds of apricots are more appropriate for drying to give high vitamins, mineral-rich products and calorific values [10]. Amounts of moisture, carbohydrate, protein, oil, total acid, cellulose and ash in apricots change with apricot varieties [9].

Amount of sulphur per unit mass of the apricot samples increases according to evaporation of water in the structure of apricot samples with drying time.

4.3 Effect of sulphur content on vitamin and phytosterol of apricot samples

Vitamin K1, vitamin D₂, and vitamin E (α tocopherol and σ tocopherol) were found in all apricot samples considered in the present study. The amount of α tocopherol in the apricot samples was found to be higher than those of other vitamins. Amount of vitamin K1 of the fresh hacihaliloglu apricot samples sulphurized in 5, 15 and 20 % SMBS solutions was illustrated in Figure 1a as a function of immersion times. As can be seen from the figure amount of vitamin K1 in the fresh hacihaliloglu apricot samples decreases with increasing both the concentrations of the SMBS solution and the immersion times, and thus, the content of sulphur in the specimen. While the highest value for vitamin K1 was obtained at the lowest concentration of the SMBS solution and the shortest immersion time, the lowest value for vitamin K1 was obtained at the highest concentration of the SMBS solution and the longest immersion time.

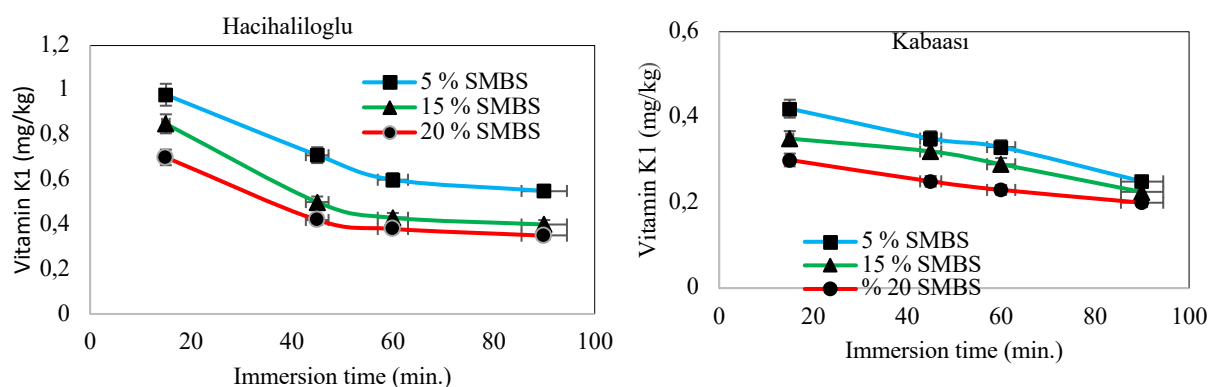


Figure 1. Variation of vitamin K1 of fresh apricot samples with immersion times for various concentrations of SMBS solution (a: Hacihaliloglu, b: Kabaası)

The trend for variation of vitamin K1 with the concentration of SMBS solution and the immersion time similar to hacihaliloglu apricot samples was observed for kabaası apricot samples as illustrated in Figure 1b. While the highest value for vitamin K1 was obtained at the lowest concentration of the SMBS solution and the shortest immersion time, the lowest value for vitamin K1 in the fresh kabaası apricot samples was obtained at the highest concentration of the SMBS solution and the longest immersion time.

Vitamin K1, resisting heat, dissolvable in oil, can be inactivated by alkali strong acids, radiation and oxidase agents. Here while acidity of apricot samples increases with sulphur content, the concentration of SMBS solution and the immersion time makes the amount of vitamin K1 decrease in the apricot samples.

Variation of σ tocopherol in hacihaliloglu apricot samples with concentration of the SMBS solutions and immersion times were depicted in Figure 2a. As can be seen in the figure while the highest value for σ tocopherol

in the fresh apricot samples sulphurized in various concentrations and immersion times was found at the lowest concentration and the shortest immersion time, the lowest σ tocopherol in the fresh apricot sample was obtained at the highest concentration of SMBS solution and the longest immersion time. The trend for variation of σ tocopherol with concentration of the SMBS solution and immersion time similar to hacihaliloglu was observed for kabaası apricot samples as evidenced in Figure 2b

Variation of vitamin D₂ in the fresh hacihaliloglu apricot samples sulphurized in 5, 15 and 20 % SMBS solution was illustrated in Figure 3a as functions of immersion times of 15, 45, 60 and 90 minutes. As seen in the figure while the highest value for vitamin D₂ in the fresh apricot samples sulphurized in various concentrations and immersion times was found at the lowest concentration of SMBS solution and the shortest immersion time, the lowest vitamin D₂ in the fresh apricot sample was obtained at the highest concentration of SMBS solution and the largest immersion time. The trend for variation of vitamin D₂ with concentration of the SMBS solution and immersion time similar to hacihaliloglu apricot specimens was observed for kabaası apricot samples as evidenced in Figure 3b.

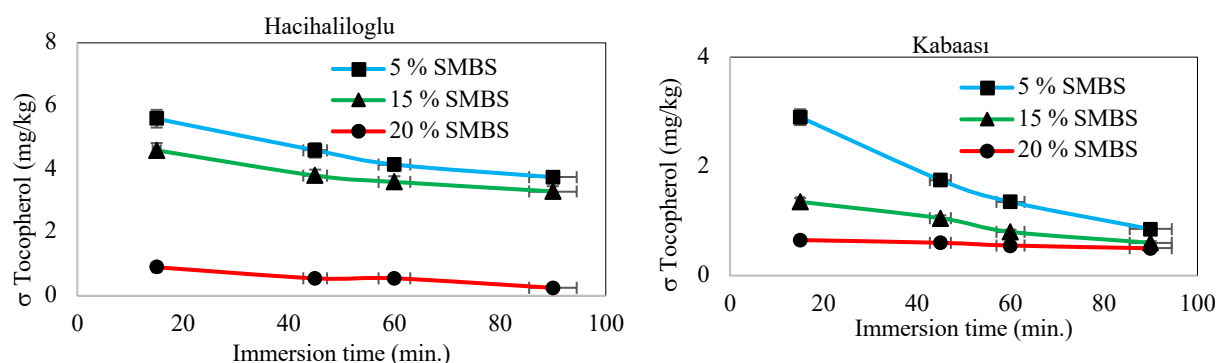


Figure 2. Variation of σ -tocopherol of fresh apricot samples with immersion times for various concentrations of SMBS solution
(a: Hacihaliloglu, b: Kabaası)

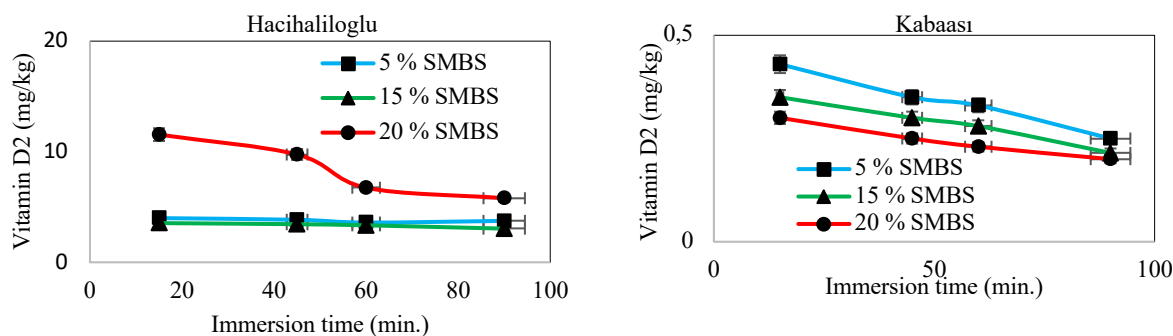


Figure 3. Variation of vitamin D₂ of fresh apricot samples with immersion times for various concentrations of SMBS solution
(a: Hacihaliloglu, b: Kabaası)

The α tocopherol (vitamin E) that is a quite powerful antioxidant decreased with increasing concentration of SMBS solution and immersion times for both sulphurized fresh hacihaliloglu and kabaası apricot samples. In other words, while the highest value of α tocopherol in both sulphurized fresh hacihaliloglu and kabaası apricot samples was observed at the lowest concentration and the shortest immersion time, the lowest value of α tocopherol in both sulphurized fresh hacihaliloglu and kabaası apricot samples was found at the highest concentration of SMBS solution and the longest immersion times as illustrated in Figure 4a and Figure 4b, respectively.

It is known that vitamins can be oxidized with time, heat and light. Amounts of vitamins decreased with increasing concentrations of SMBS solution and prolonging immersion times as evinced in Figs. 1-4. In this study, the enzyme causing oxidation may be inhibited with acidification in some apricot samples (pH less than 4.2). As

mentioned earlier, Jiang et al. [24] reported that no polyphenol oxidase activity was observed in the enzymatic reaction below pH 4.2. Moreover, it was indicated that co-pigmentation of anthocyanins in litchi fruit can be formed with a suitable treatment with acids and thus, stabilized the anthocyanin pigments [25].

Processing time, temperature, oxygen concentration in drying atmosphere, light, and pH value of a sample affect the loss of vitamins during fruit and vegetable processing. As can be seen from Figs. 1-4, amounts of vitamins of K1, D2 and E in both kinds of apricot samples sulphurized in various concentrations of SMBS solution at different immersion times decreased with increasing concentrations of SMBS solution and prolonging immersion times. This observation agrees with previous studies ([27], [4], [26], [28]). Karabulut et al. [26] reported that the light accelerated degradation in vitamin C. Furthermore, it was reported that degradation in vitamin C can be accelerated with light intensity and an increase in Sulphur content of samples ([28] and [4]).

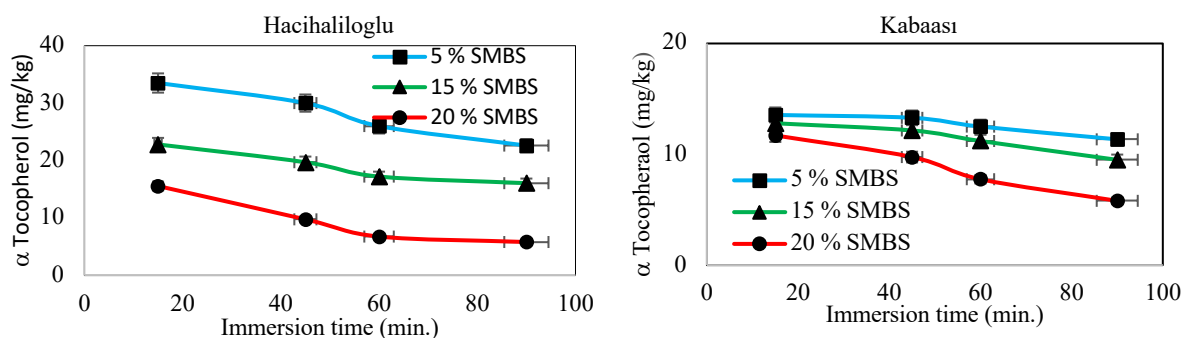


Figure 4. Variation of α -tocopherol of fresh apricot samples with immersion times for various concentrations of SMBS solution (a: Hacihaliloglu, b: Kabaası)

The ergosterol, stigmasterol and β -sitosterol were found in both hacihaliloglu and kabaası apricot samples. The stigmasterol among the phytosterols was observed to be the largest one in the hacihaliloglu apricot samples. Amounts with standard deviations of the β -sitosterol, the stigmasterol and ergosterol in the fresh hacihaliloglu and kabaası apricot samples sulphurized in various concentrations of the SMBS solutions at different immersion times are given in Table 1 and Table 2, respectively. As can be seen in the tables the relation between amount of ergosterol and sulphur content in the samples is not in order. Amount of ergosterol in the fresh hacihaliloglu apricot samples sulphurized in 5 and 15 % of the SMBS solution are higher than those in the fresh kabaası apricot samples sulphurized in the same concentration of SMBS solution.

The relationship between concentrations of SMBS solution and thus, sulphur content and the stigmasterol content in both kinds of apricot samples are not in order as seen in Table 1 and Table 2. The stigmasterol in both kinds of apricot samples are usually higher than that of the ergosterol. As being the ergosterol and the stigmasterol, β -sitosterol contents in both kinds of apricot samples do not change orderly with concentrations of the SMBS solution and immersion times as illustrated in Table 1 and Table 2, respectively.

While the myristic acid, palmitic acid (16:0), linoleic acid (18:2, n6t) and α -linoleic acid (18:3, n3) were found to be in all apricot samples considered in present study, the other types of fatty acids were encountered some of the apricot samples. The contents of palmitic acid of fresh hacihaliloglu and kabaası apricot samples sulphurized in various concentrations of SMBS solution at different immersion times were found to be 91 mg/kg and 110 mg/kg, respectively. The given value of palmitic acid for each kind of apricot sample was an average of lots of apricot samples sulphurized in various concentrations of SMBS solution at different immersion times.

The contents of myristic acid of fresh hacihaliloglu and kabaası apricot samples sulphurized in various concentrations of SMBS solution at different immersion times were found to be 198.1 mg/kg and 121.1 mg/kg, respectively. The given value of myristic acid for each kind of apricot sample was an average of a lot of apricot samples sulphurized in various concentrations of SMBS solution at different immersion times.

Table 1. Values of phytosterols for hacihaliloglu apricot samples

Immersion time (min.)	Concentration of SMBS solution								
	5 %	15 %	20 %	5 %	15 %	20 %	5 %	15 %	20 %
	β-sitosterol (mg/kg)			Stigmasterol (mg/kg)			Ergosterol (mg/kg)		
15	48,75 ±4.2	77 ±6.5	42 ±3.35	88,6 ±6.34	95,7 ±8.2	54,2 ±5.16	1,7 ±0.165	6,7 ±0.93	1,95 ±0.113
45	39,2 ±3.43	63 ±5.23	42,5 ±3.85	99,9 ±8.35	90,6 ±7.2	0,1 ±0.012	1,5 ±0.132	4,6 ±0.82	0,95 ±0.054
60	26,15 ±2.3	85,05 ±6.4	85,85 ±8.2	111,05 ±10.52	92,15 ±8.5	ND ±0	1,4 ±0.135	2,25 ±0.213	1,7 ±0.144
90	68,6 ±5.25	92,15 ±7.3	53,2 ±4.87	157,6 ±13.65	90,3 ±7.6	0,35 ±0.028	3,51 ±0.292	1,5 ±0.145	0,45 ±0.075

The numbers after ± sign point out standard deviation. ND: not detected

Table 2. Values of phytosterols for kabaasi apricot samples

Immersion time (min.)	Concentration of SMBS solution								
	5 %	15 %	20 %	5 %	15 %	20 %	5 %	15 %	20 %
	β-sitosterol (mg/kg)			Stigmasterol (mg/kg)			Ergosterol (mg/kg)		
15	84,8 ±6.2	35,65 ±3.25	49,45 ±4.85	98,6 ±7.62	87,2 ±7.65	89,1 ±8.65	0,25 ±0.025	0,05 ±0.0042	2,6 ±0.18
45	75,3 ±6.54	33,1 ±2.83	53,05 ±5.25	66 ±6.35	89,8 ±7.85	98,8 9.35	ND ±0	0,075 ±0.0035	3,2 ±0.22
60	29,6 3.15	26,2 ±2.03	39,45 ±4.35	56,8 ±4.85	88,25 ±8.38	67,7 ±5.78	0,1 ±0.015	0,125 ±0.021	23 ±2.43
90	94,2 ±8.5	39,55 ±3.52	11,8 ±1.15	107 ±9.82	84,85 ±7.85	41,6 ±3.83	0,95 ±0.097	0,145 ±0.0135	1,2 ±0.097

The numbers after ± sign indicate standard deviation. ND: not detected

While the average values of linoleic acid (18:2, n6t) and α-linoleic acid (18:3, n3) of fresh hacihaliloglu apricot samples sulphurized in various concentrations of SMBS solution at different immersion times were found to be 121.5 mg/kg and 77.3 mg/kg, respectively, the average values of those acid in kabaası apricot samples sulphurized at the conditions that were applied to hacihaliloglu apricot samples were found to be 63 mg/kg and 64.3 mg/kg, respectively.

The acids such as palmitoleic acid (16:1, n7), stearic acid (18:0), oleic acid (18:1, n9t), oleic acid (18:1, n9c), linoleic acid (18:2, n6c) and arachidonic acid (20:4, n6) were encountered in some samples.

5. Conclusions

Two kinds of apricot samples locally known hacihaliloglu and kabaası were sulphurized in various concentrations of SMBS solution at different immersion times. The sulphur contents of fresh apricot samples as a function of immersion time were depicted for each kind of apricot samples for various concentrations of SMBS solution. Furthermore, the sulphur contents of the apricot samples dried open air for a week were determined as a function of immersion time for each kind of apricot samples for various concentrations of SMBS solution. Variations of vitamins of K1, D2 and E and phytosterols in each fresh apricot sample were determined as a function of immersion time for various concentrations of SMBS solutions and thus, the sulphur contents of apricot samples. It was observed that amount of vitamins of K1, D2 and E decreased with increasing concentration of SMBS solution and prolonging immersion time and thus, increasing sulphur content of both kinds of apricot samples. Variations of phytosterol in both kinds of apricot samples sulphurized in various concentration of SMBS solution at different immersion times were not in order. While fatty acids such as the myristic acid, palmitic acid and oleic acid were determined in all apricot samples sulphurized in various concentrations of SMBS solution at different immersion times, the palmitoleic acid, stearic acid, oleic acid and arachidonic acid were encountered in some samples.

References

- [1] Yıldız F. New Technologies in Apricot Processing. Standard, Special Issue for apricot, 1994; 67-69 (in Turkish).
- [2] Inserra L, Cabaroglu T, Şen K, Arena E, Ballistreri G, Fallico B. Effect of sulphuring on physicochemical characteristics and aroma of dried Alkaya apricot: a new Turkish variety. *Turk J Agricult and Forestry* 2017; 41(1): 59–68.
- [3] Ihns R, Diamante LM, Savage GP, Vanhanen L. Effect of temperature on the drying characteristics, color, antioxidant and beta-carotene contents of two apricot varieties. *Int J Food Sci and Tech* 2011; 46(2): 275–283.
- [4] Garcia-Martinez E, Igual M, Martin-Esparza M, Martinez-Navarrete N. Assessment of the bioactive compounds, color, and mechanical properties of apricots as affected by drying treatment. *Food Bioproc Tech* 2013; 6(11): 3247–3255.
- [5] Albanese D, Cinquanta L, Cuccurullo G, Di Matteo M. Effects of microwave and hot-air drying methods on color, β -carotene and radical scavenging activity of apricots. *Int J Food Sci Tech* 2013; 48: 1327–1333.
- [6] Karatas F, & Kamisli F. Variations of vitamins (A, C and E) and MDA in apricots dried in IR and microwave. *J Food Eng* 2007; 78: 662–668.
- [7] Horoz E, Bozkurt H, Karatas H, Maskan M. Effects of hybrid (microwave-convectonal) and convectonal drying on drying kinetics, total phenolics, antioxidant capacity, vitamin C, color and rehydration capacity of sour cherries. *Food Chem* 2017; 230: 295–305.
- [8] Ozbek HN., Elik A, Koçak-Yanık, D, Işınay B, Sever M. et al. Effect of sequential-combined solar energy assisted hot air and hot air assisted radio frequency drying on the physical and chemical properties of dried apricots. *J. Food Sci and Tech* 2022; 59: 2894–2904.
- [9] Pala M, Ackurt F, Löker M & Saygı YB. Composition of apricot varieties. Standard, specific issue for apricot, 1994; May. pp. 64–66 (in Turkish).
- [10] Belloso MO & Barriobero LE. Proximate composition, minerals and vitamins in selected canned vegetables. *European Food Res and Tech* 2001; 212: 182–187.
- [11] Stryer, L. *Biochemistry*. 4th edition, Pp. 452–455. NY, W.H. Freeman and Company, 1995.
- [12] Laila G, Yues A, Bernard H, Claude J, Gerard C & Gerard S. Biological variability of superoxide dismutase, glutathione peroxidase and catalase in blood. *Clinical Chem* 1991; 37: 1932–1937.
- [13] Halliwell B. Free radical antioxidants in human disease. Curiosity, cause or consequence. *Lancet* 1994; 344: 72–74.
- [14] Pizzoferrato L, Di Lullo G & Quattrucci E. Determination of free, bound and total sulfites in foods by indirect photometry-HPLC. *Food Chem*, 1998; 63: 275–279.
- [15] Jiang YM, Liu SX, Chen F, Li YB & Zhang DL. The control postharvest of browning of litchi fruit by sodium bisulfite and hydrochloric acid. *Trop Sci* 1997; 37: 189–192.
- [16] Hayashi T & Namiki M. Role of sugar fragmentation in an early stage browning of amino-carbonyl reaction of sugar with amino acids. *Agri and Bio Chem* 1986; 50: 1965–1970.
- [17] Coskun AL, Turkyilmaz M, Aksu OT, Koc BE, Yemis O, Ozkan M. Effects of various sulphuring methods and storage temperatures on the physical and chemical quality of dried apricots. *Food Chem* 2013; 141(4): 3670–3680.
- [18] Salur-Can A, Turkyilmaz M, Ozkan M. Effects of sulfur dioxide concentration on organic acids and b-carotene in dried apricots during storage. *Food Chem* 2017; 221: 412–421.
- [19] Sabarez H, Price WE, Back PJ, Woolf LA. Modelling the kinetics of drying of d' Agen plums (*prunus domestica*). *Food Chem* 1997; 60: 371-382.
- [20] Monier-Williams, GW. Determination of sulphur dioxide. *The Analyst* 1927; 52: 415–416.
- [21] Catignani, GL. Simultaneous determination of retinol and a-tocopherol in serum or plasma by liquid chromatography. *Clinical Chemistry*, 1983; 2914, 708–712.
- [22] Miller, KW, Lorr NA & Yang CS. Simultaneous determination of plasma retinol a-tocopherol, lycopene, a-carotene, and b-carotene by high performance liquid chromatography. *Analytical Biochemistry*, 1984; 138, 340–345.
- [23] Christie WW. Preparation of methyl ester and other derivatives. In *Gas Chromatography and Lipids. A Practical Guide*, 1st ed.; Christie, W.W., Ed.; Oily Press: Glasgow, UK, 1989; pp. 36–47.
- [24] Jiang YM, Zauberman G & Fuchs Y. Partial purification and some properties of polyphenol oxidase extracted from litchi pericarp. *Postharvest Bio and Tech* 1997; 10: 221–226.
- [25] Ketsa S, Leelawatana K, & Subhadrabandhu S. Effect of pre- and post-storage acid dipping on browning of leychiee fruits. *Acta Horticultureae* 1992; 321: 726–731.
- [26] Karabulut I, Bilenler T, Sislioglu K, Gokbulut I, Ozdemir IS, Seyhan F, Ozturk K. Chemical composition of apricots affected by fruit size and drying methods. *Dry Tech* 2018; 36(16): 1937–1948.
- [27] Kamisli F & Karatas F. Effects of sulphurisation on vitamins (A, C and E) and malondialdehyde in apricots. *Int J Food Sci and Tech* 2009; 44: 987–993.
- [28] Zhou X, Xu R, Zhang B, Pei S, Liu Q, Ramaswamy HS, Wang S. Radio frequency-vacuum drying of kiwifruits: Kinetics, uniformity, and product quality. *Food and Bioproc Tech* 2018; 11(11): 2094–2109.

Weighted Visibility Graph Based WiFi Indoor Positioning Method Using Heuristic Optimization

Turan Göktuğ ALTUNDOĞAN^{1*}, Mehmet KARAKÖSE²

¹ Computer Engineering, Engineering Faculty, Manisa Celal Bayar University, Manisa, Türkiye

² Computer Engineering, Engineering Faculty, Firat University, Elazığ, Türkiye

*¹ turan.altundogan@cbu.edu.tr, ² mkarakose@firat.edu.tr

(Geliş/Received: 05/02/2023;

Kabul/Accepted: 13/01/2024)

Abstract: With the widespread use of wireless communication technologies and IoT applications, researchers are developing approaches that utilize WiFi signals for indoor location determination. In this study, indoor positioning process based on heuristic optimization-based methods was performed by creating weighted visibility matrices of access points based on WiFi signal strength (RSSI) values. In the proposed method, the PSO and GA approaches determine the position of the mobile user using a common fitness function based on the visibility weight matrices. The proposed method has been tested on a virtual scenario where position ranges based on RSSI ranges are determined. Both heuristic optimization methods are compared according to different criteria and the positioning process is performed with a maximum error of 3m for the GA based method and a maximum of 1.5m for the PSO based method.

Key words: WiFi Indoor Positioning, Visibility Graphs, PSO, GA.

Sezgisel Optimizasyon Kullanan Ağırlıklı Görünürlük Grafi Tabanlı Kapalı Alan WiFi Konumlandırma Yöntemi

Öz: Kablosuz iletişim teknolojilerinin ve IoT uygulamalarının yaygınlaşmasıyla birlikte araştırmacılar, WiFi sinyallerini iç mekân konum tespiti için kullanan yaklaşımlar geliştirmektedir. Bu çalışmada WiFi sinyal gücü (RSSI) değerlerine dayalı erişim noktalarının ağırlıklı görünürlük matrisleri oluşturularak sezgisel optimizasyon tabanlı yöntemlere dayalı iç mekân konumlandırma işlemi gerçekleştirilmiştir. Önerilen yöntemde, PSO ve GA yaklaşımları, görünürlük ağırlık matrislerine dayalı ortak bir uygunluk fonksiyonu kullanarak mobil kullanıcının konumunu belirler. Önerilen yöntem, RSSI aralıklarına dayalı konum aralıklarının belirlendiği sanal bir senaryo üzerinde test edilmiştir. Her iki sezgisel optimizasyon yöntemi farklı kriterlere göre karşılaştırılmış ve GA tabanlı yöntem için maksimum 3m, PSO tabanlı yöntem için maksimum 1,5m hata ile konumlandırma işlemi gerçekleştirilmiştir.

Anahtar kelimeler: WiFi, Kapalı Alan Konumlandırma, Görünürlük Grafları, PSO, GA.

1. Introduction

Shopping malls, parking garages, airports etc. determination of location information in large indoor areas such as, has become an important need for service users and business managers. Today, indoor positioning systems can be realized with different approaches with the development of wireless communication technologies and the spread of IoT applications. The types of wireless communication used here are generally communication technologies such as WiFi and Bluetooth that every user can carry on their smartphone. WiFi communication technology is communication in the 2.4 – 2.5 GHz or 5.0 GHz frequency range and with the IEEE 802.11 protocol. In WiFi indoor positioning applications, since the distance between the mobile wireless communication source and the communication with the access point can be calculated with a scalar (non-directional) value, there are more than one reference access point in positioning systems. At this point, features such as signal strength (RSSI, Strength) and response time to the signal of wireless communication between access points and mobile users are used.

In the literature, there are many studies focused on indoor positioning [1-14]. In a study, a high-performance positioning process was performed with a method based on the round-trip time (RTT) of WiFi signals [1]. Here, researchers have developed two different position estimation approaches, which they call coarse and fine. The methods proposed in the literature study were tested in an area of 96m² with 8 reference access points, and in 80% of the test scenarios, the position determination process was performed below the deviation value of 2.5m.

In another study, the authors investigated the effects of antenna number and antenna connection methods for indoor positioning systems using triangulation [2]. In another study, a comparison of the error depending on the communication frequency was carried out in the WiFi signal strength-based (RSSI) positioning process [3]. In the

* Corresponding author: turan.altundogan@cbu.edu.tr. ORCID Number of authors: ¹ 0000-0002-8677-3105, ² 0000-0002-3276-3788

proposed method, WiFi positioning is performed with a Knn-based method. As a result of the comparison made in the method applied for the 2.4 and 5.0 GHz frequency communications, it was concluded that the location estimation process with the 5.0 GHz communication was more successful. In addition, in the study, the positioning method based on signal strength (RSS) and positioning methods based on path loss were also compared. As a result of this comparison, it was seen that the positioning methods depending on the signal strength gave a higher performance. In another study, an image-based method that automatically configures floor plans for indoor positioning systems (IPS) is proposed [4]. In another study, they developed a classifier in an encoder-decoder structure by using past WiFi signal intensity data for indoor positioning and performed floor and building determination with this classifier [5]. In another study, a method using qr code technology was proposed for IPS [6]. In some studies, Ultra-Wide-Band wireless communication technologies were used [7,8]. With UWB wireless communication technology, indoor positioning can be performed very successfully. So much so that in IPS where WiFi or Bluetooth signals are used, the position error is calculated in the order of meters, while in the UWB-based systems, the error is calculated in the order of centimeters. As a matter of fact, in the study numbered [8], the indoor positioning process was carried out with an error of approximately 9 cm. Despite the high performance of UWB-based methods in positioning applications, they are less preferred in such applications because they have high costs. Table 1 includes the technologies used in studies focused on indoor positioning systems in the literature.

In this study, the visibility weight matrixes depending on the WiFi strength characteristics of the wireless communication of WiFi access points and mobile users are determined and the wireless communication environment is expressed with visibility graphs. Then, the moving position was estimated by heuristic optimization methods using the fitness function based on the visibility weight matrix. Two different methods using GA and PSO heuristic optimizations have been developed to solve the problem. Each method was compared according to calculation speed and performance criteria.

Table 1. Approaches belong to indoor positioning focused studies.

Literature Study	Approach	Motivation
[1]	WiFi	Weighted Scaling
[2]	WiFi	Triangulation
[3]	WiFi	Comparative Study
[4]	Image Processing	Image Processing
[5]	WiFi	Fingerprinting
[6]	QR Code	QR Code Landmark
[7]	UWB	Fingerprinting
[8]	UWB	Range Error Calibration
[9]	WiFi	Fingerprinting
[10]	Bluetooth Beacons	BLE
[11]	WiFi	Triangulation
[12]	WiFi	Temporal – Spatial Fetures
[13]	Bluetooth Beacons	Triangulation
[14]	WiFi	Comparative Study

2. Visibility Graphs

It will be useful to explain the Visibility Graphs in detail for a better understanding of the proposed method. Visibility Graphs, objects, signals, etc. They are graphs in which a weight matrix is used that deals with the visibility relations with each other. Today, visibility graphs are used in many fields such as robotics, signal processing and path planning. In computer science, graphs are expressed as a vector of nodes (V) and a matrix of edges (E). Visibility graphs are also expressed with $G=(V, E)$ as in classical graphs. For a better understanding of the mentioned structure, the visibility matrix of the objects in the environment given in Figure 1 is given in Table 2 and the visibility graph expressed by this matrix is given in Figure 2. As you see, the neighborhoods of objects can see each other in Fig 1, has been assigned 1 and the other neighborhoods has been assigned 0 in weight matrix given in Table 2.

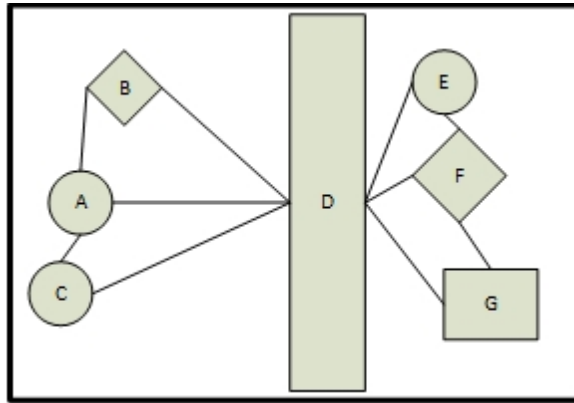


Figure 1. Sample environment belong to given visibility graph in Fig 2.

Table 2. Visibility Matrix Belong To Given Visibility Graph In Fig 2.

	A	B	C	D	E	F	G
A	0	1	1	1	0	0	0
B	1	0	0	1	0	0	0
C	1	0	0	1	0	0	0
D	1	1	1	0	1	1	1
E	0	0	0	1	0	1	0
F	0	0	0	1	1	0	1
G	0	0	0	1	0	1	0

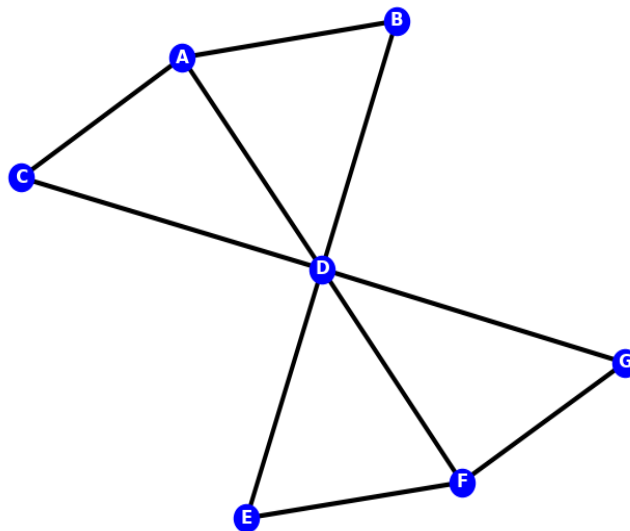


Figure 2. A sample visibility graph.

There are many studies using Visibility Graphs in the literature [15-22]. In one of these, the EEG activities of people with Alzheimer's disease were performed using a visibility graph-based method [15]. The study is a very important example for signal processing applications of Visibility Graphs. Visibility graphs are widely used in signal processing applications today. Especially in neurology, the use of visibility graphs is quite common for the detection of epileptic seizures that occur with the irregularity of EEG signals. In one of the literature studies we discussed, it

focused on the classification of motor images obtained from EEG signals with a versatile, weighted visibility graph and a deep learning-based method [16]. In another study, a method using visibility graphs was used to detect bearing failures in asynchronous motors [17]. In another study, pulse variability-related visibility graphs were used to detect late-onset sepsis in premature infants [18]. In another study, visibility graphs were used to determine the routes of ships [19]. In other studies, methods using visibility graphs are suggested for radar antenna scanning type detection and recognition [20-21]. In another study focused on radars, a visibility graph-based method has been proposed for low probability intercept (LPI) radar signal detection and recognition [22].

In this study, a weighted visibility graph based on the ability of indoor wifi sources to communicate with each other and the RSSI values of wifi signals has been constructed. Reference access points and the visibility of the wifi source to be determined are discussed in the graph. Since the location of the reference points is known, the estimation of the location of the mobile wifi source is performed with two separate methods based on GA and PSO. The proposed methods are tested on a virtual scenario. Existing positioning approaches usually focuses on fingerprinting of WiFi signals broadcasted from different sources. Our motivation in this study is predicting position by constructing a visibility graph using WiFi signals strength and position optimization using heuristic methods. By this way, data collection and tagging which the most difficult step of fingerprinting become unnecessary and this situation makes our method very applicable.

In the virtual scenario, the mobile WiFi source is assumed to be a smartphone, and the WiFi communication distance limit is configured to match the wireless communication capabilities of the smartphones. Since wifi signals are highly susceptible to noise in distance conversions based on RSSI values, value ranges are used. Visibility weights were determined with values between 0-1 assigned to each weight. After testing, the proposed methods were compared according to different criteria.

3. Proposed Approach

In this study, as mentioned before, an indoor positioning method based on Visibility Graphs and heuristic optimization is proposed. The wireless communication technology to be used for positioning here is WiFi. In indoor positioning methods where WiFi communication is used, signal characteristics such as signal strength (RSSI), round-trip time (RTT) belonging to more than one access point and a mobile WiFi source are generally used. In this study, visibility graphs are created based on RSSI values. The weight matrix of the visibility graphs created based on the RSSI values is used in the fitness function in the intuitive optimization step. The general block diagram of the proposed method is given in Figure 3.

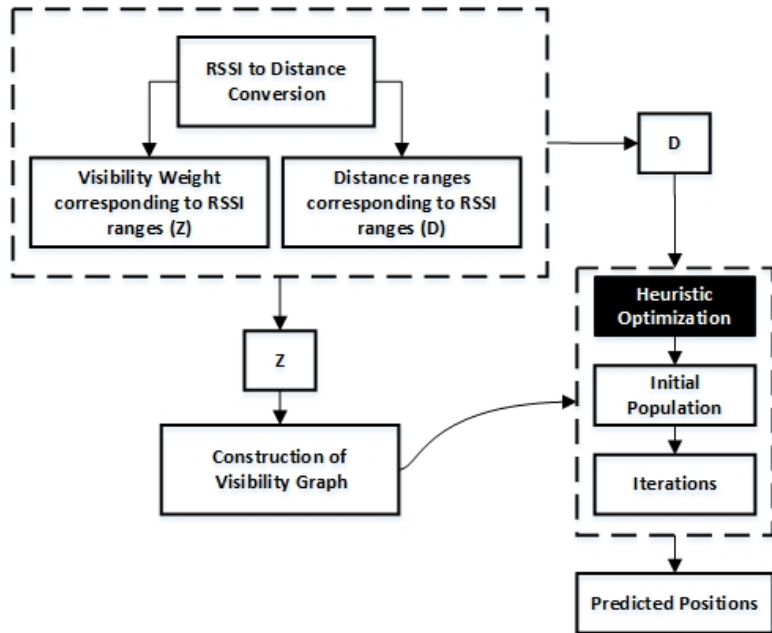


Figure 3. An overall block diagram of Proposed Method.

3.1. RSSI to Distance Conversion and Construction of Visibility Graph

In the proposed method, the aim is to estimate the location of the WiFi source, whose location is desired to be determined, by using the relationship between the RSSI value and the distance to the access point, with a method based on the distances from more than one access point. The mathematical expression used to calculate the RSSI value is given in Equations (1) to (6) [23].

$$P_L(d) = P_L(d_0) + 10n \log\left(\frac{d}{d_0}\right) + X_\sigma \quad (1)$$

$$\text{RSSI} = P_t - P_L(d) \quad (2)$$

$$P(d) = P(d_0) - 10n \log\left(\frac{d}{d_0}\right) - X_\sigma \quad (3)$$

$$\text{RSSI} = A - 10n \log\left(\frac{d}{d_0}\right) - X_\sigma \quad (4)$$

$$\text{RSSI}' = A - 10n \log(d) \quad (5)$$

$$d = 10^{(A - \text{RSSI})/10n} \quad (6)$$

Here, $P_L(d)$ represents the path loss of the received signal when the distance is d meters. $P_L(d_0)$ refers to the path loss of the reference distance received signal. n denotes the path loss index in a given environment. It shows the speed of path loss increasing with increasing distance. X_σ is in dB and represents the coverage factor. A represents the signal strength received from the reference point. Here, RSSI' refers to the RSSI values measured multiple times. As can be seen from the equation sets, distance conversion from RSSI can be performed with more than one RSSI value taken from the reference points. But as mentioned before, wifi signals are very sensitive to noise. Therefore, distance ranges corresponding to RSSI value ranges were used while creating visibility graphs. In addition, visibility weights between 0 and 1 are assigned to each value range. In Figure 4, the pseudo-code of the approach introduced for the creation of visibility graphs is given. Here, visibility weights are created according to RSSI intervals. N stands for RSSI intervals, Z stands for visibility weights corresponding to this interval. V represents the wifi resources in the environment and W represents the weight matrix.

3.2. Heuristic Optimization

After the visibility graph was built, two separate methods based on Genetic Algorithm (GA) and Particle Swarm Optimization (PSO) were developed to perform position estimation. In Figure 5, the block diagrams of both methods are given, and in Figure 6, the block diagram that expresses the operations of the individual module used in both methods. As can be seen here, the initial populations for both methods were generated using a random approach. Then, the Euclidean distances of each individual in the population to the reference access points were determined. After this process, the visibility weights corresponding to the distance intervals obtained were determined and the visibility graphs of the individuals were constructed. Here, the fitness function is determined based on the difference averages between the visibility matrices. In both methods, iterations continue until an individual with a fitness value of 1.

```

1. W= zeros(size(v),size(v))
2. for i in size(v):
3. for j in size(v):
4. if(i==j):
5. continue
6. end
7. for k in size(N):
8. if rssi(V[i],V[j]) between N[k]:
9. W[i][j] = Z[k]
10. end
11. end
12. end
13. end

```

Figure 4. Obtaining of the weight matrix.

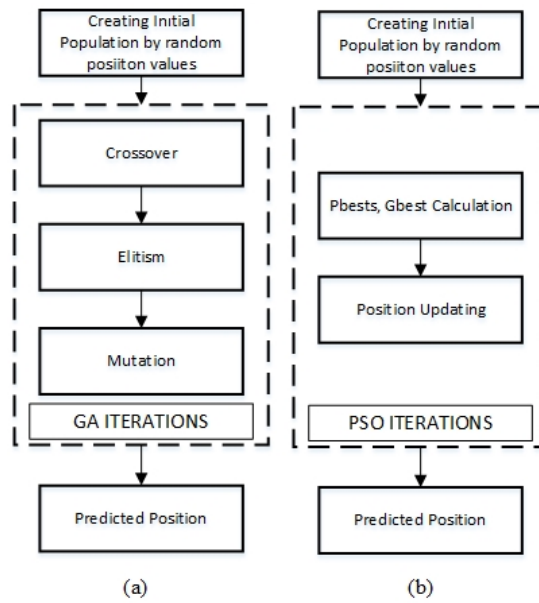


Figure 5. Heuristic optimization methods.(a:GA,b:PSO)

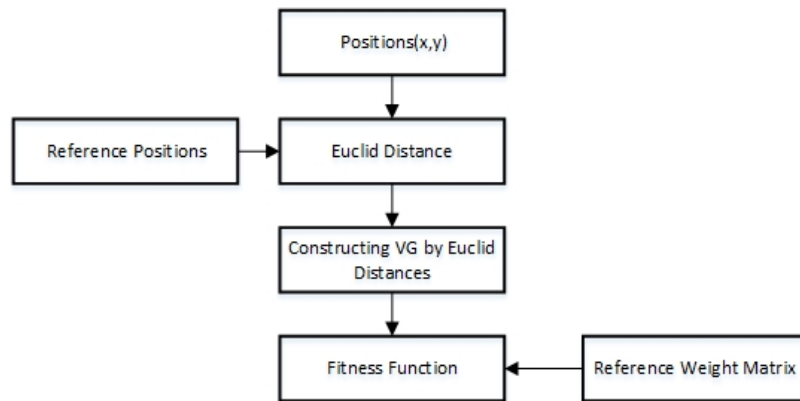


Figure 6. Processes of individual module using in Heuristic Optimization step.

4. Experimental Results

A virtual scenario was set up to test the proposed method. The first thing to consider here is the maximum distance that the WiFi sources used in the virtual scenario can reach. As it is known, the wifi communications of smart phones have a range of about 30m indoors. However, WiFi communications with an RSSI value below -80 dBm are unstable. Therefore, in the configuration made, a communication scenario with an RSSI value of -80dBm at a distance of 30m was emphasized. RSSI library is integrated into Python programming language for distance and RSSI value conversions. This library provides a function that takes the reference RSSI-distance pair and returns the corresponding RSSI value in meters. At this point, the reference RSSI value we give to the relevant function is -80dBm, and the distance value is 30 meters. In Figure 7, the graph showing the change of the distance value depending on the RSSI value in the relevant configuration is given. In Table 3, the distance ranges and visibility weights corresponding to the selected RSSI intervals are given. As seen in Figure 7, the curve in the graph has a logarithmic character. The reason for this is understood from the mathematical expressions given in Equation 1-6. The proposed method will be tested in a 1800m² virtual area. The area mentioned here has dimensions of 30mx60m. Access points are located at 15m intervals horizontally and vertically.

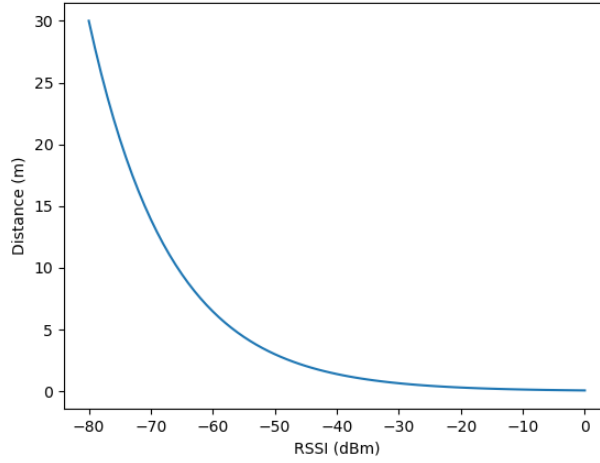


Figure 7. Distance graph based on RSSI.

Table 3. Visibility weights corresponding to rssi and distance range.

RSSI Range (dBm)	Distance Range (m)	Visibility Weight
<-80	>30	0
-80, -75	30,20	0.2
-75,-70	13,20	0.4
-70,-60	6,13	0.6
-60,-40	1.5,6	0.8
>-40	0,1.5	1.0

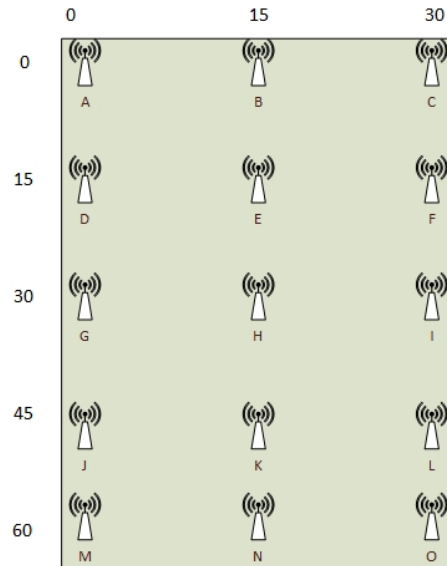


Figure 8. Virtual indoor environment.

In Figure 8, a diagram expressing the placement of access points in the virtual environment is given. In Figure 9, the graph expressing the visibility relations of the access points with each other is given.

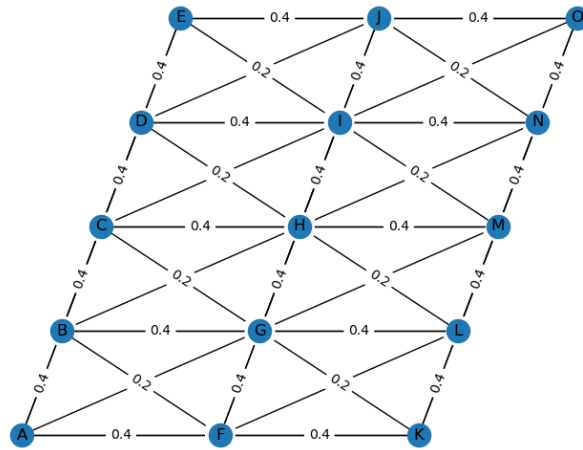


Figure 9. Visibility graph belongs to Access Points.

4.1. Experimental Results of PSO

Users at random positions were added to the virtual environment created for testing the PSO-based positioning method. In Table 4, the randomly added user positions and the predicted positions of these users with PSO, and the Euclidean distance of the predicted position from the actual position are given. The PSO was run at 50 population counts and 150 iterations. In Figure 10, the actual position, and the predicted position of the test case no. In Figure 11, the visibility graph of the test case numbered III is given. In Figure 12, the positions of Test Case V are marked. Figure 13 shows the convergence graph of the PSO.

Table 4. Test results of PSO.

Test No.	Real Position	Predicted Position	Euclid Distance
I	(25,50)	(26,50)	1m
II	(12,20)	(12.43,20.38)	58cm
III	(18,27)	(19.42,26.96)	1.42m
IV	(2,5)	(2.59,5.39)	72cm
V	(7,29)	(7.35,29.07)	36cm

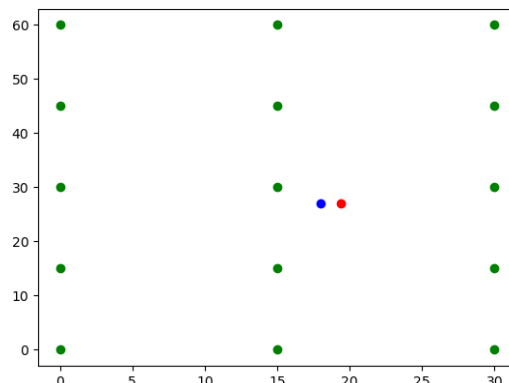


Figure 10. Real and predicted positions belong to Test Case III, (red: Predicted, blue:Real, green:Reference Access points).

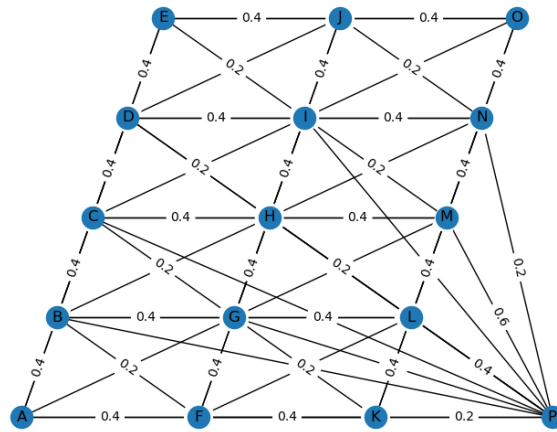


Figure 11. Visibility graph belongs to Test Case III.

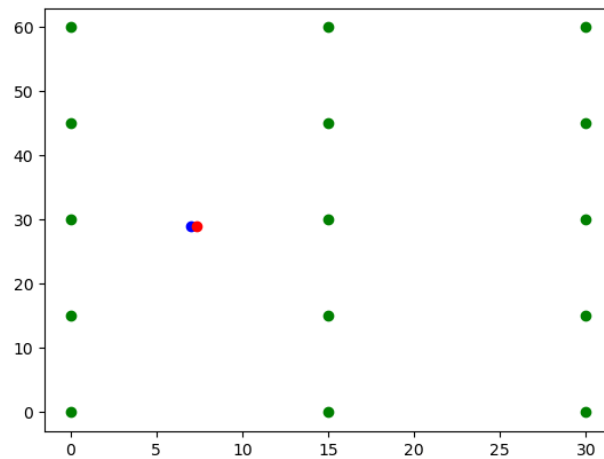


Figure 12. Real and predicted positions belong to Test Case V, (red: Predicted, blue:Real, green:Reference Access points).

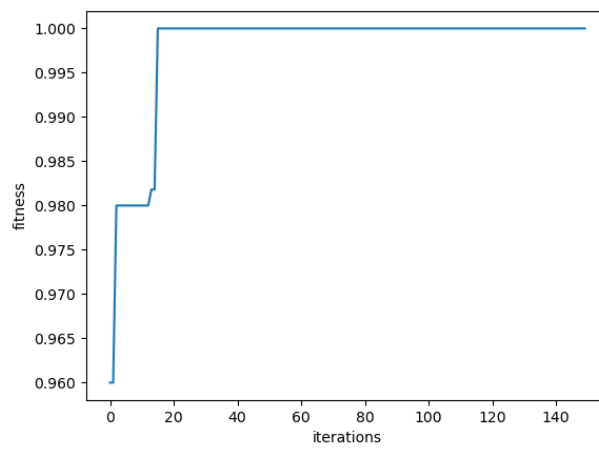


Figure 13. Fitness values belong to iterations.

4.2. Experimental Results of GA

Users at random positions were added to the virtual environment created for testing the GA-based positioning method. In Table 5, randomly added user positions and their predicted positions with PSO, and the Euclidean distance of the predicted position from the actual position are given. The GA was run for 10 populations and 1500 iterations. In Figure 14, the actual position and the predicted position of the test case IV on the virtual environment are marked. In Figure 15, the visibility graph of the test case no. III is given. In Figure 16, the positions of Test Case V are marked. Figure 17 shows the convergence graph of the GA.

Table 5. Test results of GA.

Test No.	Real Position	Predicted Position	Euclid Distance
I	(25,50)	(25,49)	1m
II	(12,20)	(11,19)	1.41cm
III	(18,27)	(18,26)	1m
IV	(2,5)	(2,8)	3m
V	(7,29)	(7,28)	1m

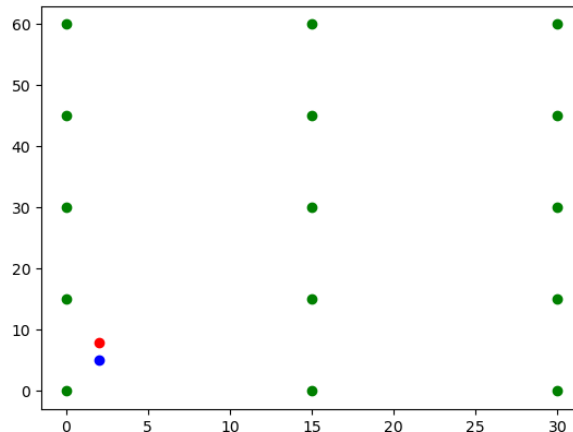


Figure 14. Real and predicted positions belong to Test Case IV, (red: Predicted, blue:Real, green:Reference Access points).

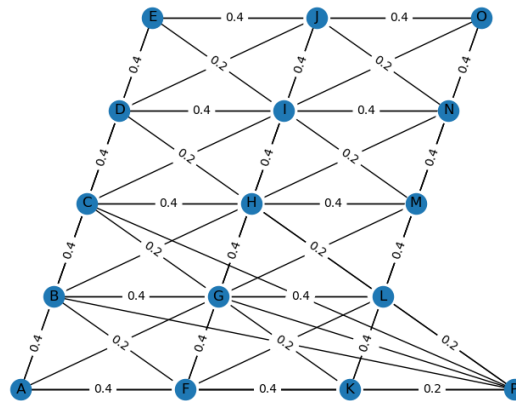


Figure 15. Visibility graph belongs to Test Case IV.

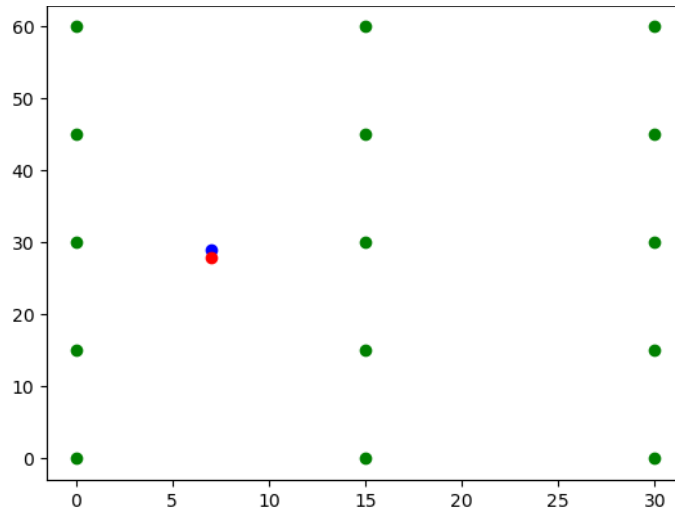


Figure 16. Real and predicted positions belong to Test Case V, (red: Predicted, blue:Real, green:Reference Access points).

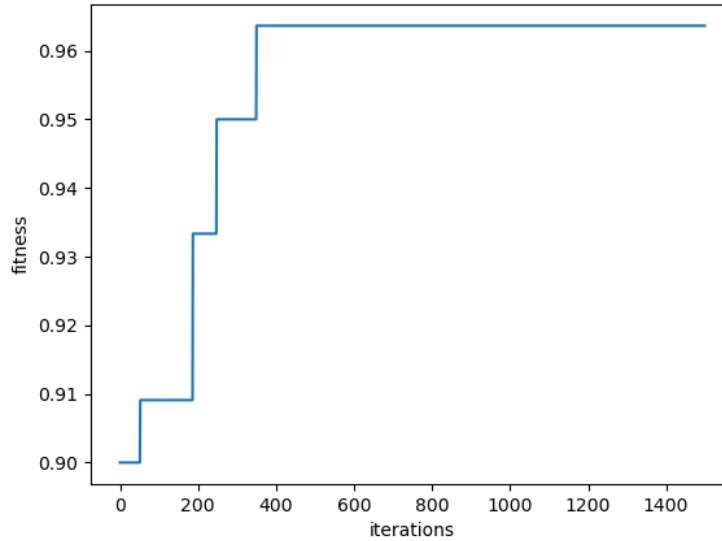


Figure 17. Fitness values belong to iterations.

5. Discussion

When the experimental results are examined, it’s seen that our position estimation approaches has achieved with a meter degree error. The results of comparisons between PSO and GA based methods proofed that the PSO based methods performance is better than GA based method. Because, almost all test error of PSO based approach is in centimeter degree, only one test error of GA based approach in centimeter degree. Besides, when Figures 13 and 17 are compared, PSO based method converges the optimum results faster than GA based method. Figure 10 and Figure 12 indicate us the real position and predicted positions and sensibility of both methods.

6. Conclusions

In this study, visibility graphs depending on Wi-Fi signal strength were created for indoor positioning and these graphs were used in the fitness function of two different heuristics for position estimation. When the experimental results are examined, it is seen that the PSO-based position estimation method works with a higher performance than the GA-based position estimation method. This situation is thought to be due to the presence of the position update approach in the working principle of the PSO and the search in the solution space with the crossover approach in GA. In addition, GA gave the results without converging the fitness value to 1.0 in many estimation

processes, PSO gave the results by obtaining a fitness value of 1.0 in each study. If we consider the working speed of the methods as another comparison criterion, it has been observed that PSO has a great advantage over GA (almost 250 times). In general, the developed approaches have achieved very efficient results in terms of performance (error < 1.5m) and position estimation time (340 ms) for PSO.

References

- [1] Yan S, Luo H, Zhao F, Shao W, Li Z and Crivello A, "Wi-Fi RTT based indoor positioning with dynamic weighted multidimensional scaling," 2019 International Conference on Indoor Positioning and Indoor Navigation (IPIN), 2019, pp. 1-8, doi: 10.1109/IPIN.2019.8911783.
- [2] Yuan D et al., "Model Checking Indoor Positioning System With Triangulation Positioning Technology," 2018 9th International Conference on Information Technology in Medicine and Education (ITME), 2018, pp. 862-866, doi: 10.1109/ITME.2018.00193.
- [3] Maung NAM, and Zaw W, "Comparative Study of RSS-based Indoor Positioning Techniques on Two Different Wi-Fi Frequency Bands," 2020 17th International Conference on Electrical Engineering/Electronics, Computer, Telecommunications and Information Technology (ECTI-CON), 2020, pp. 185-188, doi: 10.1109/ECTI-CON49241.2020.9158211.
- [4] Jaworski W, Wilk P, Juszczak M, Wysoczańska M and Lee AY, "Towards automatic configuration of floorplans for Indoor Positioning System," 2019 International Conference on Indoor Positioning and Indoor Navigation (IPIN), 2019, pp. 1-7, doi: 10.1109/IPIN.2019.8911747.
- [5] Joseph R and Sasi SB, "Indoor Positioning Using WiFi Fingerprint," 2018 International Conference on Circuits and Systems in Digital Enterprise Technology (ICCSDET), 2018, pp. 1-3, doi: 10.1109/ICCSDET.2018.8821184.
- [6] Li Z and Huang J, "Study on the use of Q-R codes as landmarks for indoor positioning: Preliminary results," 2018 IEEE/ION Position, Location and Navigation Symposium (PLANS), 2018, pp. 1270-1276, doi: 10.1109/PLANS.2018.8373516.
- [7] Blazek J, Jiranek J and Bajer J, "Indoor Passive Positioning Technique using Ultra Wide Band Modules," 2019 International Conference on Military Technologies (ICMT), 2019, pp. 1-5, doi: 10.1109/MILTECHS.2019.8870099.
- [8] Perakis H and Gikas V, "Evaluation of Range Error Calibration Models for Indoor UWB Positioning Applications," 2018 International Conference on Indoor Positioning and Indoor Navigation (IPIN), 2018, pp. 206-212, doi: 10.1109/IPIN.2018.8533755.
- [9] Molina B, Olivares E, Palau CE and Esteve M, "A Multimodal Fingerprint-Based Indoor Positioning System for Airports," in IEEE Access, vol. 6, pp. 10092-10106, 2018, doi: 10.1109/ACCESS.2018.2798918.
- [10] Andrushchak V, Maksymyuk T, Klymash M and Ageyev D, "Development of the iBeacon's Positioning Algorithm for Indoor Scenarios," 2018 International Scientific-Practical Conference Problems of Infocommunications. Science and Technology (PIC S&T), 2018, pp. 741-744, doi: 10.1109/INFOCOMMST.2018.8632075.
- [11] Teoman E and Ovatman T, "Trilateration in Indoor Positioning with an Uncertain Reference Point," 2019 IEEE 16th International Conference on Networking, Sensing and Control (ICNSC), 2019, pp. 397-402, doi: 10.1109/ICNSC.2019.8743240.
- [12] Shao W, Luo H, Zhao F, Tian H, Yan S and Crivello A, "Accurate Indoor Positioning Using Temporal-Spatial Constraints Based on Wi-Fi Fine Time Measurements," in IEEE Internet of Things Journal, vol. 7, no. 11, pp. 11006-11019, Nov. 2020, doi: 10.1109/JIOT.2020.2992069.
- [13] Pakanon N, Chamchoy M and Supanakoon P, "Study on Accuracy of Trilateration Method for Indoor Positioning with BLE Beacons," 2020 6th International Conference on Engineering, Applied Sciences and Technology (ICEAST), 2020, pp. 1-4, doi: 10.1109/ICEAST50382.2020.9165464.
- [14] Ang JLF, Lee WK and Ooi BY, "GreyZone: A Novel Method for Measuring and Comparing Various Indoor Positioning Systems," 2019 International Conference on Green and Human Information Technology (ICGHIT), 2019, pp. 30-35, doi: 10.1109/ICGHIT.2019.00014.
- [15] Cai L, Deng B, Wei X, Wang R and Wang J, "Analysis of Spontaneous EEG Activity in Alzheimer's Disease Using Weighted Visibility Graph," 2018 40th Annual International Conference of the IEEE Engineering in Medicine and Biology Society (EMBC), 2018, pp. 3100-3103, doi: 10.1109/EMBC.2018.8513010.
- [16] Samanta K, Chatterjee S and Bose R, "Cross-Subject Motor Imagery Tasks EEG Signal Classification Employing Multiplex Weighted Visibility Graph and Deep Feature Extraction," in IEEE Sensors Letters, vol. 4, no. 1, pp. 1-4, Jan. 2020, Art no. 7000104, doi: 10.1109/LSSENS.2019.2960279
- [17] Roy SS, Chatterjee S, Barman R, Roy S and Dey S, "Bearing Fault Detection in Induction Motors Employing Difference Visibility Graph," 2020 IEEE International Conference on Power Electronics, Drives and Energy Systems (PEDES), 2020, pp. 1-4, doi: 10.1109/PEDES49360.2020.9379635.
- [18] León C, Carrault G, Pladys P and Beuchée A, "Early Detection of Late Onset Sepsis in Premature Infants Using Visibility Graph Analysis of Heart Rate Variability," in IEEE Journal of Biomedical and Health Informatics, vol. 25, no. 4, pp. 1006-1017, April 2021, doi: 10.1109/JBHI.2020.3021662.
- [19] Kulbiej E, "Autonomous Vessels' Pathfinding Using Visibility Graph," 2018 Baltic Geodetic Congress (BGC Geomatics), 2018, pp. 107-111, doi: 10.1109/BGC-Geomatics.2018.00026.

- [20] Songtao L, Zhenshuo L, Yang G and Zhenming W, "Automatic radar antenna scan type recognition based on unlimited penetrable visibility graph," in *Journal of Systems Engineering and Electronics*, vol. 32, no. 2, pp. 437-446, April 2021, doi: 10.23919/JSEE.2021.000037.
- [21] Wan T, Fu X, Jiang K, Zhao Y and Tang B, "Radar Antenna Scan Pattern Intelligent Recognition Using Visibility Graph," in *IEEE Access*, vol. 7, pp. 175628-175641, 2019, doi: 10.1109/ACCESS.2019.2957769.
- [22] Tao W, J. Kaili, Jingyi L, Yanli T and Bin T, "Detection and recognition of LPI radar signals using visibility graphs," in *Journal of Systems Engineering and Electronics*, vol. 31, no. 6, pp. 1186-1192, Dec. 2020, doi: 10.23919/JSEE.2020.000091.
- [23] Shang F, Su W, Wang Q, Gao, H and Fu Q. "A location estimation algorithm based on RSSI vector similarity degree" *International Journal of Distributed Sensor Networks*, 10(8), 2014, 371350.

Classification of the Cardiac Arrhythmia Using Combined Feature Selection Algorithms

Murat TUNÇ^{1*}, Gülnur Begüm CANGÖZ²

^{1,2}Elektrik-Elektronik Mühendisliği, Mühendislik Fakültesi, Başkent Üniversitesi, Ankara, Türkiye
¹murattunc0110@gmail.com

(Geliş/Received: 12/07/2023;

Kabul/Accepted: 26/03/2024)

Abstract: The prediction of heart disease has gained great importance in recent years. Efficient monitoring of cardiac patients can save tremendous number of lives. This paper presents a method for classification and prediction of electrocardiogram data obtained from 452 patients representing the risk of cardiac arrhythmia. The aim of the study is to select highly related features with arrhythmia risk by using three different feature selection algorithms. In addition, various machine learning models are utilized for the classification task such as k-Nearest Neighbors (k-NN), Support Vector Machines (SVM) and Decision Tree (DT). The experimental results show that combination of a purposed feature selection method which later is called "Matched Selection" using SVM classifier outperforms other combinations and have an accuracy of 81.27% while k-NN and DT classifiers have an accuracy of 69.66% and 73.50% respectively. The study, in which detailed analyses are presented comparatively, is promising for the future studies.

Keywords: Arrhythmia, Classification, Feature Selection, Matched Selection.

Öz nitelik Seçim Algoritmalarının Kombinasyonu ile Kardiyak Aritminin Sınıflandırılması

Öz: Kalp hastalıklarının önceden tahmin edilmesi son yıllarda büyük önem kazanmıştır. Kalp hastalarının etkin bir şekilde izlenmesi, sayısız hayatın kurtarılmasını sağlayabilir. Bu makale, kardiyak aritmi riski taşıyan 452 hastadan elde edilen elektrokardiyogram verilerinin sınıflandırılması ve hastalıkların tahmin edilmesi için yenilikçi bir yöntem sunmaktadır. Bu çalışmanın ana hedefi, üç farklı öz nitelik seçme algoritmasını kullanarak aritmi riski ile yüksek derecede bağlantılı gösteren öz niteliklerin seçilmesidir. Ayrıca, sınıflandırma görevi için En yakın komşular algoritması(k-NN), Destek Vektör Makineleri (SVM) ve Karar Ağaçları (DT) gibi çeşitli makine öğrenimi modelleri kullanılmaktadır. Deneysel sonuçlar, Destek Vektör Makineleri (SVM) sınıflandırıcısı ve "Eşleştirilmiş Seçim" öz nitelik seçim yönteminin diğer kombinasyonları geride bıraktığını göstermektedir. Bu kombinasyon %81.27 doğruluk oranına sahipken, k-NN ve DT sınıflandırıcılarının doğruluk oranları sırasıyla %69.66 ve %73.50'dir. "Detaylı analizlerin karşılaştırmalı olarak sunulduğu bu çalışma, gelecekteki araştırmalar için umut vadetmektedir.

Anahtar Kelimeler: Aritmi, Sınıflandırma Öz nitelik Seçimi, Eşleştirilmiş Seçim.

1. INTRODUCTION

Cardiac diseases are considered as life threatening among chronic diseases which are responsible for many casualties around the world. Prevention or early detection can save many lives by monitoring heart activity. There are some technological methods such as ECG to examine these cardiac activities. An electrocardiogram (ECG) is the basic technique used to monitor heart activity in human beings. This technique can detect and diagnose various heart conditions, including arrhythmias (irregular heartbeats), heart attacks, and heart disease [1]. During an ECG, electrodes are placed on the chest, arms, and legs, and they pick up the electrical impulses generated by the heart. The impulses are then transmitted to a machine that records the data and produces a graph of the heart's activity. The results of an ECG can help doctors determine if there are any problems with the heart's rhythm or if the heart muscle is damaged [2]. The P, Q, R, S, and T waves are components of an electrocardiogram (ECG) that represent different phases of the cardiac electrical cycle [3]. Certain features of these waves such as peaks, duration and pauses between two waves provide key information to diagnose any abnormalities. In an arrhythmia, the electrical impulses that control the heart's rhythm are disrupted, causing the heart to beat too fast, too slow, or irregularly. There are many types of arrhythmias, including atrial fibrillation, atrial flutter, supraventricular tachycardia, ventricular tachycardia, and ventricular fibrillation [4]. Arrhythmia can cause a range of symptoms, including palpitations (a feeling of fluttering or racing in the chest), dizziness, shortness of breath, and chest pain. In some cases, arrhythmias can be life-threatening. Thus, early detection of arrhythmia is essential. If left untreated, arrhythmia can also lead to more serious complications, such as stroke, heart attack, or even sudden cardiac death. However, if detected early, arrhythmia can often be effectively managed with medication, lifestyle changes, or medical procedures such as ablation or implantation of a pacemaker or defibrillator [4].

* Corresponding author: murattunc0110@gmail.com ORCID numbers of authors ¹0009-0008-4994-3858; ²0000-0001-8469-5484

In summary, early detection of arrhythmia is important because it can lead to effective management and prevention of serious complications. For the reasons described, there are many studies in the literature. In a work, Güvenir et. al. used VFI5 algorithm which is majority deterministic algorithm for classification of Arrhythmia data set. Arrhythmia data set is also used in this study. By using the VFI Algorithm with 10-fold cross validation technique, the accuracy was obtained as 62%. Authors also used genetic algorithm to make VFI5 Algorithm effective and increased the accuracy to 68%. Moreover, 50% and 53% accuracy were obtained in regarding study, respectively, by applying Naive Bayes and Nearest Neighbors classifiers [3]. In another work, Niazi et. al. analyzed the same data set, Arrhythmia. They classified the data set using SVM and k-NN algorithms. They applied improved F-score and sequential forward search (IFSFS) for the feature selection process. After performing 20-fold cross validation on their presented model, average accuracy of 73.8% in case of KNN, and 68.8% in case of SVM [5]. Isin and his colleague Ozdalili used pre-trained deep learning models for ECG arrhythmia diagnosis. They employed AlexNet as a feature extractor and basic neural network for the classification of the extracted features. They obtained 98.51% accuracy while the testing accuracy is around 92%. In the light of their findings, they claimed that transfer learning can be an efficient automatic cardiac arrhythmia detection method [6]. Sannino and Pietro presented a study of ECG beat classification using MIT-BIH Arrhythmia Database. They proposed a deep learning approach developed by using Tensor Flow and Google deep learning library. Their experimental results show that the accuracy, sensitivity, and specificity metrics of the model are more efficient than the state of the art [7]. Alfaras et. al. proposed an automatic ECG arrhythmia classifier based on machine learning technique known as Echo State Networks which are a type of recurrent neural network (RNN) that have gained popularity in the field of machine learning. They used the MIT-BIH AR and the AHA ECG databases. They declared that the obtained results are comparable with the state of the art [8]. In another study Togaçar M. and his colleagues classified chest CT's by using different ML models and improved the results by integrating MRMR algorithm to their model [9].

One of the most important parameters effecting the success of a machine learning (ML) application is the data set used in the model training process. The reliability, precision and efficiency of ML model is directly dependent on the data set. In order to achieve high performance, the data set with high numbers of features and samples must be pre-processed before the training phase. These improvements in the data set can be achieved by using feature selection methods [10]. Feature selection algorithms reduce the size of the data and make the data set suitable for training phase by choosing the most relevant features in the data set. Yasar Çiklacandır and her colleague reduced their sample size by 90% by using feature selection methods such as; CHI2, MRMR and ReliefF in their work. Authors obtained 83.58% and 89.89% using DT and SVM classifiers respectively. [11]

The main goal of feature selection is to identify the most informative and relevant features which are most strongly associated with the target variable. By reducing the number of features, feature selection can help to improve the accuracy and generalizability of the model, as well as reduce the risk of overfitting [12]. In this paper, an improved feature selection method is proposed achieving higher classification accuracies for the Arrhythmia data set. Three different feature selection methods are applied on the data set for obtaining the most discriminative features. After the feature selection process, ML algorithms are implemented for the classification.

The aim of the study is to determine the most effective combination of the feature selection method and the classification algorithm. The study divided into three parts consists of the following scheme: In the first part, the data set and the methods used in this study are presented. Additionally, the usage of feature selection algorithms and classification processes are explained. In the next section, the findings obtained from the applied methods are presented. In the final section, the obtained results are revealed and recommendations for further studies are given.

This study aimed to effectively diagnose cardiac arrhythmias using the data set from the UCI Machine Learning Repository. By employing different feature selection methods and classification algorithms. Our research experiments led to the development of an improved feature selection method, achieving superior classification accuracies. Notably, the matched selection method consistently outperformed its alternatives, with a maximum accuracy of 81.27% when used with the SVM classifier. A similar result is obtained by Alshamlan H. and his colleagues. They identified and classified genes involved in the progression of the Alzheimer's Disease. Authors used SVM classifier with various feature selection methods such as; MRMR, CFS, CHI2 and F-Score. They achieved classification accuracy of 84% with the MRMR and F-Score filter methods. [13] Despite slightly longer completion times, our proposed method demonstrated remarkable accuracy and robustness, offering promising implications for improving cardiac arrhythmia diagnosis.

2. MATERIALS AND METHODS

2.1. Data Set: The purpose of this study is to classify the presence and the types of cardiac arrhythmia disease by using an ECG data set created from various patients. To serve this purpose, the data set taken from UCI Machine Learning Repository, contains ECG recordings of 452 patients. There are 279 features for all measurements, represented by the columns of the data set. Labels of the classes from 1 to 16 in the 280th column is representing the type of arrhythmia patients encounter [14]. The data set contains missing measurements. Regarding missing data is handled by setting as zero. The most occurring three classes in the data set are normal rate, right bundle branch block and coronary artery disease with their respective occurrence rates are 54.2, 11.1, 9.7 per hundred subjects. All the features of the data set are given in Table 1. below.

Table 1. Features in the data set

Number of Feature	Features	Number of Feature	Features
1	f_1 : Age	19	f_{19} : R' wave, small peak just after R
2	f_2 : Sex	20	f_{20} : S' wave
3	f_3 : Height	21	f_{21} : Number of intrinsic deflections, linear
4	f_4 : Weight	22	f_{22} : Existence of ragged R wave, nominal
5	f_5 : QRS duration	23	f_{23} : Existence of diphasic derivation of R wave, nominal
6	f_6 : P-R interval	24	f_{24} : Existence of ragged P wave, nominal
7	f_7 : Q-T interval	25	f_{25} : Existence of diphasic derivation of P wave, nominal
8	f_8 : T interval	26	f_{26} : Existence of ragged T wave, nominal
9	f_9 : P interval	27	f_{27} : Existence of diphasic derivation of T wave, nominal
10	f_{10} : QRS	160.	f_{160} : JJ wave, linear
11	f_{11} : T	161.	f_{161} : Q wave, linear
12	f_{12} : P	162.	f_{162} : R wave, linear
13	f_{13} : QRST	163.	f_{163} : S wave, linear
14	f_{14} : J	164.	f_{164} : R' wave, linear
15	f_{15} : Heart rate	165.	f_{165} : S' wave, linear
16	f_{16} : Q wave	166.	f_{166} : P wave, linear
17	f_{17} : R wave	167.	f_{167} : T wave, linear
18	f_{18} : S wave		

All of the above features from 16 to 27 measured for the DI channel are also measured for the DII channel (f_{28} - f_{39}), DIII channel (f_{40} - f_{51}), AVR (Augmented Vector Right) channel (f_{52} - f_{63}), AVL (Augmented Vector Left) channel (f_{64} - f_{75}), AVF (Augmented Vector Foot) channel (f_{76} - f_{87}), V1 channel (f_{88} - f_{99}), V2 channel (f_{100} - f_{111}), V3 channel (f_{112} - f_{123}), V4 channel (f_{124} - f_{135}), V5 (f_{136} - f_{147}), V6 channel (f_{148} - f_{159}). AVL, AVR, AVF, V1, V2, V3, V4, V5, and V6 are the names of the channels used in a standard 12-lead ECG to record the electrical activity of the heart from different perspectives. AVL is a modified chest lead that provides a view of the heart's electrical activity from the left lateral perspective. Likewise, AVR provides this activity from a right side. AVF is a modified limb lead that provides a view of the heart's electrical activity from the foot or inferior perspective. V1 to V6 are chest leads that are placed on specific locations on the chest to provide a view of the heart's electrical activity from different angles. Together, these leads or channels allow healthcare professionals to assess the electrical activity of the heart from multiple perspectives, which helps them diagnose a wide range of cardiac conditions, including arrhythmias, and other abnormalities. The following measurements from 160 to 167 are obtained from the DI channel. Features 168 (f_{168}) and feature 169 (f_{169}) named QRSA and QRSTA, respectively, are derived from some of the metrics detailed as follows:

QRSA = sum of areas of all segments divided by 10. (Area = width \times height \div 2)

QRSTA = QRSA + 0.5 \times width of T wave \times 0.1 \times height of T wave. (If T is diphasic then the bigger segment is considered).

The features from 160 to 167 measured for the DI channel are also measured for the DII channel ($f_{170-f_{179}}$), DIII channel ($f_{180-f_{189}}$), AVR channel ($f_{190-f_{199}}$), AVL channel ($f_{200-f_{209}}$), AVF channel ($f_{210-f_{219}}$), V1 channel ($f_{220-f_{229}}$), V2 channel ($f_{230-f_{239}}$), V3 channel ($f_{240-f_{249}}$), V4 channel ($f_{250-f_{259}}$), V5 ($f_{260-f_{269}}$), V6 channel ($f_{270-f_{279}}$).

2.2. Feature Selection: The data set contains many features, and using all of these features can lead to long processing times, incorrect classification and low prediction results. It may be sufficient to consider only some of the features in determining the disease that the patient will encounter. The selection of relevant features is an important step in machine learning as it can reduce the complexity of the model and increase its accuracy, interpretability, and efficiency [15]. There are several methods for feature selection, and they can be classified into three categories: filter methods, wrapper methods, and embedded methods.

2.2.1. Wrapper Methods: Wrapper methods select features by evaluating the performance of a machine learning model with different subsets of features. They can select the most relevant features and account for the interaction between features. However, they can be computationally expensive and prone to overfitting. Examples of wrapper methods include recursive feature elimination, forward selection, and backward elimination [16].

2.2.2. Embedded Methods: These methods select features during the training of a ML model. They can be computationally efficient and select the most relevant features for a specific model. However, they may not always select the most relevant features for other models, and they can be sensitive to the choice of the model. Examples of embedded methods are Lasso Regularization, Ridge Regularization, and Decision Tree-Based feature selection [17].

2.2.3. Filter Methods: Filter methods select features based on their statistical properties without considering the performance of the model. They can be fast and efficient. However, like the embedded methods, they may not always select the most relevant features. Examples of filter methods include chi-squared, mutual information, correlation-based feature selection, and variance threshold [17].

In a nutshell, filter methods are computationally efficient but may not always select the most relevant features. Wrapper methods can select the most relevant features but can be computationally expensive. Embedded methods can be efficient and select the most relevant features for a specific model but may not always be suitable for other models. Therefore, two different filter methods and a purposed hybrid approach are performed in the paper. Feature selection algorithms are applied before the classification process, such as a pre-processing filter operation. In this study, three different feature selection algorithms were applied including Minimum Redundancy Maximum Relevance, Chi-square, and Matched Feature Selection Method. These methods are briefly described in the following subsection.

Minimum Redundancy Maximum Relevance (MRMR) Feature Selection Method: This method creates the smallest set of features which consists of highly related features with class labels. This algorithm calculates relevance and redundancy of the respective feature with class labels and create a score list by using these calculations. In every loop, algorithm reduce the size of the data set until it reaches the determined set size or maximum number of repetitions. Therefore, processing time of the algorithm increases as the desired size of the data set is decreased [18].

Chi-square Feature Selection (Chi2) Method: Chi-Square test to all features and create list of features with their respective scores. Desired features can be obtained via setting a number of features or setting threshold score to take all features with higher score values. The processing time of this method is independent from the desired number of features as it calculates for all features once [19].

Matched Feature Selection (MFS) Method: This purposed method combines the two different methods mentioned the previous subsections: MRMR and Chi-square. The algorithm works by calculating both MRMR and Chi-square test scores for all of the features once. After this stage, algorithm calculates the mean scores for all of the features. Finally, as in the second method, a threshold can be set for selecting the relevant features for prediction. This algorithm provides a robust set of features, also has a similar completion time to Chi-square test

and similar performance to the MRMR algorithm. All of the algorithms have the same inputs including features, labels and the threshold level that can be set by the user. Output of the algorithms are the first set scores assigned to each feature. Number of features they selected according to the threshold level, the reduced data set is created with the important features. Afterwards, the created data set is employed for the train and the test procedures of the selected ML models.

2.3. Classification: Machine learning classification is a process of predicting a categorical label or class for a given input based on the patterns and relationships learned from a labeled training dataset. The classification process involves several steps:

- Data preparation
- Feature selection
- Model selection.
- Training, validation, and test the selected model.

Overall, the purpose is to create an accurate and efficient model which can generalize well to unseen data and automate the classification task. The classification process is carried out by using the ML models which described in the following subsections.

2.3.1. k-Nearest Neighbors (k-NN): The k-NN algorithm is one of the easiest and simplest algorithms for classification and prediction tasks. k-NN classifies new data based on its respective distances with the other samples. In order to utilize k-NN algorithm, it is necessary to determine the number of the neighbors which is demonstrated as 'k'. The key point of the algorithm is the selection of the k value, which directly affects the performance of the output [20].

Algorithm calculates all the distance between new data and each existing sample, these distances are listed and sorted from low to high. First k samples are considered from the list. Number of k class labels are counted, and new data are assigned to a class with the highest number of a certain class labels.

The algorithm is a distance based and there are numerous ways to calculate distances. However, the most common method is Euclidian Distance calculation and normalization. The visual representation of the algorithm can be seen in the Figure 1.

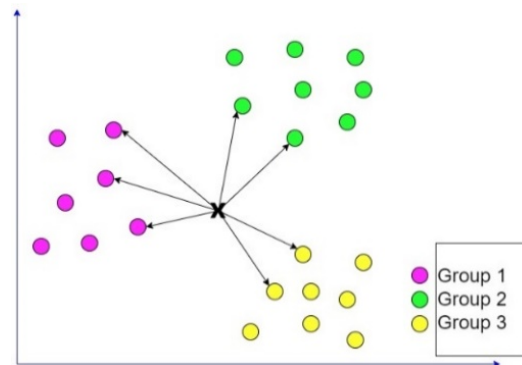


Figure 1. Visual representation of the k-NN algorithm.

2.3.2. Support Vector Machines (SVM): Support Vector Machines Algorithm is capable of determining difference between the samples. SVM uses decision functions to classify new data. Decision functions are created during the training process of the model [21]. SVM uses different methods for classification of multi-class data sets. In this study, two different SVM classification methods are concerned: one vs. one (OvO), and one vs. all (OvA). One vs. one considers only two classes while creating the support vectors which helps to separate the classes. For every combination of two classes, there must be a different decision vector in order to separate classes from each other. On one hand, this method results in high precision of classification and prediction rate. On the

other hand, process needs a high requirement of processing time since every two class combinations require a decision vector, particularly in a great number of classes.

The second method, one vs all, considers all classes while creating the support vectors. Thus, every class requires only one decision function. This method results in low precision of classification and prediction, also high chance of errors in the process. However, all classes need only one decision function completion time of this model would be lower than the first method. Main differences between these methods are their completion time and the precision. Both algorithms classify the new data by inserting the data in the decision functions created during the training process.

2.3.3. Decision Trees (DTs): This algorithm is based on the comparison of class parameters. This algorithm is used tree-like structures for classifying the new data [22]. The algorithm uses root-node-leaf relation. Every leaf of the tree is corresponding to a class label. Nodes of the tree are representing the features of the data set. For the root node feature which has the highest relation with the class label must be used.

Entropy and gain calculations are utilized in the algorithm in order to determine the level of feature – class relation. First entropy of the class labels is calculated, then entropy of all features with the class labels are computed. Finally, the gain is calculated by subtracting the second value from the first. Feature with the highest gain is used for the regarding specific node. This algorithm mostly uses with great amounts of samples in the data set and have small amounts of features. Structure of the algorithm is visualized in the Figure 2.

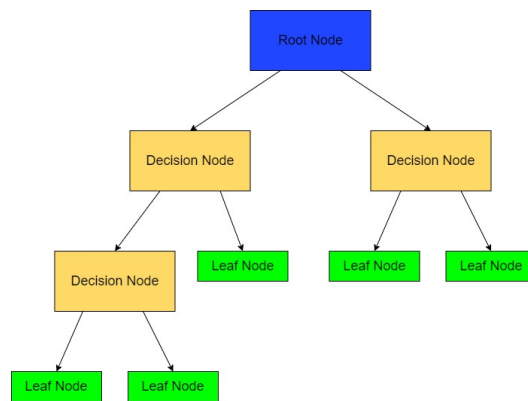


Figure 2. Structure of the Decision Tree Algorithm.

2.4. Proposed Feature Selection Method: The proposed model operates by subjecting the dataset to the MRMR and CHI2 feature selection algorithms. These algorithms compute relevancy score values for each feature, which are subsequently normalized. After normalization, these scores are multiplied by specific coefficients to create a combined value. This combined value is compared to the predetermined threshold value. Those exceeding the threshold value are stored to include in the newly created dataset. Finally, a new dataset is created with the original ranks and contents of the stored features. This dataset, along with the number of features, is returned as output to the main function.

3. FINDINGS AND DISCUSSION

Purpose of this study is to determine the risk of cardiac arrhythmias based on the ECG data from the patients. For realizing this purpose, experimental setup is created by implementing all described algorithms. A block diagram consists of the functions created and their respective input and output parameters also the interconnections between them are given Figure 3.

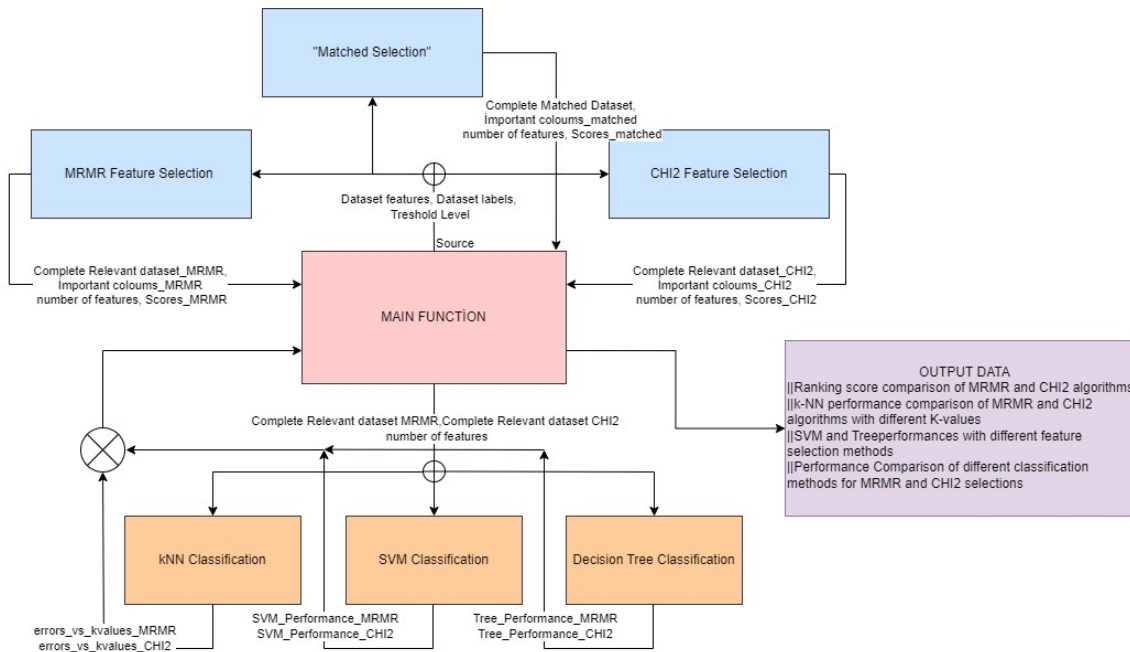


Figure 3. Block diagram of the experimental setup.

Upon successful implementation of the code and addition of a result evaluation section, the setup undergoes testing. The test results for a threshold level of 0.35 are given in the Figure 4 and Figure 5.

The test procedure is repeated for various threshold values, resulting in varying success rates. The table consisting of the results from different tests is created and it can be seen in Table 2. Using the results from the table, performance comparison graphs are created and illustrated in Figure 6, Figure 7, and Figure 8 for the k-NN, SVM and DT algorithms respectively. Comparison of different feature selection algorithms for each classification algorithm can be seen in those figures.

While the model tested with different threshold values, the completion time of feature selection algorithms were recorded to use in the performance evaluation. These records can be seen in the Table 3.

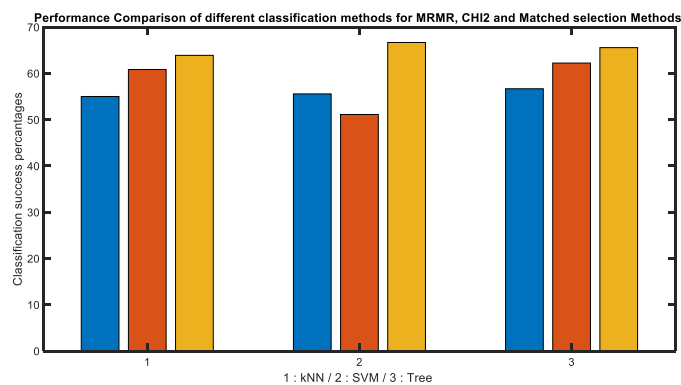


Figure 4. Accuracy of the classifiers for different feature selection algorithms.

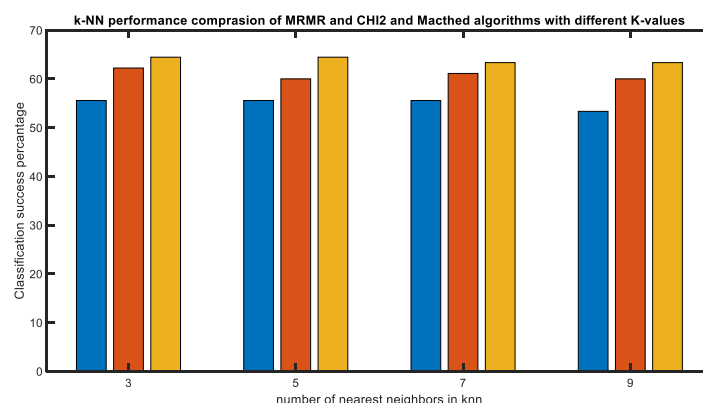


Figure 5. Accuracy of k-NN classifier for the different feature selection algorithms and different k values.

Table 2. Results of the algorithm tests

Threshold level	Completion time(Total)	K-NN			SVM			DT		
		MRMR	CHI2	Matched	MRMR	CHI2	Matched	MRMR	CHI2	Matched
0,1	5,33	55,87	44,99	51,72	55,47	62,94	62,28	59,00	55,00	63,34
0,15	5,06	47,36	53,41	58,67	56,71	51,82	60,81	50,65	59,28	57,60
0,2	4,87	54,51	52,18	60,66	53,89	64,67	69,49	54,40	55,47	57,71
0,25	5,52	55,25	59,00	49,27	66,50	59,12	58,80	57,00	55,95	68,60
0,3	5,06	47,79	59,42	53,79	46,35	66,82	70,96	54,77	64,07	73,24
0,35	4,89	60,80	50,94	52,37	51,17	54,31	72,10	59,28	63,38	64,09
0,4	4,94	53,07	58,67	69,66	53,84	53,84	74,56	49,87	53,78	73,34
0,45	5,47	49,25	47,00	60,37	47,02	62,36	81,27	56,71	55,73	53,71
0,5	5,05	52,18	51,67	59,59	59,28	49,06	70,88	51,00	57,00	58,66
0,55	5,77	59,15	48,53	68,43	56,05	54,97	69,03	46,48	52,41	60,56
0,6	5,97	57,09	55,28	62,65	49,09	50,13	64,09	44,00	54,75	64,09
0,65	7,79	50,81	43,73	63,60	46,48	54,39	74,20	51,42	50,44	73,02
0,7	9,04	50,40	59,46	66,21	55,95	52,78	68,84	46,40	54,13	73,50
0,75	7,79	48,56	56,32	49,50	59,93	54,77	63,80	44,00	54,75	46,20
0,8	8,68	53,15	54,39	56,53	68,20	52,70	59,73	53,40	46,48	51,20
0,85	10,25	52,80	49,38	68,95	54,40	68,27	63,01	44,44	49,60	51,12
0,9	9,75	59,68	59,93	53,88	59,34	59,34	75,38	42,47	50,56	55,35
0,95	7,72	49,60	53,48	57,00	61,43	54,97	52,78	52,78	48,55	55,95
1	4,85	52,23	36,03	51,42	44,98	56,22	59,45	49,06	44,98	47,55
Mean		53,13	52,31	58,65	55,06	57,03	66,92	50,90	54,02	60,46
Standart Deviation		3,92	6,17	6,46	6,40	5,46	6,99	5,11	4,87	8,62
Maximum Value		60,80	59,93	69,66	68,20	68,27	81,27	59,28	64,07	73,50

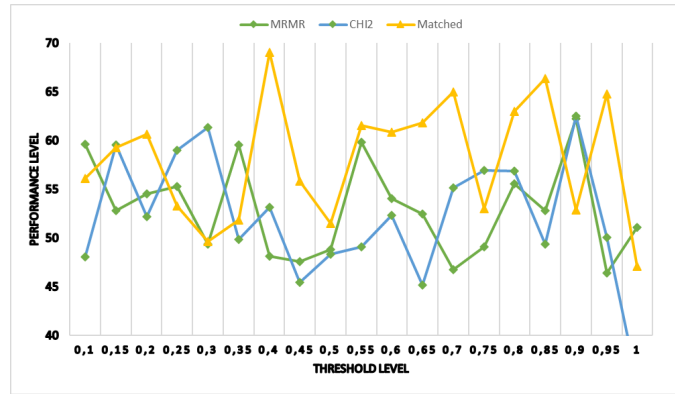


Figure 6. Performance of different feature selection algorithms with k-NN classification algorithm.

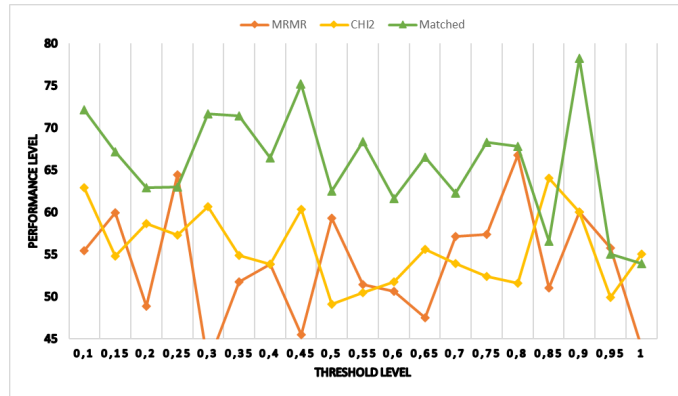


Figure 7. Performance of different feature selection algorithms with SVM classification algorithm.

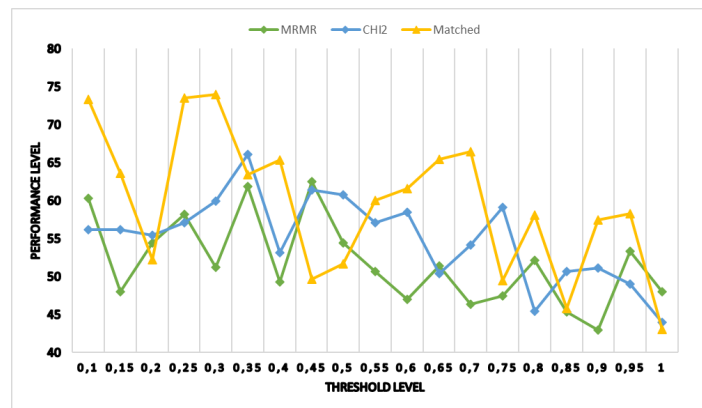


Figure 8. Performance of different feature selection algorithms with DT classification algorithm.

Table 3. Completion time of individual feature selection algorithms

Threshold level	Completion time(Total)	Completion time(Matched)	Completion time(MRMR)	Completion time(CHI2)
0,1	5,33	0,6179	0,2791	0,0386
0,15	5,06	0,5984	0,216	0,0377
0,2	4,87	0,5647	0,3237	0,0422
0,25	5,52	0,5745	0,2067	0,0378
0,3	5,06	0,5597	0,2103	0,0369
0,35	4,89	0,7307	0,2185	0,0389
0,4	4,94	0,5703	0,2026	0,0384
0,45	5,47	0,6006	0,1942	0,0368
0,5	5,05	0,5729	0,0264	0,038
0,55	5,77	0,5768	0,2057	0,0379
0,6	5,97	0,5748	0,2038	0,0371
0,65	7,79	0,57	0,2039	0,0375
0,7	9,04	0,5732	0,2022	0,0373
0,75	7,79	0,5646	0,2123	0,0371
0,8	8,68	0,6105	0,2132	0,0375
0,85	10,25	0,5635	0,2084	0,0374
0,9	9,75	0,6238	0,2199	0,0416
0,95	7,72	0,5576	0,2007	0,038
1	4,85	0,5668	0,2123	0,0366

Performance of the system is evaluated using the accuracy and algorithm completion time. The visualization of this evaluation metrics is depicted in the Figure 9, Figure 10, and Figure 11.

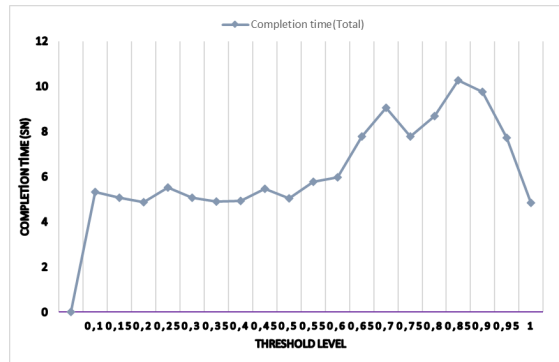


Figure 9. Variation of total completion time according to threshold level.

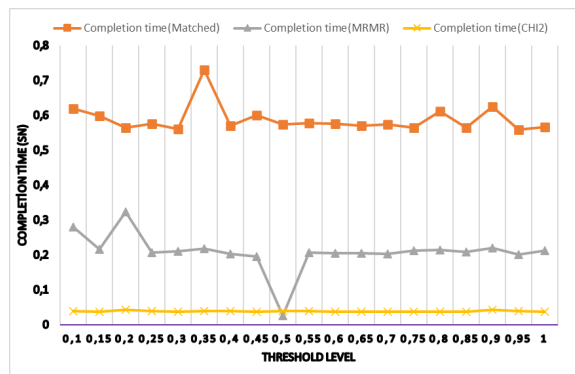


Figure 10. Change in individual completion time of feature selection algorithms with threshold level.

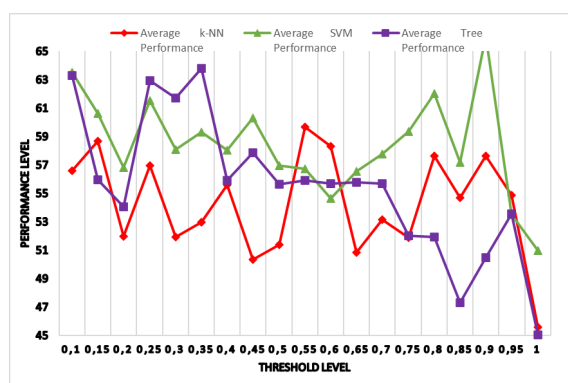


Figure 11. Average classifier performances for all the feature selection algorithms.

As it is stated before Figure 6, Figure 7, and Figure 8 reveals differences between performance of the feature selection algorithms with all classification algorithms.

For k-NN classification method MRMR and CHI2 algorithms shows almost identical performance in terms of mean accuracy. However, the proposed matched selection algorithm outperforms these two algorithms by an average of 6%. Considering standard deviation, the MRMR feature selection method is the most precise method. When considering both accuracy and precision simultaneously, the most suitable model to use with k-NN classification is the proposed matched selection model. Upon comparing the feature selection algorithms for the SVM classification model, it is evident that the most accurate feature selection algorithm is matched selection. Similar to results of the k-NN algorithm MRMR and CHI2 feature selection algorithms show close performance. Again, matched selection algorithm outperforms both algorithms by 11%. When considering precision, the CHI2 method outperforms other methods. The matched selection algorithm demonstrates similar precision performance when used with k-NN and SVM classification algorithms. Upon evaluating both accuracy and precision, the matched selection algorithm provides superior results compared to other feature selection algorithms. Additionally, it can be said that. Matched selection algorithm performs best when paired with the SVM classification algorithm. When the performance of feature selection algorithms used with the DT classification algorithm is investigated, it is apparent that the matched selection algorithm outperforms other feature selection algorithms by approximately 7% in the matter of accuracy. However, on the subject of precision matched feature selection algorithms algorithm demonstrates significantly inferior performance. The most precise feature selection model to use with DT classification is CHI2 method. Based on these it can be said that matched selection algorithm is not the most suitable model to use with DT classification algorithm.

Reviewing the information provided in Table 1, it can be concluded that the matched selection algorithm demonstrates superior performance in terms of accuracy across all classification algorithms. Moreover, proposed model generally exhibits precision performance comparable to others except when used in conjunction with the DT algorithm. Consequently, it can be asserted that the model demonstrates a noticeable superior performance compared to other models in this scenario.

Based on the data presented in Table 2, the performance of feature selection algorithms can be evaluated based on their completion times. The proposed matched selection model takes approximately 2.5 times longer to complete compared to the MRMR model and about 15 times longer compared to the CHI2 model. The completion time of all models, including the proposed model, generally decreases as the threshold level increases. Under these circumstances, it would be more sensible to use the proposed model in situations requiring high accuracy, such as healthcare, rather than time-sensitive scenarios.

The proposed matched selection algorithm combines various feature selection methods, making it versatile and robust. It offers comprehensive selection criteria, enhancing adaptability across tasks. Moreover, it consistently achieves high accuracy, especially when used with k-NN and SVM methods, making it ideal for accuracy-focused applications. Overall, the proposed algorithm represents an advancement, offering higher accuracy, with the potential to enhance classification systems in various domains.

The proposed model combines various existing feature selection algorithms to form a hybrid algorithm. This approach enables achieving higher accuracy at the expense of completion time. This innovative methodology leverages the strengths of individual algorithms while mitigating their limitations, resulting in a more comprehensive and effective solution to feature selection. Emphasizing higher accuracy, at the expense of completion time, underlines the innovative nature of this study. In summary, the proposed model represents a significant advancement in feature selection, promising improved performance.

4. CONCLUSION

The objective of this study is to determine the presence and classify the types of cardiac arrhythmia disease effectively by using the ECG data set taken from UCI Machine Learning Repository. To achieve this purpose, different feature selection methods and classification algorithms are engaged. Determining the most effective combination of the feature selection method and the classification algorithm for the data set, named Arrhythmia, is the motivation of the work.

In this paper, an improved feature selection method that achieves higher classification accuracies for the Arrhythmia data set is proposed. Besides, different feature selection methods are applied on the data set for obtaining the most discriminative features. After the feature selection process, machine learning algorithms are implemented for the classification task.

Experimental evaluation focused on determining the performance of feature selection methods and classification algorithms in predicting arrhythmias. The matched selection feature method consistently outperformed alternatives in terms of accuracy with different classification algorithms, achieving superior accuracy of 81.27% when used with SVM classifier. In addition to accuracy and precision, computational efficiency was evaluated by recording completion times of individual feature selection methods. Despite slightly longer completion times, the proposed matched selection method's superior accuracy and robustness make it a viable choice for real-world applications prioritizing accuracy rather than time-sensitivity.

References

- [1] Krikler DM. "Historical aspects of electrocardiography." *Cardiol Clin*, vol. 5, no. 3, pp. 349-355, Aug. 1987.
- [2] Zimetbaum PJ, Josephson ME. "Use of the electrocardiogram in acute myocardial infarction." *N Engl J Med*, vol. 348, no. 10, pp. 933-940, Mar. 06, 2003.
- [3] Güvenir HA, Acar B, Demiroz G, Cekin A. "A supervised machine learning algorithm for arrhythmia analysis." *Computers in Cardiology 1997*, pp. 433-436.
- [4] Fu, Dg. "Cardiac Arrhythmias: Diagnosis, Symptoms, and Treatments." *Cell Biochem Biophys*, vol. 73, pp. 291–296, 2015. DOI: <https://doi.org/10.1007/s12013-015-0626-4>.
- [5] Niazi KAK, Khan SA, Shaikat A, Akhtar M. "Identifying best feature subset for cardiac arrhythmia classification." In *Proceedings of the 2015 Science and Information Conference, SAI 2015, London, UK, 28–30 July 2015*, pp. 494–499.
- [6] Isin, A., Ozdalili, S. "Cardiac arrhythmia detection using deep learning." *Procedia Computer Science*, vol. 120, pp. 268-275, 2017. DOI: <https://doi.org/10.1016/j.procs.2017.11.238>.
- [7] Sannino, G., De Pietro, G. "A deep learning approach for ECG-based heartbeat classification for arrhythmia detection." *Future Generation Computer Systems*, vol. 86, pp. 446-455, 2018. DOI: <https://doi.org/10.1016/j.future.2018.03.057>.
- [8] Alfaras, M., Soriano, M.C., Ortín, S. "A Fast Machine Learning Model for ECG-Based Heartbeat Classification and Arrhythmia Detection." *Frontiers in Physics*, vol. 7, 2019. DOI: <https://doi.org/10.3389/fphy.2019.00103>.
- [9] Toğaçar, M., Ergen, B., Cömert, Z. "Detection of lung cancer on chest CT images using minimum redundancy maximum relevance feature selection method with convolutional neural networks." *Biocybernetics and Biomedical Engineering*, vol. 40, no. 1, pp. 23-39, 2020.
- [10] Güney, S., Ergün, G.B. "Classification of Canine Maturity and Bone Fracture Time Based on X-Ray Images of Long Bones." *IEEE Access*, vol. 9, pp. 109004-109011, 2021. DOI: 10.1109/ACCESS.2021.3101040.
- [11] Çıklaçandır Y., Karabiber Cura F., Özlem O. "A Comparative Study on Different Feature Selection Methods for Malaria Detection." 1-4, 2023. DOI: 10.1109/TIPTEKNO59875.2023.10359193.

- [12] Ergün GB, Güney S. "A Comparison of the Multivariate Calibration Methods with Feature Selection for Gas Sensors' Long-Term Drift Effect." *Uluslararası Teknolojik Bilimler Dergisi*, c. 11, sayı. 3, ss. 170-176, Ara. 2019.
- [13] Alshamlan, H., Omar, S., Aljurayyad, R., Alabduljabbar, R. "Identifying Effective Feature Selection Methods for Alzheimer's Disease Biomarker Gene Detection Using Machine Learning." *Diagnostics*, 13, 1771, 2023. DOI: 10.3390/diagnostics13101771.
- [14] Newman D, Hettich S, Blake C, Merz C (1998). "UCI Repository of machine learning databases." <http://www.ics.uci.edu/~mllearn/MLRepository.html>.
- [15] Ergün GB, Güney S. "A Comparison Study for Image Classification and Feature Selection." 4th International Conference on Computational Mathematics and Engineering Sciences, Antalya, 20-22 April 2019.
- [16] Chen G., Chen J. "A novel wrapper method for feature selection and its applications." *Neurocomputing*, vol. 159, pp. 219-226, 2015. DOI: <https://doi.org/10.1016/j.neucom.2015.01.070>.
- [17] Chandrashekar G., Sahin F. "A survey on feature selection methods." *Computers & Electrical Engineering*, vol. 40, no. 1, pp. 16-28, 2014. DOI: <https://doi.org/10.1016/j.compeleceng.2013.11.024>.
- [18] Bugata P., Drotar P. "On some aspects of minimum redundancy maximum relevance feature selection." *Sci. China Inf. Sci.*, vol. 63, p. 112103, 2020. DOI: <https://doi.org/10.1007/s11432-019-2633>.
- [19] Thaseen IS., Kumar CA. "Intrusion detection model using fusion of chi-square feature selection and multi class SVM." *Journal of King Saud University - Computer and Information Sciences*, vol. 29, no. 4, pp. 462-472, 2017. DOI: <https://doi.org/10.1016/j.jksuci.2015.12.004>.
- [20] Cover TM., Hart PE. "Nearest neighbor pattern classification." *IEEE Transactions on Information Theory*, vol. 13, no. 1, pp. 21-27, 1967. DOI: 10.1109/TIT.1967.1053964.
- [21] Cristianini N., Ricci E. "Support Vector Machines." In: Kao MY. (eds) *Encyclopedia of Algorithms*. Springer, Boston, MA, 2008. DOI: https://doi.org/10.1007/978-0-387-30162-4_415.
- [22] Quinlan JR. "Induction of Decision Trees." *Mach. Learn.*, vol. 1, no. 1, pp. 81-106, Mar. 1986.

Migration of a Vehicle Tracking System Running on Relational Database to Big Data Environment

Ferhat KOÇER¹, Selim BAYRAKLI^{2*}

¹ R&D/Wireless Department, Huawei Telecommunications, Istanbul, Türkiye

² Department of Computer Engineering, Air Force Academy Turkish National Defence University, Istanbul, Türkiye

*¹ ferhatkocer25@gmail.com, ² hbayrakli@hho.msu.edu.tr

(Geliş/Received: 21/09/2023;

Kabul/Accepted: 22/03/2024)

Abstract: Building a high-performance and scalable system has always been a challenge in tracking systems. At the root of this problem lies the excessive and real-time data overload. This paper aims to replace traditional approaches with big data approaches. In this study, a new big data ecosystem design for vehicle tracking system architecture is presented. The aim is to process real-time and extremely fast-generated location/tracking data very fast and increase the overall system performance. The process speed performance of the newly developed big data ecosystem is compared with the table query speed performance of a relational database. As a result of the comparison, the query speed of the big data ecosystem was found to be much faster than that of the relational database management system.

Key words: vehicle tracking system, satellite tracking system architecture, big data, cassandra, kafka.

İlişkisel Veri Tabanında Çalışan Araç Takip Sisteminin Büyük Veri Ortamına Taşınması

Öz: Yüksek performanslı ve ölçeklenebilir bir sistem oluşturmak, takip sistemlerinde her zaman bir sorun olmuştur. Bu sorunun temelinde aşırı ve gerçek zamanlı veri yoğunluğu yatmaktadır. Bu makale geleneksel yaklaşımların yerine büyük veri yaklaşımlarını uygulamayı amaçlamaktadır. Bu çalışmada araç takip sistemi mimarisi için geleneksel yöntemlerin dışına çıkarak yeni bir büyük veri ekosistem tasarımı ortaya koyulmuştur. Bunu yapmadaki amaç; gerçek zamanlı ve aşırı hızlı üretilen konum/takip verilerinin çok hızlı işlenmesi ve genel sistem performansının artırılmasıdır. Yeni geliştirilen büyük veri ekosisteminin hız performansı, ilişkisel veri tabanının tablo sorgulama hız performansı ile karşılaştırılmıştır. Karşılaştırma sonucunda büyük veri ekosisteminin sorgulama hızının ilişkisel veri tabanı yönetim sistemine kıyasla çok daha hızlı olduğu görülmüştür.

Anahtar kelimeler: araç takip sistemi, uydu takip sistemi mimarisi, büyük veri, cassandra, kafka.

1. Introduction

The cumulative developments in recent history occupy an important position in human life. Technological developments brought on remarkable changes in our lives and there was a considerable increase in the number of technological software and hardware. This increase led to competition among organizations participating in the race for technology, and this in turn resulted in the introduction of the concept of the internet of things (IoT), which aims for customer satisfaction, to our lives. The internet of things can be defined as network of devices with communication channels which makes it possible to collect or send the data on media, as well as tracking and performing actions over the data [1]. Smart home systems and GPS systems can be given as examples for IoT. Since all this communication network data is borne by the internet, a massive amount of data has been generated and processing of this data has brought up a new problem [2]. This problem, in turn, has introduced us to the concept of big data. This concept was articulated for the first time by Michael Cox and David Ellsworth at the IEEE 8th Conference on Visualization, during which the researchers stated that the excessive amount of data in their study entirely filled their computer's memory as well as external hard drives, referring to the incident as the "Big Data Problem" [3].

The popularity of vehicle tracking systems has gradually increased in recent times. In general, vehicle tracking systems operate over Global Navigation Satellite Systems (GNSS). Determination of location and speed through these systems is useful in search and rescue, target detection, measurement in areas of limited sight, tourism, animal agriculture and many other fields [4].

In order to resolve the 3 main issues related to tracking of vehicles and collection and analysis of data at a single hub, the essential requirements that should be met by the data analyses are as follows:

- Real-time cleansing, addition, organization and interpretation of collected data.
- High speed in data input to the system and data output from the system.

* Corresponding author: hbayrakli@hho.msu.edu.tr. ORCID Number of authors: ¹ 0000-0002-5313-7903, ² 0000-0003-3115-6721

- For purposes of customer satisfaction, real-time transfer of information and historical data to users as well as delivery of instant alerts when necessary.

Since data producers generate data at varying formats and intervals, the size of the generated data differs as well. The storage of these varying data types and analysis of real-time streaming data is very difficult through the database management systems and architectures that are currently used. The definition of big data is storage and reading of data in a significant and scalable manner [5].

Vehicle tracking systems are technological systems which make it possible for vehicles and vessels used in road, air and marine transportation to be located and tracked via electronic hardware and software. Tracking devices calculate the vehicle's speed by determining the latitude and longitude values of the vehicle, and send the data acquired from sensors such as RFID, navigation and panic button through the TCP/IP protocol.

In [6], the performance of store and query operations in NoSQL databases is described, with estimates made for the read and write speed using both basic and sophisticated queries. The results show that the performance NoSQL based Apache Cassandra's query read/write processes outperform relational database system.

2. Design of Vehicle Tracking Systems

The structure of vehicle tracking systems is very similar to that of IoT (Internet of Things). It requires for many hardware components to be controlled and used as data producers through the internet. It may not be possible to predict the scaling for the data generated by data producers. Therefore, it was intended for the designed system to be fault-tolerant and solution-oriented. In the 2016 article by Fatih Aydemir and Aydin Cetin which refers to a structure designed for border security, a similar configuration was prepared for border security vehicles [6]. This study, however, intends to address the data intensity that has occurred in vehicle tracking systems through current technology and innovative solutions.

The closest study that has been conducted so far involves the pipeline design by Fatih Aydemir. This study aims to ensure border security and includes a pipeline design in which a data stream is provided between data resources and servers [8]. However, its design is more suited to military purposes. Our study, on the other hand, rather focuses on the field of vehicle tracking. The study is based on the common protocol and modes of operation of vehicle tracking systems.

3. Real-Time Reading of Data from Multiple Resources on The Speed Layer

Many solutions have been created to provide optimization for enabling data transfer, and Apache ActiveMQ is one of these. The data is read and distributed by Apache ActiveMQ and the distributed data is captured by Apache Spark; it is then introduced to the Map/Reduce application and served over ActiveMQ to NodeJS as a topic associated with the JSON language for analysis of processed data such as Web service, mobile access and Web interface.

3.1 ActiveMQ

The ActiveMQ structure involves producers, consumers and brokers. Data producers provide the resource for the data and transmit the data to brokers. Depending on the state of the system, brokers send the data to consumers. Messages can be sent in the queue structure or with a topic. Flow control is performed at the brokers and can be shut off if desired. When flow control is on, the producer enables data delivery by receiving a confirmation message from the consumer. This ensures for the data to be retained at the broker in unfavorable conditions such as a full cache at the receiver. When flow control is off, however, the brokers remain connected to any slow consumers and stopping of the system is prevented. If a fast receiver sends a message to a slow or blocked receiver, the sent message changes direction and the system continues to operate through data transmission to the fast consumer [9].

Devices which are interconnected over TCP/IP and send data in seconds are kept in parallel to Java. Data blockages are prevented through processing at a minimum level. The processing of the collected raw data is carried out with Apache Spark. The data captured with simultaneously operating threads is sent with a queue that is associated with ActiveMQ. In this case, port listeners act as producers.

3.2 Apache Spark

Real-time reading and processing of data in vehicle tracking systems does not always yield all of the necessary solutions. Various capabilities such as interpretation, grouping and customization of the read data, as well as

interventions on it, are required. In order to achieve these, it was intended to perform distributed processing on large amounts of data through the use of Apache Spark. Apache Spark possesses the capability of real-time data processing and retains incoming requests until the action function is recalled; it keeps the acquired data in temporary storage and continues to operate.

The data flow library of Apache Spark is Apache Spark Streaming. In addition to locally supporting many messaging systems such as Kafka, Flume, Kinesis and Sockets, Apache Spark Streaming also supports data reading from external resources [10].

Javed Awan et al. aimed to support retail companies create personalized deals and promotions for their customers, using a big data framework that allows them to handle huge sales volumes with more efficient models [11]. Using the Apache Spark big data framework, they trained two machine learning models: linear regression and random forest to forecast future pricing and sales. At first, they implemented the two models without using the Spark framework and achieved accuracies of 68% and 74%, respectively. Later they trained these models on the Spark machine learning big data framework and achieved an accuracy of 72% for the linear regression model and 81% for the random forest model.

3.3 NodeJS

NodeJS is a popular server-side programming language which can work asynchronously, has a language based on Javascript as well as a powerful, fast and flexible structure, and is integrated with many current libraries [12].

3.4 Openlayers

Openlayers has an open source and powerful mapping structure. It can be directly integrated into maps such as Google Map, BingMap and OpenMap, as well as an external map service. It has a structure designed on layers. Openlayers is a map layering library developed with Javascript. Data which is broadcast with NodeJS is captured with Javascript on the client side and instantaneously reflected on maps through use of the required APIs of Openlayers.

4. Recording Meaningful Data in The Database

The data which is read through being distributed according to the server load status at the consumer with Spark is both broadcast over NodeJS at the speed layer and recorded in the database. At the stage of recording, it is subjected to the Map/Reduce processes of Apache Spark. Apache Cassandra, which carries out column-oriented recording in the NoSQL structure that serves as a big data solution, was selected as the database. Compared to relational databases, NoSQL databases are more advantageous in terms of speed [13]. They are more suitable for batch processing and the internet of things. Various industrial requirements, continuous data production, digitalization of existing data types, consolidation and each similar factor form different resources for big data [14].

4.1 Apache Cassandra

Apache Cassandra is a scalable, open source NoSQL database management system which is designed on the basis of the Apache Cassandra column structure and can be applied on distributed systems. Apache Cassandra is also used by some large companies such as Apple (10 PB of data storage with 75,000 nodes), Netflix (420 TB of data and over 1 trillion daily requests with 2,500 nodes) and eBay (100 TB of data with over 100 nodes) [15].

Apache Cassandra is designed to process big data over multiple data. The multiple node connections of data established between clusters ensures for it to be fault-tolerant. Each node communicates by using the Gossip protocol between pairs and status information is updated continuously. Apache Cassandra allows for an authorized user to access and query a node at any data center and write data by means of the CQL language.

4.1.1 Key Structures of Apache Cassandra

Node: The building block of Cassandra which retains the information as to where the data is kept.

Data center: The group formed by related nodes. Data centers can be virtual or real data centers. Different workloads should use different data centers; this applies for both physical and virtual data centers.

Cluster: Contains one or more data centers. **Commit log:** All data is first written in the commit log for purposes of durability. Following transfer to SSTables, they can be recorded, deleted or retained for reuse.

CQL Table: Tables formed by rows that are entered in the columns with the primary key.

4.1.2 The Components Required for Configuration of Apache Cassandra

Gossip: The peer-to-peer protocol over which the status and location information of nodes are periodically shared among themselves for exploratory purposes.

Partitioner: Determines in which clusters and nodes the data segment copies of nodes will be kept. A partitioner is the function which subjects the relevant row and its primary key to the hash process.

Replication factor: The total replication number for clusters. A replication factor indicates only one-time replication for each row in the node. The replication amount increases in proportion to this value. All copies are equally important and there are no primary or backup copies. In general, the number of copies is higher than 1 and lower than the number of clusters.

System operating tables: These allow for changes to be made on the main tables in order to modify the storage properties through use of the CQL language.

Replica placement strategy: Recording copies are kept in multiple nodes. Replica placement strategy determines the location of the nodes in which the copies will be kept.

Snitch: Defines the machine groups at the data center and the topologies in which replica placement strategy is used. Cassandra.yaml configuration file is the main configuration file. It is the file in which many adjustments such as property identification for clusters, cache parameters for their tables, resource use parameters for performance, timeout, client connection limitations, backup and security are carried out.

5. System Design and Modules

The basis of the structure design relies on adaptability, flexibility and sustainability of the system. The properties which the system should possess in the structure design are as follows:

- minimizing the interaction time between clients and devices,
- performing a higher number of tasks with a lower amount of load through correct use of system resources,
- increasing data reliability,
- performing a higher number of tasks with a lower amount of work through correct use of system resources,
- facilitate system growth in parallel to data growth by forming a horizontally scalable system.

Vehicle tracking systems require real-time and bi-directional processing on real big data. Therefore, Apache Spark was chosen to process the real-time data. The data of vehicle tracking hardware, which is sent with TCP over GSM, was received with multiple sockets via ports and the use of parallel programming capabilities. Due to being open source, powerful, free of charge and fault-tolerant, Apache ActiveMQ messaging service was chosen to distribute the received data over servers. For analysis of the raw data captured with ActiveMQ, Apache Spark was chosen due to being the most suitable structure for real-time parsing and easy integrability with Cassandra, which is being used to store the data.

5.1 Design of the Structure

In structure design, each segment should perform its duty in the form of small modules and the system should be as sustainable and scalable as possible. The stages of the structure completed according to this principle are as follows.

Stage 1: The raw input received from multiple data providers with ActiveMQ is assimilated with the queue and in a manner which is independent from the receiver.

Stage 2: The data which is read over the queue is combined with Apache Spark and subjected to the Map/Reduce process.

Stage 3: The data which is analyzed and interpreted with Spark is assimilated and broadcast if it has a receiver, and all data is recorded in the Cassandra database.

Stage 4: The parsed data is read at the consumer with NodeJS and sent to the relevant user with the Socket.IO library over WebSocket. NodeJS allows application development on the server side with the JavaScript programming language and is suitable for asynchronous tasks. Its powerful structure ensures for it to process instantaneous operations with low resource consumption and high performance.

Stage 5: Multiple map integration is performed through use of Openlayers within the web page with a user interface. Openlayers is an open source, free of charge map layering library which is integrated with multiple maps

and developed with Javascript. Data which is broadcast with NodeJS is captured with Javascript on the client side and instantaneously reflected on maps through use of the required APIs of Openlayers. The stages provided above show the data analysis and its reflection on the user panel; the flow chart of the whole process is given in Figure 1.

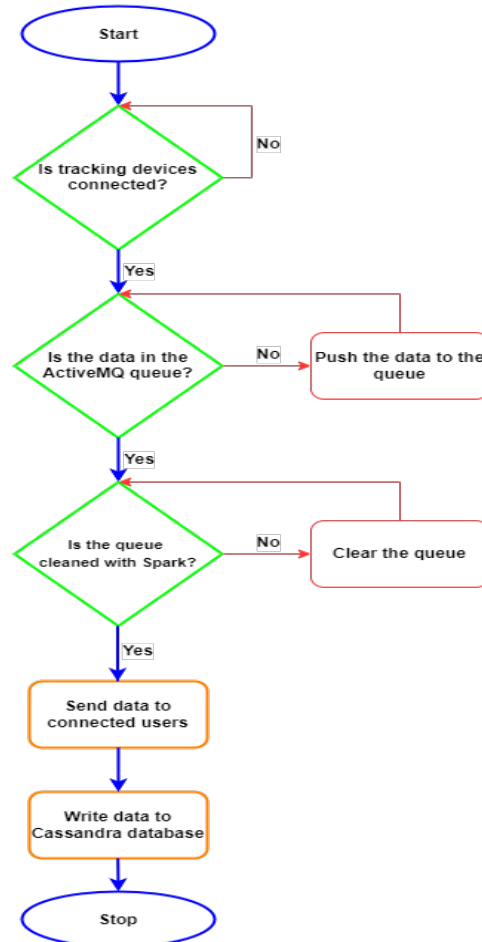


Figure 1. Flow chart of the migration process

5.2 Instantaneous Delivery of Data

In instantly delivered data, it is possible for there to be congestion and bottlenecks in the system due to changes in the data transmission frequency of data providers. In order to prevent this, the listener processes each received message at the minimum level before transferring it to the queue. Each connection on the port is assigned to the independent thread and the producer initiates data flow by using the capabilities of parallel programming.

The data from the data providers is received through use of ServerSocket and Socket classes with TCP. Each device that establishes a connection continues the process as an independent thread with a derivative object from its own Socket class. The data which is read over the port is transferred to the queue in a similar manner to threads. A failover operation is performed during data transfer with ActiveMQ to ensure data delivery to servers in situations such as interruption of instantaneous communication or timeout among servers.

5.3 Processing, Interpretation and Cleansing

In vehicle tracking systems, it is not always sufficient for the data to be instantaneously read and processed. Various capabilities such as interpretation, grouping, customization and intervention on the read data should also be provided. In order to achieve these capabilities, it was intended to perform distributed processing on large-scale

data through the use of Apache Spark. Apache Spark keeps incoming requests until the action function is recalled (lazy evaluation). It keeps the acquired findings in temporary storage and continues to operate without waiting.

Spark Stream forms a DStream (Discretized Stream) for the streaming data in the Apache ActiveMQ and Apache Spark integration. DStreams are series of the same type in which RDDs (Resilient Distributed Datasets) are continuously created. The data on ActiveMQ are deleted from the queue after the required operations are carried out. This also ensures cleansing in the queue.

5.4 Data Storage and Broadcasting

Apache Spark and Cassandra integration was provided by the Spark Cassandra Connector library. Due to operating in coordination with Apache Spark, this library also carries out recording processes with Map/Reduce. In order for the data of end users to be shown in real time over the system, the data is broadcast in JSON format over ActiveMQ before being recorded in the database. When broadcasting is performed with a topic, delivery to the subscribers is only carried out if the broadcast has any current subscribers. In order to capture the broadcast data, NodeJS acts as an ActiveMQ client. In order to prevent unnecessary use of system resources through broadcasting of all data, the user information which is active over the system is delivered to the software which interprets data over ActiveMQ with NodeJS.

NodeJS pairs the relevant data with the relevant users. Socket.IO was used to provide communication between the end user and the web client. With Socket.IO, a request can be returned in case of data arrival on the server side when there are no requests on the user side. Socket.IO allows bi-directional and simultaneous communication. Location data captured on the client side is positioned and reflected on the map through use of Openlayers.

Requests such as speed limit adjustment, region identification and data transmission to sensors connected to vehicle tracking hardware (VTH) are required for VTH on the data client side. It is required for the system to send a request to the server on the web client side. In this case, the operations are carried out in the opposite direction to the process of data acquisition from VTH. The web client sends its message to NodeJS with Web Socket. NodeJS attaches a queue with ActiveMQ and performs broadcasting. The message is read over Spark and recorded in Cassandra with Resilient Distributed Datasets (RDDs); delivery to the relevant devices is simultaneously carried out over ports and the TCP listener.

5.5 Configuration

After the reading and interpretation operations in the data sources are concluded, the data is transmitted in JSON format. The data acquired from VTH and other sensors is recorded in the table of locations through use of the IMEI (International Mobile Equipment Identity) number of VTH and the time at which the incident occurred as a primary key. The data which is sent to web clients on the NodeJS side with Socket.IO is reflected on the maps through use of the Javascript APIs of Openlayers. The map shows the location, speed, status and direction information for vehicles with icons (Figure 2).



Figure 2. Openlayers map view

6. Results and Conclusion

The conducted research led to Apache Cassandra, a column-oriented NoSQL solution, to be chosen as the database for recording the data. Apache Cassandra was preferred due to being fault-tolerant, distributed, scalable and compatible with many software products. This study involves a comparison between Apache Cassandra and the relational database MYSQL. The same tables were generated on the two databases. MYSQL and Cassandra were installed on two different virtual machines of the same properties. The virtual machines in question ran the Ubuntu 14.04 LTS operating system. Cassandra was chosen because it was fast in adding, deletion and reporting processes, as well as allowing operations over the columns. It is designed to provide high write and read throughput. It excels in write-heavy workloads and can handle a large number of concurrent writes across the distributed cluster. With this feature, Apache Cassandra is perfect for targeted work.

The results of the INSERT SQL-CQL queries ran on the databases are shown in Figure 3. It is impossible for the INSERT operation intensity to be predicted for IoT structures such as vehicle tracking systems. It is critical for the operations to be performed in the lowest amount of time possible in order for the system resources to be used correctly and data loss to be prevented. The INSERT operations which were carried out indicated that Cassandra yielded better results in terms of speed for each query directed at the two database systems installed on the same type of system.

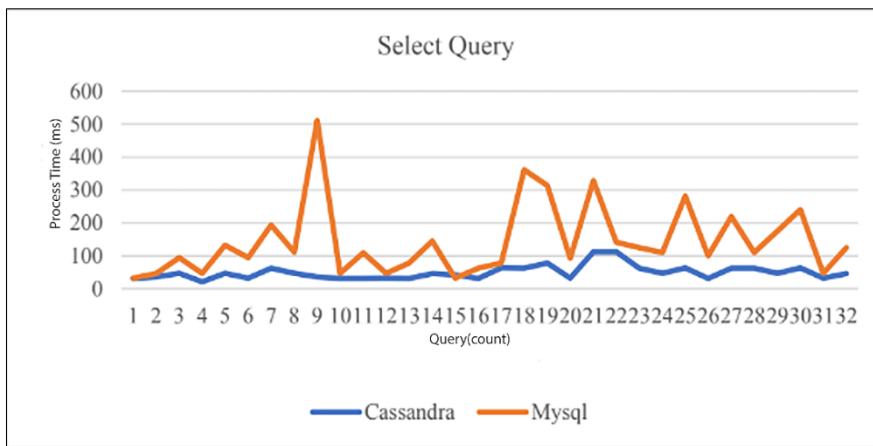


Figure 3. MYSQL-Cassandra record fetch time comparison

Data records from 16 different devices were kept for a period of 6 months for both systems. The following queries were ran in the two systems on completely identical data records and the relevant time was measured (Figure 4).

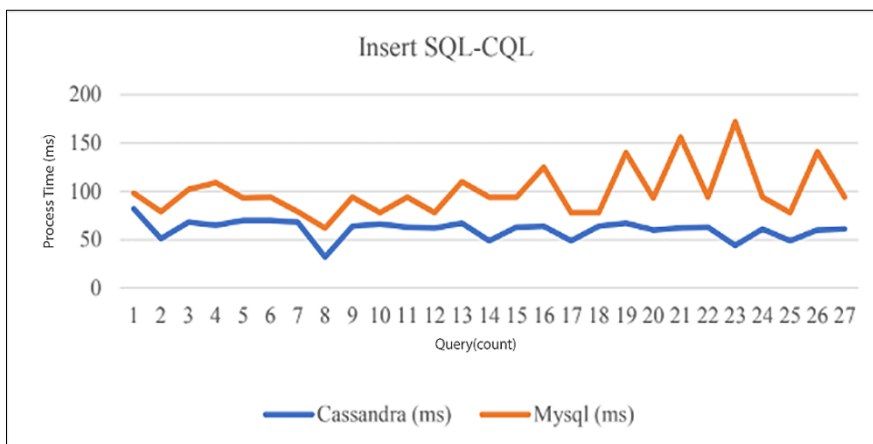


Figure 4. MYSQL-Cassandra insert record comparison

References

- [1] Giusto D, Iera A, Morabito G, Atzori L. (Eds.). The internet of things: 20th Tyrrhenian workshop on digital communications. New York, USA: Springer Science & Business Media, 2010.
- [2] Goes PB. Design science research in top information systems journals. *MIS Q.: Manag. Inf. Syst.* 2014; 38(1): iii-viii.
- [3] Cox, M., & Ellsworth, D. Application-controlled demand paging for out-of-core visualization. In: *Proceedings. Visualization'97* (Cat. No. 97CB36155); 1997 October; Phoenix, AZ, U.S.A. New York, USA: IEEE. pp. 235-244.
- [4] Koca B, Ceylan A. Uydu konum belirleme sistemlerindeki (GNSS) güncel durum ve son gelişmeler [Current Status and Recent Developments in Global Positioning Satellite Systems (GNSS)]. *Geomatik* 2018; 3(1): 63-73.
- [5] Eger Ö. "Big Data'nın (Büyük Veri) Endüstriyel Kullanımı". Türkiye'nin endüstri 4.0 platformu. 2017. <https://www.endustri40.com/big-datanin-buyuk-veri-endustriyel-kullanimi> (accessed March 28, 2018).
- [6] Kumar, M. Sandeep. "Comparison of NoSQL database and traditional database-an emphatic analysis." *JOIV: International Journal on Informatics Visualization* 2.2 (2018): 51-55.
- [7] Aydemir F, Cetin A. Designing a Pipeline with Big Data Technologies for Border Security. *Mugla Journal of Science and Technology* 2016; 2(1): 98-101.
- [8] Aydemir F. Sınır Güvenliği İçin Büyük Veri Teknik ve Teknolojileri ile Boru Hattı Tasarımı [Designing a pipeline with big data Techniques and technologies for border security] (Unpublished Master Thesis). Gazi University, Ankara, Turkey, 2012.
- [9] Apache Active MQ, 2015. <https://activemq.apache.org> (accessed October 28,2018).
- [10] Apache Spark. Apache Spark-Unified Analytics Enginefor Big Data. Apache software foundation. 2018. <https://spark.apache.org/> (accessed November 11, 2018).
- [11] Javed Awan M, Mohd Rahim MS, Nobanee H, Yasin A, Khalaf OI. A big data approach to black friday sales. *Intell. Autom. Soft Comput.* 2021; 27(3): 785-797.
- [12] Linux foundation. Node.js. 2018. <https://nodejs.org> (accessed March 29, 2018).
- [13] Öztürk S, Atmaca HE. İlişkisel ve ilişkisiz olmayan (NoSQL) veri tabanı sistemleri mimari performansının yönetim bilişim sistemleri kapsamında incelenmesi. [The examination of relationaland non-relational (NoSQL) database system's architectural performances in terms of management of information systems]. *Bilişim Teknolojileri Dergisi [Journal of Information Technologies]* 2017; 10(2): 199-209.
- [14] Aktan E. Büyük veri: Uygulama alanları, analitiği ve güvenlik boyutu [Big data: Application areas, analytics and security dimension]. *Ankara Üniversitesi Bilgi Yönetimi Dergisi [Ankara University Journal of Information Management]* 2018; 1(1): 1-22.
- [15] Apache Cassandra. "Apache Cassandra Unified Analytics Engine for Big Data". Apache software foundation. 2016. <http://cassandra.apache.org/> (accessed November 29, 2018).

Digital Pathology Image Reconstruction with Alternating Direction Method of Multipliers using Wavelet, Contourlet and Shearlet Transforms

Esra ŞENGÜN ERMEYDAN^{1*}, İlyas ÇANKAYA²

^{1,2} Department of Electrical and Electronics Engineering, Faculty of Engineering and Natural Sciences, Ankara Yıldırım Beyazıt University, Ankara, Türkiye

*¹ esrasengunermeydan@aybu.edu.tr, ² ilyas.cankaya@aybu.edu.tr

(Geliş/Received: 27/09/2023;

Kabul/Accepted: 02/03/2024)

Abstract: Digital pathology refers to image-based environment in which acquisition, extraction and interpretation of pathology information is supported by computational techniques. It has a huge potential to facilitate the diagnostic process, however, big data size and necessity of large storage areas are challenging. Therefore, in this research, Compressed Sensing (CS) scheme is studied with digital pathology images in order to reduce the amount of data for reconstruction. CS requires the sparsity of signals for a successful recovery which means that different sparsifying bases can alter the final performance. Wavelet, Contourlet and Shearlet Transforms are investigated to sparsify the digital pathology images, it is seen that Contourlet Transform is superior. Alternating Direction Method of Multipliers (ADMM) is chosen for reconstruction since it is a robust and fast convex optimization method. Despite the fact that digital pathology images are less sparse than classical images, CS reconstruction is satisfactory, which emphasizes the potential of CS for digital pathology. This study can be pioneering in the field of CS with digital pathology so it can encourage further studies of CS based imaging with different type of microscopes or at different wavelengths.

Key words: Compressed Sensing, Digital Pathology, Wavelet Transform, Contourlet Transform, Shearlet Transform.

Dalgacık, Contourlet ve Shearlet Dönüşümleri Kullanılarak Çarpanların Alternatif Yön Yöntemi ile Dijital Patoloji Görüntüsü Geriçatılması

Öz: Dijital patoloji, patoloji bilgilerinin elde edilmesi, çıkarılması ve yorumlanmasının hesaplamalı tekniklerle desteklendiği görüntü tabanlı ortamı ifade eder. Teşhis sürecini kolaylaştırma açısından büyük bir potansiyele sahiptir ancak büyük veri boyutu ve geniş depolama alanlarının gerekliliği zorlayıcıdır. Bu nedenle, bu araştırmada, yeniden yapılandırma için veri miktarını azaltmak amacıyla Sıkıştırılmış Algılama (CS) şeması dijital patoloji görüntüleri ile incelenmiştir. CS, başarılı bir kurtarma için sinyallerin seyrekliğini gerektirir; bu, farklı seyrekleştirici bazların nihai performansı değiştirebileceği anlamına gelir. Dijital patoloji görüntülerini seyrekleştirmek için Dalgacık, Contourlet ve Shearlet Dönüşümleri incelenmiştir, Contourlet Dönüşümünün üstün olduğu görülmüştür. Geriçatma için Alternatif Yön Çarpan Yöntemi (ADMM) sağlam ve hızlı bir dışbükey optimizasyon yöntemi olduğundan seçilmiştir. Dijital patoloji görüntülerinin klasik görüntülere göre daha az seyrek olmasına rağmen CS geriçatması tatmin edicidir, bu da CS'nin dijital patoloji için potansiyelini vurgulamaktadır. Bu çalışma, dijital patoloji ile CS alanında öncü olabilir ve farklı tipte mikroskoplarla veya farklı dalga boylarında CS tabanlı görüntülemeye yönelik daha ileri çalışmaları teşvik edebilir.

Anahtar kelimeler: Sıkıştırılmış Algılama, Dijital Patoloji, Dalgacık Dönüşümü, Contourlet Dönüşümü, Shearlet Dönüşümü.

1. Introduction

Medical imaging is a general term for using several different technologies to view the human body or human specimens in order to diagnose, monitor, or treat medical conditions. Through medical images, the area of the human body that is invisible or too small to be observed with the naked eye can be visualized and examined. Medical images provide very important data in the treatment process. Digital pathology is a dynamic branch of medical imaging which enables the acquisition, extraction and interpretation of pathology information using a very high-resolution picture of a microscope slide containing a sample of tissue in a digital environment [1]. The collaboration and engagement of professionals from different medical institutions are facilitated by digital pathology methods. The clinicians in other locations can easily be consulted for second opinion and obviously time and cost for diagnose are saved considerably. Besides, the risks associated with physically transporting slides are eliminated. The COVID-19 pandemic's emphasis on leveraging digital infrastructure for remote patient monitoring [2] also underscored the potential of digital pathology, which can allow pathologists to analyze and diagnose disease from anywhere, improving both healthcare accessibility and efficiency. Moreover, there are lots of studies to develop automated pathology techniques to make the diagnosis less subjective and less time consuming [3]. It is estimated that the global digital pathology market size will reach USD 1.74 billion by 2030,

* Corresponding author: esrasengunermeydan@aybu.edu.tr. ORCID Number of authors: ¹ 0000-0002-5953-4301, ² 0000-0002-6072-3097

registering a CAGR of 7.5% [4]. However, digital pathology slide images are big in size and need large storage areas therefore both the storage and the transmission of pathological images for diagnosis and monitoring purposes are still challenging. One of the solutions for reducing the data is compressing the images after they are sampled at Nyquist rate [5,6]. On the other hand, the drawback of these conventional compression methods is that acquiring too much data in a fast way is hard and quite expensive due to physical constraints. Besides, there is an obvious question asking whether there is a way of getting the data which contains information directly. The efforts for answering this question have led to a novel sensing paradigm called as Compressed Sensing (CS) in 2006. CS basically claims that signals can be reconstructed with lower sampling rates than Shannon-Nyquist theorem dictates [7, 8]. In other words, the signal is compressed at the time of sensing [9] so the number of measurements for reconstruction, acquisition time and energy are reduced.

CS has applied to a wide range of areas such as astronomy, communications, signal processing and imaging beyond the visible band. It is claimed that CS has a big potential on medical imaging [10]. In fact, first application of CS was reducing the measurement time of data acquisition for MRI [11]. The technology using CS in MR imaging has been quite mature so that in 2017, FDA has approved the clinical usage of Compressed Sensing MRI [12]. It is indicated that cardiac cine imaging is reduced from 4 minutes to just 16 seconds if CS is applied to acquire the required data. In addition to MRI, compressed sensing methods are also intensively studied in medical fields such as x-ray, computed tomography, ultrasound imaging, and compression of ECG/EEG signals [10]. Another application area of CS is the possibility of imaging with single-pixel architecture at different wavelengths such as THz or infrared [13]. Advances in CCD and CMOS technology made it much easier and cheaper to obtain high resolution images in digital cameras. However, at wavelengths where silicon cannot be used, cameras are still too expensive and/or too large in size. Therefore, there is a need for inexpensive and accessible microscopes that can be used for imaging biological samples, for quality control in industry or for research in materials science. In order to satisfy this need, single pixel microscope with compressed sensing techniques has drawn attention in academia [14]. Besides, CS with different type of microscopes such as electron, fluorescence, photoacoustic and laser scanning are also promising since they reduce the measurement time and increase the quality of imaging [15–17]. In this study, compressed sensing of digital pathology images with different sparsifying transforms is considered. Wavelet, Contourlet and Shearlet Transforms are studied as sparsifying bases. Contourlet and Shearlet Transforms are multi resolution and multi scale, therefore these transforms are attractive for medical imaging applications. Alternating Direction Method of Multipliers (ADMM) [18] is selected for the reconstruction part. It is a robust convex optimization algorithm that breaks the problem into smaller pieces, each of which is easier to handle. In the previous work [19], CS based single pixel microscope configuration was studied, Gaussian and Bernoulli random matrices were used as measurement matrices, during that study it was observed that, random matrices require large storage and cause slow reconstruction. Moreover, total variation and ℓ_1 norm minimization algorithms which were used for recovery part need the inverse matrix of the sparsifying transform. However, obtaining a compact single matrix when multi resolution and multi scale transformation is not possible. Therefore, in this study, reconstruction algorithm is changed to ADMM, another outcome of this choice is the possibility of studying higher resolution images than the previous work [19]. The performance of compressed sensing of digital pathology images is compared with classical peppers image and the quality of reconstruction is evaluated using different image similarity indices such as Structural Similarity Index (SSIM) [20], Haar Wavelet-Based Perceptual Similarity Index (HaarPSI) [21] and Peak Signal to Noise Ratio (PSNR). CS scheme ensures compression during the acquisition of data therefore digital pathology images could be reconstructed using fewer data, besides this study can encourage CS based microscopic configurations beyond the visible band or with different type of microscopes.

2. Materials and Methods

2.1 Compressed Sensing

Compressed Sensing theory [7], [8] claims that if a signal is sparse or compressible, then the signal can be reconstructed using considerably less data than Shannon-Nyquist theorem states [5]. The data acquisition process can be modeled as in equation 1:

$$z = Mx \quad (1)$$

where z are measurements, M is the measurement matrix or masking operator, x is the signal that is desired to be reconstructed. In CS, the measurement matrix M is not full rank, meaning that there will be infinitely many solutions corresponding to same z due to the null space of M , so the reconstruction problem is an ill posed problem, however, these kind of problems can be solved by convex optimization methods [8], [9] thanks to the sparsity of

the signal x . The problem in Equation 1 is known to have a unique sparse solution if the masking operator M satisfies the Restricted Isometry Property (RIP) [22] which geometrically means that the projection of M preserves the geometry of the set of sparse signals. Designing a combinatorial RIP matrix is unfortunately NP hard problem; however random matrices are known to satisfy RIP with high probability [23]. Although the problem of masking operator with RIP can be solved with random matrices, another key assumption for a successful reconstruction is that the signal x should be sparse. In many real-life applications, the signal x is not directly sparse but it becomes sparse if a suitable transform is applied. For images, Wavelet Transform (WT) [24] is the most prominent sparsifying transform, it is at the heart of JPEG2000 [6] which is widely used compression scheme. On the other hand, for cartoon-like images such as digital pathological ones, multilevel and multi scale transforms like shearlets and contourlets can represent the edges and curves better that are present in the image [25], [26].

2.2 Wavelet, Contourlet and Shearlet Transforms

Wavelet Transform is generally defined as a technique in which a signal/image is analyzed in the time/spatial domain by using shifted or contracted versions of a basis function called the mother wavelet. By using a set of wavelet orthonormal basis functions constructed by Mallat and Daubechies [24], [27], [28] both the frequency and time/spatial information can be captured simultaneously. Therefore, following the introduction of wavelets, they have been applied to a diverse range of areas from seismic signal analysis to data compression, medical imaging, pattern recognition, computer graphics. Although it is used in a wide range of areas, one of the most popular applications of WT is in image processing. It specifically sparsifies the images by decomposing it in low and high frequencies. The detail parts of the image are represented by high frequencies whereas smooth parts of the images are decomposed in the low frequencies. In WT, the mother wavelet ψ is dilated and translated to form a basis for image representation. In other words, the high frequency part of image is stored in the wavelet function ψ_{jk} and the low frequency part is described by the scaling function φ , as in (2) and (3):

$$\varphi_{j,k}(x) = 2^{j/2}\varphi(2^jx - k) \quad (2)$$

$$\psi_{j,k}(x) = 2^{j/2}\psi(2^jx - k) \quad (3)$$

Scaling functions are orthogonal to wavelet functions ($\langle \varphi_{j,k}(x), \psi_{j,k}(x) \rangle = 0$ for $k \neq l$). N-point Discrete Wavelet Transform of a function $f(x)$ can be written as in the equations (4) to (6) [29]:

$$f(x) = \frac{1}{\sqrt{N}} \left[\sum_{k=0}^{2^j-1} T_\varphi(j_0, k) \varphi_{j_0,k}(x) + \sum_{j=0}^{J-1} \sum_{k=0}^{2^j-1} T_\psi(j, k) \psi_{j,k}(x) \right] \quad (4)$$

$$T_\varphi(j_0, k) = \langle f(x), \varphi(x) \rangle = \frac{1}{\sqrt{N}} \sum_0^{N-1} f(x) \overline{\varphi(x)} \quad (5)$$

$$T_\psi(j, k) = \langle f(x), \psi_{j,k}(x) \rangle = \frac{1}{\sqrt{N}} \sum_0^{N-1} f(x) \overline{\psi_{j,k}(x)} \quad (6)$$

The functions $T_\varphi(j_0, k)$ are called scaling or approximation/low frequency coefficients and $T_\psi(j, k)$ are called wavelet or detail/high frequency coefficients, $\overline{\varphi(x)}$ and $\overline{\psi_{j,k}(x)}$ are the duals of $\varphi(x)$ and $\psi(x)$. The Wavelet Transform is a powerful and right tool for approximating and analyzing one-dimensional piecewise smooth signals. Thanks to the separable extension from 1-D bases, it can isolate the discontinuities at edge points for images. However, its performance degrades for contours or curvilinear singularities, therefore directional representational transforms such as contourlets and shearlets are introduced [25], [26]. Contourlet Transform uses non-separable filterbank approach in order to capture and represent the directional information present in the images. There are mainly two parts to obtain the Contourlet Transform representation of an image. In the first part, the image is decomposed into sub-bands by using Laplacian Pyramid and point discontinuities in the sub-band decomposition stage are captured. In the second part, the details of the image are analyzed by directional filter banks [25]. Shearlet Transform detects image saline features such as directional singularities and geometrical features by defining the direction using shearing matrices. This transform forms an affine system by generating one single function which is dilated by a parabolic scaling and a shear matrix and translated in the time domain [26]. The multiscale of shearlets are obtained using A_a the parabolic scaling matrix and S_s the shear matrix for $a > 0$ and $s \in \mathbb{R}$ [26] and the resulting shearlet system is given by (7) and (8) :

$$A_a = \begin{pmatrix} a & 0 \\ 0 & \sqrt{a} \end{pmatrix} S_s = \begin{pmatrix} 1 & -s \\ 0 & 1 \end{pmatrix} \quad (7)$$

$$\{\psi_{jkm}(x) = 2^{-j\frac{3}{2}}\psi(S_{-k}A_{4-j}x - m): j, k \in \mathbb{Z}, m \in \mathbb{Z}^2\} \quad (8)$$

where ψ is a shearlet, j , k and m denote the scale, shear and translation parameters, respectively. In this study, to see the practical perspective of these three sparsifying transforms, a synthetic image of letters O, G, R and S which have contours or curvilinear properties have been considered. The transform coefficients have been computed and depicted in Figure 1.

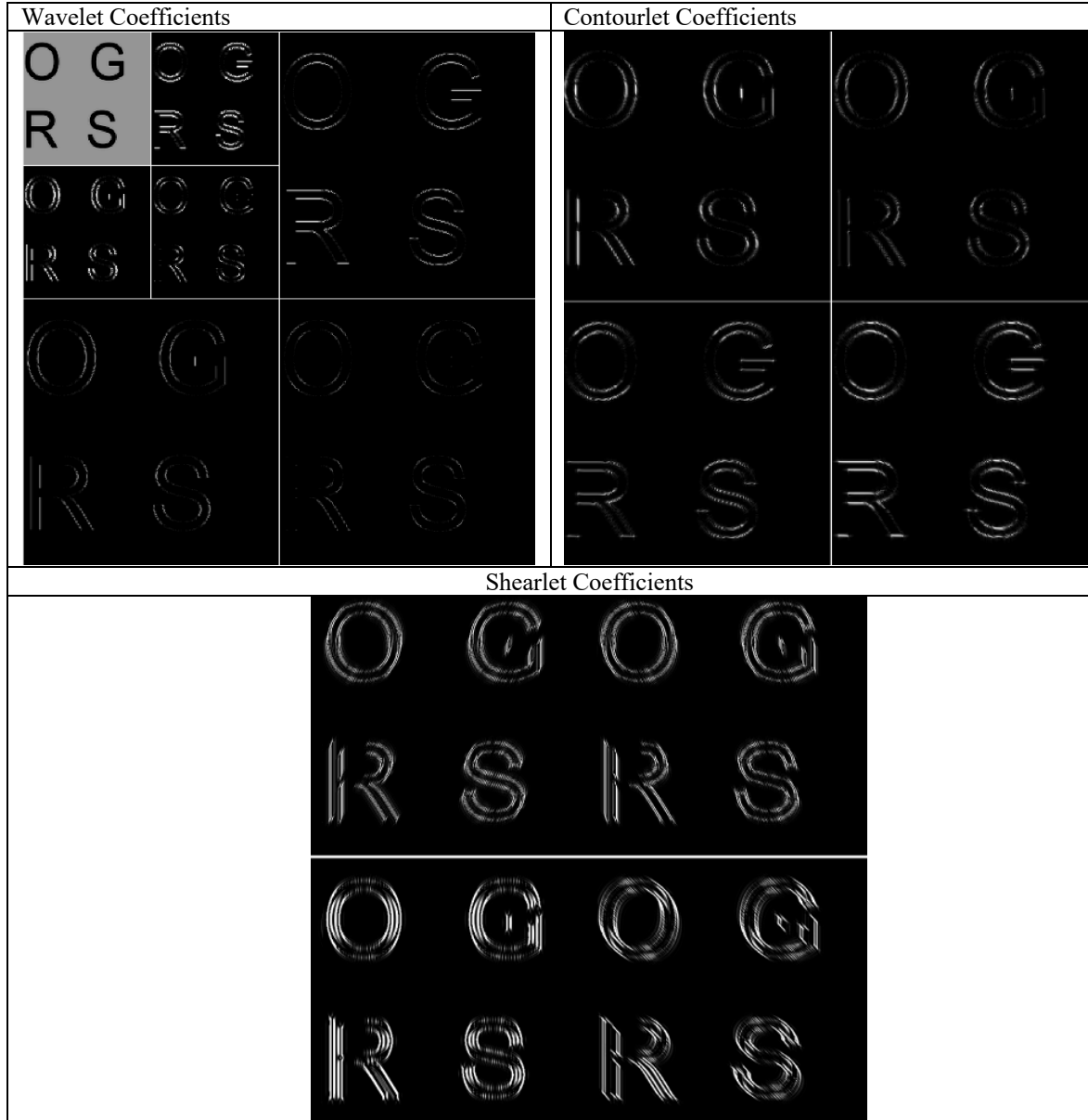


Figure 1. Wavelet, Contourlet and Shearlet Coefficients illustrations for letters O, G, R and S.

2.2 Alternating Direction Method of Multipliers (ADMM)

ADMM is a powerful convex optimization algorithm that combines the advantages of augmented Lagrangian and dual decomposition [18], [30]. ADMM is closely related to the Bregman iterative algorithms for ℓ_1 problems, proximal methods and Douglas–Rachford splitting algorithms in the literature. The algorithm is basically formed on a decomposition–coordination procedure with a goal to find a solution to a large scale problem by solving small local subproblems [18]. ADMM solves the following constrained optimization problem:

$$\text{minimize } f_1(x) + f_2(x) \text{ subject to } Ax + By = c \quad (9)$$

where $x \in \mathbb{R}^n$, $y \in \mathbb{R}^m$, $A \in \mathbb{R}^{p \times n}$, $c \in \mathbb{R}^p$, f_1, f_2 are convex functions. As it is seen, the main difference of (9) from the general linear equality-constrained problem is that the variables have been split into two parts.

The problem in (9) takes the form in (10) for compressed sensing or lasso or our image reconstruction problem:

$$\text{minimize } \tau \|z - Mx\|_2^2 + \|y\|_1 \text{ subject to } y = \Phi x \quad (10)$$

where z are measurements, M is masking operator and Φ is the sparsifying operator which is Wavelet, Contourlet or Shearlet Transform in our study. There are three main steps in ADMM: x -minimization step, y -minimization step and dual variable update. As the name of ADMM implies, the variables x and y are updated in an *alternating* manner [18]. The steps of ADMM of the convex minimization problem in (10) can be expressed as in the equations (11) to (13):

x -minimization step:

$$x^{k+1} = \operatorname{argmin}_x \tau \|z - Mx\|_2^2 + \frac{\rho}{2} \|y^k - \Phi x + u^k\|_2^2 \quad (11)$$

y -minimization step:

$$y^{k+1} = \operatorname{argmin}_y \|y\|_1 + \frac{\rho}{2} \|y - \Phi x^{k+1} + u^k\|_2^2 \quad (12)$$

dual variable update step:

$$u^{k+1} = u^k + y^{k+1} - \Phi x^{k+1} \quad (13)$$

where u is the dual variable and the penalty parameter $\rho > 0$.

3. Results

By using CS scheme, we have reconstructed peppers and Breast Cancer digital pathology image taken from TCGA [31] under different sparsifying transforms with MATLAB. As it is stated, Wavelet, Contourlet and Shearlet Transforms are used as sparsifying bases and the compression ratio is 8, in other words, 12.5 % of the pixels in the ground truth is used for reconstruction. The original and reconstructed images for 512×512 peppers and digital pathology image are given in Figure 2 and Figure 3 respectively.

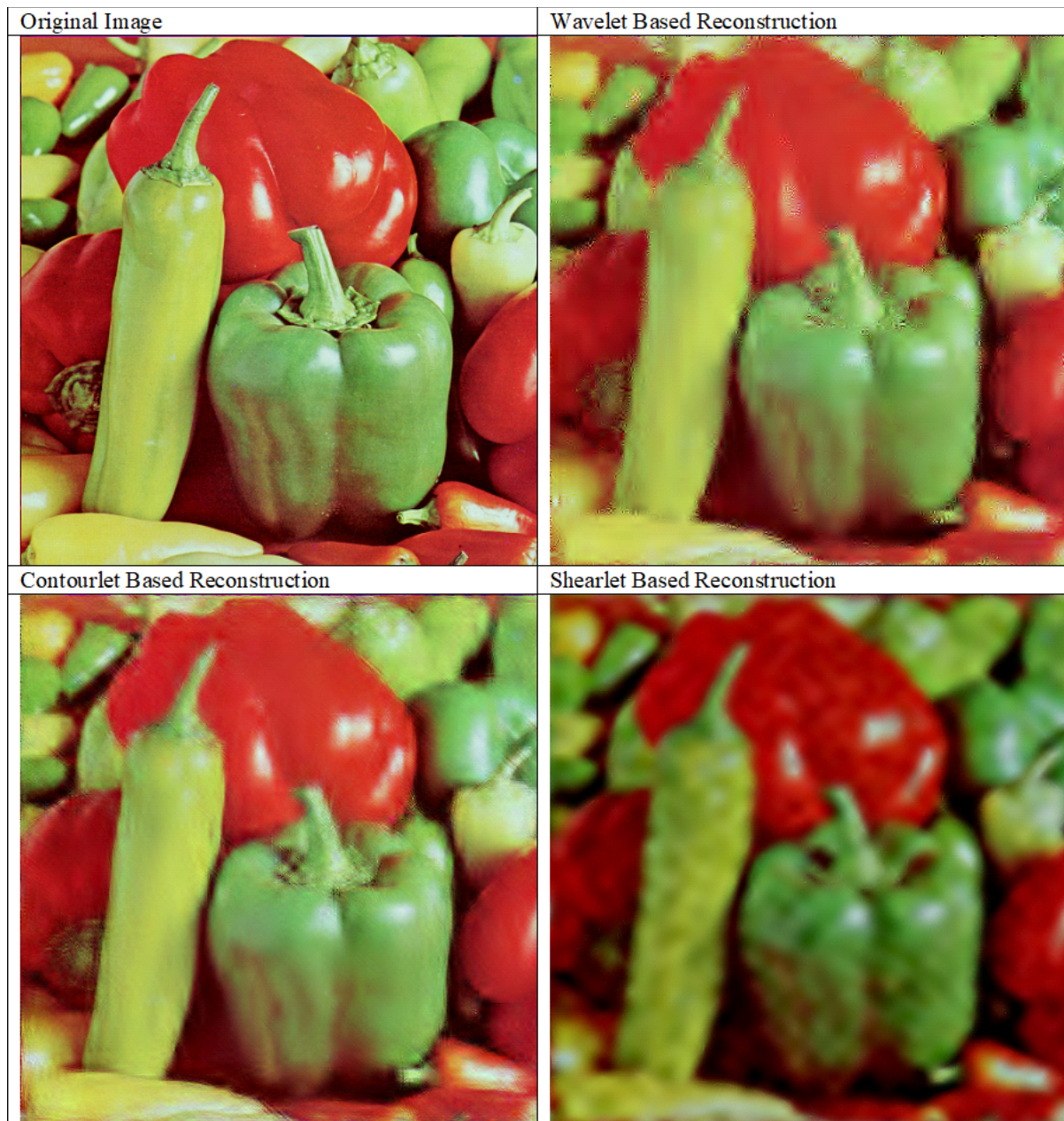


Figure 2. Peppers Image Reconstruction 512×512 .

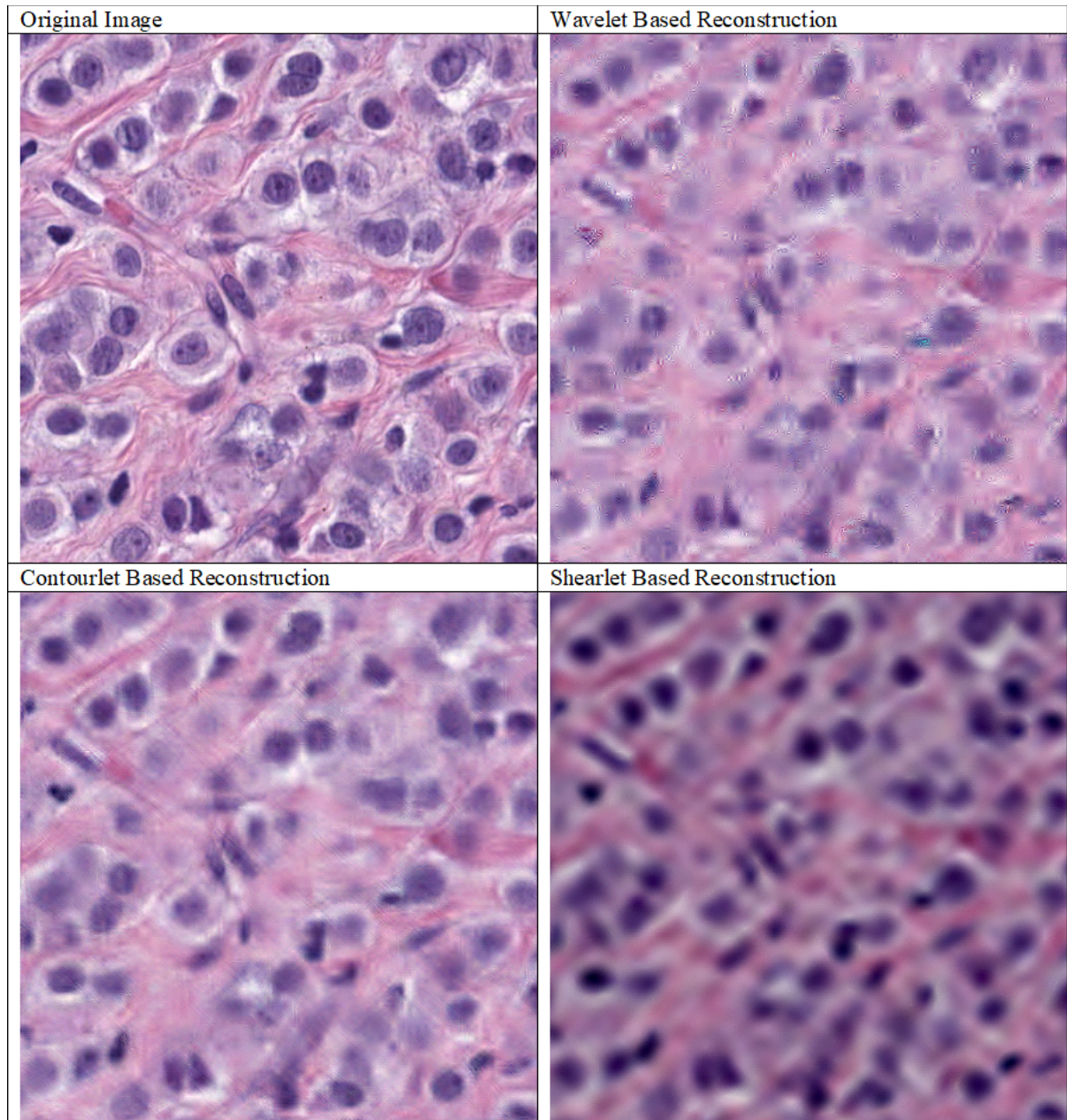


Figure 3. Digital Pathology Image Reconstruction 512×512 .

The quality of the reconstructed images are evaluated using reference based Image Quality Assessment (IQA) methods, namely SSIM [20], HaarPSI [21] and PSNR. SSIM basically compares local patterns of pixel intensities that have been normalized for luminance and contrast [20]. On the other hand, HaarPSI makes decomposition with Haar wavelet to assess local similarities between two images and the obtained coefficients are utilized to make image comparison [21]. The calculated SSIM, HaarPSI and PSNR metrics for the reconstructed images are given Table 1. In order to investigate the performance of CS in digital pathology images profoundly, 10 different 512×512 images are extracted from different Breast Cancer whole slide images. After the reconstruction process, SSIM and HaarPSI metrics are calculated for each image, they are given Figure 4 and Figure 5 respectively.

Table 1. SSIM and HaarPSI metrics for Peppers and Digital Pathology Image.

Transform Type	Peppers			Digital Pathology Image		
	SSIM	HaarPSI	PSNR	SSIM	HaarPSI	PSNR
Wavelet	0.659	0.516	70.27	0.551	0.526	70.71
Contourlet	0.688	0.599	72.47	0.628	0.605	72.63
Shearlet	0.588	0.503	63.51	0.518	0.527	63.00

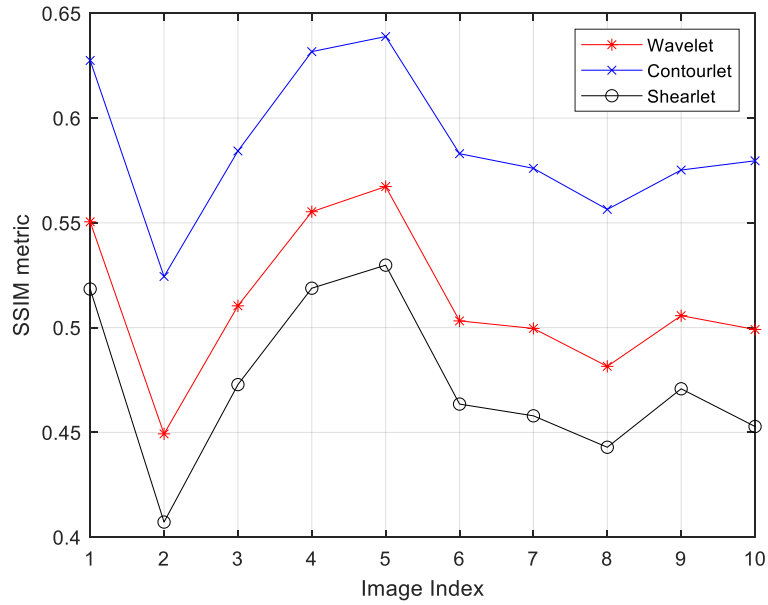


Figure 4. SSIM metrics for 10 different digital pathology images.

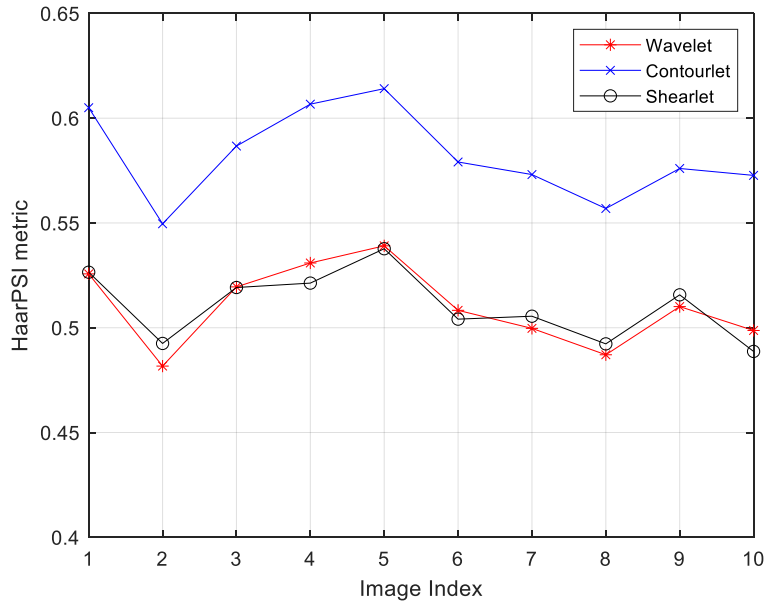


Figure 5. HaarPSI metrics for 10 different digital pathology images.

4. Discussion

In this research, compressed sensing with different sparsifying bases is considered specifically for digital pathology image. Figure 2 and Figure 3 show that the reconstruction is successful even when a few percent of the data (12.5 % for this particular case) is used. The quality measures changes for SSIM, HaarPSI and PSNR, however, if Table 1 is considered, it is seen that the performance of Contourlet Transform is better than Wavelet and Shearlet Transforms in every metrics. This observation aligns with the findings presented in Figure 1, which displays the transforms of synthetic image letters O, G, R, and S. These letters, characterized by their smooth curves and contours, serve as an effective analogy for the patterns and cellular structures typically observed in digital pathology images. In this context, the Contourlet Transform demonstrates a distinct advantage. Not only does it yield a sparse representation, but it also more accurately captures the edges, curves, and contours of these letters compared to both the Wavelet and Shearlet Transforms. This is clearly illustrated in Figure 1. The Contourlet Transform is particularly effective at showing smooth contours and continuous edges in images. It smoothly handles different levels of detail, allowing for a clearer and more accurate depiction of complex patterns. This feature is especially useful in digital pathology, where images often contain detailed and complicated structures.

During the study, it is observed that the fastest computation of coefficients is for the wavelet case. However, Contourlet Transform is faster to compute than Shearlet Transform, even though both transforms are considered as multilevel and multi resolution, the filter bank approach in Contourlet Transform is advantageous for the speed of computation. Besides, the reconstructions of digital pathology image are satisfactory compared to the reconstructions of classical peppers image when SSIM, HaarPSI and PSNR metrics are taken as a reference. While Table 1 shows that our reconstructions exhibit high quality based on PSNR values exceeding 40 dB, this metric does not accurately reflect the true quality of our images. This discrepancy arises because PSNR is traditionally geared towards grayscale images and may not correlate well with human visual perception, particularly in the context of color nuances and high dynamic range images. Figures 4 and 5 demonstrate the effectiveness of the Contourlet Transform, showcasing its application in 10 varied digital pathology images. In these figures, we have primarily focused on the results obtained from SSIM and HaarPSI measurements, which offer a more accurate and perceptually relevant assessment of image quality compared to PSNR. However, Wavelet and Shearlet Transforms result in similar quality in reconstruction specifically when the HaarPSI metric is taken into account. Digital pathology slide images can be more challenging than classical images, on the other hand, the results show that CS is very promising for digital pathology which is a growing medical industry. CS can be advantageous for imaging at different wavelengths; therefore, this study can initiate CS based imaging of digital pathology samples beyond the visible band.

Acknowledgements

This study is partially funded under the Ankara Yıldırım Beyazıt University's Projects Office Grant No. AYBU-2018-BAP-4981 about compressive sensing of digital pathology images. Open-source convex optimization toolbox UNLocBoX is utilized for ADMM based reconstruction. The results shown here are in part based upon data generated by the TCGA Research Network: <https://www.cancer.gov/tcga>.

References

- [1] Jahn S, Plass M, and Moinfar F. "Digital Pathology: Advantages, Limitations and Emerging Perspectives," *J. Clin. Med.*, vol. 9, p. 3697, Nov. 2020, doi: 10.3390/jcm9113697.
- [2] Elgendi M, Fletcher RR, Abbott D, Zheng D, Kyriacou P, and Menon C, "Editorial: Mobile and wearable systems for health monitoring," *Front. Digit. Health*, vol. 5, 2023, doi: 10.3389/fgth.2023.1196103.
- [3] Freire D, de Faria P, Travençolo B, and Zanchetta do Nascimento M. "Automated detection of tumor regions from oral histological whole slide images using fully convolutional neural networks," *Biomed. Signal Process. Control*, vol. 69, p. 102921, Aug. 2021, doi: 10.1016/j.bspc.2021.102921.
- [4] Joshi B, "Digital Pathology Market Size, Share, Trends Analysis Report by Application (Academic Research, Disease Diagnosis), by Product (Software, Device), by End-use (Diagnostic Labs, Hospitals), and Segment Forecasts, 2022-2030." 2022.
- [5] Shannon CE, "A Mathematical Theory of Communication," *Bell Syst. Tech. J.*, vol. 27, no. 3, pp. 379–423, 1948, doi: <https://doi.org/10.1002/j.1538-7305.1948.tb01338.x>.
- [6] Taubman D and Marcellin M. *JPEG2000 Image Compression Fundamentals, Standards and Practice*. Springer Publishing Company, Incorporated, 2013.

- [7] Donoho DL, “Compressed sensing,” *IEEE Trans. Inf. Theory*, vol. 52, no. 4, pp. 1289–1306, 2006, doi: 10.1109/TIT.2006.871582.
- [8] Candes EJ, and Tao T. “Stable signal recovery from incomplete and inaccurate measurements,” *Commun. Pure Appl. Math.*, vol. 59, no. 8, pp. 1207–1223, 2006, doi: <https://doi.org/10.1002/cpa.20124>.
- [9] Candes EJ, J. R Romberg JK, and Tao T. “Robust uncertainty principles: exact signal reconstruction from highly incomplete frequency information,” *IEEE Trans. Inf. Theory*, vol. 52, no. 2, pp. 489–509, 2006, doi: 10.1109/TIT.2005.862083.
- [10] Graff C and Sidky E. “Compressive sensing in medical imaging,” *Appl. Opt.*, vol. 54, pp. C23-44, Mar. 2015, doi: 10.1364/AO.54.000C23.
- [11] Lustig M, Donoho D, and Pauly JM, “Sparse MRI: The application of compressed sensing for rapid MR imaging,” *Magn. Reson. Med.*, vol. 58, no. 6, pp. 1182–1195, 2007, doi: <https://doi.org/10.1002/mrm.21391>.
- [12] Bell J. “FDA Clears Compressed Sensing MRI Acceleration Technology From Siemens Healthineers.” 2017.
- [13] Radwell N, Mitchell K, Gibson G, Edgar M, Bowman R, and Padgett M. “Single-pixel infrared and visible microscope,” *Optica*, vol. 1, pp. 285–289, Oct. 2014, doi: 10.1364/OPTICA.1.000285.
- [14] Hahamovich E, Monin S, Hazan Y, and Rosenthal A. “Single pixel imaging at megahertz switching rates via cyclic Hadamard masks,” *Nat. Commun.*, vol. 12, Jul. 2021, doi: 10.1038/s41467-021-24850-x.
- [15] Calisesi G. et al., “Compressed sensing in fluorescence microscopy,” *Prog. Biophys. Mol. Biol.*, vol. 168, pp. 66–80, 2022, doi: <https://doi.org/10.1016/j.pbiomolbio.2021.06.004>.
- [16] Binev P, Dahmen W, DeVore R, Lamby P, Savu D, and Sharpley R. “Compressed Sensing and Electron Microscopy,” in *Modeling Nanoscale Imaging in Electron Microscopy*, T. Vogt, W. Dahmen, and P. Binev, Eds., Boston, MA: Springer US, 2012, pp. 73–126. doi: 10.1007/978-1-4614-2191-7_4.
- [17] Pavillon N, and Smith NI. “Compressed sensing laser scanning microscopy,” *Opt Express*, vol. 24, no. 26, pp. 30038–30052, Dec. 2016, doi: 10.1364/OE.24.030038.
- [18] Boyd S, Parikh N, Chu E, Peleato B, and Eckstein J. “Distributed Optimization and Statistical Learning via the Alternating Direction Method of Multipliers,” *Found. Trends Mach. Learn.*, vol. 3, pp. 1–122, Jan. 2011, doi: 10.1561/22000000016.
- [19] Şengün Ermeýdan E, Değirmenci A, Çankaya I, and Erdoğan F. “The Effects of Measurement Matrix and Reconstruction Algorithms on Compressed Sensing of Pathology Images,” *Düzce Üniversitesi Bilim Ve Teknol. Derg.*, vol. 8, no. 1, pp. 880–890, 2020, doi: 10.29130/dubited.626880.
- [20] Wang Z, Bovik AC, Sheikh HR, and Simoncelli EP. “Image quality assessment: from error visibility to structural similarity,” *IEEE Trans. Image Process.*, vol. 13, no. 4, pp. 600–612, 2004, doi: 10.1109/TIP.2003.819861.
- [21] Reisenhofer R, Bosse S, Kutyniok G, and Wiegand T. “A Haar wavelet-based perceptual similarity index for image quality assessment,” *Signal Process. Image Commun.*, vol. 61, pp. 33–43, 2018, doi: <https://doi.org/10.1016/j.image.2017.11.001>.
- [22] Candes EJ, “The restricted isometry property and its implications for compressed sensing,” *Comptes Rendus Math.*, vol. 346, no. 9, pp. 589–592, 2008, doi: <https://doi.org/10.1016/j.crma.2008.03.014>.
- [23] Baraniuk R, Davenport M, DeVore R, and Wakin M. “A Simple Proof of the Restricted Isometry Property for Random Matrices,” *Constr. Approx.*, vol. 28, pp. 253–263, Dec. 2008, doi: 10.1007/s00365-007-9003-x.
- [24] Daubechies I. *Ten Lectures on Wavelets*. USA: Society for Industrial and Applied Mathematics, 1992.
- [25] Do MN and Vetterli M. “The contourlet transform: an efficient directional multiresolution image representation,” *IEEE Trans. Image Process.*, vol. 14, no. 12, pp. 2091–2106, 2005, doi: 10.1109/TIP.2005.859376.
- [26] Kutyniok G and Sauer T. “Adaptive Directional Subdivision Schemes and Shearlet Multiresolution Analysis,” *SIAM J. Math. Anal.*, vol. 41, pp. 1436–1471, Jan. 2009, doi: 10.1137/08072276X.
- [27] Mallat SG, “A theory for multiresolution signal decomposition: the wavelet representation,” *IEEE Trans. Pattern Anal. Mach. Intell.*, vol. 11, no. 7, pp. 674–693, 1989, doi: 10.1109/34.192463.
- [28] Meyer Y. *Wavelets and Operators*, vol. 1. in *Cambridge Studies in Advanced Mathematics*, vol. 1. Cambridge University Press, 1993. doi: 10.1017/CBO9780511623820.
- [29] Gonzalez RC and Woods RE. *Digital image processing*. Upper Saddle River, N.J.: Prentice Hall, 2008. [Online]. Available: <http://www.amazon.com/Digital-Image-Processing-3rd-Edition/dp/013168728X>
- [30] Bauschke HH, Burachik RS, Combettes PL, Elser V, Luke DR, and Wolkowicz H. *Fixed-Point Algorithms for Inverse Problems in Science and Engineering*. Springer Publishing Company, Incorporated, 2013.
- [31] Gutman DA et al. “Cancer digital slide archive: An informatics resource to support integrated in silico analysis of TCGA pathology data,” *J. Am. Med. Inform. Assoc. JAMIA*, vol. 20, no. 6, pp. 1091–1098, 2013, doi: 10.1136/amiajnl-2012-001469.

Drought assessment of Yeşilirmak Basin Using Long-term Data

Veysi KARTAL^{1*}

^{1*}Department of Civil Engineering, Engineering Faculty, Siirt University, Siirt, 56000, Türkiye

*¹veysikartal@siirt.edu.tr

(Geliş/Received: 17/11/2023;

Kabul/Accepted: 13/02/2024)

Abstract: Drought is a prolonged period of inadequate rainfall, such as one season, one year or several years, on a statistical multi-year average for a region. Drought is a natural disaster effective on several socio-economic activities from agriculture to public health and leads to deterioration of the environment sustainability. The drought starts with meteorological drought, continues with agricultural and hydrological drought, and when it is in the socioeconomic dimension, the effects begin to be observed. Generally, drought studies are based on drought indices in the literature. This study applied long-term precipitation, temperature, and evaporation data from Samsun, Tokat, Merzifon, Çorum and Amasya meteorological stations from 1961 to 2022 to investigate the drought in the Yeşilirmak basin of Turkey. The present study applied Standardized Precipitation Index (SPI), and Effective Drought Index (EDI), China Z- Index (CZI) and Standardized Precipitation Evapotranspiration Index (SPEI) based on daily, monthly, seasonal, and annual time periods to evaluate drought. The Sen slope and Mann-Kendall test were employed for data analysis. The results revealed that the monthly drought indices for the study area were almost identical for the study area. Although dry and wet periods were observed.

Key words: Drought, EDI, Mann-Kendall, Sen slope.

Yeşilirmak Havzası'nın uzun vadeli veriler kullanılarak kuraklığının değerlendirilmesi

Öz: Kuraklık, tarımdan halk sağlığına kadar birçok sosyo-ekonomik faaliyeti etkileyen ve çevrenin sürdürülebilirliğini bozulmasına neden olan doğal bir afettir. Kuraklık meteorolojik kuraklıkla başlar, tarımsal ve hidrolojik kuraklıkla devam eder, sosyoekonomik boyuta geçtiğinde ise etkileri görülmeye başlar. Literatürde genellikle kuraklık çalışmaları kuraklık indekslerine dayandırılmaktadır. Bu çalışmada, Türkiye'nin Yeşilirmak havzasındaki kuraklık özelliklerini incelemek için 1961-2022 yılları arasında Samsun, Tokat, Merzifon, Çorum ve Amasya meteoroloji istasyonlarından elde edilen uzun süreli yağış, sıcaklık ve buharlaşma verileri kullanılmıştır. Bu çalışmada, kuraklığı değerlendirmek için aylık, mevsimlik ve yıllık zaman dilimleri kullanılarak günlük verilere dayalı CZI, SPEI, SPI ve EDI değerleri elde edilmiştir. Veri analizi için Sen eğimi ve Mann-Kendall testi kullanılmıştır. Sonuçlar, çalışma alanı için aylık kuraklık indekslerinin neredeyse aynı olduğunu ortaya koymuştur. Özellikle şiddetli ve yağışlı dönemler gözlemlenmiş olmasına rağmen, genel olarak normal kuraklık seviyeleri gözlemlenmiştir.

Anahtar kelimeler: Kuraklık, EDI, Mann-Kendall, Sen eğimi.

1. Introduction

Drought is a life-threatening natural disaster leading to several socio-economic activities such as agriculture, public health, and leads to deterioration of the sustainability of environmental systems. There is not a precise definition of drought in the literature. However, drought effects are increasingly seen across the world. Humans usually feels drought when water scarcity begins [1]. There are four main types of droughts in the literature: meteorological, hydrological, socioeconomic, and agricultural droughts. The drought starts with meteorological drought, continues with agricultural and hydrological drought, and when it is in the socioeconomic dimension, the effects begin to be observed. Therefore, it is crucial to analyze the drought situation [2].

Generally, drought studies are based on drought indices in the literature. Several indices are employed in the literature to evaluate drought such as SPI (Standardized Precipitation Index, [3], CZI (China-Z Index), [4], EDI (Effective Drought Index), [5], PDSI (Palmer Drought Severity Index) [6], SPEI (Standardized Precipitation Evapotranspiration Index) [7], RDI (Reconnaissance Drought Index) [8], SDI (Streamflow Drought Index) [9], SWSI (Surface Water Supply Index) [10], SMDI (Soil Moisture Deficit Index) [11], ARI (Agricultural Rainfall Index) [12], ETDI (Evapotranspiration Deficit Index) [11]], etc.

The SPI has been commonly applied in Turkey ([13–15] and worldwide [16–19])

Morid et al. [18] used several drought indices for drought and compared them with each other. They concluded that EDI and SPI are better at identifying the start of drought, but EDI outperforms the SPI based on the sensitivity. Mishra and Singh [20] compared the strong and weak points of different indices against each other

* Corresponding author: veysikartal@siirt.edu.tr. ORCID: 0000-0003-4671-1281

in their drought study. They stated that the best results are obtained with SPI when Gamma distribution is used since rainfall fits the Gamma distribution better than other distributions.

Yacoup and Tayfur [16] conducted a comparison of various meteorological drought indices for the Trarza Region of Mauritania for 1, 3, 6 and 12 months. They found that SPI values obtained from gamma and log-normal distributions can detect more severe droughts than SPI and CZI values obtained from normal distribution. Malik et al. [21] studied drought with the EDI for the Uttarkand State of India and used Mann-Kendall and the Innovative Sen Method for trend detection. It was determined that Innovative Sen method outperformed the MK method when different drought types are studied in the study. This advantage is due to the fact that the trend that cannot be studied with the MK method can be examined with the Innovative Sen method. Drought studies are widespread in Turkey as several parts of world.

Dogan et al. [22] performed a drought study in the Konya Closed Basin and performed a comparison of several drought indices and reported that EDI provides better performance than the others. Tugrul et al. [23] identified the droughts that are important for the region with EDI for the Southeastern Anatolia Region, studied the droughts occurring in the provinces in the region, and determined the percentages of drought events in total time. Gumus et al. [24] analyzed drought with monthly total precipitation data for the Southeastern Anatolia Project region and investigated the trend of drought with nonparametric MK and Mann-Kendall Rank Correlation tests. It was stated that a downward trend was determined in the majority of the region. Katipoglu et al. [25] analyzed SDI values with MK and Modified MK tests to detect trends in the hydrological drought of the Euphrates basin. It was reported that downward trends were determined in the Euphrates basin in summer and fall months.

Katipoglu et al. [26] applied Innovative Sen method and Mann-Kendall to detect the trend in the hydrological droughts of Yeşilirmak basin. It was found that upward trends were dominant at monthly and annual scale. Şimşek et al. [27] analyzed meteorological drought for the Çoruh Basin using the SPI method. It was found that the longest dry time was observed after 2010 and drought increased with increasing time scale. Tuğrul and Hınıs [28] conducted meteorological and hydrological drought trend analysis in Konya Apa Dam Basin. Trend analysis demonstrated that there is an upward trend in all data in the findings obtained from ITA and in SPI-6, SPI-9 and SPI-12 in the findings obtained from MK at 0.01 significance level. Yuce et al. [29] analyzed drought in Samsun province with SPI and SPEI. Normal drought was observed more than the other drought types in Samsun while very severe drought was observed less. There is little difference between the two indices.

Değer et al. [30] analyzed hydrological drought using SDI and Innovative Trend Analysis (ITA) for 1, 3, 6, 9, 12-scale for the Kızılırmak Basin. The results show that mild drought was observed more. The Drought analysis in the Yeşilirmak Basin was studied with RDI and SPI indices by Hınıs and Geyikli [31]. They show that the SPI and RDI methods generally indicate similar values for wet periods, whereas the RDI defines more extreme dry periods than the SPI during extreme dry periods. Zeybekoglu et al. [32] compared drought indices for Yeşilirmak Basin to assess the drought. They found that these indices yield similar results and SPI determines drought at an earlier stage than the other indices. Simsek et al. [33] evaluated the drought for the Black Sea region in Turkey. It was observed that the occurrence of severe and extreme droughts is nearly 15%. Yuce et al. [34] studied the hydrological drought analysis of Yeşilirmak Basin of with SDI and ITA. It was observed that drought categories are less than wet categories.

The drought indices, as given above, can be analyzed according to the drought type and the data to be used, as well as the function and the area of application of the indices. This study used SPI, CZI, SPEI and EDI compatible with the literature. The EDI, which is considered in this study, is frequently preferred as indices that provides satisfactory results because it can be calculated using daily temperature and precipitation values to assess drought [21–23].

This study was conducted using the most updated data (1961-2022) of Amasya, Çorum, Merzifon, Samsun and Tokat monitoring stations in Yeşilirmak Basin in Turkey. CZI, SPEI, SPI, and EDI values were used in the drought assessment of Yeşilirmak basin. It is seen in the literature that drought assessments have been made for the Yeşilirmak basin according to many different drought indices. Nevertheless, SPI, SPEI and CZI drought indices commonly used in the literature were used. In addition, the EDI was employed in the present study, which is different from the literature and adds originality to the study. In addition, Mann Kendall method and Sen slope were used to determine the trends in precipitation and mean temperature for 95% confidence interval.

2. Study area

Yeşilirmak Basin is located at 35° 49' 52" East longitude and 40° 38' 54" North latitude. It occupies an area of approximately 40.000 km², which is 5% of Turkey's total area (Fig. 1). The basin is bordered by the Seyhan, Kızılırmak, Western and Eastern Black Sea, Euphrates-Tigris basins [34].

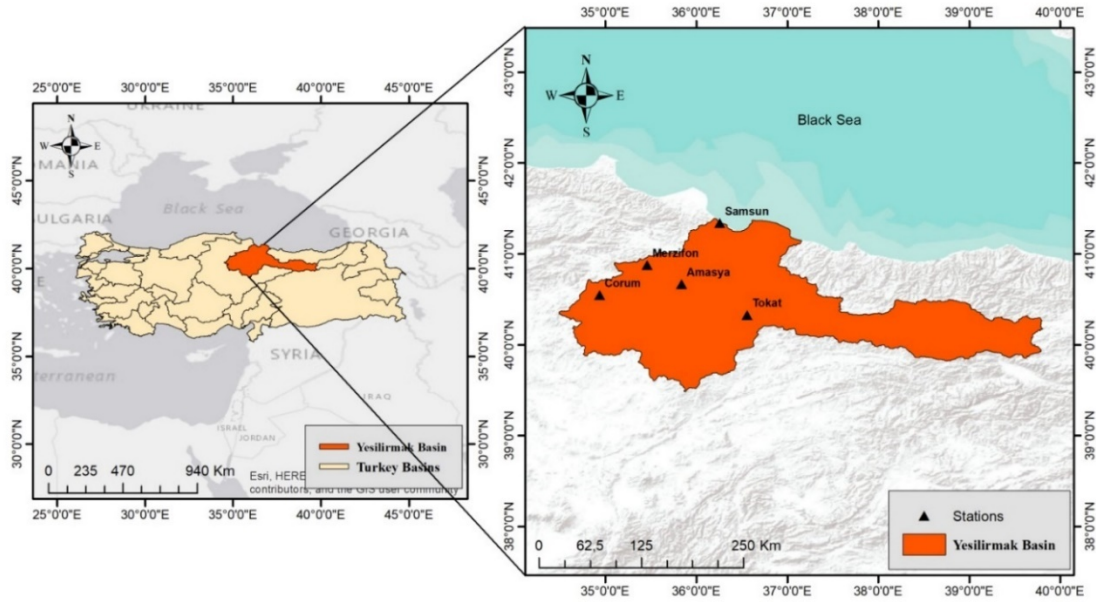


Figure 1. Location map of the present study

3. Methods and Materials

3.1. Data analysis

The meteorological data were provided from the General Directorate of Meteorology in daily average, maximum and minimum temperature, and daily precipitation data (P). In this study, homogeneity procedure was applied to complete the missing data. SPI, CZI, SPEI and EDI were calculated using daily values. Station details are shown in Table 1.

Table 1. Meteorological Monitoring Station

Station names	Latitude	Longitude	Altitude	Daily			
				T _{min} (C)	T _{ave} (C)	T _{max} (C)	P (mm)
17083-Merzifon	40.8793	35.4585	754	-21	11.5	42.6	1.17
17085-Amasya	40.6668	35.8353	409	-21	13.6	45	1.26
17086-Tokat	40.3312	36.5577	611	-22.1	12.5	45	1.17
17084-Çorum	40.5461	34.9362	776	-27.2	10.8	42.6	1.22
17030-Samsun	41.3442	36.2564	4	-7	14.6	38.7	1.95

3.2. Sen slope

It is a nonparametric test to detect the trend slope, developed by Sen [35]. Sen's slope is effective in large data errors and is employed to compute the trend in the time series data [36]. The magnitude of the trend is computed in (1) as follows [37,38]:

$$\beta = \text{median} \left(\frac{x_i - x_j}{t_i - t_j} \right) \quad (1)$$

in which x_i : value at time t_i and x_j : data value at time t_j ($i > j$). β indicates the magnitude of the trend.

3.3. Mann-Kendall test

Mann-Kendall test is employed commonly in the literature to detect the trend of meteorological and hydrological parameters in the hydrology [39–46]. The trend slope of time series can be computed using the Mann-Kendall test [47–49] as given in equations (2) to (5).

$$S = \sum_{k=1}^{n-1} \sum_{j=k+1}^n \text{sgn}(x_j - x_k) \quad (2)$$

$$\text{sgn}(x_j - x_k) = f(x) = \begin{cases} 1, & \text{if}(x_j - x_k) > 0 \\ 0 & \text{if}(x_j - x_k) = 0 \\ -1 & \text{if}(x_j - x_k) < 0 \end{cases} \quad (3)$$

in which n is the data length. A downward trend refers to for $S < 0$, but an upward trend refers to for $S > 0$.

$$\sigma^2(s) = \frac{n(n-1)(2n+5) - \sum_{i=1}^p t_i(t_i-1)(2t_i+5)}{18} \quad (4)$$

where p =number of groups, t_i =data number at p^{th} group. The Z value is calculated as below.

$$Z = \begin{cases} \frac{S-1}{\sqrt{\sigma^2(s)}}, & \text{if } S > 0 \\ 0 & \text{if } S = 0 \\ \frac{S+1}{\sqrt{\sigma^2(s)}}, & \text{if } S < 0 \end{cases} \quad (5)$$

There has a tendency if $|Z| > Z_{1-\alpha/2}$, while there is no statistical trend if the condition $|Z| < Z_{1-\alpha/2}$. A significance level of 5% was used for the analysis.

3.4. Drought indices

3.4.1. Effective Drought Index (EDI)

The EDI is computed on a daily time scale and Byun and Wilhite [5] pioneered the development of the EDI, aiming to overcome some of the shortcomings observed in other indices such as the SPI. The EDI has a numerical range of -2.5 to 2.5. The EDI is calculated by applying the equations (6) to (8):

$$EP_i = \sum_{DS=1}^{n-1} \left[\frac{(\sum_{t=m}^{m+1} P_{t-m})}{n} \right] \quad (6)$$

$$DEP_i = EP_i - MEP \quad (7)$$

$$EDI_i = \frac{DEP_i}{\sigma(DEP)} \quad (8)$$

Here, DS is the number of days (usually 365 or 15) used for rainfall accumulation to compute drought severity, while σ is a standard deviation and MEP is the mean EP. The EDI ranges from -2.5 to 2.5. The drought range is different from SPI and SPEI (Table 2).

3.4.2. China Z Index (CZI)

CZI was developed by China International Climate Centre to evaluate drought in China [4,22,50]. CZI is calculated in the following equations (9) to (11) [4,22,50]:

$$CZI_j = \frac{6}{C_{st}} \left(\frac{C_{st}}{2} \varphi_j + 1 \right)^{\frac{1}{3}} - \frac{6}{C_s} + \frac{C_{st}}{6} \quad (9)$$

$$C_{st} = \sum_{j=1}^N \frac{(X_j - \bar{X})^3}{N \times \sigma^3} \quad (10)$$

$$\varphi_j = \frac{X_j - \bar{X}}{\sigma} \quad (11)$$

where t is the time (1, 2, 3, ..., 9, 12, 24, 36, 48 months), C_{st} is a skewness coefficient for t , φ_j is a standard deviation, N is the total number of observation years, σ and \bar{X} are the standard deviation and average of the rainfall X_j , respectively.

3.4.3. Standardized Precipitation Index (SPI)

The SPI is the dominant drought index on a global scale used for monitoring and comprehensive analysis [51–53]. As seen in the studies of [22,54,55], SPI has been recognized as an important tool for the identification of

meteorological drought patterns. The pioneering work of [3] has shown that the SPI can be measured at multiple temporal scales (1, 3, 6, 9, 12, 24, and 48 month scale). The SPI values vary from +2.0 to -2.0.

SPI is based only rainfall data that can be cumulated over different time scales, and can be computed as in (12):

$$g(x) = \frac{p^{\alpha-1} e^{-\frac{x}{\beta}}}{\beta^\alpha \Gamma(\alpha)} \tag{12}$$

In this context, the gamma function is denoted by Γ , where P is the rainfall, α is the shape parameter, and β is the scale parameter [22].

3.4.4. Standardized Precipitation Evapotranspiration Index (SPEI)

SPEI is employed to assess the meteorological drought considered rainfall and temperature in a region [7]. Firstly, the SPEI is computed using potential evapotranspiration (PET). The equation of water balance is applied to compute the monthly deficit (D_i) in the following equations (13) and (14).

$$D_i = P_i - PET_i \tag{13}$$

in which P_i is the total precipitation at i^{th} month. SPEI is computed by Eq. (14) [15,56].

$$SPEI_i = W_i - \frac{2.515517 + 0.802853W_i + 0.010328W_i^2}{1 + 1.432788W_i + 0.189269W_i^2 + 0.001308W_i^3} \tag{14}$$

$$W_i = \begin{cases} p < 0.5, & \sqrt{-2 \ln p} \\ p > 0.5, & \sqrt{-2 \ln (1 - p)} \end{cases}$$

where p is the exceeding probability of calculated D_i values.

In the computation of SPEI and SPI, the methodology of the studies of McKee et al. [3], Mersin et al. [15] and Vicente Serrano et al. [54] were employed. The drought classification calculated indices is shown in Table 2.

Table 2. Drought classification of CZI, EDI, SPI and SPEI [18,54,57]

Conditions	CZI, SPI and SPEI	EDI
Extremely wet	value ≥ 2.00	value ≥ 2.50
Very wet	$1.50 \leq \text{value} < 2.00$	$1.50 \leq \text{value} < 2.50$
Moderately wet	$1.00 \leq \text{value} < 1.50$	$0.7 \leq \text{value} < 1.50$
Near normal	$-1.00 \leq \text{value} < 1.00$	$-0.70 \leq \text{value} < 0.70$
Moderately dry	$-1.50 \leq \text{value} < -1.00$	$-1.50 < \text{value} < -0.70$
Severely dry	$-2.00 \leq \text{value} < -1.50$	$-1.50 \leq \text{value} < -2.50$
Extremely dry	value ≤ -2.00	value ≤ -2.50

4. Results and Discussions

The present study was conducted by using monthly, seasonal, and annual time scales to compute the EDI, CZI, SPEI and SPI values to assess the drought of Yeşilirmak basin. In the present study, precipitation data for the Yeşilirmak basin for the years 1961-2022 were analyzed by applying the Sen slope and Mann-Kendall test and shown in Table 3. A downward trend was determined in rainfall data for all meteorological stations at 95% confidence interval based on Sen's slope. These trends were also evaluated with Mann-Kendall test.

Table 3. Mann-Kendall and Sen's slope results and descriptive statistics of rainfall

Station name	Descriptive statistics			Mann-Kendall		Sen's slope
	Maximum	Mean	Std. deviation	Kendall's tau	p-value	
Amasya	71.2	1.26	3.713	-0.001	0.770	-0.001
Çorum	58.4	1.22	3.635	-0.016	0.002	-0.001
Merzifon	95.8	1.17	3.464	-0.010	0.055	-0.001
Samsun	238.2	1.95	5.896	0.008	0.128	-0.001
Tokat	52.5	1.17	3.322	-0.001	0.805	-0.001

Figure 2 shows the variation of SPI-1, SPEI-1 and CZI-1 values derived between 1961 and 2022. In this date range, dry and wet periods were obtained for SPI-1, SPEI-1 and CZI-1. According to the findings, it is realized that especially SPI-1 values differ from the other indices. As seen in Fig. 2, the values below the -2 line represent an extremely dry situation, while the values above the +2 line represent an extremely wet situation. As seen in Fig. 2, for SPI-1, SPEI-1 and CZI-1, very severe, severe, and moderate drought and very severe, severe, and moderate wet periods were observed.

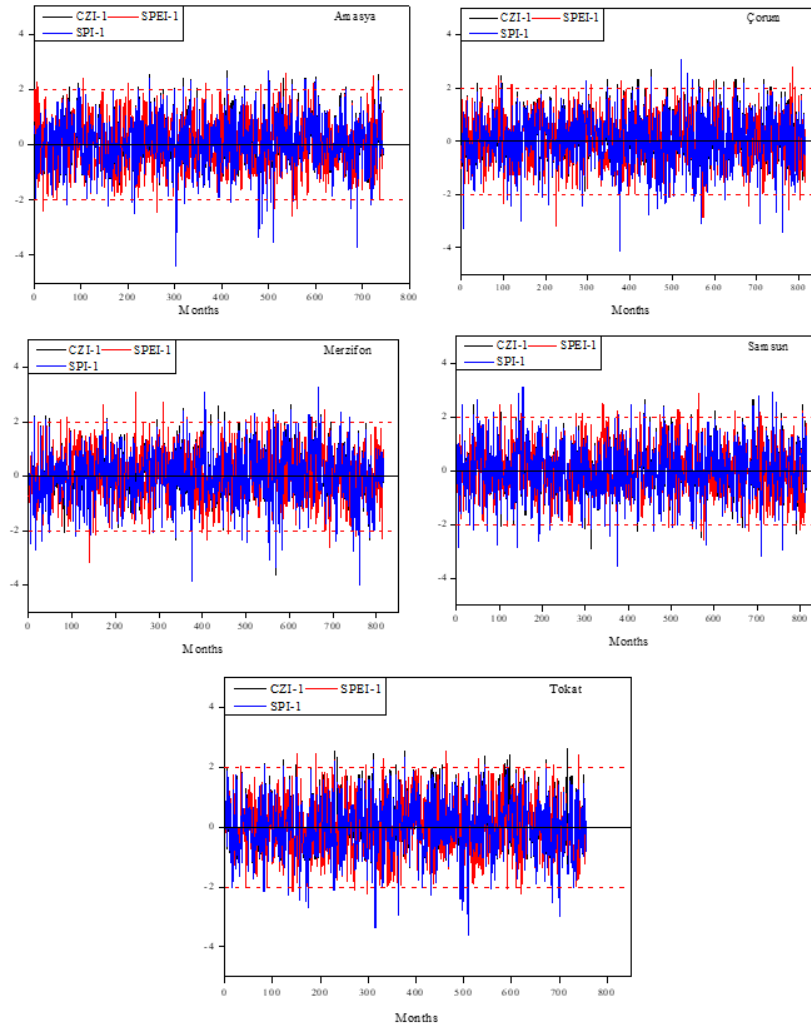


Figure 2. Monthly variation of CZI, SPEI and SPI values

Figure 3 presents the variation of SPI-3, SPEI-3 and CZI-3 values between the years 1961-2022. Dry and wet periods were obtained for SPI-3, SPEI-3, and CZI-3 between 1961-2022. The findings show that especially SPI-3 values are different from other indices. As mentioned above, values below the -2 line represent extremely dry conditions, whereas values above the +2 line represent extremely wet conditions. As shown in Fig. 3, there are very severe drought, severe and moderate drought and very severe, severe, and moderate wet periods for SPI-3, SPEI-3, and CZI-3. It was observed that droughts occurred in almost all seasons in Yeşilırmak basin, but extremely droughts generally occurred in the fall season.

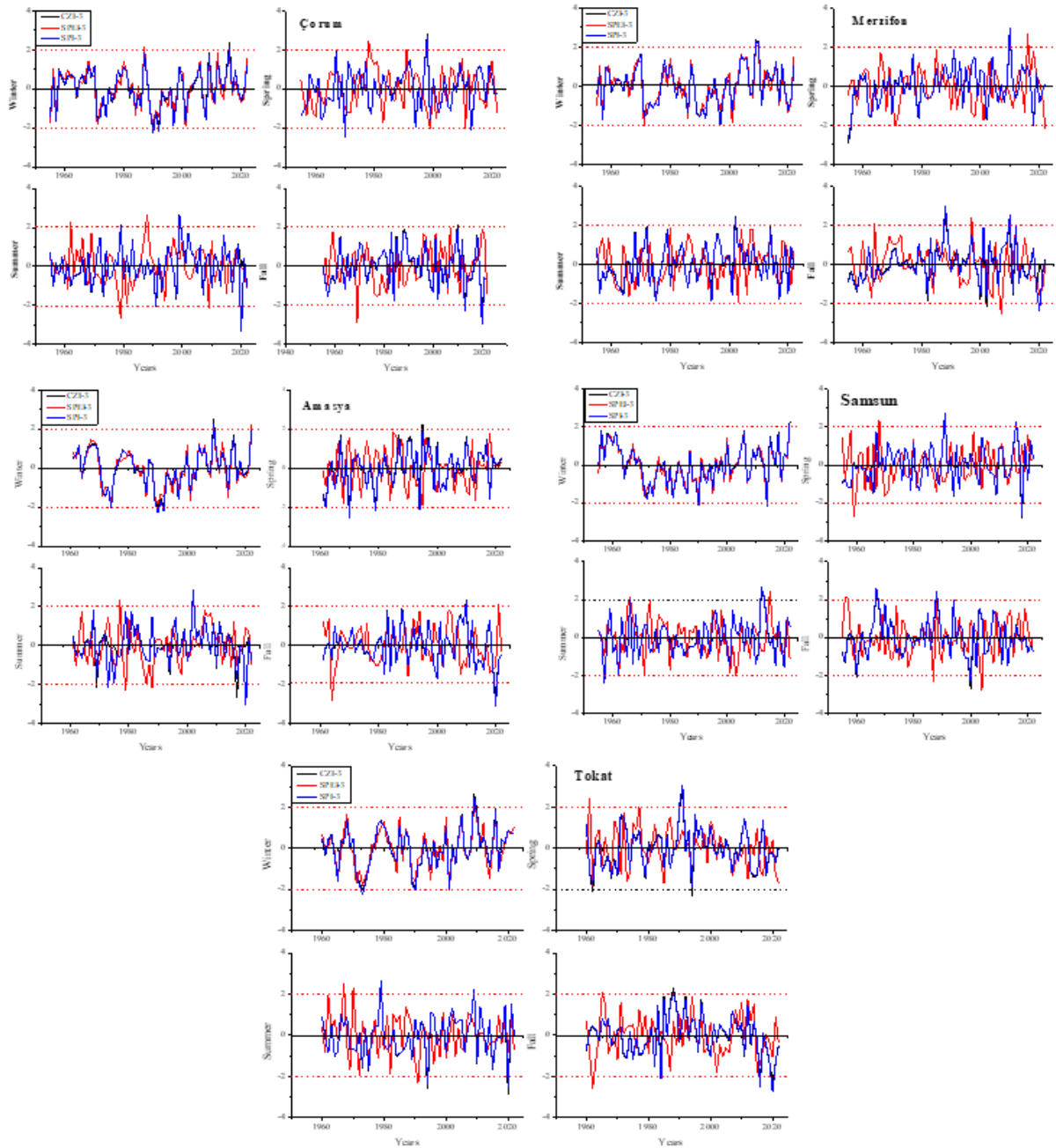


Figure 3. Seasonal variation of CZI, SPEI and SPI values

Figure 4 shows the variation of SPI-12, SPEI-12 and CZI-12 values obtained between 1961 and 2022. Wet and dry periods were observed for SPI-12, SPEI-12 and CZI-12 during this period. As seen in Fig. 4, extremely dry, severe and moderate drought and extremely wet, severe and mild wet periods were detected for SPI-12, SPEI-12 and CZI-12.

In general, the results of drought indices are compatible with each other. As seen in the Fig. 4, extremely dry periods occurred in Amasya in 2020s, in Çorum in 1960, 2010 and 2020s, in Merzifon in 1960 and 2020s, and in Samsun in 1980s. However, almost no extremely dry conditions were observed at Tokat station.

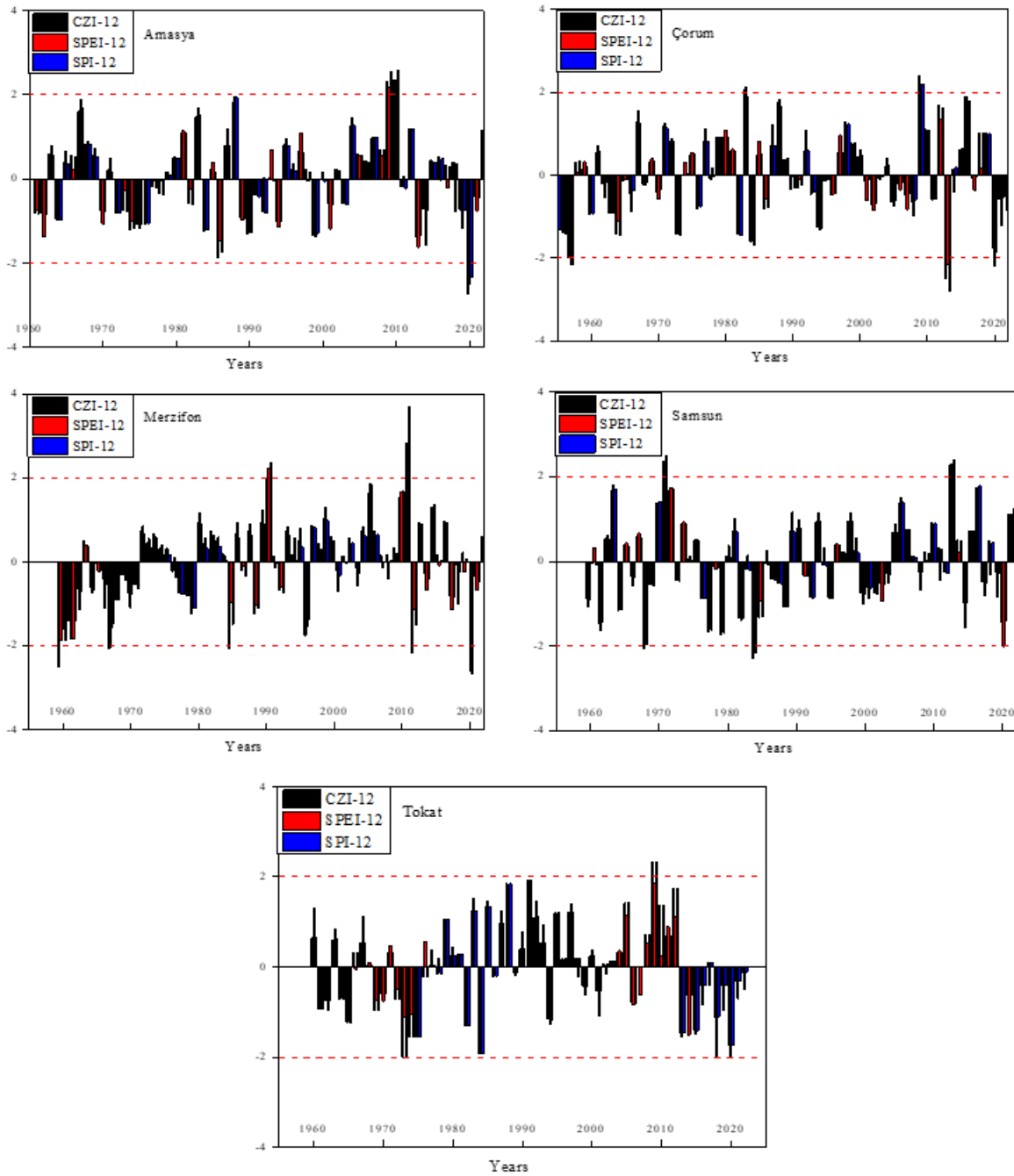


Figure 4. The variation of CZI, SPEI and SPI at annual time scale

Figure 5 shows the correlation between SPEI, CZI and SPI used for drought for Tokat. The linear correlation for SPEI, CZI and SPI shows a strong relationship. The R^2 values were used to analyze the correlation between SPEI, CZI and SPI ($\frac{\sum_{i=1}^n (o_i - o_{mean})^2 - \sum_{i=1}^n (o_i - p_i)^2}{\sum_{i=1}^n (o_i - o_{mean})^2}$). p is the predicted value and o is the observed value, o_i and p_i are the observed and predicted i^{th} values. R^2 values close to 1 mean that they have the most accurate prediction results possible [58]. As seen in Fig. 5, the lowest R^2 value was obtained between SPEI and SPI with 0.817 in the 1-month time scale. As shown in Fig. 5, consistent results were obtained between SPEI, CZI and SPI values at Tokat station. The results are more consistent between SPI and CZI.

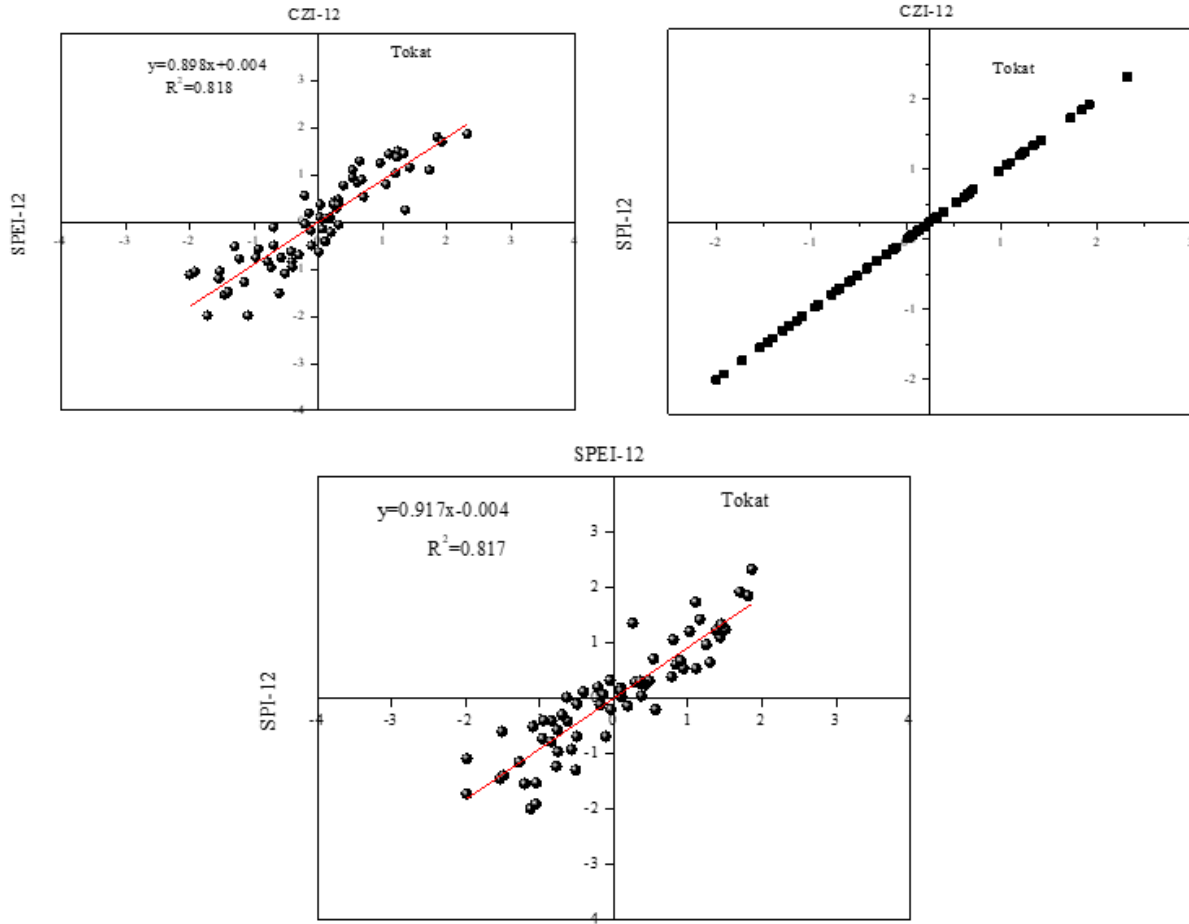


Figure 5. The comparisons of CZI-1, SPI-1 and SPEI-1

Figure 6 depicts the variation of EDI-1, EDI-3 and EDI-12 values obtained between 1961 and 2022. As seen in Fig. 6, the values below the -2.5 line represent an extremely dry situation, while the values above the +2.5 line represent an extremely wet situation. As shown in Fig. 6, for EDI-1, EDI-3 and EDI-12, extremely dry, severe and moderate drought and extremely wet, severe and moderate wet periods were observed. For EDI-1, extremely dry conditions occurred at all stations except Amasya station. Moreover, Figure 6 shows that droughts occur in almost all seasons in Yeşilırmak basin in EDI-3. According to EDI-3 and EDI-12, no extremely dry condition occurred at any station.

Drought assessment of Yeşilırmak Basin using long-term data

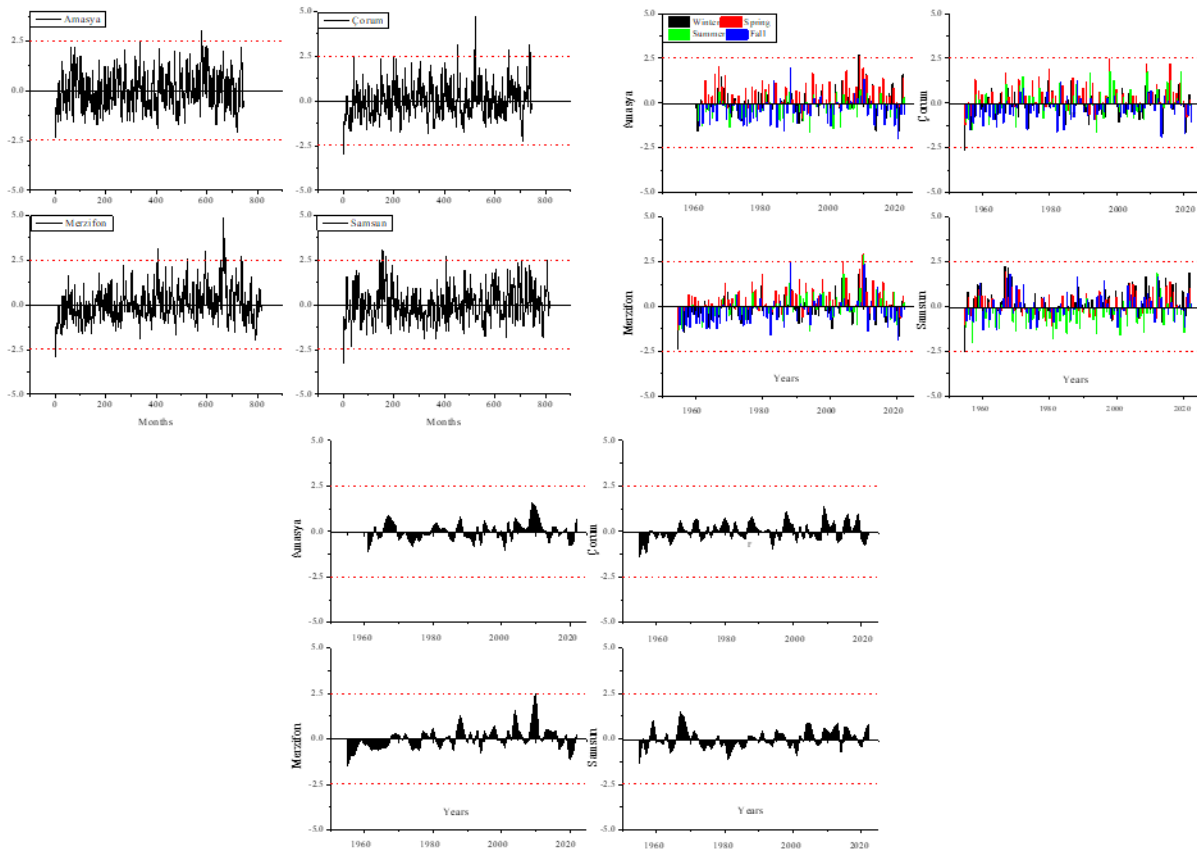


Figure 6. The variation of EDI-1, EDI-3 and EDI-12

The number of dry and wet months between 1961 and 2022 for the Yeşilırmak basin is given in Fig. 7. While SPEI, SPI and CZI are subject to the same drought classification, EDI is subject to a different drought class. Therefore, the number of dry and wet months obtained was used to make comparisons between the indices. For example, when $SPI, SPEI$ and $CZI < -2.00$, extremely dry occurs, while the same is true for $EDI < -2.5$ in EDI (Table 2). Considering the 1-month time series, the normal condition occurred at most in all stations for CZI-1, SPEI, EDI-1 and SPI-1. When EDI-1 drought index is considered, extremely dry did not occur in any station. Extremely dry occurred 6, 6 and 19 times for CZI-1, SPEI-1 and SPI-1 for Amasya station, respectively. Extremely dry occurred 4, 8 and 21 times for Çorum, 9, 13 and 16 times for Merzifon, 14, 12 and 18 times for Samsun and 6, 8 and 21 times for Tokat.

Extremely dry occurred 14 times for Samsun according to CZI index, 13 times for Merzifon according to SPEI index, 21 times each for Tokat and Çorum according to SPI index and no extremely dry events occurred according to EDI. As seen in the Fig. 7, the highest number of extremely dry conditions was obtained according to SPI index. The driest month in Yeşilırmak basin occurred in Çorum in March 1986 with $SPI-1 = -4.12$. The driest month according to CZI index was in Merzifon in May 2002 with $CZI-1 = -3.65$, the driest month according to SPEI was in Çorum in October 1973 with $SPEI-1 = -3.21$ and the driest month according to EDI was in Çorum in January 2014 with $EDI-1 = -2.30$.

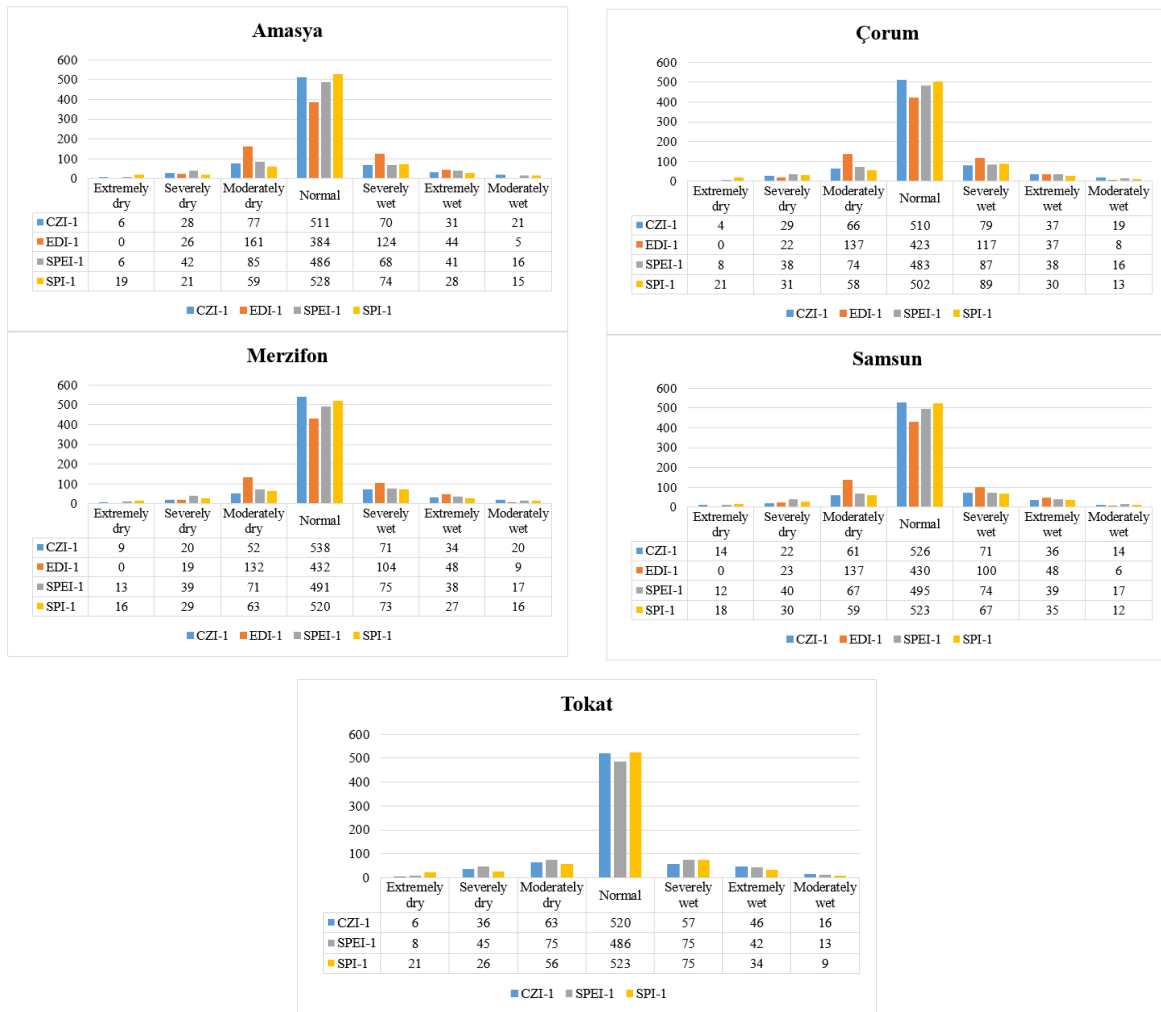


Figure 7. The number of dry and wet months

The precipitation and temperature trend behaviors of the Yeşilirmak basin were reported by Serencam [59] using ITA. The downward trends at low, medium, and high levels, with an average of -3.4%, -3.8% and -2.4% were detected, respectively. They also indicated that temperature and precipitation records showed increasing (5-10%) and decreasing trends, respectively. Although the rainfall of the basin is higher than the national average, it has a decreasing trend. Katipoğlu et al. [26] found that many moderate droughts were observed and only a few extreme droughts were observed in the monthly and annual series using SDI in the hydrologic drought assessment of Yeşilirmak Basin. Katipoğlu et al. [26] applied the ITA method to trend analysis of hydrological droughts in the Yeşilirmak basin to classify wet (SDI > 0) and dry periods (SDI < 0) reported that, except for some stations, the trends in both dry and wet periods showed downward trends.

Aktürk et al. [14] conducted a meteorological drought assessment for 1967-2017 with SPI for the Kızılırmak River Basin, neighboring the Yeşilirmak Basin, and reported that thirty one years of the period were affected by drought categories and twenty eight of the thirty one years belonged to mild drought categories. Yuce et al. [29] analyzed drought in Samsun province with SPI and SPEI. Normal drought was observed more than the other drought types in Samsun while very severe drought was observed less. There is little difference between the two indices As seen in the study of Yuce et al. [29], they used the Mann-Kendall test to rainfall data of Samsun, the findings show that there is a relative decrease in this parameter in the trend of the rainfall based on the 95% confidence interval (-0.118). The degree of trend was measured by Sen's slope method for the rainfall (-0.102). The trend in the rainfall data for Samsun in the present study was detected 0.001 based on Mann-Kendall test and -0.001 was detected for Samsun based on Sen's slope. The reason for the difference between the present study and Yuce et al. [29] can be due to the different period and data format. In this study daily data was used to assess the drought of Yeşilirmak

Basin. In the present study downward trends were determined in the rainfall data of Yeşilirmak Basin for all stations based on Sen's slope whereas an upward trend was determined in the rainfall data for Samsun based on Mann-Kendall test.

5. Conclusions

In this study, China Z Index (CZI), Standardized Precipitation Index (SPI) and Standardize Potential Evapotranspiration Index (SPEI) and Effective Drought Index (EDI) indices based on daily data were obtained by using rainfall, temperature and evaporation data measured by MGM between 1961 and 2022 for Samsun, Tokat, Merzifon, Çorum and Amasya stations located in Yeşilirmak basin. Drought analysis based on monthly, seasonal, and annual time scales was performed using different indices. According to CZI, SPI, SPEI and EDI indices, the number of dry and wet months at each station, as well as the seasonal and annual variations were obtained. The findings of the study were generally in parallel with each other. In addition, according to SPI, SPEI and CZI indices, extremely dry periods occurred in the same time periods. However, according to the EDI index, which is based on daily data, extremely dry periods never occurred at any station. The correlation between SPEI, SPI and CZI values showed that all three indices give similar results. Trend analysis of precipitation data by applying Sen and Mann-Kendall test showed that precipitation showed a decreasing trend. This study represents a step towards a comprehensive understanding of historical drought characteristics in the Yeşilirmak basin. Therefore, the following recommendations for future studies are made. The combination of meteorological drought with hydrological as well as agricultural and groundwater drought can be investigated to highlight the effects of climate change conditions.

Acknowledgements

Special thanks to the General Directorate of Meteorology (MGM) for providing the database used in this study.

References

- [1] Hezarani AB, Zeybekoğlu U, Keskin AÜ. Hydrological and Meteorological Drought Forecasting for the Yesilirmak River Basin, Turkey. *Sürdürülebilir Mühendislik Uygulamaları ve Teknolojik Gelişmeler Dergisi*. 2021;4(2):121–35.
- [2] Partal T, Yavuz E. Application of Trend Analysis on Drought Indices in the West Black Sea Region. *Artvin Çoruh University Journal of Natural Hazards and Environment*. 2020;6(2):345–53.
- [3] McKee, T.B., Doesken, N.J.; Kleist J. The relationship of drought frequency and duration to time scales. In: *Eighth Conference on Applied Climatology*. Colifornia; 1993.
- [4] Wu H, Hayes MJ, Weiss A, Hu Q. An evolution of the standardized precipitation index, the China-Z index and the statistical Z-score. *International Journal of Climatology*. 2001;21(6):745–58.
- [5] Byun H-R, Wilhite DA. Objective quantification of drought severity and duration. *Journal of climate*. 1999;12(9):2747–56.
- [6] Palmer WC. *Meteorological drought*. Vol. 30. US Department of Commerce, Weather Bureau; 1965.
- [7] Vicente-Serrano SM, Beguería S, López-Moreno JI. A multiscale drought index sensitive to global warming: The standardized precipitation evapotranspiration index. *Journal of Climate*. 2010;23(7):1696–718.
- [8] Tsakiris G, Vangelis H. Establishing a drought index incorporating evapotranspiration. *European Water*. 2005;9(10):3–11.
- [9] Nalbantis I, Tsakiris G. Assessment of hydrological drought revisited. *Water Resources Management*. 2009;23(5):881–97.
- [10] Garen DC. Revised surface-water supply index for western United States. *Journal of Water Resources Planning and Management*. 1993;119(4):437–54.
- [11] Narasimhan B, Srinivasan R. Development and evaluation of Soil Moisture Deficit Index (SMDI) and Evapotranspiration Deficit Index (ETDI) for agricultural drought monitoring. *Agricultural and forest meteorology*. 2005;133(1–4):69–88.
- [12] Nieuwolt S. Tropical rainfall variability—The agroclimatic impact. *Agriculture and Environment*. 1982;7(2):135–48.
- [13] Danandeh Mehr A, Sorman AU, Kahya E, Hesami Afshar M. Climate change impacts on meteorological drought using SPI and SPEI: case study of Ankara, Turkey. *Hydrological Sciences Journal [Internet]*. 2020;65(2):254–68. Available from: <https://doi.org/10.1080/02626667.2019.1691218>

- [14] Zeybekoğlu U, Aktürk G. A comparison of the China-Z Index (CZI) and the Standardized Precipitation Index (SPI) for drought assessment in the Hirfanlı Dam basin in central Turkey. *Arabian Journal of Geosciences*. 2021;14(24).
- [15] Mersin D, Gulmez A, Safari MJS, Vaheddoost B, Tayfur G. Drought Assessment in the Aegean Region of Turkey. *Pure and Applied Geophysics*. 2022;179(8):3035–53.
- [16] Yacoub E, Tayfur G. Evaluation and Assessment of Meteorological Drought by Different Methods in Trarza Region, Mauritania. *Water Resources Management*. 2017;31(3):825–45.
- [17] Payab AH, Türker U. Comparison of standardized meteorological indices for drought monitoring at northern part of Cyprus. *Environmental Earth Sciences* [Internet]. 2019;78(10):1–19. Available from: <https://doi.org/10.1007/s12665-019-8309-x>
- [18] Morid S, Smakhtin V, Moghaddasi M. Comparison of seven meteorological indices for drought monitoring in Iran. *International Journal of Climatology*. 2006;26(7):971–85.
- [19] Zou R, Yin Y, Wang X, Zhang Z, Ma X, Liu M, et al. Characteristics and propagation of meteorological and hydrological droughts in eastern Gansu, a typical semi-arid region, China. *International Journal of Climatology*. 2023;(February):1–21.
- [20] Mishra AK, Singh VP. A review of drought concepts. *Journal of Hydrology* [Internet]. 2010;391(1–2):202–16. Available from: <http://dx.doi.org/10.1016/j.jhydrol.2010.07.012>
- [21] Malik A, Kumar A, Pham QB, Zhu S, Linh NTT, Tri DQ. Identification of EDI trend using Mann-Kendall and Sen-Innovative Trend methods (Uttarakhand, India). *Arabian Journal of Geosciences*. 2020;13(18).
- [22] Dogan S, Berktaş A, Singh VP. Comparison of multi-monthly rainfall-based drought severity indices, with application to semi-arid Konya closed basin, Turkey. *Journal of Hydrology* [Internet]. 2012;470–471:255–68. Available from: <http://dx.doi.org/10.1016/j.jhydrol.2012.09.003>
- [23] Tuğrul T, Doğan S, Dursun Ş. Drought Analysis of Provinces in Southeastern Anatolia Region. *Konya Journal of Engineering Sciences*. 2019;7(4):705–12.
- [24] Gumus V, Simsek O, Avsaroglu Y, Agun B. Spatio-temporal trend analysis of drought in the GAP Region, Turkey. *Natural Hazards* [Internet]. 2021;109(2):1759–76. Available from: <https://doi.org/10.1007/s11069-021-04897-1>
- [25] Katipoglu OM, Acar R, Şenocak S. Spatio-temporal analysis of meteorological and hydrological droughts in the Euphrates Basin, Turkey. *Water Science and Technology: Water Supply*. 2021;21(4):1657–73.
- [26] Katipoglu OM, Yeşilyurt SN, Dalkılıç HY. Trend analysis of hydrological droughts in Yeşilirmak basin by Mann Kendall and Sen Innovative Trend Analysis. *Gümüşhane Üniversitesi Fen Bilimleri Enstitüsü Dergisi*. 2022;12(2):422–42.
- [27] Şimşek O, Soydan Oksal NG, Uncu EM, Gümüş V, Şeker M. Long-term (1969–2020) meteorological drought analysis of the Çoruh basin using the SPI method. *Journal of Polytechnic*. 2023;0900.
- [28] Tuğrul T, Hınıs MA. Trend Analysis of Meteorological and Hydrological Drought at Apa Dam (Konya) Basin. *Karaelmas Fen ve Mühendislik Dergisi*. 2023;13(1):151–63.
- [29] Yüce, M. İ., Aksoy, H., Aytekin, A., Eşit, M., Uğur, F., Yaşar, İ., Şimşek, A., & Değer İH. Samsun Province Drought Analysis with SPI and SPEI. *Kahramanmaraş Sutcu Imam University Journal of Engineering Sciences*. 2022;25(3):285–95.
- [30] Değer İH, Yüce Mİ, Eşit M. An Investigation of Hydrological Drought Characteristics in Kızılırmak Basin, Türkiye: Impacts and Trends. *Bitlis Eren University Journal of Science*. 2023;12(1):126–39.
- [31] Hınıs MA, Geyikli MS. Accuracy Evaluation of Standardized Precipitation Index (SPI) Estimation under Conventional Assumption in Yeşilirmak, Kızılırmak, and Konya Closed Basins, Turkey. *Advances in Meteorology*. 2023;2023.
- [32] Zeybekoğlu U, Hezarani AB, Keskin AU. Comparison of four precipitation based meteorological drought indices in the Yeşilirmak Basin, Turkey. *Idojaras*. 2023;127(1):123–42.
- [33] Simsek O, Yıldız-Bozkurt S, Gumus V. Analysis of meteorological drought with different methods in the Black Sea region, Turkey. *Acta Geophysica* [Internet]. 2023;(0123456789). Available from: <https://doi.org/10.1007/s11600-023-01099-0>
- [34] Yuce MI, Deger IH, Esit M. Hydrological drought analysis of Yeşilirmak Basin of Turkey by streamflow drought index (SDI) and innovative trend analysis (ITA). *Theoretical and Applied Climatology*. 2023;153(3–4):1439–62.
- [35] Sen PK. Journal of the American Statistical Estimates of the Regression Coefficient Based on Kendall's Tau. *Journal of the American Statistical Association*. 1968;63(324):1379–89.
- [36] Yu Y, Zou S, Whittemore DW. Non-parametric trend analysis of water quality data of rivers in Kansas. *Journal of Hydrology*. 1993;150:61–80.
- [37] Mersin D, Tayfur G, Vaheddoost B, Safari MJS. Historical Trends Associated with Annual Temperature and Precipitation in Aegean Turkey, Where Are We Heading? *Sustainability* (Switzerland). 2022;14(20).

- [38] Adnan S, Ullah K, Shuanglin L, Gao S. Comparison of various drought indices to monitor drought status in Pakistan. *Climate Dynamics* [Internet]. 2018;51(5):1885–99. Available from: <http://dx.doi.org/10.1007/s00382-017-3987-0>
- [39] Liu B, Zhou X, Li W, Lu C, Shu L. Spatiotemporal characteristics of groundwater drought and its response to meteorological drought in Jiangsu province, China. *Water (Switzerland)*. 2016;8(11).
- [40] Hırca T, Eryılmaz Türkan G, Niazkar M. Applications of innovative polygonal trend analyses to precipitation series of Eastern Black Sea Basin, Turkey. *Theoretical and Applied Climatology*. 2022;147(1–2):651–67.
- [41] Kahya E, Kalayci S. Trend analysis of streamflow in Turkey. *Journal of Hydrology*. 2004;289(1–4):128–44.
- [42] Gumus V, Avsaroglu Y, Simsek O. Streamflow trends in the Tigris river basin using Mann–Kendall and innovative trend analysis methods. *Journal of Earth System Science*. 2022;131(1).
- [43] Kuriqi A, Ali R, Pham QB, Montenegro Gambini J, Gupta V, Malik A, et al. Seasonality shift and streamflow flow variability trends in central India. *Acta Geophysica* [Internet]. 2020;68(5):1461–75. Available from: <https://doi.org/10.1007/s11600-020-00475-4>
- [44] Korkmaz M. Statistical and Trend Analysis of Long-Term Rainfall in Ayvalık. *International Journal of Technology and Emerging Sciences (IJTES)*. 2022;02(04):34–9.
- [45] Saplıoğlu K, Güçlü YS. Combination of Wilcoxon test and scatter diagram for trend analysis of hydrological data. *Journal of Hydrology*. 2022;612(June).
- [46] Korkmaz M. Drought research and trend analysis in Yozgat province. *Engineering Sciences*. 2022;17(3):21–34.
- [47] Mann HB. Nonparametric Tests Against Trend. *Econometrica*. 1945;13(3):245–59.
- [48] Acar R. Evaluation of Susurluk Basin Flows Using Trend Analysis Methods. *Firat University Journal of Experimental and Computational Engineering*. 2024;3(1):65–74.
- [49] Acar R. A comparison of the performance of different innovative trend assessment approaches for air temperature and precipitation data : an application to Elazığ Province (Turkey). *Journal of Water and Climate Change*. 2024;00(0).
- [50] Jain VK, Pandey RP, Jain MK, Byun HR. Comparison of drought indices for appraisal of drought characteristics in the Ken River Basin. *Weather and Climate Extremes* [Internet]. 2015;8:1–11. Available from: <http://dx.doi.org/10.1016/j.wace.2015.05.002>
- [51] Aksoy YC and H. Spatial Drought Characterization for Seyhan River Basin in the Mediterranean Region of Turkey. *Water (Switzerland)*. 2019;11:1–18.
- [52] Hsin-Fu Yeh HF, Chang CF. Using Standardized Groundwater Index and Standardized Precipitation Index to Assess Drought Characteristics of the Kaoping River Basin, Taiwan. *Water Resources*. 2019;46(5):670–8.
- [53] Katipoğlu OM, Acar R, Şengül S. Comparison of meteorological indices for drought monitoring and evaluating: A case study from euphrates basin, Turkey. *Journal of Water and Climate Change*. 2020;11(1S):29–43.
- [54] Vicente-Serrano SM, Beguería S, Lorenzo-Lacruz J, Camarero JJ, López-Moreno JI, Azorin-Molina C, et al. Performance of drought indices for ecological, agricultural, and hydrological applications. *Earth Interactions*. 2012;16(10):1–27.
- [55] Berhail S, Katipoğlu OM. Comparison of the SPI and SPEI as drought assessment tools in a semi-arid region: case of the Wadi Mekerra basin (northwest of Algeria). *Theoretical and Applied Climatology* [Internet]. 2023;1373–93. Available from: <https://doi.org/10.1007/s00704-023-04601-2>
- [56] Danandeh Mehr A, Vaheddoost B. Identification of the trends associated with the SPI and SPEI indices across Ankara, Turkey. *Theoretical and Applied Climatology*. 2020;139(3–4):1531–42.
- [57] Salehnia N, Alizadeh A, Sanaeinejad H, Bannayan M, Zarrin A, Hoogenboom G. Estimation of meteorological drought indices based on AgMERRA precipitation data and station-observed precipitation data. *Journal of Arid Land*. 2017;9(6):797–809.
- [58] Katipoğlu OM, Sarıgöl M. Coupling machine learning with signal process techniques and particle swarm optimization for forecasting flood routing calculations in the Eastern Black Sea Basin, Türkiye. *Environmental Science and Pollution Research* [Internet]. 2023;46074–91. Available from: <https://doi.org/10.1007/s11356-023-25496-6>
- [59] Serencam U. Innovative trend analysis of total annual rainfall and temperature variability case study: Yesilirmak region, Turkey. *Arabian Journal of Geosciences*. 2019;12(23):1–9.

Improved Spatial Modulation with Mapping Diversity

Mümtaz YILMAZ^{1*}

¹ Department of Electrical and Electronics Engineering, Faculty of Engineering, Aydın Adnan Menderes University,
Aydın, Türkiye

*¹ mumtaz.yilmaz@adu.edu.tr

(Geliş/Received: 30/07/2023;

Kabul/Accepted: 27/03/2024)

Abstract: In this work, the mapping diversity technique is exploited for generalized spatial modulation. In this context, multiple constellations, obtained as the solution of the optimization problem that maximizes Euclidean distance between the elements of the signal set, are employed in the active transmit antennas of the generalized spatial modulation scheme. Supported by analytical analysis and simulation results, the proposed scheme is shown to enhance the error rate performance of conventional generalized spatial modulation.

Key words: Spatial modulation, mapping diversity, constellation design, fading channel.

Eşleme Çeşitliliği ile İyileştirilmiş Uzaysal Modülasyon

Öz: Bu çalışmada geliştirilmiş uzaysal modülasyon için eşleme çeşitliliği tekniğinden faydalanılmıştır. Bu kapsamda, geliştirilmiş uzaysal modülasyon şemasındaki aktif iletim antenlerinde sinyal kümesindeki elemanlar arası Öklit mesafesini maksimize eden optimizasyon probleminin çözümü olarak elde edilen çoklu işaret kümeleri kullanılmıştır. Tasarlanan şemanın geleneksel uzaysal modülasyon tekniğinin hata oranı performansını iyileştirdiği analitik analiz ve benzetim sonuçları ile desteklenerek gösterilmiştir.

Anahtar kelimeler: Uzaysal modülasyon, eşleme çeşitliliği, işaret kümesi tasarımı, sönmülemeli kanal.

1. Introduction

Using multiple antennas in both transmitter and receiver nodes of a wireless communication system [1] is a promising solution to improve capacity and throughput. In this context, there have been tremendous works in the literature in the first decade of this century that develop multiple input – multiple output (MIMO) transmission techniques. The two well-known approaches in MIMO systems are spatial multiplexing [2] and space-time block codes [3]. Although it is possible to achieve high bandwidth efficiency by employing spatial diversity, interference arises as an important drawback in detection at the receiver. On the other hand, space-time block codes have been shown to attain high diversity order with reasonable receiver complexity.

Spatial modulation is an enhanced MIMO technique that exploits the antenna index in addition to conventional modulation techniques to increase the number of information bits per symbol [4-10]. Specifically, for each channel use in a spatial modulated system, a certain number of the data bits are utilized to identify the active antennas used for transmission, while the remaining bits are used to select the corresponding symbol from the constellation diagram. Consequently, it is possible to improve the bandwidth efficiency by employing spatial modulation techniques. Spatial modulation is designed for quadrature amplitude modulation (QAM) and phase shift keying (PSK) modulation schemes and shown to outperform maximum ratio combining for different data rates in one of the pioneering works [4]. Space shift keying (SSK) [5] can be considered the simplest form of spatial modulation because it only uses antenna indices to transmit information without any specific modulation scheme. Specifically, SSK is a special case of spatial modulation in which the active antenna index is determined by data bits and the unmodulated carrier signal is transmitted from the corresponding active antenna/antennas. Spatial modulation is extended for OFDM in [6] and analytical performance results are supported with simulation results. In the general survey paper [7], transceiver design and link adaptation techniques are provided together with spatial constellation optimization. The results in [7] show that with proper spatial constellation design, it is possible to decrease the bit error ratio (BER) in spatial modulation systems.

In the spatial modulation technique, the overall system consists of a combination of two domains, namely space and signal domains. Increasing the constellation size of one of them requires decreasing the other, so it is critical to balance the constellation size of these two domains. Related to this issue, the optimal constellation sizes

* Corresponding author: mumtaz.yilmaz@adu.edu.tr. ORCID Number of authors: ¹ 0000-0002-1121-7331

of signal and space domains in spatial modulation are found in [8] using the union bound of the bit error probability parameter. In the milestone work [9], spatial modulation is combined with the space-time block coding technique, and in addition to the increase in spectral efficiency provided by spatial modulation, the diversity and coding gains are attained due to the use of space-time block codes. In another related work [10], a spatial modulation multiple-input–multiple-output (SM-MIMO) system is proposed with spatial constellation diagrams and shaping filters being used as design parameters. It was shown in [10] that properly designed SM-MIMO systems achieve better performance than their counterpart MIMO systems, even with lower decoding complexity. Trellis-coding schemes are also considered in spatial modulation systems and like trellis-coded modulation, trellis coding is introduced in spatial modulation as well [11].

Generalized spatial modulation (GSM) [12-14] is an extension of spatial modulation in which the constraint of using only one transmit antenna for each message symbol is removed and multiple antennas are activated simultaneously for each group of information bits to be transmitted. By increasing the number of active transmit antennas, it is possible to improve spectral efficiency and error resilience. In GSM, an active set of transmit antennas is selected through a predetermined mapping table, and by using a maximum likelihood detector at the receiver, both the used antenna combinations and the transmitted symbols are detected [12]. The BER performance and capacity analysis of GSM is presented in [13]. In a concurrent work [14] the general framework of the GSM system is presented in which multiple active transmit antennas transmit the same information. Since multiple simultaneous transmission occurs in GSM, the performance may be enhanced with proper signal constellation design. In this context, there exist several works [15-18] in the literature that investigate the effect of constellation design on spatial modulation schemes. In [15], the rotated versions of the original constellation are used at several active transmit antennas carrying different information symbols. In the other related paper [16], it was shown that for the quadrature spatial modulation system, a remarkable increase in performance may be attained with optimized constellations compared with standard PSK and QAM constellations. A related paper [17] employs union bound to analyze the bit error probability of quadrature spatial modulation and reveals that in addition to Euclidean distance and energy, the in-phase and quadrature components of the symbols have an impact on the error performance. As an extension in [18], three constellation designs are suggested to improve the error performance of MIMO systems with spatial modulation.

The automatic repeat protocol (ARQ) is probably the simplest but the most effective solution for error-free transmission [19]. It has a simple signaling rule that forces the source to retransmit the packets detected erroneously by the receiver. Instead of simple repetition, Benelli proposed a method for automatic repeat request (ARQ) [20] which improves the Euclidean distance and consequently increases throughput by using two different mappings for transmitting the same symbol. In this context, employing different constellations for different retransmissions of the same information block is generally referred to as mapping diversity (MD) or mapping rearrangement in the literature. The motivation behind the idea of multiple transmissions of the same data block is the potential to improve the reliability of the link affected by channel conditions [21]. Symbol mapping diversity is applied for multiple packet transmissions in [21] using M different rotated versions of 8-PSK, 16-PSK, and 16-QAM. The uncoded BER upper bound is minimized by optimizing the mapping. In a related work, it was shown in [22] that by altering bit-to-symbol mappings, the increase rate of minimum squared Euclidean distance is larger than that of the number of transmissions. Constellation Rearrangement (CoRe) is a particular form of mapping diversity and is proposed [23] for equalizing the reliabilities of the individual bits in a single symbol. Such a need for equalization is necessary because the variations in bit reliabilities naturally increase if identical constellations and mappings are employed when identical symbols are retransmitted. It was shown in [23] that in the case of 16-QAM for the AWGN channel, the average log-likelihood ratios of bits can be equalized with a total of four different mappings. CoRe is also used to enhance the performance of the relay channel [24].

Since simultaneous transmission of the same symbol from all active antennas occurs in a MIMO system employing GSM, the constellation rearrangement technique is embedded in the system design to enhance the error correction capability in this work. Specifically, multiple different signal constellations obtained by the constellation rearrangement method are used individually at active transmit antennas at each time slot. The constellation optimization in mapping diversity is based on increasing the Euclidean distance of the successive constellations considered together. The overall effect can be regarded as an increase in BER performance like coding gain. Since embedding mapping diversity in the generalized spatial modulation system requires only using a second predetermined constellation obtained with optimization, no additional complexity arises compared to standard GSM. So, it can be stated that embedding mapping diversity in GSM system has the potential to enhance the BER without bringing any increase in the complexity of the system. Therefore, the main difference between the system structure of this paper and those of existing ones in the literature can be explained from the implementation aspect. In this work, multiple versions of the same symbol are transmitted using multiple

constellations which are obtained by optimization. The organization of the paper is as follows: In the following second section, the system model is introduced together with transmission protocols. The analytical BER performance analysis is presented in the third section. Following the Monte Carlo simulation results in Section IV, the paper is concluded in Section V.

2. System Model and Transmission Protocols

The general framework of the GSM transceiver is given in Fig. 1. It is assumed that a total of $m = m_l + m_s$ information bits are grouped to message vector \mathbf{b} . Next vector \mathbf{b} is partitioned into two parts, while the first m_l bits are used for antenna mapping, the last m_s bits constitute the transmitted modulation symbol. There exists a total of N_T transmit antennas and N_R receive antennas. Among N_T transmit antennas, N_A of them are active at each time slot and they all transmit the same symbol. The number of possible combinations of active antennas out of all transmit antennas can be given as $\mathbb{C} N_T, N_A$ where $\mathbb{C} \cdot$ stands for binomial coefficient.

Since the first m_l bits of data vector \mathbf{b} is used for antenna selection, it is enough to use only $N = 2^{\lfloor \log_2 \mathbb{C} N_T, N_A \rfloor}$ combinations among all these possible combinations and straightforward to define $m_l = \lfloor \log_2 \mathbb{C} N_T, N_A \rfloor$ where $\lfloor k \rfloor$ is the largest integer less than or equal to k and $N = 2^{m_l}$. Let us define the set of all used combinations by \mathbf{L} . Each combination, $l = \{l_1, l_2, \dots, l_{N_A}\} \in \mathbf{L}$, is a set, elements of which gives indices of the N_A active antennas. As mentioned before, the last m_s bits are used to form the M-ary modulated symbol $s \in \mathbf{S}$ where $M = 2^{m_s}$. In each period, the same symbol, s , is transmitted simultaneously from all N_A active antennas, and the remaining $N_T - N_A$ antennas remain silent. The overall spectral efficiency is $m = m_l + m_s$ bits per transmission.

The Rayleigh flat fading transmission channel \mathbf{H} is a matrix whose individual elements are complex independent and identically distributed (i.i.d.) Gaussian random variables. Additionally, there exists an additive white Gaussian noise (AWGN) with zero mean and σ_n^2 variance in each transmission path. The transmitted signal is a $N_T \times 1$ sized vector \mathbf{x} , whose elements are the same symbol, s , at indices $\{l_1, l_2, \dots, l_{N_A}\}$ and the remaining elements are zeros. Following this definition, let \mathbf{s} be a length $N_A \times 1$ vector with all elements s . In this context, the received signal can be expressed as given in equation (1),

$$\mathbf{y} = \mathbf{H}\mathbf{x} + \mathbf{n} = \sum_{n=1}^{N_A} \mathbf{h}_{l_n} s + \mathbf{n} = \mathbf{H}_l \mathbf{s} + \mathbf{n} \quad (1)$$

where \mathbf{h}_{l_n} is the l_n^{th} column of the channel matrix \mathbf{H} and \mathbf{H}_l is a sized submatrix of \mathbf{H} formed by extracting the $l = \{l_1, l_2, \dots, l_{N_A}\}$ indexed columns of \mathbf{H} . At the receiver, maximum likelihood detection is employed to jointly detect the active antenna set and transmitted symbol. Spatial modulation (SM) detector employs maximum likelihood algorithm and implements an exhaustive search over the sets \mathbf{L} and \mathbf{S} to find possible transmitted signal. It is assumed that perfect channel state information is available in respective receivers. The estimate of transmitted symbol and active antenna set can be found following the work [13] and is given in Eq (2).

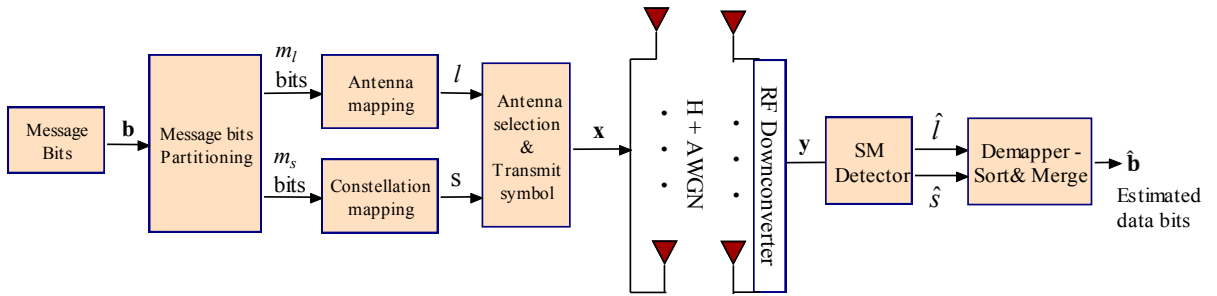


Figure 1. General block diagram of GSM system

$$\left[\hat{l}, \hat{s} \right] = \arg \min_{l \in \mathbf{L}, s \in \mathbf{S}} \left\| \mathbf{y} - \mathbf{H}_l \mathbf{s} \right\|_F^2 \quad (2)$$

In this work, a special case of the general spatial modulation is evaluated and specifically, it is assumed that there exists a total of four transmit antennas, two of which are active in each transmission at the transmitter node. In classical generalized spatial diversity scheme, as previously stated, the same symbol is transmitted from both two active antennas. Moreover, the same constellation is used for two simultaneous transmissions from two antennas. Additionally, to enhance the performance, mapping diversity is embedded in spatial modulation, and it is proposed to use two different constellations obtained by solving the optimization problem that aims to minimize the symbol error rate.

In this context, let the two different constellations used for mapping diversity be defined as $\mathbf{S}^{(1)}$ and $\mathbf{S}^{(2)}$ respectively. Since two active antennas are selected among all four transmit antennas, the set of antenna combination, $L = \{1,4, 2,3, 2,4, 3,4\}$, is selected and the corresponding four possible \mathbf{x} vectors representing transmitted signals from four transmit antennas is given in Table 1. Without loss of generality, the while first active antenna uses the constellation $\mathbf{S}^{(1)}$ to determine the transmitted symbol, the second antenna employs the constellation diagram $\mathbf{S}^{(2)}$. In the spatial domain, $m_l = 2$ data bits are used to select one element of the set of antenna combinations.

Table 1. Transmit Antenna Mapping Table

bits used for antenna mapping	Transmitted vector
00	$\mathbf{x} = \begin{bmatrix} s^{(1)} & 0 & 0 & s^{(2)} \end{bmatrix}$
01	$\mathbf{x} = \begin{bmatrix} 0 & s^{(1)} & s^{(2)} & 0 \end{bmatrix}$
10	$\mathbf{x} = \begin{bmatrix} 0 & s^{(1)} & 0 & s^{(2)} \end{bmatrix}$
11	$\mathbf{x} = \begin{bmatrix} 0 & 0 & s^{(1)} & s^{(2)} \end{bmatrix}$

3. Analytical Performance Analysis

In mapping diversity technique, the constellation diagrams can be found by solving the optimization problem that tries to minimize the BER. In this context, assuming a message out of M elements is transmitted through the N channel uses each with different constellation diagrams, the union bound for error probability [25] can be defined as given in Eq. (3),

$$P_b \leq \frac{1}{\log_2 M} \frac{1}{M} \sum_{i=1}^M \sum_{j=1, j \neq i}^M d_H(\mathbf{s}_i, \mathbf{s}_j) P(\mathbf{s}_i \rightarrow \mathbf{s}_j) \quad (3)$$

Here $\mathbf{s}_i = \left[s_i^{(1)}, s_i^{(2)}, \dots, s_i^{(N)} \right]$ is the i^{th} message vector formed by collecting all the i^{th} indexed message symbols from a total of N different constellations and $s_i^{(k)}$ is the i^{th} element of the constellation $\mathbf{S}^{(k)}$. Additionally, $d_H(\mathbf{s}_i, \mathbf{s}_j)$ represents the Hamming distance between vectors \mathbf{s}_i and \mathbf{s}_j and $P(\mathbf{s}_i \rightarrow \mathbf{s}_j)$ is the pairwise error probability of detecting \mathbf{s}_j although \mathbf{s}_i is transmitted. Assuming that maximum ratio combining is employed at the receiver, the pairwise error probability, given in Eq.(4), can be expressed using the Chernoff bound as [26]

$$P(\mathbf{s}_i \rightarrow \mathbf{s}_j) \leq \frac{4(N_0)^N}{\prod_{k=1}^N |s_i^{(k)} - s_j^{(k)}|^2} \quad (4)$$

The pairwise error probability expression given in Eq. (4) shows that to minimize the symbol error rate, the term $\prod_{k=1}^N |s_i^{(k)} - s_j^{(k)}|^2$ should be maximized. For $N=2$ (single retransmission) we can express this optimization problem [24] mathematically as given in Eq.(5).

$$\min_{\substack{s_i^{(1)}, s_i^{(2)} \\ i=1,2,\dots,M}} \sum_{i=1}^M \sum_{j=i+1}^M \frac{2C}{|s_i^{(1)} - s_j^{(1)}|^2 |s_i^{(2)} - s_j^{(2)}|^2} \quad (5)$$

such that $\frac{1}{M} \sum_{i=1}^M |s_i^{(k)}|^2 \leq 1 \quad \forall k$

In Eq. (5), $C=(4N_0)^2$ is a constant where $N_0/2$ is the noise variance. This optimization problem can be solved using an exhaustive search method. To obtain the optimum solution, the classical uniform constellations are chosen as the first constellation set, $\mathbf{S}^{(1)}$, as a baseline reference. Upon this selection, $\mathbf{S}^{(2)}$ is found by minimizing the metric given in Eq. (5). The constellations obtained by this search are given in Fig. 2 for 16-QAM.

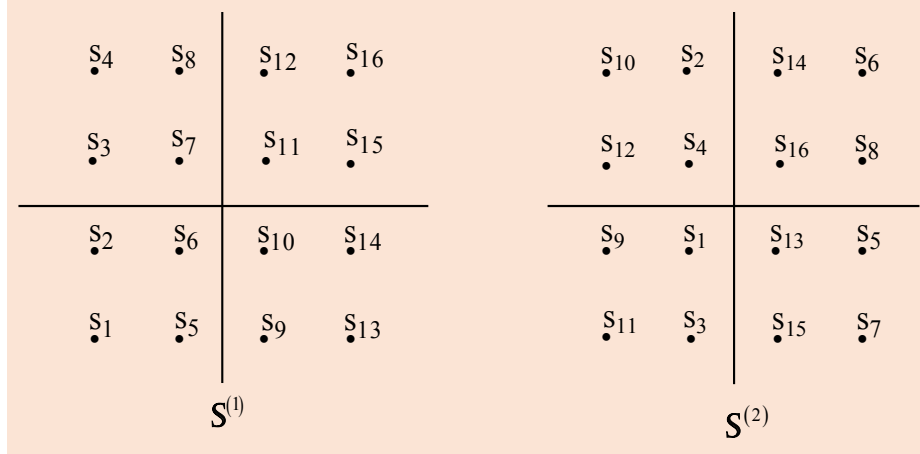


Figure 2. Mapping diversity constellations for 16-QAM

To derive the analytical average error probability of GSM the union bounding technique is applied [12,25]. Since the transmitted symbol in spatial modulation is the combination of spatial symbol and data symbol, a maximum likelihood joint detection of active antenna set, and transmitted data is realized at the receiver. Therefore, the pairwise error probability (PEP) can be defined as the probability that rather than deciding in favor of the actual transmitted spatial and data symbols (l,s) another set of symbols is detected. Following the analysis in [12,13] the PEP can be expressed mathematically as given in Eq.(6).

$$\begin{aligned} PEP(l, s \rightarrow \tilde{l}, \tilde{s}) &= \Pr\left(\|\mathbf{y} - \mathbf{H}_l \mathbf{s}\|_F^2 > \|\mathbf{y} - \mathbf{H}_{\tilde{l}} \tilde{\mathbf{s}}\|_F^2 \mid \mathbf{H}\right) \\ &= Q\left(\frac{\|\mathbf{H}_l \mathbf{s} - \mathbf{H}_{\tilde{l}} \tilde{\mathbf{s}}\|_F^2}{2\sigma_n^2}\right) = Q\left(\sqrt{\sum_{r=1}^{N_R} \gamma_r}\right) \end{aligned} \quad (6)$$

where $Q(\alpha) = \frac{1}{2\pi} \int_{\alpha}^{\infty} e^{-x^2/2} dx$ is the well-known Q function and $\gamma_r = |h_{l,r}s - h_{\tilde{l},r}\tilde{s}|^2$. Also $h_{l,r}$ is the r^{th} element of

the vector \mathbf{h}_l . The random variable $\kappa = \sqrt{\sum_{r=1}^{N_R} \gamma_r}$ is chi-squared distributed and its probability distribution function [27] can be given as in Eq.(7),

$$f_{\kappa}(\kappa) = \frac{1}{\Gamma(N_R)\gamma^{N_R}} \kappa^{(N_R-1)} \exp\left(-\frac{\kappa}{\bar{\gamma}}\right) \quad (7)$$

where $\bar{\gamma}$ is the mean value of γ . Since two different constellations are applied for two simultaneous transmissions from two active antennas, $\bar{\gamma}$ can be defined as given in Eq.(8),

$$\bar{\gamma} = \begin{cases} |s^{(1)} - \tilde{s}^{(1)}| |s^{(2)} - \tilde{s}^{(2)}| & \text{if } \tilde{l} = l \\ |s^{(1)}s^{(2)}| + |\tilde{s}^{(1)}\tilde{s}^{(2)}| & \text{if } \tilde{l} \neq l \end{cases} \quad (8)$$

Following the works [28,29], the average value of PEP can be calculated as given in Eq. (9).

$$\begin{aligned} E[Q(\sqrt{\kappa})] &= \int_{\kappa} f_{\kappa}(\kappa) Q(\sqrt{\kappa}) d\kappa \\ &= \int_{\kappa} \frac{1}{\Gamma(N_R)\gamma^{N_R}} \kappa^{(N_R-1)} \exp\left(-\frac{\kappa}{\bar{\gamma}}\right) Q(\sqrt{\kappa}) d\kappa \\ &= \beta^{N_R} \sum_{i=0}^{N_R-1} \mathbb{C}((N_R - 1 + i), i) (1 - \beta)^i \end{aligned} \quad (9)$$

$$\text{where } \beta = \frac{1}{2} \left(1 - \sqrt{\frac{\bar{\gamma}/2}{1 + \bar{\gamma}/2}} \right)$$

Consequently, the analytical BER [25,28] can be obtained as given in Eq.(10) ,

$$\text{BER} = \frac{1}{2^n} \sum_{\tilde{l}, \tilde{s}} \sum_{l, s} \frac{e}{\eta} \beta^{N_R} \sum_{i=0}^{N_R-1} \mathbb{C}((N_R - 1 + i), i) (1 - \beta)^i \quad (10)$$

where e is the Hamming distance of the PEP event between (l, s) and (\tilde{l}, \tilde{s}) .

4. Simulation Results

The performance of the proposed scheme is evaluated for the Rayleigh fading channel. In all the simulations presented in this work, perfect channel state information is assumed at all the receivers. Additionally, the average signal energy is chosen as unity for all modulation schemes. The derived analytical BER performances are presented together with simulation results. Following the main framework with four transmit antennas among which two are active at each transmission and two receive antennas, the BER performances with respect to signal-to-noise ratio (SNR) value are obtained for both conventional GSM system and the proposed GSM system with mapping diversity. For a fair comparison between the conventional GSM system without mapping diversity and the proposed GSM system with mapping diversity, all common parameters (block size, transmit power) are chosen as the same.

In terms of modulation technique, uniform decomposable QAM schemes are applied initially. The two different constellations used in mapping diversity for 16-QAM are already given in Fig. 2. For the conventional GSM system in which mapping diversity is not employed, the conventional 16-QAM ($\mathcal{S}^{(1)}$ in Fig. 2) constellation is used at both two active transmit antennas. The simulation results of the proposed mapping diversity embedded generalized spatial modulation for 16-QAM modulation are presented in Fig. 3. The main observation from simulation results is that a remarkable gain in terms of BER can be achieved by incorporating mapping diversity in spatial modulation. Defining the gain as the decrease in required SNR for a certain BER, it can be stated that this gain increases with increasing SNR and is almost constant in the high SNR regime. For instance, the gain is around 1,2 dB for a BER level of 10^{-3} . Also, the derived analytical BER bound is shown to align perfectly with simulation results for high SNR values. To determine its effect, the number of receive antennas is increased to four, and the results are given in Fig. 4. It can be easily stated that, since increasing the number of receive antennas increases the diversity as well, the BER performance increases with the number of receive antennas. Additionally, the proposed GSM system with mapping diversity still outperforms the conventional GSM system without mapping diversity.

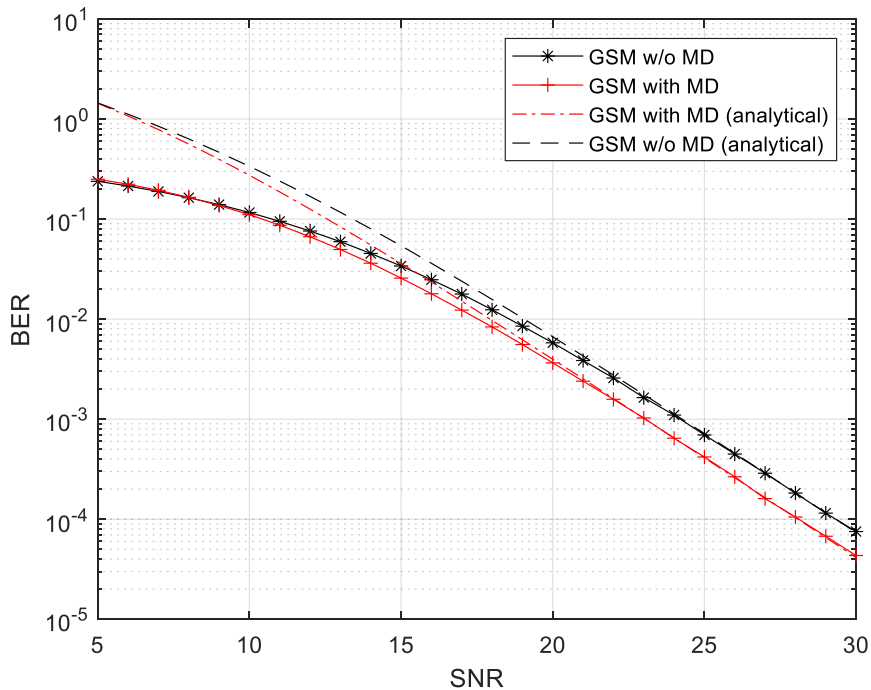


Figure 3. Analytical and simulation results for 16-QAM modulation

To determine the effect of constellation size, the M value is increased to 64 and another uniform, decomposable QAM scheme, namely 64-QAM is also considered. Following the optimization technique given in Section 3, two different constellations are obtained to be used in mapping diversity. The analytical and simulation results of the proposed system for 64-QAM modulation are presented in Fig. 5. Likewise, embedding mapping diversity in generalized spatial modulation achieves a larger gain in terms of BER than the 16-QAM case. To compare, the gain for the BER level of 10^{-3} is 2,1 dB which is 0,9 dB larger than 16-QAM modulation. The reason for this is that the potential of improvement with mapping diversity increases with modulation level, i.e., increasing modulation level value (M) from 4 (16-QAM) to 6 (64-QAM) results in a better improvement in average BER.

Lastly, two non-decomposable QAM schemes, 8-QAM and 32-QAM are used as the modulation technique, and the performances of the proposed systems are presented in Fig. 6 and Fig. 7 respectively. The analytical results still align with simulation results and embedding mapping diversity in the GSM system improves the BER performance. Numerically, while the gain for 8-QAM is 0,9 dB at a BER level of 10^{-3} (Fig. 6), which is 0,3 dB smaller than that of 16-QAM, it reaches a value of 1,4 dB for 32-QAM (Fig. 6) which is slightly larger (0,2 dB) than 16-QAM case.

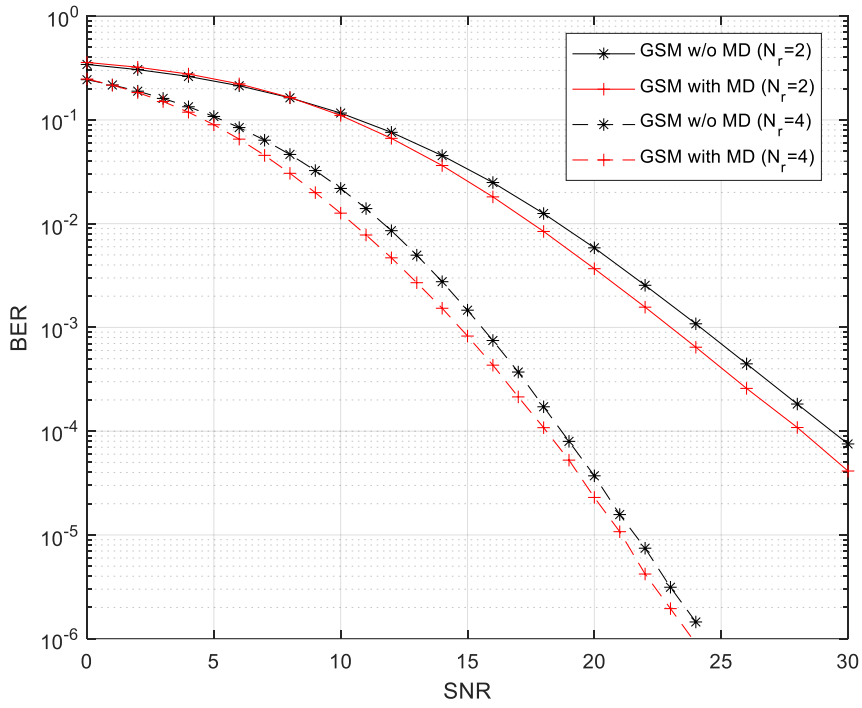


Figure 4. Simulation results for 16-QAM modulation for different number of receive antennas.

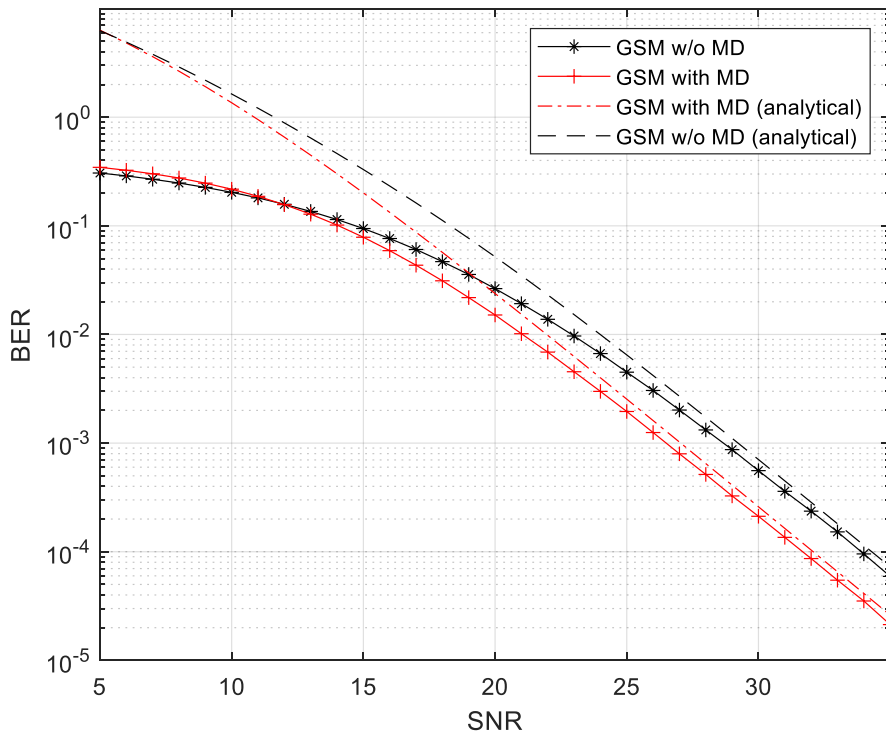


Figure 5. Analytical and simulation results for 64-QAM modulation.

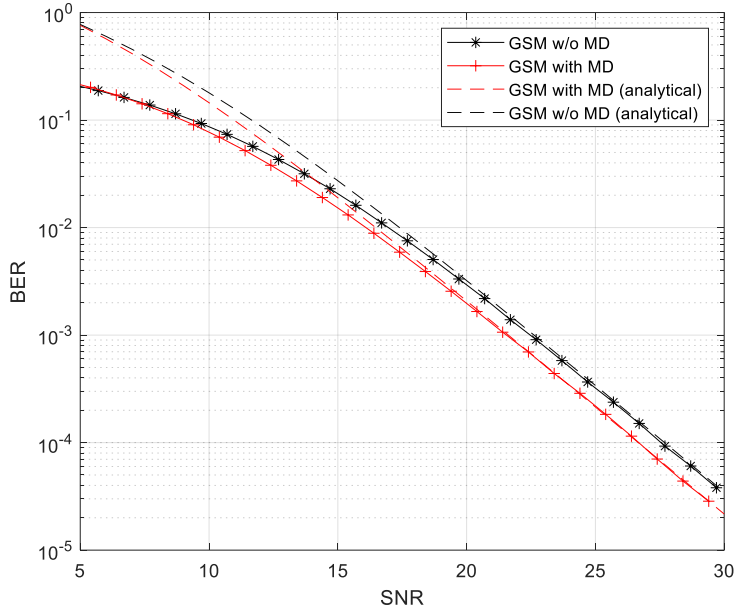


Figure 6. Analytical and simulation results for 8-QAM modulation.

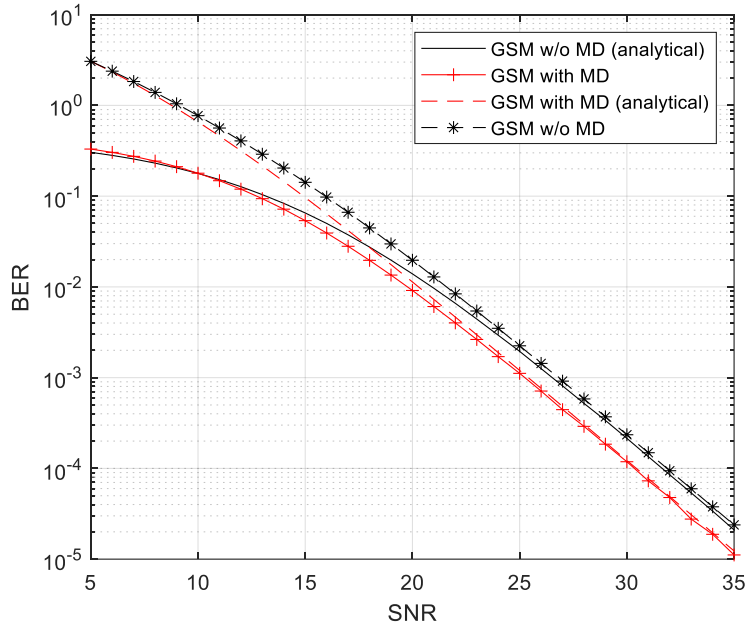


Figure 7. Analytical and simulation results for 32-QAM modulation.

5. Conclusion

In this work, mapping diversity is deployed in a MIMO system with generalized spatial modulation. Precisely, differently from conventional generalized spatial modulation in which the same constellation is applied in the transmission phase, multiple distinct constellations optimized for mapping diversity are used individually from all the active antennas in the setup. The potential of the proposed system is first evaluated analytically and then quantified with simulations. The results revealed that the performance of the generalized spatial modulation can be enhanced with the mapping diversity technique. Since perfect channel state information is assumed in this work, investigating the effect of channel estimation errors on overall performance is a future work of this paper.

References

- [1] Mietzner J, Schober R, Lampe L, Gerstacker WH, Hoeher PA. Multiple-antenna techniques for wireless communications - a comprehensive literature survey. *IEEE Communication Surveys & Tutorials* 2009; 11(2):87–105.
- [2] Zheng L, Tse DNC. Diversity and multiplexing: a fundamental tradeoff in multiple-antenna channels. *IEEE Transactions on Information Theory* 2003; 49(5): 1073-1096.
- [3] Tarokh V, Jafarkhani H, Calderbank A. Space-time block codes from orthogonal designs. *IEEE Transactions on Information Theory* 1999; 45(5):1456–1467.
- [4] Mesleh R, Haas H, Ahn CW, Yun S. Spatial Modulation - A New Low Complexity Spectral Efficiency Enhancing Technique. In: 2006 First International Conference on Communications and Networking; 2006; Beijing, China, pp. 1-5.
- [5] Jeganathan J, Ghrayeb A, Szczecinski L, Ceron A. Space shift keying modulation for MIMO channels. *IEEE Transactions on Wireless Communications* 2009; 8(7): 3692-3703.
- [6] Mesleh RY, Haas H, Sinanovic S, Ahn CW, Yun S. Spatial Modulation. *IEEE Transactions on Vehicular Technology* 2008; 57(4): 2228-2241.
- [7] Yang P, Di Renzo M, Xiao Y, Li S, Hanzo L. Design Guidelines for Spatial Modulation. *IEEE Communications Surveys & Tutorials* 2015; 17(1): 6-26.
- [8] Maleki M, Bahrami HR, Alizadeh A, Tran NH. On the Performance of Spatial Modulation: Optimal Constellation Breakdown. *IEEE Transactions on Communications* 2014; 62(1): 144-157.
- [9] Başar E, Aygözü Ü, Panayircı E, Poor HV. Space-time block coded spatial modulation. *IEEE Transactions on Commun.* 2011; 59(3): 823–832.
- [10] Di Renzo M, Haas H. On Transmit Diversity for Spatial Modulation MIMO: Impact of Spatial Constellation Diagram and Shaping Filters at the Transmitter. *IEEE Transactions on Vehicular Technology* 2013; 62(6); 2507-2531.
- [11] Başar E, Aygözü Ü, Panayircı E, Poor HV. New trellis code design for spatial modulation. *IEEE Trans. Wireless Commun.* 2011; 10(9): 2670–2680.
- [12] Younis A, Serafimovski N, Mesleh R, Haas H. Generalised spatial modulation. In: 2010 Conference Record of the Forty Fourth Asilomar Conference on Signals, Systems and Computers; 2010; pp. 1498-1502.
- [13] Younis A, Basnayaka DA, Haas H. Performance Analysis for Generalised Spatial Modulation. In: European Wireless 2014; 20th European Wireless Conference; 2014; Barcelona, Spain, pp. 1-6.
- [14] Fu J, Hou C, Xiang W, Yan L, Hou Y. Generalised spatial modulation with multiple active transmit antennas. In 2010 IEEE Globecom Workshops; 2010; Miami, FL, USA, pp. 839-844
- [15] Wang J, Jia S, Song J. Generalised Spatial Modulation System with Multiple Active Transmit Antennas and Low Complexity Detection Scheme. *IEEE Transactions on Wireless Communications* 2012; 11(4): 1605-1615.
- [16] Maleki M, Bahrami HR, Alizadeh A. Constellation design for spatial modulation. In: 2015 IEEE International Conference on Communications (ICC); 2015; London, UK, pp. 2739-2743.
- [17] Vo BT, Nguyen HH, Tuan HD. Constellation Design for Quadrature Spatial Modulation. In: 2017 IEEE 86th Vehicular Technology Conference (VTC-Fall); 2017; Toronto, ON, Canada, pp. 1-5.
- [18] Vasavada Y, John BB. Constellation Designs for the Spatial Modulation MIMO Systems. In: 2022 IEEE International Conference on Signal Processing and Communications (SPCOM); 2022, Bangalore, India, pp. 1-5
- [19] Lin S, Costello DJ, Miller MJ. Automatic-repeat-request error-control schemes. *IEEE Communications Magazine* 1984; 22(12), 5-17.
- [20] Benelli G. A new method for the integration of modulation and channel coding in an ARQ protocol. *IEEE Transactions on Communications* 1992; 40(10): 1594–1606.
- [21] Samra H, Ding Z, Hahn PM. Symbol mapping diversity design for multiple packet transmissions. *IEEE Transactions on Communications* 2005; 53(5): 810–817.
- [22] Szczecinski L, Bacic M. Constellations design for multiple transmissions: maximizing the minimum squared Euclidean distance. In: 2005 Proceedings of IEEE Wireless Communications and Networking Conference (WCNC '05); 2005; New Orleans, LA, USA, pp.1066–71.
- [23] Wengert C, von Elbwart AGE, Seidel E, Velez G, Schmitt MP. Advanced hybrid ARQ technique employing a signal constellation rearrangement. In: 2002 Proceedings of the 56th IEEE Vehicular Technology Conference; 2002; Vancouver, BC, Canada, pp.2002–6.
- [24] Khormuji MN, Larsson EG. Improving Collaborative Transmit Diversity by Using Constellation Rearrangement. In 2007 IEEE Wireless Communications and Networking Conference, Hong Kong, China, 2007, pp. 803-807,
- [25] Proakis JG. *Digital Communications*, 4th ed. New York: McGraw-Hill Higher Education; 2000. ISBN: 9780071181839
- [26] Chernoff H. A Measure of Asymptotic Efficiency for Tests of a Hypothesis Based on the sum of Observations. *The Annals of Mathematical Statistics* 1952; 23(4): 493–507.
- [27] Abramowitz M, Stegun IA. *Handbook of Mathematical Functions with Formulas, Graphs, and Mathematical Tables*. ninth Dover printing, tenth GPO printing New York: Dover, 1964.
- [28] Simon MK, Alouini MS. *Digital Communication over Fading Channels*. 2nd ed. New York: John Wiley & Sons, Inc.; 2005. ISBN: 9780471649533.
- [29] Alouini MS, Goldsmith AJ. A unified approach for calculating error rates of linearly modulated signals over generalized fading channels. *IEEE Transactions on Communications* 1999;47(9), 1324-1334.

Molecular Dynamics Simulation of Bauschinger Effect in Cu Nanowire with Different Crystallographic Orientation

Sefa KAZANÇ¹, Canan AKSU CANBAY^{2*}

¹ Mathematics and Science Education, Faculty of Education, Fırat University, Elazığ, Türkiye

² Department of Physics, Faculty of Science, Fırat University, 23119 Elazığ, TÜRKİYE

¹ skazanc@firat.edu.tr, ^{2*} caksu@firat.edu.tr

(Geliş/Received: 11/09/2023;

Kabul/Accepted: 27/03/2024)

Abstract: In this study, the Bauschinger Effect (BE) resulting from tension-compression deformation applied to nanowires obtained by placing Cu atoms in $\langle 100 \rangle$, $\langle 110 \rangle$ and $\langle 111 \rangle$ highly symmetric crystallographic directions was investigated using the Molecular Dynamics (MD) simulation method. The forces between atoms were determined from the gradient of the Embedded Atom Method (EAM) potential function, which includes many-body interactions. It was determined that there is an asymmetry between the stress-strain curves obtained as a result of the tension and compression deformation process applied to the model system. From this asymmetry, it was determined that the yield stress obtained in the drawing process for nanowire with $\langle 100 \rangle$ crystallographic orientation was greater than the yield strain obtained as a result of the compression process. In contrast, the opposite was found for nanowires with crystallographic orientation $\langle 110 \rangle$ and $\langle 111 \rangle$. In addition, after the yield strain value is exceeded as a result of the drawing process applied to the model nanowire system, compression deformation process was applied at different pre-strain values. The existence of the Bauschinger Effect (BE), which is expressed as the yield strength value as a result of forward loading corresponding to the tension operation, is smaller than the yield value obtained as a result of the compression process in which the loading is removed, was determined. To clarify the effect of BE on Cu nanowires with different crystallographic orientations, Bauschinger Stress parameter (BSP) and Bauschinger Parameter (BP) values were calculated.

Key words: Nanowire, Bauschinger effect, crystallographic orientation, mechanical properties, molecular dynamics.

Farklı Kristalografik Yönelime Sahip Cu Nano Telindeki Bauschinger Etkisinin Moleküler Dinamik Benzetimi

Öz: Bu çalışmada, Cu atomlarının $\langle 100 \rangle$, $\langle 110 \rangle$ ve $\langle 111 \rangle$ yüksek simetrik kristalografik doğrultulara yerleştirilmesiyle elde edilen nano tellere uygulanan çekme-sıkıştırma deformasyonu sonucu oluşan Bauschinger Etkisi (BE) Moleküler Dinamik (MD) benzetim yöntemi kullanılarak incelendi. Çok cisim etkileşimlerini içeren Gömülmüş Atom Metodu (GAM) potansiyel fonksiyonunun gradientinden atomlar arasındaki kuvvetler belirlendi. Model sisteme uygulanan çekme ve sıkıştırma deformasyon işlemi sonucu elde edilen zor-zorlanma eğrileri arasında bir asimetri olduğu belirlendi. Bu asimetriden $\langle 100 \rangle$ kristalografik yönelime sahip nano tel için çekme işleminde elde edilen akma geriliminin sıkıştırma işlemi sonucu elde edilen akma geriliminden daha büyük olduğu belirlendi. Buna karşılık $\langle 110 \rangle$ ve $\langle 111 \rangle$ kristalografik yönelime sahip nano teller için tam tersi bir durum tespit edildi. Ayrıca model nano tel sistemine uygulanan çekme işlemi sonucu akma gerinim değeri aşıldıktan sonra farklı ön-gerinim değerlerinde sıkıştırma deformasyon işlemi uygulandı. Çekme işlemine karşılık gelen ileri yüklemeye sonucu akma dayanımı değerinin yüklenmenin kaldırıldığı sıkıştırma işlemi sonucu elde edilen akma değerinden küçük olması olarak ifade edilen Bauschinger Etkisi (BE)'nin varlığı belirlendi. BE'nin farklı kristalografik yönelimlere sahip Cu nano telleri üzerindeki etkisini açıklığa kavuşturmak için Bauschinger Stress parametresi (BSP) ve Bauschinger Parametresi (BP) değerleri hesaplandı.

Anahtar kelimeler: Nano tel, Bauschinger etkisi, kristalografik yönelim, mekanik özellikler, moleküler dinamik.

1. Introduction

Nanowires are of great technological importance due to their potential applications in nanoscale electrical, optical, thermal and mechanical systems. These nanowires allow for the construction of nanoelectromechanical systems with unprecedented functions [1-4]. However, in addition to their physical and chemical properties, since these devices are exposed to external forces and deformation where they are used, it is extremely important to know their mechanical properties. Therefore, it is necessary to know the deformation mechanisms of nanowires under complex stress conditions. Since nanowires have a large surface area to volume ratio compared to bulk materials, their structure and properties are quite different from bulk materials.

The different crystallographic orientations of nanowires significantly affect their mechanical properties such as Young's modulus, yield stress, yield strain plastic deformation mechanism. Diano et al. [5] observed an

* Corresponding author: caksu@firat.edu.tr. ORCID Number of authors: ¹0000-0002-8896-8571, ²0000-0002-5151-4576

unsymmetrical yield stress in the Au nanowire for $\langle 100 \rangle$, and $\langle 110 \rangle$, orientations due to surface-acting internal forces and different shear systems during tension-compression. Park et al. [6,7] studied the effects of stress deformation for fcc nanowires with different crystallographic orientations.

It is known that during the tension-compression deformation process applied to the sample, the symmetry in the stress-strain relationship is preserved only within the elastic region boundaries. Bauschinger observed in 1886 that this symmetry breaks down when the yield stress of the material is exceeded. If a material is plastically deformed in one direction, plastic yielding in the reverse loading direction occurs at a lower stress than in the forward loading direction. In general, during plastic deformation, dislocations stack up against obstacles of different kinds. This decrease in yield stress in the reverse loading direction is known as the Bauschinger effect (BE) [8, 9]. BE; It is observed in many single and polycrystalline metallic materials, including Al [10], Cu [11], Nb [12,], steel [13]. However, its amount varies from metal to metal, depending on its microstructural properties. Many industrial applications are affected by BE, such as metal forming processes, flattening of sheets and bars [14-16]. This effect minimizes the accumulation of defects and significantly affects the service life and performance of metallic components during cyclic loading processes such as fatigue [17], wear [18,19] by reducing stress concentrations. Although many studies have been conducted to investigate the origin of BE, the number of models and theories developed is very few [20].

Cu element exhibits anisotropic properties depending on the crystal orientation and its mechanical properties such as yield strength and modulus of elasticity vary considerably [21,22]. However, Cu is widely used in many nano/micro electromechanical systems in circuit construction [23].

Many studies have been carried out to experimentally determine the mechanical properties of nanowires [24-26]. However, atomistic simulation methods, especially MD simulations, produce very realistic results in this area [27,28]. Today, MD simulations are widely and effectively used in materials science research with the latest developments in computer technology. Researchers have carried out extensive experiments and atomistic simulation studies to understand the deformation behavior of fcc, bcc metallic nanowires [29-32]. Compared to experimental measurements, simulation studies provide more structural detail during deformation, allowing us to examine the mechanism from a microscopic perspective. Among many atomic models such as effective medium theory [33], tight binding model [34], Finnis-Sinclair dual function formulation [35], EAM [36] has a solid theoretical basis, density function theory and It is one of the most successful approaches because of its simple analytical expression. To date, EAM has been applied to various systems such as liquids, metals and alloys, semiconductors, ceramics, polymers, nanostructures and composite materials. Structural [37], mechanical [38,39], and thermal properties [40] have been extensively studied in studies.

In this study, the Bauschinger effect in the tension-compression deformation process applied to Cu nanowires with different crystallographic orientations at 10K temperature and $1 \times 10^{10} \text{s}^{-1}$ strain value was investigated by MD simulation method. Large-scale Atomic/Molecular Massively Parallel Simulator (LAMMPS) open source MD simulation program was used for modeling nanowire structures [41]. Plastic deformation of nanowires as a result of tension-compression cycle was determined by CNA analysis method from OVITO [42] program. It was determined that crystallographic orientations had a significant effect on the stress-strain curve of the nanowire system and the BE effect was clearly seen.

1. Simulation Details

The Lagrangian function of the system to be modeled in the MD method is given in (1) below.

$$L_{PR}(\mathbf{r}^N, \dot{\mathbf{r}}^N, \mathbf{h}, \dot{\mathbf{h}}) = \frac{1}{2} \sum_{i=1}^N m_i (\dot{\mathbf{s}}_i^t \mathbf{G} \dot{\mathbf{s}}_i) - \sum_{i=1}^N \sum_{j>i}^N \phi(|\mathbf{h} \mathbf{s}_{ij}|) + \frac{1}{2} M \text{Tr}(\dot{\mathbf{h}}^t \dot{\mathbf{h}}) - P_{ext} V \quad (1)$$

where s_i , \mathbf{h} , \mathbf{G} and P_{ext} parameters define the scaled coordinate, the axes of the calculation cell, the metric tensor and the external pressure, respectively. The equations of motion obtained from this function for the particles and the calculation cell are given in equations (2) and (3), respectively.

$$\ddot{\mathbf{s}}_i = -\frac{1}{m_i} \mathbf{F}_i - \mathbf{G}^{-1} \dot{\mathbf{G}} \dot{\mathbf{s}}_i \quad (2)$$

$$\ddot{\mathbf{h}} = M^{-1} (\Pi - \mathbf{I} P_{ext}) V (\mathbf{h}^t)^{-1} \quad (3)$$

For a system subjected to deformation, the stress is calculated by the microscopic stress tensor as given in equation (4) [43,44].

$$\sigma_{ij} = V^{-1} \left[\sum_{i=1}^N m_i \vartheta_i \vartheta_i - \sum_{i=1}^N \sum_{j>i}^N \frac{F_{ij}}{r_{ij}} \mathbf{r}_i \cdot \mathbf{r}_j \right] \quad (4)$$

An object under the influence of external forces is said to be in a strain state. The state of the stress at any point in the matter is determined by the nine-component stress tensor as in (5).

$$\sigma_{ij} = \begin{pmatrix} \sigma_{11} & \sigma_{12} & \sigma_{13} \\ \sigma_{21} & \sigma_{22} & \sigma_{23} \\ \sigma_{31} & \sigma_{32} & \sigma_{33} \end{pmatrix} \quad (5)$$

The components of the stress tensor σ_{11} , σ_{22} , σ_{33} (which can also be expressed as σ_x , σ_y , σ_z , respectively) are known as the normal components of the stress, and the other components are known as the shear components of the stress. The positive values of the normal components correspond to the tension stress and the negative values to the compression stress. In uniaxial loading applied to the system along the x-axis, only the σ_x component changes. In contrast, the other components are zero [45,46].

EAM is a quasi-experimental potential energy function, which includes many-body interactions and is used to model systems of monoatomic elements and alloys. In EAM, the energy of the system is determined from the energy required to embed an atom in the charge density of other atoms around it. Total energy of the system in EAM is expressed in (6) as;

$$E_{top} = \sum_i^N F_i(\rho_i) + \frac{1}{2} \sum_{i \neq j} \Phi(r_{ij}) \quad (6)$$

The first term in the function, $F_i(\rho_i)$, gives the embedding energy including many-body interactions, and the second term $\Phi(r_{ij})$ gives the two-body interaction [47]. EAM parameters of Cu element can be found in the literature [48].

In this study, nanowire systems were formed by placing Cu atoms at fcc lattice points along the $\langle 100 \rangle$, $\langle 110 \rangle$ and $\langle 111 \rangle$ high symmetry directions. Periodic boundary conditions were applied only along the x-direction. No boundary conditions were applied along the y and z directions. The numerical solution of the equations of motion was carried out with the velocity form of the Verlet algorithm. In order for the pre-tension value of the nanowire to be zero, 5×10^4 MD steps were stabilized using the system NVT canonical ensemble without applying shrinkage for all crystallographic orientations. The strain rate and an integration step were determined as $1 \times 10^{10} \text{ s}^{-1}$ and 1 fs, respectively, in the study. The conjugate gradient algorithm was used to minimize the energy in the initial structure.

Cu nanowires with $\langle 100 \rangle$, $\langle 110 \rangle$ and $\langle 111 \rangle$ orientations used in the study consist of 4647, 4857 and 4903 atoms, respectively. The length of the nanowire was determined as 10.8 nm in the x direction and 2.17 nm in the y and z directions. In the whole study, compression deformation was applied to different oriented Cu nanowires by tension deformation and removal of this deformation at different pre-strain values. Several atomic layers were fixed in the two end regions along the x-direction of the model nanowire system. Dynamic behavior of the remaining atoms in the intermediate region is allowed. In order to comply with the experimental pulling method, one of the fixed ends was kept motionless, while the other end was pulled.

2. Results and Discussion

In this study, the BE of the model systems was investigated by applying tension deformation along the x-axis and compression at certain pre-strain values to nanowires in which Cu atoms were placed at fcc lattice points along the $\langle 100 \rangle$, $\langle 110 \rangle$ and $\langle 111 \rangle$ high symmetry directions. In Figure 1, the initial structures of Cu nanowires with these three different crystal orientations are given. The tension-compression mechanical processing process was applied by keeping the left fixed end of the nanowire motionless, pulling the right fixed end with a strain rate of $1 \times 10^{10} \text{ s}^{-1}$ and removing the tension strain with the same strain rate. Both fixed ends of the nanowire consist of three fixed atomic layers.

In Figure 2(a-c), stress-strain curves obtained as a result of applying the initial tension and compression deformation process separately along the x-axis direction to the initial structures of Cu nanowire systems with crystallographic orientations of $\langle 100 \rangle$, $\langle 110 \rangle$ and $\langle 111 \rangle$ are given. It is noteworthy that crystallographic orientations have a significant effect on the stress-strain curves obtained as a result of the calculations. Cu nanowires show elastic anisotropy as a function of crystal orientation. As seen in Figure 2(a), point A where the strain is 0.11 in the drawing process applied to the $\langle 100 \rangle$ Cu nanowire is the yield point at 7.18 GPa at which plastic deformation begins. Then the voltage drops abruptly to 2.23 GPa at point B. This change in voltage is 4.95

GPa. These changes in tension for $\langle 110 \rangle$ and $\langle 111 \rangle$ nanowires were determined as 3.83 GPa and 8.97 GPa, respectively. This sudden change in the voltage value is known as the nucleation of dislocations within the nanowire system [7,49,50]. Partial dislocations dominated by Shockley partial dislocations slide rapidly along the $\{111\}$ crystal plane, causing a sharp drop in stress [51]. It can be said that the greatest stress variation occurs in the $\langle 111 \rangle$ nanowire and this crystallographic orientation is the optimal arrangement of atoms in the nanowire for nucleation, growth and movement of dislocations. During the compression process applied to the $\langle 100 \rangle$, $\langle 110 \rangle$ and $\langle 111 \rangle$ nanowires, this change in stress was determined as 0.405 GPa, 6.31 GPa and 12.09 GPa, respectively.

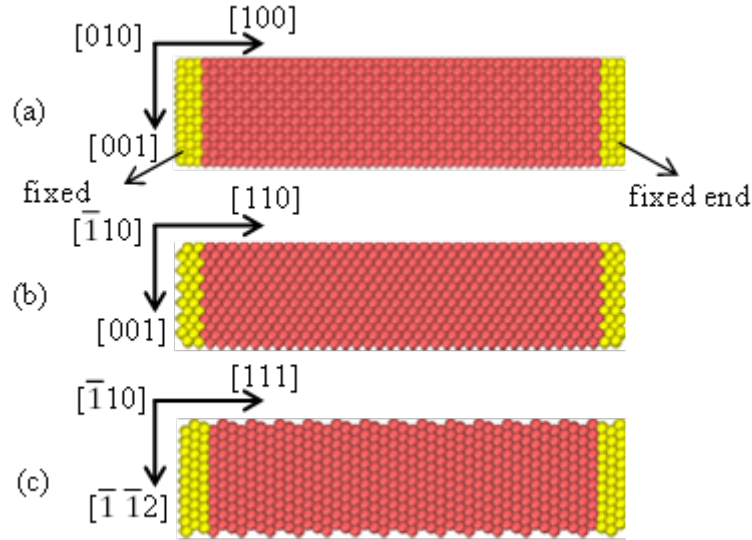


Figure 1. (a) $\langle 100 \rangle$, (b) $\langle 110 \rangle$ and (c) $\langle 111 \rangle$ Initial atomic structures of Cu nanowires. The yellow colored spheres indicate the stationary boundary atoms defined as the fixed end, the red colored spheres the dynamic atoms.

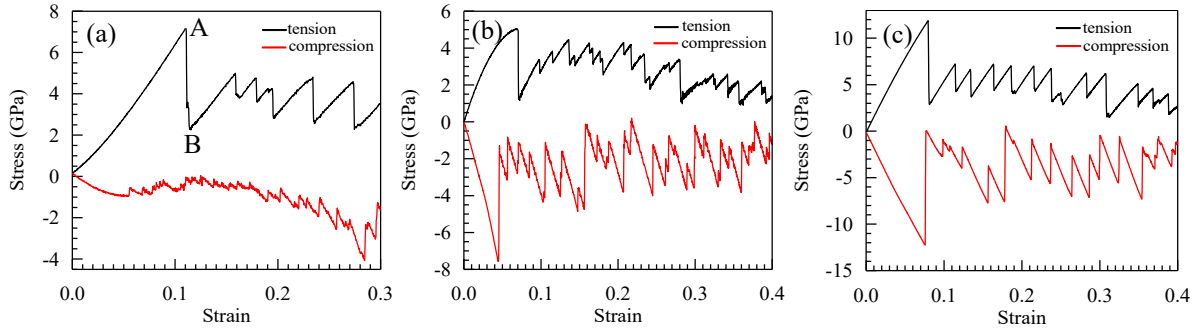


Figure 2. Stress-strain curves for (a) $\langle 100 \rangle$, (b) $\langle 110 \rangle$ and (c) $\langle 111 \rangle$ Cu nanowires obtained as a result of tension-compression deformation.

Figure 3 shows the yield stress (σ_y) in the tension direction, the pre-strain stress (σ_f) in the tension direction and the yield stress (σ_r) in the compression direction in the stress-strain curve obtained as a result of the tension-compression process applied to the nanowire system. Tension and compression deformation in nanowires with all three crystallographic orientations show an asymmetry in mechanical properties related to free surface effects in wires. When the strain reaches 0.056 as a result of the compression applied to the $\langle 100 \rangle$ nanowire system, $\sigma_r = 0.985$ GPa. This value is quite small compared to $\sigma_y = 7.18$ GPa. However, for $\langle 110 \rangle$ and $\langle 111 \rangle$ nanowires, the situation is the opposite ($\sigma_r > \sigma_y$). It is also seen for nanowires with three different crystallographic orientations that the stress-strain curve exhibits a zig-zag change as the strain value continues to increase. It can be said that the reason for this change is due to the growth and spread of nucleated dislocations [52,53]. If both tension and compression yield stresses are equal, the material behaves isotropically. To compare the difference in strength under tension and compressive loads, the tension-compression asymmetry $(\sigma_y - \sigma_r) / \sigma_y$ formula was used [51]. The tension-compression yield strength and calculated tension-compression asymmetry for Cu nanowires with

three different atomic orientations are given in Table 1. It can be clearly seen that the tension compression asymmetry of the $\langle 100 \rangle$ nanowire is more pronounced than that of the $\langle 110 \rangle$ and $\langle 111 \rangle$ nanowires. Tension-compression asymmetry is usually caused by different microscopic mechanisms. However, the different tension-compression asymmetries and BE exhibited by monocrystalline and polycrystalline materials await investigation [51].

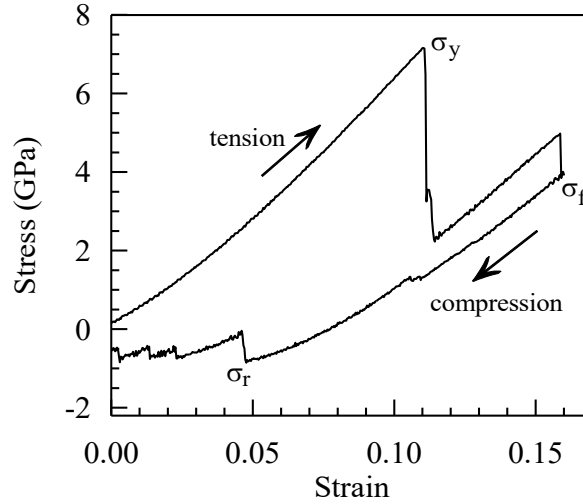


Figure 3. The yield stress in the tension direction (σ_y), the pre-strain stress in the tension direction (σ_f) and the yield stress in the compression direction (σ_r) points in the stress-strain curve obtained as a result of the tension-compression process applied to the Cu nanowire system.

The stress-strain curves obtained as a result of the tension-compression deformation process applied to Cu nanowires with three different crystallographic orientations within elastic limits are given in Figure 4(a-c). First, as seen in Figure 4(a), the $\langle 100 \rangle$ nanowire was subjected to tension processing up to a pre-strain value of 0.08 within the elastic region boundaries. After reaching this strain value, the applied load was removed and compression was performed. The compression yield stress was determined to be 0.985 GPa. This value is the same as the original compression yield stress given in Figure 2(a). The same processes were applied to the $\langle 110 \rangle$ and $\langle 111 \rangle$ nanowires within the elastic region limits, as seen in Figure 4(b-c). The resulting compression yield stresses were found to be the same as the original compression yield stresses. In this case, it was determined that BE was not observed for all three nanowire systems, since the nanowires were not plastically deformed.

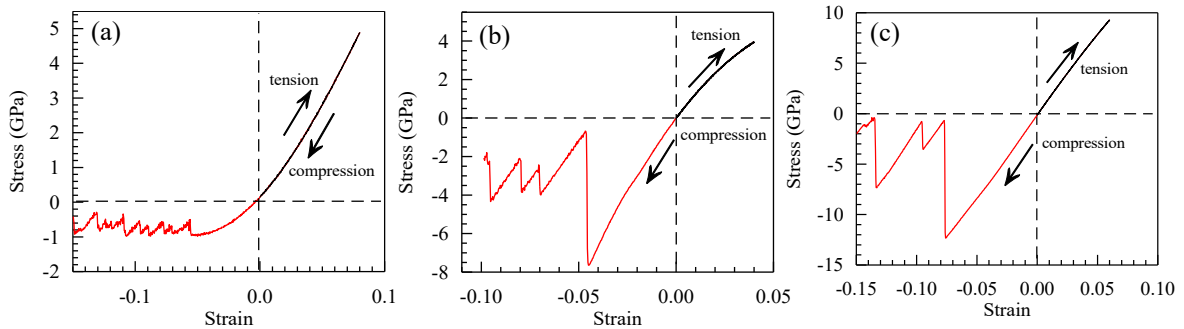
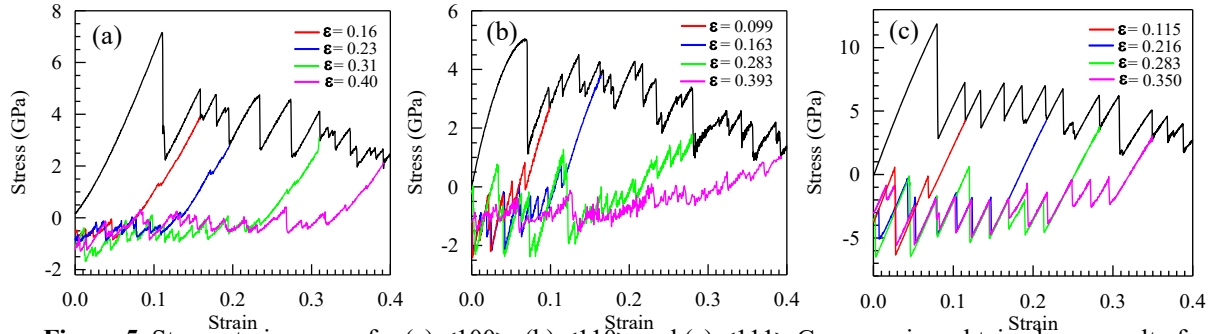


Figure 4. Stress-strain curves for (a) $\langle 100 \rangle$, (b) $\langle 110 \rangle$ and (c) $\langle 111 \rangle$ Cu nanowires obtained as a result of tension and compression deformation within elastic region boundaries.

Table 1. Tension-compression yield stresses and asymmetry of Cu single crystal nanowire.

Orientation	σ_f^t (GPa)	σ_f^c (GPa)	Asymmetry (%)
<100>	7.18	0.98	86.3
<110>	5.06	7.57	-49.6
<111>	11.88	12.29	-3.45

The mechanical response of metals subjected to plastic deformation depends not only on the current stress state, but also on their deformation history. This history can be seen as the difference between tension and compression yield stress in a ductile material [54]. In order to determine the Bauschinger effect depending on the deformation history, as seen in Figure 5(a-c), after the plastic deformation started to occur as a result of the tension loading applied to the nanowires with different crystallographic orientations, reverse loading was performed at different pre-strain values. As seen in Figure 5(a), tension deformation was applied to the <100> nano wire up to the pre-strain values of 0.16, 0.23, 0.31 and 0.40, and after these values, the load was removed and the compression process was performed. The same operations were performed at different pre-strain values in nanowires with other crystallographic orientation, as seen in Figure 5(b-c).

**Figure 5.** Stress-strain curves for (a) <100>, (b) <110> and (c) <111> Cu nanowires obtained as a result of compression deformation for different pre-strain values.

There are two types of mechanisms behind BE. The first mechanism is that during plastic deformation, dislocations accumulate in barriers, producing both long-range and short-range interactions, and dislocation stacks are formed. As a result, back stress develops in the material, which aids the reverse loading dislocation motion. In the second mechanism, when the loading direction is reversed, opposite sign dislocations are produced from the same source. Dislocations attract each other and dislocations disappear. Since stress hardening is related to the dislocation density, decreasing the number of dislocations reduces the strength. The result is that the compression yield strength is smaller than the tension yield strength [55,56]. However, the Bauschinger effect is affected by many factors such as grain boundaries, twinning, interphase boundaries, and second phases [57].

Table 2. BSP and BP values of Cu single crystal nanowire for different crystal orientations and pre-strain values.

Orientation	pre-strain (ϵ)	0.16	0.23	0.31	0.40
<100>	σ_f (GPa)	3.95	3.55	3.10	2.09
	σ_r (GPa)	-0.85	-0.66	-0.52	-0.29
	BSP	0.78	0.81	0.83	0.85
	BP	0.13	0.32	0.47	0.70
ϵ		0.09	0.16	0.28	0.39
<110>	σ_f (GPa)	2.72	3.83	1.80	1.03
	σ_r (GPa)	-0.13	-0.06	0.85	0.35
	BSP	0.95	0.98	0.52	0.66
	BP	0.98	0.99	0.88	0.95
ϵ		0.11	0.21	0.28	0.35
<111>	σ_f (GPa)	4.32	4.31	3.82	3.12
	σ_r (GPa)	-6.35	-4.57	-4.56	-2.38
	BSP	-0.47	-0.06	-0.19	0.23
	BP	0.48	0.63	0.62	0.81

Many different definitions have been used to measure the magnitude of the Bauschinger effect. The Bauschinger effect can be observed qualitatively from stress-strain curves. In order to quantitatively explain the Bauschinger effect for nanoscale simulation studies, Abel (1987) introduced a parameter called the Bauschinger stress parameter (BSP), which is a function of the pre-stress [58,59]. The BSP defines the relative reduction in stress from the forward bias stress to the reverse yield stress. However, Caceres et al. He stated that BSP is a parameter that measures the amount of back stress that particles exert on dislocations in the matrix [60]. where σ_f is the pre-strain stress in the tension direction and σ_r is the yield stress in the compression direction is determined as in eq. (7) below [8];

$$\text{BSP} = \frac{|\sigma_f| - |\sigma_r|}{|\sigma_f|} \quad (7)$$

At the nanoscale, the plastic region of the stress-strain curve appeared to exhibit a saw-like pattern. Since a specific hardening pattern cannot be predicted for the material at this scale, the Bauschinger parameter (BP) is defined in (9) to clarify this effect.

$$\text{BP} = \frac{\sigma_r^o - \sigma_r^c}{\sigma_r^o} \quad (9)$$

In this equation, σ_r^o is the original compression yield stress and σ_r^c is the compression yield stress obtained at different pre-strain values. The definition of the BP parameter indicates that the stronger Bauschinger effect leads to a greater BP value [53]. The calculated BSP and BP values of Cu nanowires with three different crystallographic orientations and different pre-strain for each orientation are given in Table 2. It is seen that the BSP increases as the pre-strain value for the <100> nanowire increases. It is thought that the increase in the pre-strain values at the completion of the tension applied to the sample will cause an increase in the plastic deformation of the material, resulting in a decrease in the difference between σ_f and σ_r values, resulting in a BE effect for this crystallographic orientation. However, it can be said that the <100> nanowire moves away with increasing pre-strain from isotropic strain, which corresponds to the $\sigma_f = \sigma_r$ state and is expressed as the expansion of the yield surface of a material with plastic deformation [54]. In addition, the increase in BP as a result of the increase in the pre-strain value indicates that a stronger BE is formed in the nanowire. In many fcc metals such as Cu, especially in nanoscale crystals, deformation at room temperature is achieved by the formation of deposition defects and the movement of partial dislocations associated with slumping defects [61,62]. Setoodah [53] et al. They found that a larger pre-strain value causes a higher dislocation density in the material and therefore a lower yield strength in the opposite direction. Also, dislocations formed under tension deformation are more likely to slip under compression deformation, resulting in premature yielding. For <110> nanowire, BSP and BP were found to be high at low pre-strains (0.099 and 0.163), and low for high pre-strains (0.283 and 0.393). This corresponds to a greater BE effect in the nanowire at low pre-strain values. With an increase in the amount of forward pre-strain, the number of mobile dislocations may decrease due to more dislocation interaction and possible formation of a more stable dislocation structure [63]. Therefore, with the increase of the amount of pre-strain, the back stress increases up to a certain pre-strain level and then decreases or becomes saturated, depending on the number of mobile dislocations present in the material [64-66]. Compared to nanowires with <100> and <110> crystallographic orientation, it is seen that σ_r value is greater than σ_f value in <111> nanowire, except for the pre-strain value of 0.35. From this, it can be said that the model nanowire structure exhibits reverse BE behavior where the compression yield strength is higher than the tension yield strength. The twin structures formed under compression deformation inhibit the movement of dislocations, causing the compression yield strength to be slightly greater than the tension yield strength, resulting in inverse BE [51]. However, it can be said from the increase in BP value that the increase in pre-strain increases the effect of BE.

3. Conclusion

In this study, the Bauschinger effect, which is the result of uniaxial tension compression deformation applied to Cu nanowires with different crystallographic orientation and modeled with the EAM potential function, was investigated by MD simulation. Crystallographic orientations have a significant effect on the stress-strain curves obtained from the calculations. The existence of tension-compression asymmetry was determined for Cu nanowires with three different atomic orientations. It was determined that the tension-compression asymmetry of the <100> nanowire was more pronounced than that of the <110> and <111> nanowires. BE was clearly seen in the Cu nanowire with different crystallographic orientations. The results of BE are important in nano-scale forming processes of nanomaterials. In single crystal structures, plastic deformation is related to dislocation shift and

twinning. Dislocations formed under tension are more likely to slip under compression, resulting in lower yield stress.

References

- [1] Wang JF, Gudixsen MS, Duan XF, Cui Y, Lieber CM. Highly polarized photoluminescence and photodetection from single indium phosphide nanowires. *Science* 2001; 293: 1455-1457.
- [2] Joyce HJ, Gao Q, Tan HH, Jagadish C, Kim Y, Zou J. et.al. III-V semiconductor nanowires for optoelectronic device applications. *Prog Quant Electron* 2011; 35: 23-75.
- [3] Cui Y, Zhong ZH, Wang DL, Wang WU, Lieber CM. High performance silicon nanowire field effect transistors. *Nano Lett* 2003; 3: 149-152.
- [4] Huang Y, Duan XF, Lieber CM. Nanowires for integrated multicolor nanophotonics. *Small* 2005;1: 142-147.
- [5] Diao J, Gall K, Dunn ML. Yield Strength Asymmetry in Metal Nanowires. *Nano Letters* 2004; 4: 1863-1867.
- [6] Park HS, Zimmerman JA. Modeling inelasticity and failure in gold nanowires. *Physical Review B* 2005; 72: 054106.
- [7] Park HS, Gall K, Zimmerman JA. Deformation of FCC nanowires by twinning and slip. *J. Mech. Phys. Solids* 2006; 54: 1862-1881.
- [8] Mahato JK, De PS, Sarkar A, Kundu A, Chakraborti PC. Effect of deformation mode and grain size on Bauschinger behavior of annealed copper. *International Journal of Fatigue* 2016; 83: 42-52.
- [9] Paul JDH, Hoppe R, Appel F. On the Bauschinger effect in TiAl alloys. *Acta Materialia* 2016; 104: 101-108
- [10] Stoltz RE, Pelloux RM. The Bauschinger effect in precipitation strengthened aluminum alloys. *Metall Trans A* 1976; 7: 1295-1306.
- [11] Pedersen OB, Brown LM, Stobbs WM. The bauschinger effect in copper. *Acta Metall* 1981; 29: 1843-1850.
- [12] Waheed S, Hao R, Bhowmik A, Balint DS, Giuliani F. A unifying scaling for the Bauschinger effect in highly confined thin films: a discrete dislocation plasticity study. *Model Simulat Mater Sci Eng* 2017; 25: 54003.
- [13] Han K, Van Tyne CJ, Levy BS. Effect of strain and strain rate on the bauschinger effect response of three different steels. *Metall Mater Trans A* 2005; 36: 2379-2384.
- [14] Gui HL, Li Q, Huang QX. The influence of Bauschinger effect in straightening process. *Math. Probl. Eng* 2015; 2015: 1-5.
- [15] Chun BK, Kim HY, Lee JK. Modeling the Bauschinger effect for sheet metals, part II: applications. *Int. J. Plast.* 2002; 18: 597-616.
- [16] Chun BK, Jinn JT, Lee JK. Modeling the Bauschinger effect for sheet metals, part I: theory, *Int. J. Plast.* 2002; 18: 571-595.
- [17] Srivatsan TS, Al-Hajri M, Troxell JD. The tensile deformation, cyclic fatigue and final fracture behavior of dispersion strengthened copper. *Mech. Mater.* 2004; 36: 99-116.
- [18] Tang CY, Li DY, Wen GW. Bauschinger's effect in wear of materials. *Tribol. Lett.* 2010; 41: 569-572.
- [19] Tang C, Wang JM, Wen GW, Wang Y, Li DY. Bauschinger effect in wear of Cu-40Zn alloy and its variations with the wear condition. *Wear* 2011; 271(9): 1237-1243.
- [20] Xiaoyu H, Chao W, Margolin H, Nourbakhsh S. The Bauschinger effect and the stresses in a strained single crystal. *Scr. Metall. Mater.* 1992; 27: 865-870.
- [21] Gao Y, Wang H, Zhao J, Sun C, Wang F. Anisotropic and temperature effects on mechanical properties of copper nanowires under tensile loading. *Computational Materials Science* 2011; 50: 3032-3037.
- [22] Sainath G, Choudhary BK. Orientation dependent deformation behaviour of bcc iron nanowires. *Computational Materials Science* 2016; 111: 406-415.
- [23] Lieber CM. Nanoscale science and technology: building a big future from small things *MRS Bull.* 2003; 28: 486-491.
- [24] Mughrabi H. Dislocation wall and cell structures and long-range internal stresses in deformed metal crystals. *Acta Metall.* 1983; 31: 1367-1379.
- [25] Liu X, Yuan F, Zhu Y, Wu X. Extraordinary Bauschinger effect in gradient structured copper. *Scr. Mater.* 2018; 150: 57-60.
- [26] Tsuru T. Origin of tension-compression asymmetry in ultrafine-grained fcc metals. *Phys. Rev. Mater.* 2017; 1: 2-4.
- [27] Park HS, Zimmerman JA. Modeling inelasticity and failure in gold nanowires. *Phys. Rev. B* 2005; 72: 054106.
- [28] Olsson PAT, Melin S, Persson C, Atomistic simulations of tensile and bending properties of single-crystal bcc iron nanobeams. *Phys. Rev. B* 2007; 76: 224112.
- [29] Sainath G, Choudhary BK, Jayakumar T. Molecular dynamics simulation studies on the size dependent tensile deformation and fracture behaviour of body centred cubic iron nanowires. *Comput. Mater. Sci.* 2015; 104: 76-83.
- [30] Zhou M, Liang W. Response of copper nanowires in dynamic tensile deformation. *Proc. Inst. Mech. Eng. Part C J. Mech. Eng. Sci.* 2004; 218(6): 599-606.
- [31] Park HS, Gall K, Zimmerman JA. Deformation of FCC nanowires by twinning and slip. *J. Mech. Phys. Solids* 2006; 54: 1862-1881.
- [32] Xie H, Yin F, Yu T, Lu G, Zhang Y. A new strain-rate-induced deformation mechanism of Cu nanowire: Transition from dislocation nucleation to phase transformation. *Acta Mater.* 2015; 85: 191-198.
- [33] Norskov JK. Covalent effects in the effective-medium theory of chemical binding: Hydrogen heats of solution in the 3d metals. *Phys. Rev. B* 1982; 26: 2875.
- [34] Cleri F, Rosato V. Tight-binding potentials for transition metals and alloys. *Phys. Rev. B* 1993; 48: 22.

- [35] Finnis MW, Sinclair JE. A Simple Empirical N- body Potential for Transition Metals. *Philos. Mag. A-Phys. Condens. Matter Struct. Defect Mech. Prop.* 1984; 50: 45.
- [36] Daw MS, Baskes M. Embedded-atom method: Derivation and application to impurities, surfaces, and other defects in metals. *Phys. Rev. B* 1984; 29: 6443.
- [37] Nam HS, Hwang NM, Yu BD, Yoon JK. Formation of an Icosahedral Structure during the Freezing of Gold Nanoclusters: Surface-Induced Mechanism. *Phys. Rev. Lett.* 2002; 89: 275502.
- [38] Cagin T, Dereli G, Uludogan M, Tomak M. Thermal and mechanical properties of some fcc transition metals. *Phys. Rev. B* 1999; 59: 3468.
- [39] Koh SJA, Lee HP, Lu C, Cheng QH. Molecular dynamics simulation of a solid platinum nanowire under uniaxial tensile strain: Temperature and strain-rate effects. *Phys. Rev. B* 2005; 72: 085414.
- [40] Sturgeon JB, Laird BB. Adjusting the melting point of a model system via Gibbs-Duhem integration: Application to a model of aluminum. *Phys. Rev. B* 2000; 62: 14720.
- [41] <http://lammmps.sandia.gov/>. LAMMPS Molecular Dynamics Simulator (Erişim Tarihi:02.04.2021).
- [42] Stukowski A. Visualization and analysis of atomistic simulation data with OVITO—the Open Visualization Tool. *Modelling and Simulation in Materials Science and Engineering* 2010; 18(1): 015012.
- [43] Kazanc S. The effects on the lattice dynamical properties of the temperature and pressure in random NiPd alloy. *Can. J. Phys.* 2013; 91(10): 833-838.
- [44] Kazanc S, Ozgen S, Adiguzel O. Pressure effects on martensitic transformation under quenching process in a molecular dynamics model of NiAl alloy. *Physica B* 2003; 334(3-4): 375-381.
- [45] Saitoh KI, Liu WK. Molecular dynamics study of surface effect on martensitic cubic-to-tetragonal transformation in Ni-Al alloy. *Computational Materials Science* 2009; 46: 531-544.
- [46] Jacobus K, Sehitoglu H, Balzer M. Effect of stress state on the stress-induced martensitic transformation in polycrystalline Ni-Ti alloy. *Metallurgical and Materials Transactions A* 1996; 27(A): 3066-3073.
- [47] Guellil AM, Adams JB. The application of the analytic embedded atom method to bcc metals and alloys. *J Mater Res* 1992; 7: 639–652.
- [48] Foiles SM, Baskes MI, Daw MS. Embedded-atom-method functions for the fcc metals Cu, Ag, Au, Ni, Pd, Pt, and their alloys. *Phys Rev B* 1986; 33: 7983.
- [49] Setoodeh AR, Attariani H, Khosrownejad, M. Nickel nanowires under uniaxial loads: A molecular dynamics simulation study. *Computational Materials Science* 2008; 44: 378-384.
- [50] Wang P, Chou W, Nie A, Huang Y, Yao H, Wang H. Molecular dynamics simulation on deformation mechanisms in bodycentered-cubic molybdenum nanowires. *J Appl Phys* 2011; 093521:110.
- [51] Zhou J, Shen J, Essa FA, Yu J. Twins and grain boundaries-dominated the reverse Bauschinger effect and tension-compression asymmetry. *Journal of materials research and technology* 2022; 18: 15 -28.
- [52] Wu HA. Molecular dynamics study of the mechanism of metal nanowires at finite temperature. *European Journal of Mechanics A/Solids* 2006; 25: 370-377.
- [53] Setoodeh AR, Attariani H. Nanoscale simulations of Bauschinger effects on a nickel nanowire. *Materials Letters* 2008; 62: 4266–4268.
- [54] Jordon JB, Horstemeyer MF, Solanki K, Xue Y. Damage and stress state influence on the Bauschinger effect in aluminum alloys. *Mechanics of Materials* 2007; 39: 920–931.
- [55] Abel A, Muir H. The Bauschinger effect and discontinuous yielding. *Phil Mag* 1972; 26: 489–504.
- [56] Brown LM. Orowan's explanation of the Bauschinger effect. *Scr Metall* 1977; 11: 127–131.
- [57] Zhu D, Zhang H, Li DY. Influence of Nanotwin Boundary on the Bauschinger's Effect in Cu: A Molecular Dynamics Simulation Study. *Metallurgical and Materials Transactions A* 2013; 44A: 2013-4207-4217.
- [58] Abel A. Historical perspectives and some of the main features of the Bauschinger effect. *Mater. Forum* 1987; 10(1): 11–26.
- [59] Horstemeyer MF. Damage influence on Bauschinger effect of a CAST A356 aluminum alloy. *Scripta Mater.* 1998; 39: 1491–1495.
- [60] Caceres CH, Griffiths JR, Reiner P. Influence of microstructure on the Bauschinger effect in an Al Si–Mg alloy. *Acta Metall.* 1996; 44: 15–23.
- [61] Prinz F, Argon AS. Dislocation cell formation during plastic deformation of copper single crystals. *Phys. Status Solidi A* 1980; 57: 741-753.
- [62] Rzychoń T, Rodak K. Microstructure characterization of deformed copper by XRD line broadening. *Arch. Mater. Sci. Eng.* 2007; 28: 605-608.
- [63] Novak V, Sittner P. Stability of dislocation structure. *Acta Universitatis Carolinae-Math et Phys* 1990; 22: 89–94.
- [64] Sohn SS, Han SY, Shin SY, Bae JH, Lee S. Effect of microstructure and pre-strain on Bauschinger effect in API X70 and X80 line pipe steel. *Met Mater Int* 2013; 19: 423–431.
- [65] Han SY, Sohn SS, Shin SY, Bae JH, Kim HS, Lee S. Effect of microstructure and yield ratio on strain hardening and Bauschinger effect in two API X80 linepipe steels. *Mat Sci Engg A* 2012; 551: 192–199.
- [66] De PS, Kundu A, Chakraborti PC. Effect of prestrain on tensile properties and ratcheting behavior of Ti-stabilised interstitial free steel. *Mat Des* 2013; 87–97

Evaluation of SNP in the *CDH8* and *CDH10* Genes Associated with Autism Using *In-Silico* Tools

Azadeh REZAEIRAD¹, Ömer Faruk KARASAKAL^{2*}, Tuğba KAMAN³, Mesut KARAHAN⁴

¹ Institute of Science, Molecular Biology, Üsküdar University, İstanbul, Türkiye

^{2,4} Vocational School of Health Services, Medical Laboratory Techniques, Üsküdar University, İstanbul, Türkiye

³ Department of Medicinal and Aromatic Plants, Vocational School of Health Services, Üsküdar University, İstanbul, Türkiye

*2 omerfaruk.karasakal@uskudar.edu.tr

(Geliş/Received: 17/08/2023;

Kabul/Accepted: 22/03/2024)

Abstract: Autism spectrum disorder (ASD) is defined as a pervasive and multifactorial neurodevelopmental disorder (ND). It is characterized by repetitive behavioral patterns as well as symptoms of social interaction and communication disorder. The cadherin (CDH) superfamily is a large group of synaptic cell adhesion molecules and has been widely related with ND, including autism. The aim of this study is to evaluate the potentially deleterious missense single nucleotide polymorphisms (SNPs) in *CDH8* and *CDH10* genes, which are related with ASD and cause amino acid changes, using internet-based software tools. To identify potentially harmful missense SNPs; all SNPs were screened using SIFT, PolyPhen-2, PROVEAN, SNPs&GO, Meta-SNP, and SNAP2 software tools, and common deleterious ones were filtered out. Its effect on protein stabilization was investigated with I-Mutant 3.0 and MUpro tools. Three-dimensional models of these common damaging amino acid changes were evaluated with the HOPE software. As a result of in silico analysis of 577 missense SNPs in the *CDH8* gene; The rs145143780 (Y572C) polymorphism common damaging SNP has been detected by all software tools. According to the results of the in silico analysis of 526 missense SNPs found in the *CDH10* gene; The rs13174039 (V459G), rs147882578 (N485K), rs201423740 (Y306C), rs201956238 (F317L) and rs373340564 (R128C) common damaging SNPs have been identified in all polymorphisms by all software tools. As a result of this study, it is thought that the data obtained will make important contributions to future relevant experimental studies.

Key words: Single nucleotide polymorphism (SNP), *CDH8*, *CDH10*, *in silico*, autism spectrum disorder (ASD).

In-Silico Araçlar Kullanılarak Otizmle İlişkili *CDH8* ve *CDH10* Genlerindeki SNP'lerin Değerlendirilmesi

Öz: Otizm spektrum bozukluğu (OSB), yaygın ve çok faktörlü bir nörogelişimsel bozukluk (NB) olarak tanımlanır. Tekrarlayan davranış kalıplarının yanı sıra sosyal etkileşim ve iletişim bozukluğu belirtileri ile karakterizedir. Kadherin (CDH) süper ailesi, büyük bir sinaptik hücre adezyon molekülleri grubudur ve otizm de dahil olmak üzere NB ile geniş çapta ilişkilendirilmiştir. Bu çalışmanın amacı, otizm spektrum bozukluğu ile ilişkili ve amino asit değişikliklerine neden olan *CDH8* ve *CDH10* genlerinde potansiyel olarak zararlı olan missense tek nükleotid polimorfizmlerinin internet tabanlı yazılım araçları kullanılarak değerlendirilmesidir. Potansiyel olarak zararlı yanlış anlamalı SNP'leri tanımlamak için; tüm SNP'ler SIFT, PolyPhen-2, PROVEAN, SNPs&GO, Meta-SNP ve SNAP2 yazılım araçları kullanılarak tarandı ve ortak zararlı olanlar filtrelendi. Protein stabilizasyonu üzerindeki etkisi, I-Mutant 3.0 ve MUpro araçlarıyla araştırıldı. Bu ortak zararlı amino asit değişikliklerinin üç boyutlu modelleri HOPE yazılımı ile değerlendirildi. *CDH8* genindeki 577 missense SNP'nin *in silico* analizi sonucunda; SNP'ye zarar veren rs145143780 (Y572C) polimorfizmi tüm yazılım araçları tarafından tespit edilmiştir. *CDH10* geninde bulunan 526 missense SNP'nin *in silico* analiz sonuçlarına göre; rs13174039 (V459G), rs147882578 (N485K), rs201423740 (Y306C), rs201956238 (F317L) ve rs373340564 (R128C) ortak zarar veren SNP'ler, tüm polimorfizmlerde tüm yazılım araçları tarafından tanımlanmıştır. Bu çalışma sonucunda elde edilen verilerin gelecekte ilgili deneysel çalışmalara önemli katkılar sağlayacağı düşünülmektedir.

Anahtar kelimeler: Tek nükleotid polimorfizmi, *CDH8*, *CDH10*, *in silico*, otizm spektrum bozukluğu (OSB).

1. Introduction

Autism spectrum disorder (ASD) is a multifactorial, pervasive neurodevelopmental disorder (ND) characterized by restricted, repetitive behavioral patterns as well as core symptoms of significant impairment in social interaction and communication [1]. ASD has been reported as a psychiatric pathology that affects almost 1% of the world's population, is more common in men (male/female ratio 4.3:1) and is generally common in children under 3 years of age [2]. Common early signs and symptoms in these children include not responding when called by name, no or very limited use of gestures in the communication process, and lack of creative play [3]. ASD is a serious ND with a strong genetic basis. However, the genetic contributions to ASD are extremely

* Corresponding author: omerfaruk.karasakal@uskudar.edu.tr . ORCID Number of authors: ¹ 0000-0002-9349-1149, ² 0000-0001-7803-3249, ³ 0000-0002-5885-0193, ⁴ 0000-0002-8971-678X

heterogeneous, and many different loci have been reported to underlie the disease to varying degrees in different individuals [4]. Despite the evidence that harmful variants in the same genes play a role in multiple ND, there has been great interest in identifying genes that, when mutated, confer a large degree of ASD-specific risk [5].

The cadherin superfamily is a large group of synaptic cell adhesion molecules and has been widely related to ND, including ASD [6,7]. Cadherin-8, which is encoded by the *CDH8* gene, a gene associated with ASDs, is known as the homophilic adhesion protein. This gene is type II from the cadherin superfamily and encodes integral membrane proteins that mediate calcium-dependent cell-cell adhesion [8]. The *CDH10* gene encodes the type II classical cadherin protein and is located in the cortex, which is thought to be critical in ASD. In addition, it has tasks such as regionalization of the brain, formation of neural circuits, and plasticity [9-11].

Among the variations in the human genome, the most common are SNPs [12]. SNPs are divided into non-synonymous ones located in the coding region of the target gene. Missense SNPs are amino acid changes that cause changes in the function of proteins [13]. These functional changes may have different impacts on the structure and function of the protein. For example, gene regulation can affect its modulation, protein hydrophobicity, charge, stability, interactions, and translation [14]. For these reasons, missense SNPs are associated with various diseases [15]. *In-silico* studies are used to analysis the impacts of variants on the structure and function of proteins [16]. Bioinformatics software tools provide significant advantages to researchers. Especially with *in silico* analysis performed before experimental studies, savings can be made in terms of cost and time. In addition, it provides rapid prediction for many compounds, allows obtaining pioneering data in drug development activities, and missense SNPs with possible harmful effects in genes known to be associated with diseases can be detected, as in our study. Thanks to this detection, instead of analyzing hundreds or thousands of SNPs, those predicted *in silico* can be studied first in research [17-19].

The aim of this study is to evaluate the potentially deleterious missense SNPs in the *CDH8* and *CDH10* genes, which are related with ASD and which cause amino acid changes, using internet-based software tools. In this relationship, it includes the evaluation of the possible consequences of the findings by estimating the possible effects of SNPs on the function, structure, and stabilization of the protein.

2. Materials and Methods

In this study, the possible impacts of missense SNPs in *CDH8* and *CDH10* genes related with ASD on protein structure, stabilization, and function were estimated, and possible high-risk SNPs that are common harms in all software tools were determined. In this context, the steps of the method applied to the selection of the target genes in the study are as follows (Figure 1).

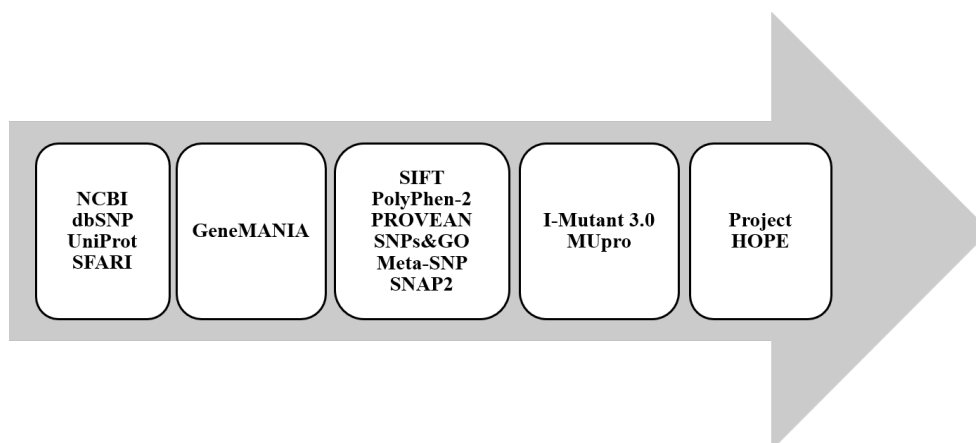


Figure 1. Workflow Diagram

2.1. Data mining

Literature searches and the SFARI database (<https://gene.sfari.org>) were used to identify the genes to be analyzed in the study. SFARI Gene is an evolving online database designed to help researchers track the ever-expanding genetic risk factors emerging in the literature [20]. SNPs in the *CDH8* and *CDH10* genes were obtained from the NCBI dbSNP database (<https://www.ncbi.nlm.nih.gov/snp/>). Among these SNPs, missense SNPs were selected.

The protein sequences encoded by the *CDH8* and *CDH10* genes and access codes were obtained from NCBI Gene (<https://www.ncbi.nlm.nih.gov/gene/>) and UniProt databases. (<http://www.uniprot.org/>).

2.2. Determination of gene-gene interactions

The relationships between the genes analyzed with bioinformatics tools and gene-gene interactions were determined via GeneMANIA (<https://genemania.org>). GeneMANIA is a comprehensive software tool that explores publicly available biological data [21,22].

2.3. Bioinformatics evaluation of missense SNPs

In order to estimate the possible effects of missense SNPs in *CDH8* and *CDH10* genes on protein function and structure, SIFT, PolyPhen-2 (Hum-Div, Hum-Var), PROVEAN, SNPs&GO, Meta-SNP, and SNAP2 software tools were used, and common damaging ones were identified in all of them. The variants predicted to be potentially harmful in each of the tools used were selected for further analysis.

SIFT (Sorting Intolerant From Tolerant) (<https://sift.bii.a-star.edu.sg/>) analyzes the physical properties and sequence homology of amino acids to understand whether an existing amino acid change in protein sequences causes a change in protein function [23]. The PolyPhen-2 (Polymorphism Phenotyping-2) (<http://genetics.bwh.harvard.edu/pph2/>) software tool is divided into two Hum-Div and Hum-Var. A tool for predicting the possible impact of amino acid changes on the function of human proteins using evolutionary and physical considerations is a software tool [24,25]. PROVEAN (Protein Variation Effect Analyzer) (<http://provean.jevl.org/index.php>) is a publicly available tool that determines whether an amino acid change or minor genetic variation has an effect on protein functionality [26,27]. SNPs&GO (<http://snps.biofold.org/snps-and-go/snpsand-go.html>), is defined as an SVM (Support Vector Machine) based web server used to estimate whether variations in protein structure are associated with the disease [28,29]. Meta-SNP (<http://snps.biofold.org/meta-snp/>) is a software tool that predicts SNPs are likely to be included in polymorphism or disease classification [30,31]. SNAP2 (<https://www.rostlab.org/services/SNAP/>) estimates the impact of missense SNPs on protein function. SNAP2 generates predictions based on machine learning methods [32,33].

2.4. Evaluation of the effect of predicted deleterious SNPs on protein stabilization

At this point, SIFT, PolyPhen-2 (Hum-Div, Hum-Var), PROVEAN, SNPs&GO, Meta-SNP, and SNAP2 were used for each amino acid change, and common harms were identified in all of them. After, the effects of these detected variants on protein stabilization were analyzed with I-Mutant 3.0 and MUpro. The I-Mutant 3.0 (<http://gpcr2.biocomp.unibo.it/cgi/predictors/I-Mutant3.0/I-Mutant3.0.cgi>) and MUpro (<http://mupro.proteomics.ics.uci.edu/>) tools were used to estimate the impacts of predicted potentially deleterious SNPs on protein stabilization. Both of these tools are publicly available tools that estimate the impacts of variants at a single location on the stabilization of proteins [34-36].

2.5. 3D-modeling of predicted harmful variations

Using the Project HOPE software, 3D models of proteins with amino acid changes, which are common in all software tools, were created. Project HOPE (<https://www3.cmbi.umcn.nl/hope/>) is a software tool that performs calculations on the three-dimensional structure of mutated proteins and provides information about the structural effects of mutation [37,38].

3. Results

The information about the SNPs in the *CDH8* and *CDH10* genes was obtained from the NCBI dbSNP database in December 2021. A total of 142242 SNPs were found in the *CDH8* gene. When the missense SNPs were filtered out among the 142242 SNPs, it was determined that only 577 of them were missense SNPs. A total of 620 different variants of these SNPs were determined. Also, a total of 59691 SNPs were found in the *CDH10* gene. When the SNPs with false meaning among 59691 SNPs were filtered, it was determined that only 526 of them were missense SNPs. A total of 615 different variants of these SNPs were reported.

When the missense SNPs in the *CDH8* gene found to be harmful in all programs were evaluated, the rs145143780 (Y572C) polymorphism was determined to be the most common damaging SNP. In the evaluation of SNPs in the *CDH10* gene that is harmful in all programs, rs13174039 (V459G), rs147882578 (N485K), rs201423740 (Y306C),

rs201956238 (F317L), and rs373340564 (R128C) polymorphisms have all been identified as the most common damaging SNPs.

3.1. Results of SNPs on protein stabilization

One variant of the *CDH8* gene, which was determined to be associated with disease in all software tools, was analyzed with I-Mutant 3.0 and MUpro tools. As a result of the study, it has been determined that one variant has the effect of reducing protein stabilization in both programs (Table 1). In addition, five variants of the *CDH10* gene, which were determined to be related with diseases in all software tools, were analyzed with the I-Mutant 3.0 and MUpro. As a result of the study, it was determined that five variants had a reducing effect on protein stabilization in both programs (Table 1).

Table 1. Results of stabilization of *CDH8* and *CDH10* genes

Gene Name	SNP Number	Amino Acid Change	I-Mutant Result	I-Mutant Reliability Value	DDG (Kcal/mol)	MUpro Result	Mupro DDG value
<i>CDH8</i>	rs145143780	Y572C	Decrease	2	0.95	Decrease	-1.0298355
	rs13174039	V459G	Decrease	9	-2.07	Decrease	-1.9914738
<i>CDH10</i>	rs147882578	N485K	Decrease	8	-2.29	Decrease	-1.2179979
	rs201423740	Y306C	Decrease	3	0.37	Decrease	-1.1597179
	rs201956238	F317L	Decrease	3	-2.19	Decrease	-1.417702
	rs373340564	R128C	Decrease	2	-0.15	Decrease	-0.18078604

3.2. Results of *CDH8* and *CDH10* gene-gene interaction

Interactions between genes were determined using the GeneMANIA software tool, and functional and interactional information for two genes was obtained. The interaction of the *CDH8* gene with *CTNND1*, *JUP*, *CTNNA1*, *CDH11*, and *PSEN1* genes the maximum has been identified. Also, *CDH10* gene with *CTNND1*, *JUP*, *CTNNA1*, *CTNNA1*, and *CDH1* genes the maximum interaction has been identified. The gene-gene interaction network of the *CDH8* and *CDH10* genes is given in Figure 2.

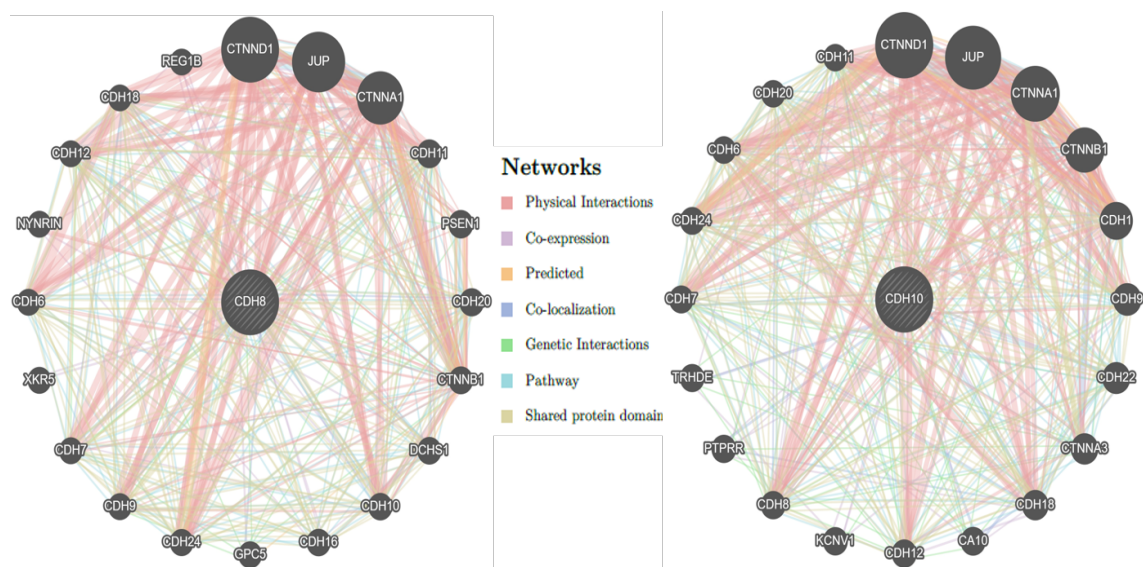


Figure 2. *CDH8* and *CDH10* gene-gene interaction network

3.3. Bioinformatics Analysis Results

Belonging to the *CDH8* and *CDH10* genes associated with autism, gene-gene interaction, prediction of possible damaging effects of SNPs, estimation of the impacts of SNPs on protein stabilization, and a three-dimensional modeling study and its results are presented below. Software tools such as SIFT, PolyPhen-2 (Hum-Div, Hum-Var), PROVEAN, SNPs&GO, SNAP2, and Meta-SNP were used to identify common harms using missense SNPs obtained from the NCBI dbSNP and amino acid change information of each SNP based on variants in the protein sequences (Table 2).

Table 2. Prediction results of *CDH8* and *CDH10* genes SNP in all software tools

Gene Name	SNP ID	Amino Acid Change	SIFT Result	SIFT Score	PolyPhen-2 Result (HumDiv)	PolyPhen-2 Score (HumDiv)	PolyPhen-2 Result (HumVar)	PolyPhen-2 Score (HumVar)	PROVEAN Result	PROVEAN Score	SNPs&GO Result	SNPs&GO Reliability Value	SNAP-2 Result	SNAP-2 Score	SNAP-2 Expected Accuracy	Meta-SNP Result	Meta-SNP Score
<i>CDH8</i>	rs145143780	Y572C	Dlt	0.002	PD	1.000	PD	0.997	Dlt	-7.172	Ds	2	Effect	48	71%	Ds	0.721
	rs13174039	V459G	Dlt	0	PD	0.998	PD	0.978	Dlt	-6.651	Ds	2	Effect	78	85%	Ds	0.661
	rs147882578	N485K	Dlt	0.015	PD	0.977	PSD	0.727	Dlt	-4.576	Ds	2	Effect	34	66%	Ds	0.74
<i>CDH10</i>	rs201423740	Y306C	Dlt	0.015	PD	1.000	PD	1.000	Dlt	-7.654	Ds	5	Effect	53	75%	Ds	0.823
	rs201956238	F317L	Dlt	0.011	PD	0.995	PSD	0.786	Dlt	-5.105	Ds	5	Effect	54	75%	Ds	0.785
	rs373340564	R128C	Dlt	0.028	PD	1.000	PD	0.999	Dlt	-5.043	Ds	5	Effect	19	59%	Ds	0.751

Dlt: Deleterious, Ds: Disease, PSD: Possibly Damaging, PD: Probably Damaging

3.4. Modeling results for *CDH8* and *CDH10* genes

The mutant residue resulting from the polymorphism often differs from the original wild-type residue. These differences are the charge, hydrophobicity, and size values specific to amino acids. The patterns of amino acid changes resulting from polymorphisms and the differences between residues are presented in Table 3.

Table 3. Wild and mutant-type residue properties of the *CDH8* and *CDH10* determined using Project HOPE

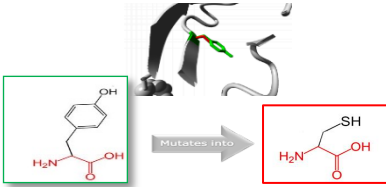
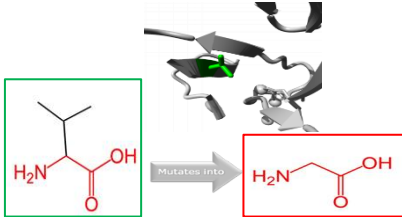
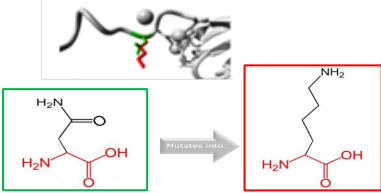
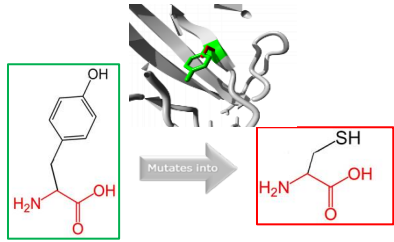
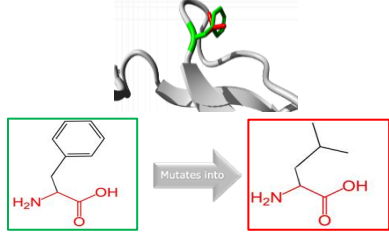
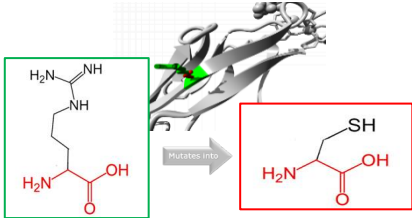
Gene Name	SNP ID	AMINO ACID CHANGE	WILD-TYPE RESIDUES			MUTANT-TYPE RESIDUES		
			Size	Charge	Hydrophobicity	Size	Charge	Hydrophobicity
<i>CDH8</i>	rs145143780	Y572C	>	-	<	<	-	>
	rs13174039	V459G	>	-	>	<	-	<
	rs147882578	N485K	<	Neutral	-	>	+charge	-
<i>CDH10</i>	rs201423740	Y306C	>	-	<	<	-	>
	rs201956238	F317L	>	-	-	<	-	-
	rs373340564	R128C	>	+charge	<	<	Neutral	>

According to the results, it was determined that the amino acid change created by SNP belonging to the *CDH8* gene, which was predicted to be high risk, was Y572C. Furthermore, amino acid changes created by high-risk SNPs of the *CDH10* gene have been identified as V459G, N485K, Y306C, F317L, and R128C. The 3D model of the protein created using the Project HOPE tool is shown in Table 4.

4. Discussions

In this study, estimation results of the possible impacts of SNPs in *CDH8* and *CDH10* genes related to ASD disorder on protein structure, function, and stabilization were obtained using *in silico* methods. *CDH8*; rs145143780 (Y572C) and *CDH10*; rs13174039 (V459G), rs147882578 (N485K), rs201423740 (Y306C), rs201956238 (F317L), rs373340564 (R128C) were identified as high-risk SNPs via bioinformatics analysis tools as shown in the workflow in Figure 1 (Table 4). During the creation of three-dimensional models by the Project HOPE, analysis is also performed in terms of hydrophobicity, charge, and size differences. It was also evaluated how the SNPs detected in both genes affect the structure or function of the protein in this respect Table 3. Changes that may occur in protein stabilization can cause proteins to deteriorate or misfold [39]. Due to the decrease in stabilization because of the amino acid change that occurs, folds with low success rates or an increase in unfolded protein sections can be seen [40]. In our study, it was determined that it decreased protein stabilization in all variants that were predicted to have a possible harmful effect. Although it has not yet been defined in autism, which is a ND, current studies show that multiple genes, epigenetic effects, or gene-gene interactions pose a risk [41,42]. Therefore, the gene-gene interactions were determined via GeneMANIA. For example, it was determined that physical and genetic interaction, co-expression, co-localization, estimated interaction, shared protein domains and pathways in *CDH8* and *CDH10* genes (Figure 2) [43].

Table 4. HOPE tool 3-D modelling results of *CDH8* and *CDH10* genes

Gene Name	SNP ID	MODELING	EXPLANATION
<i>CDH8</i>	rs145143780 (Y572C)		As a result of the rs145143780 polymorphism, the amino acid tyrosine is converted to cysteine at position 572.
	rs13174039 (V459G)		As a result of the rs13174039 polymorphism, the amino acid valine is converted to glycine at position 459.
<i>CDH10</i>	rs147882578 (N485K)		As a result of the rs147882578 polymorphism, the amino acid Asparagine is converted to Lysine at position 485.
	rs201423740 (Y306C)		As a result of the rs201423740 polymorphism, the amino acid Tyrosine is converted to Cysteine at position 306.
	rs201956238 (F317L)		As a result of the rs201956238 polymorphism, the amino acid phenylalanine is converted to leucine at position 317.
	rs373340564 (R128C)		As a result of the rs373340564 polymorphism, the amino acid Arginine is converted to Cysteine at position 128.

In a study conducted on the *CDH8* gene, they reported that *CDH8* showed a predisposition to autism and learning disabilities as a result of rare familial 16q21 microdeletions and expression analysis [6]. In an ASD study in which genetic analysis was performed, including more than 10,000 people of European origin, it was determined that *CDH10* and *CDH9* genes showed a significant relationship in the pathogenesis of ASD [44]. To understand the role of classical Type II cadherins (*CDH8* and *CDH11*) in the etiology of ASD, their expression patterns were analyzed during mouse brain development and in autism-specific human tissue (induced pluripotent stem cell (iPSC)). The results show that both cadherins may have a critical role in ASD [45].

5. Conclusions

As a result of this study, high-risk missense SNPs, which are predicted to have potentially harmful effects, were detected in each of the online analysis tools used. In addition to making more cost-effective, target-oriented studies in a shorter time with *in-silico* methods, it also makes a great contribution to providing preliminary information for experimental studies that are planned by making pre-laboratory preliminary studies. In particular, it is predicted that it will be useful in SNP research and genotyping studies on the *CDH8* and *CDH10* genes.

References

- [1] Mostafavi M, Gaitanis J. Autism spectrum disorder and medical cannabis: review and clinical experience. *Semin Pediatr Neurol.* 2020; 35, 100833.
- [2] Ozdemir, O. The green tea polyphenol EGCG modulates NGF, BDNF, and CAMKII- α pathways to alleviate neurological damage in autism-induced rats. *Acta Pol. Pharm. Drug Res.* 2021; 77, 889-895.
- [3] Hirota T, King BH. Autism spectrum disorder: A review. *Jama.* 2023; 329(2), 157-168.
- [4] Persico AM, Napolioni V. Autism genetics. *Behav. Brain Res.* 2013; 251, 95–112.
- [5] Myers SM, Challman TD, Bernier R, Bourgeron T, Chung WK, Constantino JN, Eichler EE, Jacquemont S, Miller DT, Mitchell KJ. Insufficient evidence for “autism-specific” genes. *The American Journal of Human Genetics.* 2020; 106(5), 587–595.
- [6] Pagnamenta AT, Khan H, Walker S, Gerrelli D, Wing K, Bonaglia MC, Giorda R, Berney T, Mani E, Molteni M. Rare familial 16q21 microdeletions under a linkage peak implicate cadherin 8 (*CDH8*) in susceptibility to autism and learning disability. *J. Med. Genet.* 2011; 48(1), 48–54.
- [7] Lin YC, Frei JA, Kilander MBC, Shen W, Blatt GJ. A subset of autism-associated genes regulate the structural stability of neurons. *Front. Cell. Neurosci.* 2016; 10, 263.
- [8] Friedman LG, Riemsdijk FW, Sullivan JM, Mesias R, Williams FM, Huntley GW, Benson DL. Cadherin-8 expression, synaptic localization, and molecular control of neuronal form in prefrontal corticostriatal circuits. *J. Comp. Neurol.* 2015; 523(1), 75–92.
- [9] Takeichi M. The cadherin superfamily in neuronal connections and interactions. *Nat. Rev. Neurosci.* 2007; 8(1), 11-20.
- [10] Maître JL, Heisenberg CP. Three functions of cadherins in cell adhesion. *Curr. Biol.* 2013; 23(14), R626–R633.
- [11] Redies C, Hertel N, Hübner CA. Cadherins and neuropsychiatric disorders. *Brain Res.* 2012; 1470, 130-144.
- [12] Ray M, Mishra J, Priyadarshini A, Sahoo S. In silico identification of potential drug target and analysis of effective single nucleotide polymorphisms for autism spectrum disorder. *Gene Reports.* 2019; 16, 100420.
- [13] Avsar O. Investigation of Putative Functional SNPs of Human HAT1 Protein: A Comprehensive “in silico” Study. *Cytol. Genet.* 2022; 56(1), 98–107.
- [14] Kucukkal TG, Petukh M, Li L, Alexov E. Structural and physico-chemical effects of disease and non-disease nsSNPs on proteins. *Curr. Opin. Struct. Biol.* 2015; 32, 18–24.
- [15] Owji H, Eslami M, Nezafat N, Ghasemi Y. In silico elucidation of deleterious non-synonymous SNPs in SHANK3, the autism spectrum disorder gene. *J. Mol. Neurosci.* 2020; 70, 1649–1667.
- [16] Tekcan A. In silico analysis of FMR1 gene missense SNPs. *Cell Biochem. Biophys.* 2016; 74, 109–127.
- [17] Bekisz S, Baudin L, Buntinx F, Noël A, Geris L. In vitro, in vivo, and in silico models of lymphangiogenesis in solid malignancies. *Cancers.* 2022; 14(6), 1525.
- [18] Hoda A, Lika M, Kolaneci V. Identification of deleterious nsSNPs in human HGF gene: in silico approach. *J. Biomol. Struct. Dyn.* 2023; 41(21), 11889–11903.
- [19] Yusuf M. Insights into the in-silico research: current scenario, advantages, limits, and future perspectives. *Life in Silico.* 2023; 1(1), 13–25.
- [20] Arpi MNT, Simpson TI. SFARI genes and where to find them; modelling Autism Spectrum Disorder specific gene expression dysregulation with RNA-seq data. *Sci. Rep.* 2022; 12(1), 10158.
- [21] Li M, He M, Xu F, Guan Y, Tian J, Wan Z, Zhou H, Gao M, Chong T. Abnormal expression and the significant prognostic value of aquaporins in clear cell renal cell carcinoma. *PloS One.* 2022; 17(3), e0264553.
- [22] Montojo J, Zuberi K, Rodriguez H, Kazi F, Wright G, Donaldson SL, Morris Q, Bader GD. GeneMANIA Cytoscape plugin: fast gene function predictions on the desktop. *Bioinformatics.* 2010; 26(22), 2927–2928.
- [23] Ng PC, Henikoff S. SIFT: Predicting amino acid changes that affect protein function. *Nucleic Acids Res.* 2003; 31(13), 3812–3814.

- [24] Adzhubei I, Jordan DM, Sunyaev SR. Predicting functional effect of human missense mutations using PolyPhen-2. *Curr. Protoc. Hum. Genet.* 2013; 76(1), 7-20.
- [25] Pshennikova VG, Barashkov NA, Romanov GP, Teryutin FM, Solov'ev AV, Gotovtsev NN, Nikanorova A A, Nakhodkin SS, Sazonov NN, Morozov IV. Comparison of predictive in silico tools on missense variants in GJB2, GJB6, and GJB3 genes associated with autosomal recessive deafness 1A (DFNB1A). *The Scientific World Journal.* 2019; 2019.
- [26] Choi Y, Chan AP. PROVEAN web server: a tool to predict the functional effect of amino acid substitutions and indels. *Bioinformatics.* 2015; 31(16), 2745–2747.
- [27] Sandell L, Sharp NP. Fitness effects of mutations: An assessment of PROVEAN predictions using mutation accumulation data. *Genome Biol. Evol.* 2022; 14(1), evac004.
- [28] Pawlina-Tyszko K, Semik-Gurgul E, Gurgul A, Oczkiewicz M, Szmatoła T, Bugno-Poniewierska M. Application of the targeted sequencing approach reveals the single nucleotide polymorphism (SNP) repertoire in microRNA genes in the pig genome. *Sci. Rep.* 2021; 11(1), 1–12.
- [29] Schwarz DF, Hädicke O, Erdmann J, Ziegler A, Bayer D, Möller S. SNPtoGO: characterizing SNPs by enriched GO terms. *Bioinformatics.* 2008; 24(1), 146–148.
- [30] Capriotti E, Altman RB, Bromberg Y. Collective judgment predicts disease-associated single nucleotide variants. *BMC Genomics.* 2013;14(3), 1–9.
- [31] Petrosino M, Novak, L, Pasquo A, Chiaraluce R, Turina P, Capriotti E, Consalvi V. Analysis and interpretation of the impact of missense variants in cancer. *Int. J. Mol. Sci.* 2021; 22(11), 5416.
- [32] AbdulAzeez S, Borgio JF. In-silico computing of the most deleterious nsSNPs in HBA1 gene. *PloS One.* 2016; 11(1), e0147702.
- [33] Munshani S, Ibrahim, EY, Domenicano I, Ehrlich BE. The impact of mutations in wolframin on psychiatric disorders. *Front. Pediatr.* 2021; 9, 718132.
- [34] Desai M, Chauhan JB. Predicting the functional and structural consequences of nsSNPs in human methionine synthase gene using computational tools. *Systems Biology in Reproductive Medicine.* 2019; 65(4), 288–300.
- [35] Lim SW, Tan KJ, Azuraiddi OM, Sathiya M, Lim EC, Lai KS, Yap WS, Afizan NARNM. Functional and structural analysis of non-synonymous single nucleotide polymorphisms (nsSNPs) in the MYB oncoproteins associated with human cancer. *Sci. Rep.* 2021; 11(1), 1–14.
- [36] Tanwar H, Kumar DT, Doss C, Zayed H. Bioinformatics classification of mutations in patients with Mucopolysaccharidosis IIIA. *Metab. Brain Dis.* 2019; 34(6), 1577–1594.
- [37] Sadakierska-Chudy A, Szymanowski P, Lebioda A, Płoski R. Identification and In Silico Characterization of a Novel COLGALT2 Gene Variant in a Child with Mucosal Rectal Prolapse. *Int. J. Mol. Sci.* 2022; 23(7), 3670.
- [38] Venkata Subbiah H, Ramesh Babu P, Subbiah U. In silico analysis of non-synonymous single nucleotide polymorphisms of human DEFB1 gene. *Egypt. J. Med. Hum. Genet.* 2020; 21(1), 1–9.
- [39] Matthews BW, Nicholson H, Becktel WJ. Enhanced protein thermostability from site-directed mutations that decrease the entropy of unfolding. *Proc. Natl. Acad. Sci. U.S.A.* 1987; 84(19), 6663-6667.
- [40] Ragoonanan V, Aksan A. Protein stabilization. *Transfus Med Hemother.* 2007; 34(4), 246-252.
- [41] Ma DQ, Whitehead PL, Menold MM, Martin ER, Ashley-Koch AE, Mei H, Ritchie MD, Delong GR, Abramson RK, Wright HH. Identification of significant association and gene-gene interaction of GABA receptor subunit genes in autism. *The American Journal of Human Genetics.* 2005; 77(3), 377–388.
- [42] Moore JH. The ubiquitous nature of epistasis in determining susceptibility to common human diseases. *Hum Hered.* 2003; 56(1–3), 73–82.
- [43] Warde-Farley D, Donaldson SL, Comes O, Zuberi K, Badrawi R, Chao P, Franz M, Grouios C, Kazi F, Lopes CT. The GeneMANIA prediction server: biological network integration for gene prioritization and predicting gene function. *Nucleic Acids Res.* 2010; 38(suppl_2), W214–W220.
- [44] Wang K, Zhang H, Ma D, Bucan M, Glessner JT, Abrahams BS, Salyakina D, Imielinski M, Bradfield JP, Sleiman PMA. Common genetic variants on 5p14. 1 associate with autism spectrum disorders. *Nature.* 2009; 459(7246), 528–533.
- [45] Frei JA, Niescier RF, Bridi MS, Durens M, Nestor JE, Kilander MBC, Yuan X, Dykxhoorn DM, Nestor M W, Huang S. Regulation of neural circuit development by cadherin-11 provides implications for autism. *Eneuro.* 2021; 8(4).

Use of 3D-CAPSNET and RNN models for 4D fMRI-based Alzheimer's Disease Pre-detection

Ali İSMAİL¹, Gonca Gökçe MENEKŞE DALVEREN^{2*}

¹ Graduate School of Natural and Applied Sciences, Atılım University, Ankara, Türkiye

² Software Engineering Department, Engineering Faculty, Atılım University, Ankara, Türkiye

¹ alykotbb95@gmail.com, ^{2*} gonca.menekse@atilim.edu.tr

(Geliş/Received: 27/11/2023;

Kabul/Accepted: 15/03/2024)

Abstract: Predicting Alzheimer's disease (AD) at an early stage can assist more successfully prevent cognitive decline. Numerous investigations have focused on utilizing various convolutional neural network (CNN)-based techniques for automated diagnosis of AD through resting-state functional magnetic resonance imaging (rs-fMRI). Two main constraints face the methodologies presented in these studies. First, overfitting occurs due to the small size of fMRI datasets. Second, an effective modeling of the 4D information from fMRI sessions is required. In order to represent the 4D information, some studies used the deep learning techniques on functional connectivity matrices created from fMRI data, or on fMRI data as distinct 2D slices or 3D volumes. However, this results in information loss in both types of methods. In order to model the spatiotemporal (4D) information of fMRI data for AD diagnosis, a new model based on the capsule network (CapsNet) and recurrent neural network (RNN) is proposed in this study. To assess the suggested model's effectiveness, experiments were run. The findings show that the suggested model could classify AD against normal control (NC) and late mild cognitive impairment (LMCI) against early mild cognitive impairment (eMCI) with accuracy rates of 94.5% and 61.8%, respectively.

Key words: Alzheimer's disease preliminary diagnosis, machine learning, magnetic resonance imaging, convolutional neural network, recurrent neural network.

4B fMRI Tabanlı Alzheimer Hastalığının Ön Tespiti için 3B-CAPSNET ve RNN Modellerinin Kullanılması

Öz: Alzheimer hastalığının (AH) ilerlemesinin erken tahmini, bilişsel gerilemenin daha etkili bir şekilde yavaşlatılmasına yardımcı olabilmektedir. Dinlenme durumu fonksiyonel manyetik rezonans görüntüleme (dd-fMRG) kullanılarak otomatik AH tanısı için evrimsel sinir ağlarına (ESA) dayalı farklı yöntemlerin uygulanmasına yönelik çeşitli çalışmalar yapılmıştır. Bu çalışmalarda tanıtılan yöntemler iki büyük zorlukla karşılaşmaktadır. Birincisi, fMRG veri kümeleri küçük boyutta olduğundan aşırı uyum gözlemlenebilmektedir. İkincisi, fMRG oturumlarının 4 boyutlu (4B) bilgilerinin verimli bir şekilde modellenmesi gerekmektedir. Çalışmalardan bazıları, derin öğrenme yöntemlerini, 4B bilgiyi modellemek için fMRG verilerinden oluşturulan fonksiyonel bağlantı matrislerine veya ayrı 2B dilimler veya 3B hacimler olarak fMRG verilerine uygulamıştır. Ancak bu durumun her iki yöntem türünde de bilgi kaybına neden olduğu gözlemlenmiştir. Bu çalışmada, AD tanısı için fMRG verilerinin uzay-zamansal (4B) bilgilerini modellemek amacıyla Kapsül ağı (CapsNet) ve tekrarlayan sinir ağını (RNN) temel alan yeni bir model önerilmektedir. Önerilen modelin etkinliğini değerlendirmek için deneyler yapılmıştır. Sonuçlara göre, önerilen modelin AH'na karşı normal kontrol (NK) ve geç hafif bilişsel bozukluk (GHBB) ile erken hafif bilişsel bozukluk (EHBB) sınıflandırma görevlerinde sırasıyla %94.5 ve %61.8 doğruluk elde edebildiği görülmüştür.

Anahtar kelimeler: Alzheimer hastalığı tespiti, makine öğrenmesi, manyetik rezonans görüntüleme, evrimsel sinir ağları, yinelenmeli sinir ağı.

1. Introduction

1.1 Preamble

Alzheimer's disease (AD) is the sixth cause of death among older people in the United States [1]. It is expected that the over-60 population will become 2 billion by 2050 which will be 21% of the world's population after it was 8% in 1950 [2]. This reveals a massive increase in the number of people affected by Alzheimer's disease estimated to be 100 million by 2050 [3]. AD is the most common type of dementia, it is a neurodegenerative disease that occurs as a result of changes in amyloid and tau protein levels causing a disability of communication between neurons and cell death in different brain regions resulting in the loss of cognitive abilities. Several brain regions can be damaged due to AD as well as a reduction in some neurotransmitters. As a result, the functionality for which a certain region or a neurotransmitter is responsible for is affected. For example, the hippocampus is responsible for learning and memory, and it is more likely to get damaged before other regions. Also, Acetylcholine (ACh), a neurotransmitter responsible for memory and learning is decreased in concentration. Other

* Corresponding author: gonca.menekse@atilim.edu.tr. ORCID Number of authors: ¹ 0000-0003-3614-114X, ² 0000-0002-8649-1909

regions that are affected by AD include the left medial orbital part of the superior frontal gyrus, left caudate nucleus, right middle frontal gyrus, left orbital part of the inferior frontal gyrus, left triangular part of the inferior frontal gyrus, and left inferior temporal gyrus [4]. Till now, there is no treatment for this disease, but an early prediction of conversion to AD helps slow down the progression of dementia more effectively. Changes in the brain associated with AD begin 20 years before AD symptoms appear [1]. It is more helpful for patients to predict the progression of a patient from mild cognitive impairment (MCI) stage toward AD than distinguishing AD from health normal control (NC) (see Figure 1 [5]). MCI is the cognitive decline stage before AD immediately, where subjects in this stage suffer from mild cognitive ability loss but they are still able to do their daily activities without any sign of dementia. This stage is categorized into early MCI (eMCI) and late MCI (lMCI). Another way of categorizing subjects in this stage is to divide them into stable MCI (sMCI) and progressive MCI (pMCI) based on developing AD or staying stable in a follow-up period [4]. The development of AD always occurs in a time range of 6 to 36 months. However, diagnosis of Alzheimer's disease in its early stages is more challenging than in later ones, as distinguishing between sMCI and pMCI or lMCI and eMCI is very hard due to the high similarities between brain changes in the distinguished cases.

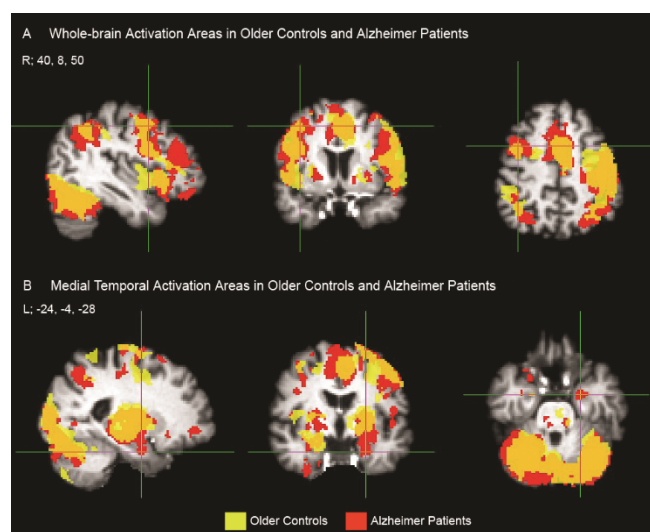


Figure 1. Demonstrates the increase in fMRI activity in neocortical (A) and medial temporal (B) brain areas of Alzheimer's disease (in red) relative to healthy older control subjects (in yellow) [5].

The human brain consists of multiple regions that interact with each other, neurodegenerative diseases such as AD are associated with a change in different brain regions' activity as well as the interaction patterns between different brain regions known as functional connectivity networks [6]. Different from structural magnetic resonance imaging (sMRI) (known traditionally as MRI) which scans the brain's anatomical structure, functional magnetic resonance imaging (fMRI) scans brain activity by capturing the blood oxygenation level-dependent (BOLD) signal as the indicator for brain activity. The information on the brain's functional disturbance provided by fMRI proved to be very helpful with the diagnosis of several brain diseases at an early stage, as brain activity changes happening as a result of AD or any of its previous cognitive decline stages happen earlier than structural (anatomical) changes scanned by sMRI [7]. There are two kinds of fMRI: resting-state fMRI (rs-fMRI) and task-based fMRI. In rs-fMRI, the session is recorded while the subject is at rest. While in task-based fMRI, the subject performs some cognitive tasks during the session. The majority of studies use rs-fMRI for automated AD diagnosis due to being easier to obtain as the subjects are not performing any task which also reduces the motion artifacts making the pre-processing of fMRI data less complicated. Still, fMRI is not yet reliable in the clinical diagnosis of AD due to two major problems. First, sophisticated statistical analysis is required for useful information extraction from raw fMRI. Second, the difficulty of fMRI visualization due to its complicated data structure. Here comes the role of applying deep learning to fMRI images for automated medical diagnosis as a step toward making fMRI applicable in clinical practice. An fMRI session is captured as a time series of brain volumes. In the literature, very few studies investigated applying deep learning in fMRI-based AD diagnosis. The brain activity information recorded by fMRI can be complementary with other neuroimaging biomarkers such as MRI and positron emission tomography (PET) for more accurate diagnosis. However, it is still early to rely on fMRI for clinical diagnosis of AD. Several challenges need to be overcome to make fMRI usage in automated diagnosis reliable and trustable. An fMRI session is captured as a time series of brain volumes. Hence, one of the main challenges is the overfitting

problem that goes back to training complex 4D models on fMRI datasets that are always available with small sizes to capture the spatial and temporal features of the fMRI time-series [7].

1.2. Related Work and Contribution

For more than a decade, various machine learning methods have been proposed for automated AD diagnosis based on rs-fMRI data. The first conventional approach introduced in the literature was using Pearson's correlation coefficients between pairs of brain regions to construct a functional connectivity (FC) network (matrix) representing the temporal functional relationships between different brain regions from an fMRI scan after using regions of interest (ROI) template (e.g., AAL) to extract the regions between which the connectivity network is of the analysis interest. Each element in this matrix denotes the Pearson correlation coefficient between the time series of a pair of ROIs. Then, using a feature extractor to extract from the FC matrices the discriminative features to be used in training a machine learning model for classifying different AD stages. For example, Jie et al. applied a graph-kernel method to FC networks to measure the topological similarity between different subjects as a feature extractor to train an SVM for classification [8]. Different from previous studies that used a single SVM, Bi et al. proposed a random SVM cluster to overcome the information loss problem encountered with a single SVM [9]. Each SVM in the cluster is built by randomly selecting a set of samples and their FC features achieving higher feature diversity. To categorize a sample, the prediction by the majority of the multiple SVMs is used. Jie et al. constructed dynamic connectivity networks (DCNs) and extracted both temporal variability features (e.g., the temporal correlation between brain regions) and spatial variability features (e.g., spatial variability within a specific brain region) neglected by most of the studies that existed before [6]. They used a manifold regularized multi-task feature learning model to extract the most important features on which a multi-kernel SVM was trained for disease classification.

However, the aforementioned methods have the disadvantages of feature extraction and the classifier's training being performed as two separate processes in addition to performing feature extraction in a handcrafted manner, which degrades the classification performance. Thanks to deep learning, both processes can be automatically combined into a single training process. Hence, the literature shifted toward applying deep learning methods, particularly convolutional neural networks (CNNs) to FC networks directly leading to significantly better classification accuracy, as feature extraction is directed by the classification feedback through the training process. Also, deep neural networks are capable of learning more hidden disease-related patterns. For example, He et al. constructed an FC matrix by calculating the time series correlation coefficient between each pair of brain regions based on both the variance of the mean value of all voxel time series in the two brain regions over time and the covariance of the time series mean value of the two brain regions [10]. Then, feeding the adjacency matrix of each subject into a simplified instance of 3D-MobileNet [11] architecture. In another study, Duc et al. applied ICA to fMRI data to generate an FC matrix representing the time-series correlations between 16 different independent components (brain regions) for each subject [12]. Then, from these matrices, 3D ICA feature maps were obtained using dual regression and fed into a 3D VGG-Net model. With another approach to decrease the fMRI dataset's small size overfitting effect, Wang et al. utilized PCANet [13] on FC matrices [14]. The choice of PCA was due to its unsupervised nature that eliminates its need for feedback adjustment parameters, making it an efficient choice for small datasets. Lin et al. introduced their end-to-end CRNN framework where they combined a CNN with an LSTM to model the 4D information [15]. They applied CNNs to dynamic FC (dFC) networks for extracting the temporal features based on which an LSTM was used to model the sequential information of the dFC networks. To perform the spatiotemporal analysis avoiding the 4D information complexity and model the 4D features at the same time, Jia et al. used mReHo transformation [16] that represents the whole time series of volumes as a single volume [17]. In the study, a 3D-PCANet was trained on the mReHo volumes as the classifier model. Due to the small size of the fMRI dataset, a disparity in sample distribution is encountered causing overfitting. As a solution for this problem, graph autoencoder (GAE) was applied over a node-edge connectivity graph that represents each node's (brain region) connectivity profile over the time series [18]. Graph theory helps to model the spatiotemporal pairwise correlation between brain regions by encoding the nodes and edges of a graph into a latent vector space to capture hidden information despite the disparity of a dataset. The GAE was trained as the generator part of a generative adversarial network (GAN) [19] that reconstructs the brain connectivity graphs to enforce the GAE to better learn the connectivity graph features benefiting from the discriminator's loss. In [20], a 3D-CNN was trained on fMRI images, and the temporal dimension was neglected. While Wang et al. applied a 2D-CNN to ROIs and then passed the extracted spatial features from sequential fMRI volumes to an LSTM to model the temporal features, they neglected the third spatial dimension [21].

Despite the classification performance improvement achieved by applying CNNs to FC networks or mReHo representations, both representations have the drawback of losing some spatial and temporal information. Also, applying 3D-CNNs to the fMRI session's volumes separately neglects the temporal dimension totally, and

applying 2D-CNNs to fMRI volumes' slices neglects the third spatial dimension resulting in information loss in both cases. To preserve both spatial and temporal information, Li et al. introduced a concatenation of a 3D-CNN with an LSTM applied directly to fMRI scans [22]. In this model, the spatial feature maps generated by the 3D-CNN from all volumes along the fMRI time-series are passed sequentially to the LSTM to model the temporal relationship along the fMRI time-series. To model the 4D information, eliminating the complexity of the CNN-RNN combination, Parmar et al. designed a 3D CNN with the first two convolutional layers of a $(1 \times 1 \times 1)$ kernel to learn the temporal features hierarchically [7], then the spatial features of the volumes in the time-series were learned through the following layers. Although CNN-based methods achieved efficient results being the best in fMRI-based AD diagnosis, an overfitting problem still exists, especially when applying CNNs to small-size datasets, which is always the case for most of the medical datasets, including fMRIs.

In this study, to develop an effective method for early-stage diagnosis of AD we introduce a CapsNet-RNN model to efficiently learn the spatiotemporal features of fMRI data for AD diagnosis tackling the small-size dataset problem that causes overfitting. We propose to utilize an enhanced version of CNNs called Capsule Network (CapsNet) introduced by Sabour et al. [23] as a solution to the overfitting problem encountered with traditional CNNs, combined with a recurrent neural network (RNN) to model the 4D information of fMRI sessions. In other words, to address the issue of overfitting in medical datasets, such as fMRIs, the Capsule Network (CapsNet), a modified version of traditional CNNs created specifically for this use, was combined with an RNN to simulate the spatiotemporal characteristics of fMRI data. The spatial characteristics of every volume in an fMRI time-series were extracted using CapsNet to create a feature vector. Next, to simulate the temporal features along the fMRI volume time-series, the vectors of the time-series are successively input to an RNN. CapsNet was introduced with two main modifications to solve two major problems in traditional CNNs. First, it replaces the scalar feature detectors lacking efficient representation of the spatial correlation between different entities (shapes) produced by a conventional CNN with the capsule concept, dividing output feature maps into several groups and viewing each group of the output feature maps as a grid of capsules. Each capsule outputs a vector and the length of a vector indicates the probability that the entity (shape) represented by its capsule exists at this capsule's location in an image, while the orientation of this vector encodes different properties of the entity such as pose, position, size, orientation, deformation, and texture. Second, instead of the pooling operation that results in information loss, it applies a routing-by-agreement algorithm to alleviate this problem and model the relationship between lower-level entities constructing higher-level ones in the image features hierarchy. In our proposed CapsNet-RNN model, the CapsNet outputs a feature vector representing the spatial features of each volume in the fMRI time series. The vector of each volume is then given to an RNN to model the temporal dependency information between the fMRI volume sequences. The proposed model is able to achieve 94.5% and 61.8% accuracy for the AD vs. NC and IMCI vs. eMCI classification tasks, respectively.

2. Proposed Model

In this section, firstly, CapsNet and RNN models are overviewed to comprehend the structure of the proposed model. Then, the architecture of the proposed model is explained.

2.1. CapsNet

CNNs have proven to be efficient with image classification, especially in the medical domain. However, CNNs still suffer from some drawbacks that are more obvious with small datasets, which is almost the case for medical image datasets. CNNs suffer from two major drawbacks [23]: first, they use scalar feature detectors, which do not efficiently capture the spatial relationships between different entities. This makes CNNs less robust to affine transformations, which means that a CNN needs to be trained on a big dataset containing most, if not all, possible transformations, while medical datasets like fMRIs are usually of small size with respect to a deep learning model's number of parameters, which causes the trained model to overfit the dataset. The second drawback is performing pooling after each convolutional layer to reduce the number of parameters for achieving a lower computational complexity. This reduction of parameters results in precise position information loss. To solve these issues, CapsNet applies two concepts: vector-output capsules and routing-by-agreement as a replacement for scalar feature detectors and max-pooling operation, respectively.

2.1.1. Vector-output capsules

A CapsNet can have one or more convolutional capsule layers; each layer performs convolution on the resulting convolutional capsules (feature maps) from the previous layer. Convolution is used to maintain the shared

weight property of CNNs (knowledge replication across space) by learning the reusable feature detectors across the entire image. Each convolutional capsule represents a shape entity, where a convolutional capsule is a group of N feature maps; the number of these feature maps is referred to as the number of atoms. This group of N feature maps can be viewed as a grid of capsules, each capsule outputting a vector. At each location on this grid, there is a capsule's N -dimensional output vector that consists of the feature detectors at the same location across this group of N feature maps forming the convolutional capsule. The length of a capsule's output vector represents the probability of the existence of the entity (e.g., rectangle, triangle, etc.) represented by its convolutional capsule at this capsule's location. While the orientation of the capsule's output vector encodes various properties of the entity it represents, including different types of instantiation parameters such as pose, position, size, orientation, deformation, and texture. The capsules of each convolutional capsule layer represent a set of entities at a certain level in a hierarchy of shape complexity, where the entities in a higher layer are constituents of entities from the layer below.

2.1.2. Routing-by-agreement

To assign parts to the wholes, an algorithm called routing-by-agreement is used to couple each capsule representing an entity in a capsule layer with the capsules of the entities (parts) in the layer below. This routing-by-agreement process iteratively takes place between each capsule layer and its previous layer for a defined number of iterations within a single training iteration for the whole network. There is a coupling coefficient between each capsule in the capsule layer and each capsule in the lower layer, indicating the extent to which a lower-level capsule (entity) is probably a part of a higher-level capsule. The input to a capsule \mathbf{s}_j is calculated as a weighted sum over all “prediction vectors” $\hat{\mathbf{u}}_{j|i}$ for this capsule. These prediction vectors are calculated by multiplying the output vectors \mathbf{u}_i of all capsules in the layer below by a weight matrix \mathbf{W}_{ij} that is learned through the training process as in (1) [23]:

$$\mathbf{s}_j = \sum_i c_{ij} \hat{\mathbf{u}}_{j|i}, \quad \hat{\mathbf{u}}_{j|i} = \mathbf{W}_{ij} \mathbf{u}_i. \quad (1)$$

The following squashing function is applied to capsule input vectors to shrink their values slightly below 1 as they are used as probability values as follows in (2):

$$\mathbf{v}_j = \frac{\|\mathbf{s}_j\|^2}{1 + \|\mathbf{s}_j\|^2} \frac{\mathbf{s}_j}{\|\mathbf{s}_j\|}, \quad (2)$$

where a capsule j receives an input \mathbf{s}_j and outputs a vector \mathbf{v}_j . The summation of prediction vectors $\hat{\mathbf{u}}_{j|i}$ is weighted by coupling coefficients c_{ij} and the coupling coefficients between capsule i and all the capsules in the layer above sum to 1. A coupling coefficient c_{ij} is computed by a “routing softmax” whose initial logits are log prior probabilities b_{ij} that a capsule i should be coupled to capsule j as in (3):

$$c_{ij} = \frac{\exp(b_{ij})}{\sum_k \exp(b_{ik})}. \quad (3)$$

The logits b_{ij} are initially set to zero, and their optimal values are learned iteratively through the dynamic routing-by-agreement process based on measuring the agreement between a capsule output \mathbf{v}_j and the prediction vector $\hat{\mathbf{u}}_{j|i}$ from capsule i . The agreement is calculated as the scalar product $a_{ij} = \mathbf{v}_j \cdot \hat{\mathbf{u}}_{j|i}$, then added to the current logit b_{ij} to calculate the new logits and coupling coefficient values for the following iteration and so on. The routing-by-agreement algorithm is demonstrated in Table 1.

Table 1. Routing algorithm.

Routing algorithm

```

1: ROUTING( $\widehat{U}_{j|i}, r, l$ )
2:   for all capsule  $i$  in layer  $l$  and capsule  $j$  in layer  $(l + 1)$ :  $b_{ij} \leftarrow 0$ .
3:   for  $r$  iterations do
4:     for all capsule  $i$  in layer  $l$ :  $C_i \leftarrow \text{softmax}(b_i)$            ▶ softmax computes Eq. 3
5:     for all capsule  $j$  in layer  $(l + 1)$ :  $S_j \leftarrow \sum_i C_{ij} \widehat{U}_{j|i}$ 
6:     for all capsule  $j$  in layer  $(l + 1)$ :  $V_j \leftarrow \text{squash}(S_j)$            ▶ squash computes Eq. 1
7:     for all capsule  $i$  in layer  $l$  and capsule  $j$  in layer  $(l + 1)$ :  $b_{ij} \leftarrow b_{ij} + \widehat{U}_{j|i} \cdot V_j$ 
   return  $V_j$ 

```

2.2 Recurrent Neural Networks

RNNs are used to label, classify, or generate sequences. Data is input to an RNN as a sequence of feature vectors [24]. An RNN can be used to predict a class for each feature vector in the sequence or to predict a class for the whole sequence. RNNs are used with any kind of data that contains sequential dependencies. Therefore, RNNs are used for applications like natural language processing and forecasting time series.

2.3 Proposed Model

The proposed model consists of two parts: a CapsNet to capture the spatial features of volumes in the fMRI time series, followed by an RNN to capture the temporal features across the time series. CapsNet first receives an fMRI time series sample of five volumes to extract the spatial features from each volume as a 32D feature vector. Then, these five vectors are fed sequentially into the RNN to model the temporal features of this volume sequence, followed by a fully connected layer for final prediction.

2.3.1. CapsNet Architecture

We designed our CapsNet architecture to start with a convolutional layer with a 3D kernel of size 5, stride 1, valid (zero) padding, and 16 output channels, followed by 2 other convolutional layers with a 3D kernel of size 5, stride 2, valid padding, 32 and 64 output channels, respectively. The convolutional layers are followed by 3 convolutional capsule layers; the output of each is 32 convolutional capsules, each consisting of 8 atoms. Note that the size of a convolutional capsule’s grid in a convolutional capsule layer is the size of the feature maps generated from the convolution operation in this layer, and the number of capsules in a convolutional capsule’s grid is equal to the size of this grid. Each convolutional capsule layer has a 3D kernel of size 3, stride 2, and padding 1. The architecture of the CapsNet is illustrated in Figure 2. It should be noted that the number of convolutional capsules from the previous layer to the first convolutional capsule layer is equal to 1, as the previous one is a traditional convolutional layer.

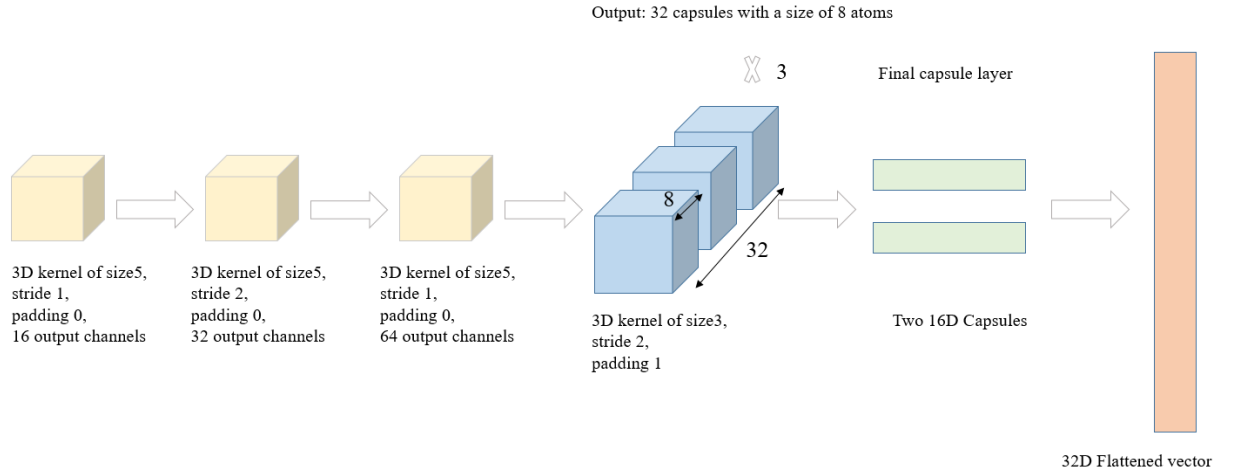


Figure 2. The CapsNet architecture used in the proposed model consisting of a convolutional layer with a 3D kernel of size 5, stride 1, valid (zero) padding, and 16 output channels, followed by 2 other convolutional layers with a 3D kernel of size 5, stride 2, valid padding, 32 and 64 output channels, followed by 3 convolutional capsule layers.

Between every two capsules in two consecutive convolutional capsule layers, there should be a weight matrix, as explained in Section 2.1.2. Thus, it is expected to have a number of weight matrices equal to (number of convolutional capsules in the lower layer \times number of convolutional capsules in the higher layer \times grid dimension of the lower convolutional capsule layer \times grid dimension of the higher convolutional capsule layer), which means an explosive number of parameters. To reduce the number of parameters and replicate knowledge across space, an approach is applied. Based on this approach, a set of filters convolving the convolutional capsules in the lower layer was used, like traditional convolution, which replaces a set of pixels equal to the kernel size by a pixel, a set of capsules is replaced by a capsule. Thus, the weights between the capsules of two convolutional capsule (convolutional capsule) layers are the weights of convolutional filters (playing the role of weight matrices \mathbf{W}_{ij} mentioned in Section 2.1.2).

The final layer in the CapsNet stage of the proposed model is composed of two 16D capsules; each of these two capsules outputs a 16D vector, where two vectors represent the spatial features of an fMRI volume, not acting as class capsules like the original CapsNet architecture introduced in [23]. Here, the capsules in the last convolutional capsule layer use a separate weight matrix \mathbf{W}_{ij} between each capsule i in this layer and each capsule j in the final layer of CapsNet. No convolution is applied between these two layers.

2.3.2 Recurrent Neural Network Architecture

In our model, we used an RNN to model the fMRI time series properties. Therefore, the two output vectors by CapsNet representing the spatial features of each volume are flattened as a single 32D vector, then all the flattened vectors are fed as a sequence to the RNN for modeling the temporal features of the volumes' time series. In the RNN architecture, there is a single layer with 64 hidden cells. Finally, the output of the RNN is passed to a fully connected layer with a single neuron, after which a sigmoid function is applied to perform the binary classification. Overall, the architecture of the proposed model based on CapsNet and RNN is illustrated in Figure 3.

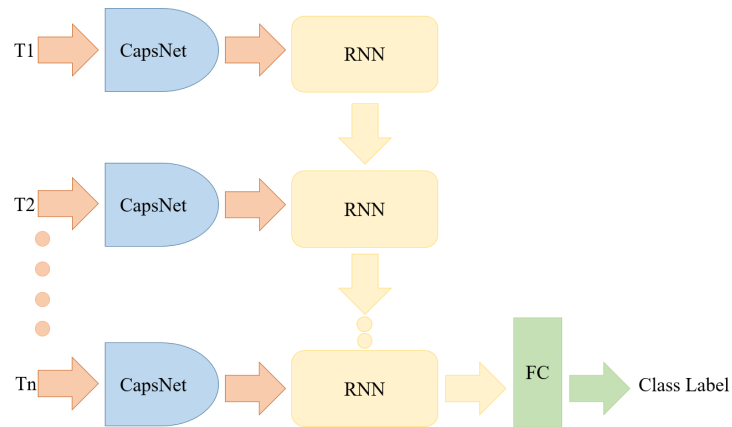


Figure 3. The architecture of the proposed model with an RNN to model the fMRI time series properties.

3. Experiments

3.1. Dataset and Pre-processing

Experiments were performed in order to evaluate the efficiency of the proposed model. In the experiments, rs-fMRI data acquired from the Alzheimer’s Disease Neuroimaging Initiative (ADNI) database [25] was used. The rs-fMRI dataset contains four classes of a total of 147 subjects, including 34 AD subjects, 34 NC subjects, and 80 MCI subjects divided into 40 eMCI and 40 IMCI. For each subject, 140 volumes were acquired in a session, with each volume consisting of 36 – 48 slices. Each slice is of size 64×64 , slice thickness is 3.1 mm, TE (echo time) is 30 ms, and TR (repetition time) is 2200 – 3100 ms. The rs-fMRI dataset was pre-processed using the SPM 12 toolbox [26] and MATLAB 2022b. The pre-processing steps included removing the first three volumes for magnetization equilibrium, head motion correction, slice timing correction, and spatial smoothing by a Gaussian kernel with a full-width-at-half-maximum (FWHM) of 6 mm. Finally, fMRIs were co-registered with T1-weighted MRIs of the same subjects to normalize the fMRIs onto the standard 152 Montreal Neurological Institute (152 MNI) space. By the end of this process, the dimension of fMRI volumes is changed from $64 \times 64 \times 48$ to $61 \times 73 \times 61$ due to the deformations applied by the spatial normalization module to register the images into the standard space.

3.1. Implementation Details

The Python-based Pytorch framework was used to implement and train the proposed model. Besides, Google Colab Pro was used to perform the experiments, utilizing the NVIDIA A-100 GPU with 40 GB of RAM and 83.5 GB of CPU RAM. The proposed model was trained for two binary classification tasks: AD vs. NC and IMCI vs. eMCI classifications. Binary cross-entropy was used as a loss function for the proposed model. The model was trained using the Adam optimizer with a learning rate of $1e-6$ and L2 regularization to prevent overfitting with a regularization coefficient of 0.1. The training was completed in 20 and 15 epochs (to avoid overfitting) for the AD vs. NC and IMCI vs. eMCI tasks, respectively. Moreover, the batch size was set to 2 for both classification tasks. The proposed model was trained for nearly 1 hour and 10 minutes. It should be noted that the number of parameters in our model is 4.4 M parameters. Furthermore, the GPU RAM consumption was 1.9 GB, and the CPU RAM consumption used mainly for holding the dataset was 49.5 GB and 43.9 GB for AD vs. NC and IMCI vs. eMCI tasks, respectively.

Before the implementation, the dataset was divided into three categories: 70% as training data, 10% as validation data, and the remaining 20% as testing data. The proposed model was trained on 34 AD, 34 NC, 40 IMCI, and 40 eMCI subjects, taking a maximum of three sessions and two sessions from each subject in AD vs. NC and IMCI vs. eMCI, respectively, due to memory constraints. Following an approach applied in [7], we obtained the first 100 volumes from each session after the pre-processing stage and divided these 100 volumes into 20 samples to have 5-volume time-series samples. Obtaining five samples from a single session increases the number of trainable samples, leading to a higher generalization of the proposed model. Thus, 1680 AD, 1680 NC, 1460 IMCI, and 1460 eMCI samples were obtained to carry out the experiments.

3.2 Results

3.2.1. Classification performance

The classification accuracy achieved by the proposed model for the two binary classification tasks is given in Table 2. For the AD vs. NC classification task, it is clear that the proposed model achieved the accuracy at 100%, 100%, and 94.5% for training, validation, and testing datasets, respectively. For the IMCI vs. eMCI task, it achieved the accuracy at 99%, 64.3%, and 61.8% accuracies for training, validation, and testing datasets, respectively.

The loss and accuracy curves for the AD vs. NC task are plotted in Figure 4 and 5, respectively, and for the IMC vs. eMCI task in Figure 6 and 7, respectively.

Table 2. Classification accuracy of the proposed model.

Accuracy	AD vs. NC	IMCI vs. eMCI
Training	100%	99%
Validation	100%	64.3%
Test	94.5%	61.8%

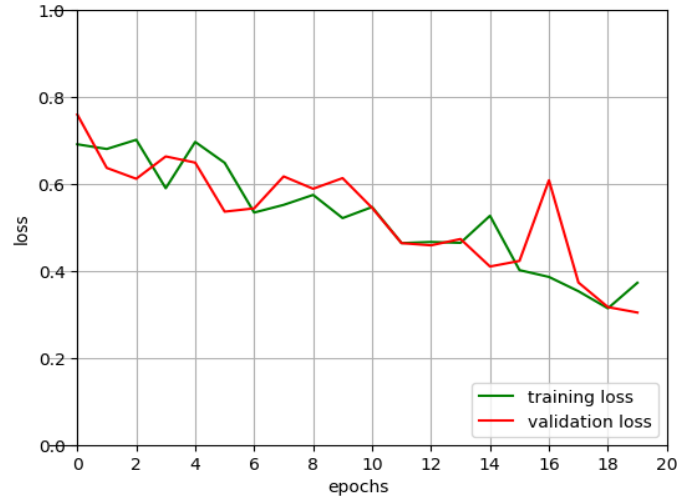


Figure 4. Loss curves of AD vs. NC.

3.2.2. Comparison with State-of-the-Art Methods

In this section, the accuracy of the proposed method is compared with several state-of-the-art methods proposed in the literature. We can see from Table 3 that the proposed model performs comparably well in terms of testing accuracy to the recent studies for the AD vs. NC task. Besides, it can be seen that nearly all the models reach high accuracies with the AD vs. NC task, while there is still a gap between the accuracies achieved by our study and studies [6], [21] when performing IMCI vs. eMCI classification and those achieved by nearly all studies in the AD vs. NC task. Thus, the IMCI vs. eMCI task and its similar sMCI vs. pMCI are reported to be challenging tasks in the literature [4]. Hence, the authors are planning to consider enhancing the accuracy of the IMCI vs. eMCI task in the near future.

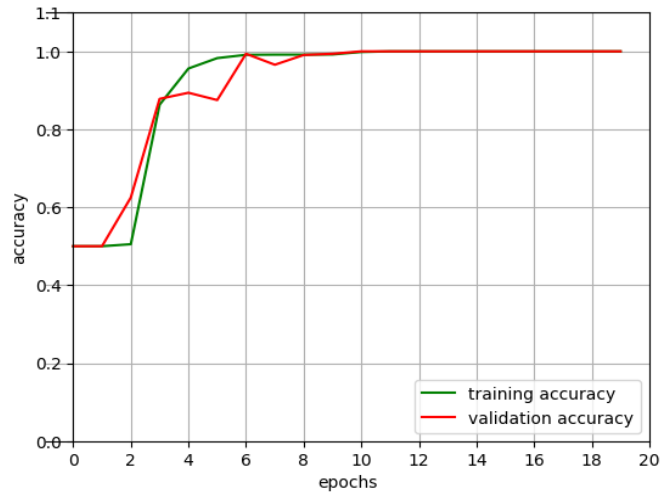


Figure 5. Accuracy curves of AD vs. NC.

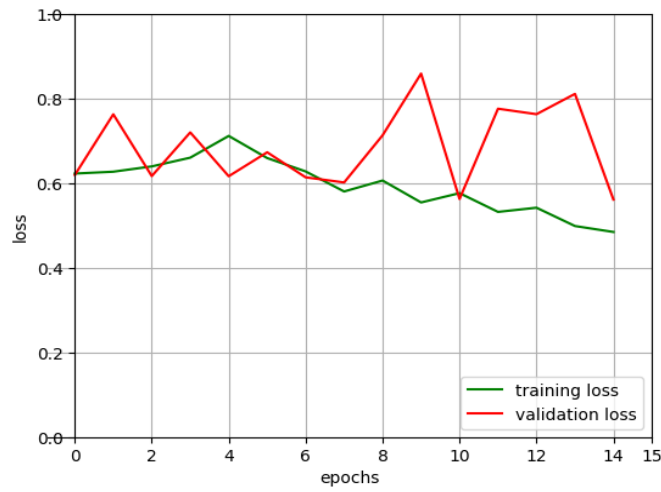


Figure 6. Loss curves of IMCI vs. eMCI.

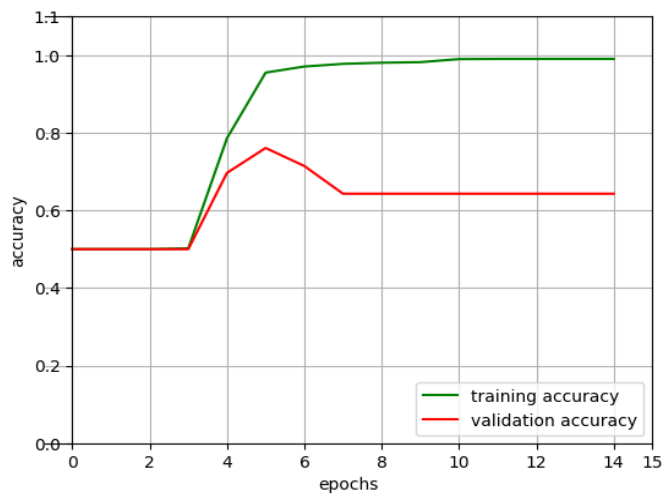


Figure 7. Accuracy curves of IMCI vs. eMCI.

Table 3. Comparison with other studies.

Study	Method	AD vs. NC	IMCI vs. eMCI	pMCI vs. sMCI	Multi-Class
He et al. [10]	2D-CNN applied to FC matrices.	93%	N/A	N/A	N/A
Duc et al. [12]	3D-CNN applied to 3D-ICA feature maps based on FC networks.	85.27%	N/A	N/A	N/A
Jie et al. [6]	Multi-task feature learning+SVM applied to FC networks.	N/A	78.8%	N/A	N/A
Wang et al. [14]	PCANet applied to FC matrices.	88%	100%	N/A	N/A
Jia et al. [17]	PCANet applied to mReHO transformation images.	80%	N/A	N/A	N/A
Mirakhorli et al [18]	Graph-CNN applied to brain connectivity node-edge graph.	97.1%	N/A	N/A	N/A
Lin et al. [15]	CNN+LSTM applied to FC networks	92.8%	N/A	N/A	AD vs eMCI vs IMCI vs NC: 61.7%
Wang et al. [21]	2D-CNN+LSTM applied to overlapping windows of ROIs.	90.28%	79.36%	N/A	AD vs. MCI vs. NC: 71.76% AD vs. eMCI vs. IMCI vs. NC: 60.67%
Li et al. [22]	3D-CNN+LSTM applied to fMRI volumes time-series.	97.37%	N/A	N/A	AD vs MCI vs NC: 89.47%
Parmar et al. [7]	A special configuration of 3D-CNN to model the 4D information applied to fMRI volumes time-series.	N/A	N/A	N/A	AD vs. eMCI vs. IMCI vs. NC: 93%
Our study	CapsNet +RNN applied to fMRI volumes time-series.	94.5%	61.8%	N/A	N/A

As discussed earlier, there are two aims behind combining a CapsNet with an RNN in the same model. The first is to model the 4D information by applying the model directly to the time series of fMRI volumes in order to avoid information loss associated with applying CNNs to FC networks or mReHo transformation images, and the second is to overcome the overfitting problem that occurs with traditional CNNs that was replaced with CapsNet. From the comparison results, it has been observed that the proposed model and the studies introduced in [7] and [22], which model the 4D information from the fMRI volume sequence directly, were able to achieve better accuracies than the models introduced in [10], [12], [14], [15] (which apply CNNs to FC networks), and [17] (that apply CNNs to mReHO images). Moreover, despite CapsNet being designed to achieve better generalization than traditional CNNs, the method which applies CNNs with LSTM directly to fMRI volumes [22] still achieves better accuracy than our model. Hence, we concluded that some enhancement is required in the pre-processing stage to improve the performance of our model, which can be considered as a future work.

4. Discussion

The proposed CapsNet-RNN-based model exhibits a high capability of generalization and learning more hidden patterns of interest from a small dataset and in a relatively small number of epochs. In addition, it efficiently models the 4D information of fMRI sessions, which is unique to fMRI different from other neuroimaging modalities.

Medical datasets generally suffer from being of small size including brain neuroimaging datasets. This is due to several reasons, such as the difficulty of acquiring medical datasets from a wide range of subjects and privacy and data protection concerns. Here, the role of CapsNet comes as a solution to one of the CNNs' drawbacks that becomes more obvious with smaller datasets. CNNs suffer from a lack of capturing sufficient affine transformation features, as discussed earlier resulting in an overfitting problem. CapsNet with its representation of shape entities as vectors and applying the routing-by-agreement algorithm can efficiently learn the relationship features of assigning parts to wholes, which alleviates the need for big datasets to learn all possible affine transformations as in the case of CNNs.

Regarding fMRI data, the CapsNet-RNN models both brain activity dynamic changes within a specific region and dynamic FC between different regions across the fMRI time series. It does not need to construct FC matrices as a pre-processing step, where it learns the spatiotemporal features entirely through the training process performed

directly on fMRI images. Thus, it avoids the information loss associated with constructing FC networks or just taking into account the spatial features and neglecting the temporal ones.

This relatively high accuracy reached in less than 20 epochs with the AD vs. NC task reveals the powerfulness of CapsNet to generalize and converge in a relatively small number of epochs with small-size datasets. Similarly, CapsNet converged to the desired classification accuracy in 10 epochs in another study utilizing it in a multi-class brain tumor classification [27]. The promising results of CapsNet in the medical domain and other various domains [28] show that CapsNet is revolutionizing computer-vision-related applications, thus it can be helpful with several medical tasks such as diagnosis, prognosis, and segmentation.

5. Conclusion and Future Work

To capture the 4D information of the rs-fMRI time-series data for AD diagnosis, an end-to-end deep learning model (CapsNet-RNN) is proposed in this study. Specifically, an RNN was concatenated with a version of standard CNNs known as CapsNet, created for this purpose, to represent the spatiotemporal aspects of fMRI data, therefore mitigating the overfitting issue associated with medical datasets, including fMRIs. The spatial characteristics of every volume in an fMRI time series were extracted as a feature vector using CapsNet. Subsequently, an RNN is trained with the time series vectors in order to model the temporal properties along the fMRI volume time series. The robustness of CapsNet to obtain a reasonable generalization level on limited datasets is demonstrated by the reasonably high accuracy (94.5%) reached in fewer than 20 epochs with the AD vs. NC task.

Although the results of applying the suggested model to fMRI data for AD diagnosis have been encouraging, the pre-processing step still needs to be revised. Furthermore, it is also essential to enhance the proposed model to achieve closer accuracy achieved by well-known models for the AD vs. NC task and to attain similar accuracy for the AD vs. NC task along with more challenging tasks like the IMCI vs. eMCI task. As a future work, combining different neuroimaging biomarkers, such as sMRI and PET with fMRI using CapsNets for AD diagnosis needs to be investigated. Combining multi-imaging modalities can lead to better diagnosis accuracy in clinical practice, as different modalities can provide complementary information to each other. Moreover, only binary classification was used in this investigation. The suggested model is anticipated to be used in the near future for multi-class classification of various phases of AD or possibly for differentiating AD from other types of dementia.

Acknowledgements

Publicly available datasets from Alzheimer's Disease Neuroimaging Initiative (ADNI) database were analyzed in this study. Data accessible from: Alzheimer's Disease Neuroimaging Initiative (ADNI) database (<https://adni.loni.usc.edu>).

References

- [1] Alzheimer's Association Report. 2017 Alzheimer's disease facts and figures. *Alzheimer's & Dementia* 2017; 13(4): 325-373.
- [2] Haux R. Health information systems - past, present, future. *Int J Med Inform* 2006; 75(3-4): 268-281.
- [3] Janghel RR, Rathore YK. Deep convolution neural network based system for early diagnosis of alzheimer's disease. *IRBM* 2021; 42(4): 258-267.
- [4] Ebrahimighahnavieh MA, Luo S, Chiong R. Deep learning to detect Alzheimer's disease from neuroimaging: a systematic literature review. *Computer Methods and Programs in Biomedicine* 2020; 187: 105242.
- [5] Kivistö J, Soininen H, Pihlajamäki M. Functional MRI in Alzheimer's Disease. *Advanced Brain Neuroimaging Topics in Health and Disease - Methods and Applications*. InTech; 2014.
- [6] Jie B, Liu M, Shen D. Integration of temporal and spatial properties of dynamic connectivity networks for automatic diagnosis of brain disease. *Med Image Anal* 2018; 47:81-94.
- [7] Parmar H, Nutter B, Long R, Antani S, Mitra S. Spatiotemporal feature extraction and classification of alzheimer's disease using deep learning 3D-CNN for fMRI data. *Journal of Medical Imaging* 2020; 7(5): 056001.
- [8] Jie B, Zhang D, Wee CY, Shen D. Topological graph kernel on multiple thresholded functional connectivity networks for mild cognitive impairment classification. *Hum Brain Mapp* 2014; 35(7):2876-2897.
- [9] Bi XA, Shu Q, Sun Q, Xu Q. Random support vector machine cluster analysis of resting-state fMRI in alzheimer's disease. *PLoS One* 2018; 13(3): e0194479.
- [10] He Y, Wu J, Zhou L, Chen Y, Li F, Qian H. Quantification of cognitive function in alzheimer's disease based on deep learning. *Front Neurosci* 2021; 15: 651920.
- [11] Howard AG, Zhu M, Chen B, Kalenichenko D, Wang W, Weyand T, Andreetto M, Adam H. MobileNets: efficient convolutional neural networks for mobile vision applications. *arXiv* 2017; 1704.04861.

- [12] Duc NT, Ryu S, Qureshi MNI, Choi M, Lee KH, Lee B. 3D-deep learning based automatic diagnosis of alzheimer's disease with joint mmse prediction using resting-state fMRI. *Neuroinformatics* 2020; 18(1), 71-86.
- [13] Chan TH, Jia K, Gao S, Lu J, Zeng Z, Ma Y. PCANet: a simple deep learning baseline for image classification? *IEEE Transactions on Image Processing* 2015; 24(12): 5017-5032.
- [14] Wang Y, Liu X, Yu C. Assisted diagnosis of alzheimer's disease based on deep learning and multimodal feature fusion. *Complexity* 2021; 2021: 6626728.
- [15] Lin K, Jie P, Dong P, Ding X, Bian W, Liu M. Convolutional recurrent neural network for dynamic functional mri analysis and brain disease identification. *Front Neurosci* 2022; 16: 933660.
- [16] Jiang L, Zuo XN. Regional homogeneity: a multimodal, multiscale neuroimaging marker of the human connectome. *Neuroscientist* 2016; 22(5): 486-505.
- [17] Jia H, Lao H. Deep learning and multimodal feature fusion for the aided diagnosis of alzheimer's disease. *Neural Comput Appl* 2022; 34(22): 19585-19598.
- [18] Mirakhorli J, Amindavar H, Mirakhorli M. A new method to predict anomaly in brain network based on graph deep learning. *Rev Neurosci* 2020; 31(6): 681-689.
- [19] Goodfellow IJ, Pouget-Abadie J, Mirza M, Xu B, Warde-Farley D, Ozair S, Courville A, Bengio Y. *ArXiv* 2014; 1406.2661.
- [20] Ghafoori S, Shalhaf A. Predicting conversion from MCI to AD by integration of rs-fMRI and clinical information using 3D-convolutional neural network. *Int J Comput Assist Radiol Surg* 2022; 17(7): 1245-1255.
- [21] Wang M, Lian C, Yao D, Zhang D, Liu M, Shen D. Spatial-temporal dependency modeling and network hub detection for functional MRI analysis via convolutional-recurrent network. *IEEE Trans Biomed Eng* 2020; 67(8): 2241-2252.
- [22] Li W, Lin X, Chen X. Detecting alzheimer's disease based on 4D fMRI: an exploration under deep learning framework. *Neurocomputing* 2020; 388: 280-287.
- [23] Sabour S, Frosst N, Hinton GE. Dynamic routing between capsules. In: *Proceedings of the 31st International Conference on Neural Information Processing Systems*; 4-9 December 2017; Long Beach, California, USA: Curran Associates Inc. pp. 3859–3869.
- [24] Schmidt RM. Recurrent neural networks (RNNs): a gentle introduction and overview. *ArXiv* 2019; 1912.05911.
- [25] Mueller SG, Weiner MW, Thal LJ, Petersen RC, Jack CR, Jagust W, Trojanowski JQ, Toga AW, et al. Ways toward an early diagnosis in alzheimer's disease: the alzheimer's disease neuroimaging initiative (ADNI). *Alzheimers Dement*. 2005; 1(1): 55-66.
- [26] The FIL Methods Group and honorary members, SPM12 Manual. Functional Imaging Laboratory, Institute of Neurology, UCL, 2015, <http://www.fil.ion.ucl.ac.uk/spm/doc/manual.pdf>.
- [27] Afshar P, Mohammadi A, Plataniotis KN. Brain tumor type classification via capsule networks. In: *25th IEEE International Conference on Image Processing (ICIP)*: 07-10 October 2018; Athens, Greece: IEEE. pp. 2381-8549.
- [28] Goceri E. Analysis of capsule networks for image classification. In: *International Conference on Computer Graphics, Visualization, Computer Vision and Image Processing: IADIS*. pp. 53-60.

Effect of Ferro-Alloys on the Properties of High Entropy Alloy with FeCoNiMnMoV Composition Produced by Arc-Melting Method

Seval Hale GÜLER^{1*}

¹ Rare Earth Elements Application and Research Center, Munzur University 62000, Tunceli, Türkiye

*sevalhaleguler@munzur.edu.tr

(Geliş/Received: 07/12/2023;

Kabul/Accepted: 26/02/2024)

Abstract: In this study, high entropy FeCoNiMnMoV and FeCoNiMn (Ferro Mo-Ferro-V) alloys were produced by arc melting method. After the arc melting process, the samples were annealed at 1000°C under argon atmosphere for 15 hours physical and thermodynamic calculations were performed to determine the properties of the alloy. In the study, both alloys were characterized. For characterization, XRD, SEM, EDS and Micro hardness were taken from the samples. The aim of my study is to examine the effect of using low-priced starting materials on the microstructure of HEA. For this purpose, ferro-alloys were added to the alloy. As a result, similar properties were obtained for the microstructure of both alloys. However, it has been determined that the hardness of samples containing ferro-alloys decreases more due to their chemical composition, especially after heat treatment.

Key words: High Entropy Alloy, Arc Melting, Ferro Alloys, SEM, Hardness.

Ark-Ergitme Yöntemi ile Üretilen FeCoNiMnMoV Bileşimine Sahip Yüksek Entropili Alaşımın Özelliklerine Ferro-Alaşımın Etkisi

Öz: Bu çalışmada yüksek entropili FeCoNiMnMoV ve FeCoNiMn (Ferro Mo-Ferro V) alaşımları ark ergitme yöntemi ile üretilmiştir. Ark ergitme işlemi sonrası numenelere 1000°C'de argon atmosferi altında 15 saat tavlama işlemi uygulanmıştır. Alaşımın özelliklerini belirlemek için fiziksel ve termodinamik hesaplamalar yapılmıştır. Çalışmada her iki alaşım karakterize edilmiştir. Karakterizasyon için numunelerden XRD, SEM, EDS, Mikro sertlik alınmıştır. Çalışmanın amacı düşük fiyatlı başlangıç malzemelerinin kullanılmasının HEA'ların mikro yapısına etkisini incelemektir. Bu amaçla alaşımın içine ferro alaşımlar ilave edilmiştir. Sonuç olarak, her iki alaşım mikro yapısı için benzer özellikler elde edilmiştir. Ancak özellikle ısıtım işleminden sonra ferro alaşımlı numunelerin kimyasal bileşimlerinden kaynaklı olarak sertliklerinin daha fazla düştüğü tespit edilmiştir.

Anahtar Kelimeler: Yüksek Entropili Alaşım, Ark Ergitme, Ferro Alaşımlar, SEM, Sertlik.

Introduction

Some properties are improved and some are worsened by the alloy. The intermetallics that are hard and brittle and form in the structure make the alloy stronger, but they also make it less plastic [1]. Each new material leads to a new application area, thus leading to the development of engineering practices. The search for new materials continues at full speed today. In many traditional alloys, a family of alloys based on the main element is obtained by adding different types of alloying elements to a main element [2]. For example, Zn, Mg, Si, Mn added to Al causes the emergence of new alloys with different properties. While Si provides increased strength, Mg causes the development of corrosion properties. [3]. The formation of complex microstructures, intermetallic compounds and precipitate phases is the result of adding different metals to the base metal in various proportion [4]. Intermetallic compounds that are typically hard and brittle are formed when the amount of minor alloy element increases. The strength of the alloys is enhanced, but the plasticity of the alloys frequently declines. [5]. In the alloy concept first proposed by YEH and her colleagues in 1995, new generation alloys that are not similar to traditional alloys have emerged [6]. This new generation alloy concept is called "high entropy alloy (HEA)". HEAs are groups of alloys containing 5 or more major elements [7, 8]. Each major element has a concentration between 5% and 35% [9, 10]. The mixing entropy in these alloys is very high compared to conventional alloys. Unlike conventional alloys, the formation of simple structured solid solution phases is observed in these alloys instead of several dozen phases and intermetallics that cause embrittlement. These simple structured solid solutions in HEAs make HEAs different from other alloys. High strength, excellent wear resistance, unusual fatigue resistance, low temperature strength, good corrosion resistance, antioxidation and excellent microstructural stability are the properties that make HEAs better than conventional alloys [11-14]. HEAs have the potential to be used in many engineering applications thanks to the unique properties they exhibit. HEAs have some disadvantages. One of them is their weight. The other is their cost, which is more important than their weight. Since HEAs are alloys obtained by adding at least 5

* Corresponding author: sevalhaleguler@munzur.edu.tr. ORCID Number of authors: 0000-0001-5888-9437

metals in equimolar and/or near-equimolar ratios, this causes their costs to increase [15]. The Ferro-alloy form of a metal is preferred over its pure form for alloying in the traditional alloy production sector. The reason is that the Ferro-alloy form of a metal is significantly less expensive than its pure form [16, 17]. The production of HEAs will be more affordable by using ferroalloys in HEAs. Ferroalloys are of two types; these are those produced in high quality and those produced in lower quality. Even in high quality Ferroalloys, there are still some impurities. The effect of these impurities found in ferroalloys on the properties of HEAs is an issue that needs to be investigated. In this study, HEA alloy in FeCoNiMnMoV composition was also produced using some Ferroalloys and the changes between the structural and some mechanical properties of both alloys were revealed.

2. Experimental Procedure

High purity V (Merck, 99.5%), Co (Merck, 99+%), Fe (Merck, 99%), Ni (Merck, 99.5%), Mo (Merck, 99.5%), Mn (Nanography, 99.5%) metals were used in the first method, and high purity Al, Co, Fe, Ni were used in the second method to produce HEA with FeCoNiMnMoV composition in this study. However, instead of high purity Mo and V, high quality Ferrovandium and Ferromolybdenum were used. Ferrovandium and Ferromolybdenum were obtained from Acarer Metal company and their compositions are given in Table 1.

Table 1. Compositions of Ferroalloys used in the study

Ferrovandium		Ferromolybdenum	
V	65 % min	Mo	70 % min
Al	1.5 % max	Cu	0.5 % max
Si	2 % max	Si	1.5 % max
P	0.1 % max	S	0.01 % max
C	0.25 % max	C	0.1 % max
		P	0.05 % max

Table 2. Sample codes, composition, processes

Sample Code	Composition	Treatment
S1 (As-Cast)	Only Elemental Metal Powders	Arc Melting
S2 (As-Cast)	Ferroalloys and Elemental Metal Powders	Arc Melting
SG1 (Cast-Annealing)	Only Elemental Metal Powders	Annealing after Arc Melting
SG2 (Cast-Annealing)	Ferroalloys and Elemental Metal Powders	Annealing after Arc Melting

Sample codes and the procedures performed on the samples are given in Table 2. The powders weighed in appropriate proportions were mixed and turned into pellets. Then, the obtained pellets were melted 3 times consecutively using Arc-melting to obtain alloys. The other group of samples were subjected to annealing at 1000°C under argon atmosphere for 15 hours after the arc melting process (Table 2). The flow chart for the experiment is given in Figure 1.

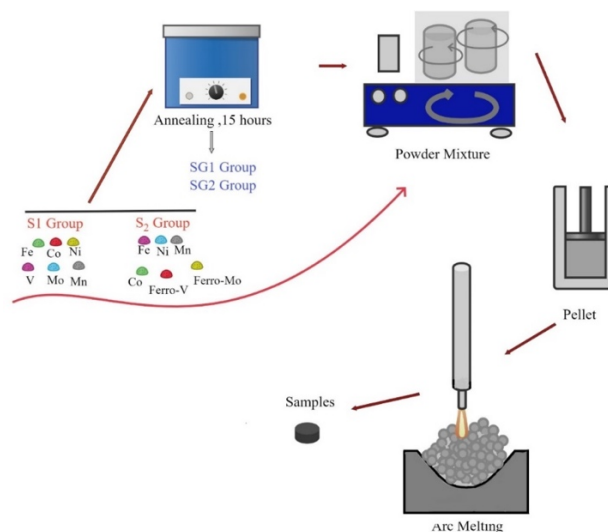


Figure 1. Experiment flow chart

The obtained samples were subjected to X-ray diffraction spectra (XRD, RIGAKU Miniflex 600) analysis for morphological examinations. Then, the samples were examined with scanning electron microscopes (SEM, Hitachi SU3500) and energy dispersive spectroscopy (EDX, Oxford AZtech) and Mitutoyo Corporation brand microhardness tester. Additionally, formulas for determining the properties of alloys are given in Table 3.

Table 3. Formulas required for physical and thermodynamic calculations of alloys

	Formulation	Amorphous	Solid solution (SS)	SS+Intermetallic (IM)
δ	$\delta = \sqrt{\sum C_i \left(\frac{1-r_i}{r}\right)^2}$ [18]	$\delta \geq 9$ [19]	$0 \leq \delta \leq 8.5$ [19]	SS and IM $3.6\% \leq \delta r < 6.6\%$ IM, $\delta r \geq 6.6\%$ [20]
Ω	$\Omega = \frac{T_m \Delta S_{mix}}{ \Delta H_{mix} }$ [18]	-	$\Omega \geq 1.1$ [18]	IM $1 \leq \Omega \leq 2$ SS and IM $1.1 \leq \Omega \leq 10$ [20]
VEC	$VEC = \sum_i^n C_i (VEC)_i$ [21]	-	VEC ≤ 6.87 BCC VEC ≥ 8 FCC $6.87 \leq VEC \leq 8$: FCC+BCC [22]	-
ΔS_{mix}	$\Delta S_{mix} = -R \sum_i^n C_i \ln C_i$ [21]	$7 \leq \Delta S_{mix} \leq 14$ Jmol ⁻¹ K ⁻¹ [19]	$11 \leq \Delta S_{mix} \leq 19.5$ Jmol ⁻¹ K ⁻¹ [19]	-
ΔH_{mix}	$\Delta H_{mix} = \sum_{i=1}^n \sum_{j \neq i} 4\Delta H_{ij}^{mix}$ [21]	$-35 \leq \Delta H_{mix} \leq -8.5$ kJmol ⁻¹ [19]	$-22 \leq \Delta H_{mix} \leq 7$ kJmol ⁻¹ [19]	Containing IM; $\Delta H_{mix} < -7.5$ [20]

In the given equations, the value of n represents the number of components (*ci* and *cj*). i and j give the mole fractions of the elements in the alloy. In addition, the binary mixing enthalpy values (ΔH_{ij}^{mix}) between the elements i and j can be calculated with the Miedema approach [23]. ΔS_{mix} , represents the mixture entropy, ΔS_{conf} represents the configuration entropy. δ gives the atomic size difference. In the formula (r) refers to the atomic diameter of the alloying elements. The term Ω refers to the probability of forming a solid solution. In this expression Ω , is a symbol of the conflict between entropy and enthalpy. VEC describes the valence electron configuration. Using the formulas in Table 3 and the Miedema approach, the thermodynamic and physical properties for the S1 and S2 alloy are given in Table 4.

Table 4. Physical and thermodynamic properties for samples S1 and S2

Sample Code	ΔS_{conf}	ΔS_{mix}	ΔH_{mix}	VEC	Ω	δ	T_m
S1	1.79R	14.88	-4.377	7.47	6.07	7.28	1990.9
S2	1.77R	14.71	-2.91	7.55	9.92	7.36	1961.7

3. Results and Discussion

Figure 2 shows the XRD analysis results of samples S1, S2, SG1 and SG2. S1 sample is the sample produced using elemental metal powders and arc melting. Sample S2 is an HEA sample produced by arc melting using both elemental powders and ferro-alloys. 3 characteristic peaks are seen in both the XRD spectra of the S1 sample and the S2 sample (Figure 2.a - b). The most intense and broad peak at approximately 43° is the peak showing BCC and FCC structure. Since the peak is strong and broad, the (111) FCC peak and the (110) BCC peak are on top.

Other characteristic peaks are the FCC peak at approximately 52° (200). The peak at approximately 73° is the (220) FCC peak.

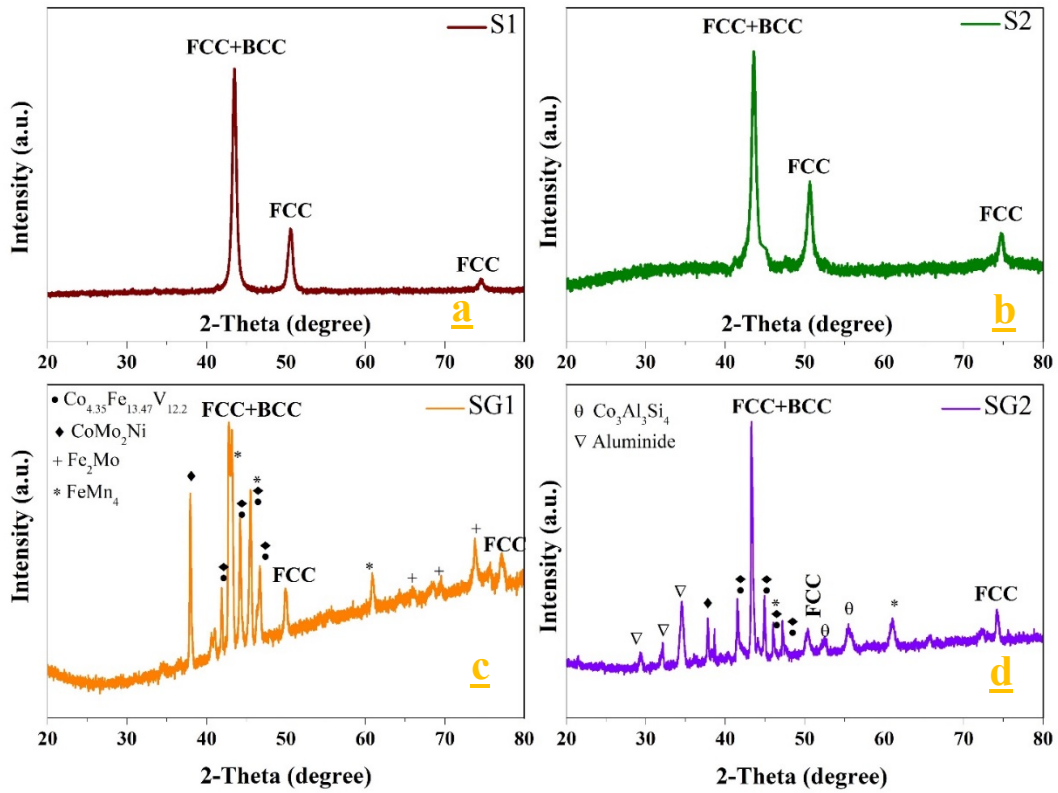


Figure 2. XRD spectra a) S1, b) S2, c) SG1, d) SG2

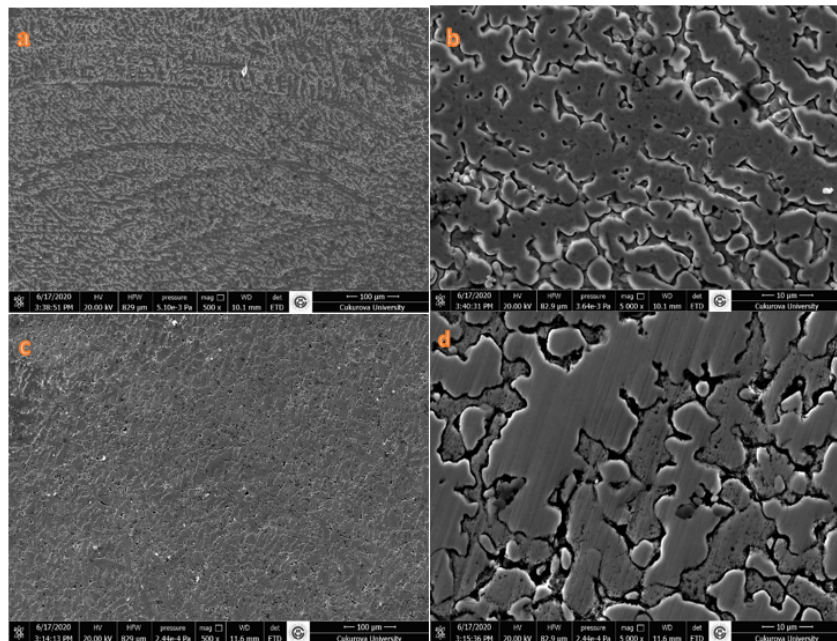


Figure 3. a) S1 (500X), b) S1 (5000X), c) S2 (500X), d) S2 (5000X)

XRD spectra of SG1 and SG2 samples are given in Figure 2c and d. SG1 and SG2 samples are the samples of S1 and S2 annealed at 1000°C for 15 hours after arc melting. As can be seen from the XRD spectra, the characteristic peaks at 43°, 52° and 73° are also present in the SG1 and SG2 samples. However, at the end of the annealing process, it is seen that $\text{Co}_{4.35}\text{Fe}_{13.47}\text{V}_{12.2}$, CoMo_2Ni , Fe_2Mo and FeMn_4 structures precipitate. Additionally, $\text{Co}_3\text{Al}_3\text{Si}_4$ and various aluminides are observed to precipitate in the SG2 sample. The high annealing temperature of 1000 °C and the long annealing time of 15 hours caused the precipitation of such structures. Because both temperature and time contributed to the diffusion conditions for the formation of these structures. The main reason why these phases cannot precipitate in S1 and S2 samples is that cooling occurs very quickly after the arc melting process and there is not enough time for the metals in solid solution to come out of the cage. Therefore, solid solutions seen in classical HEAs were observed in samples S1 and S2. Although there is no Al and Si in the composition of the alloy, it was observed that $\text{Co}_3\text{Al}_3\text{Si}_4$ and various aluminides were formed in the SG2 sample. The reason for this situation is due to the ferro-alloys used in the SG2 sample. As seen in Table 1, Ferro-alloys contain up to 1.5% Al and Si.

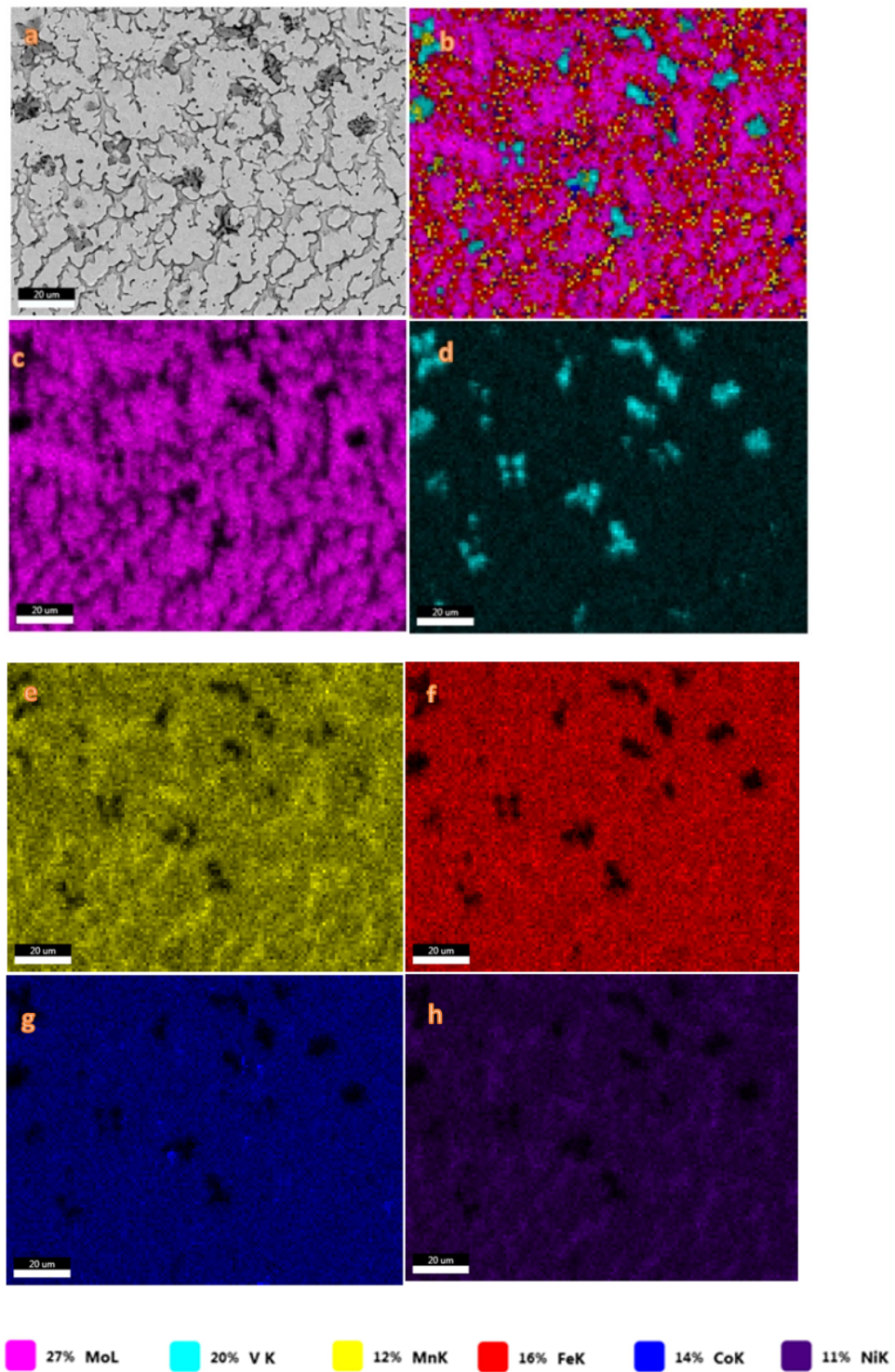
Figure 3 shows the SEM images of S1 (Figure 3.a-b) and S2 (Figure 3.c-d) samples at different magnifications after casting. It is seen that the S1 sample has a thinner casting structure than the S2 sample and the dendritic structure is longer and more continuous. It is seen that the dendritic structure in the S2 sample is discontinuous and the grains are coarser compared to the S1 sample.

Each sample was inspected and analysed by scanning electron microscopy (SEM) and energy-dispersive X-ray spectroscopy (EDS), and mapping was carried out to verify the spatial distribution of the alloy components. A SEM image and typical mapping of a 6-component alloy is shown in Figure 4.(a-b). The regions in the mapping with a good distribution of alloying elements showed the formation of the high-entropy alloys that were the objective of this study. From these results, when the elemental mapping given in Figure.4 for the S1 sample of the microstructure of this alloy is examined, it is seen that Mo, V, Co, Fe elements are concentrated in the dendritic phase, while Ni and Mn are in the dendritic phase in less density. The mapping for each element is shown in the Figure.4 (c-h). It is seen that the regions rich in vanadium element are concentrated as a separate phase within this dendrite phase. In the interdendritic structure, Mn, Fe, Ni, Co elements are predominantly seen. V is not seen in the interdendritic structure.

In Figure 5.(a-b), SEM image and the elemental mapping for the sample S2 is given. The mapping for each element is shown in the Figure.5 (c-h). Here, similar to the S1 sample, it is seen that Mo, V are more concentrated in the dendritic phase, Mn and Ni elements are more concentrated between the dendrites, and Co and Fe are concentrated in both regions.

Figure 6 shows the microstructure images of SG1 (Figure 6.a-b) and SG2 (Figure 6.c-d) samples at different magnifications. SG1 and SG2 samples are the samples after heat treatment. Therefore, especially in the SG1 sample, it is seen that the dendritic arms in the structure have transformed into equiaxed grains. The structure is coarser in the SG2 sample. This suggests that the different elements in the ferro alloy cause a slow diffusion effect in the homogenization annealing.

Figure 7. (a-b) shows SEM image and the elemental distribution mapping for the SG1 sample. The mapping for each element is shown in the Figure.7 (c-h). With the effect of heat treatment, the elements are distributed more homogeneously between grains and grains. We can say that only Mo is present in the grain and the other elements are more homogeneously distributed. According to the XRD analysis given in Figure 2, different precipitates formed in the structure due to the effect of heat treatment. These precipitates are $\text{Co}_{4.35}\text{Fe}_{13.47}\text{V}_{12.2}$, CoMo_2Ni , Fe_2Mo and FeMn_4



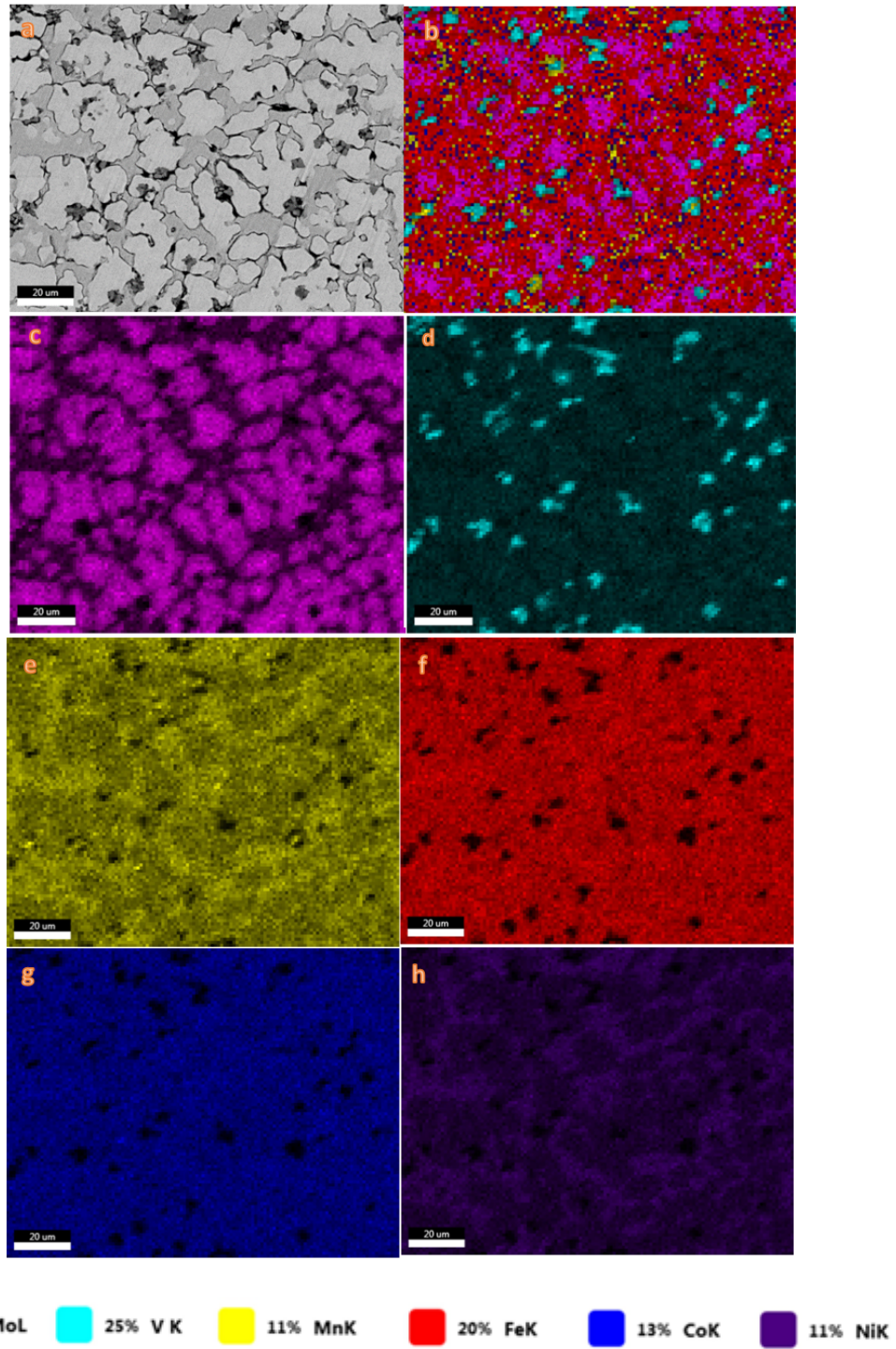


Figure 5. S2 sample a) SEM image b) Elemental distribution mapping for the sample c-h) The mapping for each element

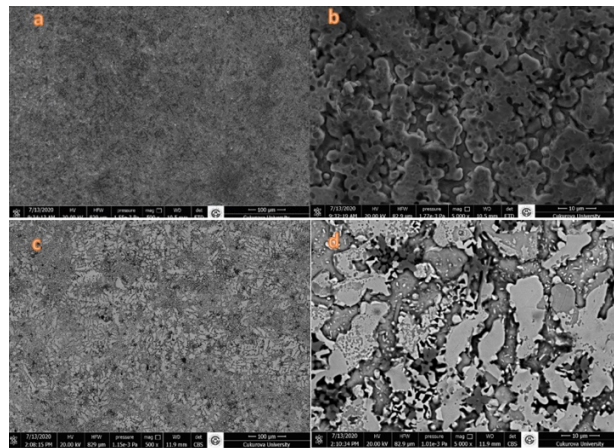


Figure 6. a) SG1 (500X), b) SG1 (5000X), c) SG2 (500X), d) SG2 (5000X)

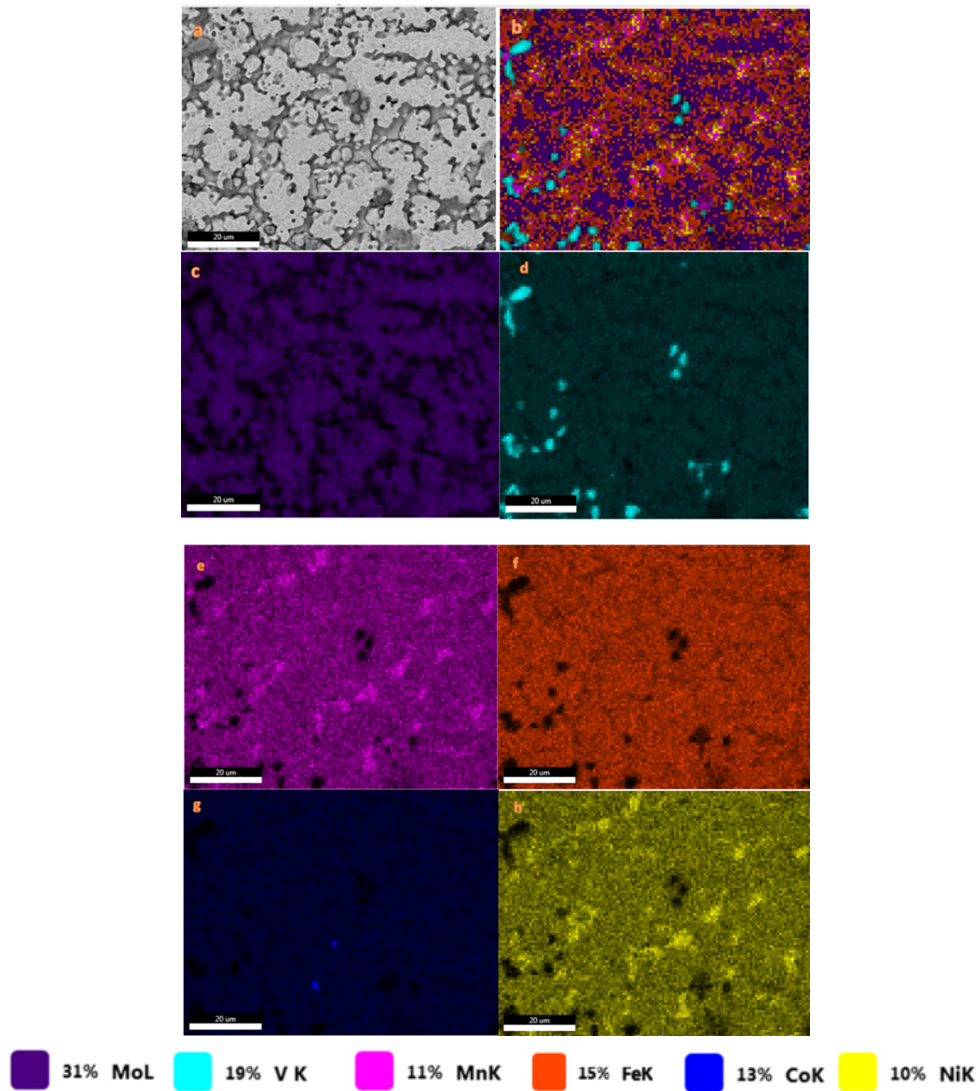


Figure 7. SG1 sample a) SEM image b)Elemental distribution mapping for the sample c-h) The mapping for each element

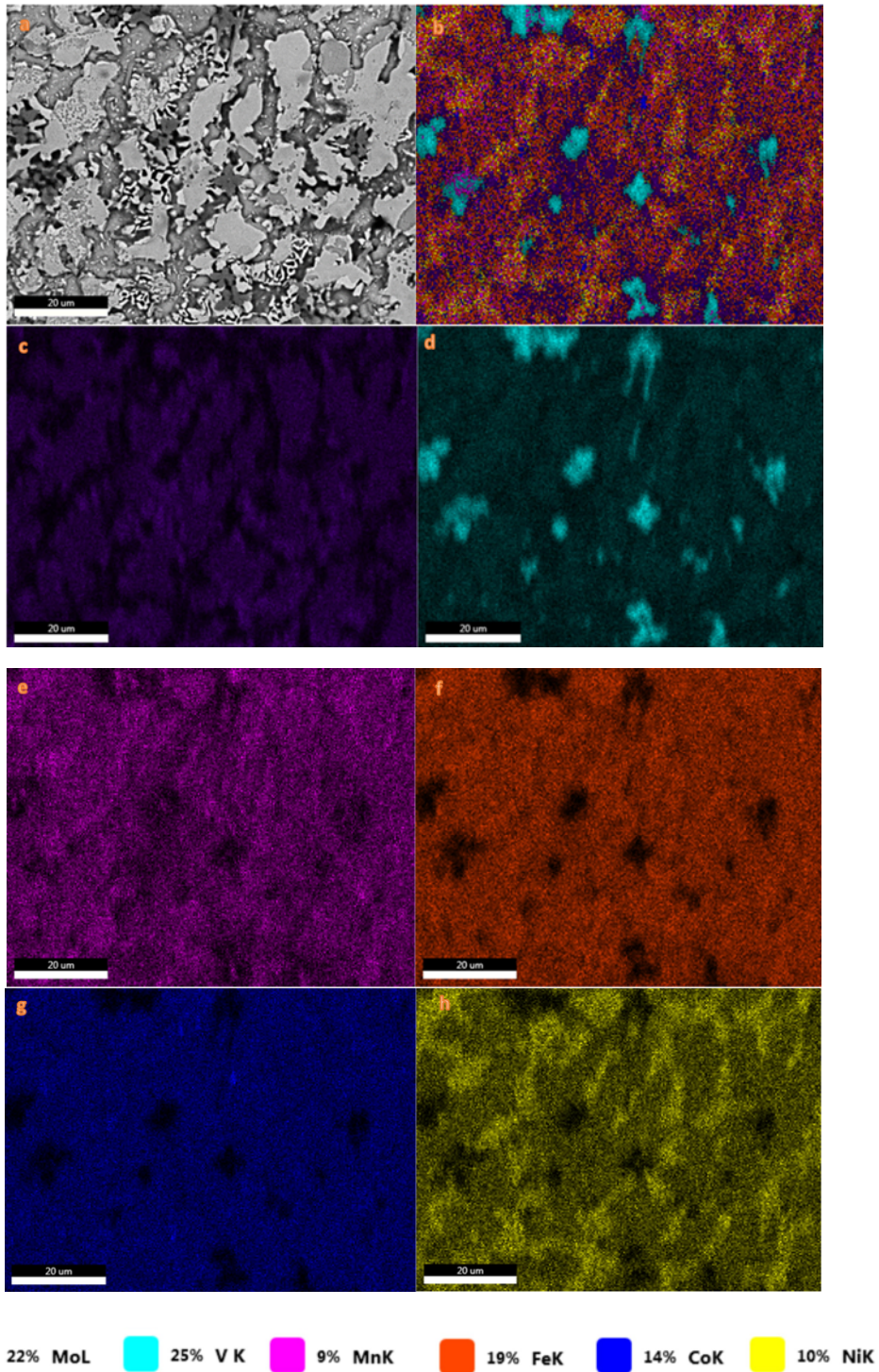


Figure 8. SG2 sample a) SEM image b)Elemental distribution mapping for the sample c-h) The mapping for each element

Figure 8. (a-b) shows the elemental distribution mapping and SEM image of the SG2 sample. The mapping for each element is shown in the Figure.8 (c-h). In Figure 8.a is seen that the regions rich in the V element have expanded. The Mo element is also present in the grain. Unlike SG1, Mn and Ni elements are concentrated at the grain boundary in the SG2 sample. According to the XRD graphs, $\text{Co}_3\text{Al}_3\text{Si}_4$ and various aluminides were

precipitated for the SG2 sample. Although they are not included in the alloy, structures containing Al and Si come from ferroalloys.

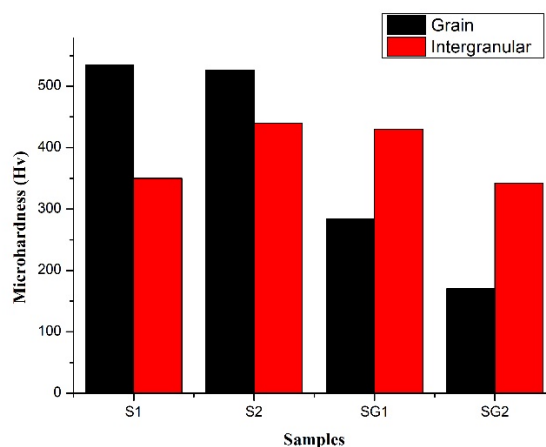


Figure 9. Microhardness of samples

In Figure 9, microhardness analysis was performed on the grain and intergranular regions of the samples. Accordingly, when S1 and SG1 samples were compared with each other, the hardness of the grain and intergranular region changed as a result of the separation and diffusion in the elements after the heat treatment. The same changes are observed in S2 and SG2 samples. Comparing S1 and S2, while the hardness within the grain does not change, the hardness in the intergranular region is higher than the S1 sample. In SG1 and SG2 samples, the effect of heat treatment is seen; while the hardness of the intragranular region decreases, an increase is observed in the intergranular region. This situation was considered as the expected effect of homogenization annealing. Because the elements had enough time to diffuse during annealing. The effect of lattice distortion provided by high entropy decreased with annealing. This caused a decrease in hardness.

4. Conclusions

This study focuses on investigating the effect of lower-priced starting materials to create high-entropy alloys. For this purpose, FeCoNiMnMoV and FeCoNiMn (Ferro Mo-Ferro-V) alloys have been successfully produced by the arc melting method. As a result of the microstructure research, a coarser grained structure was observed, especially in the samples with ferroalloy addition, after casting and after heat treatment. As a result of the microhardness test, it was observed that the hardness decrease was greater in ferro-alloy samples, especially after heat treatment.

References

- [1] George EP, Raabe D, and Ritchie RO. High-entropy alloys. *Nature reviews materials*. 2019; 4:8: 515-534.
- [2] Tsai M-H and Yeh J-W. High-entropy alloys: a critical review. *Materials Research Letters*. 2014; 2:3: 107-123.
- [3] Rambabu P, Eswara Prasad N, Kutumbarao V, and Wanhill R. Aluminium alloys for aerospace applications. *Aerospace materials and material technologies*. 2017: 29-52.
- [4] Shi Y, Collins L, Feng R, Zhang C, Balke N, Liaw PK, and Yang B. Homogenization of Al_xCoCrFeNi high-entropy alloys with improved corrosion resistance. *Corrosion Science*. 2018; 133: 120-131.
- [5] Xiao D, Zhou P, Wu W, Diao H, Gao M, Song M, and Liaw P. Microstructure, mechanical and corrosion behaviors of AlCoCuFeNi-(Cr, Ti) high entropy alloys. *Materials & Design*. 2017; 116: 438-447.
- [6] Yeh JW, Chen SK, Lin SJ, Gan JY, Chin TS, Shun TT, Chang SY. Nanostructured high-entropy alloys with multiple principal elements: novel alloy design concepts and outcomes. *Advanced engineering materials*. 2004; 6:5: 299-303.
- [7] Zhang Y, Zuo TT, Tang Z, Gao MC, Dahmen KA, Liaw PK, and Lu ZP. Microstructures and properties of high-entropy alloys. *Progress in materials science*. 2014; 61: 1-93.
- [8] Murty BS, Yeh J-W, Ranganathan S, and Bhattacharjee P. *High-entropy alloys*. 2019: Elsevier.
- [9] Santodonato LJ, Zhang Y, Feyngenson M, Parish CM, Gao MC, Weber RJ, Liaw PK. Deviation from high-entropy configurations in the atomic distributions of a multi-principal-element alloy. *Nature communications*. 2015; 6:1: 1-13.

- [10] Zhang Y, Yang X, and Liaw P. Alloy design and properties optimization of high-entropy alloys. *Jom*. 2012; 64:7: 830-838.
- [11] Wu Z, Bei H, Pharr GM, and George EP. Temperature dependence of the mechanical properties of equiatomic solid solution alloys with face-centered cubic crystal structures. *Acta Materialia*. 2014; 81: 428-441.
- [12] Verma A, Tarate P, Abhyankar A, Mohape M, Gowtam D, Deshmukh V, and Shanmugasundaram T. High temperature wear in CoCrFeNiCu_x high entropy alloys: The role of Cu. *Scripta Materialia*. 2019; 161: 28-31.
- [13] George EP, Curtin W, and Tasan CC. High entropy alloys: A focused review of mechanical properties and deformation mechanisms. *Acta Materialia*. 2020; 188: 435-474.
- [14] Shi Y, Yang B, and Liaw PK. Corrosion-resistant high-entropy alloys: A review. *Metals*. 2017; 7:2: 43.
- [15] Fu X, Schuh CA, and Olivetti EA. Materials selection considerations for high entropy alloys. *Scripta Materialia*. 2017; 138: 145-150.
- [16] Güler SH. The Effect of Using Ferro-Alloy on the Properties of AlCoFeNiMoTi High-Entropy Alloy Produced by Arc-Melting Method: Design of Low Cost. *International Journal of Metalcasting*. 2023: 1-10.
- [17] Özkul İ. Characterization of AlCoCrFeNiVTi High Entropy Alloy Produced with Different Alloying Sources. *Journal of Materials Engineering and Performance*. 2023: 1-7.
- [18] Youssef KM, Zaddach AJ, Niu C, Irving DL, and Koch CC. A novel low-density, high-hardness, high-entropy alloy with close-packed single-phase nanocrystalline structures. *Materials Research Letters*. 2015; 3:2: 95-99.
- [19] Sheng G and Liu CT. Phase stability in high entropy alloys: Formation of solid-solution phase or amorphous phase. *Progress in Natural Science: Materials International*. 2011; 21:6: 433-446.
- [20] Senkov O and Miracle D. A new thermodynamic parameter to predict formation of solid solution or intermetallic phases in high entropy alloys. *Journal of Alloys and Compounds*. 2016; 658: 603-607.
- [21] Tian F, Varga LK, Chen N, Shen J, and Vitos L. Empirical design of single phase high-entropy alloys with high hardness. *Intermetallics*. 2015; 58: 1-6.
- [22] Yang S, Lu J, Xing F, Zhang L, and Zhong Y. Revisit the VEC rule in high entropy alloys (HEAs) with high-throughput CALPHAD approach and its applications for material design-A case study with Al-Co-Cr-Fe-Ni system. *Acta Materialia*. 2020; 192: 11-19.
- [23] Takeuchi A and Inoue A. Classification of bulk metallic glasses by atomic size difference, heat of mixing and period of constituent elements and its application to characterization of the main alloying element. *Materials transactions*. 2005; 46:12: 2817-2829.

Physicochemical Effects of PEG Content in Alginate-based Double Network Hydrogels as Hybrid Scaffolds

Ozgul Gok*

¹Department of Biomedical Engineering, Faculty of Engineering and Natural Sciences, Acibadem Mehmet Ali Aydinlar University, Istanbul, Turkey
*ozgul.gok@acibadem.edu.tr

(Geliş/Received: 26/12/2023;

Kabul/Accepted: 26/03/2024)

Abstract: This study aims to prepare a double-network hydrogel as hybrid networks bearing both natural and synthetic polymers to obtain scaffolds with increased swelling capacity and tunable mechanical and morphological properties. Physically cross-linked alginate hydrogel was reinforced with various ratios of Poly(ethylene glycol) (PEG) polymers which were chemically gellated via UV light exposure with a water soluble initiator. Physicochemical properties of the resulting hydrogels were systematically investigated via Fourier-transform infrared (FT-IR) spectroscopy for chemical composition and Scanning Electron Microscopy (SEM) for their morphological features like porosity. Furthermore, the effect of PEG amount in the final hydrogel (10, 20 and 40%) on swelling capacity was evaluated as well as the rheological properties. Prepared double-network hydrogels were demonstrated to be composed of both natural alginate polymer and synthetic PEG chains in FT-IR spectrum. Although 10%PEG containing hydrogel was not significantly different in terms of swelling capacity from the alginate hydrogel alone, increasing PEG amount seems to have improved the swelling ability. Comparative rheological studies presented that introducing covalently cross-linked PEG network into alginate one increased crosspoint of storage and loss moduli almost 12 times more providing a stiffer scaffold. Increasing PEG content decreased the pore size on SEM images, indicating more crosslinking points in hydrogel structure.

Key words: Hybrid Hydrogels, Physical Cross-linking, UV Curing, Porous Scaffolds.

Hibrit İskeleler Olarak Aljinat Bazlı Çift Ağ Hidrojellerindeki PEG İçeriğinin Fizikokimyasal Etkileri

Öz: Bu çalışma, artan şişme kapasitesine ve ayarlanabilir mekanik ve morfolojik özelliklere sahip iskeleler elde etmek için hem doğal hem de sentetik polimerleri taşıyan hibrit ağlar olarak çift ağı bir hidrojel hazırlamayı amaçlamaktadır. Fiziksel olarak çapraz bağlı aljinat hidrojel, suda çözünür bir başlatıcı ile UV ışığına maruz bırakılarak kimyasal olarak jelleştirilen çeşitli oranlarda Poli(etilen glikol) (PEG) polimerleri ile güçlendirildi. Elde edilen hidrojellerin fizikokimyasal özellikleri, kimyasal bileşimleri için Fourier dönüşümü kızılötesi spektroskopisi (FT-IR) ve gözeneklilik gibi morfolojik özellikleri açısından Taramalı Elektron Mikroskopu (SEM) aracılığıyla sistematik olarak araştırıldı. Ayrıca reolojik özelliklerin yanı sıra son hidrojeldeki PEG miktarının (%10, 20 ve 40) şişme kapasitesine etkisi de değerlendirildi. Hazırlanan çift ağ yapılı hidrojellerin, FT-IR spektrumunda hem doğal aljinat polimerinden hem de sentetik PEG zincirlerinden oluştuğu gösterilmiştir. Her ne kadar %10 PEG içeren hidrojel şişme kapasitesi açısından tek başına aljinat hidrojelden önemli ölçüde farklı olmasa da, artan PEG miktarının iyileştirici etkisi vardır. Karşılaştırmalı reolojik çalışmalar, kovalent olarak çapraz bağlı PEG ağının aljinata dahil edilmesinin, depolama çapraz noktasını ve kayıp modülünü neredeyse 12 kat artırdığını ve daha sert bir yapı iskelesi sağladığını ortaya koydu. PEG içeriğinin artırılması, SEM görüntülerinde gözenek boyutunun azalmasına neden oldu ve bu da hidrojel yapısında daha fazla çapraz bağlanma noktasının olduğunu gösterdi.

Anahtar kelimeler: Hibrit Hidrojeller, Fiziksel Çapraz Bağlama, UV Kütleme, Gözenekli İskeleler

1. Introduction

Regarding the rapidly growing field of tissue engineering, the need for innovative biomaterials remains very significant and is desired to address the complexities of mimicking native tissue microenvironments [1,2]. As powerful scaffold platforms, hydrogels have emerged as very advantageous scaffolds for three-dimensional (3D) networks, owing to their inherent biocompatibility, tunable mechanical properties and porosity levels, together with their potential for controlled release of biomolecules like bioactive agents and growth factor [3,6]. Although there are numerous hydrogel designs in the literature, most of them depend on either physical interactions like electrostatic interactions or self-assembly of amphiphilic polymers or chemical cross-linking like UV-based radicalic gelation or wellknown coupling reactions such as NHS/EDC coupling dependent amidation, 1,4 Michael addition or click reactions [7,14]. With the need for better control on hydrogel scaffolds by improving the complexity coming from the composite designs, it has been recently switched to combine both natural and

* Corresponding author: ozgul.gok@acibadem.edu.tr. ORCID Number of authors:0000-0001-5960-2397

synthetic polymeric biomaterials with different cross-linking strategies to come up with more advantageous polymeric networks.

Double network hydrogels are such systems providing step-wise cross-linking ability of different types of materials in a more controlled fashion [15,16]. Each part can be cured independently from each other and this orthogonal cross-linking strategy can be seen as a new, yet more powerful tool to obtain more tough and biomimetic scaffolds for the target tissue modeling [17,19]. In the literature, there are several examples of interpenetrating networks that involve two different types of polymers, one of which is cured and the other one is entrapped in the generated pores [20,21]. However, based on their degradation tendencies and pore size, the mechanical properties of the resultant scaffold might be weaker than desired. The above-mentioned hydrogel systems are obtained by orthogonally cross-linked two polymeric biomaterials in the same environment in a sequential or simultaneous fashion so that the resultant scaffold becomes more stable and modular, enabling more possibilities for the adjustment of final properties of the obtained scaffold [22].

Literature reveals that the double-network hydrogels have been mostly prepared by the combination of natural polymers. Alginate, a naturally occurring polysaccharide derived from brown seaweed, possesses inherent biocompatibility and gel-forming properties based on electrostatic interactions with divalent cations like Ca^{+2} , making it an attractive candidate for tissue engineering applications [23]. Despite their biomimetic features for a solid tissue, high degradation rate and low stability require the urgent need for the contribution of synthetic, yet biocompatible polymers, among which biodegradable polyesters have a very limited use due to their hydrophobicity. On the other side, PEG (Poly(ethylene glycol)) remarkably stands as a potential solution for both introducing the increased hydrophilicity to the final scaffold structure and providing more options for cross-linking process with its versatile functional groups. In 2015, Chee et al. presented the preparation of alginate hydrogel integrated with polymerized PEG monomethyl methacrylate, which was cured under UV light to obtain injectable gel-like material [24]. However, the PEG chains in this study were appended to the main polymer backbone, hence less likely to contribute to the stiffness of the final scaffold. In a very recent study released in 2023, Zhu and coworkers prepared alginate/PEG double network hydrogels containing anthracene-functionalized 4-arm PEG polymer which crosslinks based on the UV-mediated dimerization of terminal anthracene moieties [25]. This structure was utilized for obtaining patterning of resultant hydrogel with photolithography and may not have a great potential for bio-applications due to the toxicity of anthracene groups [26]. As a more relevant study, Huang et al. has shown the alginate/PEG based double network hydrogels, prepared by different weight ratios of alginate in PEG-based scaffold [16]. Although they have concluded that the contribution of alginate to the final hydrogel structure helped to get smaller pores and improve mechanosensing against adipose derived stem cells, taking PEG network as the basis and introducing alginate polymer with a relatively higher molecular weight would complicate the reproducibility of the final construct as PEG length and branching degree increases. As a more relevant study, Hong et al. prepared hydrogels with interpenetration of only 40% acrylated PEG chains in alginate network, supporting the idea of this polymer pair to obtain highly stretchable and tough scaffolds [27].

Based on the lights of these findings, the study presented in this paper suggests a systematic approach for the preparation of alginate/PEG double network hydrogels, which takes the alginate hydrogel as the main network and reinforce it with the UV-light mediated crosslinking of dimethacrylated linear PEG chains of various ratios in alginate network depending on the ionic interaction with the added CaCl_2 solution. By incorporating PEG, a synthetic polymer known for its versatility and hydrophilicity, into the alginate network, this demonstrated double-network hydrogels provide better control over the synthetic part of this hybrid scaffold with tunable features for swelling capacity, mechanical strength and porosity (Fig. 1). The prepared double-network hydrogels containing a natural polymer, alginate, and a synthetic one, PEG, aimed to benefit from their synergistic advantages to develop more stable and biomimetic environments for further tissue engineering applications. Characterization results for the obtained hydrogels with varying PEG content revealed that increased PEG amounts have enhanced the swelling ability of scaffolds tremendously and improved their mechanical properties with micron-sized pores visualized under SEM.

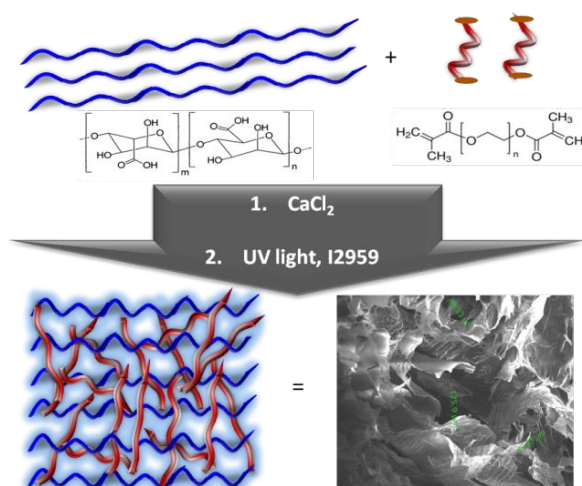


Figure 1. General scheme for the preparation of Alginate/PEG double-network hydrogel.

2. Materials and Methods

Materials and Instrumentation

Alginic acid sodium salt from brown algae-medium viscosity was purchased from Sigma-Aldrich. Poly(ethyleneglycol) dimethacrylate (PEGdiMA) was obtained from Sigma-Aldrich, with an average $M_n=750$ gmol^{-1} and contains 900-1100 ppm MEHQ as inhibitor, which was removed by passing through basic alumina column prior to use. Calcium Chloride (CaCl_2) and Irgacure 2959 (98% purity) were purchased from Merck Millipore. All used organic solvents were reagent-grade.

FT-IR spectroscopy measurements were done on a Perkin Elmer Spectrum Two FT-IR spectrometer. For SEM visualization, conductive carbon tabs and mounts were obtained from Ted Pella, and samples were prepared as coated with 20 nm of gold (Au/Pb) under vacuum. Images were taken under low vacuum at Thermo Fisher Scientific (FEI) Quattro S ESEM. Mechanical evaluation of hydrogels was performed by Malvern Kinexus Pro and J2 SR 4703 SS geometry, obtained from ©Malvern, was used in rheological experiments. The strain-dependent oscillatory rheology measurements of hydrogel scaffolds (500 mg for each sample) was tested at $f=1\text{Hz}$ and with $\gamma=0.01$, at 37°C (30 data points).

Preparation of Alginate/PEG Double-Network Hydrogel (AA/PEG-HG)

Only alginate polymer containing control hydrogels (AA-HG) were prepared by physical cross-linking of alginate chains with Ca^{+2} ions in aqueous environment. Briefly, alginate polymer (100 mg) was dissolved in ddH_2O (10mL) to obtain a solution of 1% by weight. On the other side, 75 mM CaCl_2 solution was prepared in ddH_2O , as well [28]. Their equi-volume mixture was prepared to obtain a homogeneous solution and then let to shake at 500 rpm in an orbital shaker for an additional 10 minutes for complete gelation. Obtained hydrogels were washed with fresh ddH_2O for three times and obtained transparent hydrogel structures were freeze-dried in lyophilizer for further characterization steps.

Double network hydrogels were prepared by the incorporation of PEGdiMA polymers into the hydrogel environment with different ratios by volume. Increasing amounts (10, 20 and 40%) of PEGdiMA polymer, determined with respect to the final solution volume, were mixed with the alginate solution. After the addition of 1% Irgacure (by weight, with respect to PEGdiMA), the final solutions were mixed with CaCl_2 solution by equal volume homogeneously and as stated for control hydrogel above, complete gelation of alginate part was obtained after its incubation for 10 minutes in the orbital shaker. Later on, these mixtures were directly exposed to UV light (365 nm) for 20 minutes for the chemical cross-linking of PEGdiMA polymers [28,29]. Then, obtained double network hydrogels were washed with fresh ddH_2O for three times and obtained scaffold were freeze-dried in lyophilizer for further characterization steps.

3. Results and Discussion

The preparation of alginate/PEG based double network hydrogels were achieved by physical cross-linking of negatively charged alginate chains with a divalent cation Ca^{+2} in aqueous environment, followed by UV light mediated chemical cross-linking of PEG polymers functionalized with methacrylate moieties at its both ends. Different ratios of PEGdiMA polymers were added into the alginate solutions and after step-wise crosslinking procedures, the obtained double-network hydrogel constructs were investigated for the effect of immobilized PEG chains interconnected in an alginate mesh on gel conversion, swelling capacity, mechanical properties and porosity. The adjustability of PEG amount in the prepared double-network scaffolds clearly provide a modular approach for tuning the final mechanical, morphological and swelling properties of alginate-based hydrogels while still preserving its major biomimetic features.

Step-wise gelation procedures were followed by slight modifications from the literature for the mixture of alginate and PEGdiMA polymers with CaCl_2 and Irgacure, respectively. The obtained hydrogels were weighed for their final amounts to calculate gel conversion, based on the equation 1. Obviously, negatively charged carboxylic acid groups of alginate polymers make electrostatic interactions with the Ca^{+2} ions included into the media readily, to give a higher yield for the gelation of alginate chains (Table 1). However, the addition of PEGdiMA polymer seems to decrease the total gel conversion, which might be due to the slower radical generation by the water soluble photoinitiator, Irgacure. Also, taking the relatively smaller molecular weight into account, it can be estimated that some of the PEGdiMA chains were not included into the gelation, when gel conversions of double network hydrogels were compared to the control hydrogel (Eq. (1)).

$$\text{Gel Conversion} = \left[\frac{\text{Weight of obtained hydrogel}}{\text{Weight of polymers used}} \right] * 100 \quad \text{Gel Conversion} = \text{Weight} \quad (1)$$

Table 1. Preparation details and calculated gel conversion for the obtained hydrogels.

No	Code	V of 1% Alginate (mL)	% of PEGdiMA (v/v)	Amount of PEGdiMA (μL)	V of 75 mM CaCl_2 (mL)	Gel Conversion
1	AA	0.5	0	0	0.5	96
2	AA-10PEG	0.5	10	50	0.5	81
3	AA-20PEG	0.5	20	100	0.5	71
4	AA-40PEG	0.5	40	200	0.5	82

Although alginate polymer is very hydrophilic and readily dissolves in water, the hydrogel dependent on its physical cross-linking demonstrate a low stability for the final construct. This might be due to not only the high degradation rate of alginate polymers in aqueous media but also their dissociation upon the removal of Ca^{+2} ion from the gel part, based on their diffusion to outside environment. Addition of chemically cross-linked PEG chains into environment, the resultant hydrogel structures were expected to preserve more stability in water, with an increased swelling capacity and lower degradation profile. With this aim, prepared AA/PEG double network hydrogels were incubated in pH7.4 PBS (phosphate buffer solution) and at body temperature (37°C) for a certain period of time to mimic the physiological conditions. At different time points, the hydrogels were removed from the solution and excess water was removed. The weight of hydrogels was recorded and the swelling ratio for the hydrogels was calculated by the Eq. (2).

$$\text{The swelling ratio} = \left[\frac{\text{Weight of wet hydrogel} - \text{Weight of dry hydrogel}}{\text{Weight of dry hydrogel}} \right] * 100 \quad (2)$$

Fig. 2 demonstrates that addition of PEG chains into the final hydrogel structure leads to an increase in the swelling ratio value. Compared to only alginate hydrogel, the capacity of hydrogels for water uptake capacity has improved with the increased amount of PEG chains incorporated into the hydrogel. 10% PEG containing hydrogel seems to show no significant difference for swelling capacity, however for 20 and 40% PEG containing ones, it is clearly seen that the swelling capacity of the resultant double-network hydrogels was dramatically increased. After 3-4 hours, the weight of hydrogels were observed to decrease, which might be due to its

degradation, and it is notable that the point at which the decrease started was later for PEG containing double-network hydrogels, compared to only alginate one. This might be an indication for the ameliorating effect of chemically cross-linked PEG network on the stability of the final scaffold structure.

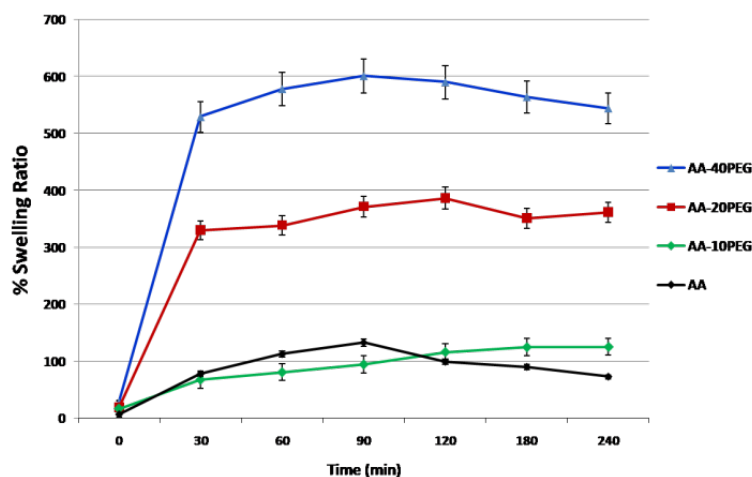


Figure 2. Swelling ratios of prepared hydrogels.

For the chemical structure analysis of the prepared hydrogels, FT-IR spectroscopy was used to compare the characteristic peak evaluations of the polymers separately and they are compared with the peaks observed at the spectra of double-network hydrogels. Fig. 3 clearly reveals that the spectra for AA-20PEG hydrogel demonstrates both the peaks belonging to alginate polymer as singlet at 1595 cm^{-1} for C=O stretching for carboxylic acid group and a broad multiplet between $1020\text{--}1070\text{ cm}^{-1}$ for C-O bonds. The broad peak seen at around 3300 cm^{-1} represents the presence of labile proton based bonds in hydrogel structure, coming from the alginate polymer. On the other site, the presence of a sharp peak at 1736 cm^{-1} comes from the ester carbonyl double bond in methacrylated ends, verifying the incorporation of PEG chains into the hydrogel structure. Moreover, the disappearance of peak for hydrogel spectrum, which appears at 1638 cm^{-1} in PEGdiMA one, points to the removal of C=C methacrylate double bond upon radicalic UV cross-linking. This chemical structure evaluation for double-network hydrogel indicates the successful network formation by PEGdiMA chains in alginate network.

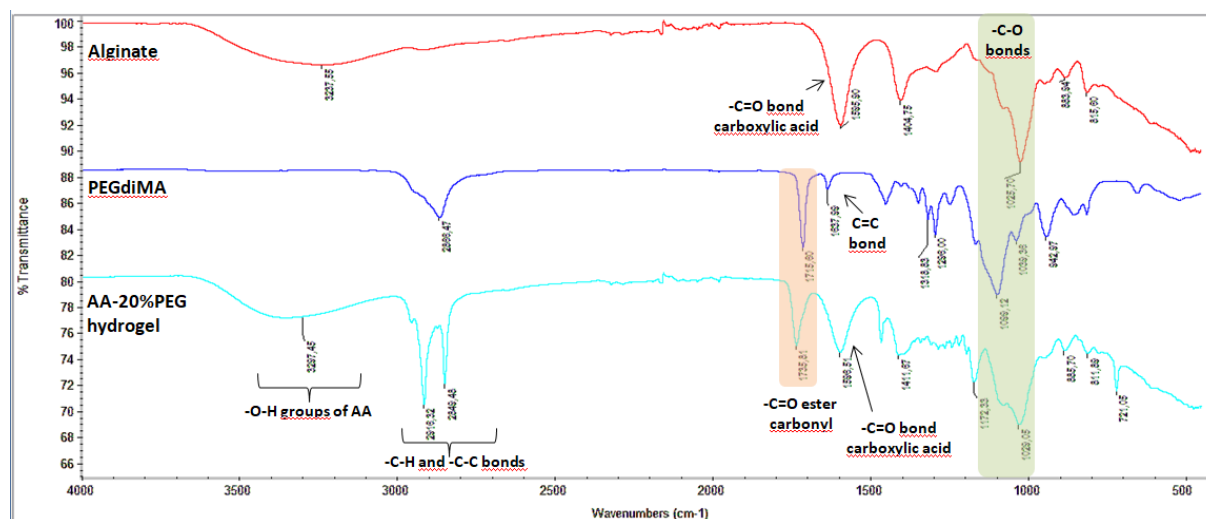


Figure 3. FT-IR spectra of Alginate polymer, pure PEGdiMA polymer and 20%PEG containing alginate (AA-20PEG) hydrogel.

The ionic interaction based physical cross-linking of alginate polymer chains are expected to provide a porous structure, which was visualized by SEM. Fig. 4 clearly shows that alginate hydrogels provide a homogenously distributed pores with mostly 150-200 μm in diameter. Incorporation of chemically cross-linked PEG chains obviously decreases the pore size of the resultant double-network hydrogel, indicating to the increased cross-linking degree in the scaffold. It can be noted that the greater the amount of PEGdiMA chains was in the hydrogel, the smaller the generated pores formed to appear around 50 μm . Especially the SEM image for AA-40PEG hydrogel provides a very clear look to very regular pore distribution, due to the high amount of PEG chains homogeneously mixed in alginate network, indicated with red arrows. These images confirm the efficient crosslinking of PEG chains in alginate network, which can be used as a powerful tool to modulate its morphological properties like porosity and pore size.

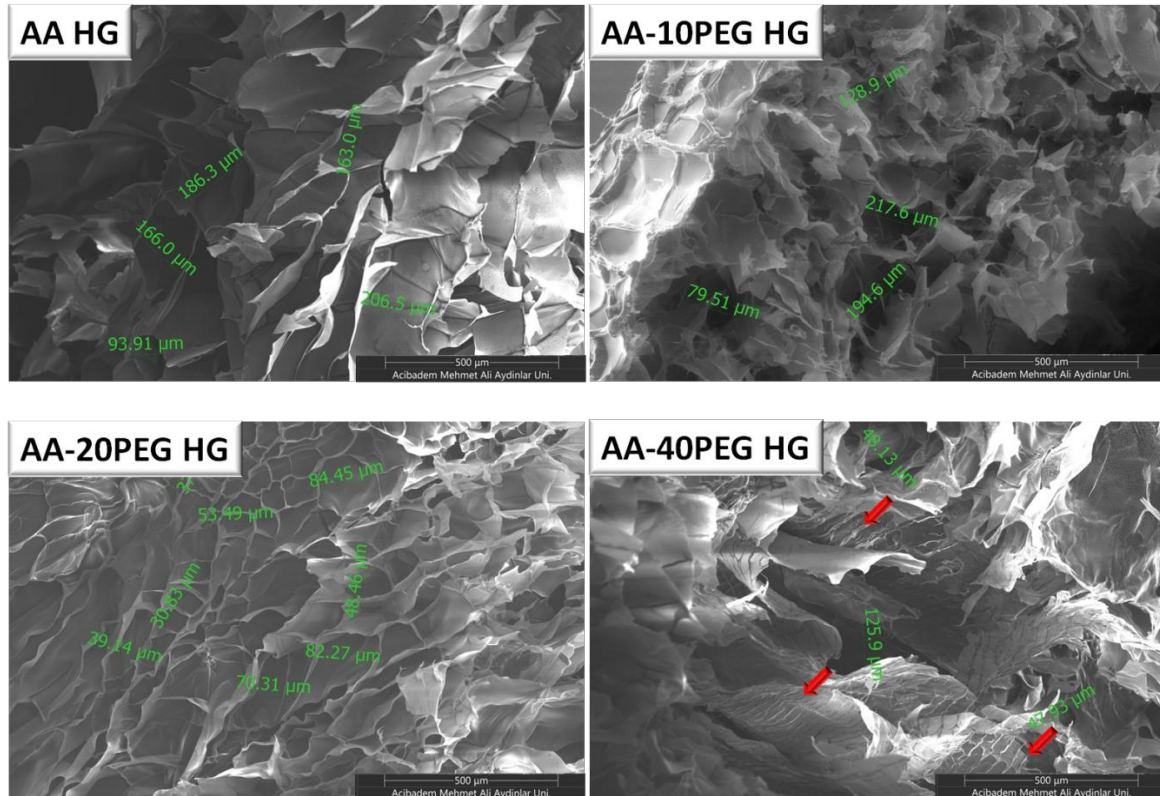


Figure 4. SEM images for prepared double-network hydrogels and their comparison with only alginate hydrogel.

One of the most commonly encountered issues for soft-tissue resembling hydrogel scaffolds is their weak mechanical properties, which have a determining impact on further cell attachment in tissue-engineering applications. Reinforcing these properties with increasing the stability of the final construct could be achieved by the incorporation of comparably less degrading synthetic polymers into the network, which was the strategy applied in this study. As a natural and biocompatible polysaccharide, alginate polymer provides a very good biomimicry for soft tissues, from which cannot be benefitted with a high yield because of its less stability and fast degradation profile in aqueous environment. In this work, we aimed to improve the mechanical stability of alginate polymer to create scaffolds with tunable stiffness by adding desired amount of PEG chains in hydrogel structure, without giving up on the main properties of alginate network. This trend of prepared double-network hydrogels were analyzed by a rheometer and compared with that of control alginate hydrogel. Fig. 5 provides the trends for both G' (storage modulus) and G'' (loss modulus) for the hydrogels, where the former one represents the elasticity (solid-like structure) of the scaffolds and the latter one is for the viscosity (liquid-like structure). The strain-dependent oscillatory rheology measurements of hydrogel scaffolds was tested at $f=1\text{Hz}$ and with $\gamma=0.01$, at 37 $^{\circ}\text{C}$. Compared to the alginate hydrogel alone, PEG containing double-network hydrogels provide an increased G' storage modulus value, indicating enhanced stiffness of the final constructs, which gets better with an increased amount of PEG (especially for 20 and 40 % content). Also, the cross point values (G'/G'') are

seen to be shifted to right, almost 12 times more compared to only alginate hydrogel, strengthening the idea of getting stiffer and more elastic for the obtained double-network hydrogels with better mechanical properties. It is more clear for 40%PEG containing alginate hydrogel, G' curve lasts up to $\gamma=100$ which indicates the hydrogel gets more viscous (liquid-like) structure at a higher strain value and withstand with more deformation compared to other hydrogels.

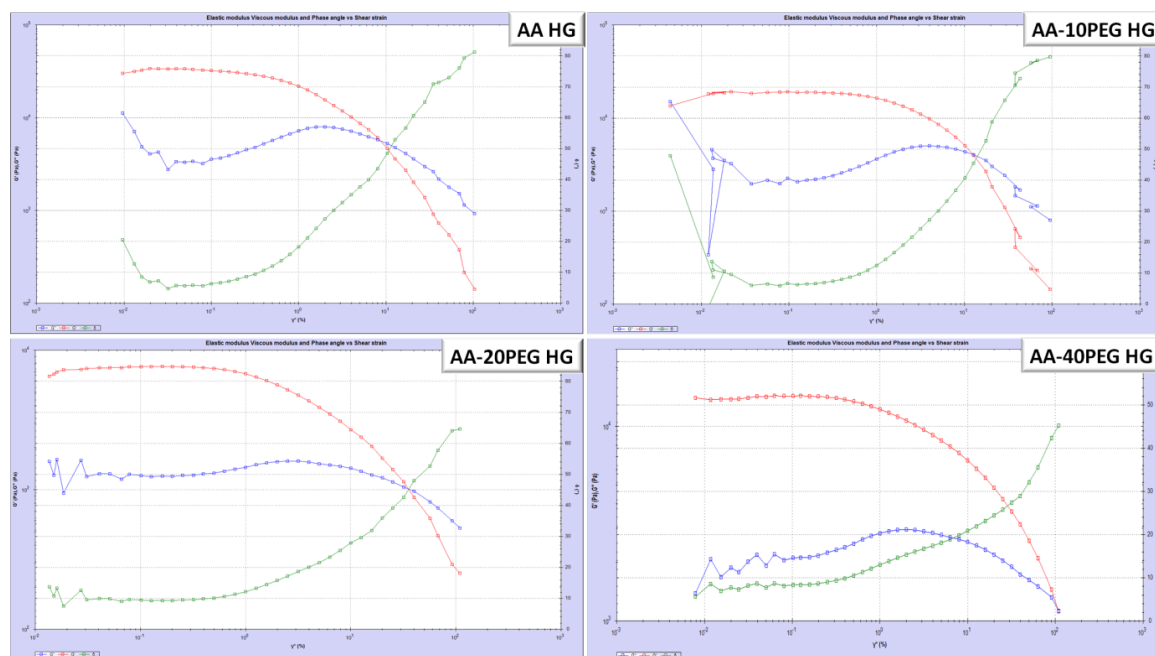


Figure 5. Mechanical evaluations for prepared double-network hydrogels and their comparison with control alginate hydrogel. (Red curve represents G' (storage modulus), Blue curve represents G'' (loss modulus))

4. Conclusion

In summary, double-network hydrogel platforms were prepared with high yield (>70%) by physical cross-linking of alginate polymers with Ca^{+2} ions, followed by chemical cross-linking of PEGdiMA chains under UV light. Alginate-based hydrogels were aimed to have better properties in terms of their swelling ability, and mechanical and morphological features without losing their biomimicry by the addition of various amounts of PEG polymers (10, 20, and 40% by volume), which were immobilized in alginate network to demonstrate the effect of incorporation of a hydrophilic and synthetic component into the scaffold structure. While these double-network hydrogels were characterized for their hybrid chemical composition successfully with the expected peak in FT-IR spectra, their improved mechanical properties as increased G' value and swelling capacity up to 600% clearly indicate the benefit of PEG content. Morphological evaluations also verify that the porosity was directly related to the increased PEG amount and its cross-linking density, which was clearly seen for 40%PEG containing hydrogels, compared to only alginate hydrogel. Overall, these hybrid scaffolds were obtained as reinforced double cross-linked networks with tunable properties by adjusting the PEG amount inside the alginate polymer, which provides a high potential to prepare the optimum scaffolds for more biomimetic environments for further tissue-engineering applications.

References

- [1] Liaw C, Ji S, Guvendiren M. Engineering 3D Hydrogels for Personalized In Vitro Human Tissue Models. *Adv Healthcare Mater* 2018;1–16.
- [2] Dhandayuthapani B, Yoshida Y, Maekawa T, Kumar DS. Polymeric Scaffolds in Tissue Engineering Application: A Review. *Int J Polym Sci* 2011; 290602.
- [3] Nicodemus GD, Bryant SJ. Cell Encapsulation in Biodegradable Hydrogels for Tissue Engineering Applications. *Tissue Eng Part B Rev* 2008;14:149–165.
- [4] Liu M, Zeng X, Ma C, Yi H, Ali Z, Mou X, Li S, Deng Y, He N. Injectable Hydrogels for Cartilage and Bone Tissue Engineering. *Bone Res* 2017; 30:17014.

- [5] Saraiva SM, Miguel SP, Ribeiro MP, Coutinho P, Correia JJ. Synthesis and Characterization of a Photocrosslinkable Chitosan-Gelatin Hydrogel Aimed for Tissue Regeneration. *RSC Adv* 2015; 5: 63478-63488.
- [6] Edri R, Gal I, Noor N, Harel T, Fleischer S, Adadi N, Green O, Shabat D, Heller L, Shapira A. Personalized Hydrogels for Engineering Diverse Fully Autologous Tissue Implants. *Adv Mater* 2019; 31:1803895.
- [7] Thornton D, Mart RJ, WebbSJ, Ulijn RV. Enzyme-Responsive Hydrogel Particles for the Controlled Release of Proteins: Designing Peptide Actuators to Match Payload. *Soft Matter* 2008;4:821-827.
- [8] Chen Y, Tan Z, Wang W, Peng YY, Narain R. Injectable, Self-Healing, and Multi-Responsive Hydrogels via Dynamic Covalent Bond Formation between Benzoxaborole and Hydroxyl Groups. *Biomacromolecules* 2019;20:1028-1035.
- [9] Guaresti O, Basasoro S, González K, Eceiza A, Gabilondo N. In Situ Cross-Linked Chitosan Hydrogels via Michael Addition Reaction Based on Water-Soluble Thiol-Maleimide Precursors. *Eur Polym J* 2019; 119:376-384.
- [10] Koehler KC, Anseth KS, Bowman CN. Diels-Alder Mediated Controlled Release from a Poly(Ethylene Glycol) Based Hydrogel. *Biomacromolecules* 2013;14:538-547.
- [11] Yan S, Chai L, Li W, Xiao LP, Chen X, Sun RC. Tuning the Properties of PH-Responsive Lignin-Based Hydrogels by Regulating Hydroxyl Content. *Colloids Surfaces A Physicochem Eng Asp* 2022;643:128815.
- [12] Summonte S, Racaniello GF, Lopodota A, Denora N, Bernkop-Schnürch A. Thiolated Polymeric Hydrogels for Biomedical Application: Cross-Linking Mechanisms. *J Control Release* 2021, 330: 470- 482.
- [13] Cengiz N, Kabadayıoglu H, Sanyal R. Orthogonally Functionalizable Copolymers Based on a Novel Reactive Carbonate Monomer. *J Polym Sci Part A Polym Chem* 2010;48:4737-4746.
- [14] Safakas K, Saravanou SF, Iatridi Z, Tsitsilianis C. Thermo-Responsive Injectable Hydrogels Formed by Self-Assembly of Alginate-Based Heterograft Copolymers. *Gels* 2023; 9(3):236.
- [15] Cai L, Dewi RE, Heilshorn SC. Injectable Hydrogels with in Situ Double Network Formation Enhance Retention of Transplanted Stem Cells. *Adv Funct Mater* 2015; 25(9):1344-1351.
- [16] Huang Y, Jayathilaka PB, Islam MS, Tanaka CB, Silberstein MN, Kilian KA, Kruzic JJ. Structural Aspects Controlling the Mechanical and Biological Properties of Tough, Double Network Hydrogels. *Acta Biomater* 2022; 138: 301-312.
- [17] Gong JP, Katsuyama Y, Kurokawa T, Osada Y. Double-Network Hydrogels with Extremely High Mechanical Strength. *Adv Mater* 2003; 15: 1155-1158.
- [18] Yasuda K, Gong JP, Katsuyama Y, Nakayama A, Tanabe Y, Kondo E, Ueno M, Osada Y. Biomechanical Properties of High-Toughness Double Network Hydrogels. *Biomaterials* 2005;26:4468- 4475.
- [19] Chen Q, Chen H, Zhu L, Zheng J. Fundamentals of Double Network Hydrogels. *J Mater Chem B* 2015;3:3654-3676.
- [20] Zhao J, Zhao X, Guo B. Multifunctional Interpenetrating Polymer Network Hydrogels Based on Methacrylated Alginate for the Delivery of Small Molecule Drugs and Sustained Release of Protein. *Biomacromolecules* 2014; 15(9): 3246-3252.
- [21] Polaske NW, McGrath DV, McElhanon JR. Thermally Reversible Dendronized Linear Ab StepPolymers via "Click" Chemistry. *Macromolecules* 2011;44:3203-3210.
- [22] Xu X, Jerca VV, Hoogenboom R. Bioinspired Double Network Hydrogels: From Covalent Double Network Hydrogels: Via Hybrid Double Network Hydrogels to Physical Double Network Hydrogels. *Mater Horizons* 2021;8:1173-1188.
- [23] Lee KY, Mooney DJ. Alginate: Properties and Biomedical Applications. *Prog Polym Sci* 2012;37:106-126.
- [24] Ma ZP, Song X, Yang BZ, Liu ST, Zheng RY, Xu XZ, Liu CH, Zhu YY. Fabrication of PEG-Anthracene/Alginate Double-Network Hydrogels and Their Application in Photolithography. *J Appl Polym Sci* 2023;140(48): 1-11.
- [25] BrackW, Altenburger R, Küster E, Meissner B, Wenzel KD, Schüürmann G. Identification of Toxic Products of Anthracene Photomodification in Simulated Sunlight. *Environ. Toxicol Chem* 2003; 22:2228-2237.
- [26] Hong S, Sycks D, Chan HF, Lin S, Lopez GP, Guilak F, Leong KW, Zhao X. 3D Printing: 3D Printing of Highly Stretchable and Tough Hydrogels into Complex, Cellularized Structures. *Adv Mater* 2015; 27:4034-4034.
- [27] Savić-Gajić IM, Savić IM, Svirčev Z. Preparation and Characterization of Alginate Hydrogels with High Water-Retaining Capacity. *Polymers (Basel)* 2023;15(12): 2592.
- [28] Wilems TS, Lu X, Kurosu YE, Khan Z, Lim HJ, Smith Callahan LA. Effects of Free Radical Initiators on Polyethylene Glycol Dimethacrylate Hydrogel Properties and Biocompatibility. *J Biomed Mater Res - Part A* 2017;105:3059-3068.
- [29] Tucker RM, Parcher BW, Jones EF, Desai TA. Single-Injection HPLC Method for Rapid Analysis of a Combination Drug Delivery System. *AAPS PharmSciTech* 2012; 13(2): 605-610.

Performance Comparison of Standard Polysomnographic Parameters Used in the Diagnosis of Sleep Apnea

Seda Arslan TUNCER¹, Yakup ÇİÇEK², Taner TUNCER^{3*}

^{1,2} Software Engineering, Faculty of Engineering, Firat University, Elazığ, Turkey

³ Computer Engineering, Faculty of Engineering, Firat University, Elazığ, Turkey

¹ satuncer@firat.edu.tr, ³ ttuncer@firat.edu.tr

(Geliş/Received: 15/01/2024;

Kabul/Accepted: 21/03/2024)

Abstract: Obstructive sleep apnea (OSAS), which is one of the leading sleep disorders and can result in death if not diagnosed and treated early, is most often confused with snoring. OSAS disease, the prevalence of which varies between 0.9% and 1.9% in Turkey, is a serious health problem that occurs as a result of complete or partial obstruction of the respiratory tract during sleep, resulting in sleep disruption, poor quality sleep, paralysis and even death in sleep. Polysomnography signal recordings (PSG) obtained from sleep laboratories are used for the diagnosis of OSAS, which is related to factors such as the individual's age, gender, neck diameter, smoking-alcohol consumption, and the occurrence of other sleep disorders. Polysomnography is used in the diagnosis and treatment of sleep disorders such as snoring, sleep apnea, parasomnia (abnormal behaviors during sleep), narcolepsy (sleep attacks that develop during the day) and restless legs syndrome. It allows recording various parameters such as brain waves, eye movements, heart and chest activity measurement, respiratory activities, and the amount of oxygen in the blood with the help of electrodes placed in different parts of the patient's body during night sleep. In this article, the performance of PSG signal data for the diagnosis of sleep apnea was examined on the basis of both signal parameters and the method used. First, feature extraction was made from PSG signals, then the feature vector was classified with Artificial Neural Networks, Support Vector Machine (SVM), k-Nearest Neighbors (k-NN) and Logistic Regression (LR).

Key words: Sleep, Sleep Apnea, PSG, Classification.

Uyku Apnesinin Teşhisinde Kullanılan Standart Polisomnografik Parametrelerin Performans Karşılaştırılması

Öz: Erken tanı konulmadığında ve tedavi edilmediği zaman ölümlerle sonuçlanabilen ve uyku hastalıklarının başından gelen Tıkaçıcı uyku apnesi (OSAS) en çok horlama ile karıştırılmaktadır. Türkiye’de görülme yaygınlığı %0,9 ila %1,9 değişen OSAS hastalığı uyku süresi boyunca solunum yollarının tamamen veya kısmen tıkanması sonucunda görülen uyku bölünmesi, kalitesiz uyku geçirme, felç olma ve hatta uykuda ölümün bile görülmesi gibi sonuçlar doğuran ciddi bir sağlık sorunudur. Bireyin yaşı, cinsiyeti boyun çapı, sigara-alkol tüketimi, diğer uyku rahatsızlıklarının görülme durumu gibi etmenlerle ilişkili olan OSAS tanı için uyku laboratuvarlarından alınan Polisomnografi sinyal kayıtları (PSG) kullanılmaktadır. Polisomnografi horlama, uyku apnesi, parasomnia (uyku esnasında anormal davranışlar), narkolepsi (gün içinde gelişen uyku atakları), huzursuz bacak sendromu gibi uyku bozukluklarının tanı ve tedavisinde kullanılır. Gece uykusu boyunca hasta vücudunun farklı bölgelerine yerleştirilen elektrotlar yardımıyla beyin dalgaları, göz hareketleri, kalp ve göğüs aktivitesinin ölçülmesi, solunum etkinlikleri, kandaki oksijen miktarı gibi çeşitli parametrelerin kayıt altına alınmasını sağlar. Bu makalede, PSG sinyal verilerinin uyku apnesinin teşhisine yönelik başarımları hem sinyal parametreleri hem de kullanılan yöntem bazında incelendi. İlk olarak PSG sinyallerinden özellik çıkartımı yapıldı daha sonra özellik vektörü yapay sinir ağları, destek vektör makinesi (DVM), k-enyakın komşu (k-NN) ve lojistik regresyon (LR) ile sınıflandırıldı.

Anahtar kelimeler: Uyku, Uyku Apnesi, PSG, Sınıflandırma.

1. Introduction

Sleep is an unconscious state in which the activity of a person's body organs decreases, brain and neural activities continue, but some stimuli from the outside world are not perceived. Sleep apnea is a breathing disorder and can be defined as a situation in which a person cannot breathe for at least 10 seconds or more during sleep. Although treatment is possible, people suffering from sleep apnea, which is often confused with snoring, may neglect treatment as a result of not being able to recognize the disease or noticing it too late. Diagnosis can be made by the physician by obtaining PSG signal data with the help of a polysomnography device in sleep laboratories [1]. Polysomnographic signal data includes data such as EEG (Electroencephalography), EOG (Electrooculography), EMG (Electromyography), ECG (Electrocardiography), Airflow, chest and abdominal movements, SpO₂ (Oxygen saturation), PTT (Pulse transit time).

* Corresponding author: ttuncer@firat.edu.tr. ORCID Number of authors: ¹ 0000-0001-6472-8306, ² 0000-0003-1414-3187, ³ 0000-0003-0526-4526

Sleep apnea types are divided into three: Obstructive Sleep Apnea (OSAS), Central Sleep Apnea (CSA) and Mixed Sleep Apnea (MSA). The incidence of these species is 85%, 14%, and 1%, respectively. It is important to examine OSAS disease due to its frequency, and the level of the disease is determined according to the AHI (Apnea Hypopnea Index) index.

AHI, which determines the severity of apnea, is the hourly average of apneas and hypopneas occurring throughout sleep. OSAS types are classified as mild OSAS patients between 5-15, moderate OSAS patients between 15-30, and severe OSAS patients 30 and above, depending on the AHI (Apnea-Hypopnea index/total number of apnea-hypopneas per hour of sleep) level [2].

In OSAS, the most common type of sleep apnea, shortness of breath occurs for more than 20 seconds and can last up to 1-2 minutes in severe cases. It is the most common of all known sleep apneas. In this type of sleep apnea, which first shows OSAS symptoms and then evolves into Compound Sleep Apnea, the disease progresses rapidly for 5-10 years, eventually confining the patient to bed. In Central Sleep Apnea, which is rarer than other types of sleep apnea, the person experiences more frequent awakenings. All known sleep apneas, CSA constitutes approximately 1%.

There are many studies in the literature on sleep apnea using clinical and computer-aided programming approaches. Xie et al. found that there was a relationship between heart rate variability (HRV) and OSAS [3]. Marcos et al. They diagnosed sleep apnea with bayesian neuron networks using oxygen saturation (SaO₂) [4]. Liu et al. analyzed the EEG signals in the ANN method and classified them for the detection of OSAS, and they achieved a 91% success rate as a result of the classification [5]. Akhter et al. obtained the OSAS model with a Naive Bayes-based model with a sensitivity of 92%, specificity of 81%, and average accuracy of 82%. They used REM and NREM data in the voice recordings taken from OSAS patients [6]. Sharma et al. reported the accuracy, sensitivity, specificity, and F1score values as 90.11%, 90.87%, 88.88%, and 0.92%, respectively, using wavelet filter bank (BAWFB) in the ECG-based OSA-CAD system for OSAS detection [7]. Jane et al. proposed a 2-layer Feedforward multilayer neural network to detect the snoring of people with OSAS and healthy people. The model has 82% sensitivity and 90% positive predictive value [8]. Konyang et al. developed a method based on hidden markov model (HMM) and deep neural network using ECG signal. The method has been reported to have approximately 85% classification accuracy and 88.9% sensitivity [9]. Banluesombatkul et al., who introduced a new approach for OSAS severity classification with the deep learning method. They used one-dimensional convolutional neural networks and deep recurrent neural networks with long short-term memory. The method used has an accuracy rate of 79.45% [10]. Akilotu et al. examined the effect of OSAS, the most common type of sleep apnea, on sleep stages and REM sleep using vector machines and artificial neural networks [11]. Khandoker et al. applied support vector machines to detect different types of OSAS by taking ECG recordings from 42 subjects, and as a result, they determined the accuracy to be 92.85% and Cohen's kappa value to be 0.85 [12]. To diagnose OSAS, Almazydeh et al. developed a neural network using the SpO₂ measurements [13]. Lin et al. examined the EEG signals they received from patients diagnosed with OSAS with classifiers such as kNN, SVM, LDA (Linear discriminant analysis) [14]. Karandikar et al. detected sleep apnea from electrocardiogram signals. In this study, sensitivity, specificity and misclassification parameters (91.93%), specificity (85.84%) and misclassification (11.94%) results were obtained [15]. Mostafa et al. developed a sleep apnea detection system using the deep learning method using SpO₂ signal data obtained from 33 subjects [16]. Jezzini et al. achieved 98.7% accuracy using classification in ECG signals for sleep apnea detection [17]. Lee et al. compared the clinical and polysomnography (PSG) features of patients with suspected OSAS in otolaryngology, neurology, and psychiatry clinics. Patients' medical records and PSG reports were analyzed retrospectively [18]. Chien et al. examined 10 years of electronic medical records of OSAS patients. Baseline PSG parameters were compared between patients with and without memory impairment. In this study, Subgroup analyzes based on OSAS severity and associations of PSG parameters with memory impairment were presented [19]. Gasa et al. applied cluster analysis to data obtained from routine polysomnography to optimize OSAS categorization. In this study, it has been emphasized that OSAS severity using the AHI approach is assessed with an inaccurate or incomplete analysis of the heterogeneity of the disorder [20]. Edis et al. evaluated possible risk factors that may lead to sleep-disordered breathing. Apnea-Hypopnea Index (AHI) scores were calculated for all patients, taking into account thorax computed tomography, respiratory function tests, carbon monoxide diffusion tests, and echocardiography polysomnography records [21]. Zhou et al. evaluated the performance of a wearable multisensory system compared to polysomnography (PSG) in measuring sleep stages and investigating OSAS [22]. Apart from these studies, compilation studies in the literature on systems that will help classify or detect sleep apnea are also presented in [23, 24, 25].

The contributions of the study to the literature are as follows.

- Identifying effective signals in the diagnosis of OSAS by examining all PSG signals in the diagnosis of OSAS
- Extracting features from PSG signals and detecting OSAS with classical machine learning algorithms of the feature vector

2. Material and Method

2.1 Material

PSG signals were collected from 30 OSAS patients and 30 healthy individuals who applied to Firat University neurology outpatient clinic, with the decision of the non-invasive ethics committee. Polysomnographic data of a total of 60 people were examined by a specialist doctor and created in two classes. The PSG signal of each patient consists of 16 channels. Table 1. Characteristics of the collected data. Figure 1 shows from which body positions the collected PSG signals were obtained.

Table 1. Dataset and features

Total Number of Data	60
Number of Patient Data	30
Number of stray data	30
Number of Sick/Healthy Men	15/15
Number of Sick/Healthy Women	15/15
Weight Range of Sick and Healthy People	50-87
Apnea-Hypopnea Index Level of Patients	Intermediate Level (AHI, Between 15-30)
Number of PSG Channels for Each Individual	16

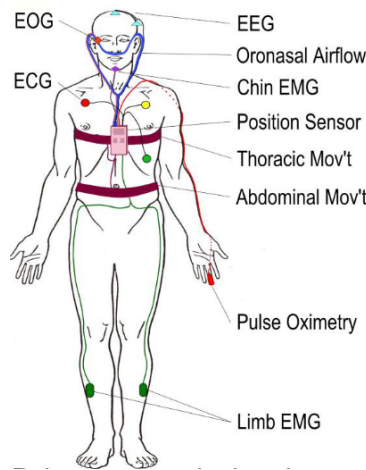


Figure 1. PSG signals

2.2. The Proposed Method

People diagnosed with sleep apnea face many serious problems both during night sleep and during the day. Daytime insomnia, headache upon awakening; Sudden death at night, paralysis, and respiratory failure in lung patients are examples of these negativities. Therefore, there is a need for information systems that will assist the physician in the decision-making process in detecting OSAS disease.

A 2-stage model is proposed for the detection of sleep apnea from PSG signal data. First, feature extraction was performed from the 16-channel PSG signals of each patient. Secondly, the resulting feature vector was classified. Figure 2. Shows the structure of the proposed model.

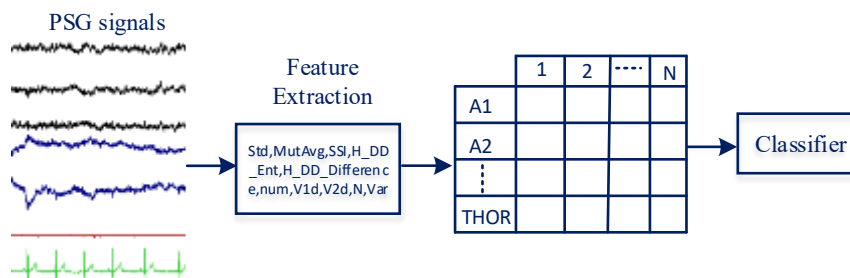


Figure 2. The proposed method

The PSG signal of each individual has 16 channels and each channel contains 960 values over time. In the feature extraction phase, features such as standard deviation, average value, total value, and entropy were extracted for each channel. The definitions of the extracted features are as in table 2.

Table 2. The extracted features

Feature	Defination
Std	Standard Deviation of the Signal
MutAvg	Absolute Average value of the signal
SSI	Sum of square of the signal
H DD Ent	Normalized Shannon wavelet entropy of the signal
H DD Difference	Difference between the maximum and minimum value of the signal
num	Sum of local maximum and local minimum values of the signal
V1d	variance of the first derivative of the signal
V2d	variance of the second derivative of the signal
N	average value of the average difference of the elements of the signal
Var	Variance of the signal

The feature vector obtained as a result of feature extraction was fed as input to the classification algorithms. Many classification algorithms were used to investigate the effect of PSG parameters on the diagnosis of OSAS disease. These are ANN, SVM, k-NN and logistic regression classifiers.

ANN is defined as a model network structure inspired by the functioning of neurons in the human brain. This network consists of nerve cells arranged in layers. The model basically has three types of layers: input, hidden, and output layers. In this study, the input and hidden layers consist of 10 nerve cells and the output layer consists of a single nerve cell.

SVM, which is used for both classification and regression problems, is especially effective in two-class problems. SVM attempts to classify data points with a specific hyperplane. It creates a decision boundary between two classes and tries to maximize the distance between these boundaries. The main goal of SVM is to determine the hyperplane that draws this decision boundary with a "maximum margin" between data points. This margin is the distance between the decision boundary and the closest data points, and this distance is tried to be maximized. Since this study had two classes, a linear kernel was used in the classification process.

In k-NN, neighboring data points are taken into account to determine the class of data. In the algorithm, the distances between all other training data points of the data are calculated. This distance is usually the Euclidean distance. A k value is selected for the Nearest Neighbor's Determination. This determines the number of neighbors of the predicted point. Euclidean distance and k value of 2 were selected in the classification process.

Logistic regression, which is widely used especially in binary classification problems, estimates the probability of an event based on input features. In the classification process, a sigmoid and a threshold value of 0.5 were selected as the logistic function.

3. Results

Confusion matrix is a matrix model that provides detailed details about the performance of the classification algorithm. The confusion matrix and the False Positive (FP), False Negative (FN), True Positive (TP) and True Negative (TN) obtained from this matrix were used to determine the performance of the proposed model.

- False Positive (FP): a healthy person is diagnosed as sick
- False Negative (FN): diagnosing the sick person as healthy
- True Positive (TP): the sick person is diagnosed as sick
- True Negative (TN): diagnosing a healthy person as healthy

The performance of the classifiers was determined by the accuracy (A), sensitivity (S), specificity (Sp), precision (P) and F1 score values shown in equations (1) to (5) which can be obtained from the confusion matrix.

$$A = \frac{TP+TN}{TP+TN+FP+FN} \quad (1)$$

$$S = \frac{TP}{TP+FN} \quad (2)$$

$$Sp = \frac{TN}{TN+FP} \quad (3)$$

$$P = \frac{TP}{TP+FP} \quad (4)$$

$$F1\ Score = \frac{2TP}{2TP+FP+FN} \quad (5)$$

The results regarding the signals trained in the artificial neural network are given in table 3. According to the table, the signals showing the best results are LOC, O1, O2 with 100% accuracy, A2 with 98.3% accuracy, AIRFLOW, C4, ECG2, NASAL, PTT, A1 with 96.7% accuracy, SPO2 with 94.5% accuracy, the accuracy degree was obtained as C3 with 91.7%, the accuracy degree as SNORE with 80% and the accuracy degree as THOR with 76.7%.

Table 3. Results obtained with the ANN algorithm.

Signal	A	S	Sp	P	F1
A1	96.7	96.7	96.7	94.5	96.7
A2	98.3	96.8	100	100	98.3
ABDO	76.7	78.6	75.0	73.3	75.8
AIRFLOW	98.3	100	96.8	96.7	98.3
C3	91.7	87.9	96.3	90	92.0
C4	98.3	96.8	100	100	98.3
ECG1	95.4	97.2	91.1	89.8	89.7
ECG2	98.3	100	96.8	96.1	98.3
LOC	100	100	100	100	100
NASAL	98.3	96.8	100	100	91.7
O1	100	100	100	100	100
O2	100	100	100	100	100
PTT	98.3	96.8	100	100	98.3
SNORE	80	82.1	78.1	76.6	79.3
SPO2	94.5	92.6	95.7	88.2	89.6
THOR	76.7	68.2	94	91.5	81.0

Table 4. SVM, k-NN and Logistic Regression classification results

Signal	Classifier	A	S	SP	P	F1
A1	k-NN	93.3	100	86.6	88.2	93.7
A2	LR	93.3	93.3	93.3	93.3	93.3
ABDO	SVM	81.7	80	80	80.6	81.9
AIRFLOW	LR	80	76.6	83.3	82.1	79.3
C3	SVM	80	90	70	75	81.8
C4	k-NN	96.7	96.7	96.7	96.7	96.7
ECG1	SVM	98.3	100	96	100	98.3
ECG2	SVM	96.7	93.3	100	100	96.5
LOC	LR	100	100	100	100	100
NASAL	SVM	91.7	90	93.3	93.1	91.5
O1	LR	98.3	96	100	100	98.3
O2	k-NN	100	100	100	100	100
PTT	SVM	96.7	96	96	87.1	96.5
SNORE	SVM	73.3	72	74	72.4	71.1
SPO2	LR	100	100	100	100	100
THOR	SVM	78.4	75	71.9	73.5	77.2

The results for the signals trained with SVM, k-NN and Logistic Regression are given in table 4 above. According to the table, the signals showing the best results are LOC, O2, SPO2 with an accuracy level of 100%, ECG1 with an accuracy level of 98.3%, O1 with an accuracy level of 96.7%, C4 with an accuracy level of 96.7%, PTT, ECG2 with an accuracy level of 93.3%, A1 with an accuracy level of 81.7%. With ABDO, the accuracy rate

was 80% for AIRFLOW, C3, 78.4% for THOR, and 73.3% for SNORE. Figure 3 shows the comparison of the results obtained with ANN and other classifiers in terms of accuracy.

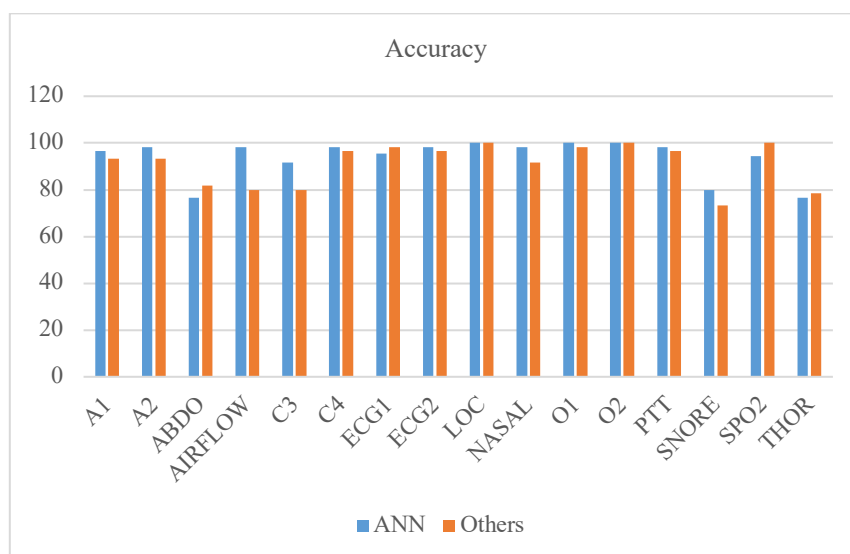


Figure 3. Comparison of ANN and other classifiers in terms of accuracy

4. Conclusion

Sleep apnea, which is often confused with snoring, is a chronic respiratory disorder that can result in stroke, suffocation, heart attack and death. Studies have been conducted on many support systems related to sleep apnea, especially to help diagnose and treat sleep apnea. Polysomnographic signal data were used in most of these studies. In our study, classification algorithms from machine learning methods were used. After the features of the PSG parameters were extracted, they were made suitable for studying with machine learning. PSG signal data subjected to machine learning methods were examined together in this study and the accuracy of the most effective parameters was determined comparatively. By comparing the accuracy, sensitivity, specificity, sensitivity and F1Score values of the PSG signal data examined in the classification algorithms, the effect on disease diagnosis was tried to be determined.

At the end of the study, the parameters that had the most impact on determining OSAS disease were determined to be LOC, O1 and O2 signals with 100% accuracy in ANN classifiers.

One of the most important gains and differences of this study is that all standard PSG signals (16) obtained from OSAS patients were examined together and the results were evaluated comparatively. It can be envisaged that PSG signals with high accuracy values will be further examined in future studies in order to produce auxiliary systems for both diagnosis and treatment of OSAS. Another important finding in the evaluation of classifiers is that signals such as LOC, O1, O2, SPO2, ECG1, which have a high level of accuracy, can be re-examined with different methods for diagnosis.

Acknowledgment

We express our gratitude to Prof. Dr. Caner Feyzi Demir from the Neurology Department at Fırat University for his invaluable contribution during the data collection and labeling process.

References

- [1] Akılotu BN, Tuncer SA. OSAS Evaluation By Means Of Machine Learning And Artificial Neural Networks By Using Polisomnographic Report Data, International Conference on Engineering Technologies (ICENTE'17), 2017.
- [2] Demir A, et al. Türk Toraks Derneği Obstrüktif Uyku Apne Sendromu Tanı Ve Tedavi Uzlaşı Raporu”, Türk Toraks Dergisi, Cilt 13, Vol.13, 2012.
- [3] Xie J, Yu W, Wan Z, Han F, Wang Q, Chen R. Correlation Analysis between Obstructive Sleep Apnea Syndrome (OSAS) and Heart Rate Variability, Iran J Public Health., 46(11), p:1502–1511, 2017.

- [4] Marcos C, Hornero JVR, Álvarez D, Nabney IT. Automated detection of obstructive sleep apnoea syndrome from oxygen saturation recordings using linear discriminant analysis, *Med Biol Eng Comput* ., 48(9):895-902, 2010.
- [5] Liu D, Pang Z, Lloyd SR. A neural network method for detection of obstructive sleep apnea and narcolepsy based on pupil size and EEG, *IEEE Transactions on Neural Networks*, 19(2), 308-318, 2008.
- [6] Akhter S, Abeyratne UR, Swarnkar V. Characterization of REM/NREM sleep using breath sounds in OSA, *Biomedical Signal Processing and Control*, 25, 130-142, 2016.
- [7] Sharma M, Agarwal S, Acharya UR. Application of an optimal class of antisymmetric wavelet filter banks for obstructive sleep apnea diagnosis using ECG signals, *Computers in Biology and Medicine*, vol.100, 100-113, 2018.
- [8] Jane R, Sola-Soler J, Fiz JA, Morera J. Automatic detection of snoring signals: validation with simple snorers and OSAS patients, *Proceedings of the 22nd Annual International Conference of the IEEE Engineering in Medicine and Biology Society*, Chicago, IL, USA, 2000
- [9] Kunyang L, Weifeng P, Yifan L, Qing J, Guanzheng L. A method to detect sleep apnea based on deep neural network and hidden Markov model using single-lead ECG signal, *Neurocomputing*, Vol.294, 94-101, 2018.
- [10] Banluesombatkul N, Rakthanmanon T, Rapaport TW. Single Channel ECG for Obstructive Sleep Apnea Severity Detection Using a Deep Learning Approach, *TENCON 2018* - pp. 2011-2016, 2018.
- [11] Akilotu BN, Tuncer SA. Evaluation of the Effect of CPAP Device on REM Sleep in OSAS Patients Using YSA and SVM, *International Conference on Engineering Technologies*”, (ICENTE’17), Dec 07-09, Konya, Turkey, 2017.
- [12] Khandoker AH, Palaniswami M, Karmakar CK. Support Vector Machines for Automated Recognition of Obstructive Sleep Apnea Syndrome From ECG Recordings, *IEEE transactions on information technology in biomedicine*, 13(1),37-48, 2009.
- [13] Almazaydeh L, Faezipour M, Elleithy K. A Neural Network System for Detection of Obstructive Sleep Apnea Through SpO2 Signal Features, *International Journal of Advanced Computer Science and Applications*, 3(5), 7-11, 2012.
- [14] Lin SY, Wu Y, Mao W, Wang P. EEG signal analysis of patients with obstructive sleep apnea syndrome (OSAS) using power spectrum and fuzzy entropy, *2017 13th International Conference on Natural Computation, Fuzzy Systems and Knowledge Discovery (ICNC-FSKD)*, Guilin, China, pp. 740-744, 2017.
- [15] Karandikar K, Le T, Sa-ngasoonsong A, Wongdhamma W, Bukkapatnam S. Detection of sleep apnea events via tracking nonlinear dynamic cardio-respiratory coupling from electrocardiogram signals, *Annu Int Conf IEEE Eng Med Biol Soc.*, 7088-91, 2013.
- [16] Mostafa SS, Mendonça F, Morgado-Dias F, Ravelo-García A. SpO2 based sleep apnea detection using deep learning, *IEEE 21st International Conference on Intelligent Engineering Systems (INES)*, Larnaca, Cyprus, 2017.
- [17] Jezzini A, Ayache M, Elkhansa L, Ibrahim Z. ECG classification for sleep apnea detection, *2015 International Conference on Advances in Biomedical Engineering (ICABME)*, Beirut, Lebanon, pp. 301-304, 2015.
- [18] Lee, E., Lee, H. Clinical and Polysomnographic Characteristics of Adult Patients with Suspected OSAS from Different Sleep Clinics at a Single Tertiary Center. *Neurol Ther*, 2024.
- [19] Chien, W.-C. Et.al. The Associations between Polysomnographic Parameters and Memory Impairment among Patients with Obstructive Sleep Apnea: A 10-Year Hospital-Based Longitudinal Study. *Biomedicines*, 11, 621, 2023.
- [20] M. Gasa, et al., Polysomnographic Phenotypes of Obstructive Sleep Apnea in a Real-Life Cohort: A Pathophysiological Approach, *Archivos de Bronconeumología* Vol. 59. Issue 10., pages 638-644 , 2023.
- [21] E.Ç. Edis, et.al. Polysomnography findings and risk factors for sleep-disordered breathing in patients with systemic sclerosis, *Archives of Rheumatology*, 36(3), 2021.
- [22] Zhou SJ, et. al. Measuring Sleep Stages and Screening for Obstructive Sleep Apnea with a Wearable Multi-Sensor System in Comparison to Polysomnography”, *Nat Sci Sleep.*, 15:353-362, 2023.
- [23] Garg VK, Bansal RK, Intelligent Computing Techniques for the Detection of Sleep Disorders: A Review, *International Journal of Computer Applications*, 110, 0975 – 8887,1, 2015.
- [24] Alvarez-Estevez D, Moret-Bonillo V. Computer-Assisted Diagnosis of the Sleep Apnea-Hypopnea Syndrome: A Review, *Sleep Disorders*, 2015:237878, 2015.
- [25] Motamedi-Fakhr S et. al. Signal processing techniques applied to human sleep EEG signals-A review, *Biomedical Signal Processing and Control*. 10, 21–33, 2014.

Realization of Fuzzy-PI Controller-Based Path Planning of Differential Drive Mobile Robot

Ahmet TOP^{1*}, Muammer GÖKBULUT²

^{1,2} Department of Electrical and Electronic Engineering, Faculty of Technology, Firat University, Elazığ, Turkey

*¹ atop@firat.edu.tr, ² mgokbulut@firat.edu.tr

(Geliş/Received: 22/01/2024;

Kabul/Accepted: 26/03/2024)

Abstract: This paper uses a cascade-connected fuzzy-PI controller to control the position and speed of a differential drive and four-wheel drive of an autonomous mobile robot for optimal path planning. The angular speed information obtained from the encoder of each motor and the instantaneous position and angle information of the robot were calculated. The angle and position error between the reference points and these values is applied to the fuzzy logic controller as an input signal. The robot angular and linear speed data obtained from the fuzzy logic output were converted into reference speed values with kinematic equations to be applied to the motors. The speed controls of the motors were carried out with a PI controller based on these reference values. The study was performed both as a simulation in the MATLAB program and experimentally in the laboratory environment for one and more reference coordinates. In the experimental study, reference values were sent to the robot via Bluetooth with the Android application designed. At the same time, the instant data of the robot was also collected on the Android device through the same application. These data collected in Excel format were transferred to the computer via e-mail and the graphics were drawn in the MATLAB program. When the results were examined, it was seen that both speed and position control were successfully implemented with the fuzzy-PI controller for optimum path planning of the robot.

Keywords: Fuzzy logic, PI, mobile robot, Android application, path planning.

Diferansiyel Sürüşlü Mobil Robotun Bulanık PI Denetleyici Tabanlı Yol Planlamasının Gerçekleştirilmesi

Öz: Bu çalışmada, diferansiyel sürüşlü ve dört tekerden tahrikli otonom mobil robotun, optimum yol planlaması için, konum ve hız kontrolü kaskad bağlantılı fuzzy-PI kontrolör ile gerçekleştirilmiştir. Her bir motorun enkoderinden alınan açısal hız bilgileri ile robotun anlık konum ve açı bilgilerini hesaplanmıştır. Referans noktalar ile bu değerler arasındaki açı ve konum hatası bulanık mantık denetleyiciye giriş sinyali olarak uygulanmıştır. Bulanık mantık çıkışından alınan robot açısal ve lineer hız verileri ise kinematik denklemler ile motorlara uygulanacak olan referans hız değerlerine dönüştürülmüştür. Motorların hız kontrolleri bu referans değerler baz alınarak PI kontrolör ile gerçekleştirilmiştir. Bir ve birden fazla referans koordinatlar için gerçekleştirilen çalışma hem MATLAB programında simülasyonda hem de laboratuvar ortamında deneysel olarak gerçekleştirilmiştir. Deneysel olarak yapılan çalışmada, tasarımı gerçekleştirilen Android uygulama ile referans değerler robota bluetooth aracılığıyla gönderilmiştir. Aynı zamanda robotun anlık verileri de yine aynı uygulama üzerinden android cihazda toplanmıştır. Excel formatında toplanan bu veriler mail yolu ile bilgisayara aktarılarak MATLAB programında grafikleri çizdirilmiştir. Alınan sonuçlar incelendiğinde robotun fuzzy-PI kontrolör ile başarılı bir şekilde hem hız hem de konum kontrolünün gerçekleştirildiği görülmüştür.

Anahtar kelimeler: Bulanık mantık, PI, mobil robot, Android uygulama, yol planlama.

1. Introduction

Robotics is a sector that is expanding quickly along with technological advancements, and robots are increasingly playing a significant role in daily life for humans. In addition to classical areas such as industrial, medical, and rehabilitation, human-robot interaction increases its impact in areas such as exploration, urban search, and rescue, due to reasons such as saving manpower and time, being more economical, and working with fewer errors. These robots can be controlled manually by humans, depending on their area of use and purpose, or they can perform the tasks assigned to them autonomously [1]. An autonomous mobile robot (AMR) is a system that operates in an unpredictable and partially unknown environment. There is little or no human intervention in autonomous mobile robot movement [2].

Mobile robot (MR) systems are separated into three main modules: information sensing, path planning, and control of motion. Path planning is the connection between information perception and motion control, and it is a crucial aspect of a mobile robotic system. The continuous development of path-planning technology brings innovations to every part of life. For example, the sweeping robot can replace people doing housework and make people's work easier; As long as the destination location is entered in driverless vehicles, it can provide an optimum route and provide safe and accurate transportation; In emergency rescue and disaster assistance, AMRs can locate

* Corresponding author: atop@firat.edu.tr. ORCID Number of authors: ¹ 0000-0001-6672-2119, ² 0000-0003-1870-1772

targets quickly, accurately, and safely in hazardous conditions. In scientific research, it can replace humans by entering harsh environments to help humans recognize unknown planets and complete the task of acquiring knowledge [3].

To assist an MR in choosing the best path, numerous algorithms have been presented by researchers since the 1950s. These algorithms can be examined in general under three headings: classical, bionic, and artificial intelligence algorithms. Cell decomposition method (CD), sampling-based method (SBM), and graph search algorithm (GSA) can be given as examples of classical algorithms that have the advantage of easily observing the calculation results. Each algorithm can also be classified among themselves, and studies related to each are available in the literature. The CD was analyzed in three parts: regular (RCD) [4-6], approximate (ACD) [7,8], and exact decomposition (ECD) [9,10]. RRT (rapidly exploring random tree) [11] and PRM (probabilistic roadmap method) [12,13] algorithms were studied under the heading of SBM. Dijkstra algorithm [14,15] and A* algorithm [16] are in the GSA group. The bionic algorithm is a random algorithm inspired by the biological herd intelligence phenomenon in nature. It can be grouped according to different path-searching mechanisms. Genetic algorithm (GA) [17,18], ant colony optimization (ACO) [19,20], and particle swarm optimization (PSO) [21,22] are some of the studied bionic algorithms related to path planning. Artificial intelligence (AI), which has basic needs such as algorithms, data, and computing capability, simulates human behaviors such as learning, reasoning, thinking, and planning. The most used AI algorithms for path planning in MRs; are bioinspired neural network algorithms [23,24] and fuzzy logic control algorithms.

Fuzzy logic (FL), presented by Zadeh in 1965 [25], is an artificial intelligence algorithm that processes real-time information from the sensors as input data and generates the output values required for the path planning of the MR as a result of its analysis. Because it is less influenced by outside forces, it is appropriate for path planning in unknown environments [26]. However, it has the disadvantage that the optimum path to be followed depends on the rule base created by experts. Many researchers have used different algorithms together with the FL algorithm to improve the performance and accuracy of FL [27]. For example, Zagradjanin et al. used the D*lite algorithm with FL [28], while Ntakolia and Lyridis obtained high-quality solutions by integrating the swarm intelligence graph-based pathfinding algorithm and the FL algorithm [29]. Gharajeh & Jond presented the adaptive neuro-fuzzy inference system (ANFIS) method and shortened the planned path by 30 percent compared to other algorithms [30]. Besides, the most common integrated use is FL and PID (proportional-integral-derivative) algorithms [31-35].

When the MR path planning studies with Fuzzy-PID in the literature are examined, it is seen that the fuzzy logic controller is generally used to regulate and adjust the proportional, integral, and derivative coefficients of the PID algorithm. In this study, unlike the studies in the literature, the reference value, not the parameters of the PI algorithm, was determined with the fuzzy logic controller. The reference target points were sent to the robot with the designed Android application and these values were compared with the instant data of the robot and the position and angle error values were calculated. These values are applied as input signals to the fuzzy logic controller. Linear and angular velocities of the robot are obtained as output signals. By using these speed values in the kinematic equations, the angular speeds that each motor must reach instantaneously are calculated. The instantaneous speed of the motors was controlled by applying the error between the instantaneous speed values obtained from the encoders and the reference motor angular speed values to the PI controller. The robot, which reached the target within the approach distance given for the reference positions, performed its next movement with the reference speed values obtained from the fuzzy logic. The instant speed, angle, and position values of the robot were transferred via Bluetooth with the same Android application and collected on the Android device in Excel format. This file was then sent to the computer by e-mail and the robot's graphics were drawn with the MATLAB program. When the graphics are examined, it is seen that the robot reaches the desired positions within the given approach distance and by taking the optimum path.

2. Materials and Methods

2.1 Mobile robot

For this study, the design and prototype of a four-wheel drive, **Symmetric Modular Robot (SMaRt)**, which can be used in many fields such as education, research, military, health, etc. have been realized. The design of the robot, which consists of the components in Figure 2 and whose final assembly is given from different angles in Figure 1; consists of 3 main parts: mechanical, electronic, and software tools. It has the advantages of weighing less than 10 kg, adding attachments such as a robot arm, and the ability to remove and replace the desired parts thanks to its modular structure.

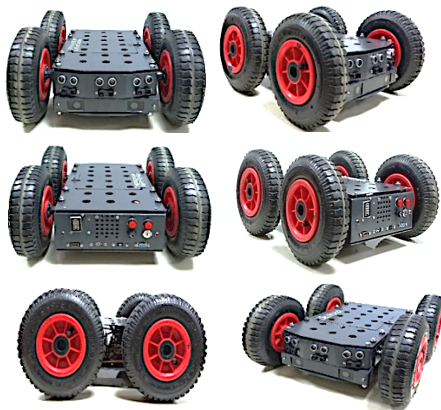


Figure 1. Symmetric modular robot-SMArt

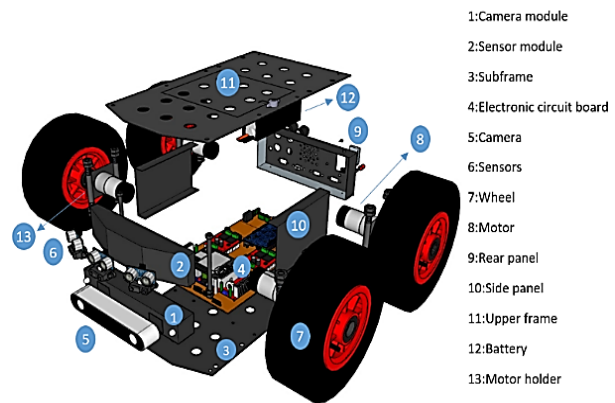


Figure 2. Components of the MR

The DC motor (No Load Speed: 76 rpm, Stall torque: 45 kg-cm, Max. Impact torque: 6 kg-cm) was selected based on the motor torque value calculated for each wheel, taking into account the robot's weight, the wheel's dimensions, and any potential tilt and acceleration. The encoder has a resolution of 64 CPR and is attached to the motor shaft from behind. The microprocessor was able to determine the motor speed using the square wave data it received from the encoder, and the motor speed control was made possible. The XOR-HWT (exclusive OR-half-wave time) method was used to detect velocity with these signals [36].

The MR's four DC motors are driven by the Sparkfun Monster motor driver modules with dual outputs shown. With this driver module, it is possible to control motors with a maximum of 16 V, a continuous current of 14A, and a maximum PWM frequency of 20kHz. [38]. There are wired and wireless connections to enable the circuits and processors in the robot to communicate with each other or with the outside world. The HM-10 Bluetooth module was used to provide the connection between Arduino and Android devices. This module is a Bluetooth 4.0 module with low power consumption (when active, the current is 9mA) [39]. It is connected to Arduino with UART communication protocol. Arduino Due is an Atmel SAM3X8E 32-bit ARM Cortex-M3 CPU-based microcontroller board. It has a total of 54 digital input/output pins, 12 of which can be used for PWM, 12 analog inputs, 4 UARTs, 84 MHz oscillator frequency, and 2 digital to analog converter pins [40]. Arduino software is made with Arduino IDE (Integrated Development Environment), an open-source development platform.

2.2 Android application

A computer or a special electronic control circuit is usually used to send target coordinates to the robot. Likewise, robot information is collected on an additional memory card or sent to the computer. In this study, an Android-based application, whose screenshots are given in Figure 3, has been developed for smart devices (mobile phones, tablets) that are widely used today, which can do both operations [41]. The MIT App Inventor, which was initially made available by the Google firm and is currently maintained by the Massachusetts Institute of Technology (MIT), was used to create and implement the app. MIT App Inventor has been transformed over the past ten years into automation systems [43], quizzes and games [44], smart home control [45–48], education [49], and more. It has been utilized for Android applications in many different projects, including. In robotic applications, there are designs only for the manual use of the robot, but in this study, robot data was collected by using it for autonomous control.

Thanks to the buttons on the main screen in Figure 3 (a), it is possible to switch to manual and autonomous control screens, as well a Bluetooth connection is provided from here. With the manual control screen in Figure 3 (b), the movement direction of the robot, its speed, and the status of the LEDs and headlights on it can be changed and the robot can be brought to the desired starting point for autonomous control. When the screen in Figure 3 (c) is reached by pressing the automatic control button on the main screen, three different coordinate points where the robot desires to go and the approach distances to these points are entered and sent to the robot. After the reference points are sent and the robot starts to move, the coordinate plane in Figure 3 (d) comes to the Android device screen, the reference points are automatically marked and the instant position of the robot is drawn on this plane. In addition, the instantaneous speed and angle information of the robot, along with the location information, can be collected on the Android device in Excel file format and shared on a desired platform. The Excel file obtained in this study was transferred to the computer by e-mail and the graphs of the data of the robot were drawn in the MATLAB program.

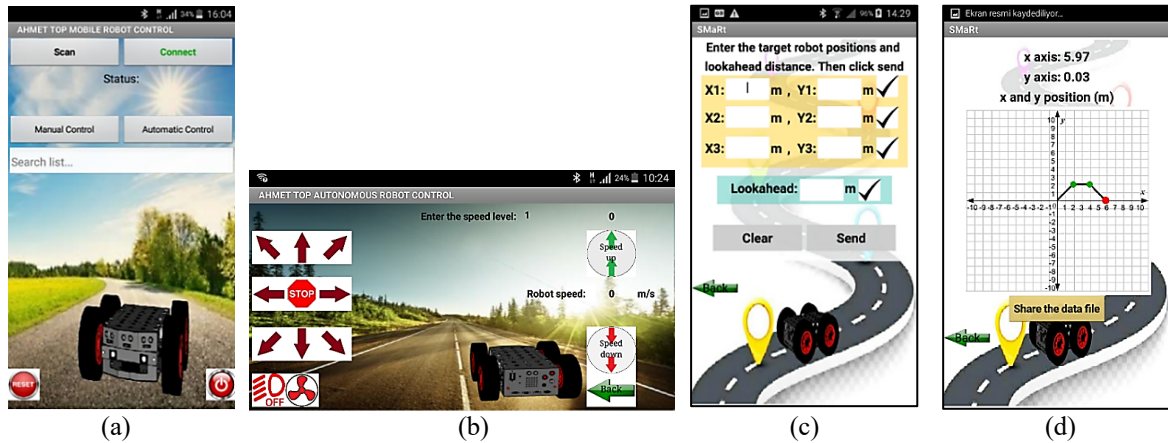


Figure 3. Android application; (a) Main screen, (b) Manual control screen, (c) Automatic control screen, (d) Instant motion graph of the robot

2.3 PID controller

PID controllers, also known as proportional, integral, and derivative (PID) controllers, are frequently used to regulate the speed of DC motors. The PID controller is regarded as the method most frequently employed in nonlinear control systems [50]. In essence, a PID controller uses a straightforward trinomial controller to increase stability and decrease steady-state error [51]. It offers the most efficient and simplest solution for many control problems, covering both transient and steady-state responses. The transfer function is usually written with the "gain notation" given by equation 1 or the "time constant notation" given by equation 2.

$$T(s) = K_p + K_i \frac{1}{s} + K_d s \tag{1}$$

$$T(s) = K_p \left(1 + \frac{1}{T_i s} + T_d s \right) \tag{2}$$

where K_p is the proportional gain, K_i is the integral gain, K_d is the derivative gain, T_i is the integral time constant and T_d is the derivative time constant. It's crucial to regulate these motors properly because the robot's position is dictated by the speed information the DC motor encoder provides. Due to this, each motor has been separately PI controlled to closely and quickly follow the reference speed values. In Figure 5, the general block diagram of the motor controls is given. In this study, the PI controller was used by setting $K_d = 0$.

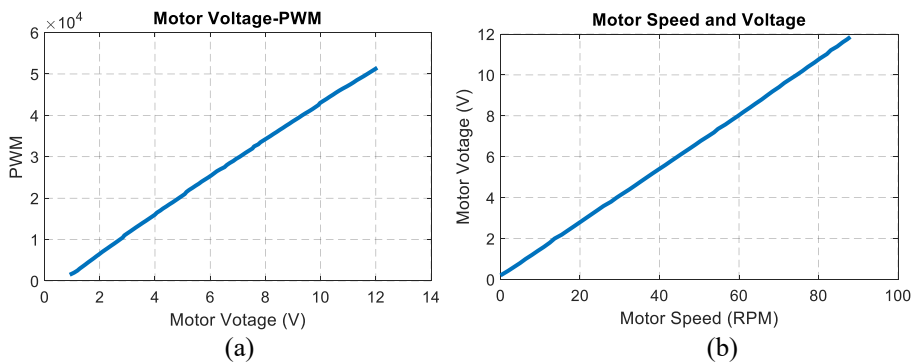


Figure 4. (a) Motor voltage-PWM graph, (b) Motor speed and voltage graph

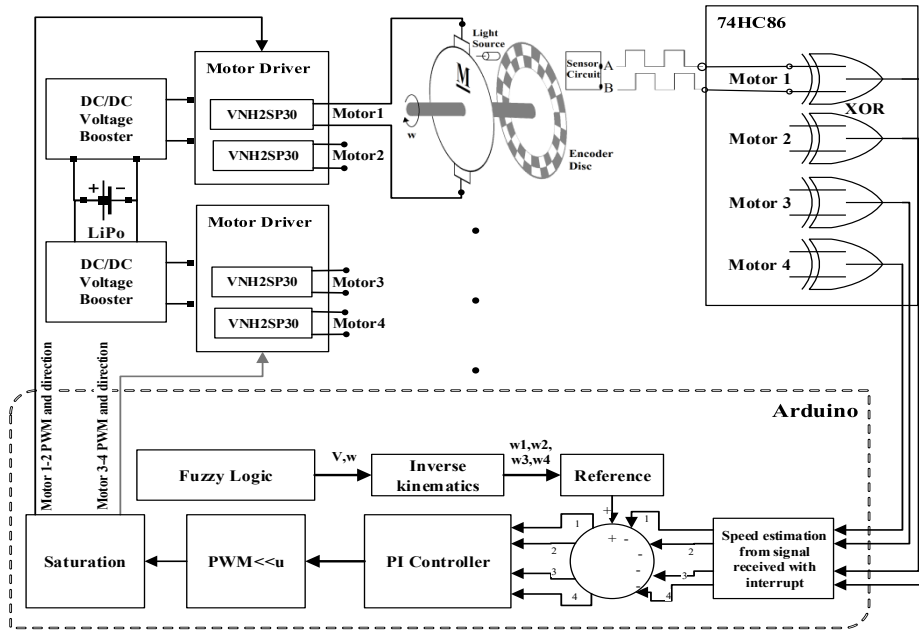


Figure 5. Motor control general block diagram with PI

According to this diagram, the output of the fuzzy logic controller used for position control of the robot is the reference linear and angular velocity of the robot. The reference angular velocities that each wheel must reach are rad./s by using these velocity values as inputs to the kinematics equations. These reference values were obtained from the output of the fuzzy controller and the instantaneous motor speeds taken from the XOR logic gate and the instantaneous and reference voltage values of the motors were obtained and the error was found by taking the difference of these values. This error has been converted to PWM values since the output value obtained when passed through the PI controller cannot be sent directly to the drivers. Experimental results revealed the association between motor speed and motor voltage as well as the relationship between the motor voltage and applied PWM. The graph of these values was drawn as in Figure 4 and the equational expression between them was created. The signals received from the encoder connected to the motor shaft are applied to the XOR logic gate input and each XOR output is connected to a different pin of the Arduino [36]. The motor and encoder disc shown in the block diagram are visually shown for only one motor. The same steps must be followed for other motors.

2.4 Fuzzy logic (FL)

The FL controller is a control algorithm that processes the input data taken from the physical environment and whose value is certain and produces outputs that can be used in the physical environment as output. In this study, Mamdani-type FL was used to perform position control and path planning in line with the target coordinates given to the robot. The controller consists of two input and two output variables. The distance error and angle error to the coordinate point where the robot should go are given as input variables. The linear and angular velocities that the robot needs to reach instant are taken as the output variable. Position error value is meter, angle error value is radian, linear velocity value is m/s and angular velocity value is radian/s evaluated in units. As seen in Figure 6, ten triangular membership functions (MFs) are used for the input membership functions created for the position error. Ten were used to gradually decrease its velocity every ten centimeters, one meter from the reference position.

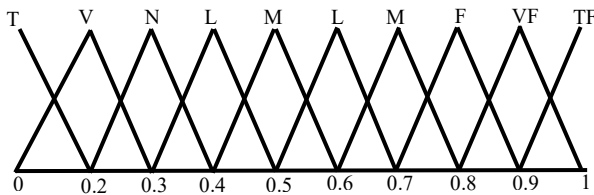


Figure 6. Position error MFs

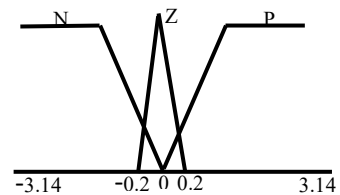


Figure 7. Angle error MFs

where, TN: Too near, VN: Very near, N: Near, LN: Little near, MN: Middle near, LF: Little far, MF: Middle far, F: Far, VF: Very far, TF: Too far. If the difference between the target and the position of the robot is more

than one meter, it is considered too far. When this error value falls below one meter, membership degrees change at each level until it reaches zero. The MFs created for the angle error are given in Figure 7. The limits of the angle error memberships consisting of two trapezoidal and one triangle membership functions are in the range of ± 3.14 radians. In angle error membership, N: Negative, Z: Zero, P: Positive. The breaking points of the positive and negative angle MFs were determined as ± 1.57 radians. There are two outputs in the system, angular velocity and linear velocity. Ten triangular MFs make up linear velocity, while three do the same for angular velocity. When the functions given in Figure 8 are examined, values are given such that the highest linear speed is 0.275 m/s and the lowest linear speed is 0.11 m/s. The reason for giving these values can be listed as the difficulties in the rotation movement of the motors at low speeds, while excessive energy consumption, microcontroller processing speed, and slips in sudden starts at high speeds.

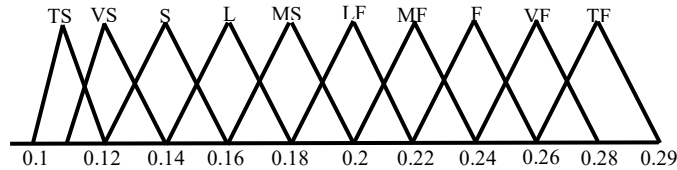


Figure 8. Linear speed MFs

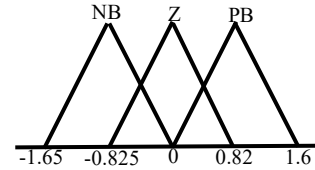


Figure 9. Angular speed MFs

where, TS: Too slow, VS: Very slow, S: Slow, LS: Little slow, MS: Middle slow, LF: Little fast, MF: Middle fast, F: Fast, VF: Very fast, TF: Too fast. The three membership functions used for the angular velocity of the robot are named NB: Negative big, Z: Zero, and PB: Positive big. The median values of the functions whose graphs are given in Figure 9 are given as -0.825, 0, and +0.825 radians, respectively. Since the mean of weights method is used in defuzzification, the value at the midpoint of each of the membership functions is used in the calculations.

Table 1. Rule base for linear speed

Position error	TN	VN	N	LN	MN	LF	MF	F	VF	TF	
	Angle error	N	S	VF	VF	F	MF	LF	TS	LF	VS
	Z	S	S	S	LS	MS	LF	MF	F	VF	TF
	P	S	VF	VF	F	MF	LF	TS	LF	VS	TS

Table 2. Rule base for angular speed

Position error	TN	VN	N	LN	MN	LF	MF	F	VF	TF
	Angle error	N	NB	NB	NB	NB	NB	NB	NB	NB
	Z	Z	Z	Z	Z	Z	Z	Z	Z	Z
	P	PB	PB	PB	PB	PB	PB	PB	PB	PB

After the membership degrees and the degrees of precision found by using the algebraic product method are passed through the rule bases in Tables 1 and 2, the addition process does not take place. It is subjected to a direct defuzzification process. As a result, the robot linear and angular velocity values obtained from the fuzzy controller output are applied as input to the inverse kinematics equation in the control system whose flow chart is given in Figure 10, and reference angular velocity values for the motors on both sides are calculated.

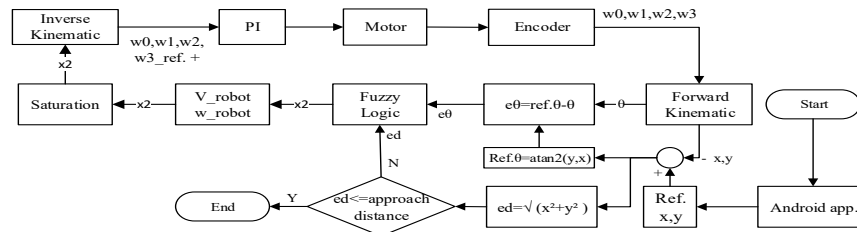


Figure 10. Position control flow chart with fuzzy logic controller

3. Simulation

Before examining the robot's performance with the experimental study, a simulation was prepared in the MATLAB/Simulink program to examine both the accuracy of the equations and the accuracy of the written algorithms and coefficient values. With different reference values for robot movements, firstly the results were obtained in the simulation, and then experimental studies were carried out in the laboratory environment.

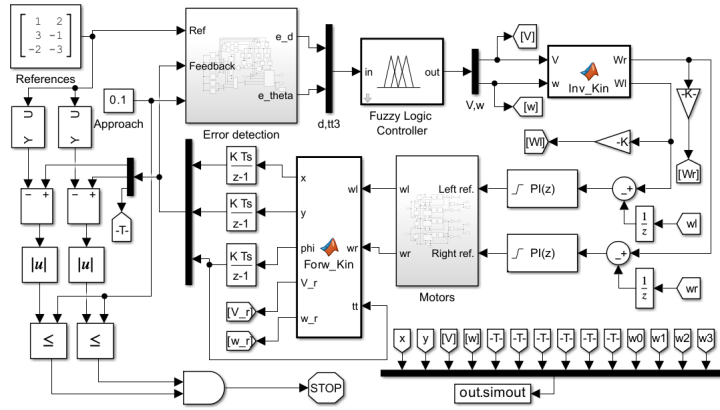


Figure 11. Robot position control simulink model

There are two input variables in the MATLAB/Simulink model in Figure 11. These are reference values and approach distance. For the robot to go to three different position points, $x_1, y_1, x_2, y_2,$ and x_3, y_3 positions are given to the reference block in matrix format. If the robot is desired to go to only one reference, zero values are entered into the points other than the x_3 and y_3 values. Similarly, if it is desired to go to two references, zero values are entered in x_1 and y_1 . The approach distance is the variable that determines how much error the robot can approach the given target coordinate. For example, if this value is entered as 0.1 m as in Figure 11, it means that the robot can stop after 0.1 meters approach to the reference point. The robot's approach can be in front of, right, left, or behind the target. Reference value, instantaneous feedback position values, and approach distance are given as input to the error detection block in Figure 12. In this block, the first reference point and instantaneous position and angle values from feedback are applied to the error function block. Here, the difference of the reference position and the instantaneous measured positions is taken and the position and angle error are calculated from these values. These values form the output of the error detection block. If the first reference is within the approach distance, the same operations are repeated by switching to the second reference with the multi-position switch block. If the second reference is reached, calculations for the third reference point begin. If the first two references are zero, since they will both be within the approach distance, the movement starts directly toward the third reference.

Position and angle error obtained from the error detection block is applied as input to the fuzzy logic block, and the reference linear and angular velocity of the robot is calculated from the block output. The reference angular velocity values of the left motor and right motors calculated by applying inverse kinematics according to Equations 3 and 4 are passed through the PI and applied to the motor models in the motors block in Figure 13.

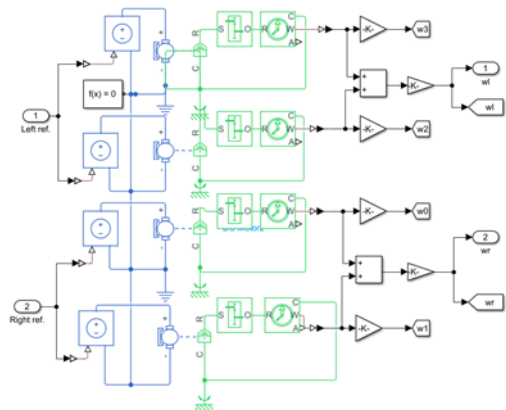
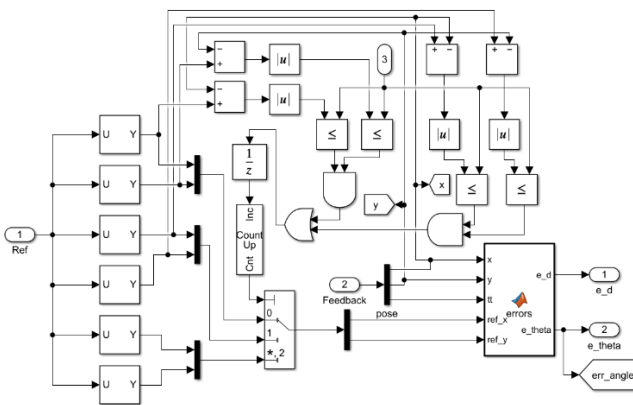


Figure 12. The internal structure of error detection block Figure 13. The internal structure of the motor block

$$w_L = \frac{1}{R} \cdot (V - W \frac{L}{2}) \tag{3}$$

$$w_R = \frac{1}{R} \cdot (V + W \frac{L}{2}) \tag{4}$$

where; w_L , is the angular velocity of the left motors, w_R is the angular velocity of the right motors, V is the robot linear velocity, W is the robot angular velocity, R is the radius of the wheels and L is the axis distance of the robot. The motor block contains four equal motors. The top two of them represent the motors on the left of the robot and the others on the right of the robot. The instantaneous speeds of the motors to which the reference speed is applied constitute the output of the block. These values, taken as left and right motor speeds, are applied as inputs to the forward kinematics block and the speed in the x direction (V_x), speed in the y direction (V_y), and angular velocity of the robot are calculated according to Equation 5-9.

$$V = \frac{R}{2} \cdot (w_R + w_L) \quad (5)$$

$$W = \frac{R}{L} \cdot (w_R - w_L) \quad (6)$$

$$\text{Robot} = [V \quad 0 \quad W]' \quad (7)$$

$$R_z = [\cos(tt) \quad -\sin(tt) \quad 0; \sin(tt) \quad \cos(tt) \quad 0; 0 \quad 0 \quad 1] \quad (8)$$

$$[V_x, V_y, V_{tt}]^T = R_z * \text{Robot} \quad (9)$$

where; tt instantaneous angle of the robot. By integrating these obtained values concerning time, x position, y position, and angle information are calculated.

4. Simulation and Experimental Results

During the period from the start of the simulation to the end, all the desired data were collected with the help of the 'out.simout' block and graphed in MATLAB/m-file. The performance of the robot with different reference values (RVs) and different approach distances (ADs), both in the simulation and experimentally, is given below.

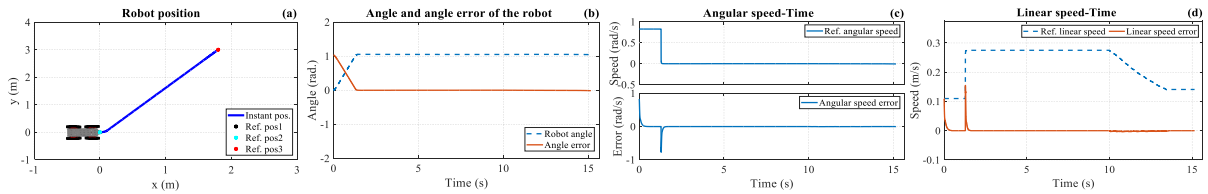


Figure 14. Simulation results for $x_1:0, y_1:0, x_2:0, y_2:0, x_3:1.8, y_3:3$ m reference and 0.05 m AD. Robot: (a) position, (b) Angle and angle error, (c) Angular speed and error, (d) Linear speed and error

In the MATLAB/Simulink program, when the $x_1:0, y_1:0, x_2:0, y_2:0, x_3:1.8, y_3:3$ m coordinates and 0.05 m approach distance are sent to the robot as a reference, the robot performances in figure 14 and figure 15 motor speed and errors were obtained. Since the reference value is $x_3:1.8$ m and $y_3:3$ m, it is seen in Figure 14 (b) that the angle to be rotated is calculated as 1.03 radians. When the angular velocity and linear velocity values in Figure 14 (c) and (d) are examined, it is observed that it first takes a turn with speeds of 0.825 radians/s and 0.11 m/s to go to the reference, and then increases to a linear velocity of 0.275 m/s over time, and its angular velocity decreases to zero.

Experimental work was carried out for the same reference values and the results in figure 16 and figure 17 were obtained. Looking at the robot position graph in Figure 16 (a), since the approach distance is given as 0.05 m, it is seen that the robot completes its movement at $x:1.78, y:2.96$ m. In cases where there is more than one reference change during the movement, a temporary state and a permanent state occur at each reference change. Therefore, the error amounts between the reference value and the instantaneous measured values in all graphs are completely taken into account without including the first transient in the evaluation. While Equation 10 gives the average absolute velocity errors of the graphs for this case, the instantaneous highest velocity error that occurs in other transients except for the initial transient case is given as the maximum velocity error.

$$\text{Performance criteria} = \frac{1}{N} \sum_{k=1}^N |e(k)| \quad (10)$$

where; $e()$ is the error value and N is the number of samples. In this case, when looking at the graphs obtained for the reference value (1.8,3) m, the maximum linear velocity error between the two signals is 0.038 m/s and the average linear velocity error is 0.0021 m/s, while the angular velocity reference is 0.179 rad./s maximum. and an average of 0.0057 rad./s. followed by an error. When the motor speed graphs in Figure 17 (a) and (b) are examined, the maximum and average absolute error values of the motors for the same situation are given in Table 3.

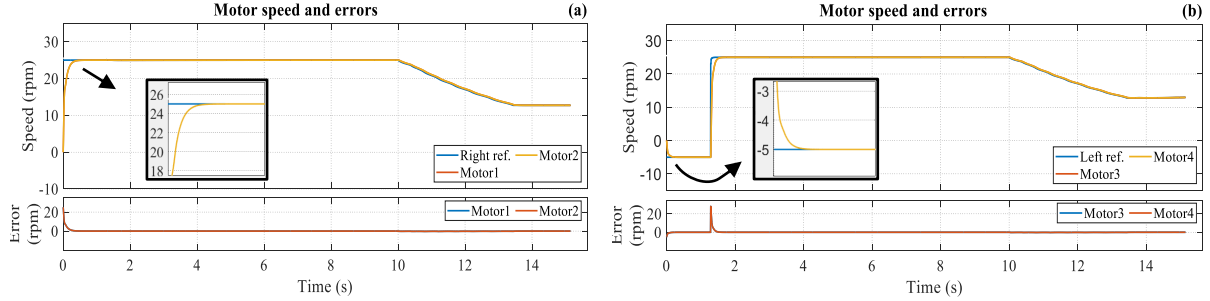


Figure 15. Simulation results for $x_1:0, y_1:0, x_2:0, y_2:0, x_3:1.8, y_3:3$ m RFs and 0.05 m AD. Robot: (a) Right motor speeds and errors, (b) Left motor speeds and errors

Table 3. Speed errors of motors for $x_1:0, y_1:0, x_2:0, y_2:0, x_3:1.8, y_3:3$ m RVs and 0.05 m AD

	Motor1	Motor2	Motor3	Motor4
Average absolute speed error (rpm)	0.194	0.134	0.229	0.249
Maximum speed error (rpm)	1.113	0.637	5.921	7.495

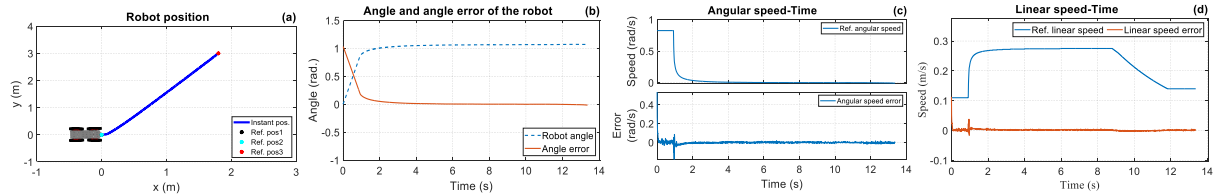


Figure 16. Experimental results for $x_1:0, y_1:0, x_2:0, y_2:0, x_3:1.8, y_3:3$ m reference and 0.05 m AD. Robot: (a) position, (b) Angle and angle error, (c) Angular speed and error, (d) Linear speed and error

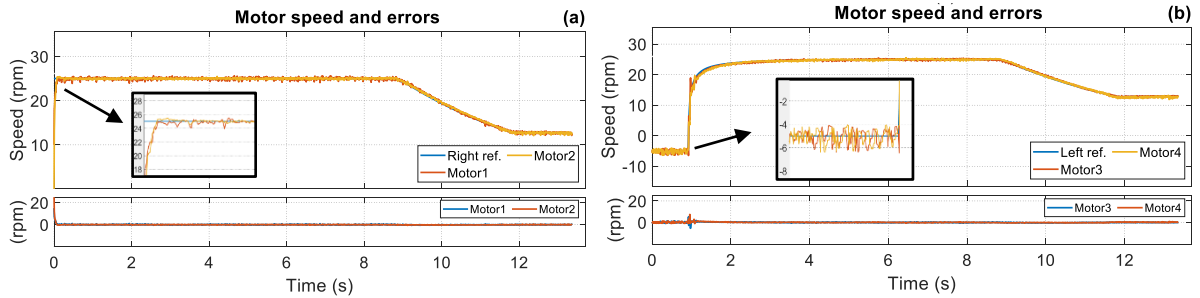


Figure 17. Experimental results for $x_1:0, y_1:0, x_2:0, y_2:0, x_3:1.8, y_3:3$ m RVs and 0.05 m AD. Robot: (a) Right motor speeds and errors, (b) Left motor speeds and errors

Performance graphics for $x_1:1, y_1:2, x_2:3, y_2:-1, x_3:-2, y_3:-3$ m reference values and 0.1 m approach distance given in different coordinate regions are given in figure 18 and figure 20. When the graphs of Figure 18 (a), and Figure 20 (a) are examined, the first target is in the first region of the coordinate plane, the second target is in the fourth region, and the last target is in the third region of the coordinate axis for both simulation and experimental work.

The angles calculated according to the point where the robot arrives and the point where it is desired to go and the angles realized as seen in figures 18(b)-20 (b) are given in Table 4.

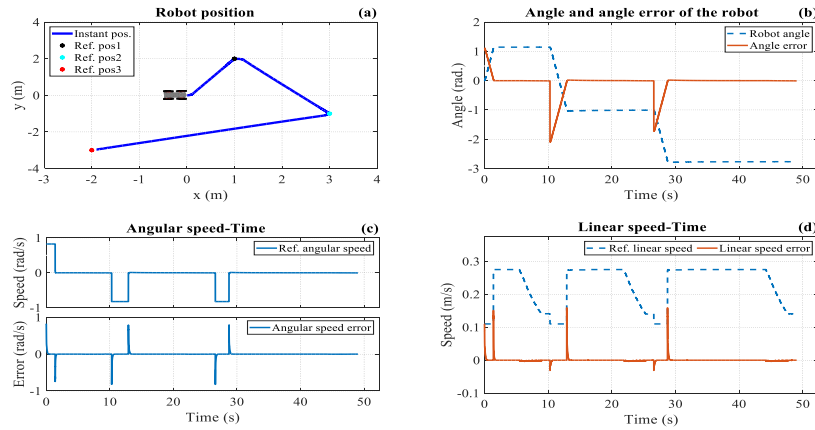


Figure 18. Simulation results for $x_1:1, y_1:2, x_2:3, y_2:-1, x_3:-2, y_3:-3$ m RVs and 0.1 m AD. Robot: (a) position, (b) Angle and angle error, (c). Angular speed and error, (d) Linear speed and error

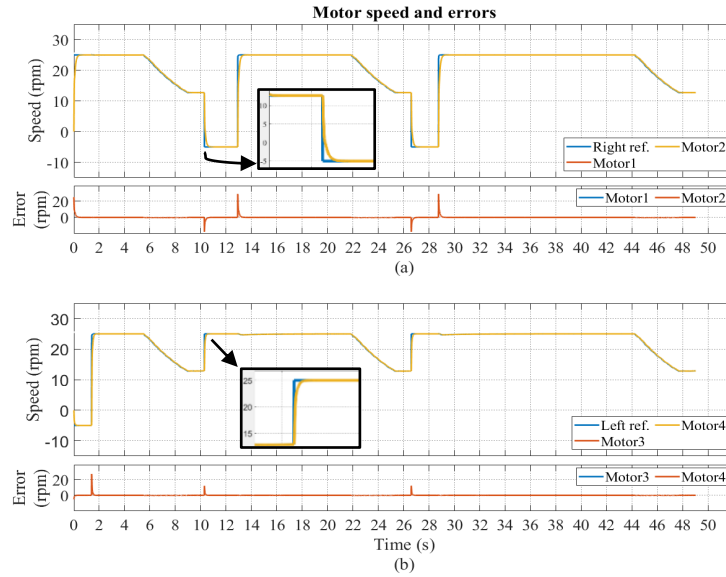


Figure 19. Simulation results for $x_1:1, y_1:2, x_2:3, y_2:-1, x_3:-2, y_3:-3$ m RVs and 0.1 m approach distance. Robot: (a) Right motor speeds and errors, (b) Left motor speeds and errors

Table 4. Calculated and actual angle values for $x_1:1, y_1:2, x_2:3, y_2:-1, x_3:-2, y_3:-3$ m RVs and 0.1 m AD

Theory			Experimental			Simulation		
Current position (m)	Target point (m)	Calculated angle (radian)	Current position (m)	Target point (m)	Realized angle (radian)	Current position (m)	Target point (m)	Realized angle (radian)
(0,0)	(1,2)	1.107	(0,0)	(1,2)	1.107	(0,0)	(1,2)	1.107
(1,2)	(3,-1)	-0.98	(0.96, 1.91)	(3,-1)	-2.1	(0.95, 1.9)	(3,-1)	-2.096
(3,-1)	(-2,-3)	-2.76	(2.97, -0.95)	(-2,-3)	-1.72	(2.94, -0.9)	(-2,-3)	-1.71

According to Table 4, when the theoretical and experimental results are compared, the rotation angle reference is 1,107 radians, since the beginning point and the first target point are the same for both. -0.98 and -2.76 radians are calculated for the second and third turns, respectively. However, in the results obtained from the experimental and simulation studies, an angle reference of -2.1 radians for the second rotation and -1.72 radians for the third rotation was determined. This is because when the robot comes to the first reference point, its instantaneous angle is relative to the x-axis $|1.117|$ is radians. Since the robot will turn 0.98 radians in the negative direction when the

instantaneous angle is added to this value, $|1.117|+|0.98|=|2.1|$ radian angle reference. Likewise, since its angle at the second point is -1.036 radians and the angle calculated for the third position is -2.76 radians, the angle at which the robot must turn is -1.72 radians. When the motor speeds given in Figure 19 and Figure 21 are examined, the speed error information in Table 5 was obtained.

Table 5. Speed errors of motors for $x_1:1, y_1:2, x_2:3, y_2:-1, x_3:-2, y_3:-3$ m RVs and 0.1 m AD

	Motor1	Motor2	Motor3	Motor4
Average absolute speed error (rpm)	0.283	0.237	0.231	0.238
Maximum speed error (rpm)	8.6660	9.1600	12.4590	12.4000

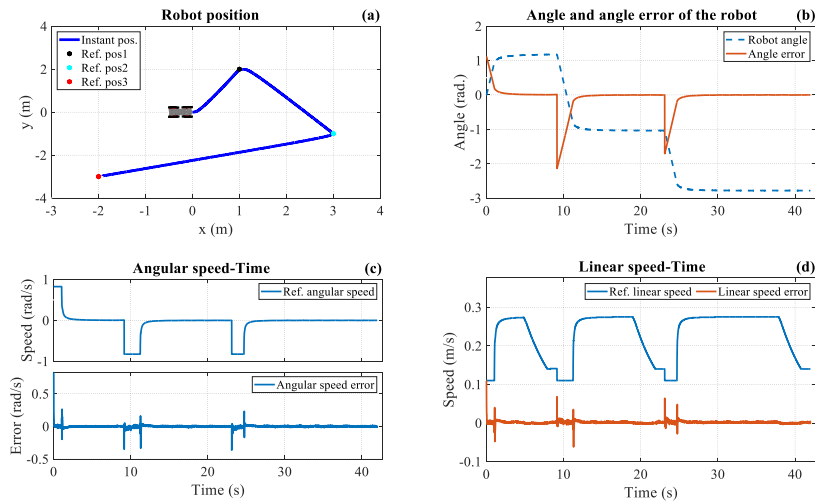


Figure 20. Experimental results for $x_1:1, y_1:2, x_2:3, y_2:-1, x_3:-2, y_3:-3$ m RVs and 0.1 m AD. Robot: (a) position, (b) Angle and angle error, (c) Angular speed and error, (d) Linear speed and error

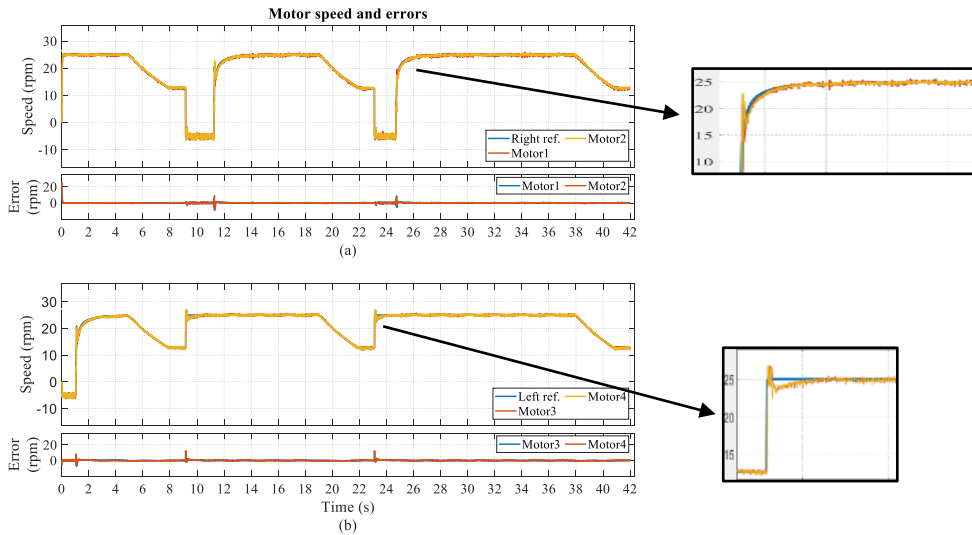


Figure 21. Experimental results for $x_1:1, y_1:2, x_2:3, y_2:-1, x_3:-2, y_3:-3$ m RVs and 0.1 m AD. Robot: (a) Right motor speeds and errors, (b) Left motor speeds and errors

5. Conclusion

In this study, a four-wheeled AMR's position control and path planning for single or multiple target coordinate points were carried out using a cascade connection of fuzzy logic and PI controllers. While the reference values of the robot were carried out remotely via Bluetooth connection with the Android application, the instant data of the robot was transferred to the Android device thanks to the same application. These data, which were collected in Excel file format, were then transferred to the computer via e-mail, and graphs were drawn in MATLAB. The position and angle information of the robot is obtained by passing the motor angular velocity information instantly from the encoders connected to the shaft of all four motors of the MR through the kinematic equations. Angle and position errors obtained by comparing reference values with instantaneous values are applied to the fuzzy logic controller as input signal. By applying the robot angular and linear velocity values obtained as the output value thanks to the created rule base to the inverse kinematic equations, the instantaneous reference angular velocity values that the motors should reach are calculated. The speed error was calculated by taking the difference between these values and the angular speed information received from the encoders and applied to the PI controller input. The motor speeds required for the position that the robot needs to reach are controlled by PI. When the graphics are examined, it was seen in both simulation and experimental studies that the MR reaches the position most shortly and without any errors in line with the given approach distance. In addition, the fact that the average absolute speed error in the motors is a maximum of 0.283 rpm shows the effectiveness of both PI and fuzzy logic controllers.

Funding: This study is supported by Firat University Scientific Research Projects Unit with the project number TEKF.19.07.

References

- [1] Shabalina K, Sagitov A, & Magid E. Comparative analysis of mobile robot wheels design. In 2018 11th International Conference on Developments in Systems Engineering; 2018; (pp. 175-179)
- [2] Alalise MB, & Hancke GP. A review on challenges of autonomous mobile robot and sensor fusion methods. *IEEE Access* 2020; 8, 39830-39846.
- [3] Liu L, Wang X, Yang X, Liu H, Li J, & Wang P. Path Planning Techniques for Mobile Robots: Review and Prospect. *Expert Systems with Applications* 2023; 120254.
- [4] Jiusheng B, Muye Z, & Shirong G. Underground driverless path planning of trackless rubber tyred vehicle based on improved A* and artificial potential field algorithm [J]. *Journal of China Coal Society* 2022; 47(03), 1347-1360.
- [5] Zhou X, Yu X, & Peng X. UAV collision avoidance based on varying cells strategy. *IEEE Transactions on Aerospace and Electronic Systems*, 2018; 55(4), 1743-1755.
- [6] Challita U, Saad W, & Bettstetter C. Deep reinforcement learning for interference-aware path planning of cellular-connected UAVs. In 2018 IEEE International Conference on Communications (ICC);2018; (pp. 1-7).
- [7] Guruprasad KR, & Ranjitha TD. CPC algorithm: Exact area coverage by a mobile robot using approximate cellular decomposition. *Robotica* 2021; 39(7), 1141-1162.
- [8] Samaniego F, Sanchis J, García-Nieto S, & Simarro R. Recursive rewarding modified adaptive cell decomposition (RR-MACD): a dynamic path planning algorithm for UAVs. *Electronics* 2019; 8(3), 306.
- [9] Jung JW, So BC, Kang JG, Lim DW, & Son Y. Expanded Douglas–Peucker polygonal approximation and opposite angle-based exact cell decomposition for path planning with curvilinear obstacles. *Applied Sciences* 2019; 9(4), 638.
- [10] Park J, Karumanchi S, & Iagnemma K. Homotopy-based divide-and-conquer strategy for optimal trajectory planning via mixed-integer programming. *IEEE Transactions on Robotics* 2015; 31(5), 1101-1115.
- [11] Wang H, Li G, Hou J, Chen L, & Hu NA path planning method for underground intelligent vehicles based on an improved RRT* algorithm. *Electronics* 2022; 11(3), 294.
- [12] Ravankar AA, Ravankar A, Emaru T, & Kobayashi Y. HPPRM: hybrid potential based probabilistic roadmap algorithm for improved dynamic path planning of mobile robots. *IEEE Access* 2020; 8, 221743-221766.
- [13] Esposito JM, & Wright JN. Matrix completion as a post-processing technique for probabilistic roadmaps. *The International Journal of Robotics Research* 2019; 38(2-3), 388-400.
- [14] Fink W, Baker VR, Brooks AJW, Flammia M, Dohm JM, & Tarbell MA. Globally optimal rover traverse planning in 3D using Dijkstra's algorithm for multi-objective deployment scenarios. *Planetary and Space Science* 2019; 179, 104707.
- [15] Balado J, Diaz-Vilariño L, Arias P, & Lorenzo H. Point clouds for direct pedestrian pathfinding in urban environments. *ISPRS Journal of Photogrammetry and Remote Sensing* 2019; 148, 184-196.
- [16] Wang YF, Cao XH, & Guo X. Warehouse AGV path planning method based on improved A* algorithm and system short-term state prediction. *Computer Integrated Manufacturing System* 2021; 1-22.
- [17] Lamini C, Benhlina S, & Elbekri A. Genetic algorithm-based approach for autonomous mobile robot path planning. *Procedia Computer Science* 2018; 127, 180-189.
- [18] Shivgan R & Dong Z. Energy-efficient drone coverage path planning using genetic algorithm. In 2020 IEEE 21st International Conference on High Performance Switching and Routing 2020; (pp. 1-6).

- [19] Miao C, Chen G, Yan C, & Wu Y. Path planning optimization of indoor mobile robot based on adaptive ant colony algorithm. *Computers & Industrial Engineering* 2021; 156, 107230.
- [20] Ji Y & Liu B. Research and Implementation of Robot Path Planning Based on Ant Colony Algorithm. In *Journal of Physics: Conference Series* 2022; (Vol. 2171, No. 1, p. 012074).
- [21] Chai R, Tsourdos A, Savvaris A, Chai S & Xia Y. Solving constrained trajectory planning problems using biased particle swarm optimization. *IEEE Transactions on Aerospace and Electronic Systems* 2021;57(3), 1685-1701.
- [22] Qiuyun T, Hongyan S, Hengwei G & Ping W. Improved particle swarm optimization algorithm for AGV path planning. *Ieee Access* 2021; 9, 33522-33531.
- [23] Wang Z, Li H & Zhang X. Construction waste recycling robot for nails and screws: Computer vision technology and neural network approach. *Automation in Construction* 2019; 97, 220-228.
- [24] Zhu D & Yang SX. Bio-inspired neural network-based optimal path planning for UUVs under the effect of ocean currents. *IEEE Transactions on Intelligent Vehicles* 2021; 7(2), 231-239.
- [25] Zadeh LA. Fuzzy sets. *Information and control* 1965; 8(3), 338-353.
- [26] Li M. Mobile robot path planning based on fuzzy control. Hebei University of Technology. 2015
- [27] Xie YN. The research for the mobile robot path planning algorithm[D]. Xi 'a University of Architecture and Technology. 2016.
- [28] Zagradjanin N, Rodic A, Pamucar D & Pavkovic B. Cloud-based multi-robot path planning in complex and crowded environment using fuzzy logic and online learning. *Information Technology and Control* 2021; 50(2), 357-374.
- [29] Ntakolia C & Lyridis DV. A swarm intelligence graph-based pathfinding algorithm based on fuzzy logic (SIGPAF): A case study on unmanned surface vehicle multi-objective path planning. *Journal of Marine Science and Engineering* 2021; 9(11), 1243.
- [30] Gharajeh MS, & Jond HB. An intelligent approach for autonomous mobile robots path planning based on adaptive neuro-fuzzy inference system. *Ain Shams Engineering Journal* 2022; 13(1), 101491.
- [31] Jin X, Chen K, Zhao Y, Ji J, & Jing P. Simulation of hydraulic transplanting robot control system based on fuzzy PID controller. *Measurement* 2020; 164, 108023.
- [32] Cao G, Zhao X, Ye C, Yu S, Li B, & Jiang C. Fuzzy adaptive PID control method for multi-mecanum-wheeled mobile robot. *Journal of Mechanical Science and Technology* 2022; 36(4), 2019-2029.
- [33] Babunski D, Berisha J, Zaev E, & Bajrami X. Application of fuzzy logic and PID controller for mobile robot navigation. In *2020 9th Mediterranean Conference on Embedded Computing*; 2020; (pp. 1-4).
- [34] Cai C. Autonomous Mobile Robot Obstacle Avoidance Using Fuzzy-PID Controller in Robot's Varying Dynamics. In *2020 39th Chinese Control Conference*; 2020; (pp. 2182-2186). IEEE.
- [35] Lee K, Im DY, Kwak B, & Ryoo YJ. Design of fuzzy-PID controller for path tracking of mobile robot with differential drive. *International Journal of Fuzzy Logic and Intelligent Systems* 2018; 18(3), 220-228.
- [36] Top A, & Gökbulut M. A novel period-based method for the measurement direct current motor velocity using low-resolver encoder. *Transactions of the Institute of Measurement and Control* 2023; 45(4), 711-722.
- [37] Pololu 37D Metal Gearmotors Datasheet 18s., www.pololu.com/product/4756/specs, Access: 08.12.2023
- [38] Sparkfun Monster Moto Shield and VNH2SP30 datasheet <https://www.sparkfun.com/products/retired/10182>, Access:20.12.2023
- [39] HM-10 bluetooth modul, [http://www.martyncurrey.com/hm-10-bluetooth-4ble-modules/#HM-10Services_and Character istics](http://www.martyncurrey.com/hm-10-bluetooth-4ble-modules/#HM-10Services_and_Characteristics), Access: 08.12.2023
- [40] Arduino Due, <https://store.arduino.cc/products/arduino-due>, Access: 08.12.2023
- [41] Top A, & Gökbulut M. Android Application Design with MIT App Inventor for Bluetooth Based Mobile Robot Control. *Wireless Personal Communications* 2022; 126(2), 1403-1429.
- [42] Hong S, & Hwang Y. design and implementation for iort-based remote control robot using block-based programming. *Issues in Information Systems* 2020; 21(4), 317-330.
- [43] De Moura Oliveira PB. Teaching automation and control with App Inventor applications. In *2015 IEEE Global Engineering Education Conference*; 2015; (pp. 879-884). IEEE.
- [44] Asghar MZ, Sana I, Nasir K, Iqbal H, Kundi FM, & Ismail S. Quizzes: Quiz application development using Android-based MIT APP Inventor platform. *International Journal of Advanced Computer Science and Applications* 2016; 7(5).
- [45] Sullivan D, Chen W, & Pandya A. Design of remote control of home appliances via Bluetooth and Android smartphones. In *2017 IEEE International Conference on Consumer Electronics-Taiwan*; 2017; (pp. 371-372).
- [46] Prayogo SS, Saptariani T, & Salahuddin NS. Rancang Aplikasi Android Pengendali Mobil dan Kamera Menggunakan APP inventor, *Seminar Nasional Aplikasi Teknologi Informasi* 2015; (Vol. 1, No. 1).
- [47] Kannapiran S, & Chakrapani A. A novel home automation system using Bluetooth and Arduino, *international journal of advances in computer and electronics engineering* 2017; 2(2), 41-44.
- [48] Adiono T, Anindya SF, Fuada S, Afifah K, & Purwanda IG. Efficient android software development using mit app inventor 2 for bluetooth-based smart home. *Wireless Personal Communications* 2019;105(1), 233-256.
- [49] Karakus M, Uludag S, Guler E, Turner SW, & Ugur A. Teaching computing and programming fundamentals via App Inventor for Android, *2012 International Conference on Information Technology Based Higher Education and Training*; 2012;(pp. 1-8). IEEE.
- [50] Kushwah M, & Patra A. Tuning PID controller for speed control of DC motor using soft computing techniques-A review. *Advance in Electronic and Electric Engineering* 2014; 4(2), 141-148.
- [51] Ang KH, Chong G, & Li Y. PID control system analysis, design, and technology. *IEEE transactions on control systems technology* 2005; 13(4), 559-576.

Comparative Analysis of Wavelet Families in Image Compression, Featuring the Proposed New Wavelet

İbrahim ÖZ^{1*}

¹ Ankara Yıldırım Beyazıt Üniversitesi, TTO, Ayvalı Mah. Ankara, Türkiye
*¹ ibrahimoz@gazi.edu.tr

(Geliş/Received: 30/01/2024;

Kabul/Accepted: 28/03/2024)

Abstract: Image compression is fundamental to the efficient and cost-effective use of digital media, including but not limited to medical imagery, satellite images, and daily photography. Wavelet transform is one of the best methods used in compression. This study conducts a meticulous comparative analysis of various established wavelet families and introduces a novel wavelet named new wavelet for image compression (NWI), shedding light on its performance compared to well-established counterparts. This research conducts a meticulous comparative analysis of various wavelet families to assess their performance in image compression. The results show that an average compression ratio of around 75% can be achieved with a 38 dB PSNR value for all test images. The best result was achieved with the test-2 image, with a compression performance (CP) of 3312.08, using the proposed NWI wavelet. The research evaluates eight wavelet families and shows that the performance of image compression depends on both image type and selected wavelet family while keeping the coding algorithm the same for all calculations of image processing scenarios. In image compression, introducing new wavelet families, such as the NWI, can enhance performance and achieve better results.

Keywords: Wavelet, image compression, image processing, compression ratio, signal-to-noise ratio

Görüntü Sıkıştırma Dalgacık Ailelerinin Karşılaştırmalı Analizi ve Yeni bir Dalgacık Ailesi Önerisi

Öz: Görüntü sıkıştırma, tıbbi görüntülerden uydu görüntülerine ve günlük fotoğrafçılığa kadar dijital medyanın verimli ve maliyet etkili kullanımı için temel bir gerekliliktir. Dalgacık dönüşümü, görüntü sıkıştırma için kullanılan en iyi yöntemlerden biridir. Bu araştırma, en çok bilinen dalgacık ailelerinin görüntü sıkıştırma performansını çeşitli analizlerle değerlendirmiştir. İlave olarak nwi adlı yeni bir dalgacık ailesi üretilmiş ve performansı bilinen dalgacık aileleri ile karşılaştırılmıştır. Sıkıştırma Oranı (CR) ve Tepe Sinyal-Gürültü Oranı (PSNR) gibi nicel ölçüleri kullanarak, tablolar ve şekillerde sunulan sonuçlar, farklı dalgacık dönüşümlerinin performansını göstermektedir. Sonuçlar, tüm test görüntüleri için ortalama %75 sıkıştırma oranının 38 dB PSNR değeri ile elde edilebileceğini göstermektedir. En iyi sonuç, önerilen NWI dalgacığı ile test-2 görüntüsünde sıkıştırma performansı (CP) 3312,08 değeri ile elde edilmiştir. Bu çalışmada, sekiz dalgacık ailesi değerlendirilmekte ve görüntü sıkıştırma performansının hem görüntü türüne hem de seçilen dalgacık ailesine bağlı olduğu sonucu çıkmaktadır. Kodlama algoritması tüm dalgacık aileleri için aynı tutularak sadece dalgacık dönüşüm performansı analiz edilmiştir. Görüntü sıkıştırma için yeni ve etkili dalgacık ailelerinin gerçekleştirilebileceği NWI önerisinde olduğu gibi gösterilmiştir.

Anahtar kelimeler: Dalgacık, görüntü sıkıştırma, sıkıştırma oranı, sinyal gürültü oranı.

1. Introduction

The ubiquity of digital images in various domains, including social media platforms, satellite imagery, and medical imaging, has led to a surge in daily usage. However, the storage and transmission of uncompressed multimedia data, encompassing videos, photos, graphics, and audio, pose challenges due to their substantial space and bandwidth requirements. Efficient systems with sufficient memory and robust processors are essential for handling the storage and processing demands associated with such unprocessed data.

Both moving and still images are frequently broadcasted for human consumption. During viewing, imperceptible details can be selectively removed from storage to mitigate data size and reduce transmission bandwidth while maintaining a predefined image quality threshold.

Compression is pivotal in addressing these challenges, allowing videos and images to occupy less storage space and utilize minimal bandwidth during transmission without compromising perceptible image quality. Raw images generated by contemporary digital devices exhibit considerable data size and transmission rates. For instance, in high-definition image systems like HD (1920x1080 pixels), a standard image requires a 16.5 Mbyte file size. In more advanced systems such as 4KHD (3840x2160 pixels), this requirement escalates to 66 Mbyte.

The transmission and storage of image signals at exceedingly high data rates pose practical challenges. Consequently, the most viable solution is to employ compression techniques to reduce the file size and data rate

* Corresponding author: ibrahimoz@gazi.edu.tr. ORCID 0000-0003-4593-917X

to manageable levels. Digital images are compressed by removing redundant information, with three primary types of redundancy addressed [1]. **Spatial Redundancy:** In natural images, neighboring pixels often exhibit very close values. As a result, identical pixels are not individually coded; instead, the information that they share the same value is stored. The focus is on preserving the different information between closely located pixels, minimizing the need for redundant coding. **Temporal Redundancy:** In video sequences, successive frames typically have minimal changes. Regions of the frame that remain unchanged over time contribute to temporal redundancy. The information indicating that these areas are consistent with the previous frame is stored to optimize storage and transmission. Temporal redundancy reduction is particularly crucial in video compression scenarios. **Spectral Redundancy:** Image portions divided into frequency bands exhibit spectral values of closely located pixels that are very similar. These subtle details, often imperceptible to the human eye, are discarded. By doing so, the method efficiently eliminates spectral redundancy, preventing the unnecessary repetition of similar information and effectively shortening the data series representing the image information [2].

These redundancy reduction methods collectively contribute to a streamlined representation of image data, ensuring more efficient transmission and storage without compromising essential visual information.

The Discrete Wavelet Transform (DWT) is a widely utilized signal and image analysis tool. It dissects data into approximation and detail coefficients using filters, capturing localized and overall variations. The hierarchical decomposition facilitated by DWT allows for efficient data representation and compression. This transformative method finds applications in diverse fields, such as compression, noise removal, and feature extraction. Despite its proficiency in preserving crucial details, it is essential to note that DWT may introduce blocking artifacts and possess higher computational complexity when compared to simpler transforms [3].

Signal processing has seen a burgeoning interest in wavelets and wavelet transforms, marking a significant area of research. Their applications, especially in the 2D Discrete Wavelet Transform (DWT) context, have become pivotal in multimedia applications such as JPEG2000 and MPEG-4 standards, multimedia information recovery systems, and digital watermarking. The discrete mayor wavelet demonstrates remarkable effectiveness in image deblurring. Biorthogonal wavelets have been proposed to expedite the processing of geometric models, while the Fejer-korovkin wavelet exhibits a commendable response in human noise identification within multimedia applications. A novel method for enhancing image contrast, termed low dynamic range histogram equalization (LDR-HE), is introduced. This method relies on the Quantized Discrete Haar Wavelet Transform (HWT) in the frequency domain [4].

In addressing the challenges associated with separating noise from partial discharge signals, efforts have been directed towards Fourier transform, applied in the frequency or time domains. However, inherent limitations arise, as acquiring information from both time and frequency domains simultaneously proves elusive. To overcome these challenges, researchers have turned to coiflet and symlet wavelet transformations.

While the 2D DWT plays a pivotal role in multimedia applications, it comes with computational complexity, especially compared to other functions like those in the JPEG2000 standard. Consequently, many architectures have been proposed to process 2D DWT efficiently. Its application extends to enhanced ultrasonic flaw detection, and innovative structures, such as a memory-efficient 2D DWT for JPEG2000, have been put forth. This proposed structure involves a 1D column processor, internal memory, and a 1D row processor, with a primary advantage being reducing memory requirements [5].

There are numerous fields where wavelet applications find relevance, and authors have introduced various image compression techniques. These contributions have been published and shared within the academic community and among professionals.

By harnessing influential frequency bands through wavelet transform and selecting high-performance features, it is possible to detect faults in power transmission lines using ensemble learning, specifically addressing discharge faults [6]. The application of wavelet transform can be employed to address the challenge of eliminating noise arising from abrupt changes in very low frequency (VLF) signals utilized in remote sensing, which is particularly crucial for the detection of sub-ionospheric events. In industrial applications, specifically asynchronous motors, misalignment faults, including issues like loose connections and angular imbalances, can be effectively analyzed using Wavelet, transform [7].

Efficient storage and transmission of medical images are pivotal in telemedicine. The application of wavelet transform proves instrumental in achieving near-lossless compression in medical image data [8]. Utilizing wavelet transform and machine learning techniques, it is feasible to classify individuals into categories of colon cancer patients and healthy subjects based on signal analysis. [9]. The method accurately classifies colon cancer patients, providing a robust methodology for distinguishing between health conditions.

Efficient and cost-effective utilization of digital medical imaging in applications like teleradiology and Picture Archiving and Communication Systems (PACS) necessitates advanced image compression techniques. In a comparative study between JPEG and Wavelet compression, the Wavelet Compression Engine and JPEG Wizard tools were employed to compress and decompress a digitized chest X-ray image at various ratios. Wavelet

compression demonstrated lower error matrices and higher peak signal-to-noise ratios, with no significant differences in diagnostic accuracy up to 30:1 compression ratios. Visual comparisons confirmed minimal image degradation, and the wavelet algorithm achieved an impressive compression ratio of up to 600:1. [10]. The Wavelet-Based Deep Auto Encoder-Decoder Network (WDAED) for image compression addresses various frequency components in images. The proposed approach incorporates Wavelet transform pre-processing and a deep super-resolution network in the decoder for improved decompression quality. The algorithm is tested on various datasets, demonstrating superior compression performance across multiple evaluation metrics. [11]. An enhanced algorithm for image compression based on wavelet properties, specifically targeting detail subbands (Diagonal, Vertical, and Horizontal), is analyzed by hard thresholding. Using the standard deviation concept, the proposed algorithm estimates an optimal threshold value for each detail subband. The experiment results demonstrate the algorithm's effectiveness in removing unnecessary wavelet coefficients without compromising image quality. This leads to increased compression ratios and reduced elapsed time, showcasing the potential of the proposed approach. A novel method for enhancing image contrast, termed low dynamic range histogram equalization (LDR-HE), is introduced. This method relies on the Quantized Discrete Haar Wavelet Transform (HWT) in the frequency domain [12].

Investigations are conducted using a hybrid transform for lossless image compression, combining the discrete wavelet transform (DWT) with prediction. The approach involves reversible denoising and lifting steps (RDLSs) with step skipping, applied in an image-adaptive manner using heuristics and entropy estimation. The research demonstrates the effectiveness of combining DWT with prediction, achieving notable compression ratio improvements over JPEG 2000. The study presents practical compression schemes with various trade-offs, providing valuable insights for optimizing compression methods. [13]. Exploring the use of 2-D multiple-level discrete Wavelet transform for image compression shows that after obtaining approximation and detail coefficients through multiple-level Wavelet transform, the superior compression performance of wavelet-based methods compared to other compression techniques was achieved. [14].

Transform coding, especially the Discrete Wavelet Transform (DWT), stands out among effective lossy compression methods. Wavelet-based image coding schemes, including transformation, quantization, and coding, delve into the principles of popular schemes like EZW, SPIHT, SPECK, and EBCOT, comparing their advantages and shortcomings. Designing efficient codecs for wavelet image compression, incorporating spline transform and improved coding schemes. [15].

To address the increasing demand for faster encoding and decoding, researchers proposed an image compression algorithm that combines 2D DWT, PCA, and canonical Huffman coding (CHC). The hybrid compression model achieves up to 60% compression while maintaining high visual quality. Their proposed method effectively utilizes storage space in the growing image data usage era. [16].

The application of two-dimensional discrete wavelet transform (2D DWT) in the compression of both video and still images has been explored, employing innovative compression techniques such as PAQ. The outcomes of this investigation demonstrate that these methods are successful and practical in their applicability [2].

The Huffman coding algorithm compresses and decomposes images by incorporating the Discrete Wavelet Transform. The approach decomposes the image into distinct sets of signals encoded into a bit stream, resulting in improved compression. The proposed algorithm surpasses other techniques in compression ratio, compression time, and bits per pixel. [17].

The critical challenge of signal identification under uncertainty, focusing on filtering and compression using the Discrete Wavelet Transform (DWT), was analyzed in a separate study. The method involved a comparison of the proximity of a one-dimensional series of wavelet coefficients, providing a robust solution. The results underscored wavelets' effectiveness in signal identification and compression, contributing substantially to the existing literature [18].

In another study, innovative image compression techniques are introduced, employing multiwavelets and multiwavelet packets. The research addresses limitations in existing wavelet filters, exploring multiwavelets to provide more design options and combine desirable transform features. Experimental results showcase the superior performance of these techniques, either matching or surpassing current wavelet filters. This research contributes to advancing image compression standards and offers valuable insights for future optimization [19].

A researcher introduces a novel approach to image compression utilizing subspace techniques and downsampling. The methodology begins by reducing the size of the image through downsampling. Subsequently, the Karhunen-Loeve transform (KLT) is employed on the downsampled image to generate a series of transform coefficients [20]. Another study delves into the efficacy of subspace-driven coding methodologies in the context of compression [21]. Another researcher analyzes different Wavelet transforms. The evaluation involves assessing performance using Peak Signal-to-Noise Ratio (PSNR) and Mean Square Error (MSE). The results highlight differences among wavelet families [22].

A researcher evaluated various wavelet difference reduction (WDR) methods, focusing on their image compression and transmission performance. WDR demonstrates coding gains compared to traditional coding approaches, emphasizing the convenience and superiority of modified WDR methods for diverse applications [23].

This study centers around the comprehensive exploration of various wavelet families to evaluate their performance in the domain of image compression.

2. Wavelet Transform

Wavelet transform is a versatile mathematical tool for analyzing signals with dynamic changes in frequency attributes over time. Its applicability extends to signals of one, two, or higher dimensions, preserving unique signal features. This transformative process involves decomposing a signal to obtain a set of basis functions known as wavelets. These wavelets, focused on both frequency and time around specific points, play a pivotal role in achieving approximation through the summation of short-lived waves, aptly named wavelets. The compact support characteristic signifies that wavelets do not extend indefinitely in the signal.

Moreover, wavelets exhibit asymmetry and irregularity, making them valuable in signal processing. The zero-sum area beneath the wavelet curve ensures equal energy distribution in both positive and negative directions. In signal processing, wavelets effectively recover weak signals from noise and analyze signals with dynamic frequency changes over time [22].

$$f = \sum_i a_i \psi_i \tag{1}$$

Choosing scales and positions based on powers of two, known as dyadic scales and positions, enhances the efficiency and accuracy of our analysis. This analytical improvement is achieved through the discrete wavelet transform (DWT), and Mallat developed a particularly efficient implementation of this approach using filters.

The practical filtering algorithm provided by Mallat facilitates a rapid wavelet transform—a process resembling a box through which a signal passes, yielding wavelet coefficients swiftly. This analysis, derived from the discrete wavelet transform (DWT) [14], initiates from the signal s and produces the coefficients $C(a, b)$.

$$C(a, b) = C(j, k) = \sum_{n \in Z} s(n) g_{j,k}(n) \tag{2}$$

In signal processing, wavelets serve to recover weak signals embedded in noise. Their asymmetric and irregular nature sets them apart. Signal decomposition occurs through scaled and shifted versions of the original Wavelet, termed the mother wavelet, in wavelet analysis. Scaling involves modifying the signal along its time attribute by expanding or compressing it.

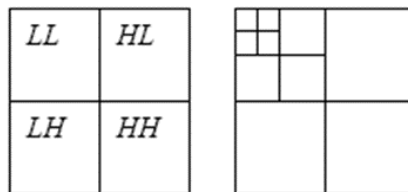


Figure 1. The multilevel decomposition of the image, displaying a 2-level decomposition in this instance

In the process of multilevel image decomposition, the image is systematically broken down into multiple levels or layers to extract detailed information. This intricate procedure involves applying Wavelet transforms that facilitate the isolation of various frequency components within the image. Each level of decomposition reveals specific details, contributing to a more comprehensive understanding of the image's structural and textural characteristics.

Furthermore, this multilevel decomposition allows for extracting both coarse and fine features in the image. The decomposition process operates iteratively, progressively unveiling hidden nuances within the visual data. Through this method, the image's complexity is effectively captured and represented at different scales, providing a hierarchical representation that enhances the analysis of its content.

2.1 Wavelet Families

Different families of wavelets are used in signal processing and analysis. Each wavelet family has its own unique properties and characteristics that make them suitable for various applications. This study investigates the

application of seven well-known wavelet families (haar, dB10, sym7, coif3, bir5.5, rbio2.6, and dmey). These wavelet families are selected based on their widespread recognition and utilization in JPEG 2000. A concise overview of seven widely recognized wavelet families, each distinguished by unique properties and applications in signal processing and image compression.

Haar Wavelet: The Haar wavelet is the most straightforward function operating with two coefficients. It's a piecewise constant function and is computationally efficient. While it lacks smoothness, it's often used in introductory studies due to its simplicity.

dB10 Wavelet: The "dB" in "dB10" stands for Daubechies, a famous family of wavelets known for its compact support and orthogonality. dB10 is a specific wavelet from the Daubechies family, characterized by 10 vanishing moments, which means it captures more complex signal features.

Sym7 Wavelet: This belongs to the Symlets family, an extension of Daubechies wavelets with slightly improved symmetry. Symlets offer good performance in compressing signals with edges and details.

Coif3 Wavelet: Coiflets, or Coiflet wavelets, are similar to Daubechies and Symlets but have a different shape. Coif3, in particular, is from this family and helps analyze signals with finite support.

Bior5.5 Wavelet: Bior stands for "Biorthogonal" wavelets, which use separate sets of functions for decomposition and reconstruction. The 5.5 represents the number of vanishing moments in each of these functions. Biorthogonal wavelets like Bior5.5 are valuable for handling non-stationary signals.

Rbio2.6 Wavelet: Another member of the biorthogonal wavelet family, Rbio2.6, has different characteristics compared to Bior5.5. The numbers in the name indicate the number of vanishing moments for the analysis and synthesis wavelets, respectively.

Dmey Wavelet: The Dmey wavelet, also known as the Meyer wavelet, is derived from a function introduced by Yves Meyer. It's characterized by smoothness and symmetry and is often used in image compression and denoising applications.

Each of these wavelets has specific properties regarding frequency response, vanishing moments, support, and other characteristics that make them suitable for different types of signal analysis, compression, and feature extraction tasks. The choice of Wavelet depends on the specific requirements and characteristics of the signal being analyzed or processed.

3. Method: Wavelet-Based Image Compression and Reconstruction

Image compression using wavelets involves transforming and analyzing individual images. Wavelet transforms and decomposes an image into its frequency components, creating a multi-resolution representation. This transformation allows for efficient compression by removing redundant or less noticeable image data while preserving crucial visual information. Figure 2 illustrates the sequential steps involved in image processing, commencing with the application of wavelet transform, followed by quantization, coding, and culminating in the generation of the compressed image.

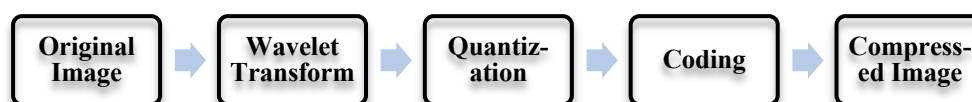


Figure 2. The block diagram illustrates the image compression process employing Wavelet transform.

Wavelet-based image compression typically involves spatial information compression. It takes advantage of the spatial redundancy present in images, identifying and reducing unnecessary pixel data while retaining essential details.

In multilevel wavelet decomposition, images are divided into sub-bands like LL (low-low), LH (low-high), HL (high-low), and HH (high-high) using the wavelet transform. These sub-bands represent different frequency components of the image.

This compression technique finds applications in various fields, such as photography, medical imaging, satellite imagery, and digital libraries, where single images must be stored, transmitted, or processed efficiently.

Upon transforming image data through wavelets, the subsequent application of thresholding and quantization processes becomes imperative. Subband thresholding is a technique used in signal processing and image compression. It involves dividing a signal or image into different frequency bands or subbands and applying a threshold to the coefficients within these subbands. This thresholding helps to reduce less significant or noisy information, leading to compression [24].

Quantization, as a crucial step in the image compression workflow, reduces the number of symbols within the data matrix. This process is essential for efficiently compressing data and optimizing memory usage. The wavelet coefficients undergo quantization using a carefully selected quantizer, ensuring that the transformed data is represented with an appropriate level of precision while effectively managing storage requirements. The meticulous application of quantization aligns with the overarching goal of image compression, enabling the preservation of essential information while minimizing the memory footprint of the compressed data.

Following the quantization process, the data undergo compression, particularly in image compression, where quantization and coding techniques are employed. In image compression workflows, lossy compression techniques are expected to be used at this stage. The outcome of this process is the acquisition of compressed images characterized by a significantly reduced file size. This reduction in file size is a key objective in image compression, allowing for more efficient storage, transmission, and handling of visual data while acknowledging the inherent trade-offs associated with lossy compression methods.

Huffman coding is a widely used entropy coding algorithm in information theory and compression. A variable-length coding method assigns shorter codes to more frequent symbols and longer codes to less frequent symbols. Huffman coding is often used to compress data efficiently, and it's a key component in many compression algorithms.

Huffman coding stands as a widely adopted algorithm for achieving image compression. This algorithm meticulously analyzes the frequencies of pixel values, assigning shorter codes to frequently occurring symbols and longer codes to those that are less common, resulting in the construction of a Huffman tree. However, the conventional Huffman coding approach necessitates the decoder to traverse the entire tree, introducing potential inconvenience. The classical Huffman algorithm has been extensively employed in both data compression and image compression applications. One notable drawback of the traditional Huffman algorithm is its reliance on variable-length codes for symbol representation dictated by their frequency of occurrence. Although this strategy effectively compresses frequently encountered symbols, it may generate lengthier codes for symbols that occur less frequently.

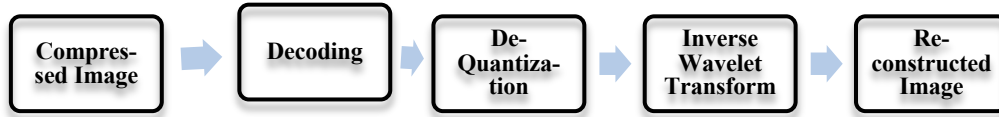


Figure 3. Block diagram for the reconstruction of the compressed image.

Following the acquisition of the compressed image, the processes mentioned above are reversed, as illustrated in the block diagram presented in Figure 3. The decoding process involves reversing compression, wherein the compressed image undergoes dequantization. Subsequently, an inverse wavelet transform is applied to restore the original data structure. The culmination of these processes leads to reconstructing the image in its original form. This intricate series of operations ensures that the information lost during compression is recuperated, restoring the visual data to its pre-compressed state.

3.1. Development of the Novel NWI Wavelet in Image Compression

In this research, a novel wavelet is developed and explicitly proposed for image compression, referred to as "new wavelet for image compression" or NWI. This new Wavelet is a variant of the Daubechies filter, with enhanced performance observed when scaling function frequency and vanishing moment are increased [24]. Well-localized elements characterize the NWI wavelet family. A set of N integer coefficients defines each Wavelet in the family represented as $k = \{0, 1, \dots, N - 1\}$, established through scale relations in Equation 3 and 4. The coefficients a_k and a_{1-k} , featured in Equations 3 and 4, are filter coefficients, and their relationships are expressed [25] as;

$$\phi(x) = \sum_{k=0}^{N-1} a_k \phi(2x - k) \quad (3)$$

$$\psi(x) = \sum_{k=2-N}^1 (-1)^k a_{1-k} \phi(2x - k) \quad (4)$$

Figure 4.a) displays the proposed wavelet family, NWI 20, while Figure 4.b) illustrates the mother wavelet, Daubechies 10. These figures provide visual representations of the wavelet functions, highlighting the distinctive characteristics of the newly introduced NWI 20 wavelet and comparing it to the well-established Daubechies 10 wavelet.

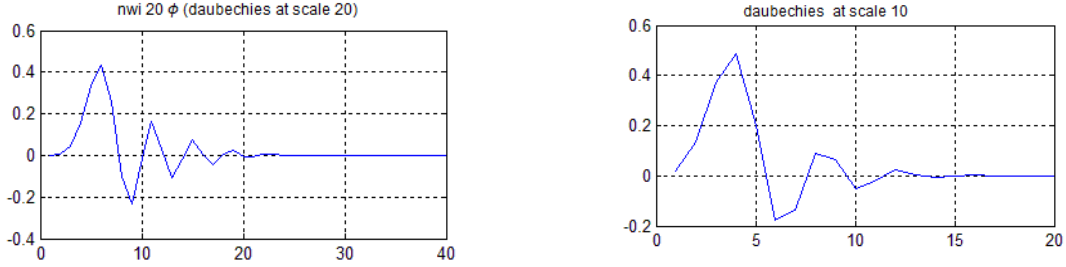


Figure 4. a) NWI wavelet b) daubechies wavelet

Standard test images such as Lena, house, lake, and tree are chosen to assess the efficacy of these wavelet transformations. These images are widely recognized and serve as benchmarks for readers' convenience in image compression.

3.2 Measurement of Image Quality

In lossy compression, the reconstructed image's pixel values differ from the original image's pixel values. If the difference between the original and reconstructed images is imperceptible to the human eye, it signifies good compression. In this study, the Peak signal-to-noise ratio (PSNR) has been used to measure the quality of the reconstructed image. The PSNR serves as a metric to quantify the peak error in decibels. Its relevance is constrained to data encoded in terms of bits per sample or bits per pixel. A higher PSNR value corresponds to enhanced quality in the compressed or reconstructed image. In the context of lossy compression, typical PSNR values for an image range between 30 and 50 dB. Notably, the two images become indistinguishable when the PSNR surpasses 40 dB. The following equation defines the PSNR:

$$PSNR = 10 \log_{10} \left(\frac{\max^2}{MSE} \right) \quad (5)$$

max: color depth. For 8 bits $\max=2^8-1=255$, and mean square error can be calculated with Equation 6;

$$MSE = \frac{1}{mn} \sum_{i=0}^{m-1} \sum_{j=0}^{n-1} |X(i, j) - X_c(i, j)|^2 \quad (6)$$

Where, M and N represents the size of the image, X represents the given input image and X_c represents the reconstructed image.

The compression ratio (CR) is defined as the proportion of elements in the compressed image to the number of elements in the original image, expressed as a percentage. It is employed to determine the compression percentage attained by a compression algorithm, calculated through the Equation 7.

$$CR = \left(1 - \frac{h_c}{h_i} \right) * 100 \quad (7)$$

Where h_c : number of bits of the compressed image, h_i : number of bits of the initial image

The Compression Performance (CP) metric, initially introduced by Bulut et al. [26], combines the Peak Signal-to-Noise Ratio (PSNR) as the quality measure and Compression Ratio (CR) as the compression metric. This hybrid metric effectively captures the correlation between PSNR and CR, enabling a comprehensive assessment of compression performance. The formulation of CP in Equation 8 as follow;

$$CP = PSNR \times CR \quad (8)$$

A higher CP value indicates superior performance in image compression, emphasizing the ability to achieve higher levels of compression without compromising image quality.

All selected test images undergo compression using the seven established wavelet families and the newly developed NWI wavelet. The results are then evaluated using two key performance metrics: Compression Ratio (CR), Peak signal-to-noise ratio (PSNR) and Compression Performance (CP). This comprehensive analysis aims to provide insights into the comparative performance of different wavelet families, including the innovative NWI wavelet, in the context of image compression.

4. Results and Discussions

This study systematically evaluates the performance of eight distinct wavelet families, including the proposed "NWI" wavelet, using eight diverse test images, consistently employing the Huffman compression method across all wavelet families. The uniform use of Huffman compression allows for an analysis of the efficacy of the wavelet families while minimizing the impact of coding variations in the process [27]. The objective is to evaluate the overall effectiveness of these wavelet families and compare them with the developed and proposed NWI Wavelet across a spectrum of images, aiming to gain a comprehensive understanding of their performance variations in diverse scenarios.

In this study, we utilized a set of standard, widely recognized test images for our analysis as shown in Figure 5. The images chosen include House, Lenna, Lake, and Tree, which were specifically selected to assess medium to low-frequency responses of the wavelet families. Additionally, Peppers, Baboon, Boat, and Airplane images were incorporated to evaluate the high-frequency response of the wavelet families.

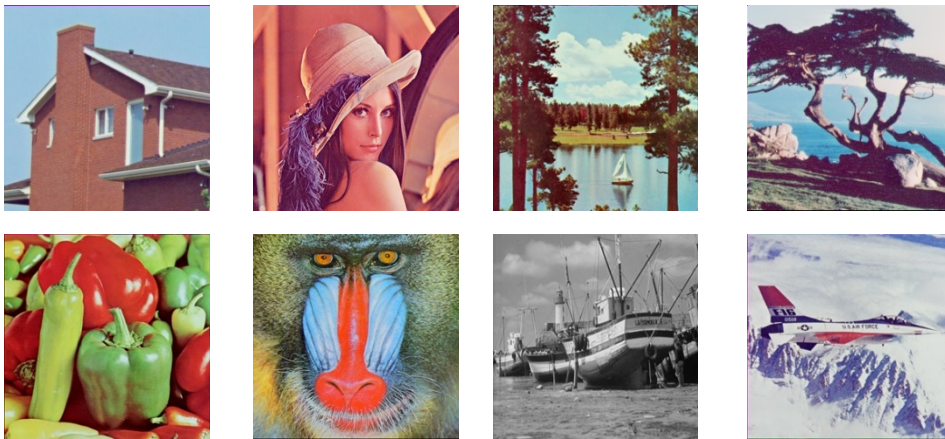


Figure 5. Eight test images, arranged from top left to right as House, Lenna, Lake, Tree, and from bottom left to right as Peppers, Baboon, Boat, and Airplane.

Figure 6 offers an exhaustive examination of the compression performances demonstrated by eight distinct wavelet families across eight test images. The analysis encompasses a range of threshold values applied with Huffman coding, allowing for exploring diverse compression ratios. This comprehensive evaluation provides valuable insights into the varying capabilities of each wavelet family in achieving optimal compression results for the specified test images under different threshold settings, thereby contributing to a nuanced understanding of their performance characteristics. The results depicted in Figure 6.a) and 6.b) highlight notable similarities in the compression outcomes for the House and Lenna images, wherein the difference in image quality between the best and worst-performing wavelet family is approximately 3 dB. Sym7 and Coif3 emerge as the top-performing wavelet families, while rbio2.6 exhibits the least favorable performance. Considering the proposed NWI wavelet, it exhibits superior performance compared to the other seven wavelet families.

The reconstructed image quality is approximately 1 dB higher than that achieved with the Coif3 wavelet. This enhancement in performance highlights the efficacy of the proposed NWI wavelet in image reconstruction, demonstrating its potential for superior results compared to established wavelet families.

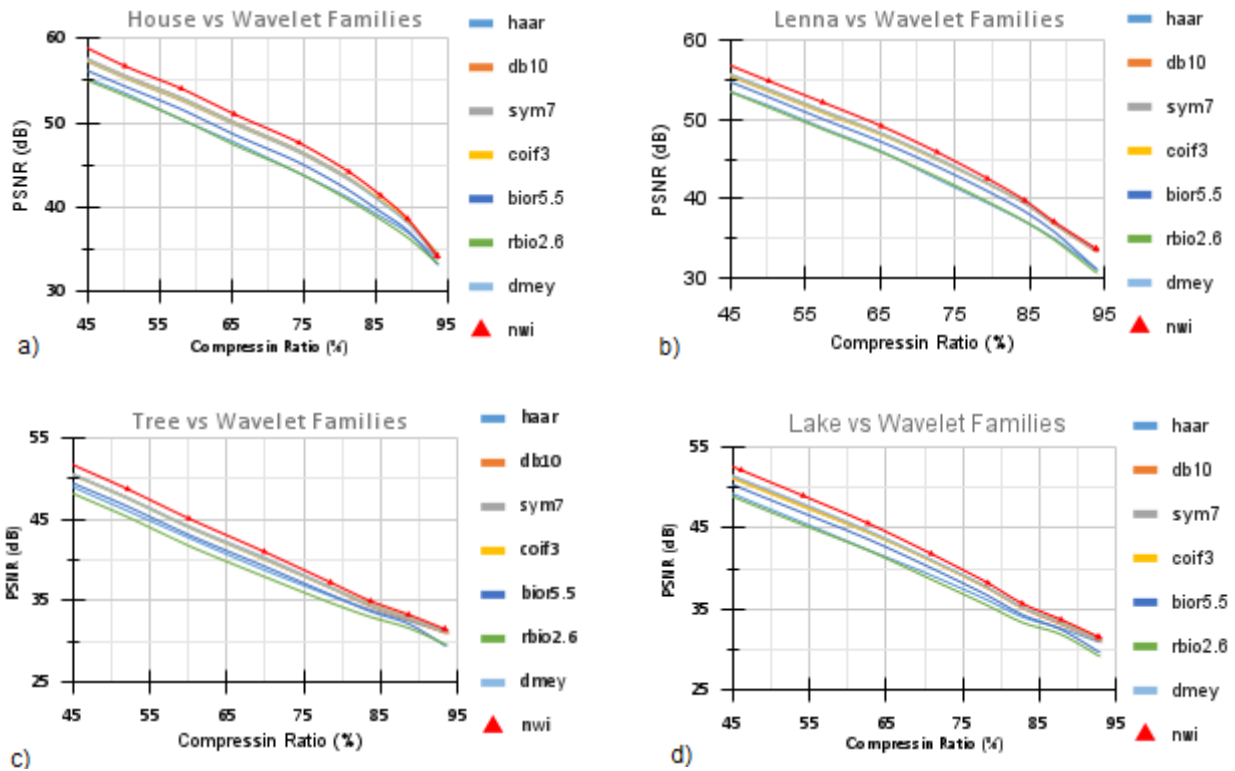


Figure 6. Comparison of Peak Signal-to-Noise Ratio (PSNR) against Compression Ratio (CR) for Eight Wavelet Families across Four Test Images.

In the case of Lake and Tree images, a consistent trend is observed, with their image quality registering approximately 5 dB lower for all wavelet families compared to the House and Lenna images, as depicted in Figure 6.c) and Figure 6.d). Sym7 and coif3 consistently deliver optimal performance, while rbio2.6 consistently yields the least favorable results. It is crucial to emphasize that the x-axis of the figure illustrates the compression ratio, ranging between 45% and 95%.

Likewise, the proposed NWI wavelet demonstrates enhanced compression performance for the tree and lake datasets. It yields results that are 1 dB superior compared to Sym7 and Coif3 wavelets. This improvement underscores the effectiveness of the proposed NWI wavelet in achieving higher compression efficiency, displaying its potential advantages over established wavelets like sym7 and coif3.

Figure 7 depicts the performance assessment of various wavelet families applied to four additional test images: Peppers, Baboon, Boat, and Airplane. Each graph within the figure represents the performance of a specific wavelet family in terms of compression ratio (CR) versus peak signal-to-noise ratio (PSNR) for each test images. This comprehensive evaluation offers valuable insights into the diverse capabilities of each wavelet family in achieving optimal compression outcomes for the specified test images across various threshold settings, thus contributing to a nuanced comprehension of their performance characteristics. Notably, the results for the Peppers image, as depicted in Figure 7.a), showcase the best performance among the four additional test images. Conversely, the Baboon image, shown in Figure 7.b), exhibits the lowest performance, registering a notable 8 dB less compared to the average performance. Among the evaluated wavelet families, Sym7 and Coif3 emerge as the top performers, while Rbio2.6 demonstrates the least favorable performance.

Introducing the proposed NWI wavelet it performs better than the other seven wavelet families. The reconstructed image quality with NWI is approximately 1 dB higher than that achieved with the Coif3 wavelet, underscoring its efficacy in image reconstruction and its potential for superior results compared to established wavelet families.

A consistent trend is observed for the Boat and Airplane images, with their image quality depicted in Figure 7.c) and Figure 7.d), respectively. Dmey and Coif3 consistently deliver optimal performance, while Rbio2.6 consistently yields the least favorable results.

Furthermore, the proposed NWI wavelet demonstrates enhanced compression performance across the four image datasets, yielding results that are 1.5 dB superior compared to Sym7 and Coif3 wavelets. This improvement underscores the effectiveness of the proposed NWI wavelet in achieving higher compression efficiency, highlighting its potential advantages over established wavelets such as Sym7 and Coif3.

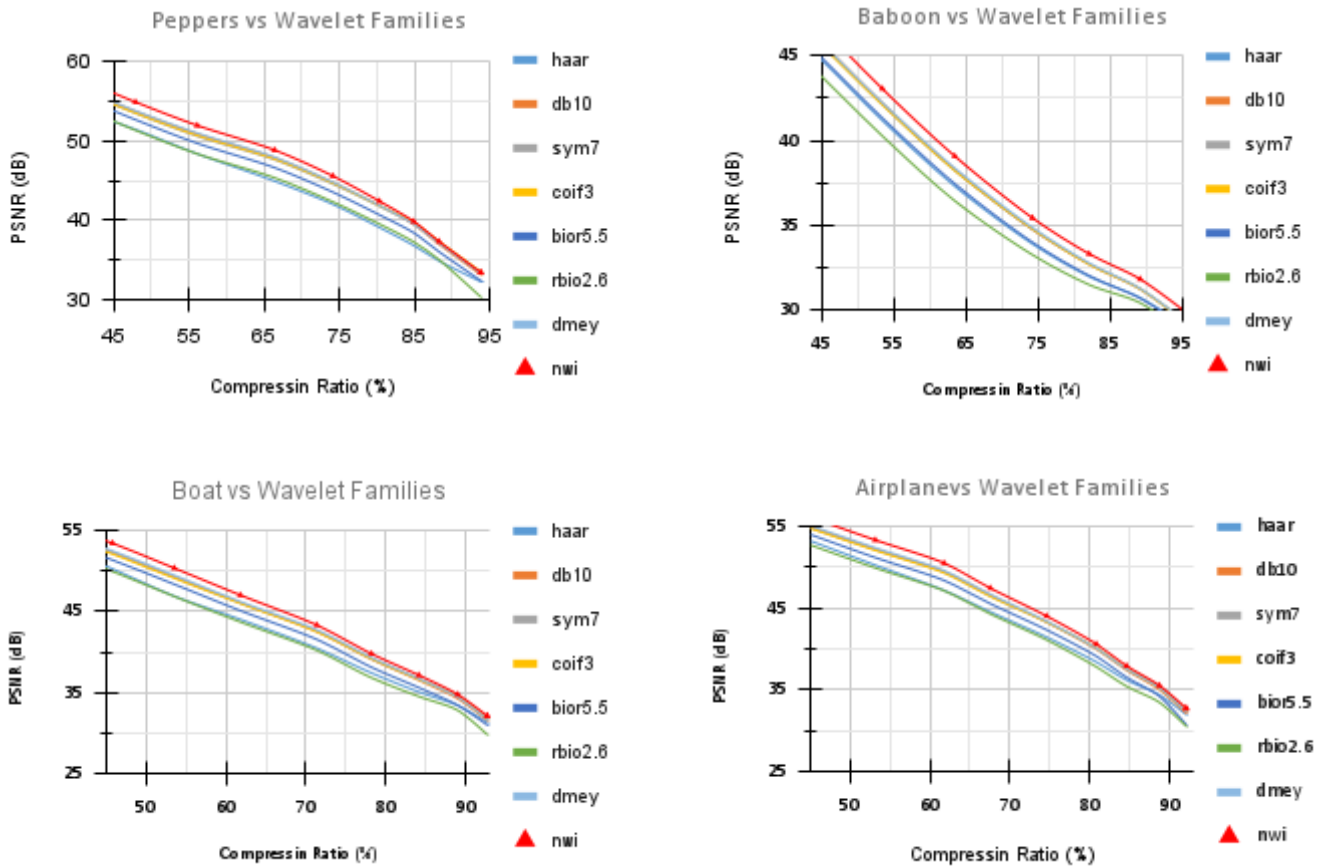


Figure 7. Comparison of Peak Signal-to-Noise Ratio (PSNR) against Compression Ratio (CR) for seven wavelet families across four additional test images..

Figure 8.a) illustrates compressed and reconstructed house images chosen from the test dataset as an exemplar leveraging the NWI wavelet family. The original and reconstructed image disparities, depicted as residuals, reveal that regions colored black signify the attainment of high image quality. This visualization effectively demonstrates the effectiveness of the NWI wavelet family in preserving image quality during the compression and reconstruction processes.

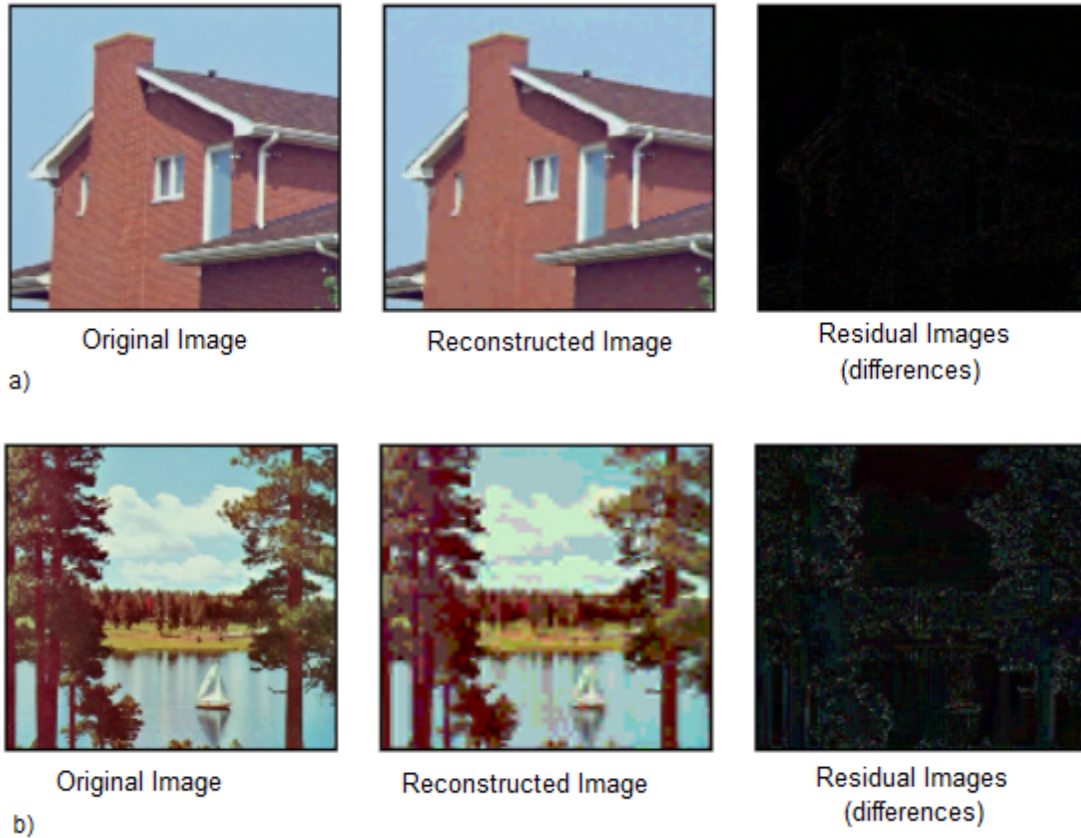


Figure 8. Utilizing the wavelet family "NWI", a) the original versus the compressed and reconstructed Test Image-1, and b) the original versus the compressed and reconstructed Test Image-4.

Figure 8.b) presents another illustrative example from our image dataset. Here, the lake image undergoes compression and reconstruction utilizing the NWI wavelet family, visually representing the process. The residuals, depicting the differences between the original and reconstructed images, exhibit certain image textures. This observation suggests a lower Peak signal-to-noise ratio (PSNR) compared to the house image. The nuanced variations in residual patterns contribute to a comprehensive understanding of the NWI wavelet family's performance across different images.

Table 1 presents a detailed analysis of the compression performances of various wavelet families while maintaining a constant Peak Signal-to-Noise Ratio (PSNR) of 40 dB. The table also includes summary statistics such as average (Avg) and standard deviation (Stdev) PSNR values across all wavelet families for each test image, providing a comprehensive overview of their performance. Notably, Nvi, Coif3, and dB10 demonstrate superior Compression Ratios (CR), achieving values of 76.00%, 75.95%, and 75.55%, respectively. In contrast, Haar and Rbio2.6 exhibit relatively lower CR performances, registering 72.62% and 72.52% values. The highest PSNR value of 41.58 dB is observed in the House image, indicating excellent compression quality, while the lowest PSNR performance of 32.5 dB is noted in the Baboon image.

Examining the standard deviation values in the last row of the table reveals variations in image quality among different wavelet families, ranging from 0.41 to 1.27. This suggests a relatively consistent performance correlation across the families. However, the standard deviation values for the average PSNR range from 7.75 to 10.06, indicating that the images' characteristics influence the performance of wavelet families.

Moreover, Coif3 and Sym7 demonstrate commendable CR values across various test images, indicating superior performance. Conversely, Rbio2.6 and Haar exhibit relatively lower CR performances. The proposed NWI wavelet shows promising CR performance, positioning it as a compelling option for image compression. Its consistent performance and good CR make it a valuable addition to existing wavelet families, potentially offering enhanced versatility in various compression scenarios.

The performance of the NWI wavelet, achieving 76% in our study, is particularly noteworthy, demonstrating superior CR values across a set of test images. This observation underscores the NWI wavelet's potential as a

valuable option for efficient image compression, competing favorably with established wavelet families like Coif3 and Sym7.

Table 1. Performance of Test Images at a Constant PSNR of 40 dB with Compression Ratio (CR).

Wave Family	Lenna	House	Lake	Tree	Peppers	Baboon	Boat	Airplane	Avg	Stdev
haar	78.36	83.28	69.41	67.78	79.36	51.2	72.34	77.6	72.42	10.06
db10	80.83	84.16	71.08	69.86	83.03	56.96	72.66	77.78	74.55	8.95
sym7	81.80	85.69	71.87	70.37	81.8	58.48	73.01	78.68	75.21	8.69
coif3	82.62	85.89	72.07	71.28	83.47	58.52	74.68	79.06	75.95	8.88
bior5.5	81.29	83.98	71.15	70.81	81.29	59.47	74.88	78.16	75.13	7.96
rbio2.6	80.08	82.47	67.86	66.00	81.06	55.1	71.2	77.22	72.62	9.42
dmey	81.54	84.05	71.47	70.96	82.13	56.03	72.29	78.74	74.65	9.14
NWI20	83.08	85.77	70.36	73.79	81.31	61.59	74.92	77.17	76.00	7.75
Avg	81.20	84.41	70.66	70.11	81.68	57.17	73.25	78.05	72.54	10.81
Stdev	1.49	1.26	1.41	2.35	1.19	2.95	1.32	0.67	1.53	0.99

Table 2 thoroughly examines the Peak Signal-to-Noise Ratio (PSNR) image quality achieved under a consistent 80% compression ratio, shedding light on the efficacy of various wavelet families applied to the test images. The inclusion of statistical metrics in the last two columns of the table further enriches the analysis by providing insights into the average and standard deviation for each wavelet family.

Significant performance disparities emerge among the wavelet families, with Nvi, Dmey, and Coif3 emerging as the top performers, boasting PSNR values of 39.10, 38.52, and 38.07 dB, respectively. Conversely, Haar and Rbio2.6 exhibit comparatively inferior PSNR performance, clocking in at 36.99 and 37.68 dB values. The disparity in PSNR values underscores the varying effectiveness of different wavelet families in preserving image quality under compression.

Table 2. Performance of Test Images at a Constant Compression Ratio of 80% with Peak Signal-to-Noise Ratio (PSNR) Values.

Wave Family	PSNR (dB) image quality									AVG	Stdev
	Lenna	House	Lake	Tree	Peppers	Baboon	Boat	Airplane			
haar	39.18	41.64	35.32	34.96	39.02	30.42	36.43	38.93	36.99	3.48	
db10	40.46	41.63	35.54	34.93	41.46	31.69	37.54	38.69	37.74	3.52	
sym7	41.45	42.42	35.93	35.18	41.05	31.72	38.02	38.75	38.07	3.64	
coif3	41.86	42.48	36.04	35.64	40.85	33.78	38.64	35.64	38.12	3.30	
bior5.5	40.98	41.08	35.58	35.4	40.21	32.52	39.13	39.22	38.02	3.13	
rbio2.6	39.68	40.21	34.82	34.45	41.55	32.63	38.24	39.82	37.68	3.26	
dmey	41.6	41.62	35.73	35.48	41.63	33.76	38.72	39.59	38.52	3.15	
NWI20	41.54	42.89	37.25	36.90	41.98	33.48	38.96	39.82	39.10	3.14	
Avg	40.84	41.58	35.57	35.15	40.97	32.50	38.21	38.81	37.62	3.61	
Stdev	0.98	0.78	0.41	0.41	0.90	1.11	0.83	1.27	1.03	0.20	

Highlighting individual image performance, the House image stands out with the highest average PSNR value of 41.58 dB, indicative of superior compression quality. On the contrary, the Baboon image demonstrates the lowest PSNR performance at 32.5 dB, signaling challenges in preserving image fidelity for certain content types.

A closer examination of the standard deviation values in the table's last row reveals the range of variation in image quality among different wavelet families, spanning from 0.41 to 1.27. This suggests a relatively consistent performance correlation across the families, indicating their overall reliability in maintaining image quality. However, the standard deviation values for the average PSNR paint a nuanced picture, ranging from 3.13 to 3.64.

This indicates that while wavelet families exhibit consistent performance trends, their effectiveness is indeed influenced by the inherent characteristics of the images themselves, underscoring the complexity of image compression dynamics.

Furthermore, the proposed NWI20 consistently delivers superior results across various image types, underscoring its efficacy in image compression. This observation aligns with our expectations, highlighting the advantageous performance of the proposed NWI wavelet. It's essential to note that the type of image significantly influences the attained image quality, emphasizing the need for tailored compression strategies based on image content.

Table 3 presents detailed information on the average Compression Ratio (CR) and Peak Signal-to-Noise Ratio (PSNR) achieved across ten compression levels for all test images. Notably, Coif3 and Sym7 demonstrate commendable CR, indicating superior performance across various test images. Conversely, Rbio2.6 and Haar exhibit relatively lower CR. The newly introduced NWI Wavelet shows promise with its CR performance. Overall, the trend highlights NWI and Coif3 as favorable choices for image compression due to their high average PSNR values and consistent performance. Low standard deviation values suggest minimal performance variations among wavelet families, indicating comparable effectiveness in diverse compression scenarios. The performance of the NWI wavelet is particularly noteworthy, demonstrating superior CR across diverse test images and showcasing competitive results compared to established wavelet families like Coif3 and Sym7. Its consistent performance and good CR make it a compelling option for applications requiring efficient image compression, potentially offering enhanced versatility in various compression scenarios.

Table 3. Average Compression Ratio (CR) and average Peak Signal-to-Noise Ratio (PSNR) achieved for the test images at 10 compression levels, utilizing various wavelet families.

		haar		db10		sym7		coif3		bior5.5		rbio2.6		dmey		NWI20	
		CR	PSNR	CR	PSNR	CR	PSNR	CR	PSNR	CR	PSNR	CR	PSNR	CR	PSNR	CR	PSNR
Lenna	Avg	72.79	41.74	71.45	43.94	72.19	43.88	72.59	43.96	74.17	42.72	74.03	41.64	72.07	44.03	72.78	44.66
	Stdev	18.28	8.28	17.41	8.31	17.54	8.15	17.29	8.14	17.82	8.65	17.79	8.38	17.59	8.26	18.78	8.63
House	Avg	73.36	43.62	69.90	45.44	71.42	45.37	71.49	45.47	72.68	44.20	72.77	43.33	70.62	45.43	71.69	46.20
	Stdev	20.12	8.76	20.33	9.36	20.54	9.09	20.32	9.16	20.54	9.35	20.51	8.95	20.52	9.33	21.75	9.76
Lake	Avg	70.65	39.25	68.46	40.63	69.04	40.64	69.47	40.62	70.69	39.63	71.24	38.54	68.27	40.75	70.95	41.44
	Stdev	19.55	7.60	21.12	8.36	21.04	8.18	20.55	8.15	20.75	8.40	21.03	8.03	21.30	8.34	22.07	8.66
Tree	Avg	70.17	39.37	68.11	40.22	68.81	40.38	69.71	40.26	70.64	39.22	70.63	38.40	68.95	40.28	70.37	41.06
	Stdev	20.58	7.82	21.85	8.43	21.29	8.34	20.99	8.28	21.24	8.46	21.24	7.99	21.54	8.34	22.81	8.73
Peppers	Avg	72.59	41.62	71.26	43.85	72.34	43.82	72.21	43.90	73.18	42.82	73.77	41.44	71.42	43.96	69.59	44.56
	Stdev	19.19	7.82	19.24	8.30	19.24	8.08	18.52	8.06	18.68	8.19	19.40	8.37	19.15	8.27	20.01	8.67
Baboon	Avg	66.33	37.75	66.06	38.54	66.55	38.51	66.74	38.49	66.66	37.86	67.00	37.10	66.69	38.60	66.08	39.33
	Stdev	24.88	8.96	24.64	9.45	24.55	9.38	24.50	9.37	24.39	9.29	24.79	9.09	24.69	9.47	24.84	9.71
Boat	Avg	70.64	40.39	68.76	41.85	69.64	41.90	70.10	41.85	70.98	40.99	71.68	39.75	68.98	42.00	67.98	42.64
	Stdev	20.09	7.99	20.64	8.58	19.88	8.45	19.83	8.41	20.08	8.47	20.64	8.32	20.39	8.56	21.52	8.83
Airplane	Avg	74.04	40.96	71.95	42.33	72.38	42.37	72.77	42.36	74.49	41.28	74.68	40.30	72.09	42.48	70.95	43.10
	Stdev	16.62	7.60	17.52	8.27	16.95	8.11	16.91	8.07	17.54	8.34	17.50	7.98	17.53	8.23	18.65	8.50

The standard deviation (Stdev) values reflect the consistency of the proposed method's performance, showing relatively lower variations. These results underscore the robustness and superior performance of the proposed NWI wavelet across various compression scenarios. However, choosing the best wavelet family may also depend on specific application requirements.

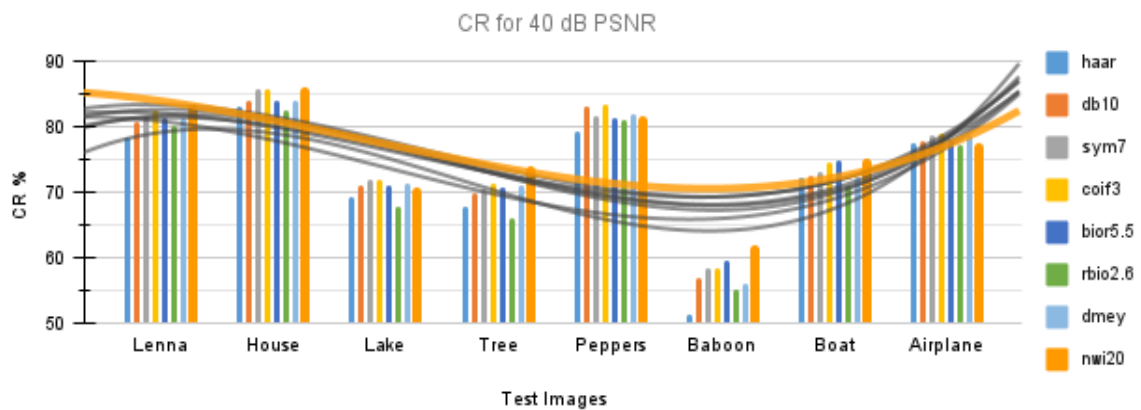
The compression performance of various wavelet families was assessed using Compression Performance (CP) values across a range of test images. Table 4 provides an overview of the Compression Performance (CP) exhibited by various wavelet families across different test images. The highest CP value observed is 3312.08, achieved by the NWI20 wavelet in the House image, which represents the proposed method. Conversely, the lowest CP value of 2485.80 is obtained with the rbio2.6 wavelet in the Baboon image.

Table 4. Compression Performance of test images, utilizing various wavelet families

	Compression Performance (CP)							
	haar	db10	sym7	coif3	bior5.5	rbio2.6	dmev	NWI20
Lenna	3038.25	3139.51	3167.70	3191.06	3168.54	3082.61	3173.24	3250.35
House	3199.96	3176.26	3240.33	3250.65	3212.46	3153.12	3208.27	3312.08
Lake	2773.01	2781.53	2805.79	2821.87	2801.44	2745.59	2782.00	2940.17
Tree	2762.59	2739.38	2778.55	2806.52	2770.50	2712.19	2777.31	2889.39
Peppers	3021.22	3125.05	3169.55	3170.12	3133.45	3057.07	3139.22	3100.80
Baboon	2504.14	2545.93	2562.75	2568.50	2523.87	2485.80	2573.96	2598.72
Baot	2853.41	2877.21	2917.75	2933.17	2908.91	2849.44	2897.32	2898.48
Airplane	3033.11	3045.38	3066.97	3082.73	3075.18	3009.88	3062.66	3057.84

Notably, NWI20 and Coif3 consistently demonstrated superior compression performance, with NWI20 exhibiting particularly high CP values, notably in the House image. Sym7 also showcased commendable compression performance across diverse test images. However, DB10 and Dmey displayed moderate performance, with CP values generally falling within a moderate range. In contrast, Haar, rbio2.6, and bior5.5 exhibited relatively lower compression performance, with CP values tending to be on the lower end of the spectrum across most test images.

Figures 9 illustrate the trend lines depicting the relationship between wavelet families and their corresponding performances in both PSNR and CR. In Figure 9, the compression ratios of eight selected wavelet families are depicted for images with a quality of 40 dB. The graph illustrates the variations in compression ratios among the wavelet families, with a discernible trend line capturing these differences. Notably, the house image attains the highest compression ratio, signifying superior compression efficiency compared to the other test images. Conversely, the Baboon image exhibits the lowest compression ratio, indicating less optimal performance in achieving data reduction. This graphical representation offers a clear visual insight into how the selected wavelet families perform regarding compression ratios at a specific image quality level.

**Figure 9.** Compression performance of wavelet families for test images.

In Figure 10, the image quality, as measured by PSNR values, is presented at a fixed compression ratio of 80%. The graph highlights the performance of various test images across this compression level. Impressively, the house image stands out with the highest quality, indicating its resilience to compression at the specified ratio. Additionally, the PSNR values for the Peppers test image closely approach those of the house image, emphasizing their comparable high-quality retention. On the other hand, the Lake and Baboon test images exhibit PSNR values approximately 8 dB lower than those of the House and Peppers. This detailed analysis provides valuable insights into the varying image qualities achieved by the tested compression methods under the defined conditions.

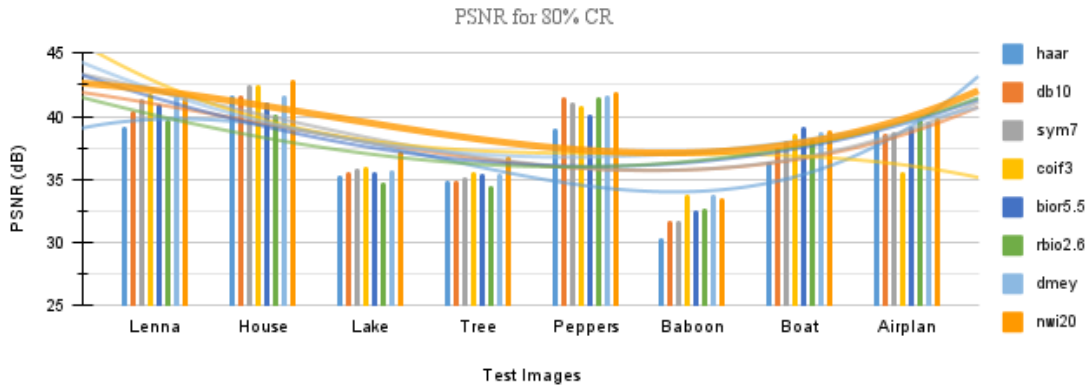


Figure 10. PSNR values of test images for fixed 80%compression ratio for different wavelet families.

The table and figure information suggests a connection between image specifications, specifically entropy, and the impact of different wavelet families on compression ratio and image quality. The observed results indicate that the choice of wavelet family significantly influences the performance. Notably, Coif3, characterized by a high-frequency converter, demonstrates superior compression ratio and image quality performance compared to other wavelet families. This emphasizes the importance of selecting an appropriate wavelet family based on specific image characteristics and compression requirements.

By assessing and comparing performance metrics, specifically Compression Ratio (CR) and Peak signal-to-noise Ratio (PSNR), one can effectively determine an appropriate wavelet transform for a specific image processing application. The CR and PSNR values analysis proves instrumental in selecting the optimal Wavelet for a given task. Notably, PSNR values ranging from 30 to 40 dB are generally deemed satisfactory across various applications. However, it is imperative to validate the suitability of wavelets individually for each application, ensuring an optimal match between the chosen Wavelet transform and the specific requirements of the image processing task at hand.

5. Conclusions

In conclusion, the comprehensive evaluation of various wavelet families for image compression performance, as detailed in the tables and figures, provides in-depth insights into their respective influences on compression ratio and image quality. The results emphasize the crucial role of selecting an appropriate wavelet family tailored to specific image characteristics and desired compression goals. Notably, Coif3, distinguished by its high-frequency conversion capabilities, is a standout performer, showcasing superior results across the assessed parameters.

Additionally, including the proposed NWI wavelet in the evaluation further enhances the understanding of its performance characteristics. The NWI wavelet consistently exhibits competitive results, demonstrating its potential as a viable option in image compression scenarios. These findings significantly contribute to the broader comprehension of wavelet-based image compression, offering practical guidance for optimizing performance across diverse applications.

As the field of image compression continues to advance, ongoing investigations and refinements in wavelet selection and compression techniques are essential to fuel continued progress in image processing. Integrating innovative wavelets, such as the NWI wavelet, into the existing landscape further expands the possibilities for achieving enhanced compression outcomes and improved image quality.

References

- [1] Ayiluri SR, Yelchuri SK, Laxumudu V, Sajan GP, Kumar, AYP, Kaur K. Jpeg Image Compression Using Matlab. International Research Journal of Modernization in Engineering Technology and Science. 2022;3(5) :663-669
- [2] Oz I. İki boyutlu ayrık dalgacık dönüşüm filtreleri kullanarak sabit ve hareketli görüntü sıkıştırma. PhD, Sakarya University, Sakarya, Turkey, 2006.
- [3] Aranzado, J. D. R., Barbosa, G. K., Linget, K. F., & Agustin, V. A. Enhancement of the Huffman Algorithm with Discrete Wavelet Transform Applied to Lossless Image Compression.
- [4] Bulut, F. Low dynamic range histogram equalization (LDR-HE) via quantized Haar wavelet transform. The Visual Computer, 2022;38(6), pp.2239-2255

- [5] Chen Y. An introduction to wavelet analysis with applications to image and jpeg 2000. In 2022 4th International Conference on Intelligent Medicine and Image Processing. 2022; pp. 49-57.
- [6] Wang D, Zhang L, Vincent, A. Improvement of JPEG2000 using curved wavelet transform. In Proceedings.(ICASSP'05). IEEE International Conference on Acoustics, Speech, and Signal Processing, 2005; Vol. 2, pp. ii-365, IEEE.
- [7] Yilmaz Ö, Aksoy M, Kesilmiş Z. Misalignment fault detection by wavelet analysis of vibration signals. *International Advanced Researches and Engineering Journal*, 2019; 3(3), 156-163.
- [8] Viswanthan P, Kalavathi P. Subband Thresholding for Near-Lossless Medical Image Compression. *International Journal of Computing and Digital Systems*. 2023;14(1), 1-1.
- [9] Toraman S, Turkoglu I. A new method for classifying colon cancer patients and healthy people from FTIR signals using Wavelet transform and machine learning techniques. *Journal of the Faculty of Engineering and Architecture of Gazi University*. 2020; 35(2), 933-942.
- [10] Saffor A, Ramli AR, Ng KHA. Comparative study of image compression between JPEG and Wavelet. *Malaysian Journal of computer science*. 2001;14(1), 39-45.
- [11] Mishra D, Singh SK, Singh RK. Wavelet-based deep auto encoder-decoder (wdaed)-based image compression. *IEEE Transactions on Circuits and Systems for Video Technology*. 2020; 31(4), 1452-1462.
- [12] Taujuddin NSAM, Ibrahim R, Sari S. An improved technique to wavelet thresholding at details subbands for image compression. *ARNP Journal of Engineering and Applied Sciences*. 2016;11(18), 10721-10726.
- [13] Starosolski R. Hybrid adaptive lossless image compression based on discrete wavelet transform. *Entropy*. 2020; 22(7), 751.
- [14] Oz I, Oz C, Yumusak N. Image compression using 2-D multiple-level discrete wavelet transform (DWT). *Eleco 2001 International Conference on Electrical and Electronics Engineering 2001; Turkey*.
- [15] Boujelbene R, Jemaa YB, Zribi M. A comparative study of recent improvements in wavelet-based image coding schemes. *Multimedia Tools and Applications*. 2019; 78, 1649-1683.
- [16] Ranjan R, Kumar P. An Improved Image Compression Algorithm Using 2D DWT and PCA with Canonical Huffman Encoding. *Entropy*. 2023; 25(10), 1382.
- [17] Aranzado JDR, Barbosa GK, Linget KF, Agustin VA. Enhancement of the Huffman algorithm with discrete wavelet transform applied to lossless image compression. *United International Journal for Research & Technology*. 2023; Volume 04, Issue 08, pp 83-90.
- [18] Onufriienko D, Taranenko Y. Filtering and compression of signals by the method of discrete wavelet decomposition into one-dimensional series. *Cybernetics and Systems Analysis*. 2023;1-8.
- [19] Martin MB, Bell AE. New Image compression techniques using multiwavelets and multiwavelet packets. in *IEEE Transactions on Image Processing*, 2001; vol. 10, no. 4, pp. 500-510.
- [20] Keser S. An image compression method based on subspace and down sampling. *Bitlis Eren Üniversitesi Fen Bilimleri Dergisi*, . 2023;12(1), 215-225
- [21] Keser S, Gerek ÖN, Seke E, Gülmezoğlu MBA. Subspace based progressive coding method for speech compression. *Speech Communication*, 2017; 94, 50-61.
- [22] Bindulal TS. Performance analysis of modified wavelet difference reduction methods in image compression and transmission. *International Journal of Advanced and Applied Sciences*. 2023; 10(10), Pages: 229-238.
- [23] Viswanthan P, Kalavathi P. Subband Thresholding for Near-Lossless Medical Image Compression. *International Journal of Computing and Digital Systems*. 2023; 14(1), 1-1.
- [24] Ahamad MG, Almazayad A, Ali SA. Design and development of new parametric wavelet for image denoising. *International Journal of Electronics and Communication Engineering*. 2011; 4 (1), pp.1-9
- [25] Da Silva PCL. Use of daubechies wavelets in the representation of analytical functions. In *Wavelet Theory*. IntechOpen. 2020.
- [26] Ince IF, Bulut F, Kilic I., Yildirim ME, Ince OF. Low dynamic range discrete cosine transform (LDR-DCT) for high-performance JPEG image compression. *The Visual Computer*, 2022;38(5), pp.1845-1870.
- [27] Bulut F. Huffman Algoritmasıyla Kayıpsız Hızlı Metin Sıkıştırma. *El-Cezeri*, 2016; 3, no. 2.

Detailed Analysis of Li-ion Batteries for Use in Unmanned Aerial Vehicles

Merve Nur KAYA¹, Zehra URAL BAYRAK^{2*}

¹ Department of Avionics, School of Aviation, Firat University, Elazığ, Turkey

¹ mervee.nur.kayaa@gmail.com, ² zural@firat.edu.tr

(Geliş/Received: 14/02/2024;

Kabul/Accepted: 26/03/2024)

Abstract: With the developing technologies in the aviation, the transition to more electrical systems is increasing day by day. For this reason, research on the development of batteries has accelerated. Nowadays, Lithium ion (Li-ion) batteries are more widely preferred due to their energy-to-weight ratio and advantages such as having a lower self-discharge rate when not working compared to other battery technologies. Batteries convert the stored chemical energy into electrical energy and heat is released as a result of the chemical reactions. The heat released negatively affects the battery's lifespan, charging/discharging time and battery output voltage. The battery must be modeled correctly to see these negative effects and intervene in time. In this way, negative situations that may occur in the battery can be intervened at the right time without any incident.

In this study, the unmanned aerial vehicle (UAV) is powered by Li-ion batteries. It is simulated in Matlab/Simulink environment using the electrical equivalent circuit. A detailed model is created, taking into account temperature, state of charge (SoC), cell dynamics and operating functions. To estimate state of health (SoH) of the battery, resistance values must be known. Resistance and capacity values in the equivalent circuit of the Li-ion battery are obtained with the help of the simulation model. So, the SoH of the Li-ion batteries can be accurately predicted with the results obtained.

Key words: Li-ion, UAV, battery model, simulation.

Li-iyon Bataryaların İnsansız Hava Araçlarında Kullanımı için Detaylı Analizi

Öz: Havacılık alanında gelişen teknolojilerle birlikte daha fazla elektrikli sistemlere geçiş günden güne artmaktadır. Bu sebeple pillerin geliştirilmesine yönelik araştırmalar hız kazanmıştır. Günümüzde, enerji-ağırlık oranına ve diğer pil teknolojilerine kıyasla, çalışmadığı zamanlarda kendi kendine daha düşük deşarj oranına sahip olması gibi avantajları bulunmasından ve diğer pil türlerine göre çevreye daha az zarar vermesinden dolayı Lityum iyon (Li-iyon) bataryalar daha yaygın olarak tercih edilmektedir. Bataryalar, depoladığı kimyasal enerjiyi elektrik enerjisine dönüştürürler ve reaksiyon sonucunda ısı açığa çıkar. Açığa çıkan ısı bataryanın kullanım ömrünü, şarj/deşarj süresini ve batarya çıkış gerilimini olumsuz olarak etkilemektedir. Bu olumsuz etkileri görebilmek ve zamanında müdahale etmek amacıyla, bataryanın müdahale edilebilecek düzeyde modellenmesi gerekmektedir. Böylece bataryada oluşabilecek arıza durumlarında, doğru zamanda ve herhangi bir olay yaşanmadan müdahale edilebilecektir.

Bu çalışmada insansız hava aracının (İHA) gücü Li-iyon piller ile sağlanmaktadır. Li-iyon pilin elektriksel eşdeğer devresi kullanılarak Matlab/Simulink ortamında benzetimi yapılmıştır. Sıcaklık, şarj durumu, hücre dinamiği ve çalışma fonksiyonları dikkate alınarak pilin ayrıntılı bir modeli oluşturulmuştur. Pilin sağlık değerini tahmin etmek için direnç değerlerinin bilinmesi gerekir. Li-iyon pilin eşdeğer devresindeki direnç ve kapasite değerleri gerçekleştirilen model yardımıyla elde edilmiştir. Elde edilen sonuçlar sayesinde Li-iyon pillerin sağlık durumu doğru bir şekilde tahmin edilebilecektir.

Anahtar kelimeler: Li-iyon, İHA, batarya modeli, benzetim.

1. Introduction

The energy needs of modern life are rapidly diversifying and expanding with constantly developing technology and increasing mobility. Many applications, from electric vehicles to portable devices, are increasing the demand for a reliable and efficient energy storage solution. In this context, battery technologies have become an indispensable element of modern life by forming the basis of energy storage systems [1].

Mathematical modeling of batteries plays a critical role in the design and optimization of energy storage systems. These models are used to understand the battery's electrochemical behavior, charge/discharge processes, and performance under various operating conditions. In particular, Li-ion batteries stand out with their advantages such as high energy density, lightness, low self-discharge rate and long life. Therefore, effective modeling of Li-ion batteries is a critical step in the advancement of energy storage technologies [2].

Some of the studies in the literature on modeling Li-ion batteries are given below.

Hlinka et al. [4] carried out a study and modeling of the charging process of Li-ion batteries. The charging process was examined to compare long-term stored Li-ion batteries with new Li-ion batteries. Charging data has been obtained experimentally through long-term tests.

* Corresponding author: zural@firat.edu.tr. ORCID Number of authors: ¹ 0009-0009-1707-5360, ² 0000-0001-8249-0063

Afraz et al. [5] investigated a compact thermal management model in Li-ion battery packs, especially for Tesla Model S vehicles. It is a study to increase the efficiency and safety of Li-ion batteries for electric vehicles. It is found that major factors such as the discharge rate (C) value of the battery and the initial liquid temperature have a significant impact on the battery temperature and maximum temperature difference. This study provides valuable results for the design and analysis of battery thermal management systems.

Ozdemir et al. [6] extensively investigated the electrical and thermal behavior of Li-ion batteries under normal and abuse conditions. A detailed sensitivity analysis was performed by developing an electrochemical-thermodynamically coupled model. Thermal and electrical properties of the Li-ion battery were predicted for varying discharge rates at temperatures of 20 and 50 °C.

In the study by Hou et al. [7], health factors that may characterize battery degradation were extracted from charging data in order to accurately predict the health status of Li-ion batteries in real time and ensure the safe operation of the relevant equipment. Correlations between health factors and battery capacity were analyzed using Spearman and Pearson coefficients.

In a study by Cheng [8], the equivalent electrical circuit of a Li-ion battery cell was examined. Extended hybrid pulse power characterization was designed and implemented to observe the dynamic response of the battery cell in the time domain. The most suitable meta-heuristic-based method to quickly and systematically determine the equivalent electrical circuit parameters of the battery cell was examined.

Mastrogiorgio et al. [9] used machine learning/deep learning to predict the probability of thermal runaway in Li-ion batteries. Three different stages, namely safe operation, critical state of thermal escape and formation of real thermal escape, were determined with the classification approach. Novel convolutional neural networks were used to predict the evolution of heat sources.

Rezk et al. [10] conducted a study stating that the optimal parameter definition of the Li-ion battery model was important to accurately capture battery behavior and performance in electric vehicle applications. They proposed optimal parameter identification with Self-adaptive Bonobo Optimizer, a meta-heuristic optimization algorithm used in electric vehicle applications.

Mavi and Arslan [11] examined the thermal management of an electric vehicle's battery module for waste heat recovery. They used a two-phase flow system to provide a more effective heat transfer in the evaluation of waste heat. In the thermal analysis of the battery module, a parametric study was carried out using computer-aided fluid dynamics for different C values and discharge depths.

Kumar et al. [12] conducted a study to accurately predict the temperature-varying orthotropic thermal properties and volumetric heat production of Li-ion batteries. Temperature-dependent orthotropic thermal conductivities, specific heat and volumetric heat production of a Panasonic NCR18650BD cylindrical battery were estimated using an inverse approach. Experimental measurements were carried out with surface temperatures taken from suitable places on the battery.

Lee et al. [13] proposed a convolutional neural network model to predict the SoH of Li-ion batteries in the early stages of qualification tests. Five different types of convolutional neural network models were developed and these models were used to predict the SoH values of Li-ion batteries. The performance and reliability of the developed models were evaluated under various experimental conditions.

Navas et al. [14] emphasized that batteries that allow storing excess energy from renewable energy sources such as solar and wind are an important component, and a dynamic Li-ion battery model was created. This model is based on an electrical equivalent circuit model.

It is very important to create a correct battery model in systems that need to store electrical energy. For this reason, in this study, a detailed model of the Li-ion battery, which is frequently used in UAVs, is created. It is simulated in Matlab/Simulink environment using the electrical equivalent circuit of the battery. Simulation results are used to examine the effect of battery parameters on the efficiency of the system. This article will especially contribute to researchers working on the modeling, development and future use potential of the Li-ion batteries.

2. Batteries

Cells are storage units that allow us to store energy chemically and then use this stored chemical energy as electrical energy with the help of electrochemical cells. Battery is a cell group formed by combining multiple cells [15].

The properties of the cells, serial or parallel connection status, number of cells and external hardware structure are used to obtain the desired characteristics [15]. Some characteristic features of the batteries, which enable us to store energy and use it at desired times, are needed in order to see their current status, to increase the battery life by ensuring that it operates under operating conditions, and to ensure safe operation against possible adverse events.

The battery is the structure that contains electrolyte, electrode and other components. More than one battery comes together to form a module, and modules come together to form a package [16, 17]. Higher voltage can be

obtained by connecting battery packs in series. This means high power with lower current. The high power generated will ensure better performance of the vehicle in which the battery group is used [17].

When current flows through a battery, the potential difference between the ends of the battery as a result of the kinetics of electrode reactions, the free enthalpy of the cell reaction and the change in cell resistance is called voltage [17, 18]. Open circuit voltage is the potential difference between the electrodes of the no loaded battery resulting from its internal resistance [16, 17].

There is a process in which the battery can be used as a result of the chemical and physical deformations it experiences during charging and discharging. The number of complete discharge-charge cycles during this process constitutes the cycle life of the battery [17, 18]. Higher C ratio, extreme temperature and high voltage range affect the cycle life as they affect the battery life [17]. The battery's lifespan is defined as its capacity value, which varies between approximately 500-1000 cycles, without falling below 80% of the initial capacity value. Problems occurring during electrochemical reactions shorten the life of the battery and cause it not to complete the required cycle life [19].

When using batteries, there is a need to determine the remaining energy in order to protect the battery, prevent over-discharge and extend battery life. This uses the SoC to determine the remaining energy and is expressed as 0%, 10%, 100%, etc. 0% corresponds to an empty battery and 100% corresponds to a fully charged battery [17, 20]. Accurate estimation of SoC information required for battery management systems and charging control is difficult and complex due to limited models and parametric uncertainties between models. That's why different methods are used to determine the SoC.

The coulomb counting method and ampere-hour methods use the standard measurement-based estimation approach. Open circuit protection and impedance measurement methods provide a more reliable estimation result. In addition, machine-based methods such as artificial neural networks and prediction logic provide a better estimate of the state of charge by taking non-consumption use into account. However, the prediction processes of these models are offline since the learning processes are very computational [20]. Equation (1) can be used to calculate SoC, which expresses the ratio of remaining capacity to rated capacity [16].

$$SoC = \frac{\text{Remaining capacity}}{\text{Rated capacity}} \quad (1)$$

Due to some irreversible chemical reactions occurring within the battery, internal resistance increases and capacity decreases. This causes the performance of the battery to decrease. Therefore, SoH is used to express the remaining useful life of batteries and the extent of aging. It is obtained by comparing the current conditions of the batteries with their initial conditions [17, 21]. It is seen from SoH information that operating the battery outside the recommended operating conditions, experiencing events such as extreme temperatures, overcharging, and overdischarging causes early aging of the battery [17, 22]. Equation (2) can be used to calculate SoH, which expresses the ratio of usable capacity to rated capacity [16].

$$SoH = \frac{\text{Usable capacity}}{\text{Rated capacity}} \quad (2)$$

Some types of batteries, which vary according to the chemical structure of the electrode and electrolyte inside, are Lead Acid (Pb-Acid), Nickel Cadmium (Ni-Cd), Nickel Metal Hydride (NiMH), Zebra, Lithium Polymer (LiPo), Lithium Air (Li-Air), Lithium Sulfur (Li-S), Zinc Air (Zn-Air), Zinc Bromide (Zn-Br), Lithium Ion (Li-ion). LiPo, Li-Air and Li-ion are commonly used batteries in the UAVs.

3. Modelling of Li-ion Batteries

The cells in Li-ion batteries, which were commercialized by Sony in 1991, consist of an anode, cathode, electrolyte and separator. These parts help in the production and storage of electricity [23-25]. The anode part, that is, the negative electrode, consists of carbon-based composites (usually graphite) as material and also a copper current collector. The cathode part consists of Lithium Cobalt Oxide (LiCoO₂), Lithium Iron Phosphate (LiFePO₄) and Lithium Manganese Oxide (LiMn₂O₄), which are transition metal oxides that have a lower discharge potential as the electrical capacity density increases. It consists of nickel-based cobalt oxide and also aluminum copper collector. LiMn₂O₄ is used in high security applications. But LiCoO₂ is widely used as cathode material [26]. The electrolyte consists of Li salt in a non-aqueous solvent [18, 25].

It is of great importance to create an appropriate battery model for the control and optimization of negative situations that may occur in the system [27]. Battery performance and health status can be determined through the created models. While electrical circuit models of batteries provide analytical predictions, chemical circuit models are very complex. There are also mathematical models in which battery parameters are expressed as variables of

a mathematical equation [28]. In this study, the electrical circuit model is preferred because it is easier to control and not complicated. While creating the battery model, many subsystems are used to eliminate complexity and is simulated in the MATLAB/Simulink environment. Electrical and thermal structure are taken into account in the battery equivalent circuit model [29, 30].

The second order Randles electrical equivalent circuit seen in Figure 1 is used while modeling. It gives better results in the literature [29]. Here, v_{ocv} is the ideal voltage source that varies depending on the current SoC of the battery, R_0 is the internal resistance, $v_0(t)$ is the voltage on the internal resistance, $R_i C_i$ ($i = 1, 2$) pair is the resistors that will represent the charge transfer, $v_1(t)$, $v_2(t)$ refers to the voltage on these pairs, and $i(t)$ refers to the current passing through the circuit. R_0, R_1, R_2 values change depending on temperature and current.

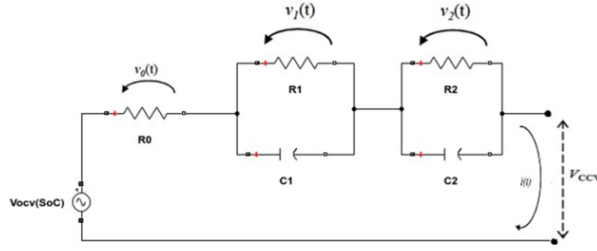


Figure 1. Second order Randles electrical equivalent circuit

The battery is simulated in MATLAB/Simulink, taking into account the Randles equivalent circuit in Figure 1 and the mathematical equations of this circuit [29]. The considered mathematical equations are obtained according to Ohm's and Kirchhoff's laws. $v_{ccv}(t)$ which represents the battery closed-circuit voltage, is obtained by Equation (3).

$$v_{ccv}(t) = v_{ocv}(t) - v_0(t) - v_1(t) - v_2(t) \quad (3)$$

The voltage on the internal resistance, the current passing through the R_1 resistor, the current passing through the C_1 and the total current passing through the circuit are given in Equations (4), (5), (6) and (7), respectively capacity.

$$v_0(t) = R_0 \cdot i(t) \quad (4)$$

$$i_1(t) = \frac{v_1(t)}{R_1} \quad (5)$$

$$i_2(t) = C_1 \cdot \frac{dv_1(t)}{dt} \quad (6)$$

$$i(t) = i_1(t) + i_2(t) \quad (7)$$

The total current value is found by adding the obtained $i_1(t)$ and $i_2(t)$. When these currents are written into Equation (7), the differential Equation (8) is obtained.

$$\frac{dv_1(t)}{dt} = \frac{1}{C_1} \cdot i(t) - \frac{1}{R_1 \cdot C_1} \cdot v_1(t) \quad (8)$$

Data tables found in the literature and obtained as a result of experiments are used for non-constant R_1, C_1, R_2, C_2 values [29, 31].

In the cell dynamics subsystem shown in Figure 2, there are impedances consisting of R_0, R_1, C_1, R_2, C_2 values, $v_{ocv,cell}$, I_{cell} are inputs of the system. At the outputs, there are V_{ccv} and V_0, V_1, V_2 terms to be used in thermal calculations.

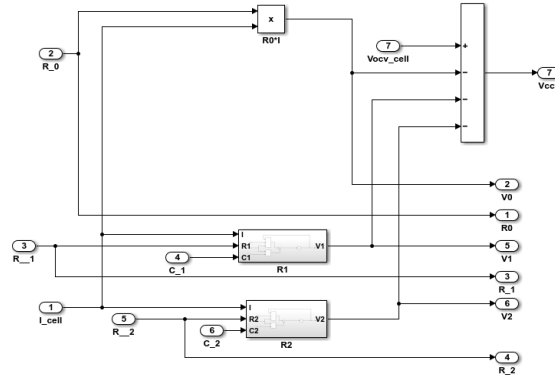


Figure 2. Model of cell dynamics subsystem

The thermal calculations subsystem is simulated with the help of the equations assuming the thermal energy balance. It is known that the heat energy stored in the system (Q_3) can be calculated by taking the difference between the heat energy given to the system (Q_1) and the heat energy removed from the system (Q_2) from the basic law of conservation of energy. This situation is shown in Equation (9). Q_1 , whose formulation is given in Equation (10), represents the heat generated due to the internal resistances of the battery and the energy loss in the resistors. The power loss on the resistors is formulated in Equation (11) by taking the energy on the resistors into account. Q_2 , which is the heat removed from the system, is transmitted in three ways: conduction, convection and heating. Q_2 , calculated by neglecting conduction and radiation, is formulated with Equation (12) [29].

$$Q_1 - Q_2 = Q_3 \quad (9)$$

$$Q_1 = \sum_{i=1}^n I^2 R_i(t) \quad (10)$$

$$\frac{Q_1}{t} = \frac{v_0(t)^2}{R_0} + \frac{v_1(t)^2}{R_1} + \frac{v_2(t)^2}{R_2} \quad (11)$$

$$Q_2 = h_c \cdot A(T(t) - T_a(t)) \quad (12)$$

where h_c is heat transfer coefficient ($\text{W}/\text{m}^2 \text{ } ^\circ\text{K}$), A is battery outer surface area, $T(t)$ is battery internal temperature ($^\circ\text{K}$), $T_a(t)$ represents the environmental temperature ($^\circ\text{K}$). The equation by which the heat stored in the system can also be calculated is given in Equation (13).

$$Q_3 = m \cdot C_p \cdot \frac{dT(t)}{dt} \quad (13)$$

where m is battery mass (kg). C_p represents the specific heat of the battery ($\text{J}/\text{kg}^\circ\text{K}$) and when multiplied, the total capacity coefficient C_i is obtained. If all these mentioned equations are replaced and arranged in Equation (13), the differential Equation (14) is obtained [29].

$$\frac{dT(t)}{dt} = \frac{1}{C_i} \left\{ \left[\frac{v_0^2(t)}{R_0} + \frac{v_1^2(t)}{R_1} + \frac{v_2^2(t)}{R_2} \right] - [h_c \cdot A(T(t) - T_a(t))] \right\} \quad (14)$$

The thermal calculations subsystem in Figure 3 is created by simulating Equation (14) in the Matlab/Simulink environment. As seen in Figure 3, the cell temperature $T(t)$ is obtained by using $T_a(t)$, which represents the initial value and entered by the user, and V_0, V_1, V_2 , values calculated as output in the cell dynamics subsystem, as input.

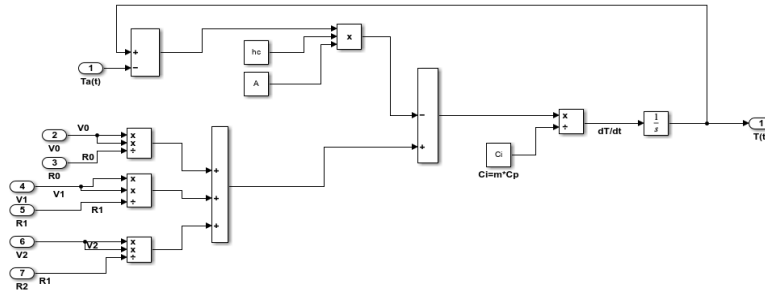


Figure 3. Model of thermal calculations subsystem

In order to determine the resistance and capacity values of R_0, R_1, C_1, R_2, C_2 which vary according to temperature and current charge state, the operating functions subsystem is created using the data tables found in the literature [20, 29, 31] and obtained from the tests carried out by the companies. Using the literature, the data table given in Table 1 is created for resistance and capacity values. These values are entered into look up tables and R and C values are obtained by interpolation method and used in subsystems. This subsystem can be seen in Figure 4. SoC and temperature input, open circuit voltage (v_{OCV_cell}) and R_0, R_1, C_1, R_2, C_2 impedance values are created as output.

Table 1. Data tables for resistances and capacities [20, 29, 31]

SoC	R_0 (Ω)			R_1 (Ω)			R_2 (Ω)		
	0 °C	25 °C	40 °C	0 °C	25 °C	40 °C	0 °C	25 °C	40 °C
0,1	0,00161	0,00205	0,00468	0,00468	0,00468	0,0008	0,00468	0,0008	0,0007
0,2	0,00149	0,00183	0,00084	0,00084	0,00084	0,00056	0,00084	0,00056	0,00054
0,3	0,00139	0,00173	0,00061	0,00061	0,00061	0,00051	0,00061	0,00051	0,0005
0,4	0,00135	0,00166	0,00056	0,00056	0,00056	0,00047	0,00056	0,00047	0,00047
0,5	0,00132	0,00163	0,00058	0,00058	0,00058	0,00049	0,00058	0,00049	0,00048
0,6	0,00136	0,00168	0,00061	0,00061	0,00061	0,00061	0,00061	0,00061	0,0006
0,7	0,00134	0,00164	0,00071	0,00071	0,00071	0,00066	0,00071	0,00066	0,00067
0,8	0,00133	0,00165	0,00076	0,00076	0,00076	0,00071	0,00076	0,00071	0,00071
0,9	0,00135	0,00168	0,00079	0,00079	0,00079	0,00069	0,00079	0,00069	0,00065
1	0,00142	0,00179	0,0007	0,0007	0,0007	0,00054	0,0007	0,00054	0,00048
SoC	C_1 (mF)			C_2 (mF)					
	0 °C	25 °C	40 °C	0 °C	25 °C	40 °C			
0,1	1932,18	19211,03	20259,19	1932,18	19211,03	20259,19			
0,2	17789,3	28931,85	28069,01	17789,3	28931,85	28069,01			
0,3	28714,76	32396,9	29206,52	28714,76	32396,9	29206,52			
0,4	29501,58	31501,14	30337,55	29501,58	31501,14	30337,55			
0,5	28762,95	31579,66	29661,89	28762,95	31579,66	29661,89			
0,6	26838,07	29368,02	26832,82	26838,07	29368,02	26832,82			
0,7	23782,12	24301,35	23832	23782,12	24301,35	23832			
0,8	22040,82	22281,47	20809,55	22040,82	22281,47	20809,55			
0,9	20772,07	20610,91	20282,04	20772,07	20610,91	20282,04			
1	22405,03	29856,73	28507,86	22405,03	29856,73	28507,86			

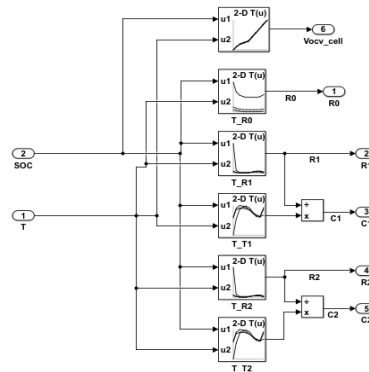


Figure 4. Model of operation functions subsystem

The calculation of SoC, which is specified by measuring the current flowing through the battery based on the coulomb counting method, is given in Equation (15) [29].

$$SoC(t) = SoC_{initial} + \frac{\int_0^t i(t).dt}{Q_{nom}} \tag{15}$$

where Q_{nom} represents the nominal capacity (Ah) of the battery. Modeling of this equation in Matlab/Simulink environment is shown in Figure 5. $SoC_{initial}$ and $Capacity_{nom}$ (Q_{nom}) values, which are defined and changed in the Matlab environment, and I_{cell} are taken as the input, and so the SoC_{cell} is obtained as output.

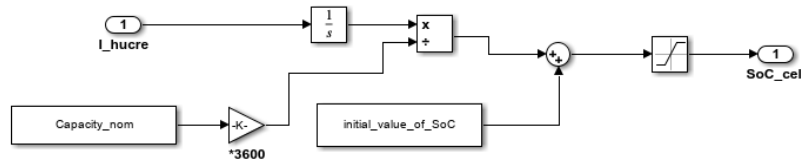


Figure 5. Model of SoC subsystem

Figure 6 shows the Li-ion battery model formed by combining all the subsystems given above.

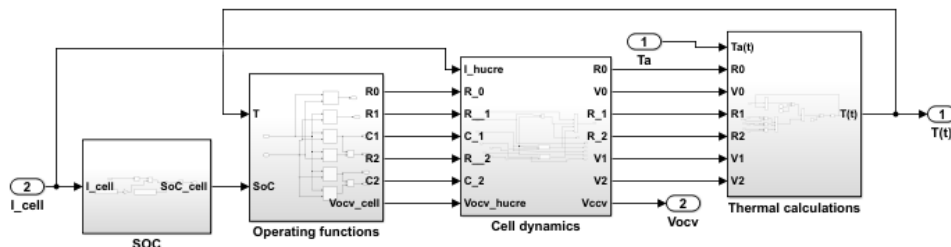


Figure 6. Li-ion battery model

4. Results and Discussions

In this study, the system containing the Li-ion battery used as the power source for UAVs is analyzed in the MATLAB/Simulink environment. The block diagram of the all system is given in Figure 7. In order to change the battery temperature, the ambient temperature change from outside is determined with the help of a signal generator. Battery block contains the battery cell created in detail in Chapter 3. An inverter is used to convert the direct voltage obtained from the battery cell into three-phase alternating voltage. In order to represent the UAV load, BLDC motor is preferred due to its features such as not requiring frequent maintenance, long life and high power.

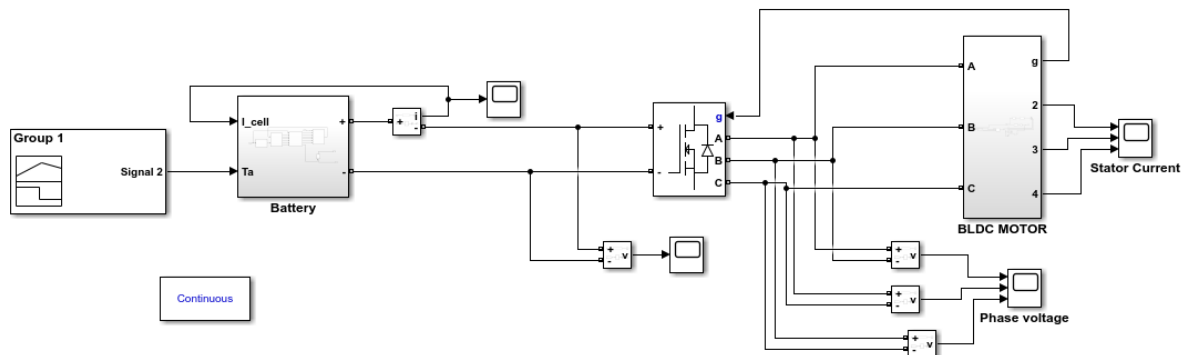


Figure 7. UAV system with Li-ion battery

Figure 8 shows the SoC change of the battery. It is obtained as a result of the load connected to the battery and the calculations made in the Charge Level Determination Subsystem. An exponential change is obtained as a result of the integrator block within the subsystem. Figure 9 shows the change graph of battery cell temperature. The T_a ambient temperature entered from outside is taken as input in the thermal calculations subsystem and is obtained as a result of the calculations made.

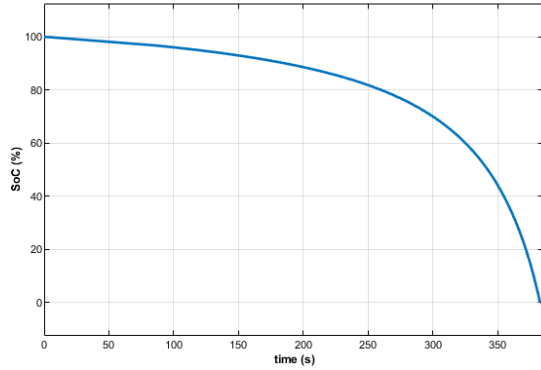


Figure 8. SoC of the battery

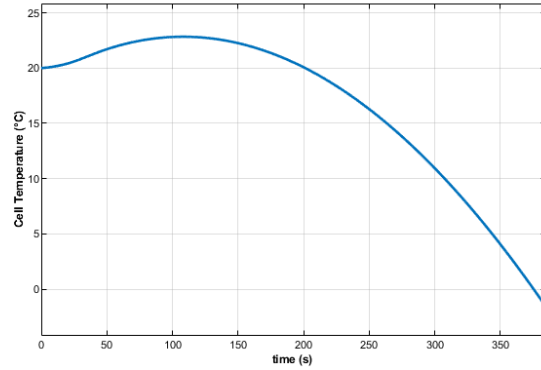


Figure 9. Battery cell temperature

The output voltage of the battery cell is seen in Figure 10. This voltage change is calculated by taking into account the voltage on the R_0, R_1, C_1, R_2, C_2 elements in the battery equivalent circuit according to the charge type, temperature and SoC state calculated with the help of look up tables in the operating functions subsystem, and the battery open circuit voltage according to the current SoC state. As can be seen from the graph, the voltage value changes depending on the usage time of the battery and the change of SoC. Voltage fluctuations between approximately 7.7 and 7.5 V can be prevented with the help of a DC/DC converter. Figure 11 shows the current drawn from the battery after the UAV load is connected to the battery. There are also fluctuations in current due to voltage fluctuation.

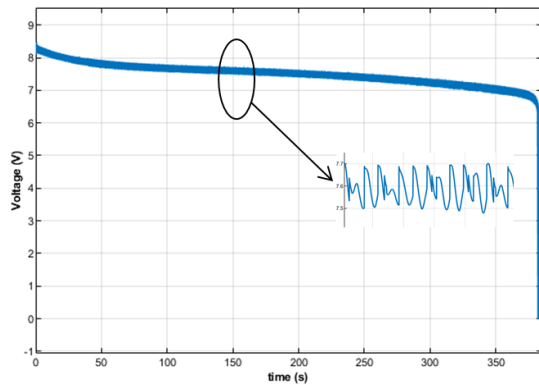


Figure 10. Battery output voltage

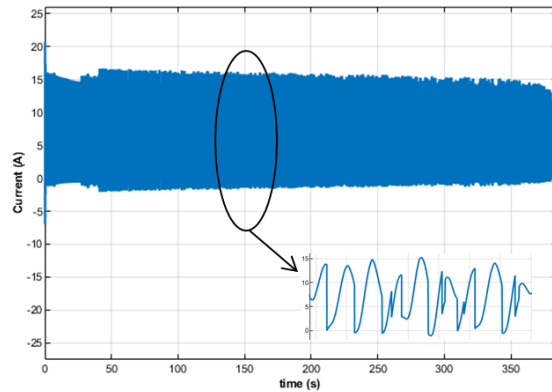


Figure 11. Current change of the battery

When the current drawn from the battery is different from zero, a change is observed in the output voltage and SoC values of the battery cell. The SoC value changes depending on the current drawn from the battery cell. The changing SoC value affects the output voltage of the battery cell. It has been observed that the battery output voltage reaches its maximum value when the SoC value is 100%. Additionally, it can be followed from Figure 8, Figure 10 and Figure 11 that when the SoC value is 0%, the battery output voltage is zero and no current is drawn from the battery.

The stator currents of the BLDC motor are given in Figure 12. The change of three-phase currents with a 120-degree phase difference between them can be observed from the figure. Figure 13 shows the output phase voltage changes of the inverter. The output voltage of one battery cell used in the system is 7.2 V. However, the output voltages are obtained by calculating the values entered in the look up tables in the operating functions using the interpolation method.

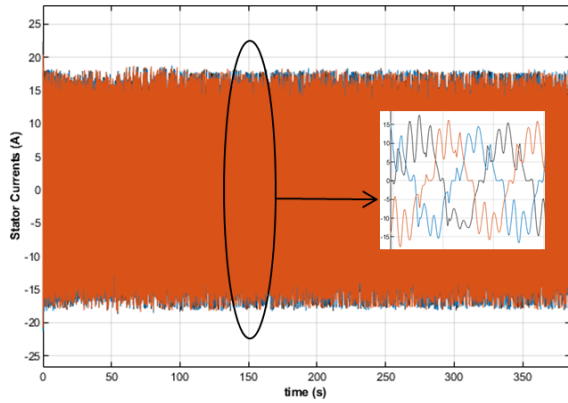


Figure 12. Stator Current Change

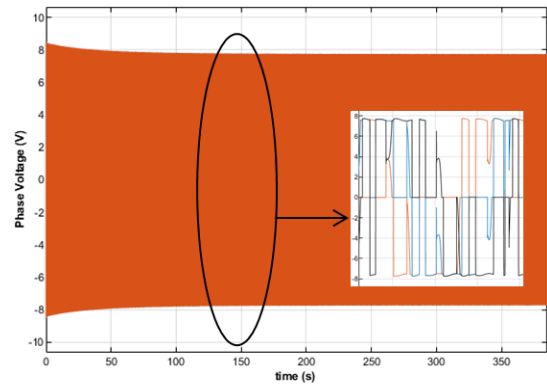


Figure 13. Phase Voltage Change

With the results obtained, changes in SoC and battery output voltage are observed depending on the usage time of the battery. It is known that if the SoC value drops below 20% while the battery is being discharged or goes above 80% while charging, it affects SoH of the battery. If these situations occur, they can be taken under control by intervening in the SoC subsystem. Depending on the battery usage rate, the output voltage value of the battery decreases in proportion to the SoC. In this study, the battery has been modeled in detail so that it can be taken under control in case of sudden voltage drops that may occur at the battery output.

5. Conclusions

With the increase in air traffic, harmful gas emissions released into the environment from gas turbine engines used in aircraft create serious problems. For this reason, studies on the increased use of electrical systems in aviation are gaining importance. However, the spread and use of electrical systems is not progressing at the desired rate. It is thought that these problems will disappear with the performance and development of batteries. For this reason, the importance of improving the performance of the battery by making an accurate simulation has become a necessity.

In this study, a Li-ion battery model is created by examining the battery models available in the literature for use in UAVs. The system, including the BLDC engine used to represent the UAV load, is modeled in the Matlab/Simulink environment. With the modeling carried out in this study, the health and charge status of the battery can be accurately determined and used in the desired system.

As a result of chemical reactions taking place inside the battery, the battery temperature increases. Increasing temperature will prevent battery reactions from occurring sequentially and completely. This will cause the internal resistance of the battery to increase. Increasing internal resistance will ensure that the battery spends its energy on its own internal resistance rather than on the system used. Thanks to these subsystems, battery temperature, voltage and internal resistances will be predicted. In this way, the battery can be intervened without any negative situation.

Acknowledgement

This study has been produced from Merve Nur KAYA's master's thesis.

References

- [1] Tarhan B, Yetik Ö, Karakoç HT. Hybrid Battery Management System Design for Electric Aircraft. *Energy* 2021; 234: 121227.
- [2] Kaya MN, Bayrak ZU. States Based EMS for Li-ion Battery & Fuel Cell Powered Unmanned Aerial Vehicle. *IHTEC 2023 7th International Hydrogen Technologies Congress*; 10-12 May 2023; Elazig, Turkey.
- [3] Li Y, Zhou Z, Wu WT. Three-Dimensional Thermal Modeling of Li-Ion Battery Cell And 50 V Li-ion Battery Pack Cooled by Mini-Channel Cold Plate. *Applied Thermal Engineering* 2019; 147: 829-840.
- [4] Vali's D, Hlinka J, Forbelsk M, Proch'azka P, Cipín R, Kořtial R, Vintr Z. Perspective Study on Charge Time Measurement of Long-Term Stored Lithium-ion Batteries Used in Electric-Powered Aircraft Assessed and Modelled by Specific Growth Model with Diffusion Process Backup. *Journal of Energy Storage* 2024; 80:110385.

- [5] Afraz MV, Mohammadi ZA, Karimi G. A Novel Compact Thermal Management Model for Performance Evaluation of Tesla-Like Lithium-ion Battery Packs. *Energy Conversion and Management* 2024; 300: 117927.
- [6] Özdemir T, Ekici Ö, Köksak M. Numerical and Experimental Investigation of The Electrical and Thermal Behaviors of The Li-ion Batteries Under Normal and Abuse Operating Conditions. *Journal of Energy Storage* 2024; 77: 109880.
- [7] Hou X, Guo X, Yuan Y, Zhao K, Tong L, Yuan C, Teng L. The State of Health Prediction of Li-ion Batteries Based On an Improved Extreme Learning Machine. *Journal of Energy Storage* 2023; 70: 108044.
- [8] Cheng Y. Identification of Parameters for Equivalent Circuit Model of Li-ion Battery Cell with Population Based Optimization Algorithms. *Ain Shams Engineering Journal* 2024; 15: 102481.
- [9] Goswami BRD., Mastrogiorgio M, Ragone M, Jabbari V, Shahbazian-Yassar R, Mashayek F, Yurkiv V. A Combined Multiphysics Modeling and Deep Learning Framework to Predict Thermal Runaway in Cylindrical Li-ion Batteries. *Journal of Power Sources* 2024; 595: 234065.
- [10] Ghadbane HE, Rezk H, Ferahtia S, Barkat S, Al-Dhaifallah M. Optimal Parameter Identification Strategy Applied to Lithium-ion Battery Model for Electric Vehicles Using Drive Cycle Data. *Energy Reports* 2024; 11: 2049-2058.
- [11] Mavi A, Arslan O. Numerical Investigation on The Thermal Management of Li-ion Batteries for Electric Vehicles Considering The Cooling Media with Phase Change for The Auxiliary Use. *Journal of Energy Storage* 2024; 77: 109964.
- [12] Kumar S, Akula R, Balaji C. An Inverse Methodology to Estimate the Thermal Properties and Heat Generation of A Li-ion Battery. *Applied Thermal Engineering* 2024; 236: 121752.
- [13] Lee G, Kwon D, Lee C. A Convolutional Neural Network Model for SOH Estimation of Li-ion Batteries with Physical Interpretability. *Mechanical Systems and Signal Processing* 2023; 188: 110004.
- [14] Navas SJ, González GMC, Pino FJ, Guerra JJ. Modelling Li-ion Batteries Using Equivalent Circuits for Renewable Energy Applications. *Energy Reports* 2023; 9: 4456-4465.
- [15] Efe Ş, Güngör ZA. Geçmişten Günümüze Batarya Teknolojisi. *European Journal of Science and Technology* 2021; Special Issue 32: 947-955.
- [16] Yıldız M. Uçaklarda Kullanıma Yönelik Batarya Isıl Yönetim Sistemlerinin Araştırılması. Doktora Tezi, Anadolu Üniversitesi, Fen Bilimleri Enstitüsü, 2016.
- [17] Ceylan M. Lityum-İyon Tabanlı Pillerin Elektriksel Eşdeğer Modelinin Çıkarılması. Yüksek Lisans Tezi, Gebze Yüksek Teknoloji Enstitüsü, Fen Bilimleri Enstitüsü, 2013.
- [18] Ekici YE. Batarya Yönetim Sistemleri, Yüksek Lisans Tezi, İnönü Üniversitesi, Fen Bilimleri Enstitüsü, 2019.
- [19] Özel MA. Elektrikli Araçlarda Kullanılan Batarya Paketinin Termal Modeli ve Analizi. Yüksek Lisans Tezi, Bursa Uludağ Üniversitesi, Fen Bilimleri Enstitüsü, 2019.
- [20] Kim J, Kowal J. Development of A Matlab/Simulink Model for Monitoring Cell State-of-Health and State-of-Charge Via Impedance of Lithium-ion Battery Cells. *Batteries* 2022; 8: 8.
- [21] Yang D, Wang Y, Pan R, Chen R, Chen Z. State-Of-Health Estimation for The Lithium-ion Battery Based on Support Vector Regression. *Applied Energy* 2018; 227: 273-283.
- [22] Zhou X, Stein JL, Ersal T. Battery State of Health Monitoring by Estimation of The Number of Cyclable Li-ions. *Control Engineering Practice*. 2017; 66: 51-50.
- [23] Erdiñç O, Vural B, Uzunođlu M. Hibrit Alternatif Enerji Sistemlerinde Kullanılan Enerji Depolama Üniteleri. *Elektrik-Elektronik ve Bilgisayar Sempozyumu* 2011.
- [24] Polat DB, Keleş Ö. Lityum İyon Pil Teknolojisi. *Türk Mühendis ve Mimar Odaları Birliđi Metalurji Mühendisleri Odası*, pp: 42-48.
- [25] Gümüşsu E. Lityum İyon Pillerin Isıl Modellemesi. Yüksek Lisans Tezi, Hacettepe Üniversitesi, Fen Bilimleri Enstitüsü, 2017.
- [26] United States Patent, Patent Number: 5,510,209, Date of Patent: Apr. 23, 1996.
- [27] Liu K, Li K, Peng Q, Zhang C. A Brief Review on Key Technologies in The Battery Management System of Electric Vehicles. *Review Article* 2019; 14(1): 47-64.
- [28] Barlak C. Batarya Model Parametrelerinin, Doluluk Durumunun, Sağlık Durumunun Kestirimi ve Ni-Mh Bataryalara Uygulanması, Doktora Tezi, Hacettepe Üniversitesi, Fen Bilimleri Enstitüsü, 2009.
- [29] Sayın AA. Elektrikli Taşıt Araçlarında Kullanılan Lityum-iyon Bataryaların Modellenmesi ve Benzetimi, Yüksek Lisans Tezi, Uludağ Üniversitesi, Fen Bilimleri Enstitüsü, 2011.
- [30] Özay O. Modelling and State of Charge Estimation for Lithium-ion Batteries, Yüksek Lisans Tezi, İstanbul Teknik Üniversitesi, Fen Bilimleri Enstitüsü, 2019.
- [31] Estevez MAP, Calligaro S, Bottesi O, Caligiuri C, Renzi M. An Electro-Thermal Model and Its Electrical Parameters Estimation Procedure in A Lithium-ion Battery Cell. *Energy* 2021; 234: 121296.

COPYRIGHT RELEASE FORM

TURKISH JOURNAL OF SCIENCE AND TECHNOLOGY (TJST) Published by Firat University

Firat University, Fen Bilimleri Enstitüsü Müdürlüğü
Turkish Journal of Science & Technology Editörlüğü
Elazığ-TURKEY,
Manuscript title:

Full names of all authors (in order to appear on manuscript):

Name, address etc. of corresponding author:

ID Number: Telephone:

E-mail: Mobile phone:

The author(s) warrant(s) that:

- a) the manuscript submitted is his/her/their own original work;
- b) all authors participated in the work in a substantive way and are prepared to take public responsibility for the work;
- c) all authors have seen and approved the manuscript as submitted;
- d) the manuscript has not been published and is not being submitted or considered for publication elsewhere;
- e) the text, illustrations, and any other materials included in the manuscript do not infringe upon any existing copyright or other rights of anyone. Notwithstanding the above, the Contributor(s) or, if applicable the Contributor's Employer, retain(s) all proprietary rights other than copyright, such as

a) patent rights;

b) to use, free of charge, all parts of this article for the author's future works in books, lectures, classroom teaching or oral presentations;

c) the right to reproduce the article for their own purposes provided the copies are not offered for sale.

However, reproduction, posting, transmission or other distribution or use of the article or any material contained therein, in any medium as permitted hereunder, requires a citation to the Journal and appropriate credit to Firat University as publisher, suitable in form and content as follows:

Title of article, author(s), journal title and volume/issue, Copyright© year.

All materials related to manuscripts, accepted or rejected, including photographs, original figures etc., will be kept by Turkish Journal of Science and Technology editority for one year following the editor's decision. These materials will then be destroyed.

I/We indemnify Firat University and the Editors of the Journals, and hold them harmless from any loss, expense or damage occasioned by a claim or suit by a third party for copyright infringement, or any suit arising out of any breach of the foregoing warranties as a result of publication of my/our article. I/We also warrant that the article contains no libelous or unlawful statements and does not contain material or instructions that might cause harm or injury.

This copyright form must be signed by all authors. Separate copies of the form (completed in full) may be submitted by authors located at different institutions; however, all signatures must be original.

ID number: ID number:

Full name (block letters) Full name (block letters)

Signature Date Signature Date

ID number: ID number:

Full name (block letters) Full name (block letters)

Signature Date Signature Date

ID number: ID number:

Turkish authors must supply their ID card number; foreign authors must supply their passport number (if possible)